THE EFFECTS OF FOOD PROCESSING ON FOOD COMPONENTS AND THEIR HEALTH FUNCTIONS

EDITED BY: Jinkai Zheng, Hang Xiao and Edoardo Capuano
PUBLISHED IN: Frontiers in Nutrition

frontiers Research Topics

ISSN 1664-8714
ISBN 978-2-88974-652-1
DOI 10.3389/978-2-88974-652-1

About Frontiers

Frontiers is more than just an open-access publisher of scholarly articles: it is a pioneering approach to the world of academia, radically improving the way scholarly research is managed. The grand vision of Frontiers is a world where all people have an equal opportunity to seek, share and generate knowledge. Frontiers provides immediate and permanent online open access to all its publications, but this alone is not enough to realize our grand goals.

Frontiers Journal Series

The Frontiers Journal Series is a multi-tier and interdisciplinary set of open-access, online journals, promising a paradigm shift from the current review, selection and dissemination processes in academic publishing. All Frontiers journals are driven by researchers for researchers; therefore, they constitute a service to the scholarly community. At the same time, the Frontiers Journal Series operates on a revolutionary invention, the tiered publishing system, initially addressing specific communities of scholars, and gradually climbing up to broader public understanding, thus serving the interests of the lay society, too.

Dedication to Quality

Each Frontiers article is a landmark of the highest quality, thanks to genuinely collaborative interactions between authors and review editors, who include some of the world's best academicians. Research must be certified by peers before entering a stream of knowledge that may eventually reach the public - and shape society; therefore, Frontiers only applies the most rigorous and unbiased reviews.
Frontiers revolutionizes research publishing by freely delivering the most outstanding research, evaluated with no bias from both the academic and social point of view. By applying the most advanced information technologies, Frontiers is catapulting scholarly publishing into a new generation.

What are Frontiers Research Topics?

Frontiers Research Topics are very popular trademarks of the Frontiers Journals Series: they are collections of at least ten articles, all centered on a particular subject. With their unique mix of varied contributions from Original Research to Review Articles, Frontiers Research Topics unify the most influential researchers, the latest key findings and historical advances in a hot research area! Find out more on how to host your own Frontiers Research Topic or contribute to one as an author by contacting the Frontiers Editorial Office: frontiersin.org/about/contact

THE EFFECTS OF FOOD PROCESSING ON FOOD COMPONENTS AND THEIR HEALTH FUNCTIONS

Topic Editors:
Jinkai Zheng, Institute of Food Science and Technology, Chinese Academy of Agricultural Sciences (CAAS), China
Hang Xiao, University of Massachusetts Amherst, United States
Edoardo Capuano, Wageningen University and Research, Netherlands

Citation: Zheng, J., Xiao, H., Capuano, E., eds. (2022). The Effects of Food Processing on Food Components and Their Health Functions. Lausanne: Frontiers Media SA. doi: 10.3389/978-2-88974-652-1

Table of Contents

frontiers in Nutrition

EDITORIAL
published: 15 February 2022
doi: 10.3389/fnut.2022.837956

Editorial: The Effects of Food Processing on Food Components and Their Health Functions

Jinkai Zheng[1]* *and Hang Xiao*[2]*

[1] *Institute of Food Science and Technology, Chinese Academy of Agricultural Sciences, Beijing, China,* [2] *Department of Food Science, University of Massachusetts, Amherst, MA, United States*

Keywords: food processing, nutrients, chemical structure, health functions, mechanism

Editorial on the Research Topic

The Effects of Food Processing on Food Components and Their Health Functions

Food processing plays an important role in our daily diet. It includes a wide variety of treatments on food materials such as mechanical treatment, heating, cooling, drying, high pressure, acid and alkaline treatments, fermentation and more. These processes can significantly influence the composition and structures (chemical structures and multiple-scale structures) of food components and their interactions with one another, thereby significantly affecting their impact on health (1, 2). Food processing could involve in every steps from harvest to the final food products (processed, unprocessed and ultra-processed) we consume.

During food processing, new compounds can be generated that may have health functions (beneficial or harmful). For example, changes induced by heat treatments can produce significant alterations in chemical composition of the food products, affecting palatability, digestibility and bioavailability (3). Both harmful compounds (e.g., acrylamide, HMF, heterocyclic amines) and beneficial compounds (e.g., AGE inhibitors, antioxidant melanoidins) can be produced depending on food formulation and processing conditions (4). Nutrients and bioactive compounds can also be modified in a way that impacts their effects on nutritional status and health: for instance, during the drying of citrus fruits polymethoxyflavones (PMFs) can be transformed to hydroxylated PMFs with more potent bioactivities than the parent compounds (e.g., antioxidative, anti-inflammatory and anti-cancer effects), enhancing the health value of citrus products (5). It is therefore of special significance to elucidate the effects of different types of food processing on food components and the subsequent impact on their health functions.

This volume contains a collection of manuscripts on the effects of food processing on food components and their health functions. Sixteen manuscripts are included: 15 original research articles and one review. They show that various food processing methods (e.g., heat treatment, acid treatment, high-pressure homogenization (HPH), fermentation, frying, emulsification, sun-drying, extraction, and separation methods) significantly influence the chemical structures and functional properties of components in various foods, including skim milk, orange juice, black garlic, soymilk, mango chips, citrus oils, Ganpu tea, deer oil, foxtail millet whole grain flour, pumpkin peptides, gluten epitopes, chrysanthemum, and finger citron.

Eight articles present the effects of processing on food components, including their abundance, chemical structures, and physicochemical properties. Li, Zhao et al. determined the effect of heat treatment on the properties, structure, and aggregation of skim milk proteins. Treating skim milk at different temperatures induced a decrease in sulfhydryl content and an increase in surface hydrophobicity with a disrupted secondary structure of skim milk proteins containing random

Edited and reviewed by:
Michael Rychlik, Technical University of Munich, Germany

***Correspondence:**
Jinkai Zheng
zhengjinkai@caas.cn; jinkai8212@163.com
Hang Xiao
hangxiao@foodsci.umass.edu

Specialty section:
This article was submitted to Food Chemistry, a section of the journal Frontiers in Nutrition

Received: *17 December 2021*
Accepted: *11 January 2022*
Published: *15 February 2022*

Citation:
Zheng J and Xiao H (2022) Editorial: The Effects of Food Processing on Food Components and Their Health Functions. Front. Nutr. 9:837956. doi: 10.3389/fnut.2022.837956

coils, β-sheets, and β-turns. These changes facilitate aggregate formation via disulfide bonds and hydrophobic interactions. Yu et al. revealed the correlations between HPH-induced changes in the structure of pectin and the stability of orange juice. Compared with non-homogenized orange juice, HPH significantly altered the pectin structure, including monosaccharide composition, molecular weight, linearity, and branching; cracks and pores of different sizes formed on the pectin surface. With increasing pressure and number of homogenization passes, HPH improved the stability of not-from-concentrate orange juice; this was related to the structural properties of pectin. Ma et al. demonstrated that *Lactobacillus* fermentation significantly influenced the physicochemical properties of black garlic extract broth, including its sensory characteristics and composition (e.g., pH, total acids, amino nitrogen, total polyphenols, total flavonoids, and 5-hydroxymethylfurfural). Gas chromatography–mass spectrometry and liquid chromatography–mass spectrometry analyses showed that the contents of several components with unpleasant baking flavors were reduced, whereas the contents of components with green grass, floral, and fruit aromas were increased. More importantly, the contents of functional components like lactic acid, Gly-Pro-Glu, and sorbose were increased after *Lactobacillus* fermentation. The results demonstrated the potential of probiotic fermentation to improve the quality of black garlic. Yang, Yang et al. determined the effect of soybean cultivars on soymilk fermentation using Kefir C. Moreover, new kefir starters were produced by adding lactic acid bacteria to kefir from three different sources: Kefir C, Chinese kefir (Kefir A), and Caucasus kefir (Kefir B). They showed that the starter culture created by adding specific probiotics to Chinese kefir significantly increased the abundance of isoflavone aglycones. Ayustaningwarno et al. evaluated the effect of ripening stage, frying temperature, and time on the quality of vacuum-fried mango. The fat content in fried ripe mango was higher, while the total ascorbic acid in unripe mango remained higher. Considering the quality parameters, vacuum frying unripe mango at the optimal conditions of 100°C for 20 min was preferred for producing high-quality fruit snacks. Yang, Zhang et al. separated essential oils from four citrus varieties into two fractions by molecular distillation. The composition, physicochemical properties, and antimicrobial activity of each essential oil were then evaluated systematically. The main components with antimicrobial activity were 1-decanol, α-terpineol, geraniol, and linalool. Notably, various components in food have low stability or bioavailability (Liu et al.). The development of processing methods such as emulsification to improve their stability and bioavailability has drawn a lot of attention. Xu et al. investigated the effects of ionic strength, heating, and freeze–thaw treatment on the stability of *Monascus* pigment double emulsions stabilized by polyglycerol polyricinoleate (PGPR) and soybean protein isolate (SPI). The *Monascus* pigment double emulsions with < 5 mM $CaCl_2$ prevented calcium from destroying the physical stability of the emulsions, while those with more than 10 mM $CaCl_2$ developed creaming. After freeze–thaw treatment, creaming occurred in the *Monascus* pigment double emulsion. However, it was stable upon heat treatment.

This volume also reports the effects of processing on the health functions of foods that were induced by the changes in their components. The extraction of components from food materials is a common processing procedure. Xia et al. demonstrated that an aqueous enzymatic extract of deer oil not only had a high extraction yield but also had little effect on the contents of active ingredients, especially unsaturated fatty acids, compared with conventional boiling extraction. These components might prevent stomach injury by reducing oxidative stress and inflammation. Hot-water extracts of *Chrysanthemum morifolium* cv. Fubaiju protected against oxidative damage in ARPE-19 cells by activating the PI3K/Akt-mediated Nrf2/HO-1 signaling pathway (Hao et al.). A continuous phase-transition extract of flavonoids from finger citron showed a strong antioxidative activity, as demonstrated by its strong 2,2-diphenyl-1-picrylhydrazyl and 2,2-azino-bis(3-ethyl-benzothiazoline-6-sulfonic acid) diammonium salt radical scavenging activities and oxygen radical absorbance capacity. It also increased the mean and maximum lifespans of *Caenorhabditis elegans* (Luo et al.). A water extract of *Potentilla discolor* improved hepatic glucose homeostasis by regulating gluconeogenesis and glycogen synthesis in mice on a high-fat diet and streptozotocin-induced type 2 diabetic mice (Li, Chang et al.). In addition to extraction, other types of processing were also investigated. Xiao et al. systematically identified and analyzed 104 water-soluble compounds in Ganpu tea and their variation during the sun-drying processing. They showed that the generation of pigments and gallic acid coincided with a sharp decrease in catechin content and significant increases in the alkaloid and flavonoid contents. The conversion of these components helped improve the sensory attributes of Ganpu tea and might be responsible for its unique flavor. Moreover, the components formed during the sun-drying of Ganpu tea had antidepressant effects *in vivo*. Zhang et al. demonstrated that fermentation and germination processing improved the protective effects of foxtail millet whole grain against dextran sulfate sodium-induced acute ulcerative colitis and gut microbiota dysbiosis in C57BL/6 mice. In addition, mice on a diet of fermented–germinated foxtail millet flour had the lowest plasma interleukin-6 levels and claudin2 expression levels in the colon, indicating reduced systemic inflammation and improved gut barrier function. Lu et al. prepared pumpkin seed protein hydrolysate (PSPH) using enzymatic hydrolysis with bromelain, papain, flavourzyme, alcalase, and pepsin. They found that peptides hydrolyzed by papain had the largest average molecular weight, smallest particle size, greatest hydrophobicity, and greatest zinc-binding capacity. Zinc had better gastrointestinal stability in PSPH chelates than as its salt. PSPH-Zn had a higher zinc-binding capacity and better stability. Gao et al. simulated the changes in solution structures of various gluten epitopes at different pH and temperatures to mimic fermentation and

baking/cooking processes, and they investigated the binding of differently processed gluten epitopes to human leukocyte antigen (HLA)-DQ2. This revealed that heating and pH change during fermentation affect the solution structure of gluten epitope. However, the binding of differently treated gluten epitope peptide to HLA-DQ2 mainly depended on its primary amino acid sequence, especially the acidic amino acid residues that play a pivotal role in their recognition by HLA-DQ2.

In summary, this collection emphasizes the important influence of food processing on food components and their health effects. This topic is gaining increasing attention. However, some areas are still poorly investigated, such as the impact of processing on the color, flavor, and texture of foods, the effects of chemical structure changes on individual nutrient bioavailability, and their health-promoting effects. Such information would provide critical scientific guidance for establishing optimal processing methods and techniques beneficial to health and is critically important for the production of the next generation of innovative healthy foods.

AUTHOR CONTRIBUTIONS

JZ and HX prepared, checked and revised the manuscript, and approved the submitted version. All authors contributed to the article and approved the submitted version.

FUNDING

The authors would like to acknowledge the financial support provided by National Natural Science Foundation of China (Nos. 32072181) and Nestle R&D Ltd. The funder was not involved in the study design, collection, analysis, interpretation of data, the writing of this article or the decision to submit it for publication.

ACKNOWLEDGMENTS

We would acknowledge the support of National Elite Youth Program from Chinese Academy of Agricultural Sciences for JZ.

REFERENCES

1. Cui JF, Zhao CY, Feng LP, Han YH, Du HJ, Xiao H, et al. Pectins from fruits: Relationships between extraction methods, structural characteristics, and functional properties. *Trends Food Sci Tech*. (2021) 110:39–54. doi: 10.1016/j.tifs.2021.01.077
2. Azeredo HMC, Tonon RV, McClements DJ. Designing healthier foods: Reducing the content or digestibility of key nutrients. *Trends Food Sci Tech*. (2021) 118:459–470. doi: 10.1016/j.tifs.2021.10.023
3. Zailani MA, Kamilah H, Husaini A, Awang Seruji AZR, Sarbini SR. Functional and digestibility properties of sago (Metroxylon sagu) starch modified by microwave heat treatment. *Food Hydrocolloid*. (2022) 122:107042. doi: 10.1016/j.foodhyd.2021.107042
4. Zhang NN, Zhou Q, Fan DM, Xiao J, Zhao YL, Cheng KW, et al. Novel roles of hydrocolloids in foods: Inhibition of toxic maillard reaction products formation and attenuation of their harmful effects. *Trends Food Sci Tech*. (2021) 111:706–715. doi: 10.1016/j.tifs.2021.03.020
5. Karn A, Zhao CY, Yang FL, Cui JF, Gao ZL, Wang MQ, et al. *In-vivo* biotransformation of citrus functional components and their effects on health. *Crit Rev Food Sci*. (2021) 61:756–76. doi: 10.1080/10408398.2020.1746234

Conflict of Interest: The authors declare that the research was conducted in the absence of any commercial or financial relationships that could be construed as a potential conflict of interest.

Publisher's Note: All claims expressed in this article are solely those of the authors and do not necessarily represent those of their affiliated organizations, or those of the publisher, the editors and the reviewers. Any product that may be evaluated in this article, or claim that may be made by its manufacturer, is not guaranteed or endorsed by the publisher.

frontiers in Nutrition

ORIGINAL RESEARCH
published: 17 July 2020
doi: 10.3389/fnut.2020.00095

Nutritional and Physicochemical Quality of Vacuum-Fried Mango Chips Is Affected by Ripening Stage, Frying Temperature, and Time

Fitriyono Ayustaningwarno [1,2,3], Elise van Ginkel [1], Joana Vitorino [1], Matthijs Dekker [1], Vincenzo Fogliano [1] and Ruud Verkerk [1]**

[1] *Food Quality and Design, Wageningen University & Research, Wageningen, Netherlands,* [2] *Department of Nutrition Science, Faculty of Medicine, Diponegoro University, Semarang, Indonesia,* [3] *Center of Nutrition Research, Diponegoro University, Semarang, Indonesia*

For the production of healthier fruit snacks, vacuum frying is a promising alternative for atmospheric frying, to reduce the oil content, while maintaining a high nutritional quality. This paper evaluates the effect of ripening stages, frying temperature, and time on the quality of vacuum-fried mango. Unripe mango was dehydrated faster than ripe mango and had a higher hardness after frying at 110 and 120°C. Fat content in fried ripe mango was higher. Total ascorbic acid and β-carotene in both ripening stages were not different, but after frying total ascorbic acid in unripe mango remains higher. A novel image analysis was applied to quantify the color distribution of fried mango. Color changes in unripe mango were more susceptible to temperature and time. Considering all quality parameters, vacuum frying of unripe mango at the optimal condition of 100°C for 20 min is preferred for producing high-quality healthier fruit snacks.

Keywords: vacuum frying, mango, ripening, vitamin C, β-carotene, fat, color, texture

OPEN ACCESS

Edited by:
Jinkai Zheng,
Institute of Food Science and Technology (CAAS), China

Reviewed by:
Kin Weng Kong,
University of Malaya, Malaysia
Alam Zeb,
University of Malakand, Pakistan

****Correspondence:***
Fitriyono Ayustaningwarno
ayustaningwarno@fk.undip.ac.id
Ruud Verkerk
ruud.verkerk@wur.nl

Specialty section:
This article was submitted to Food Chemistry, a section of the journal Frontiers in Nutrition

Received: *19 March 2020*
Accepted: *26 May 2020*
Published: *17 July 2020*

Citation:
Ayustaningwarno F, van Ginkel E, Vitorino J, Dekker M, Fogliano V and Verkerk R (2020) Nutritional and Physicochemical Quality of Vacuum-Fried Mango Chips Is Affected by Ripening Stage, Frying Temperature, and Time. Front. Nutr. 7:95. doi: 10.3389/fnut.2020.00095

INTRODUCTION

Consumers have a strong desire for fried food products because of their unique flavor–texture combination. However, the increased awareness of consumers toward the relationship between food, nutrition, and health stimulates the food industry to use alternative processing methods complying the demand for healthier snacks. In this paper, we study an alternative frying process to meet these demands by reducing the oil uptake and maintaining a high nutritional value.

Technically deep-frying is heating and dehydrating foods with associated oil uptake by immersing them in an edible fat at 165–190°C (1). Compared to other cooking methods, deep-frying generates products with a unique color, texture, and flavor.

Deep-frying dries the product, giving it a crust and making it crispy (2). However, excessive oil absorption is an undesired side effect of the process that could be limited by various strategies such as dripping and post-frying centrifugation (3). Additionally, a high frying temperature might reduce the content of nutrients present in the raw material (4). In the framework of the increasing demand for healthier snack choices, industries are developing low-fat alternatives. Techniques such as drying, extrusion, and baking have not always been able to satisfactorily meet the sensory characteristics of fried foods (5). Consumers do not want to compromise on organoleptic properties in exchange for healthier products (6). Altogether, vacuum frying might be a promising technology for healthier fried products.

Vacuum frying is similar to atmospheric frying but is carried out under reduced pressure below 10 kPa, causing a decrease in the boiling point of water in the fried products (4). Therefore, the frying temperature can be reduced to as low as 90°C, which allows preservation of the food nutritional characteristics, flavor, and aroma. This is of particular relevance for fruits which contain high amounts of thermolabile vitamins and phytochemicals. In this respect, characteristics of the fruit matrix can play a very important role and is an underexposed factor in the scientific literature up to now (7).

Several studies on vacuum-fried food have been done for pineapple (8) and apple (9). The effect of ripening on the physicochemical quality of vacuum-fried fruit has already been investigated for banana and jackfruit. Yamsaengsung and Ariyapuchai (10) found that vacuum-fried ripe banana has a higher volume expansion than unripe banana, even though there was no difference between them in overall sensory acceptability. Diamante (11) found that vacuum-fried ripe jackfruit has a higher moisture and fat content, while it was more yellow and less crunchy, has more aroma, and is sweeter than half-ripe jackfruit.

Studies on vacuum-fried mango have been done to compare the vacuum frying technique to atmospheric frying on the oil content, color, texture, total carotenoid content, and the like (12) and to study the effect of osmotic dehydration on moisture and oil content, expansion, density porosity, color, texture, and total carotenoid and sensory characteristics (13). However, the effect of ripening stage on the quality of vacuum-fried mango has not been studied before.

As a climacteric fruit, mango quality is strongly influenced by ripening. During ripening, physiological, biochemical, and molecular changes are initiated in the mango matrix by the autocatalytic production of ethylene and increase in respiration rate. Some of these changes include increased biosynthesis of carotenoids, a decrease in ascorbic acid, conversion of starch into sugars, and the softening of the fruit promoted by the pectinase action on the cell wall. Another influenced quality attribute is color. Color changes in mango result from carotenoid accumulation in the pulp (14).

The objective of this study was to investigate the effect of ripening stages, frying temperature, and time on the nutritional and physicochemical quality of vacuum-fried mango. The physicochemical quality was characterized by measuring the key parameters moisture and fat content, color and texture. While the nutritional value was assessed by analyzing vitamin C and β-carotene content as key parameters for, respectively, water- and fat-soluble nutrients in mango. The research hypothesis was that quality of vacuum-fried mango chips is affected by ripening stage, frying temperature, and time.

MATERIALS AND METHODS

Raw Material

Unripe (stage 2, firmness 68.4–87.9 kg/m^2) and ripe (stage 4, firmness 24.4–39.1 kg/m^2) mango (*Mangifera indica* L. cv. Kent) from Brazil were supplied by Bakker Barendrecht B.V. (The Netherlands) and stored at 11°C and used within 5 days after arrival. Just prior to the frying experiment, the mangoes were selected based on ripeness indicators, including total soluble solids (TSS), to indicate the sugar content and firmness (15) as shown in **Table 1**. In order to study the role of the physiological maturity, stages 2 and 4 were selected to represent the unripe and ripe mango with enough internal matrix differences, while still having suitable properties for handling the fruit.

TABLE 1 | Initial values for firmness and total soluble solid content of unripe and ripe mangoes used for vacuum-frying experiments.

Ripeness	Firmness (kg/m^2)	TSS (°Brix)
Unripe	78.25 ± 0.44 [a]	16.03 ± 0.08 [a]
Ripe	31.91 ± 0.26 [b]	16.41 ± 0.11 [b]

Different superscripts at firmness and TSS values show significant difference ($p \leq 0.01$) between ripe and unripe mango N = 423.

TABLE 2 | Settings used for vacuum frying mango chips.

Oil temperature (°C)	Frying time (minutes)					
90	5	10	15	25	35	50
100	5	10	15	20	27.5	35
110	2.5	5	10	15	20	25
120	2.5	5	7.5	10	12.5	15

Firmness was measured using fruit penetrometer FT327, equipped with an 8-mm tip (Nieuwkoop B.V., the Netherlands). The firmness measurements were done on each peeled mango cheek with three repetitions and were expressed in kg/m^2. TSS content was measured three times from juice obtained from mango cheek using a refractometer (HI96801, Hanna Instruments) and was expressed in °Brix. After selection, mangoes were peeled, and the seed was removed and halved. The halved fruits were cut into 4-mm-thick slices with a mandolin (V5 Power, Börner, Germany) to ensure the fast heat penetration to the center of the chips but not collapse during the processing.

Vacuum Frying Procedure

Mango slices were vacuum fried in 2-kg batches using a pilot scale industrial vacuum fryer (Florigo Industry B.V., The Netherlands) containing 250 L fresh high oleic sunflower oil. A high oil-to-fruit ratio was needed to diminish temperature drop after the fruit was submerged into the oil. The vacuum fryer was equipped by an automatic basket rotator, two heat exchangers to cool and heat the oil, and an atmospheric spinner to remove surface oil. Some pilot experiments have been carried out to determine the optimal conditions for thickness of mango slices and vacuum frying pressure. Based on these results, 4-mm mango slices were fried at 10 kPa at times and temperatures as listed in **Table 2**. This working pressure produces water boiling at 44.3°C.

Two samples of mango slices (1 kg of each of the two ripening stages) were loaded into the vacuum chamber. After 60 s, the desired vacuum pressure was reached, and the basket was submersed into the oil to initiate the frying time. During frying, the basket was rotated back and forth at 17 rpm for 60 s to ensure that the heat and oil were evenly distributed. To stabilize

the temperature, a heat exchanger to heat and cool the oil was used. Once the frying was finished, the basket was lifted from the oil and shaken for 20 s inside the vacuum chamber to remove excess of oil. The vacuum chamber was then pressurized, and the vacuum-fried mango was centrifuged to remove surface oil for 60 s at 100 g (MSD-500HD, Eillert B.V., the Netherlands). Then, mango chips were packed in sealed plastic bags and stored at −20°C until further use. All frying experiments were performed in duplicate.

Moisture and Fat Content

Moisture content of the samples was determined in triplicate per frying experiment with a forced convection oven at 100°C until constant weight and described in % fresh weight. Fat content of the fried mango chips was determined in duplicate per frying experiment with the Soxhlet method using 200 ml petroleum ether 40–60°C after drying overnight and then described in % dry basis (db) (16).

Texture

Texture of the mango chips was measured with a texture analyzer (TA.XT.Plus, Stable Micro Systems, UK) using a three-point bending test according to Da Silva and Moreira (17) with some modifications. One mango chip was placed on two parallel edges (16 mm wide), and the probe selected was a 1-mm-thick steel blade. Settings used were as follows: 0.50 mm/s test speed, 10.00 mm/s post-test speed, 15 mm distance, and 5 kg load cell. Results from ten replications per frying experiment were expressed as hardness in N.

Total Ascorbic Acid

Since ascorbic acid (AA) easily oxidized into L-dehydroascorbic acid (DHA), vitamin C was calculated as total ascorbic acid (TAA) which sums of AA and DHA. AA was reduced into DHA using TCEP (tris-2-carboxyethyl phosphine) and then calculated together into TAA. The extraction and HPLC analysis was conducted according to the methods of Hernández, Lobo (18), and Wechtersbach and Cigić (19) with modification. Two grams of sample was used and homogenized with 25 ml metaphosphoric acid-tert-butylhydroquinone (MPA-TBHQ) solution using Ultra Turrax at high speed for 45 s and was centrifuged for 20 min at 4,000 rpm at 4°C. The supernatant was then centrifuged again in a 5-ml preweighed reaction tube at 10,500 rpm for 20 min at 4°C. An amount of 1.485 ml sample was added by 15 μl TCEP, filtered using a 0.2-μm CA filter to an amber vial and ready to be injected into the HPLC. Three measurements per frying experiment were conducted, and the values are expressed in mg TAA/100 g of dry basis (db). A calibration curve was prepared using 10 mg/ml ascorbic acid in MPA TBHQ, filtered through a 0.2-μm CA filter, and diluted in 8 steps to get a range from 200 μg/ml to 1.56 μg/ml with $R^2 = 0.997$. HPLC analysis was done using thermo separation products Spectra Series HPLC with a binary gradient pump and UV detector at 245 nm and Polaris 5 C18 A 150 × 4.6 mm 5 μm column. The twenty-μl sample was injected using orthophosphoric acid 0.2% in Milli Q water as mobile phase, with a 5.5-min run time at a 1.0-ml/min flow.

β-Carotene

The extraction and HPLC analysis of β-carotene was conducted according the methods of Salur-Can, Türkyilmaz (20), with modification. During extraction, 1 g sample was used and dissolved into 1.5 ml of Milli Q water and 7 ml hexane, then the samples were homogenized using Ultra Turrax and centrifuged 5 min for 3,000 rpm to get the supernatant; the pellets were extracted again two times, on a third time using 10 ml tetrahydrofuran (THF) instead of hexane. The orange upper liquid then taken out (from hexane and THF extraction), the solvents were evaporated using vacuum evaporator at 40°C, 270 mbar vacuum. The extract then dissolved into 2 ml buffer MeOH-THF 1:1 + 0.01% BHT, filtered through a 0.2-μm filter, ready to be injected into HPLC. Three measurements per frying experiment were conducted, and the values are expressed in μg/g dry basis (db) of β-carotene. A calibration curve was prepared using 0.1 mg/ml β-carotene (Sigma Aldrich, 22040) in THF including 0.1% BHT, filtered through a 0.2-μm filter, and diluted in 6 steps to get a range from 50 to 0.78 μg/ml with $R^2 = 0.999$. HPLC analysis was done using HPLC with a Dionex Ultimate 3000 RS equipped with Phenomenex Onyx monolithic C18 column (100 × 4.6 mm, pore size of 130 Å). Twenty μl of sample was injected with 60% acetonitrile (ACN), 30% MeOH, 10% ethyl acetate (ETAC), and 0.1% trimethylamine (TEA) mobile phase, with a run time of 10 min at flow rate of 1.0 ml/min. Compounds were detected at a wavelength of 445 nm.

Color

The color distribution of mango chips was described by a new approach developed specially for this study (21). Therefore, a detailed description will be given. Four pieces of mango chips from each frying experiment were photographed and analyzed via a color quantization for each pixel based on a method described by Wu (22).

Images of mango chips were taken using a color digital camera (Canon 1000D with Canon EFS 18-55 mm F3.5-5.6 IS lens) mounted on Kaiser RT1 base 25 cm from the product and were placed inside a closed picture chamber. The light used was produced by a 4 × 36 watt 5,400 k 40 Hz fluorescent light mounted at 22° from the sample axis. Color calibration was done using X-Rite ColorChecker Passport and Adobe Lightroom.

An uncompressed picture file (CR2) with image size 3,888 × 2,592 pixel was produced and later converted to another uncompressed file (Exif-tiff 8 bit) at the same resolution by image processing software (Canon Digital Photo Professional, version 3.14.40.0) prior to further analysis. Image background was removed using a quick selection tool from an image processing software (Adobe Photoshop CC 2015). The tiff images were then analyzed using Color Inspector 3D v 2.3(21) within Fiji (22), an Image J 1.52 g repository (23), according to color quantization for each pixel. The obtained RGB color table was converted into L^* a^* b^* values using the method developed by (24). Only the L^* and a^* values were used, as they describe the most important changes in color of vacuum-fried products (6). The L^* value describes the lightness with 0 for darkest black and 100 for brightest white and was divided into 3 levels, $0 \leq$ dark ≤ 60, $60 <$ medium-light ≤ 80, and $80 <$ light ≤ 100. The a* value describes the transition

from green to red, ranging from −128 for the purest green and +128 for the purest red, and were divided into 3 levels, green ≤ 0, 0<medium-red ≤ 10, and red >10. The number of pixel in each lightness and redness level is then divided by total pixel of the mango chips and multiplied by 100% to produce % of pixels of each lightness and redness level.

Statistical Analysis

Data analysis was performed using R software by independent *T*-Test for TSS and firmness to test the difference between ripe and unripe mango. On the other hand, ANOVA with Tukey *post hoc* analysis was performed for moisture, fat, texture, TAA, β-carotene, and color. Numbers and graphs were made based on mean and standard error. Standard error of the mean (SEM) was used to describes the uncertainty of how the sample mean represents the population mean, which is possible at a large number of measurements (23).

RESULTS AND DISCUSSION

Firmness and TSS of Fresh/Raw Mango

Firmness and TSS content of raw mangoes were measured to determine the required ripeness stages (**Table 2**). Commonly during mango ripening, the TSS content increases due to hydrolysis of starch into sugars (14), while firmness of the fruits declines due to breakdown of the cell wall polysaccharide such as pectin (24). However, our data just show just a slight though significant increase in TSS from unripe to ripe mango (0.38 °Brix). While Ibarra-Garza and Ramos-Parra (14) found a higher increase during ripening in Keitt mango, from 10.1 to 12.7 °Brix. This difference could be ascribed by variation among varieties.

Moisture Content

Overall, moisture loss during vacuum frying exhibited a classical drying profile (**Figure 1**). As frying time increases, moisture content rapidly decreases. For all temperatures, an initial rapid decrease in water content was observed, followed by a more gradual decline until a constant moisture value is reached. Moreover, moisture loss increased with increasing temperature; consequently, a shorter frying time led to the same final moisture content.

At 10 min of frying, the moisture content of unripe mango ranged from 34.4 ± 4.4% at 90°C to 5.2 ± 0.5% at 120°C, while for ripe mango the content was 37.8 ± 2.9% and 14.5 ± 2.4% for the respective temperatures. Even though not significant, this result shows that the moisture of ripe mango was more difficult to evaporate during frying than for unripe mango. This difference could be explained by the structure, soluble solids, and texture differences. Pectin is an important compound influencing those physical characteristics. Pectin is more abundantly present in unripe mango, thereby increasing the water-binding properties (25). In unripe mango, large pectin molecules firmly hold the water and, when heated, the polysaccharides shrink expelling water out and increase the moisture loss (26). On the other hand, in the ripened fruit the water is already more free because pectin was enzymatically hydrolyzed.

Moreira (1) described that a moisture content of <10% is needed to keep the product stable upon storage. To produce fried chips with <10% moisture content, vacuum frying at 120°C will need 7.5 min for unripe mango compared to 15 min that is required for ripe mango. A similar effect was observed for air-drying of 1-cm-thick banana slices, for which the rate constant of ripe banana was lower than in unripe banana, even though the difference was not significant (27).

Fat Content

During vacuum frying, there is an increase in the fat content for mango parts of both ripening stages; however, the fat content of unripe mango showed a sigmoid trend, while ripe mango showed an almost linear increase in fat content during frying (**Figure 1**). A similar increase in fat content is also observed in vacuum frying of apple (5).

Fat uptake during vacuum frying is a direct effect of moisture loss. When the mango slices were submerged in hot oil, moisture rapidly evaporated from the surface and allowed oil to adhere to the dry surface (28) and further infiltrate to the chips (29).

At most frying conditions, fat content in unripe and ripe mango shows no significant differences, except at the most intense treatments in which the fat content in unripe mango is lower as shown at 90°C for 50 min ($p = 0.0150$) and 110°C for 25 min ($p = 0.0034$), but at 120°C, there was no significant difference for all frying times. The difference could be caused by the higher pectin content in unripe mango; BeMiller (30) describes that pectin consists of hydrophilic and hydrophobic molecules. Pectin could become a barrier to oil absorption (31).

Texture

After vacuum frying started, the hardness of fried mango chips initially drops for both ripening stages and at all temperatures and subsequently increases in time. Dueik and Robert (32) divided the vacuum frying into fast and slow phases. During the fast phase, the plant tissue initially softens and then hardens in the slow phase. The tissue softens because the middle lamella between the cells is solubilized (33). However, during the slow phase there is tissue hardening because the mango dehydrates and forms a crust.

The hardening process accelerates at higher temperatures. Unripe mango chips fried for 15 min at 90°C had a hardness value of 3.9 ± 0.6 N; this value was at the beginning of the slow phase which increased at a longer frying time. On the other hand, unripe mango chips fried at 120°C for 15 min had a hardness value of 10.6 ± 0.9 N; this value was at the end of the slow phase. Nunes and Moreira (13) did a similar research on Tommy Atkins mango chips and found that when the oil temperature was increased from 120 to 130°C, the maximum force (N) and the work (N * mm) values also increased. However, when the temperature was increased to 138°C, these maximum force and work values decreased because of the brittleness of the chips. A phenomenon was also observed in our data for unripe mango fried at 90 and 100°C and ripe mango fried at 110°C.

Overall, there was no significant difference between hardness of unripe and ripe mango after vacuum frying at 90 and 100°C at all-time points. At higher temperatures, the hardening was

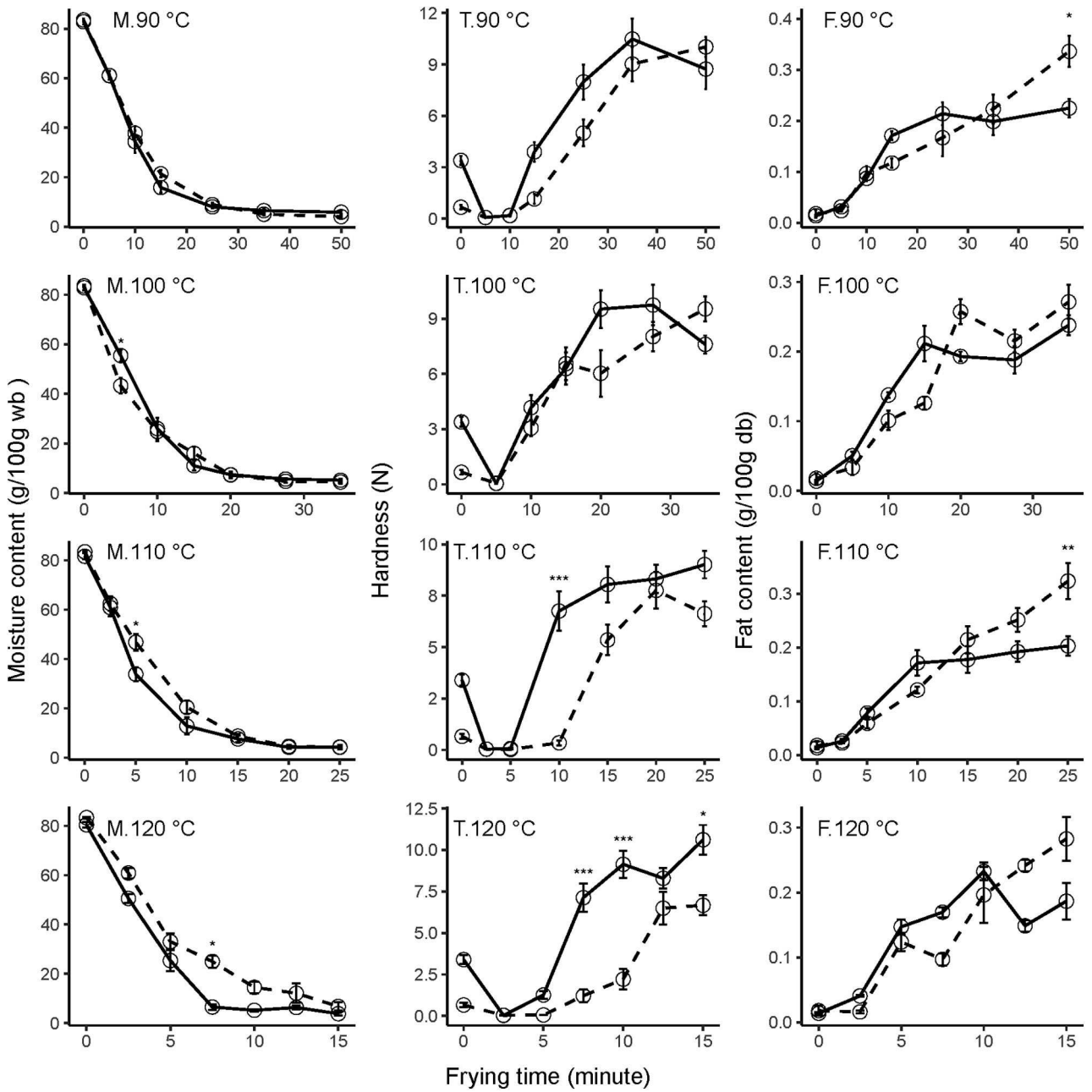

FIGURE 1 | Effect of frying temperatures, time, and ripening stage on moisture content (M), texture (T), and fat content (F) of mango chips during vacuum frying at 90, 100, 110, and 120°C. Solid lines are unripe mango, and dashed lines are ripe mango. Error bars are standard error. Asterisk shows significant difference between ripening stages (*$p \leq 0.05$, **$p \leq 0.01$, ***$p \leq 0.001$, ****$p \leq 0.0001$). $N = 6$ (two frying experiments × 3 replications) for moisture content; 4 (two frying experiments × 2 replications) for fat content; 20 (two frying experiments × 10 replications) for texture.

faster for unripe mango compared to ripe mango. A significant difference ($p = 0.000$) is observed after frying at 110°C for 10 min, with a hardness of 6.8 ± 1.0 N for unripe mango and 0.3 ± 0.1 N for ripe mango. When the temperature increased to 120°C, the difference ($p = 0.000$) was observed at a shorter frying time (7.5 min): 7.1 ± 0.9 N for unripe mango, and 1.2 ± 0.4 N for ripe mango. Again, the difference in matrix could play a role here. The crust formed by unripe fried mango is harder because the pectin polymer is still there, and when the water evaporates, it is able to form a stronger network and becomes hard (34).

Ascorbic Acid

Vitamin C (AA + DHA) is an important nutritional parameter for fried food products. The raw material used in this study is

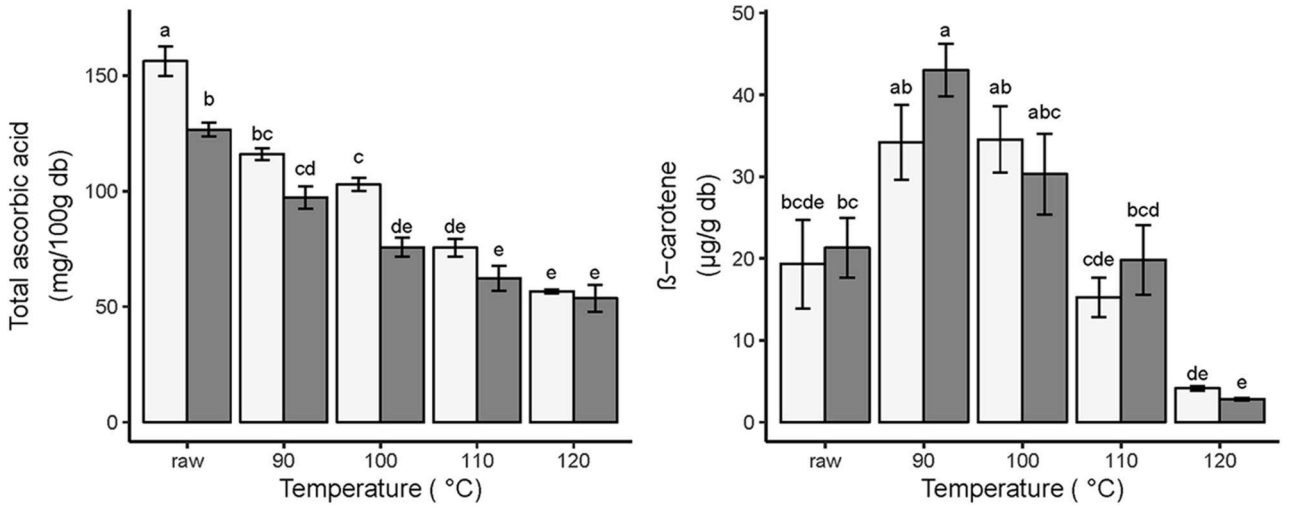

FIGURE 2 | Effects of vacuum frying and ripening stages of mango on total ascorbic acid (mg/100 g db) (left) and β-carotene (μg/g db) (right) during vacuum frying. Light bars represent unripe mango; dark bars represent ripe mango. The different frying temperatures also represent the different final frying times; 90°C (50 min); 100°C (35 min); 110°C (25 min); 120°C (15 min). Error bars are standard error. Different letters above the error bars show significant difference between treatments $N = 6$.

characterized by a high total ascorbic acid content; raw unripe mango had a higher TAA content of 156.2 ± 6.4 mg /100 g compared to ripe mango (126.6 ± 3.0 mg/100 g). The TAA decrease could be a result of ascorbate peroxidase (APX) activity which uses ascorbates as electron donor to remove hydroxyl radical from the cell that produced during fruit ripening (35).

As expected, thermal degradation of total ascorbic acid (TAA) increased with increasing frying temperature; a similar pattern was observed in both ripening stages (**Figure 2**). AA loss was described to have a linear relationship with temperature in vacuum-fried gold kiwi fruit (36) but also by first-order kinetics and the Arrhenius equation (37). Reduction in ascorbic acid content (AA) is possible in the absence of oxygen and at relatively low frying temperatures as it can follow an anaerobic pathway of non-enzymatic browning reactions (5). It has been shown in apple and potato that frying at atmospheric pressures substantially reduces the vitamin C content in comparison with vacuum-frying conditions (4). Under vacuum pressure, no dehydroascorbic acid is formed in significant amounts; ascorbic acid degrades by the cleavage of ring and the addition of water, decarboxylation, and intermolecular rearrangement, followed by dehydrations to produce furfural (38).

However, the TAA values remain higher in the unripe mango for all temperatures, although only significantly at 100°C. Frying for 35 min at 100°C retained 65.8 and 59.8% of TAA in unripe and ripe mango. Even at this severe heating, 100 g unripe and ripe vacuum-fried mango is able to provide 114.3 and 84.1% of the recommended daily allowance of vitamin C for adults (90 mg), respectively. This difference shows the importance of the fruit matrix as the container of the ascorbic acid. Davey et al. (39) mentioned that L-ascorbic acid was present at the subcellular level in various cell compartments including in chloroplast, cytoplasm, mitochondria, and apoplast. This arrangement could protect ascorbic acid inside the cell, but due to the lower amount of pectin in the cell walls of the ripe mango cell (34) could increase ascorbic acid heat damage in comparison to unripe mango cells.

β-Carotene

Raw ripe mango had a higher β-carotene content compared to unripe mango, even though not significant (27.2 ± 3.6 and 19.3 ± 5.4 μg/g db, respectively). This result was expected since carotenoid content increases during mango ripening (14).

There was no significant difference in β-carotene content for each temperature/time combination between the two ripening stages. While in both ripening stages the initial low β-carotene value increases after frying at 90 and 100°C, there is a clear decline in β-carotene content for both ripening stages when temperature is increased (**Figure 2**).

The possible explanations for the increased ß-carotene concentrations after frying at 90 and 100°C, which were also found in vacuum-fried apricot at 70–90°C (40), could be connected to the role of the changing fruit matrix on the accessibility of ß-carotene. In mango, β-carotene is located in lipid-dissolved and liquid-crystalline tubular elements of mesocarp chloroplasts. Thermal treatment and the presence of lipids improve the β-carotene accessibility (41).

However, after vacuum frying at 110 and 120°C, the ß-carotene concentrations decreased, which shows the thermal sensitivity of ß-carotene in vacuum frying. Da Silva and Moreira (12) confirm that vacuum frying of mango at 1.33 kPa, 120°C, for 3 min resulted in a decrease by 71.3% of the ß-carotene content. So, it was clear that to maintain ß-carotene content in vacuum-fried mango chips, a high-temperature processing should be avoided.

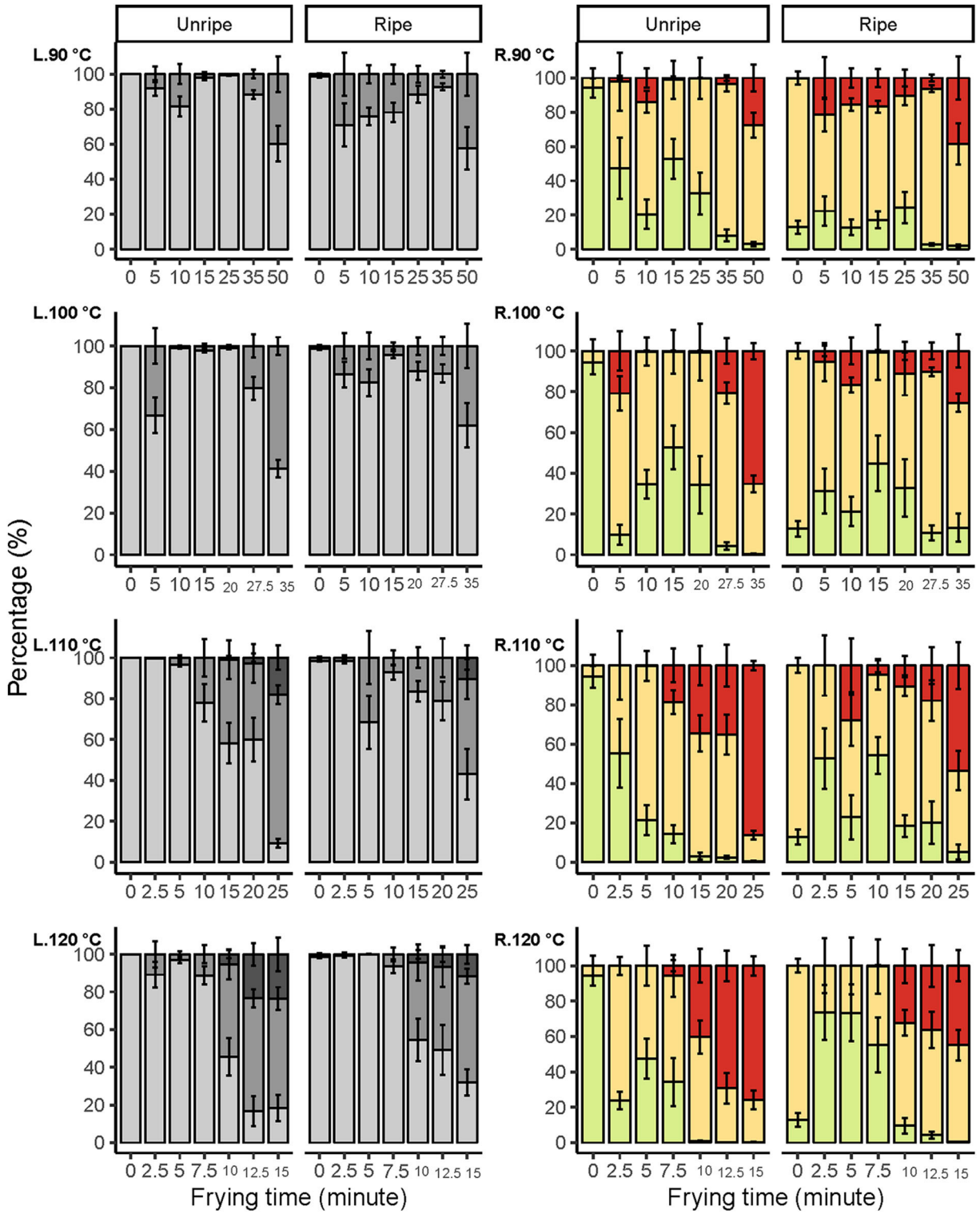

FIGURE 3 | Color distribution in terms of lightness L^* (L) and green to red a^* (R) changes during vacuum frying at different ripening stages of mango, fried at 90, 100, 110, and 120°C. Lightness levels of mango were represented in three levels: $0 \leq$ dark ≤ 60, $60 <$ medium-light ≤ 80, $80 <$ light ≤ 100. Meanwhile, red to green were represented in three levels; green ≤ 0, $0 <$ medium-red ≤ 10, red > 10. Error bars are standard error $N = 8$.

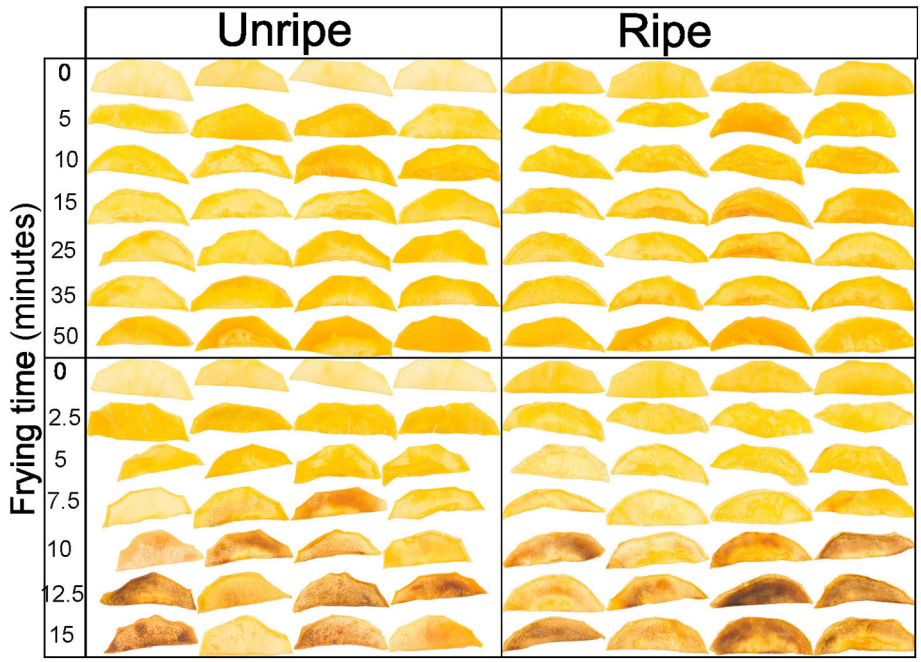

FIGURE 4 | Unripe (left) and ripe (right) mango slices vacuum fried at 90 (top) and 120°C (bottom) for different times.

Color

The color of fried mango chips is often inhomogeneous with strong local differences, e.g., the occurrence of brown spots in a lighter background. This phenomenon is present in most fried or baked foods. Therefore, measuring the overall color changes, e.g., expressed as L*a*b* values, is not representative for the visual appearance. In many cases, the food matrix and surface are not homogenous and have different structures at micro- and macroscopic scales (42). Image analysis of photographs taken under standard lighting gives the opportunity to assess the local differences in color values in a quantitative way. Instrumental color distribution analysis has been done for food for a variety of applications, including for microwaved pizza (43); however, application of this method in vacuum-fried food and especially as a time-series analysis is a novel approach. The effects of vacuum frying and ripening stages on the color changes have been assessed in terms of the percentage of surface area in levels of lightness (L^*) and green to red (a^*) (**Figures 3**, **4**).

The area in levels of lightness decreased gradually upon increasing frying time and temperature. However, a faster trend in lightness reduction was observed for the unripe mango chips, which was most distinct at 110°C and 120°C. The reduction in levels of the light area clearly led to an increase in levels of medium-light and dark areas, also differentiating between the two maturities. Similar results were found by Maity and Bawa (44), which state that vacuum-fried jackfruit bulb at 90°C for 25 min could reduce lightness by 15% and, when extended for another 5 min, reduced to 32%.

Similarly, the areas for medium-red and red increased progressively as the frying time and temperature increased, which was also observed by Maity and Bawa (44), stating that vacuum-fried jackfruit bulb at 90°C for 10 min increased the a* value by 168% and by 303% when extended to 20 min of frying. Furthermore, when fried at 100°C, the a* value was increased to 367% after 20 min, whereby a faster and stronger increase in redness areas was observed for unripe compared with ripe mango chips. At all temperatures, the green area decreased in unripe mango, while a fluctuation was seen in ripe mango chips. This trend was most pronounced at the highest temperatures. Additionally, as water evaporated, the boiling point of the moisture in the fruit will be increased and so will the fruit temperature (41), which indirectly contributed to color changes.

It was clear that the combination of ripening stage, frying time, and temperature has a substantial influence on the color of the mango chips. Unripe mango fried for a longer time at a higher temperature has a darker and redder surface compared to ripe mango. So, unripe mango seems more susceptible to the temperature–time treatments toward changes in lightness and redness compared to ripe mango. Similar effects were also found in apple, although they were measured as having an average color value of the fried apple surface (28). The change in color at 110 and 120°C at different frying times is probably due to the Maillard reaction and/or caramelization. The darker areas (**Figure 4**), and sometimes spots, would then be caused by locally higher amounts of reducing sugars, which could increase the rate of both the Maillard reaction and caramelization (40). Caramelization is likely to occur due to the high amount of sugars (45), also confirmed by (46) in vacuum-fried jackfruit. However, ripe mango has a significantly higher sugar content (**Table 2**), so the darker color was expected to be dominating, but this is not the

case; frying time and temperature and other mechanisms could play more roles on the color change.

CONCLUSION

Moisture loss of unripe mango chips was faster than that of ripe mango chips. There was no significant difference between hardness of unripe and ripe mango after vacuum frying at low temperatures (90–100°C), but at higher temperatures (110–120°C), unripe mango had a higher hardness value compared to ripe mango. Vacuum-fried ripe mango had a higher fat content compared to unripe mango. No differences between the ripening stages were found on the degradation of ascorbic acid and β-carotene during frying. Unripe mango is more susceptible to temperature and time toward lightness and redness changes compared to ripe mango. Considering all quality parameters, unripe mango is preferred over ripe mango for vacuum-frying processing. Furthermore, vacuum frying at 100°C for 20 min was sufficient to decrease the moisture content and produce high-hardness chips without adsorbing too much oil, maintain the color without losing too much ascorbic acid, and preserve the β-carotene content.

DATA AVAILABILITY STATEMENT

The raw data supporting the conclusions of this article will be made available by the authors, without undue reservation.

AUTHOR CONTRIBUTIONS

FA did the study conception and design, acquisition of data, analysis and interpretation of data, and drafting of the manuscript. EG and JV did the study, acquisition of data, analysis and interpretation of data, and drafting of the manuscript. MD did the analysis and interpretation of data, study conception and design, drafting of the manuscript, and critical revision. VF did the drafting of manuscript and critical revision. RV did the study conception and design, drafting of the manuscript, and critical revision. All authors contributed to manuscript revision and read and approved the submitted version.

FUNDING

Financial support for this study was provided by the Indonesia Endowment Fund for Education (LPDP) within the Ministry of Finance, Indonesia (grant number PRJ-201/LPDP/2015).

REFERENCES

1. Moreira RG. Vacuum frying versus conventional frying - An overview. *Eur J Lipid Sci Technol.* (2014) 116:723–34. doi: 10.1002/ejlt.201300272
2. Bouchon P. Food deep-fat frying. In: Brennan JG, Grandison AS, Editors. *Food Processing Handbook*. Wiley-VCH Verlag GmbH & Co. KGaA (2011). p. 455–89. doi: 10.1002/9783527634361.ch14
3. Sothornvit R. Edible coating and post-frying centrifuge step effect on quality of vacuum-fried banana chips. *J Food Eng.* (2011) 107:319–25. doi: 10.1016/j.jfoodeng.2011.07.010
4. Dueik V, Bouchon P. Development of healthy low-fat snacks: understanding the mechanisms of quality changes during atmospheric and vacuum frying. *Food Rev Int*. (2011) 27:408–32. doi: 10.1080/87559129.2011.563638
5. Dueik V, Bouchon P. Vacuum frying as a route to produce novel snacks with desired quality attributes according to new health trends. *J Food Sci*. (2011) 76:E188–95. doi: 10.1111/j.1750-3841.2010.01976.x
6. Mariscal M, Bouchon P. Comparison between atmospheric and vacuum frying of apple slices. *Food Chem*. (2008) 107:1561–9. doi: 10.1016/j.foodchem.2007.09.031
7. Ayustaningwarno F, Dekker M, Fogliano V, Verkerk R. Effect of vacuum frying on quality attributes of fruits. *Food Eng Rev*. (2018) 10:154–64. doi: 10.1007/s12393-018-9178-x
8. Perez-Tinoco MR, Ana P, Marco S-C, Max R, Fabrice V, et al. Effect of vacuum frying on main physicochemical and nutritional quality parameters of pineapple chips. *J Sci Food Agricul*. (2008) 88:945–53. doi: 10.1002/jsfa.3171
9. Shen X, Zhang M, Bhandari B, Guo Z. Effect of ultrasound dielectric pretreatment on the oxidation resistance of vacuum-fried apple chips. *J Sci Food Agricul*. (2018) 98:4436–44. doi: 10.1002/jsfa.8966
10. Yamsaengsung R, Ariyapuchai T, Prasertsit K. Effects of vacuum frying on structural changes of bananas. *J Food Eng.* (2011) 106:298–305. doi: 10.1016/j.jfoodeng.2011.05.016
11. Diamante LM. Vacuum fried jackfruit: effect of maturity, pre-treatment and processing on the physiochemical and sensory. In: Brough L, editor. *Annual Scientific Meeting of the Nutrition Society of Australia*. New Zealand: Nutrition Society of New Zealand (Inc). (2008), p. 138–42.
12. Da Silva PF, Moreira RG. Vacuum frying of high-quality fruit and vegetable-based snacks. *LWT-Food Sci Technol.* (2008) 41:1758–67. doi: 10.1016/j.lwt.2008.01.016
13. Nunes Y, Moreira RG. Effect of osmotic dehydration and vacuum-frying parameters to produce high-quality mango chips. *J Food Sci*. (2009) 74:E355–62. doi: 10.1111/j.1750-3841.2009.01257.x
14. Ibarra-Garza IP, et al. Effects of postharvest ripening on the nutraceutical and physicochemical properties of mango (*Mangifera indica* L. cv Keitt). *Postharvest Biol Technol.* (2015) 103:45–54. doi: 10.1016/j.postharvbio.2015.02.014
15. National Mango Board. *Mango Maturity & Ripeness Guide.* (2010). Available online at: http://www.mango.org/Mangos/media/Media/Documents/Retail-Quality%20Assessment/Mango-Maturity-and-Ripeness-Guide.pdf (accessed December 04, 2016).
16. Su Y, Zhang M, Adhikari B, Mujumdar AS, Zhang W. Improving the energy efficiency and the quality of fried products using a novel vacuum frying assisted by combined ultrasound and microwave technology. *Innovat Food Sci Emerg Technol.* (2018) 50:148–59. doi: 10.1016/j.ifset.2018.10.011
17. Alvis A, González A, Arrázola G. Effect of edible coating on the properties of sweet potato slices (Ipomoea Batatas Lam) cooked by deep-fat frying. part 2: thermophysical and transport properties. *Inform Tecnol.* (2015) 26:103–16. doi: 10.4067/S0718-07642015000100012
18. Hernández Y, Lobo MG, González M. Determination of vitamin c in tropical fruits: a comparative evaluation of methods. *Food Chem*. (2006) 96:654–64. doi: 10.1016/j.foodchem.2005.04.012
19. Wechtersbach L, Cigić B. Reduction of dehydroascorbic acid at low pH. *J Biochem Biophys Methods*. (2007) 70:767–72. doi: 10.1016/j.jbbm.2007.04.007
20. Salur-Can A, Türkyilmaz M, Özkan M. Effects of sulfur dioxide concentration on organic acids and β-carotene in dried apricots during storage. *Food Chem.* (2017) 221:412–21. doi: 10.1016/j.foodchem.2016.10.081
21. Ayustaningwarno F, Verkerk R, Fogliano V, Dekke M. The pivotal role of moisture content in the kinetic modelling of the quality attributes of vacuum fried chips. *Innovat Food Sci Emerg Technol.* (2020) 59:102251. doi: 10.1016/j.ifset.2019.102251
22. Wu X. Color quantization by dynamic programming and principal analysis. *ACM Trans. Graph.* (1992) 11:348–72. doi: 10.1145/146443.146475

23. Biau DJ. In brief: Standard deviation and standard error. *Clin Orthop Related Res*. (2011) 469:2661–4. doi: 10.1007/s11999-011-1908-9
24. Nambi VE, Thangavel K, Rajeswari KA, Manickavasagan A, Geetha V. Texture and rheological changes of Indian mango cultivars during ripening. *Postharvest Biol Technol*. (2016) 117:152–60. doi: 10.1016/j.postharvbio.2016.02.009
25. Willats WGT, Knox JP, Mikkelsen JD. Pectin: new insights into an old polymer are starting to gel. *Trends Food Sci Technol*. (2006) 17:97–104. doi: 10.1016/j.tifs.2005.10.008
26. Pilgrim GW, Walter RH, Oakenfull DJams G. Jellies, and Preserves. In: Walter RH, Editor. *The Chemistry and Technology of Pectin*. San Diego: Academic Press (1991). p. 23-50. doi: 10.1016/B978-0-08-092644-5.50007-8
27. Nguyen M-H, Price WE. Air-drying of banana: Influence of experimental parameters, slab thickness, banana maturity and harvesting season. *J Food Eng*. (2007) 79:200–7. doi: 10.1016/j.jfoodeng.2006.01.063
28. Shyu S-L, Hwang LS. Effects of processing conditions on the quality of vacuum fried apple chips. *Food Res Int*. (2001) 34:133–42. doi: 10.1016/S0963-9969(00)00141-1
29. Deng K, Chen J, Tian J, Miao S, Zheng B. Optimization of process variables on physical and sensory attributes of shiitake (*Lentinula edodes*) slices during vacuum frying. *Innovative Food Sci Emerg Technol*. (2019) 54:162–71. doi: 10.1016/j.ifset.2019.04.009
30. BeMiller JN. An introduction to pectins: structure and properties. In: Fishman ML, Jen JJ. Editors. *Chemistry and Function of Pectins*. American Chemical Society (1986). p. 2–12. doi: 10.1021/bk-1986-0310.ch001
31. Albert S, Mittel GS. Comparative evaluation of edible coatings to reduce fat uptake in a deep-fried cereal product. *Food Res Int*. (2002) 35:445–58. doi: 10.1016/S0963-9969(01)00139-9
32. Dueik V, Robert P, Bouchon P. Vacuum frying reduces oil uptake and improves the quality parameters of carrot crisps. *Food Chem*. (2010) 119:7. doi: 10.1016/j.foodchem.2009.08.027
33. Pedreschi F, Moyano P. Oil uptake and texture development in fried potato slices. *J Food Eng*. (2005) 70:557–63. doi: 10.1016/j.jfoodeng.2004.10.010
34. Daraei Garmakhany A, Mirzaei HO, Maghsudlo Y, Kashaninejad M, Jafari SM. Production of low fat french-fries with single and multi-layer hydrocolloid coatings. *J Food Sci Technol Mysore*. (2014) 51:1334–41. doi: 10.1007/s13197-012-0660-9
35. Gomez MLP, Lajolo FM. Ascorbic acid metabolism in fruits: activity of enzymes involved in synthesis and degradation during ripening in mango and guava. *J Sci Food Agricul*. (2008) 88:756–62. doi: 10.1002/jsfa.3042
36. Diamante LM, Savage GP, Vanhanen L. Response surface methodology optimization of vacuum-fried gold kiwifruit slices based on its moisture, oil and ascorbic acid contents. *J Food Process Preserv*. (2013) 37:432–40. doi: 10.1111/j.1745-4549.2011.00659.x
37. Gregory JF III. Vitamis. In: Damodaran S, Parkin KL. Editors. *Fennema's Food Chemistry*. Boca Raton: CRC Press (2017), p. 543–26.
38. Yuan JP, Chen F. Degradation of ascorbic acid in aqueous solution. *J Agricult Food Chem*. (1998) 46:5078–82. doi: 10.1021/jf9805404
39. Davey MW, Montagu MV, Inzé D, Sanmartin D, Kanellis A, Smirnoff N, et al. Plant L-ascorbic acid: chemistry, function, metabolism, bioavailability and effects of processing. *J Sci Food Agricult*. (2000) 80:825–60. doi: 10.1002/(SICI)1097-0010(20000515)80:7<825::AID-JSFA598>3.0.CO;2-6
40. Diamante LM, Savage GP, Vanhanen L, Ihns R. Effects of maltodextrin level, frying temperature and time on the moisture, oil and beta-carotene contents of vacuum-fried apricot slices. *Int J Food Sci Technol*. (2012) 47:325–31. doi: 10.1111/j.1365-2621.2011.02842.x
41. Boon CS, McClements DJ, Weiss J, and Decker EA. Factors Influencing the Chemical Stability of Carotenoids in Foods. *Crit Rev Food Sci Nutr*. (2010) 50:515–32. doi: 10.1080/10408390802565889
42. Capuano E, Oliviero T, van Boekel MAJS. Modeling food matrix effects on chemical reactivity: challenges and perspectives. *Crit Rev Food Sci Nutr*. (2017) 2017:1–15. doi: 10.1080/10408398.2017.1342595
43. Yam KL, Papadakis SE. A simple digital imaging method for measuring and analyzing color of food surfaces. *J Food Eng*. (2004) 61:137–42. doi: 10.1016/S0260-8774(03)00195-X
44. Maity T, Bawa AS, Raju PS. Effect of vacuum frying on changes in quality attributes of jackfruit (*Artocarpus heterophyllus*) bulb slices. *Int J Food Sci Technol*. (2014) 2014:752047. doi: 10.1155/2014/752047
45. Kroh LW. Caramelisation in food and beverages. *Food Chem*. (1994) 51:373–9. doi: 10.1016/0308-8146(94)90188-0
46. Maity T, Bawa AS, Raju PS. Use of hydrocolloids to improve the quality of vacuum fried jackfruit chips. *Int Food Res J*. (2015) 22:1571–7.

Conflict of Interest: The authors declare that the research was conducted in the absence of any commercial or financial relationships that could be construed as a potential conflict of interest.

frontiers in Nutrition

REVIEW
published: 18 August 2020
doi: 10.3389/fnut.2020.00132

Current Understanding of the Structure and Function of Fungal Immunomodulatory Proteins

Yusi Liu[1,2,3], *Shanna Bastiaan-Net*[2] *and Harry J. Wichers*[2,3]*

[1] *Laboratory of Food Enzyme Engineering, Institute of Food Science and Technology, Chinese Academy of Agriculture Sciences, Beijing, China,* [2] *Wageningen Food and Biobased Research, Wageningen University and Research, Wageningen, Netherlands,* [3] *Laboratory of Food Chemistry, Wageningen University, Wageningen, Netherlands*

Fungal immunomodulatory proteins (FIPs) are a group of proteins found in fungi, which are extensively studied for their immunomodulatory activity. Currently, more than 38 types of FIPs have been described. Based on their conserved structure and protein identity, FIPs can be classified into five subgroups: Fve-type FIPs (Pfam PF09259), Cerato-type FIPs (Pfam PF07249), PCP-like FIPs, TFP-like FIPs, and unclassified FIPs. Among the five subgroups, Fve-type FIPs are the most studied for their hemagglutinating, immunomodulating, and anti-cancer properties. In general, these small proteins consist of 110–125 amino acids, with a molecular weight of ∼13 kDa. The other four subgroups are relatively less studied, but also show a noticeable influence on immune cells. In this review, we summarized the protein modifications, 3-dimensional structures and bioactivities of all types of FIPs. Moreover, structure-function relationship of FIPs has been discussed, including relationship between carbohydrate binding module and hemagglutination, correlation of oligomerization and cytokine induction, relevance of glycosylation and lymphocyte activation. This summary and discussion may help gain comprehensive understanding of FIPs' working mechanisms and scope future studies.

Keywords: immunomodulatory proteins, FIPs, glycosylation, immunomodulaion, hemagglutination, structure-function relationship

OPEN ACCESS

Edited by:
Hang Xiao,
University of Massachusetts Amherst, United States

Reviewed by:
Xuanwei Zhou,
Shanghai Jiao Tong University, China
Marcin Szymanski,
Adam Mickiewicz University, Poland
Thiago Henrique Napoleão,
Federal University of Pernambuco, Brazil
Bruno Rocha,
Federal University of Ceara, Brazil

***Correspondence:**
Harry Wichers
harry.wichers@wur.nl

Specialty section:
This article was submitted to Food Chemistry, a section of the journal Frontiers in Nutrition

Received: *25 March 2020*
Accepted: *09 July 2020*
Published: *18 August 2020*

Citation:
Liu Y, Bastiaan-Net S and Wichers HJ (2020) Current Understanding of the Structure and Function of Fungal Immunomodulatory Proteins. Front. Nutr. 7:132. doi: 10.3389/fnut.2020.00132

INTRODUCTION

Fungi can potentially contain many bioactive proteins, including lectins, ribosome-inactivating proteins, laccases, nucleases, glycoproteins/glycopeptides, and immunomodulatory proteins (1–3). Fungal immunomodulatory proteins (FIPs) are a group of proteins found in fungi, which show noticeable immunomodulatory activity (4, 5). In recent decades, they have been widely studied for their pharmaceutical utilizations (2, 3). Ling-Zhi 8 (LZ-8) is the first FIP discovered in *Ganoderma lucidum* (6). Till now, more than 38 types of FIPs have been identified (see **Table 1**).

Based on the conserved structure and protein identity (see **Figure 1**), FIPs can be classified into 5 subgroups: Fve-type FIPs, Cerato-type FIPs, PCP-like FIPs, TFP-like FIPs, and unclassified FIPs (see **Figure 1** and **Table 1**). Among the five subgroups, Fve-type FIPs are the largest subgroup with 29 members which have the assigned Pfam Fve family domain signature PF09259. *Antrodia camphorate* immunomodulatory protein (ACA) and *Trametes versicolor* "Yun-Zhi" protein (YZP) belong to the second subgroup, named Cerato-type FIPs, which contains the Pfam PF07249 domain. The third subgroup is formed by the PCP-like FIPs with only one member till now, *Poria cocos* immunomodulatory protein (PCP). Besides PCP, three kinds of hypothetical proteins from

Wolfiporia cocos (Accession PCH39154.1, PCH35963.1, and PCH34729.1) might also belong to this subgroup. Currently, the fourth subgroup just contains *Tremella fuciformis* protein (TFP), with no other high-identity proteins having been identified by BLAST. This group is indicated as TFP-like FIPs. The other FIPs could not be classified since their amino acid sequence has not yet been elucidated. Hence, they are categorized as unclassified FIPs, including *Auricularia polytricha* immunomodulatory protein (APP), *Pleurotus citrinopileatus* immunomodulatory protein (PCiP), the immunomodulatory protein from *T. versicolor* (named TVC), the immunomodulatory protein from *Hericium erinaceus* (named HEP3), and the immunomodulatory protein from *Pleurotus eryngii* (named PEP 1b).

In general, Fve-type FIPs consist of 110–125 amino acids, with a molecular weight of ∼13 kDa. This subgroup of FIPs was mainly studied for their hemagglutinating, immunomodulating, and anti-cancer properties, which have been reviewed in several articles. These reviews mostly focused on the their bioactivities, heterologous production, physicochemical properties, and proposed molecular anti-tumor mechanisms (5, 35–37). However, the mechanism behind their immunomodulatory activity needs to be updated, and the detailed information about their protein structure and function relationship have not yet been reviewed. Proteins belonging to the other four FIP subgroups have shown a noticeable influence on immune cells. However, they were neither extensively studied, nor critically discussed. In this review, we have summarized protein modifications like glycosylation, the 3-dimensional structure, and bioactivity of all types of FIPs, and try to find relationships between structural features and immunomodulatory activity, in order to gain a better understanding of the mechanism of FIPs' bioactivity and scope further research.

TABLE 1 | Summary of FIPs and classification.

Classification	Name	Accession	Source	References
Fve-type FIPs	rFIP-bbo	KDQ10166.1	*Botryobasidium botryosum*	(7)
	rFIP-cru	AKU37620.1	*Chroogomphis rutilus*	(8)
	rFIP-dsp2	XP_007363541	*Dichomitus squalens*	(9)
	FIP-fve	P80412.1	*Flammulina velutipe*	(4)
	rFIP-gap1	AEP68179.1	*Ganoderma applanatum*	(10)
	rFIP-gap2	ART88472.1	*Ganoderma applanatum*	(10)
	rFIP-gat	AJD79556.1	*Ganoderma atrum*	(11)
	LZ-8	P14945.2	*Ganoderma lucidum* (Ling Zhi)	(6)
	rLZ-9	na	*Ganoderma lucidum*	(12)
	rFIP-gmi	3KCW	*Ganoderma microsporum*	(13)
	rFIP-gsi	na	*Ganoderma sinensis*	(14–16)
	FIP-gts	na	*Ganoderma tsugae*	(17)
	rFIP-SN15	na	Intergeneric shuffled library	(18)
	rFIP-SJ75	na	Intergeneric shuffled library	(19)
	rFIP-lrh	na	*Lignosus rhinocerotis*	(20)
	rFIP-lti1	na	*Lentinus tigrinus*	(21)
	rFIP-lti2	na	*Lentinus tigrinus*	(21)
	rFIP-nha	EEU37941.1	*Nectria haemotococca*	(12)
	rFIP-ppl	AJL35148.1	*Postia placenta*	(9)
	rFIP-sch2	AQQ80204.1	*Stachybotrys chlorohalonata*	(22)
	rFIP-sch3	KEY70185.1	*Stachybotrys chlorohalonata*	(22)
	rFIP-tvc	na	*Trametes versicolor*	(23)
	FIP-vvo	na	*Volvariella volvacea*	(24)
	rFIP-vvo77	na	*Volvariella volvacea*	(25)
	rFIP-vvo78	na	*Volvariella volvacea*	(25)
	rFIP-vvo79	na	*Volvariella volvacea*	(25)
	rFIP-vvo80	na	*Volvariella volvacea*	(25)
	rFIP-vvo82	na	*Volvariella volvacea*	(25)
	rFIP-vvo98	na	*Volvariella volvacea*	(25)
Cerato-type FIPs	ACA	AAT11911.1	*Antrodia camphorata*	(26)
	YZP	AGH06133.1	*Trametes versicolor (Yunzhi)*	(27)
PCP-like FIPs	PCP	AEM91639.1	*Poria cocos*	(28)
TFP-like FIPs	TFP	ABL96299.1	*Tremella fuciformis*	(29)
Unclassified FIPs	APP	na	*Auricularia polytricha*	(30)
	HEP3	na	*Hericium erinaceus*	(31)
	PCiP	na	*Pleurotus citrinopileatus*	(32)
	PEP 1b	na	*Pleurotus eryngii*	(33)
	TVC	na	*Trametes versicolor*	(34)

na, not available.

STRUCTURE ANALYSIS

Structure of FIPs

In general, the amino acid sequence of reported Fve-type FIPs is rich in valine and aspartic acid, and short of cysteine and histidine. Based on the circular dichroism spectrum analysis and prediction of ExPASy, they consist of 1-3 α-helixes, 7-9 β-sheets, and some random coils (see **Supplementary Table 1**). The 3-dimensional structures of three FIPs have been determined via X-ray diffraction in earlier studies: FIP-fve (PDB code: 1OSY), LZ-8 (PDB code: 3F3H) and FIP-gmi (PDB code: 3KCW) (see **Figures 2A–C**). The structure showed that monomers of Fve-type FIPs consist of two parts, the N-terminal and C-terminal domains. The N-terminal domain starts with an N-terminal α-helix, which is an essential structure for all Fve-type FIPs. The α-helix is followed by a β-sheet (1OSY and 3F3H), which is essential for the dimeric structure, or a stretch of random coil (3KCW). The C-terminal domain is a sandwich-type Fibronectin III domain, which mainly consists of 7 β-sheets (13, 43, 44). The monomer of Fve-type FIPs assembles into a homodimeric (1OSY and 3F3H) or tetrameric structure (3KCW) via non-covalent interaction, such as hydrophobic interactions and hydrogen bonds. The dimerization sustained by domain swapping (45, 46)

Abbreviations: APCs, antigen-presenting cells; CD, cluster of differentiation; D, aspartic acid; DCs, Dendritic cells; ERK, extracellular signal-regulated kinase; F, phenylalanine; FIP, fungal immunomodulatory protein; GM-CSF, Granulocyte-macrophage colony-stimulating factor; HLA, human leukocyte antigen; hPBL, human peripheral blood lymphocyte; I, isoleucine; IFN, interferon; ICAM, intercellular cell adhesion molecule; Ig, immunoglobulin; IL, interleukin; IL-2R, interleukin-2 receptor; L, leucine; LPS, lipopolysaccharide; LT, lymphotoxin; MAPK, mitogen-activated protein kinase; MHC II, major histocompatibility complex; Mr, relative molecular mass; MyD88, myeloid differentiation primary response 88; N, asparagine; NF-kB, nuclear factor-kB; NO, nitric oxide; PBL, peripheral blood lymphocyte; PBMC, peripheral blood mononuclear cell; PKC, protein kinase C; PLC, phospholipase C; PTK, protein tyrosine kinase; ROS, reactive oxygen species; RSV, respiratory syncytial virus; S, serine; T, threonine; Th, T helper; TLR, Toll-like receptor; TNF, tumor necrosis factor; TRAF, TNF receptor-associated factor; VEGF, vascular endothelial growth factor; W, tryptophan.

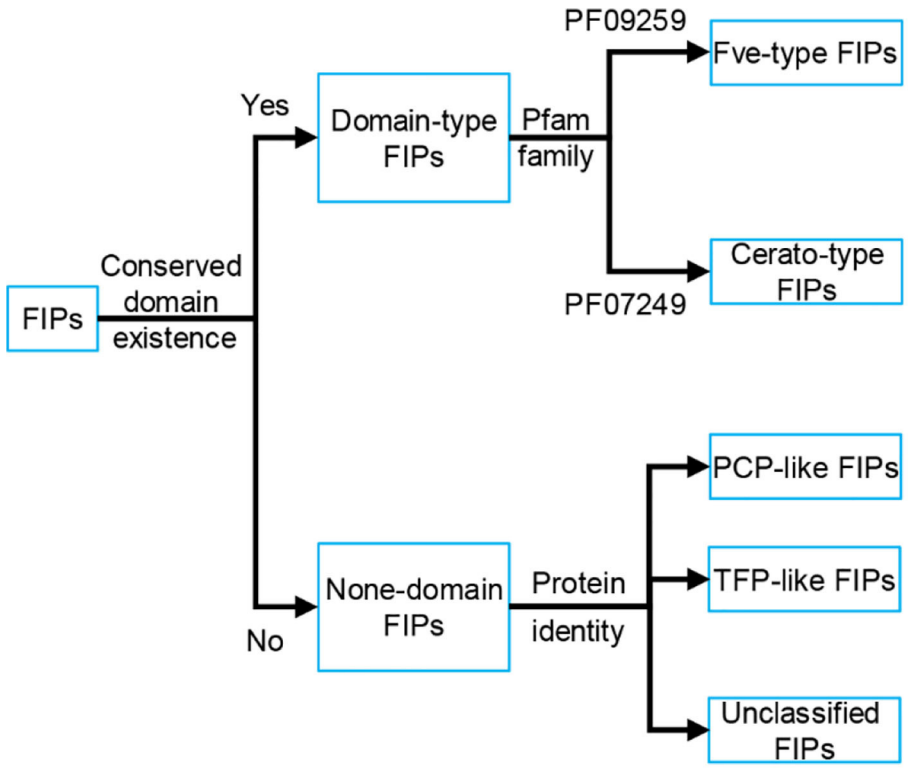

FIGURE 1 | Classification of FIPs based on the conserved structure and protein identity. Depending on the existence of conserved domains, FIPs could be classified into domain-type FIPs and none-domain FIPs. In domain-type FIPs, Fve-type FIPs have the assigned Pfam Fve family domain signature PF09259, while Cerato-type FIPs contain the Pfam PF07249 domain signature. In none-domain FIPs, FIPs were separated into PCP-like FIPs, TFP-like FIPs and unclassified FIPs based on protein identity. As the amino acid sequence of unclassified FIPs has not yet been elucidated, they could not be classified and have been placed separately.

mainly depends on the N-terminal α-helix and β-sheet (43, 44), while there is no detailed information about the dynamics of tetramer formation. Notably, after the N-terminal α-helix in FIP-gmi (3KCW), there is a stretch of random coil, instead of a β-sheet. This difference may be relevant for the occurrence of the different oligomeric states, while further study is needed to clarify the underlying mechanism.

Till now, only the amino acid sequence of ACA, YZP, PCP, and TFP has been identified, and no primary structure information is available about unclassified FIPs. Though no amino acid sequence is known, some articles report the amino acid composition. For instance, APP is relatively rich in threonine (11.5%), but contains no histidine, little methionine (1.05%) and cysteine (1.08%) (30). Besides, PCiP has a high leucine content (10.76%), but little cysteine (0.56%), and methionine (1.22%) (32). We predicted their secondary structure via ExPASy based on the known sequence (see **Supplementary Table 1**). Protein structures of FIPs at crystal level or relevant NMR data for proteins from other subgroups have not been provided. A structure prediction of Cerato-type FIPs could be obtained via SWISS-MODEL using 3m3g.1.A and 3suk.1.A (Cerato-platanin proteins) as modeling template for ACA and YZP, respectively (see **Figures 2D,E**) (38–42). Cerato-platanin proteins are small, secreted proteins involved in the various stages of the host-fungus interaction process, acting as phytotoxins, elicitors, and allergens (47, 48). Modeled ACA and YZP show a spheroid-like structure, formed by short α-helixes, three (ACA) or five β-sheets (YZP), and lots of random coils (see **Figures 2D,E**). The three β-sheets of ACA exits in one layer, while the five β-sheets of YZP fold into two perpendicular layers, which may lead to a more stable core.

Glycosylation Modification of FIPs

Protein glycosylation is an important post-translational modification that may influence protein structure and function in eukaryotes (49–52). Till now, we found that 8 native or heterologous expressed specimens of FIPs could be glycosylated, and 12 specimens of FIPs have potential glycosylation sites.

As shown in **Table 2**, several Fve-type FIPs have potential N-glycosylation sites, and some of them were glycosylated in heterologous expression systems. In 2013, Bastiaan-Net et al. expressed recombinant FIP-fve in *Picha pastoris*, which resulted in three bands on SDS-PAGE gel, representing the non-glycosylated, single glycosylated and double glycosylated FIP-fve respectively, demonstrating that both predicted glycosylation sites (N36 and N54) could be glycosylated. Whether these results correspond to the glycosylation state of native FIP-fve could not be concluded with certainty, as proteins will be over-glycosylated in the yeast expression systems (52).

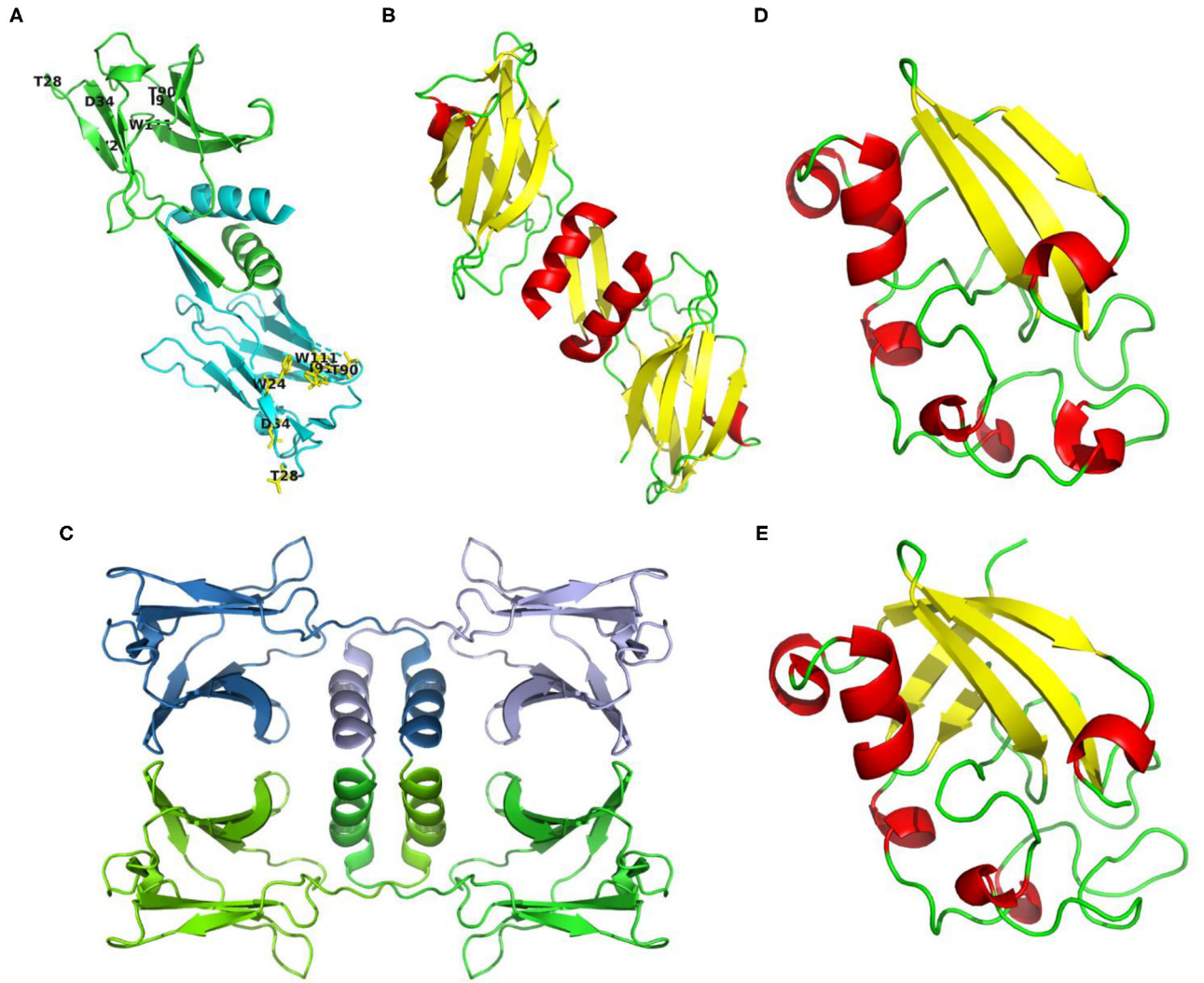

FIGURE 2 | Structures or structure predictions of FIPs. **(A)** FIP-fve (PDB code: 1OSY) colored by monomer in cyan and green, and labeled with purposed CBM34-like structure in yellow (W24, T28, D34, T90, I91, and W111 of FIP-fve); **(B)** LZ-8 (PDB code: 3F3H) colored by secondary structure (helixes in red, sheets in yellow, loops in green); **(C)** FIP-gmi (PDB code: 3KCW) colored by monomer in skyblue, lightblue, chartreuse, and green; **(D)** Structure prediction of ACA based on 3m3g.1. via SWISS-MODEL (38–42), and colored by secondary structure (helixes in red, sheets in yellow, loops in green); **(E)** Structure prediction of YZP based on 3suk.1.A via SWISS-MODEL (38–42), and colored by secondary structure (helixes in red, sheets in yellow, loops in green).

Interestingly, rFIP-gts expressed in Sf21 cells can be produced in glycosylated (relative molecular mass (Mr) ∼15 kDa) as well as in non-glycosylated forms (Mr ∼13.5 kDa), which was confirmed by glycoprotein staining. Specifically, the glycosylated rFIP-gts was guided by a signal peptide from bombyxin (SP_{bbx}; the recombinant vector vAcP10SP_{bbx}Gts), while the rFIP-gts without this signal peptide (the recombinant vector vAcP10Gts) existed as a non-glycosylated form. Wu et al. thought that the signal peptide (SP_{bbx}) upstream of rFIP-gts facilitated entry into the endoplasmic reticulum where the glycosylation process takes place (8). However, no putative glycosylation site was demonstrated in the article, nor was it predicted by the NetNGlyc 1.0 Server and NetOGlyc 4.0 Server.

Also, native ACA and PCP are glycoproteins (26, 28). ACA is predominately an N-glycosylated protein, as deglycosylated ACA (treated with N-glycosidase F, a specific N-glycosylation protease) shows the same molecular weight as rACA expressed by *Escherichia coli*. Predicted by GlyNGly 1.0 Service, asparagine at residue 20 (N20) of the full-length ACA (16 kDa) had the highest possibility (80.53%) to be N-glycosylated, followed by N31 and N87 (with 63.51 and 66.68% possibility, respectively) (26). Native PCP (35.6 kDa) is a disulfide-linked heterodimeric glycoprotein consisting of 14.3 and 21.3 kDa subunits with N- and O-glycosylation which contributes ∼7 kDa to its molecular mass (28). Interestingly, there is only one predicted N-glycosylation site (N142, with 52.90% possibility) found by the NetNGlyc 1.0 and NetOGlyc 4.0 Servers. Meanwhile, there

TABLE 2 | Glycosylation modification of FIPs.

FIPs	Glycosylation	Native/heterologous expression/predicted	References
ACA	N-glycosylated protein	Native	(26)
PCP	Disulfide-linked heterodimeric glycoprotein with N- and O-glycosylation.	Native	(28)
rFIP-gts	Can be glycosylated when expressed by Sf21 insect cells	Sf21 insect cells	(8)
rFIP-fve	Two N-glycosylated sites: N36 and N54	*P. pastoris*	(12)
rFIP-nha	Two N-glycosylated sites: N5 and N39	*P. pastoris*	(12)
rFIP-cru	One confirmed and one potential glycosylation sites: N29 (79.64%*) and N36 (76.59%*)	*P. pastoris*	(53)
rFIP-gap1	One N-glycosylated sites: N38	*P. pastoris*	(10)
rFIP-gap2	Two N-glycosylated sites: N31 (79.49%*) and N38 (76.40%*)	*P. pastoris*	(10)
FIP-lrh	Four potential O-linked glycosylation: S1, T4, T6, and S58	Predicted[#]	(20)
rFIP-gsi	One potential N-glycosylated site: N36 (74.31%)	Predicted*	(15, 16)
FIP-lti1	Two potential glycosylation sites: N27 (61.63%*) and N34 (57.98%*)	Predicted*	(21)
FIP-lti2	Two potential glycosylation sites: N30 (81.12%*) and N37 (61.80%*)	Predicted*	(21)
FIP-SN15	Two potential glycosylation sites: N29 (80.11%*) and N36 (74.30%*)	Predicted*	(18)
FIP-SJ75	Two potential glycosylation sites: N31 (76.10%*) and S34 (50%*)	Predicted*	(19)
FIP-dsp2	Two potential glycosylation sites: N36 (66.49%) and S32 (58.80%)	Predicted*	(22)
FIP-gat	Two potential glycosylation sites: N29 (80.10%) and N36 (74.29%)	Predicted*	(11)
FIP-gmi	One potential glycosylation sites: S32 (64.29%)	Predicted*	(54)
FIP-gsi	Two potential glycosylation sites: N29 (80.11%) and N36 (74.31%)	Predicted*	(15)
FIP-sch2	One potential glycosylation sites: S33 (50.90%)	Predicted*	(22)
FIP-sch3	One potential glycosylation sites: S33 (53.04%)	Predicted*	(22)

**Predicted by NetNGlyc 1.0 (http://www.cbs.dtu.dk/services/NetNGlyc/) and NetOGlyc 4.0 (http://www.cbs.dtu.dk/services/NetOGlyc/).*

[#]Means FIP-lrh has no positive O-glycan site predicted by NetOGlyc 4.0 (http://www.cbs.dtu.dk/services/NetOGlyc/), but Pushparajah et al. obtained the results by NetOGlyc 4.0 and GlycoEP (http://www.imtech.res.in/raghava/glycoep/) (20).

is some controversy as to the composition of PCP. Lu et al. thought PCP to be composed of two identical 12.8 kDa protein subunits (73 residues cleaved); however, these subunits would be asymmetrically modified by N- and O- glycosylation (55). Still, PCP was not heterologous expressed to verify such hypothesis. In contrast, Li et al. expressed rPCP (19 residues cleaved as signal peptide) in *P. pastoris* system, and showed that rPCP existed as two bands (Mr ∼18 and ∼20 kDa) under reducing condition and one band (Mr ∼37 kDa) under non-reducing condition. Besides, rPCP was only N-glycosylated, as confirmed by PNGase F (specific for N-glycans) treatment (56). Though the rPCP had to some extent a similar bioactivity to native PCP, such as upregulation of interleukin (IL)-1β and tumor necrosis factor (TNF)-α gene expression next to induction of macrophage TNF-α secretion (28, 55, 56), it's utilization to replace native PCP still need consideration.

HEALTH-PROMOTING ACTIVITIES OF FIPs

As the antitumor activity of FIPs has been described clearly in recent reviews (36, 37), we focus here specifically on immunomodulatory activity and hemagglutination properties.

Immunomodulatory Activity of Fve-Type FIPs

Fve-type FIPs can regulate cellular and humoral immunity (**Figure 3**), which includes activation of immune cells, leading to immune-mediated anti-allergic, anti-inflammatory, and anti-tumor effects.

Activation of Immune Cells

Fve-type FIPs activate immune cells via inducing secretion of cytokines and chemokines, increasing expression of cell adhesion molecules, as well as enhancing lymphocyte proliferation. As shown in **Table 3**, FIPs behave distinctively in activation of immune cells. For instance, FIP-vvo and FIP-gsi could induce transcriptional expression of IL-4, TNF-α, and lymphotoxin (LT) (14, 24), whereas no significant regulation of IL-4 secretion was reported following treatment with LZ-8 (58) or FIP-fve (64). However, most FIPs could proliferate mouse splenocytes and human peripheral blood lymphocytes (hPBLs), as well as induce IL-2, interferon (IFN)-γ, and IL-2 receptor (IL-2R) transcriptional expression.

LZ-8 is one of the most studied FIPs for immune modulation effects. It could induce mitogenesis toward mouse splenocytes (59), hPBLs (60), human mixed lymphocyte (purified T cells and allogeneic B cells) (61). Its behavior on hPBLs is monocyte-dependent, similar to phytohemagglutinin and other lectin mitogens (60) which can activate T cells and Dendritic cells (DCs), and induces the production of quite a few cytokines and cell adhesion molecules.

There is some insight into the mechanism of LZ-8 in regulating IL-2 transcriptional expression in T cells. As shown in **Figure 3**, the rLZ-8-mediated signal-transduction pathways

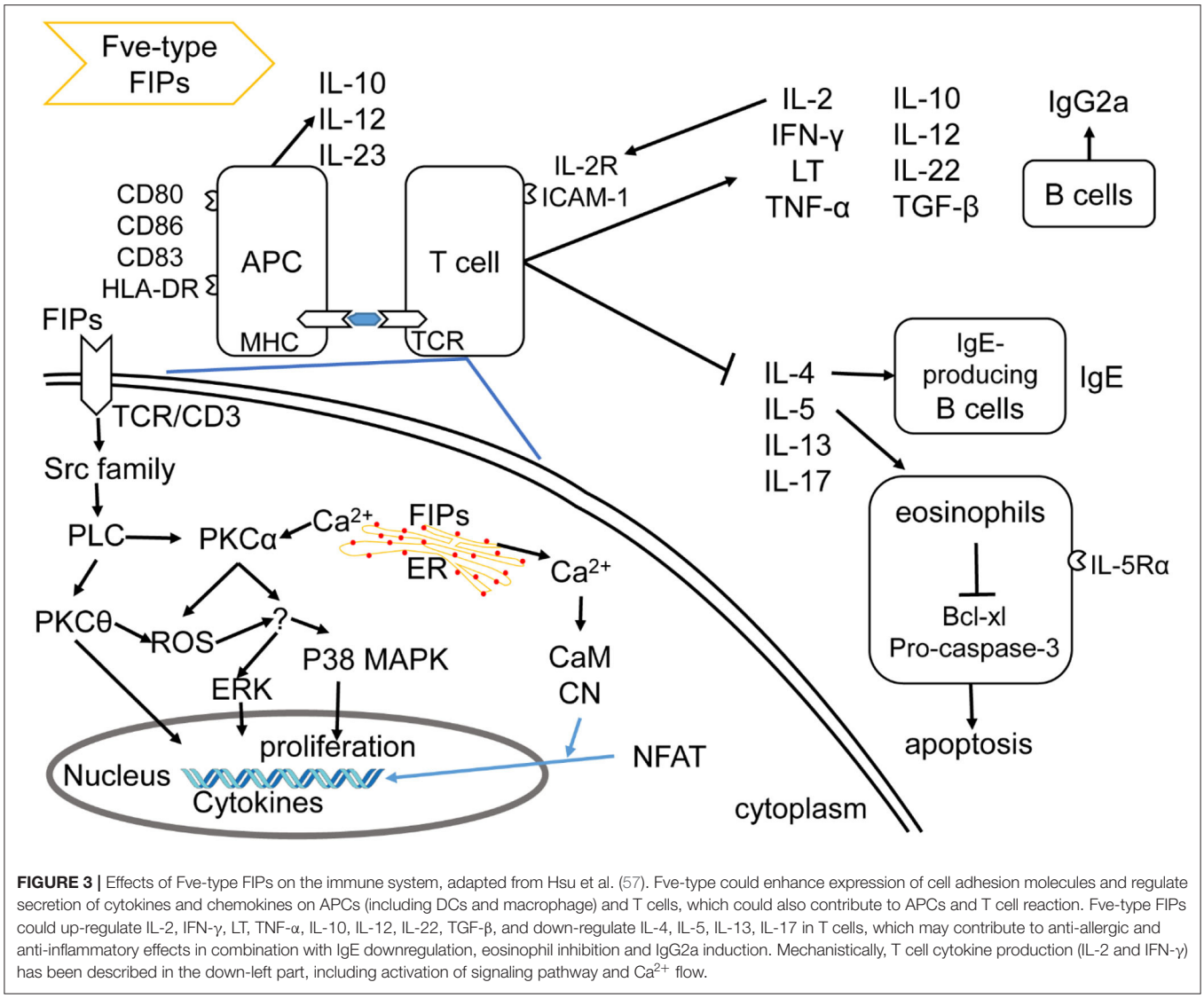

FIGURE 3 | Effects of Fve-type FIPs on the immune system, adapted from Hsu et al. (57). Fve-type could enhance expression of cell adhesion molecules and regulate secretion of cytokines and chemokines on APCs (including DCs and macrophage) and T cells, which could also contribute to APCs and T cell reaction. Fve-type FIPs could up-regulate IL-2, IFN-γ, LT, TNF-α, IL-10, IL-12, IL-22, TGF-β, and down-regulate IL-4, IL-5, IL-13, IL-17 in T cells, which may contribute to anti-allergic and anti-inflammatory effects in combination with IgE downregulation, eosinophil inhibition and IgG2a induction. Mechanistically, T cell cytokine production (IL-2 and IFN-γ) has been described in the down-left part, including activation of signaling pathway and Ca^{2+} flow.

such as protein tyrosine kinase (PTK)/protein kinase C (PKC)/reactive oxygen species (ROS), PTK/phospholipase C (PLC)/PKCα/extracellular signal-regulated kinase (ERK)1/2, and PTK/PLC/PKCα/p38, could up-regulate IL-2 transcriptional expression in T cells (57). Meanwhile, TCR/cluster of differentiation (CD)3 complex is one of the putative binding sites of, or receptors for, rLZ-8 in T cell activation (57). With respect to the IL-2 secretion, inhibition of PKC, Ca^{2+} influx, mitogen-activated protein kinase kinase (MEK)1/ERK1/2 pathway, or Src-family kinases could result in a significant reduction and inhibition of IL-2 secretion (upon incubation with rLZ-8). These evidences indicate the mentioned signaling pathways and Ca^{2+} influx to be important for the rLZ-8-mediated IL-2 secretion by T cells (57).

Most likely, LZ-8 is also able to activate antigen-presenting cells (APCs). Specifically, Lin et al. (58) demonstrated the ability of LZ-8 to induce activation and maturation of DCs (58). In addition, Li et al. (62) suggested that LZ-8 activates the PI3K/Akt and MAPK signaling pathways after internalization by macrophages. However, the exact underlying mechanism of DCs (58, 73) and macrophages (62) activation by LZ-8 still needs to be further explored, especially its supposed TLR4 binding, since minor lipopolysaccharide (LPS) contamination could cause similar results in DCs and macrophages (74, 75). FIP-SJ75, which is a chimera composed of LZ-8, FIP-fve and FIP-vvo (19), triggered similar cytokine expression profiles in macrophages as seen for LZ-8 (shown in **Table 3**). Its underlying mechanism was still unknown, which needs further investigation.

FIP-fve is also a potent T-cell activator, mediating its effects via cytokine regulation of p38 mitogen-activated protein kinase (MAPK), especially IFN-γ secretion (64). Besides, FIP-fve stimulates IFN-γ transcriptional expression in human peripheral blood mononuclear cells (hPBMCs) via the modulation of Ca^{2+} release and the activation of PKCα (65). Notably, p38 MAPK activation, PKC pathways, and Ca^{2+} flow are vital in both FIP-fve and LZ-8 mediated cytokine transcriptional expression

TABLE 3 | Activation of immune cells induced by Fve-type FIPs.

FIPs	Induction of cell proliferation	Cytokines secretion	Cytokines expression	Cell adhesion molecules	References
LZ-8	Mouse splenocytes; hPBLs; T cell (monocyte dependent); hPBMCs	IFN-γ$^{\uparrow}$, TNF-α$^{\uparrow}$, IL-1β$^{\uparrow}$, IL-2$^{\uparrow}$, IL-12 p40$^{\uparrow}$, IL-12p70$^{\uparrow}$, IL-23$^{\uparrow}$, IL-4^{N}	CCL2$^{\uparrow}$, IL-10$^{\downarrow}$, CXCL10$^{\downarrow}$, IL-6^{N}	CD25^{+}(T cells)$^{\uparrow}$; IL-2R (T cells)$^{\uparrow}$; ICAM-1 (PBLs)$^{\uparrow}$; CD54 (T cells)$^{\uparrow}$; HLA-DR (DCs)$^{\uparrow}$, CD80 (DCs)$^{\uparrow}$, CD86 (DCs)$^{\uparrow}$, CD83 (DCs)$^{\uparrow}$, CD44 (T cells)$^{\uparrow}$, CD154 (T cells)$^{\uparrow}$, CD86 (macrophages)$^{\uparrow}$; MHCII (macrophages)$^{\uparrow}$	(57–63)
FIP-fve	hPBLs (G1/G0 to S)	IL-2$^{\uparrow}$, IFN-γ$^{\uparrow}$, IL-10$^{\uparrow}$, TGF-β$^{\uparrow}$, IL-22$^{\uparrow}$, IL-4^{N}, IL-5$^{\downarrow}$, IL-6$^{\downarrow}$, IL-13$^{\downarrow}$, IL-17$^{\downarrow}$		ICAM-1 (hPBMCs)$^{\uparrow}$, IL-5R (eosinophils)$^{\downarrow}$, CD95 (eosinophils)$^{\uparrow}$, MHCI (PBMCs)$^{\uparrow}$, MHCII (PBMCs)$^{\uparrow}$, CD80 (PBMCs)$^{\uparrow}$	(4, 64–71)
FIP-vvo	hPBLs		IL-2$^{\uparrow}$, IL-4$^{\uparrow}$, IFN-γ$^{\uparrow}$, TNF-α$^{\uparrow}$, LT$^{\uparrow}$, IL-1^{N}, IL-3^{N}, IL-5^{N}, IL-6^{N}	IL-2R (mouse splenocytes)$^{\uparrow}$	(24)
FIP-gsi			IL-2$^{\uparrow}$, IL-3$^{\uparrow}$, IL-4$^{\uparrow}$, IFN-γ$^{\uparrow}$, TNF-α$^{\uparrow}$, IL-1α^{N}, IL-5^{N}, IL-6^{N}, LT^{N}	IL-2R (mouse splenocytes)$^{\uparrow}$	(14)
FIP-cru		IL-2$^{\uparrow}$			(53)
FIP-gaps	Mouse splenocytes	IL-2$^{\uparrow}$, IFN-γ$^{\uparrow}$			(10)
FIP-SJ75	RAW264.7 cells		TNF-α$^{\uparrow}$, IL-6$^{\uparrow}$, IL-10$^{\uparrow}$, TGF-β1$^{\uparrow}$,		(19)
FIP-ltis			IL-1β$^{\downarrow}$, IL-6$^{\downarrow}$, TNF-α$^{\downarrow}$	CD4^{+}(T cells)$^{\uparrow}$; CD25^{+}(T cells)$^{\uparrow}$	(21)
FIP-nha	Mouse spleen lymphocyte	IL-2$^{\uparrow}$			(72)
FIP-ppl	Mouse splenocytes	IL-2$^{\uparrow}$			(9)
FIP-tvc			IL-1α$^{\uparrow}$, IL-2$^{\uparrow}$, IL-5$^{\uparrow}$, IL-6$^{\uparrow}$, TNF-α$^{\uparrow}$, LT$^{\uparrow}$, IL-3^{N}, IL-4^{N}, IFN-γ^{N}	IL-2R (mouse splenocytes)^{N}	(23)

$^{\uparrow}$*In the superscript means up-regulation.*
$^{\downarrow}$*In the superscript means down-regulation.*
^{N}*In the superscript means no significant change.*
(Cells) in which the adhesion molecules were detected.

(57, 64). FIP- fve initially induces Ca^{2+} release which results in facilitating the activation of Ca^{2+}-dependent PKC-α (65), while the mechanism underlying Ca^{2+} influx in LZ-8 treated T cells is not known (57). Meanwhile, both FIP-fve and LZ-8 can aggregate hPBLs and consequently increase the intercellular cell adhesion molecule (ICAM)-1 expression, which is associated with increasing IFN-γ, TNF-α, IL-1β secretion levels (30, 60), and may contribute to their immunomodulation properties.

Anti-allergic and Anti-inflammation Effects

Fve-type FIPs have been studied for their anti-allergic and anti-inflammatory properties for quite a few years. These studies focus on asthma, airway inflammation, food allergy, systemic anaphylaxis reactions, and other graft-tolerance or inflammation reactions.

Allergic asthma is a chronic airway inflammation, which would cause activation of $CD4^{+}$ T cell, eosinophils, and IgE-producing B cells, polarize T helper (Th)2 cells, as well as induce Th2 cytokines (such as IL-4, IL-5, IL-13) and secretion of other cytokines (IL-17, IL-33, IL-25) (76, 77). FIP-fve could suppress allergen-induced asthma, airway inflammation (66, 67, 78, 79), respiratory syncytial virus (RSV) replication, RSV-induced inflammation (80), as well as eosinophil-related allergic inflammation *in vitro* or *in vivo* (68). More specifically, in allergen-induced asthma or airway inflammation mice models, both pre-treatment and post-treatment with orally administrated FIP-fve suppressed the airway hyperresponsiveness in allergen-sensitized mice (66, 79). Upon methacholine challenge, significantly decreased the number of infiltrating inflammatory cells (neutrophils and eosinophils) as well as secretion of IL-17 and Th2 cytokines (IL-4, IL-5, IL-13), and increased Th1 cytokines (IFN-γ, IL-10, IL-12, IL-22, TGF-β) production in bronchoalveolar lavage fluid and serum (66, 67, 79). In addition, allergen-specific immunoglobulin IgE in serum was significantly decreased, whereas the serum IgG2a level increased significantly (66, 67, 79). Even the structural changes of inflammatory lung tissue would become nearly normal via oral FIP-fve treatment based on lung histopathological studies (66). Regarding RSV-related disease, pre-treatment with FIP-fve inhibited RSV replication after 24 h infection *in vitro*, and oral administered FIP-fve decreased RSV-induced airway hyperresponsiveness, airway inflammation, and IL-6 expression in bronchoalveolar lavage fluid of RSV-infected mice (80). What's more, in eosinophil-related allergic inflammation, FIP-fve can inhibit IL-5-mediated survival of eosinophils through down-regulating IL-5Rα expression on the cells' surface, and enhancing eosinophil apoptosis via down-regulation of BCL-XL [a pro-survival protein in apoptosis regulating BCL-2 protein family (81)] and pro-caspase 3 expressions *in vitro* (68). In summary, oral FIP-fve treatment

in mice is described to exert beneficial effects on both airway allergic or inflammatory symptoms, as well as on secondary makers such as secreted cytokines, except for eosinophil-related allergic inflammation.

Hsieh et al. intraperitoneally injected ovalbumin to mimic food allergy in a murine model. Oral administration of FIP-fve during allergen sensitization upregulated IFN-γ and downregulated IL-5 expressions in splenocytes, decreased ovalbumin-specific IgE response, and enhanced IgG2a response, which is similar to airway inflammation (82). Besides, it could protect the mice from systemic anaphylaxis-like symptoms after subsequent oral challenge with the same allergen (82).

Allergic asthma, IgE mediated food allergy and symmetric anaphylaxis reaction are all type I hypersensitivity reactions involving antibody-mediated immune cell responses to an allergen (83). However, the Arthus reaction is a type III hypersensitivity reaction that is immune complex-mediated, and involves the deposition of antigen/antibody complexes in the vascular walls (83). LZ-8 and FIP-fve could suppress bovine serum albumin-induced Arthus reaction and systemic anaphylaxis reaction in mice, which was explained by reduction of antibody production (4, 84). Fip-vvo significantly reduced the production of bovine serum albumin-induced Arthus reaction in mice *in vivo*, whereas there was no apparent effect in the prevention of systemic type I anaphylaxis reactions (24). Mechanistically, FIP-vvo induced mostly Th1-specific transcriptional expression of cytokines (IL-2, IFN-γ, and LT), next to the transcription of Th2-specific IL-4 (within 4 h) in mouse spleen cells (24), while there is no information about the secretion of cytokines. In conclusion, the immunomodulatory activity of FIP-vvo may, to some extent, be lower than FIP-fve or LZ-8.

Other benefits of FIPs include suppression of local swelling of mouse footpads by FIP-fve (4). LZ-8 suppressed effects in allogeneic tissue transplantation without side effects (61), helped increase immunity on leukopenia (low white blood cell count) induced by cyclophosphamide in mice (85), and improved both non-alcoholic fatty liver disease and early atherogenesis (fat-deposits in the arteries) because of its anti-inflammatory effect (86). FIP-lti1 and FIP-lti2 have been shown to mitigate ConA-induced liver oxidative injury (21). FIP-gmi was recently found to exert anti-inflammatory effects on neuron/glia cells (87), human fibrotic buccal mucosal fibroblasts (88), as well as intestinal mucosa and the tongue (89).

As Tumor Vaccine or Adjuvant

LZ-8 may be a promising adjuvant to enhance the efficacy of DNA vaccines by activating DCs. DCs activation could induce antigen-specific T cell activation, which contributed to Th1 and cytotoxic T lymphocyte responses induced by the vaccine against mouse bladder tumor (73). FIP-fve might help tumor immunotherapy via both innate and adaptive immunity. $CD4^+$ T cells, $CD8^+$ T cells, and IFN-γ play critical roles in conferring the anti-tumor effects. More specifically, co-immunized mice by tumor antigen and FIP-fve showed induction of antigen-specific antibodies and increased the expansion of antigen-specific IFN-γ-producing $CD4^+$ T cells and $CD8^+$ T cells, leading to an enhanced antigen-specific humoral and cellular type 1 anti-tumor immune response (90). Oral administration of FIP-fve significantly increased the tumoricidal capacity of peritoneal macrophages and tumor-specific splenocytes, and up-regulated the expression levels of MHC class I and II molecules and costimulatory molecule CD80 on peripheral blood mononuclear cell to inhibit tumor growth and angiogenesis (91). Oral treatment of FIP-fve did not influence body weight, and the tumoricidal effect of FIP-fve was significantly decreased when the mice were co-injected with IFN-γ neutralization, confirming that FIP-fve exerts its function via immune, rather than via a cytostatic mechanism (91).

Immunomodulatory Activity of Other Subgroups of FIPs

The other four subgroups of FIPs were identified to modulate macrophage activity by regulating cytokine and chemokine production, activating signaling pathways (28, 29, 33), and/or M1 (classically activated macrophages) polarization (see **Table 4**). Besides, some of them could activate lymphocytes or enhance lymphocytes activation (see **Table 4**). As shown in **Figure 4**, FIPs mentioned in the yellow arrow on the left side (APP, PCiP, ACA, PCP, TVC, TFP, and PEP 1b) can induce an LPS-mimicking pro-inflammatory response or enhance the response, while others (YZP and HEP3; right-hand side) could suppress LPS-induced responses (similar with Fve-type FIPs) or inhibit tumor growth indirectly via gut microbiota. However, most research used native FIPs extracted from fungi, and in some cases there was no check for other immunomodulatory compounds (especially endotoxin contamination) reported, which may have biased outcomes.

Induction of LPS-Mimicking Pro-Inflammatory Response

LPS and other endotoxins polarize macrophages toward the M1 phenotype by binding to TLR4 and activating downstream signaling (92). This would lead to the induction of nitric oxide (NO) synthase and secretion of TNF-α and IL-6, which might contribute to increased inflammation, immune stimulation, and tumor suppression (93, 94). FIPs in the left side arrow (see **Figure 4**) could activate macrophages, or enhance the LPS-induced pro-inflammatory response toward macrophages (APP and TVC). Specifically, these FIPs could induce NO secretion or inducible nitrogen oxide synthase (iNOS) expression; up-regulate production of pro-inflammatory cytokines or chemokines; and enhance synthesis of cell adhesion molecules, phagocytosis, as well as M1 polarization (**Table 4**). Mechanistically, TLR2/myeloid differentiation primary response (MyD)88 may play a critical role in ACA-induced macrophage activation and polarization (26). The TLR2-triggered NF-κB activation would lead the expressions of express M1 related genes (26). PCP, TFP, and PEP 1b all rely on the TLR4-mediated NF-κB signaling pathway with the involvement of MyD88 to induce expression of cytokines and chemokines in macrophages (28, 29, 33). In these specimens, endotoxins in PCP were neutralized (28); though PEP 1b could induce NO production without endotoxin (33), the content of endotoxin in PEP 1b and TFP (see **Table 4**) might have contributed to activation of macrophages via the

TABLE 4 | Activation of immune cells induced by other subgroups of FIPs.

FIPs	Cells modulation	NO induction	Cytokines/chemokines secretion	Cytokines/chemokines expression	Cell adhesion molecules	Endotoxin contamination	References
APP	Enhance activation of macrophages	NO$^{\uparrow}$	IFN-γ$^{\uparrow}$			NT	(30)
	Murine splenocytes proliferation$^{\uparrow/\downarrow}$		TNF-α$^{\uparrow}$				
PCP	Macrophage activation	iNOS$^{\uparrow}$	TNF-α$^{\uparrow}$, IL-1β$^{\uparrow}$	IL-6$^{\uparrow}$, IL-12$^{\uparrow}$, IL-18$^{\uparrow}$		Neutralized LPS	(28, 55)
	Mouse splenocytes proliferation		IL-2$^{\uparrow}$, IFN-γ$^{\uparrow}$, TNF-α$^{\uparrow}$, IL-4^{N}, IL-5^{N}	IL-4$^{\uparrow}$, IL-5$^{\uparrow}$	CD44 (T cells)$^{\uparrow}$, CD69 (T cells)$^{\uparrow}$		
ACA	M1 polarization and differentiation	iNOS$^{\uparrow}$, NO$^{\uparrow}$	TNF-α$^{\uparrow}$, IL-1β$^{\uparrow}$, IL-12$^{\uparrow}$	TNF-α$^{\uparrow}$, IL-1β$^{\uparrow}$, IL-6$^{\uparrow}$, IL-12$^{\uparrow}$, IL-10^{N}, CCL3$^{\uparrow}$, CCL4$^{\uparrow}$, CCL5$^{\uparrow}$, CCL10$^{\uparrow}$, CCL17^{N}, CCL22^{N}, CCL24^{N}	MHCII$^{\uparrow}$, CD86$^{\uparrow}$, CD80^{N}	NT	(26)
PCiP	Macrophage activation	NO$^{\uparrow}$	TNF-α$^{\uparrow}$			NT	(32)
	Murine splenocytes proliferation$^{\uparrow/\downarrow}$		IFN-γ$^{\uparrow}$				
TVC	Enhance macrophage activation	NO$^{\uparrow}$	TNF-α$^{\uparrow}$			NT	(34)
	Enhance the proliferation of splenocytes and hPBLs						
TFP	M1-polarization		TNF-α$^{\uparrow}$, IL-1β$^{\uparrow}$, IL-1ra$^{\uparrow}$, IL-12$^{\uparrow}$	CCL3$^{\uparrow}$, CXCL10$^{\uparrow}$, CCL4^{N}, CCL5^{N}, CCL17^{N}, CCL24^{N}	CD86$^{\uparrow}$, MHCII$^{\uparrow}$, CD80^{N}	0.14 EU/mg	(29)
PEP 1b	M1-polarization	NO$^{\uparrow}$, iNOS$^{\uparrow}$	TNF-α$^{\uparrow}$, IL-1β$^{\uparrow}$, IL-6$^{\uparrow}$, IL-8^{N}			0.570 ± 0.085 EU/mL	(33)
YZP	B cell activation and differentiation		IL-6$^{\uparrow}$, IL-10$^{\uparrow}$		CD1d$^{\uparrow}$, CD25$^{\uparrow}$, CD69$^{\uparrow}$	Less than 0.013 EU/mg	(27)
	Suppress LPS-activated macrophage		TNF-α$^{\downarrow}$, IL-1β$^{\downarrow}$	TNF-α$^{\downarrow}$, IL-1β$^{\downarrow}$, IL-6$^{\downarrow}$, IL-12$^{\downarrow}$, IL-10$^{\uparrow}$			
HEP3	Splenocytes proliferation, and T cells proliferation and differentiation		GM-CSF$^{\uparrow}$, IFN-γ$^{\uparrow}$, IL-4$^{\uparrow}$, IL-12$^{\uparrow}$, IL-17$^{\uparrow}$, TNF-α$^{\downarrow}$, IL-10$^{\downarrow}$, VEGF$^{\downarrow}$		CD3$^{\uparrow}$, CD4$^{\uparrow}$, CD8$^{\uparrow}$, CD28$^{\uparrow}$	NT	(31)
	Suppress LPS-activated macrophage	NO$^{\downarrow}$, iNOS$^{\downarrow}$	TNF-α$^{\downarrow}$, IL-1β$^{\downarrow}$, IL-6$^{\downarrow}$				

$^{\uparrow}$*In the superscript means up-regulation.*
$^{\downarrow}$*In the superscript means down-regulation.*
^{N}*In the superscript means no significant change.*
$^{\uparrow/\downarrow}$*Indicates that APP and PCiP can proliferate splenocytes, but suppress concanavalin A-induced proliferation in vitro (30, 32).*
NT means no test mentioned in the reference.
(Cells) in which the adhesion molecules were detected.

TLR4 signaling pathway or enhanced its activation (74, 75). Meanwhile, PEP1b depended on the MAPK signaling pathway as well. Since TNF receptor-associated factor (TRAF)6 is involved in both TLR2/NF-κB and TLR4/NF-κB signaling pathways (95–98), it may be the connecting factor in these two signaling pathways (see **Figure 4**).

These FIPs also show effects on splenocytes. APP and PCiP both can activate murine splenocytes, but suppress concanavalin A-induced proliferation of splenocytes *in vitro* (30, 32). The mechanism for this may be competition for the same mediators in signaling pathways (30, 32). Besides, PCiP may decrease 3-(4,5-dimethyldiazol-2-yl)-2,5 diphenyl tetrazolium bromide (MTT) metabolism of concanavalin A-induced splenocytes without the induction of cytotoxicity (32). TVC enhanced the proliferation of splenocytes and hPBLs, while it could not proliferate $CD4^{+}$ and $CD8^{+}$ T cells (34). However, PCP could activate $CD8^{+}$ T cells, induce the secretion of IFN-γ and IL-2 in $CD4^{+}$ T cells, as well as regulate Th1/Th2 response. More specifically, oral-treatment with PCP could increase IgG2a and Th1-related cytokines in splenocytes, and decrease IgG1, IgE, and Th2-related cytokines in an atopic dermatitis mice model. Further, PCP increased T-bet (a transcription factor that stimulates Th1 response) while inhibiting Th2 response (99) and STAT4 (Th1 transcription factor) expression (55). These observations indicate that PCP might be a regulator of Th1/Th2 balance that favors the Th1 response.

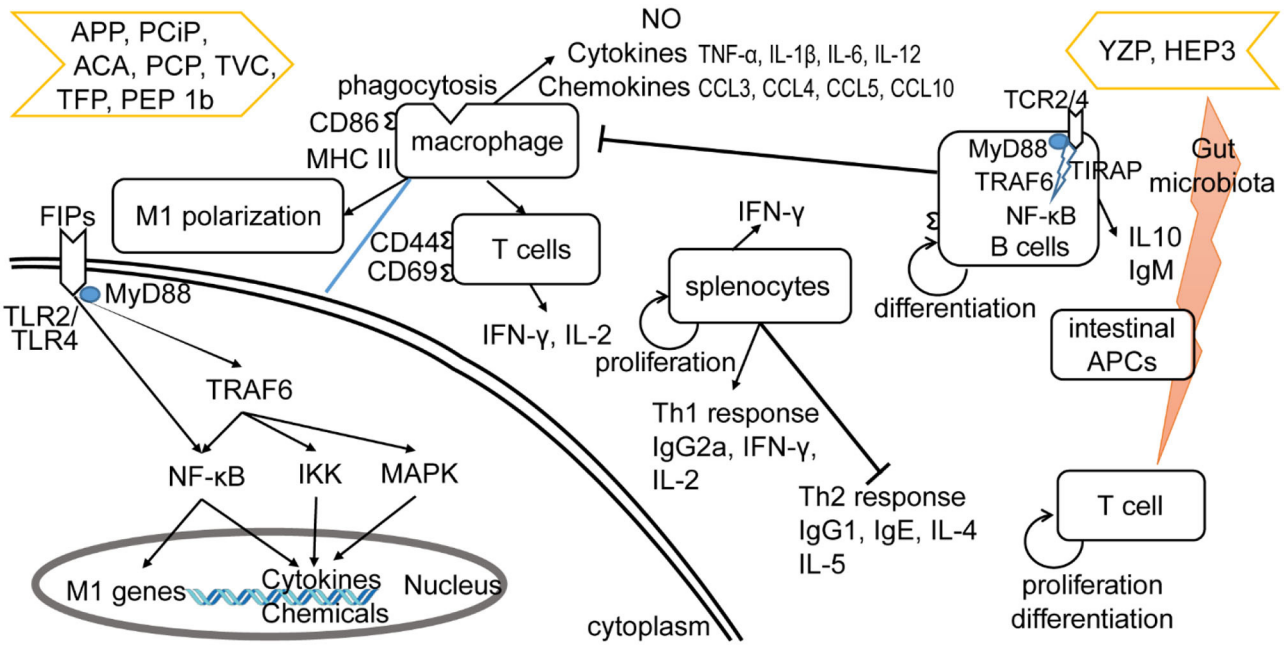

FIGURE 4 | Effects of other type of FIPs on the immune system. FIPs mentioned on the left side (APP, PCiP, ACA, PCP, TVC, TFP, and PEP 1b) induce an LPS-mimicking proinflammatory response or enhance the response. More specific, FIPs in the left side could activate macrophages, T cells, and splenocytes. The mechanism of macrophage activation has been shown in down-left part. FIPs in the right side (YZP and HEP3) could reduce activation of LPS-activated macrophages, suppress inflammatory cytokine expression, and show other anti-inflammatory and anti-tumor effects via B cell regulation (YZP) or gut microbiota (HEP3).

Anti-inflammatory and Anti-tumor Effects

YZP and HEP3 could reduce activation of LPS-activated macrophages, suppress inflammatory cytokine expression, and show other anti-inflammatory and anti-tumor effects as well (27, 31). YZP could modulate humoral immunity through regulating B-cell activation and suppressing macrophages via B cell in a mixed leukocyte reaction. More specifically, it can enhance IL-10 and IgM secretion, CD25, CD69, and CD1d expression in B cells, and trigger B-reg differentiation, for which the signaling pathway relies on TLR2/NF-κB and TLR4/NF-κB (see **Figure 4**). For instance, YZP was tested as a colonic inflammatory therapy on an acute colitis murine model, and the effects observed were primarily by B cell regulation (27). Comparably, HEP3 showed stronger potential as a colonic inflammatory treatment, and even in tumor therapy (31). It could suppress LPS-activated macrophages by reducing inflammatory cytokines and downregulating the expression of inducible NO synthase and NK-κB p65 *in vitro*. Further investigation showed that HEP3 could induce proliferation and differentiation of T cells via the gut microbiota, stimulate intestinal APCs in an inflammatory model in mice, and act as anti-tumor inhibitor via an immune mechanism in tumor-grafted mice.

Hemagglutination Properties of FIPs

Quite a few types of FIPs can agglutinate mouse or rat, rabbit, sheep, or human red blood cells (RBCs) (see **Table 5**). There are some conflicting data, and some variations in e.g., threshold values in the chart, maybe because of interference of artifacts. In the hemagglutination test, concanavalin A and phytohemagglutinin (both lectins from legume plants) are commonly used as positive control while PBS is always used as a negative control. Since lectin recognition of sugars is rather specific, most agglutination reactions induced by lectins can be inhibited by monosaccharides or oligosaccharides (106). Nevertheless, no inhibition of hemagglutination via several kinds of mono- and disaccharides has been described in FIP-fve (4), LZ-8 (6), APP (30), respectively. FIPs resemble lectins in their hemagglutinating properties but in other features they act clearly different from lectins (12). FIPs may interact with other types of saccharides, or the mechanism behind FIP-induced agglutination is different. Specifically, Fve-type FIPs have a putative carbohydrate binding module (CBM)34-like structure (for details, please see CBM34-Like Structure) linked to glycan chain-binding properties (69).

STRUCTURE AND FUNCTION RELATIONSHIP

The protein structures of Fve-type FIPs are all modeled based on the crystal structures of FIP-fve (PDB code: 1OSY), LZ-8 (PDB code: 3F3H), and FIP-gmi (PDB code: 3KCW). No other FIP-structures have been described yet. Evaluation of FIPs' bioactivity has been done with many read-out systems. Therefore, no conclusive conclusions can be drawn so far. However, the impact of key residues, CBM34-like structure, oligomeric states, and glycosylation have been described to some extent.

TABLE 5 | The FIPs concentration required [μg/ml] to hemagglutinate different origins of RBCs.

FIPs	Origin of RBCs				References
	Mouse/(rat)	Rabbit	Sheep	Human	
LZ-8	NT	NT	6.25	F	(84)
rLZ-8 (*E. coli*)	10	NT	NT	F	(100)
rLZ-8 (*P. pastoris*)	10/1.25	2.5	12.5/20	0.16 (O type)	(12, 100, 101)
rLZ-9 (*P. pastoris*)	1.25	2.5	5	0.156 (O type)	(12)
FIP-fve	NT	NT	F	2/12.5	(4, 71)
rFIP-fve (*E. coli*)	NT	NT	NT	2 (O type)	(102)
rFIP-fve (*P. pastoris*)	F	5	F	2	(12, 103)
OsDp2Fve (rice cell)	NT	NT	NT	F	(104)
FIP-vvo	1.1/0.52 (rat)	0.13	NT	F	(24)
rFIP-vvo (*P. pastoris*)	0.2 (rat)	NT	1.0	F	(105)
rFIP-nha (*P. pastoris*)	0.625	5	0.62	0.16 (O type)	(12)
rFIP-nha (*E. coli*)	NT	1.28	NT	100	(72)
FIP-lrh (*E. coli*)	5	NT	NT	5	(20)
FIP-cru	2	NT	2	F	(53)
rFIP-gap1 (*P. pastoris*)	1	NT	1	1	(10)
rFIP-gap2 (*P. pastoris*)	8	NT	8	8	(10)
rFIP-ppl (*E. coli*)	NT	64	NT	F	(9)
rFIP-tvc (*E. coli*)	1/2 (rat)	NT	NT	NT	(23)
APP	4	NT	NT	NT	(30)
ACA	F	NT	NT	F	(26)
PciP	F	NT	NT	NT	(32)
PCP	F	NT	NT	NT	(28)
TFP	F	NT	NT	NT	(29)
TVC	F	NT	NT	NT	(34)

F means fail to aggregate the red blood cell.
NT means not tested.

CBM34-Like Structure

CBM structures always exist in glycoside hydrolases to promote substrate association (107). The CBM family has 86 members listed in CAZy (http://www.cazy.org/) (108). FIP-fve mimics CBM34, a β-sandwich folding family that shows granule starch-binding functionality (109). W24, T28, D34, T90, I91, and W111 of FIP-fve (see **Figures 2A**, **5**) are the key residues for the CBM34-like structure formation (69). This structure may contribute to hemagglutination and induction of IFN-γ secretion in hPBMCs (69). Hemagglutination activity seems to be specifically related to W24, D34, I91, and W111, while the immunomodulatory activity is more associated with W24, D34, T90, and W111 that are essential for ligand-like glycoproteins binding interaction on the surface of hPBMCs (69). Liu et al. also tested the inhibition effects of 15 kinds of saccharides in hPBMCs: N-acetylneuraminic acid, maltotriose, cyclodextrin, and dextrin could inhibit IFN-γ secretion significantly (69). This suggests that the CBM34-like structure might have a preference in sugar binding. Interestingly, 6 kinds of mono- and disaccharides could not inhibit hemagglutination by FIP-fve (4). Amid these saccharides, N-acetylgalactosamine could weakly block FIP-fve-induced IFN-γ production of hPBMCs at 30 mM, while there is no impact on hemagglutination even at 0.1 M (4, 69).

In the amino acid composition of the predicted CBM34-like structure, T28 is only present in FIP-fve, while there are small position shift or residues variation in other Fve-type FIPs (**Figure 5**), which may impact their hemagglutination (**Table 5**) and IFN-γ inducing properties (**Table 3**). Prediction of the CBM34-like structure has been confirmed in FIP-lrh, consisting of W25, D35, I92, W110, as well as two residues variation, N29 and K90 (see **Figure 5**). Docking predictions of FIP-lrh and FIP-fve on several glycans (commonly found on cellular surfaces) showed their binding energy, although the binding energy of FIP-lrh is lower than FIP-fve (20). Evidentially, the threshold of FIP-fve on human erythrocyte agglutination was 2 μg/mL, while the threshold of FIP-lrh was up to 5 μg/mL (20). Although not only the structure contributes to erythrocytes agglutination, the glycan type on the erythrocyte cell surface can also influence the agglutination. This may explain why the same FIPs behave differently on erythrocytes from different species, and that there is variation in thresholds for various types of FIPs on the same type of erythrocytes (see **Table 5**). Meanwhile, IFN-γ secretion in hPBMCs induced by FIP-fve is related to the interaction with glycans on the cell surface and the supposed CBM34-like structure (69). It is tempting to investigate cell surface glycosylation further and to see whether bioactivities of FIPs can be affected by such modifications.

Oligomeric States

Some articles hint that the dimerization state of Fve-type FIPs plays a vital role in their activity. For example, the monomer of FIP-gts did not induce cytokine production on hPBLs (17, 111). L5, F7, L9, and the N-terminal α-helix of Fip-gts, which affects its dimerization, are essential in inducing IL-2 and IFN-γ secretion (17). L10, W12, and D45, which are located in the interface of dimerized LZ-8, are pivotal in triggering IL-2 secretion on hPBLs (110). Furthermore, the crystal structures of FIP-fve (43, 112) and LZ-8 (113) also show that the N-terminal α-helix is highly conserved in Fve-type FIPs, and the conserved N-terminal β-sheet may sustain the dimerization state via domain swapping (46).

Glycosylation Modification

The effects of glycosylation of FIPs manifest in the induction of cytokine production/secretion, cell adhesion molecules expression, and lymphocyte proliferation. For instance, the level of IL-2 induction resulting from the non-glycosylated rFIP-gts was lower than for the glycosylated form (8, 114), indicating that the post-translational processing of rFIP-gts might play an essential role in enhancing and maintaining the required immunomodulatory activity on T lymphocytes. Besides, there were more noticeable cellular lymphocytes aggregates of murine splenocytes when treated with glycosylated rFIP-gts than with the non-glycosylated form (8). As reported in literature, hPBL cellular aggregation coincides with the upregulation of ICAM-1 expression and T cell proliferation (115–117). Therefore, the glycosylated rFIP-gts might be more potent in the induction of ICAM-1 expression and T cell proliferation.

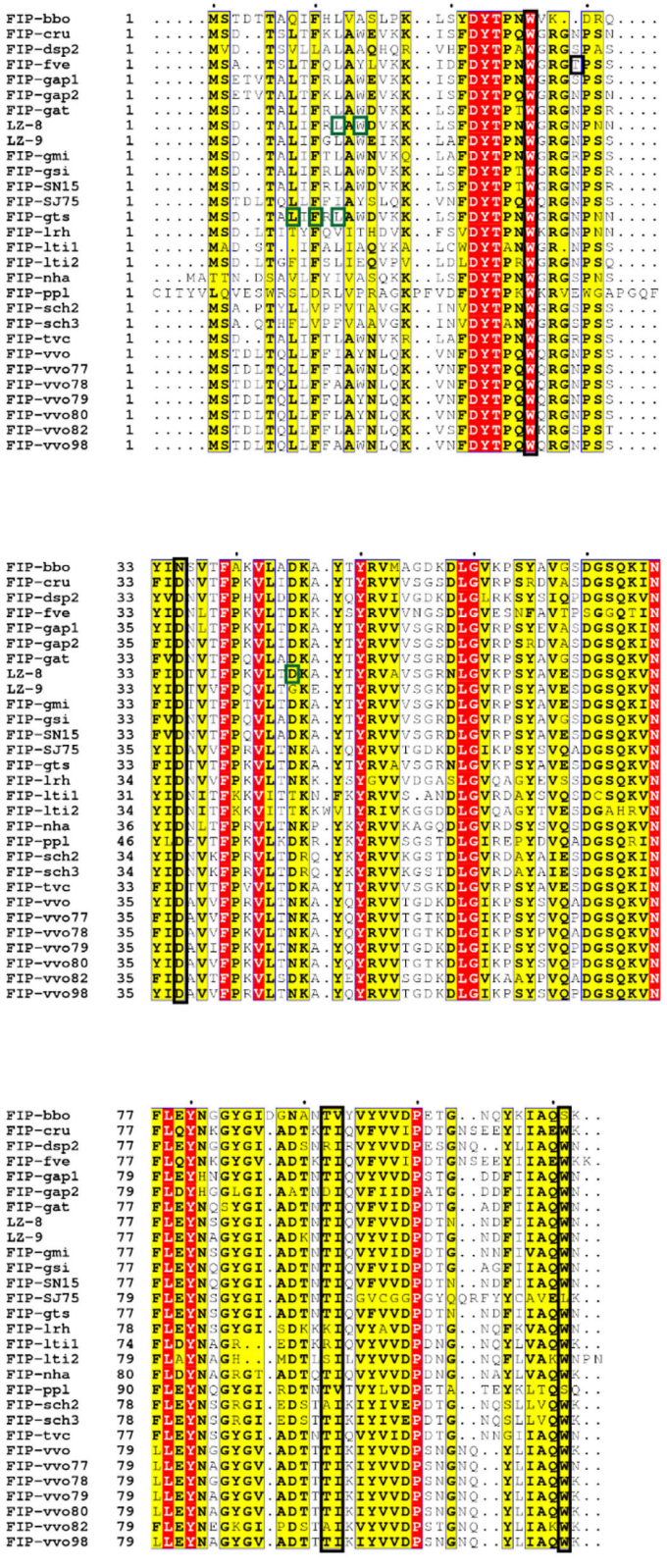

FIGURE 5 | Sequence alignment of Fve-type FIPs (**Table 1**) via ESPript (http://espript.ibcp.fr/ESPript/cgi-bin/ESPript.cgi) with vital molecules or domains indicated [adapted from (110)]. The black blocked amino acids may be essential for hemagglutination and induction of IFN-γ in hPBMCs, which has been investigated on FIP-fve (W24, T28, D34, T90, I91, and W111) (69) and confirmed on FIP-lrh (W25, D35, I92, and W110) (20); the green blocked units are imported for IL-2 expression induced by LZ-8 (L10, W12, and D45) (110) or IL-2 and IFN-γ secretion induced by FIP-gts (L5, F7, and L9) (17).

Comparably, only native PCP (glycosylated fraction) was able to increase the cell surface expression of TLR4 in peritoneal macrophages from wild type mice; deglycosylated PCP, or LPS cannot (28). This evidence indicated that PCP-induced macrophage activation was directly correlated with the polysaccharide moiety of PCP. In contrast, in Sheu's research, both the native ACA (glycoprotein) and rACA (expressed by *E. coli*) showed dose-dependent induction of TNF-α in macrophages, and the level of TNF-α induction was higher in response to rACA than to native ACA (26). Similar activation differences were observed for IL-1β and NO by the presence of ACA (26). The most apparent difference between PCP and ACA in activating macrophages is in the involved receptors on the cell surface. PCP activates macrophages via the TLR4/MyD88 signaling pathway (28), while ACA activates macrophages via the TLR2/MyD88 signaling pathway and induces M1 polarization and differentiation (26). There is no evidence showing that FIPs are taken up by a macrophage, and the TLR2/MyD88 as well as TLR4/MyD88 signaling pathway will not induce endocytosis (97, 98). The different sensitivity of TLR4 and TLR2 for activation of the signaling pathway, when being exposed to glycosylated or other types of FIPs, may play a role. Hence, more research is needed to elucidate the further mechanisms of FIPs and the role of glycosylation. Another kind of explanation may be LPS contamination, as rACA was expressed in *E. coli,* and no LPS investigation or removal method is mentioned in their study (26).

PROSPECTS

Fungi contain many bioactive molecules, including polysaccharides, lectins, and FIPs. Until now, more than 38 types of FIPs have been described, which can be divided into 5 subgroups. However, the list of Fve-type FIPs and Cerato-type FIPs could be expanded in the future. For instance, FIP-gja from *Ganoderma japonicum* (Genbank: AAX9824) could be a Fve-type FIP, ACA2 from *Antrodia camphorate* (GenBank: ABE01080) and TVCs (GenBank: EIW60955.1, EIW60914.1, EIW60949.1) from *T. versicolor* would be expected to belong to Cerato-type FIPs.

Fve-type FIPs are highly interesting because of their anti-allergic, anti-inflammatory, and anti-cancer bioactivity, especially as they have not shown side-effects in allergy treatment or as an adjuvant to attack drug-resistant tumor cells based on current findings. Co-treatment of medicine and Fve-type FIPs is important to investigate as well, since Fve-type FIPs have shown intense immunomodulatory activity and promising options in drug-resistant tumor cells. Research has shown that some Fve-type FIPs can retain their bioactivity upon oral administration. That means they are rather digestion-resistant, or that some vital domain, responsible for their bioactivity, reaches the intestinal tract intact. In some articles, the thermal stability and digestion resistance of FIPs have been described (111, 118–120). Additional research will deliver details about essential domains as well as their utilization.

Regarding the other four subgroups, their bioactivity is obviously worth further study. Those FIPs which can induce/enhance an LPS-mimetic response could be used as an adjuvant to enhance the immune response in the host. FIPs that can suppress an LPS-induced response could be used in anti-inflammatory therapy. Two types of FIPs show benefits for reducing colonic inflammation, and even toward cancer via the gut microbiota. It will be meaningful and useful to deeper investigate their mechanisms and applications.

Up to now, only three Fve-type FIP structures have been solved. Several articles show protein structure and function relationships and use the amino acid sequence to predict their function or activity (121–123). This suggests that more structural information on Fve-type FIPs, as well as on the other subgroups of FIPs, will increase comprehension of their bioactivity. Although a precise mechanism is still unknown, there are relevant illustrations of some structural-related bioactive functions. For instance, FIP-gts (124), FIP-nha (125), and LZ-8 (126) can be transported into tumor cells and exert toxicity, and LZ-8 could even enter the nucleus of NB4 cells (127). The way they distinguish tumor cells and normal cells, the vital structure which enters the cell and behaves toxically, and the mechanism of their anti-tumor activity need further investigation. Regarding the glycosylation modification, multiple results indicate that it may influence FIPs' bioactivity, which has been describing in "4.3 Glycosylation modification." Meanwhile, there are more FIPs shown in **Table 2** with potential glycosylation sites, which could be further investigated to shed further light on the influence of glycosylation on bioactivity of FIPs systematically.

AUTHOR CONTRIBUTIONS

YL and SB-N wrote the first draft of the paper. All authors read and contributed to the final version of the paper.

FUNDING

This study was supported by the Dutch Ministry of Agriculture Nature and Food Quality via the knowledge- and innovation KB37 program Healthy and Safe food systems (Grant Number KB-37-001-007), and the National Key Research and Development Plan modern food processing and food storage and transportation technology and equipment (No. 2017YFD0400204) from Chinese government.

ACKNOWLEDGMENTS

I would like to thank Dr. Fengjiao Xin and Dr. Yingying Xie for their nice suggestions on the review; Dr. Coen CFM Govers for his support and explanation on MHC and endotoxin contamination; and Ph.D. candidates Khandaker Md. Sharif Uddin Imam and Lei Deng for some language suggestions.

SUPPLEMENTARY MATERIAL

The Supplementary Material for this article can be found online at: https://www.frontiersin.org/articles/10.3389/fnut.2020.00132/full#supplementary-material

REFERENCES

1. Xu X, Yan H, Chen J, Zhang X. Bioactive proteins from mushrooms. *Biotechnol Adv.* (2011) 29:667–74. doi: 10.1016/j.biotechadv.2011.05.003
2. Li LD, Mao PW, Shao KD, Bai XH, Zhou XW. *Ganoderma* proteins and their potential applications in cosmetics. *Appl Microbiol Biotechnol.* (2019) 103:9239–50. doi: 10.1007/s00253-019-10171-z
3. Zhou R, Liu ZK, Zhang YN, Wong JH, Ng TB, Liu F. Research progress of bioactive proteins from the edible and medicinal mushrooms. *Curr Protein Peptide Sci.* (2019) 20:196–219. doi: 10.2174/1389203719666180613090710
4. Ko JL, Hsu CI, Lin RH, Kao CL, Lin JY. A new fungal immunomodulatory protein, FIP-fve isolated from the edible mushroom, *Flammulina velutipes* and its complete amino acid sequence. *Eur J Biochem.* (1995) 228:244–9. doi: 10.1111/j.1432-1033.1995.tb20256.x
5. Li QZ, Wang XF, Zhou XW. Recent status and prospects of the fungal immunomodulatory protein family. *Crit Rev Biotechnol.* (2011) 31:365–75. doi: 10.3109/07388551.2010.543967
6. Tanaka S, Ko K, Kino K, Tsuchiya K, Yamashita A, Murasugi A, et al. Complete amino acid sequence of an immunomodulatory protein, ling zhi-8 (LZ-8), an immunomodulator from a fungus, *Ganoderma lucidium*, having similarity to immunoglobulin variable regions. *J Biol Chem.* (1989) 264:16372–7.
7. Wang Y, Gao YN, Bai R, Chen HY, Wu YY, Shang JJ, et al. Identification of a novel anti-cancer protein, FIP-bbo, from *Botryobasidium botryosum* and protein structure analysis using molecular dynamic simulation. *Sci Rep.* (2019) 9:5818. doi: 10.1038/s41598-019-42104-1
8. Wu TY, Chen HA, Li FY, Lin CT, Wu CM, Hsieh FC, et al. High-level expression, purification and production of the fungal immunomodulatory protein-gts in baculovirus-infected insect larva. *Appl Biochem Biotechnol.* (2013) 169:976–89. doi: 10.1007/s12010-012-0049-2
9. Li SY, Shi LJ, Ding Y, Nie Y, Tang XM. Identification and functional characterization of a novel fungal immunomodulatory protein from *Postia placenta*. *Food Chem Toxicol.* (2015) 78:64–70. doi: 10.1016/j.fct.2015.01.013
10. Zhou S, Guan S, Duan Z, Han X, Zhang X, Fan W, et al. Molecular cloning, codon-optimized gene expression, and bioactivity assessment of two novel fungal immunomodulatory proteins from *Ganoderma applanatum* in Pichia. *Appl Microbiol Biotechnol.* (2018) 102:5483–94. doi: 10.1007/s00253-018-9022-5
11. Xu H, Kong YY, Chen X, Guo MY, Bai XH, Lu YJ, et al. Recombinant FIP-gat, a fungal immunomodulatory protein from *Ganoderma atrum*, induces growth inhibition and cell death in breast cancer cells. *J Agric Food Chem.* (2016) 64:2690–8. doi: 10.1021/acs.jafc.6b00539
12. Bastiaan-Net S, Chanput W, Hertz A, Zwittink RD, Mes JJ, Wichers HJ. Biochemical and functional characterization of recombinant fungal immunomodulatory proteins (rFIPs). *Int Immunopharmacol.* (2013) 15:167–75. doi: 10.1016/j.intimp.2012.11.003
13. Wu M, Hsu M, Huang CS, Fu H, Huang CT, Yang CS. A 2.0 Å structure of GMI a member of the fungal immunomodulatory protein family from Ganoderma microsporum. *Protein crystallogr.* (2007) 2:132. Available online at: https://www.researchgate.net/publication/287118125_A_20_A_Structure_of_the_Fungal_Immunomodulatory_Protein_GMI_from_Ganoderma_microsporum/link/588a401da6fdccb538f1f27c/download
14. Li Q, Wang X, Chen Y, Lin J, Zhou X. Cytokines expression induced by *Ganoderma sinensis* fungal immunomodulatory proteins (FIP-gsi) in mouse spleen cells. *Appl Biochem Biotechnol.* (2010) 162:1403–13. doi: 10.1007/s12010-010-8916-1
15. Zhou X, Xie M, Hong F, Li QZ. Genomic cloning and characterization of a FIP-gsi gene encoding a fungal immunomodulatory protein from *Ganoderma sinense* Zhao et al. (Aphyllophoromycetideae). *Int J Med Mushrooms.* (2009) 11:77–86. doi: 10.1615/IntJMedMushr.v11.i1.90
16. Han F, Liu Y, Guo LQ, Zeng XL, Liu ZM, Lin JF. Heterologous expression of the immunomodulatory protein gene from *Ganoderma lucidium* in the basidiomycete *Coprinopsis cinerea*. *J Appl Microbiol.* (2010) 109:1838–44. doi: 10.1111/j.1365-2672.2010.04811.x
17. Lin WH, Hung CH, Hsu CI, Lin JY. Dimerization of the N-terminal amphipathic alpha-helix domain of the fungal immunomodulatory protein from *Ganoderma tsugae* (Fip-gts) defined by a yeast two-hybrid system and site-directed mutagenesis. *J Biol Chem.* (1997) 272:20044–8. doi: 10.1074/jbc.272.32.20044
18. Cong WR, Xu H, Liu Y, Li QZ, Li W, Zhou XW. Production and functional characterization of a novel fungal immunomodulatory protein FIP-SN15 shuffled from two genes of *Ganoderma* species. *Appl Microbiol Biotechnol.* (2014) 98:5967–75. doi: 10.1007/s00253-014-5539-4
19. Shao K-D, Mao P-W, Li Q-Z, Li L-D-J., Wang Y-l, Zhou X-W. Characterization of a novel fungal immunomodulatory protein, FIP-SJ75 shuffled from *Ganoderma lucidum*, *Flammulina velutipes* and *Volvariella volvacea*. *Food Agr Immunol.* (2019) 30:1253–70. doi: 10.1080/09540105.2019.1686467
20. Pushparajah V, Fatima A, Chong CH, Gambule TZ, Chan CJ, Ng ST, et al. Characterisation of a new fungal immunomodulatory protein from tiger milk mushroom, *Lignosus rhinocerotis*. *Sci Rep.* (2016) 6:30010. doi: 10.1038/srep30010
21. Gao Y, Wang Y, Wang Y, Wu Y, Chen H, Yang R, et al. Protective function of novel fungal immunomodulatory proteins Fip-lti1 and Fip-lti2 from *Lentinus tigrinus* in concanavalin A-induced liver oxidative injury. *Oxid Med Cell Longev.* (2019) 2019:3139689. doi: 10.1155/2019/3139689
22. Li S, Jiang Z, Xu W, Xie Y, Zhao L, Tang X, et al. FIP-sch2, a new fungal immunomodulatory protein from *Stachybotrys chlorohalonata*, suppresses proliferation and migration in lung cancer cells. *Appl Microbiol Biotechnol.* (2017) 101:3227–35. doi: 10.1007/s00253-016-8030-6
23. Li F, Wen H, Liu X, Zhou F, Chen G. Gene cloning and recombinant expression of a novel fungal immunomodulatory protein from *Trametes versicolor*. *Protein Expr Purif.* (2012) 82:339–44. doi: 10.1016/j.pep.2012.01.015
24. Hsu HC, Hsu CI, Lin RH, Kao CL, Lin JY. Fip-vvo, a new fungal immunomodulatory protein isolated from *Volvariella volvacea*. *Biochem J.* (1997) 323 (Pt 2):557–65. doi: 10.1042/bj3230557
25. Wang Y, Wa Ng Y, Gao Y, Li Y, Wan JN, Yang RH, et al. Discovery and characterization of the highly active Fungal Immunomodulatory Protein Fip-vvo82. *J Chem Inf Model.* (2016) 56:2103–14. doi: 10.1021/acs.jcim.6b00087
26. Sheu F, Chien PJ, Hsieh KY, Chin KL, Huang WT, Tsao CY, et al. Purification, cloning, and functional characterization of a novel immunomodulatory protein from *Antrodia camphorata* (bitter mushroom) that exhibits TLR2-dependent NF-kappaB activation and M1 polarization within murine macrophages. *J Agric Food Chem.* (2009) 57:4130–41. doi: 10.1021/jf900469a
27. Kuan YC, Wu YJ, Hung CL, Sheu F. *Trametes versicolor* protein YZP activates regulatory B lymphocytes-gene identification through *de novo* assembly and function analysis in a murine acute colitis model. *PLoS ONE.* (2013) 8:e72422. doi: 10.1371/journal.pone.0072422
28. Chang HH, Yeh CH, Sheu F. A novel immunomodulatory protein from *Poria cocos* induces Toll-like receptor 4-dependent activation within mouse peritoneal macrophages. *J Agric Food Chem.* (2009) 57:6129–39. doi: 10.1021/jf9011399
29. Hung CL, Chang AJ, Kuo XK, Sheu F. Molecular cloning and function characterization of a new macrophage-activating protein from *Tremella fuciformis*. *J Agric Food Chem.* (2014) 62:1526–35. doi: 10.1021/jf403835c
30. Sheu F, Chien PJ, Chien AL, Chen YF, Chin KL. Isolation and characterization of an immunomodulatory protein (app) from the jew's ear mushroom auricularia polytricha. *Food Chem.* (2004) 87:593–600. doi: 10.1016/j.foodchem.2004.01.015
31. Diling C, Chaoqun Z, Jian Y, Jian L, Jiyan S, Yizhen X, et al. Immunomodulatory activities of a fungal protein extracted from *Hericium erinaceus* through regulating the gut microbiota. *Front Immunol.* (2017) 8:666. doi: 10.3389/fimmu.2017.00666
32. Sheu F, Chien PJ, Wang HK, Chang HH, Shyu YT. New protein PCiP from edible golden oyster mushroom pleurotus citrinopileatus activating murine macrophages and splenocytes. *J Sci Food Agric.* (2010) 87:1550–8. doi: 10.1002/jsfa.2887
33. Hu Q, Du H, Ma G, Pei F, Ma N, Yuan B, et al. Purification, identification and functional characterization of an immunomodulatory protein from *Pleurotus eryngii*. *Food Funct.* (2018) 9:3764–75. doi: 10.1039/C8FO00604K
34. Li F, Wen H, Zhang Y, Aa M, Liu X. Purification and characterization of a novel immunomodulatory protein from the medicinal

mushroom *Trametes versicolor*. *Sci China Life Sci.* (2011) 54:379–85. doi: 10.1007/s11427-011-4153-2
35. Wang XF, Su KQ, Bao TW, Cong WR, Chen YF, Li QZ, et al. Immunomodulatory effects of fungal proteins. *Curr Topics Nutraceuticals Res.* (2012) 10:1–11.
36. Ariel LGG. Fungal immunomodulatory proteins in the context of biomedicine. *Front Biosci.* (2017) 9:286–306. doi: 10.2741/e803
37. Li QZ, Zheng YZ, Zhou XW. Fungal immunomodulatory proteins: characteristic, potential antitumor activities and their molecular mechanisms. *Drug Discov Today.* (2018) 24:307–14. doi: 10.1016/j.drudis.2018.09.014
38. Guex N, Peitsch MC, Schwede T. Automated comparative protein structure modeling with SWISS-MODEL andSwiss-PdbViewer: a historical perspective. *Electrophoresis.* (2009) 30:S162–73. doi: 10.1002/elps.200900140
39. Benkert P, Biasini M, Schwede T. Toward the estimation of the absolute quality of individual protein structuremodels. *Bioinformatics.* (2011) 27:343–50. doi: 10.1093/bioinformatics/btq662
40. Bertoni M, Kiefer F, Biasini M, Bordoli L, Schwede T. Modeling protein quaternary structure of homo- and hetero-oligomers beyond binary interactions by homology. *Sci Rep.* (2017) 7:10480. doi: 10.1038/s41598-017-09654-8
41. Bienert S, Waterhouse A, de Beer TAP, Tauriello G, Studer,G., Bordoli L, et al. The SWISS-MODEL Repository - new features andfunctionality. *Nucl Acids Res.* (2017) 45:D313–D9 doi: 10.1093/nar/gkw1132
42. Waterhouse A, Bertoni M, Bienert S, Studer G, Tauriello G, Gumienny R, et al. SWISS-MODEL: homology modelling of protein structures and complexes. *Nucl Acids Res.* (2018) 46:W296–W303 doi: 10.1093/nar/gky427
43. Paaventhan P, Joseph JS, Seow SV, Vaday S, Robinson H, Chua KY, et al. A 1.7A structure of Fve, a member of the new fungal immunomodulatory protein family. *J Mol Biol.* (2003) 332:461–70. doi: 10.1016/S0022-2836(03)00923-9
44. An M, Gao GF, Qi J, Li F, Liu X. Expression and crystallographic studies of a fungal immunomodulatory protein LZ-8 from a medicinal fungus *Ganoderma lucidum*. *Sheng Wu Gong Cheng Xue Bao.* (2010) 26:1563–8.
45. Vangelista L, Cesco-Gaspere M, Lamba D, Burrone O. Efficient folding of the FcepsilonRI alpha-chain membrane-proximal domain D2 depends on the presence of the N-terminal domain D1. *J Mol Biol.* (2002) 322:815–25. doi: 10.1016/S0022-2836(02)00853-7
46. Mascarenhas NM, Gosavi S. Understanding protein domain-swapping using structure-based models of protein folding. *Prog Biophys Mol Bio.* (2017) 128:113–20. doi: 10.1016/j.pbiomolbio.2016.09.013
47. de Barsottini OMR, de Oliveira JF, Adamoski D, Teixeira PJ, do Prado PF, Tiezzi HO, et al. Functional diversification of cerato-platanins in Moniliophthora perniciosa as seen by differential expression and protein function specialization. *Mol Plant Microbe Interact.* (2013) 26:1281–93. doi: 10.1094/MPMI-05-13-0148-R
48. Gaderer R, Bonazza K, Seidl-Seiboth V. Cerato-platanins: a fungal protein family with intriguing properties and application potential. *Appl Microbiol Biotechnol.* (2014) 98:4795–803. doi: 10.1007/s00253-014-5690-y
49. Higel F, Seidl A, Sörgel F, Friess W. N-glycosylation heterogeneity and the influence on structure, function and pharmacokinetics of monoclonal antibodies and Fc fusion proteins. *Eur J Pharm Biopharm.* (2016) 100:94–100. doi: 10.1016/j.ejpb.2016.01.005
50. Karav S, German JB, Rouquie C, Le Parc A, Barile D. Studying lactoferrin N-glycosylation. *Int J Mol Sci.* (2017) 18:870. doi: 10.3390/ijms18040870
51. Cymer F, Beck H, Rohde A, Reusch D. Therapeutic monoclonal antibody N-glycosylation - Structure, function and therapeutic potential. *Biologicals.* (2018) 52:1–11. doi: 10.1016/j.biologicals.2017.11.001
52. Vieira Gomes AM, Souza Carmo T, Silva Carvalho L, Mendonca Bahia F, Parachin NS. Comparison of yeasts as hosts for recombinant protein production. *Microorganisms.* (2018) 6:38. doi: 10.3390/microorganisms6020038
53. Lin JW, Guan SY, Duan ZW, Shen YH, Fan WL, Chen LJ, et al. Gene cloning of a novel fungal immunomodulatory protein from *Chroogomphis rutilus* and its expression in *Pichia pastoris*. *J Chem Technol Biotechnol.* (2016) 91:2761–8. doi: 10.1002/jctb.4881
54. Lin CH, Sheu GT, Lin YW, Yeh CH, Huang YH, Lai YC, et al. A new immunomodulatory protein from *Ganoderma microsporum* inhibits epidermal growth factor mediated migration and invasion in A549 lung cancer cells. *Process Biochem.* (2010) 45:1537–42. doi: 10.1016/j.procbio.2010.06.006
55. Lu YT, Kuan YC, Chang HH, Sheu F. Molecular cloning of a *Poria cocos* protein that activates Th1 immune response and allays Th2 cytokine and IgE production in a murine atopic dermatitis model. *J Agric Food Chem.* (2014) 62:2861–71. doi: 10.1021/jf405507e
56. Li H, Bu X, Li K, Wu D. Production of a novel *Poria cocos* immunomodulatory protein in *Pichia pastoris*: cloning, expression, purification and activities assays. *World J Microbiol Biotechnol.* (2019) 35:27. doi: 10.1007/s11274-019-2602-4
57. Hsu HY, Hua KF, Wu WC, Hsu J, Weng ST, Lin TL, et al. Reishi immunomodulation protein induces interleukin-2 expression via protein kinase-dependent signaling pathways within human T cells. *J Cell Physiol.* (2008) 215:15–26. doi: 10.1002/jcp.21144
58. Lin YL, Liang YC, Tseng YS, Huang HY, Chou SY, Hseu RS, et al. An immunomodulatory protein, Ling Zhi-8, induced activation and maturation of human monocyte-derived dendritic cells by the NF-kappaB and MAPK pathways. *J Leukoc Biol.* (2009) 86:877–89. doi: 10.1189/jlb.0708441
59. Kino K, Mizumoto K, Sone T, Yamaji T, Watanabe J, Yamashita A, et al. An immunomodulating protein, Ling Zhi-8 (LZ-8) prevents insulitis in non-obese diabetic mice. *Diabetologia.* (1990) 33:713–8. doi: 10.1007/BF00400340
60. Haak-Frendscho M, Kino K, Sone T, Jardieu P. Ling Zhi-8: a novel T cell mitogen induces cytokine production and upregulation of ICAM-1 expression. *Cell Immunol.* (1993) 150:101–13. doi: 10.1006/cimm.1993.1182
61. van der Hem LG, van der Vliet JA, Bocken CF, Kino K, Hoitsma AJ, Tax WJ. Ling Zhi-8: studies of a new immunomodulating agent. *Transplantation.* (1995) 60:438–43. doi: 10.1097/00007890-199509000-00006
62. Li QZ, Chang YZ, He ZM, Chen L, Zhou XW. Immunomodulatory activity of *Ganoderma lucidum* immunomodulatory protein via PI3K/Akt and MAPK signaling pathways in RAW264.7 cells. *J Cell Physiol.* (2019) 234:23337–48. doi: 10.1002/jcp.28901
63. Yeh CH, Chen HC, Yang JJ, Chuang WI, Sheu F. Polysaccharides PS-G and protein LZ-8 from Reishi (*Ganoderma lucidum*) exhibit diverse functions in regulating murine macrophages and T lymphocytes. *J Agric Food Chem.* (2010) 58:8535–44. doi: 10.1021/jf100914m
64. Wang PH, Hsu CI, Tang SC, Huang YL, Lin JY, Ko JL. Fungal immunomodulatory protein from *Flammulina velutipes* induces interferon-gamma production through p38 mitogen-activated protein kinase signaling pathway. *J Agric Food Chem.* (2004) 52:2721–5. doi: 10.1021/jf034556s
65. Ou CC, Hsiao YM, Wu WJ, Tasy GJ, Ko JL, Lin MY. FIP-fve stimulates interferon-gamma production via modulation of calcium release and PKC-alpha activation. *J Agric Food Chem.* (2009) 57:11008–13. doi: 10.1021/jf902725s
66. Lee YT, Lee SS, Sun HL, Lu KH, Ku MS, Sheu JN, et al. Effect of the fungal immunomodulatory protein FIP-fve on airway inflammation and cytokine production in mouse asthma model. *Cytokine.* (2013) 61:237–44. doi: 10.1016/j.cyto.2012.09.024
67. Lee YT, Wu CT, Sun HL, Ko JL, Lue KH. Fungal immunomodulatory protein-fve could modulate airway remodel through by affect IL17 cytokine. *J Microbiol Immunol Infect.* (2018) 51:598–607. doi: 10.1016/j.jmii.2017.06.008
68. Hsieh CW, Lan JL, Meng Q, Cheng YW, Huang HM, Tsai JJ. Eosinophil apoptosis induced by fungal immunomodulatory peptide-fve via reducing IL-5alpha receptor. *J Formos Med Assoc.* (2007) 106:36–43. doi: 10.1016/S0929-6646(09)60214-X
69. Liu YF, Chang SH, Sun HL, Chang YC, Hsin IL, Lue KH, et al. IFN-gamma induction on carbohydrate binding module of fungal immunomodulatory protein in human peripheral mononuclear cells. *J Agric Food Chem.* (2012) 60:4914–22. doi: 10.1021/jf300957k
70. Wu CC, Liao EC, Lee MF, Tsai JJ. Augmentation of regulatory T cells in allergic individuals by recombinant Der f 2 peptide with fungal immunomodulatory peptide fve. *Ann Allergy Asthma Immunol.* (2009) 102:216–22. doi: 10.1016/S1081-1206(10)60084-1
71. Kong X, Zhang J, Han X, Zhang P, Dai X, Liu J, et al. High-yield production in *Escherichia coli* of Fungal Immunomodulatory Protein isolated from

Flammulina velutipes and its bioactivity assay *in vivo*. *Int J Mol Sci.* (2013) 14:2230–41. doi: 10.3390/ijms14022230
72. Li S, Nie Y, Ding Y, Shi L, Tang X. Recombinant expression of a novel fungal immunomodulatory protein with human tumor cell antiproliferative activity from *Nectria haematococca*. *Int J Mol Sci.* (2014) 15:17751–64. doi: 10.3390/ijms151017751
73. Lin CC, Yu YL, Shih CC, Liu KJ, Ou KL, Hong LZ, et al. A novel adjuvant Ling Zhi-8 enhances the efficacy of DNA cancer vaccine by activating dendritic cells. *Cancer Immunol Immunother.* (2011) 60:1019–27. doi: 10.1007/s00262-011-1016-4
74. Schwarz H, Schmittner M, Duschl A, Horejs-Hoeck J. Residual endotoxin contaminations in recombinant proteins are sufficient to activate human CD1c+ dendritic cells. *PLoS ONE.* (2014) 9:e113840. doi: 10.1371/journal.pone.0113840
75. Govers C, Tomassen MMM, Rieder A, Ballance S, Knutsen SH, Mes JJ. Lipopolysaccharide quantification and alkali-based inactivation in polysaccharide preparations to enable *in vitro* immune modulatory studies. *Bioact Carbohydr Diet Fibre.* (2016) 8:15–25. doi: 10.1016/j.bcdf.2016.09.001
76. Hirose K, Iwata A, Tamachi T, Nakajima H. Allergic airway inflammation: key players beyond the Th2 cell pathway. *Immunol Rev.* (2017) 278:145–61. doi: 10.1111/imr.12540
77. Boonpiyathad T, Sozener ZC, Satitsuksanoa P, Akdis CA. Immunologic mechanisms in asthma. *Semin Immunol.* (2019) 46:101333. doi: 10.1016/j.smim.2019.101333
78. Chang YC, Hsiao YM, Hung SC, Chen YW, Ou CC, Chang WT, et al. Alleviation of Dermatophagoides microceras-induced allergy by an immunomodulatory protein, FIP-fve, from *Flammulina velutipes* in mice. *Biosci Biotechnol Biochem.* (2015) 79:88–96. doi: 10.1080/09168451.2014.956682
79. Chu PY, Sun HL, Ko JL, Ku MS, Lin LJ, Lee YT, et al. Oral fungal immunomodulatory protein-*Flammulina velutipes* has influence on pulmonary inflammatory process and potential treatment for allergic airway disease: a mouse model. *J Microbiol Immunol Infect.* (2017) 50:297–306. doi: 10.1016/j.jmii.2015.07.013
80. Chang YC, Chow YH, Sun HL, Liu YF, Lee YT, Lue KH, et al. Alleviation of respiratory syncytial virus replication and inflammation by fungal immunomodulatory protein FIP-fve from *Flammulina velutipes*. *Antiviral Res.* (2014) 110:124–31. doi: 10.1016/j.antiviral.2014.08.006
81. Czabotar PE, Lessene G, Strasser A, Adams JM. Control of apoptosis by the BCL-2 protein family: implications for physiology and therapy. *Nat Rev Mol Cell Biol.* (2014) 15:49–63. doi: 10.1038/nrm3722
82. Hsieh KY, Hsu CI, Lin JY, Tsai CC, Lin RH. Oral administration of an edible-mushroom-derived protein inhibits the development of food-allergic reactions in mice. *Clin Exp Allergy.* (2003) 33:1595–602. doi: 10.1046/j.1365-2222.2003.01790.x
83. Justiz Vaillant AA, Zito PM. *Immediate Hypersensitivity Reactions.* Treasure Island, FL: StatPearls PublishingStatPearls Publishing LLC. Abstract Abstract retrieved from NCBI (Accession Number: 30020687) (2020).
84. Kino K, Yamashita A, Yamaoka K, Watanabe J, Tanaka S, Ko K, et al. Isolation and characterization of a new immunomodulatory protein, ling zhi-8 (LZ-8), from *Ganoderma lucidium*. *J Biol Chem.* (1989) 264:472–8.
85. Zhou H, Sun F, Li H, Zhang S, Liu Z, Pei J, et al. Effect of recombinant *Ganoderma lucidum* immunoregulatory protein on cyclophosphamide-induced leukopenia in mice. *Immunopharmacol Immunotoxicol.* (2013) 35:426–33. doi: 10.3109/08923973.2013.791834
86. Lee MF, Chiang CH, Lin SJ, Song PP, Liu HC, Wu TJ, et al. Recombinant Lactococcus lactis expressing Ling Zhi 8 protein ameliorates nonalcoholic fatty liver and early atherogenesis in cholesterol-fed rabbits. *Biomed Res Int.* (2020) 2020:3495682. doi: 10.1155/2020/3495682
87. Chen WY, Chang CY, Li JR, Wang JD, Wu CC, Kuan YH, et al. Anti-inflammatory and neuroprotective effects of Fungal Immunomodulatory Protein involving microglial inhibition. *Int J Mol Sci.* (2018) 19:3678. doi: 10.3390/ijms19113678
88. Lee PH, Hsieh PL, Liao YW, Yu CC. Inhibitory effect of GMI, an immunomodulatory protein from *Ganoderma microsporum*, on myofibroblast activity and proinflammatory cytokines in human fibrotic buccal mucosal fibroblasts. *Environ Toxicol.* (2018) 33:32–40. doi: 10.1002/tox.22489
89. Li CH, Ko JL, Ou CC, Lin WL, Yen CC, Hsu CT, et al. The protective role of GMI, an immunomodulatory protein from *Ganoderma microsporum*, on 5-Fluorouracil-induced oral and intestinal mucositis. *Integr Cancer Ther.* (2019) 18:1534735419833795. doi: 10.1177/1534735419833795
90. Ding Y, Seow SV, Huang CH, Liew LM, Lim YC, Kuo IC, et al. Coadministration of the fungal immunomodulatory protein FIP-Fve and a tumour-associated antigen enhanced antitumour immunity. *Immunology.* (2009) 128:e881–94. doi: 10.1111/j.1365-2567.2009.03099.x
91. Chang HH, Hsieh KY, Yeh CH, Tu YP, Sheu F. Oral administration of an Enoki mushroom protein FVE activates innate and adaptive immunity and induces anti-tumor activity against murine hepatocellular carcinoma. *Int Immunopharmacol.* (2010) 10:239–46. doi: 10.1016/j.intimp.2009.10.017
92. Liu YC, Zou XB, Chai YF, Yao YM. Macrophage polarization in inflammatory diseases. *Int J Biol Sci.* (2014) 10:520–9. doi: 10.7150/ijbs.8879
93. Zhou D, Huang C, Lin Z, Zhan S, Kong L, Fang C, et al. Macrophage polarization and function with emphasis on the evolving roles of coordinated regulation of cellular signaling pathways. *Cell Signal.* (2014) 26:192–7. doi: 10.1016/j.cellsig.2013.11.004
94. Zhu L, Zhao Q, Yang T, Ding W, Zhao Y. Cellular metabolism and macrophage functional polarization. *Int Rev Immunol.* (2014) 34:82–100. doi: 10.3109/08830185.2014.969421
95. de Oliviera Nascimento L, Massari P, Wetzler L. The role of TLR2 in infection and immunity. *Front Immunol.* (2012) 3:79. doi: 10.3389/fimmu.2012.00079
96. Yang L, Seki E. Toll-like receptors in liver fibrosis: cellular crosstalk and mechanisms. *Front Physiol.* (2012) 3:138. doi: 10.3389/fphys.2012.00138
97. Li J, Lee DS, Madrenas J. Evolving bacterial envelopes and plasticity of TLR2-dependent responses: basic research and translational opportunities. *Front Immunol.* (2013) 4:347. doi: 10.3389/fimmu.2013.00347
98. Awasthi S. Toll-like receptor-4 modulation for cancer immunotherapy. *Front Immunol.* (2014) 5:328. doi: 10.3389/fimmu.2014.00328
99. Peng SL. The T-box transcription factor T-bet in immunity and autoimmunity. *Cell Mol Immunol.* (2006) 3:87–95.
100. Xue Q, Ding Y, Shang C, Jiang C, Zhao M. Functional expression of LZ-8, a fungal immunomodulatory protein from *Ganoderma lucidium* in *Pichia pastoris*. *J Gen Appl Microbiol.* (2008) 54:393–8. doi: 10.2323/jgam.54.393
101. Liang C, Zhang S, Liu Z, Sun F. *Ganoderma lucidum* immunomodulatory protein(Lz-8) expressed in *Pichia pastoris* and the identification of immunocompetence. *Sheng Wu Gong Cheng Xue Bao.* (2009) 25:441–7.
102. Ko JL, Lin SJ, Hsu CI, Kao CL, Lin JY. Molecular cloning and expression of a fungal immunomodulatory protein, FIP-fve, from *Flammulina velutipes*. *J Formos Med Assoc.* (1997) 96:517–24.
103. Lin JW, Jia J, Shen YH, Zhong M, Chen LJ, Li HG, et al. Functional expression of FIP-fve, a fungal immunomodulatory protein from the edible mushroom *Flammulina velutipes* in *Pichia pastoris* GS115. *J Biotechnol.* (2013) 168:527–33. doi: 10.1016/j.jbiotec.2013.09.013
104. Su CF, Kuo IC, Chen PW, Huang CH, Seow SV, Chua KY, et al. Characterization of an immunomodulatory Der p 2-FIP-fve fusion protein produced in transformed rice suspension cell culture. *Transgenic Res.* (2012) 21:177–92. doi: 10.1007/s11248-011-9518-6
105. Wang XF, Li QZ, Bao TW, Cong WR, Song WX, Zhou XW. *In vitro* rapid evolution of fungal immunomodulatory proteins by DNA family shuffling. *Appl Microbiol Biotechnol.* (2013) 97:2455–65. doi: 10.1007/s00253-012-4131-z
106. Singh RS, Bhari R, Kaur HP. Mushroom lectins: current status and future perspectives. *Crit Rev Biotechnol.* (2010) 30:99–126. doi: 10.3109/07388550903365048
107. Boraston AB, Bolam DN, Gilbert HJ, Davies GJ. Carbohydrate-binding modules: fine-tuning polysaccharide recognition. *Biochem J.* (2004) 382(Pt 3):769–81. doi: 10.1042/BJ20040892
108. Lombard V, Golaconda Ramulu H, Drula E, Coutinho PM, Henrissat B. The carbohydrate-active enzymes database (CAZy) in 2013. *Nucl Acids Res.* (2014) 42:D490–5. doi: 10.1093/nar/gkt1178
109. Abe A, Tonozuka T, Sakano Y, Kamitori S. Complex structures of thermoactinomyces vulgaris R-47 α-Amylase 1 with malto-oligosaccharides demonstrate the role of domain N acting as a starch-binding domain. *J Mol Biol.* (2004) 335:811–22. doi: 10.1016/j.jmb.2003.10.078
110. Bao DP, Bai R, Gao YN, Wu YY, Wang Y. Computational insights into the molecular mechanism of the high immunomodulatory activity of

LZ-8 protein isolated from the Lingzhi or Reishi medicinal mushroom *Ganoderma lucidum* (Agaricomycetes). *Int J Med Mushrooms.* (2018) 20:537–48. doi: 10.1615/IntJMedMushrooms.2018026264
111. Ou CC, Hsiao YM, Wang WH, Ko JL, Lin MY. Stability of fungal immunomodulatory protein, FIP-gts and FIP-fve, in IFN-γ production. *Food Agr Immunol.* (2009) 20:319–32. doi: 10.1080/09540100903247688
112. Seow SV, Kuo IC, Paaventhan P, Kolatkar PR, Chua KY. Crystallization and preliminary X-ray crystallographic studies on the fungal immunomodulatory protein Fve from the golden needle mushroom (*Flammulina velutipes*). *Acta Crystallogr D Biol Crystallogr.* (2003) 59(Pt 8):1487–9. doi: 10.1107/S0907444903011879
113. Huang L, Sun F, Liang C, He YX, Bao R, Liu L, et al. Crystal structure of LZ-8 from the medicinal fungus *Ganoderma lucidium*. *Proteins.* (2009) 75:524–7. doi: 10.1002/prot.22346
114. Jinn TR, Wu CM, Tu WC, Ko JL, Tzen JT. Functional expression of FIP-gts, a fungal immunomodulatory protein from *Ganoderma tsugae* in Sf21 insect cells. *Biosci Biotechnol Biochem.* (2006) 70:2627–34. doi: 10.1271/bbb.60232
115. Arkin S, Naprstek B, Guarini L, Ferrone S, Lipton JM. Expression of intercellular adhesion molecule-1 (CD54) on hematopoietic progenitors. *Blood.* (1991) 77:948–53. doi: 10.1182/blood.V77.5.948.948
116. Hubbard AK, Rothlein R. Intercellular adhesion molecule-1 (ICAM-1) expression and cell signaling cascades. *Free Radic Biol Med.* (2000) 28:1379–86. doi: 10.1016/S0891-5849(00)00223-9
117. Amaout MA, Mahalingam B, Xiong JP. Integrin structure, allostery, bidirectional signaling. *Annu Rev Cell Dev Biol.* (2005) 21:381–405. doi: 10.1146/annurev.cellbio.21.090704.151217
118. Chang HH, Chien PJ, Tong MH, Sheu F. Mushroom immunomodulatory proteins possess potential thermal/freezing resistance, acid/alkali tolerance and dehydration stability. *Food Chem.* (2007) 105:597–605. doi: 10.1016/j.foodchem.2007.04.048
119. Tong MH, Chien PJ, Chang HH, Tsai MJ, Sheu F. High processing tolerances of immunomodulatory proteins in Enoki and Reishi mushrooms. *J Agric Food Chem.* (2008) 56:3160–6. doi: 10.1021/jf800205g
120. Huang WN, Yang CY, Chen DC, Chuang LT. Correlation of the structure and bioactivity of recombinant Fungal Immunomodulatory Protein, LingZhi-8 (LZ-8) following exposure to denaturing conditions. *J Food Biochem.* (2014) 38:328–36. doi: 10.1111/jfbc.12057
121. Sturzbecher H, Deppert W. The tumor-suppressor protein p53-relationship of structure to function (review). *Oncol Rep.* (1994) 1:301–7. doi: 10.3892/or.1.2.301
122. Sadowski MI, Jones DT. The sequence-structure relationship and protein function prediction. *Curr Opin Struct Biol.* (2009) 19:357–62. doi: 10.1016/j.sbi.2009.03.008
123. Wildhagen KC, Lutgens E, Loubele ST, ten Cate H, Nicolaes GA. The structure-function relationship of activated protein C. Lessons from natural and engineered mutations. *Thromb Haemost.* (2011) 106:1034–45. doi: 10.1160/TH11-08-0522
124. Liao CH, Hsiao YM, Sheu GT, Chang JT, Wang PH, Wu MF, et al. Nuclear translocation of telomerase reverse transcriptase and calcium signaling in repression of telomerase activity in human lung cancer cells by fungal immunomodulatory protein from *Ganoderma tsugae*. *Biochem Pharmacol.* (2007) 74:1541–54. doi: 10.1016/j.bcp.2007.07.025
125. Xie Y, Li S, Sun L, Liu S, Wang F, Wen B, et al. Fungal immunomodulatory protein from *Nectria haematococca* suppresses growth of human lung adenocarcinoma by inhibiting the PI3K/Akt pathway. *Int J Mol Sci.* (2018) 19:3429. doi: 10.3390/ijms19113429
126. Wang X, Liang C, Li H, Li B, Sun F. Recombinant *Ganoderma lucidum* immunoregulatory protein (rLZ-8) induces nuclear-stress apoptosis in K562 cells. *Chin J Immunol.* (2010) 26:616–23. Available online at: https://www.cabdirect.org/cabdirect/abstract/20103261811
127. Liang CY, Xu WQ, Cao YX, Liu LX, Zhang SQ, Liu ZY, et al. Dynamic observation of cellular localization of fluorescein isothiocyanate labeled recombinant ganoderma lucidum immunoregulatory protein(rLz-8) in NB4 APL cell. *Chem J Chin Univers.* (2009) 30:479–83. Available online at: https://www.researchgate.net/publication/286772396_Dynamic_Observation_of_Cellular_Localization_of_Fluorescein_Isothiocyanate_Labeled_Recombinant_Ganoderma_Lucidum_Immunoregulatory_ProteinrLz-8_in_NB4_APL_Cell

Conflict of Interest: The authors declare that the research was conducted in the absence of any commercial or financial relationships that could be construed as a potential conflict of interest.

frontiers in Nutrition

ORIGINAL RESEARCH
published: 15 September 2020
doi: 10.3389/fnut.2020.00161

Water Extract of *Potentilla discolor* Bunge Improves Hepatic Glucose Homeostasis by Regulating Gluconeogenesis and Glycogen Synthesis in High-Fat Diet and Streptozotocin-Induced Type 2 Diabetic Mice

Tiange Li[1], *Rui Chang*[1], *Huijuan Zhang*[1], *Min Du*[2] *and Xueying Mao*[1]*

[1] *Beijing Advanced Innovation Center for Food Nutrition and Human Health, Key Laboratory of Precision Nutrition and Food Quality, Key Laboratory of Functional Dairy, Ministry of Education, College of Food Science and Nutritional Engineering, China Agricultural University, Beijing, China,* [2] *Department of Animal Sciences, Washington State University, Pullman, WA, United States*

OPEN ACCESS

Edited by:
Jinkai Zheng, Chinese Academy of Agricultural Sciences (CAAS), China

Reviewed by:
Viduranga Y. Waisundara, Australian College of Business and Technology—Kandy Campus, Sri Lanka
Dongmin Liu, Virginia Tech, United States

***Correspondence:**
Xueying Mao
maoxueying@cau.edu.cn

Specialty section:
This article was submitted to Food Chemistry, a section of the journal Frontiers in Nutrition

Received: *01 June 2020*
Accepted: *10 August 2020*
Published: *15 September 2020*

Citation:
Li T, Chang R, Zhang H, Du M and Mao X (2020) Water Extract of Potentilla discolor Bunge Improves Hepatic Glucose Homeostasis by Regulating Gluconeogenesis and Glycogen Synthesis in High-Fat Diet and Streptozotocin-Induced Type 2 Diabetic Mice. Front. Nutr. 7:161. doi: 10.3389/fnut.2020.00161

Potentilla discolor Bunge, as a traditional Chinese medicine, exhibits many phytochemical activities. The aim of the present study was to investigate the effects of *Potentilla discolor* Bunge water extract (PDBW) and its underlying mechanisms on gluconeogenesis and glycogen synthesis in high-fat diet/streptozotocin (HFD/STZ)-induced type 2 diabetic mice. LC-MS/MS analyses of PDBW identified 6 major compounds including apigenin-7-O-β-D-glucoside, epicatechin, quercetin 3-O-β-D-glucuronide, kaempferol-3-O-β-D-glucopyranoside, scutellarin, and quercitrin. In the study, a mouse model of type 2 diabetes was induced by 4-week HFD combined with STZ (40 mg/kg body weight) for 5 days. After oral administration of PDBW at 400 mg/kg body weight daily for 8 weeks, the mice with type 2 diabetes showed significant decrease in the levels of fasting blood glucose and glycated hemoglobin A1c (HbA1c), and increase in the insulin level. PDBW improved the glucose tolerance, insulin sensitivity and lipid profiles. Furthermore, PDBW inhibited the mRNA levels of key gluconeogenic enzymes [phosphoenolpyruvate carboxykinase (PEPCK) and glucose-6-phosphatase (G6Pase)] in liver. PDBW also promoted glycogen synthesis by raising the liver glycogen content, decreasing the phosphorylation of glycogen synthase (GS) and increasing the phosphorylation of glycogen synthase kinase3β (GSK3β). Besides, PDBW induced the activation of protein kinase B (Akt) and AMP-activated protein kinase (AMPK), which might explain changes in the phosphorylation of above enzymes. In summary, PDBW supplementation ameliorates metabolic disorders in a HFD/STZ diabetic mouse model, suggesting the potential application of PDBW in prevention and amelioration of type 2 diabetes.

Keywords: ***Potentilla discolor*** **Bunge, gluconeogenesis, glycogen synthesis, insulin sensitivity, type 2 diabetes**

INTRODUCTION

Type 2 diabetes (T2D) is one of the largest global health problems affecting over 400 million people worldwide in recent years (1). As a complex and progressive metabolic disease, T2D is characterized by chronic hyperglycemia resulting from defects in insulin secretion and action due to β-cell dysfunction and insulin resistance in target organs (2). T2D requires long-term glycemic control and can trigger a steep increase in the risk of severe complications including diabetic nephropathy, cardiovascular and stroke (3). In clinical practice, metformin and thiazolidinediones were often used to treat diabetes while they have side effects such as digestive discomfort, increased cardiovascular morbidity and potential toxicities (4). Therefore, it is of great urgency to find effective methods on the blood glucose control to improve T2D.

Insulin sensitivity of peripheral tissues is critical for preventing hyperglycemia after meals (5). Liver plays an important role in the maintenance of glucose homeostasis by regulating glucose storage *via* glycogen synthesis (glycogenesis) and glucose production *via* the breakdown of glycogen (gluconeogenesis) (6). In diabetic individuals, glycogenesis is reduced while gluconeogenesis is strongly elevated, which leads to the increased rate of hepatic glucose output and causes hyperglycemia ultimately (7). The reduced glycogenesis is associated with the phosphorylation of glycogen synthase kinase-3 (GSK3), which subsequently inactivates glycogen synthase (GS) (8). Gluconeogenesis is mainly modulated by phosphoenolpyruvate carboxykinase (PEPCK) and glucose-6-phosphatase (G6Pase). PEPCK and G6Pase are up-regulated during the development of T2D (9). Glucose utilization in liver is mainly regulated by phosphoinositide-3-kinase and its activity is regulated by protein kinase B (PI3K/Akt). PI3K/Akt signaling pathway decreased hepatic glucose output mainly through inducing the phosphorylation of GSK3, thereby stimulating glycogen synthesis (10). AMPK is a key regulator of energy balance (11). AMPK activation can lower blood glucose level and inhibit lipid accumulation by decreasing gluconeogenesis and fatty acid synthesis, and increasing fatty acid oxidation in liver (12). Therefore, maintaining the homeostasis of hepatic glycogenesis and gluconeogenesis is important for T2D prevention and treatment.

The traditional Chinese medicine, *Potentilla discolor* Bunge (PDB), has a long history of clinical application for the treatment of hepatitis, diarrhea or traumatic hemorrhage (13). In recent years, several benefits of PDB and its extracts, such as anti-tumor, anti-cancer, and anti-ulcerogenic activity, have been reported (14). Especially, PDB has drawn much attention in protection against T2D. The extract of PDB dose-dependently reduced the blood glucose levels in alloxan-induced diabetic mice (15). Four weeks' treatment with water extract of PDB ameliorated the development of hyperglycemia and hyperlipidemia in obese mice (16). However, the underlying mechanisms on the hypoglycemic effects of PDB remain largely undefined.

The purpose of this study was to investigate the effects of *Potentilla discolor* Bunge water extract (PDBW) on hepatic glucose homeostasis in high-fat diet and streptozotocin (HFD/STZ)-induced type 2 diabetic mice. To study the hypoglycemic mechanisms of PDBW, the expression of key factors regulating glycogenesis and gluconeogenesis and the alteration of PI3K/Akt and AMPK signaling were evaluated.

MATERIALS AND METHODS

Materials

The air-dried plant of PDB was provided by Tangxian Dandelion Tea Manufacturing Co., Ltd (Tang country, Hebei Province, China) and was identified and authenticated by the taxonomist of Beijing University of Chinese Medicine. Streptozotocin (STZ) and insulin were purchased from Sigma-Aldrich (St. Louis, MO, USA). The mouse insulin enzyme-linked immunosorbent assay (ELISA) kit was purchased from Mercodia (Uppsala, Sweden). RIPA buffer, phosphatase cocktails and protease for western blot, and BCA protein assay kit were purchased from Beyotime Biotech (Haimen, Jiangsu, China). Primary antibodies against p-GS (Ser641), GS, p-GSK3β (Ser9), GSK3β, p-Akt (Ser473), Akt, p-AMPK (Thr172), and AMPK were purchased from Cell Signaling Technology (Beverly, MA). The primary antibody against β-actin was purchased from Biosynthesis Biotechnology (Beijing, China). The anti-rabbit secondary antibody was purchased from Beyotime Biotech (Haimen, Jiangsu, China). All other chemicals were of analytical grade and obtained from Sinopharm Chemical Reagent Co., Ltd (Shanghai, China).

Preparation of PDBW

One kilogram of PDB was soaked in 10 L of boiling water for 1 h, and the process was repeated twice. The combined extract was filtered using double gauze and then centrifuged before concentrated on a rotary evaporator under reduced pressure at 40°C. The concentrate was lyophilized to obtain the powder.

LC-MS/MS Analysis of Components From PDBW

Components in PDBW were analyzed with a LC-MS/MS system. Chromatographic separation was performed using an Agilent 1,290 Infinity II UPLC system (Agilent, Santa Clara, CA, USA) equipped with an Agilent Eclipse XDB-C18 column (100 mm × 2.1 mm i.d., 3.5 μm). The column temperature was set at 35°C and the UV absorption wavelengths were set as 254 and 320 nm, respectively. Elution were accomplished on a gradient of formic acid (0.1%) in water (mobile phase A) vs. formic acid (0.1%) in acetonitrile (mobile phase B) at a flow rate of 0.3 mL/min and the injection volume was 10 μL. An optimal gradient elution program was applied to separate the components effectively: 0–15 min, 5–90% B; 15–20 min, 90% B. MS/MS analysis was operated using a high resolution mass spectrometer (Q-Exactive Focus, Thermo Fisher Scientific). The MS data were acquired from an electrospray ionization (ESI) source in positive and negative ion mode, respectively. The parameters of the source were set as follows: nebulizer gas pressure 45.00 psi; electrospray voltage 4,000 V; fragmentor 150 V; desolvation gas (nitrogen > 99.99%) flow 600 L/h; desolvation temperature 350°C and source

temperature 100°C; target mass m/z 400; scan range m/z 100–1,500. Data acquisition processing was carried out using Thermo Fisher Xcalibur workstation (Xcalibur software, version 4.0).

Animal Treatments

The C57BL/6J mice (5 weeks old, male) were purchased from Beijing Vital River Laboratory Animal Technology Co., Ltd. (Beijing, China). Additionally, mice were housed at a controlled temperature (22 ± 1°C) and humidity (40 ± 10%) with a 12-h light-dark cycle. All mice were weighed and given free access to food and water. Body weight and food consumption were monitored throughout the study. All the experimental procedures, animal care and handling were performed according to the guidelines provided by the Animal Care Committee and approved by the Ethics Committee of China Agricultural University (Approval No. KY160018).

After 1-week adaptation, the diabetic mice were established with some modification of methods described previously (17). Mice were fed by a normal chow diet (CON group, KeAoXieLi Feed Co., Ltd., Beijing, China) ($n = 10$) or a high-fat diet (KeAoXieLi Feed Co., Ltd., Beijing, China) ($n = 20$) for 4 weeks. The normal chow diet contains 19.38% (w/w) protein, 45.79% (w/w) carbohydrate, and 4.48% (w/w) fat, whereas the high-fat diet contains 26.2% (w/w) protein, 26.30% (w/w) carbohydrate, and 34.90% (w/w) fat. After fasting overnight, high-fat-fed mice were injected with streptozotocin (40 mg/kg body weight, dissolved in freshly prepared 100 mmol/L citrate buffer) for consecutive 5 days and the mice in the CON group were injected with an equal amount of citrate buffer. The mice with fasting blood glucose level more than 11.1 mmol/L were considered diabetic and then selected for study. Then the diabetic mice were divided into two groups and fed with high-fat diet (T2D group, $n = 8$) or high-fat diet with PDBW at 400 mg/kg body weight (T2DP group, $n = 8$) by intragastric administration for another 2 months. The CON and T2D group were orally administered with an equal amount of sterile physiological saline. At the end of the experiment, all mice were euthanized after overnight fasting. Blood samples were collected and stored at 4°C overnight. Afterwards, samples were centrifuged (4°C, 1,300 × g, 15 min) to obtain serum for analysis. The livers were collected, rinsed and stored at −80°C.

Measurement of Fasting Blood Glucose and Serum Insulin Levels

After overnight fasting, the blood glucose levels from tail vein of mice were measured using a glucose meter (Roche Diagnostics, Mannheim, Germany). After treatment with PDBW for 8 weeks, the serum insulin level was determined by mouse insulin enzyme-linked immunosorbent assay (ELISA) kit (R&D Systems, Minneapolis, MN, USA).

Measurement of Glycated Hemoglobin, Serum Lipid Parameters, and Hepatic Glycogen Content

The level of glycated hemoglobin (HbA1c) was determined using glycated hemoglobin kit (Enzyme-linked Biotechnology, Shanghai, China) according to the manufacturer's instructions. The serum lipid parameters [triglyceride (TG), total cholesterol (TC), high-density lipoprotein (HDL-C), low-density lipoprotein (LDL-C) cholesterol, and free fatty acids (FFA)] were measured using commercially diagnostic kits (Jiancheng Bioengineering Institute, Nanjing, China). Glycogen contents in the liver were determined using a colorimetric assay kit (Jiancheng Bioengineering Institute, Nanjing, China).

Oral Glucose Tolerance Test (OGTT), Intraperitoneal Insulin Tolerance Test (IPITT), and Pyruvate Tolerance Test (PTT)

OGTT was performed after treatment with PDBW for 7 weeks. Mice were orally given glucose at a dose of 2.0 g/kg body weight after an overnight fast, and blood glucose levels were measured at 0, 30, 60, 90, and 120 min after administration using a glucose meter. IPITT and PTT were performed after treatment with PDBW for 8 weeks. After an overnight fast, mice were injected intraperitoneally with insulin at 1.0 U/kg body weight or sodium pyruvate solution at 2.0 g/kg body weight, respectively. Then blood glucose levels were measured at 0, 30, 60, 90, and 120 min. The results of OGTT, IPITT, and PTT were expressed as area under the curve (AUC) calculated according to the previous study (18).

Real-Time Quantitative Polymerase Chain Reaction

Total RNA was extracted from liver using Trizol reagent (Tiangen Biotech, Beijing, China). First strand cDNA was synthesized from 10 μL of total RNA in a 20 μL reaction volume using 5 × All-In-One RT Master Mix kit (Abm, Richmond, BC, Canada) according to the manufacturer's instructions in a C1000 Thermal Cycler (Bio-Rad, Hercules, USA). The SYBR green-based RT-PCR assay was implemented with a Techne Quantica real-time PCR system (Hangzhou Bioer Technology, Hangzhou, China). The RT-PCR program was as follows: 40 cycles of 95°C for 180 s, 95°C for 30 s, 60°C for 30 s and 72°C for 30 s. The specific primers which include both sense and antisense were showed in **Table S1**. The mRNA expression was normalized to the house keeping gene GAPDH. Data was presented as the fold change relative to the control group.

Histological Analysis

The liver was fixed in 4% paraformaldehyde solution and embedded in paraffin wax followed by sectioning into 4 μm thickness. Sections were then stained with hematoxylin-eosin and examined with an electron microscope (Olympus Corporation, Tokyo, Japan).

Western Blot Analysis

The liver was lysed in RIPA buffer with phosphatase cocktails and protease. The homogenates were then centrifuged at 12,000 × g at 4°C for 15 min and then the supernatants were collected. After measurement of protein concentration by quantification using BCA protein assay reagent (Beyotime Biotech, Haimen, Jiangsu, China), equal amounts of protein samples were separated by 10% sodium dodecyl sulfatepolyacrylamide gel electrophoresis

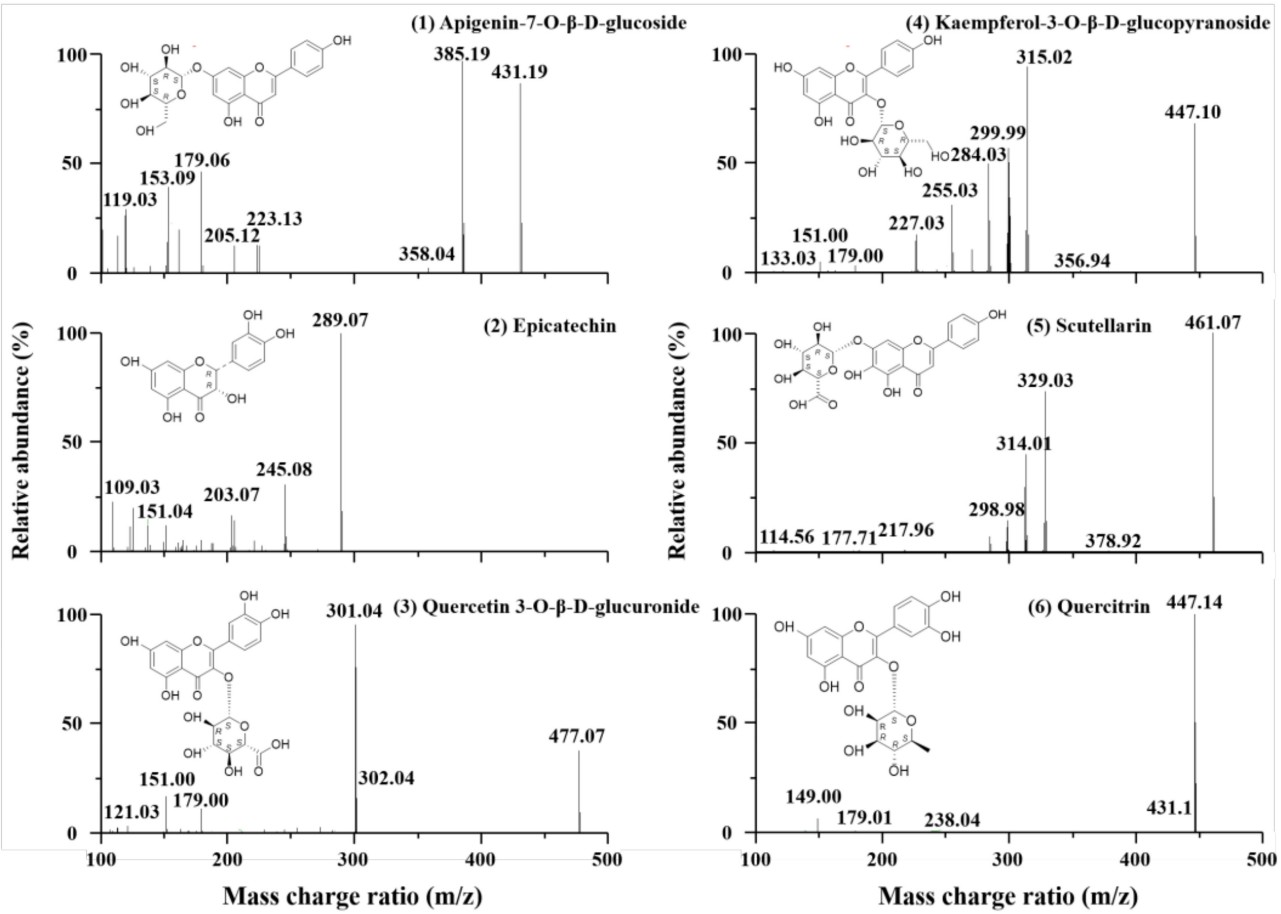

FIGURE 1 | LC-MS/MS spectra of main components in *Potentilla discolor* Bunge water extract (PDBW): (1) apigenin-7-O-β-D-glucoside, (2) epicatechin, (3) quercetin 3-O-β-D-glucuronide, (4) kaempferol-3-O-β-D-glucopyranoside, (5) scutellarin, and (6) quercitrin.

and transferred to polyvinylidene fluoride membranes on a wet transfer apparatus (Bio-Rad, Hercules, USA). The membranes were blocked by 5% non-fat milk power in tris-buffered saline containing 0.1% Tween-20 (TBS-T) for 2 h at room temperature, followed by incubation with primary antibodies overnight at 4°C. After washed by TBS-T, the membranes were incubated with a peroxidase conjugated secondary antibody for 2 h at room temperature. Protein bands were detected by an enhanced chemiluminescenece method using enhanced chemiluminescence (ECL) reagents (Millipore, Billerica, MA, USA). The band intensities were analyzed using software ImageJ 1.47v (Wayne Rasband, Bethesda, MD, USA). All protein expressions were normalized by β-actin.

Statistics Analysis

Data were expressed as means ± standard error of the mean (SEM) and analyzed by SPSS 20.0 software. Significant differences ($p < 0.05$) between means were evaluated with one way ANOVA followed by Duncan's multiple-comparison test.

RESULTS

Identification of Components in PDBW

To identify the main components of PDBW, LC-MS/MS was applied to characterize their chemical structures. As shown in **Figure S1A**, UV chromatograms of the components in PBDW at 254 and 320 nm suggested that six major components can be well-separated within 20 min and their λ_{max} were all at 254 nm. The characteristic ions of the detected components presented in MS total ion chromatogram profiles in negative ion mode were stronger than those in positive ion mode (**Figure S1B**). The characteristic fragment ions of compounds 1–6 are shown in MS/MS spectra (**Figure 1**). For fragmentation analysis, taking compound 4 as an example, the quasi-molecular ($[M–H]^-$) ion at m/z 447.10 was identified as $C_{21}H_{20}O_{11}$ by element matching. By comparing the UV absorption, it was speculated as a glycoside compound. As shown in **Figure 1**, the characteristic ion of aglycone radical $[Y_0\text{-}H]^-$ at m/z 284.03 by loss of 163 Da ($C_6H_{11}O_5$, a glucose) from the precursor ion $[M–H]^-$ had higher abundance than that of aglycone $[Y_0^-]$ at m/z 285.03 (not marked in **Figure 1**), which suggested that the aglycone and glucose were

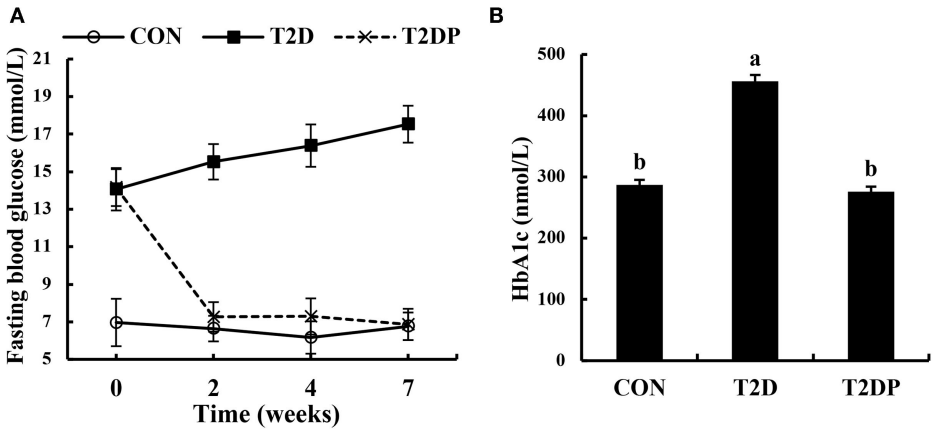

FIGURE 2 | Effects of *Potentilla discolor* Bunge water extract (PDBW) on fasting blood glucose and HbA1c levels in HFD-STZ induced diabetic mice. **(A)** The levels of fasting blood glucose after PDBW treatment. **(B)** The levels of HbA1c after 8 weeks treatment with PDBW. All values are means ± SEM ($n = 8$); Values marked with different lower-case letters in superscript format indicate significant differences among groups ($p < 0.05$).

linked by 3-O glucosidic band. Prominent ions at m/z 315.02 $[(M–H)–^{1,5}X_0]^-$ and m/z 299.99 $[(M–^{0,1}X_0)^-]$ was obtained from the quasi-molecular ($[M–H]^-$) ion and molecular ($[M^-]$) ion by fracturing of chemical bond at the 1,5-position and 0,1-position of the glucose, respectively. Besides, the characteristic fragment ions of the aglycone radical $[Y_0\text{-}H]^-$ at m/z 284.03 was also matched to that of a flavonol (Mass Spectrum data from the SciFinder Database: scifinder.cas.org). For flavonols, there were some low abundance ions that were generated from the fragmentation pathways of retro-Diels–Alder (RDA) cleavage from the 1,4-position of their C-ring. The fragment ions at m/z 151.00 $[^{1,3}A^-]$, m/z 133.03 $[^{1,3}B^+]$ and m/z 179.00 $[^{1,2}A^-]$ indicated that there were two hydroxyl substituents on ring A, one on ring B and one on ring C. In addition, flavonols are more likely to lose basic radicals or some small molecular fragments, like H (1), $CH_3^{\cdot}$ (15), H_2O (18), CO (28), H+CO (29), CO+$CH_3^{\cdot}$ (43), and CO+H_2O (46), H+2CO (57), *etc.*, in their structures and yield the basic fragment peaks. The diagnostic fragment ions of compounds 4 at m/z 255.03 $[(Y_0\text{-}H)–(H+CO)]^-$ and m/z 227.03 $[(Y_0\text{-}H)–(H+2CO)]^-$ were derived from the aglycone radical. Based on the retention time and UV absorption, MS/MS spectrum library and other literature data, this component was identified as kaempferol-3-O-β-D-glucopyranoside with the retention time of 5.92 min, and its fragmentation pathways in negative ion mode was listed in **Figure S2** (19, 20). Following the same pattern, compounds 1, 2, 3, 5, and 6 were identified as apigenin-7-O-β-D-glucoside, epicatechin, quercetin 3-O-β-D-glucuronide, scutellarin, and quercitrin with the retention time of 4.09, 4.55, 5.03, 6.63, and 9.62 min, respectively.

PDBW Decreased Glucose Level in HFD/STZ-Induced Diabetic Mice

The blood glucose levels were measured after PDBW oral administration for 2, 4, and 7 weeks. As shown in **Figure 2A**, diabetic mice showed a higher blood glucose level compared to that in the CON group ($p < 0.05$). After oral administration of PDBW, blood glucose level was significantly reduced in comparison with that of T2D group ($p < 0.05$, **Figure 2A**). In line with the blood glucose level, T2D group had higher HbA1c level compared to the CON group while PDBW administration significantly decreased the HbA1c level ($p < 0.05$, **Figure 2B**).

TABLE 1 | Effects of *Potentilla discolor* Bunge water extract (PDBW) on body weight, food intake, and serum biochemical profiles.

	CON	T2D	T2DP
Initial body weight (g)	24.80 ± 0.58^a	24.93 ± 0.31^a	24.59 ± 0.38^a
Body weight before PDBW treatment (g)	30.76 ± 0.31^a	28.20 ± 0.42^b	28.85 ± 0.41^b
Final body weight (g)	32.82 ± 0.53^a	28.77 ± 0.35^b	31.33 ± 0.68^a
Food intake (g/d)	3.75 ± 0.15^a	3.79 ± 0.15^a	3.74 ± 0.17^a
Insulin (μg/L)	0.48 ± 0.05^a	0.30 ± 0.034^b	0.46 ± 0.07^a
TG (mmol/L)	0.85 ± 0.11^c	2.85 ± 0.06^a	1.86 ± 0.07^b
TC (mmol/L)	2.72 ± 0.19^c	4.60 ± 0.10^a	3.77 ± 0.1^b
HDL-c (mmol/L)	1.68 ± 0.10^a	0.93 ± 0.04^c	1.09 ± 0.04^b
LDL-c (mmol/L)	0.97 ± 0.05^c	1.89 ± 0.08^a	1.32 ± 0.05^b
FFA (mmol/L)	0.90 ± 0.09^c	3.80 ± 0.11^a	2.75 ± 0.06^b
AST (nmol/min/mL)	110.42 ± 13.53^b	180.46 ± 20.42^a	140.66 ± 15.32^a
ALT (nmol/min/mL)	70.34 ± 6.75^c	150.67 ± 19.46^a	102.34 ± 14.23^b

All values are the mean ± standard error (n = 8); Values marked with different lower-case letters in superscript format indicate significant differences between three groups (p < 0.05).

PDBW Ameliorated Body Weight Loss and Dyslipidemia in HFD/STZ-Induced Diabetic Mice

As shown in **Table 1**, compared to the CON group, T2D group showed lower body weight, while PDBW treatment to T2D mice increased body weight ($p < 0.05$). Meanwhile, there was no significant difference in the amount of food intake among the

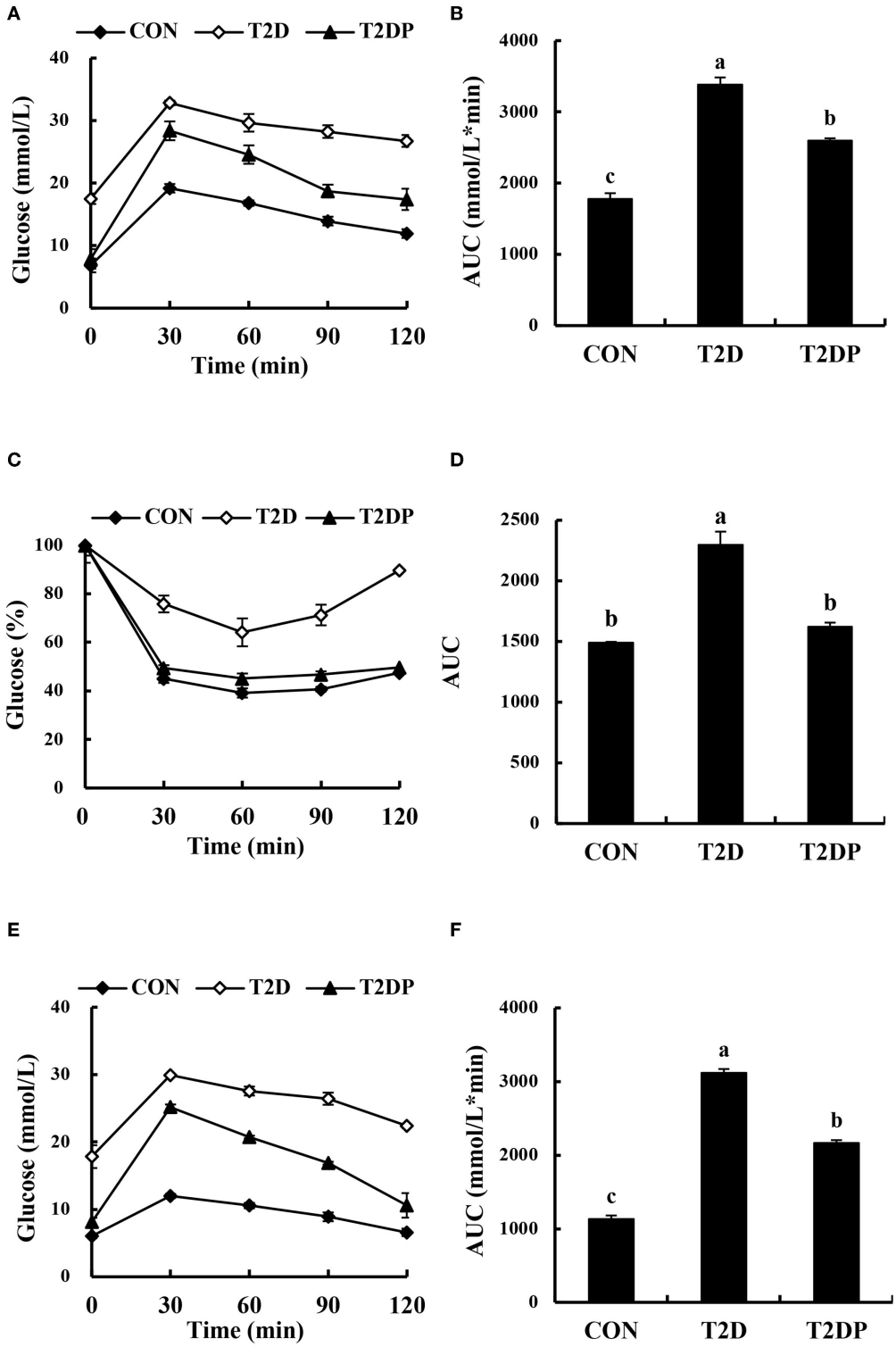

FIGURE 3 | Effects of *Potentilla discolor* Bunge water extract (PDBW) on oral glucose tolerance (OGTT), intraperitoneal insulin tolerance (IPITT), and pyruvate tolerance test (PTT) in HFD-STZ induced diabetic mice. Blood glucose levels **(A)** and area under the curve (AUC) **(B)** for the blood glucose levels during OGTT. Blood glucose levels **(C)** and AUC **(D)** for the blood glucose levels during IPITT. The graph displays blood glucose levels expressed as a percentage of the initial blood glucose level following an overnight fast. Blood glucose levels **(E)** and AUC **(F)** for the blood glucose levels during PTT. All values are the mean ± standard error (n = 8); Values marked with different lower-case letters in superscript format indicate significant differences between three groups ($p < 0.05$).

three groups (**Table 1**). The T2D group presented a lower insulin level than that of the CON group. Compared to T2D group, PDBW improved the insulin level by 53.3% ($p < 0.05$). T2D mice exhibited a higher level of TG, TC, LDL-c, and FFA and a lower level of HDL-c in serum than that of the CON group ($p < 0.05$), while PDBW treatment reversed these effects with a lower levels of TG, TC, LDL-c and FFA, and a higher level of HDL-c level in T2D mice ($p < 0.05$). Moreover, compared to the CON group, T2D group showed a higher level of AST and ALT in serum, whereas PDBW treatment improved the level of ALT and AST in T2D mice.

PDBW Improved Glucose Tolerance and Insulin Sensitivity in HFD/STZ-Induced Diabetic Mice

To investigate the effect of PDBW on glucose tolerance, insulin tolerance and pyruvate tolerance, the OGTT, IPITT, and PTT were carried out. As shown in **Figures 3A,B**, fasting blood glucose was significantly increased in the T2D mice compared to that of the CON group mice ($p < 0.05$). The T2DP group, by contrast, showed a decrease in fasting blood glucose levels compared to the T2D group ($p< 0.05$). The blood glucose levels of all groups showed an increase and reached the highest at 30 min after glucose oral administration, and then decreased until the end. The area-under-the-curve (AUC) of T2D group during OGTT was significantly higher than that of the CON group ($p < 0.05$). PDBW treatment reduced the AUC compared to T2D group ($p < 0.05$), suggesting a reverse in impaired glucose tolerance induced by HFD/STZ. The curves of blood glucose vs. time in the IPITT showed that the blood glucose levels of mice from all groups bottomed at 60 min after insulin injection and then increased until the end (**Figures 3C,D**). The blood glucose levels of the mice in T2DP group were lower than those of T2D group at all the time points in IPITT. The AUC of T2D group was significantly higher than that of the CON group ($p < 0.05$) while PDBW treatment significantly decreased the AUC ($p < 0.05$) and improved insulin tolerance.

The effect of PDBW on PTT was presented in **Figures 3E,F**. The pyruvate tolerance capacity of the T2D group was severely impaired comparing with the CON group, as shown by the increase in blood glucose levels and higher AUC of PTT after sodium pyruvate solution injection. When the T2D mice were supplemented with PDBW, the blood glucose level and the AUC during PTT were markedly reduced ($p < 0.05$), suggesting the improvement in gluconeogenesis.

PDBW Prevented Hepatic Lipid Accumulation in HFD/STZ-Induced Diabetic Mice

To investigate the effects of PDBW on the lipid accumulation of liver in HFD-STZ induced diabetic mice, H&E staining of liver tissues was performed. Histologic analysis of liver showed a remarkable increase in the amount of lipid vacuoles within hepatocytes in mice from the T2D group compared to the CON group (**Figure 4**). However, treatment of PDBW significantly decreased lipid droplets, suggesting PDBW effectively prevents hepatic lipid accumulation.

PDBW Down-Regulated mRNA Expressions of Key Gluconeogenic Enzymes in Liver of HFD/STZ-Induced Diabetic Mice

To investigate the effects of PDBW on gluconeogenesis in HFD-STZ induced diabetic mice, the mRNA expression of key gluconeogenic enzymes (PEPCK and G6Pase) was determined. As revealed in **Figure 5**, compared to the CON group, the mRNA expression levels of PEPCK and G6Pase were significantly increased in T2D group ($p < 0.05$). After PDBW treatment, the mRNA expression levels of PEPCK and G6Pase were decreased by 63.13 and 68.03%, respectively, compared to the T2D group ($p < 0.05$). The data suggests that PDBW might modulate the glucose gluconeogenesis through down-regulation of key enzymes involved in liver gluconeogenesis.

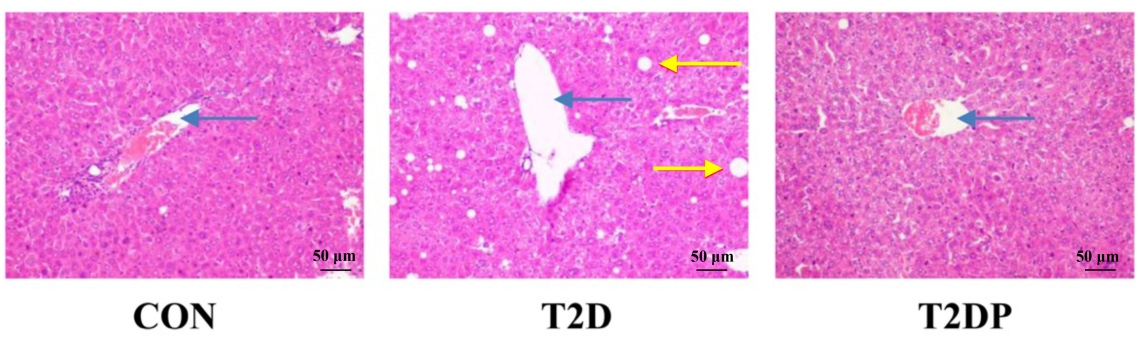

FIGURE 4 | Effects of *Potentilla discolor* Bunge water extract (PDBW) on histological changes in liver (H&E, 200×) of HFD-STZ induced diabetic mice. Blue arrows indicate central veins. Yellow arrows indicate lipid droplets.

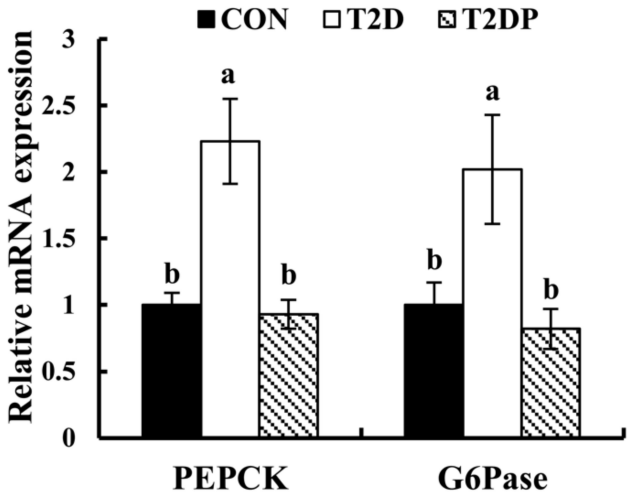

FIGURE 5 | Effects of *Potentilla discolor* Bunge water extract (PDBW) on the phosphoenolpyruvate carboxykinase and glucose-6-phosphatase mRNA gene expression in liver of HFD-STZ induced diabetic mice. All values are the mean ± standard error ($n = 6$); Values marked with different lower-case letters in superscript format indicate significant differences between three groups ($p < 0.05$).

PDBW Regulated Hepatic Glycogen Content and Phosphorylation Levels of Key Glycogenic Enzmyes in Liver of HFD/STZ-Induced Diabetic Mice

To investigate the effects of PDBW on glycogenesis, the glycogen content and protein expression of enzymes involved in glycogen synthesis were determined. As shown in **Figure 6A**, compared to the CON group, the glycogen content was significantly reduced in diabetic mice of T2D group. However, PDBW supplementation increased the glycogen content by 108.64% compared to T2D group. As shown in **Figure 6B**, the ratio of p-GS/GS in T2D group was remarkably higher than that in the CON group ($p < 0.05$). After treatment with PDBW, the p-GS/GS ratio was significantly decreased ($p < 0.05$), suggesting the inhibition of GS phosphorylation. Besides, diabetic mice showed a lower p- GSK3β/GSK3β ratio in comparison with the CON group ($p < 0.05$). PDBW elevated the ratio of p-GSK3β/GSK3β, showing the increased phosphorylation of GSK3β. These results indicate that PDBW increased glycogen content by regulating the phosphorylation of GS and GSK3β in diabetic mice.

PDBW Activated the PI3K/Akt and AMPK Signaling in Liver of HFD/STZ-Induced Diabetic Mice

To further explore whether PDBW regulates gluconeogenesis and glycogenesis by activating Akt and AMPK pathway, the contents of p-Akt and p-AMPK were assessed. As shown in **Figure 7**, compared to the CON group, the ratio of p-Akt/Akt and p-AMPK/AMPK were reduced in T2D group ($p < 0.05$), while PDBW treatment increased the ratio of p-Akt/Akt and p-AMPK/AMPK. This result suggests that the effects of PDBW on the gluconeogenesis and glycogenesis are related to the activation of Akt and AMPK pathways.

DISCUSSION

Type 2 diabetes, one of the most common metabolic disorders, is associated with an abnormal modulation of glucose metabolism. Therefore, effective blood glucose control improves the living quality of T2D patients. In the present study, we found that PDBW decreased blood glucose level and increased serum insulin level, and improved glucose tolerance, insulin sensitivity and lipid profiles in HFD/STZ-induced diabetic mice. PDBW also regulated the liver glucose metabolism by inhibiting gluconeogenesis and increasing glycogen synthesis, which contributed to the alleviation of metabolic disorders in T2D.

In T2D, hyperglycemia is the consequence of insufficiency of insulin secretion from the pancreatic β cells and inability of target organs to respond to insulin (21). Afterwards, pancreas β cells succumb to the consistent high glucose level, leading to a series of metabolic syndrome (22). In order to initiate the insulin dysregulation related to T2D, the high-fat diet to animals is an effective method to induce obesity, which acts as a known risk factor for T2D (23). Besides, a low dose of β cell toxin STZ can cause a mild impairment of insulin secretion attributed to the later stage of T2DM and is often used to hasten the T2D development in mice similar to the condition observed in human (23). Therefore, a murine model of T2D induced by high fat diet combined with multiple low doses of STZ could mimic the metabolic characteristics of type 2 diabetes in humans (24). In our study, the HFD/STZ-induced diabetic mice exhibited high blood glucose concentrations and low plasma insulin levels with impaired glucose tolerance and insulin sensitivity, which are in concert with previous studies (25).

After PDBW treatment, the HFD/STZ-induced diabetic mice showed a significant decrease in blood glucose level and an increase in serum insulin level, paralleling the increase in insulin sensitivity shown by greater improvement in OGTT and IPITT. Another report also showed that treatment of ob-db mice with PDB decoction for 4 weeks caused a decrease in the blood glucose values (16). Besides, HbA1c reflects long-term glycaemic exposure and has better pre-analytical stability for diabetes than single measures of glucose concentration such as fasting blood glucose or OGTT (26). In our study, HbA1c of diabetic mice was remarkably increased while PDBW prevented the elevation, indicating the anti-diabetic effects of PDBW. It has been reported that some of the major compounds of PBDW could attenuate hyperglycemia and related metabolic disorders. Epicatechin has been shown to lower blood glucose levels in diabetic patients and restored insulin sensitivity and improved glucose metabolism in HFD-fed mice (27). Cyclocarya paliurus with a high content of quercetin 3-O-β-D-glucuronide was beneficial to reverse body weight loss and to reduce glucose levels in OGTT and IPITT tests of STZ-induced diabetic

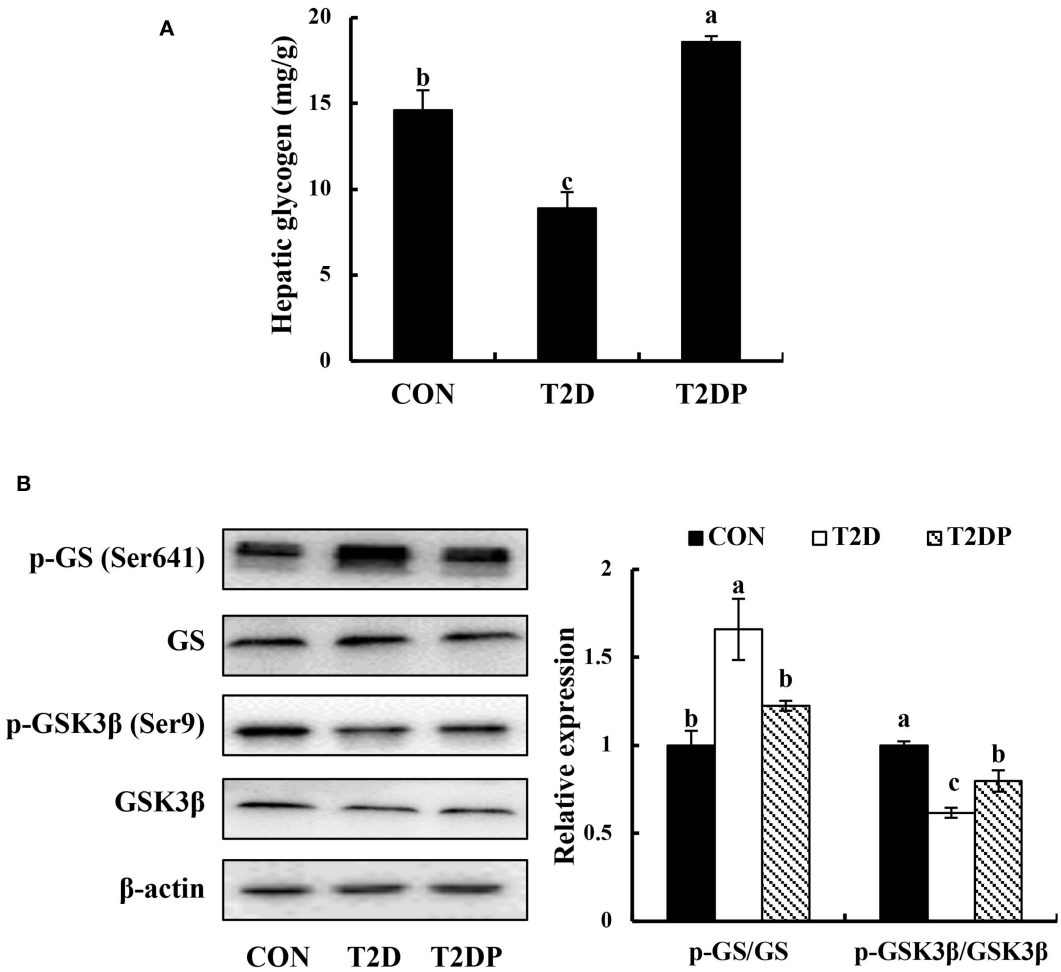

FIGURE 6 | Effects of *Potentilla discolor* Bunge water extract (PDBW) on glycogenesis in liver of HFD-STZ induced diabetic mice. **(A)** Hepatic glycogen content. **(B)** Hepatic protein expression of p-GSK3β, GSK3β, p-GS, and GSK3β. All values are the mean ± standard error ($n = 6$); Values marked with different lower-case letters in superscript format indicate significant differences between three groups ($p < 0.05$).

mice (28). Pilea microphylla rich in apigenin-7-O-β-D-glucoside produced significant reduction in plasma glucose in HFD/STZ-induced diabetic mice (29). Besides, α-glucosidase inhibitors are used and marketed as anti-diabetic drugs that can prevent carbohydrates from producing glucose (30). Quercetin 3-O-β-D-glucuronide and apigenin-7-O-glucoside exhibited remarkable α-glucosidase inhibitory activity and might serve as effective α-glucosidase inhibitor and insulin sensitizer (31). Therefore, the anti-hyperglycemic effects of PDBW may involve in these bioactive compounds-induced improvement in blood glucose control.

Notably, hyperlipidemia is closely related with hyperglycemia in diabetic patients with poor glucose metabolic control and increase the risk of diabetic vascular complications (5). Previous studies have demonstrated that HFD-fed mice become more sensitive to the development of hyperlipidemia under STZ treatment (25). In the present study, diabetic mice had a significant increase in TG, TC, LDL-c, and FFA levels and a decrease in HDL-c level while PDBW administration reversed these effects. Additionally, the H&E staining of liver showed that PDBW treatment significantly reduced lipid accumulation, demonstrating that PDBW prevented the abnormalities in lipid metabolism. Consistent with our results, the major component of PDBW, epicatechin, alleviated liver fat accumulation and reduced the contents of TC, LDL-c, and TG while increased HDL-c in hyperlipidemic rats (32). Scutellarin given to patients with hyperlipidemia decreased the levels of TC, LDL-c, and TG, but increased the level of HDL-c (33). The flavonoid rich fraction containing apigenin-7-O-β-D-glucoside decreased the TG and TC contents in plasma of HFD/STZ-induced diabetic mice (29).

The liver is primarily responsible for the maintenance of blood glucose levels by its ability to produce glucose from gluconeogenesis and to store glucose as glycogen (6). Hepatic glucose output is primarily regulated by PEPCK and G6Pase, which are the rate-limiting enzymes in gluconeogenesis (34). In the present study, PDBW reduced the elevated mRNA levels of

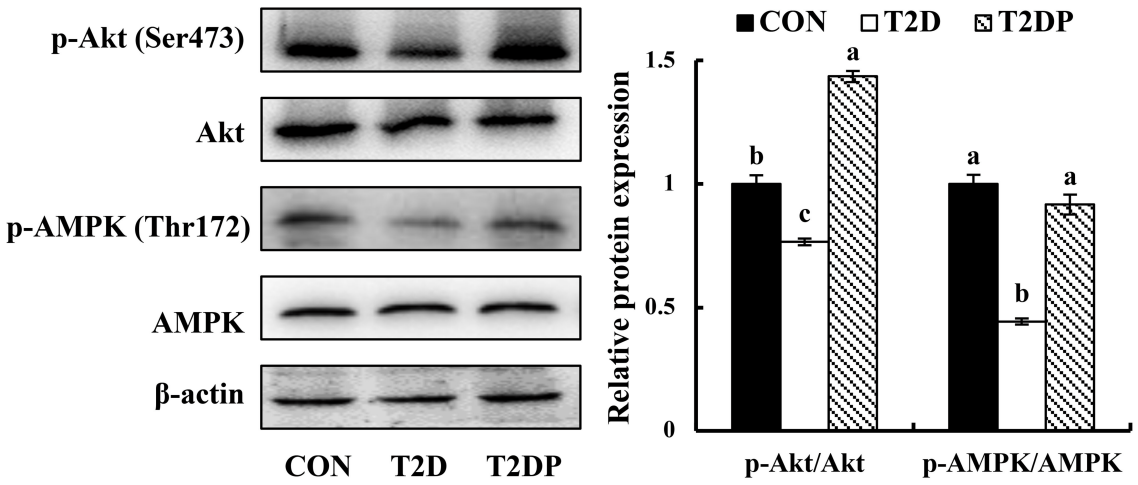

FIGURE 7 | Effects of *Potentilla discolor* Bunge water extract (PDBW) on hepatic protein contents of p-Akt, Akt, p-AMPK, and AMPK. All values are the mean ± standard error ($n = 6$); Values marked with different lower-case letters in superscript format indicate significant differences between three groups ($p < 0.05$).

PEPCK and G6Pase induced by HFD/STZ. Moreover, PDBW-treated diabetic mice exhibited significant decrease in blood glucose levels after an injection of pyruvate, indicating that gluconeogenesis from pyruvate decreased *in vivo*. Glycogen synthase is a key rate-limiting enzyme for glycogen synthesis, which catalyzes the incorporation of UDP-glucose into glycogen chains. GSK3β has been implicated in mediating the development of insulin resistance, mainly by inhibition of glycogen synthesis (35). GSK3β inhibits glycogen biosynthesis through inactivation of GS by inhibitory phosphorylation (35). In our study, PDBW improved accumulation of hepatic glycogen in T2D mice, as evidenced by the raise in the hepatic glycogen contents. PDBW treatment reversed the elevation in the phosphorylation level of GS and up-regulated the phosphorylation level of GSK3β, indicating that PDBW promoted glycogenesis. These findings are similar to previous reports showing that epicatechin possessed insulin-like effects and modulated the expression of PEPCK, leading to a diminished hepatic glucose production (36). Quercitrin increased the insulin secretion and improved glucose homeostasis along with the restoration of glycogen content and alteration of gluconeogenic enzymes in streptozotocin-induced diabetic rats (37).

In relation to T2D, many protein kinases have been shown to play vital roles in the regulation of hepatic glucose metabolism and insulin sensitivity, such as Akt and AMPK. The serine/threonine kinase Akt, also known as protein kinase B (PKB), plays a central but diverse role in cell signaling downstream of hormones, growth factors, cytokines, and other cellular stimuli (10). Insulin-mediated regulation of glycogenesis and gluconeogenesis are associated with the phosphorylation of insulin receptor substrate mediated by the insulin receptor, thus activating the PI3K/Akt signal pathway (38). The impairment of signaling through PI3K/Akt may predispose to the development of diabetes (38). Besides, AMPK, the key regulator of energy balance, has the potential to control whole-body glucose metabolism against obesity and T2D (12). Particularly, the activation of AMPK can lead to a decrease in gluconeogenesis-related gene transcription, increased fatty acid oxidation, and decreased fatty acid synthesis in liver, thereby lowering the blood glucose level and lipid accumulation (39). Epicatechin from cocoa strengthened the insulin signaling by Akt phosphorylation and suppressed hepatic gluconeogenesis through AMPK activation in HepG2 cells (36). Quercetin 3-O-β-D-glucuronide ameliorated insulin resistant endothelial dysfunction by positive regulation of Akt (40). Scutellarin could promote glucose uptake in adipocytes by management of AMPK or Akt activity (41). Herein PDBW increased the phosphorylation of both Akt and AMPK in HFD/STZ mice, which demonstrated that PDBW provided strong impacts on insulin signaling regulation by Akt and AMPK activation.

Many metabolomics studies have showed that the metabolites including glucose, pyruvate, lactate, β-hydroxybutyrate, succinate, citrate, and 2-oxoglutarate have been generally identified as biomarkers in diabetic models and most of them are related to the carbohydrate metabolism, particularly glycolysis/gluconeogenesis and TCA cycle (42). Glucose can be broken down and converted into pyruvate that is closely correlated with the glycolysis/gluconeogenesis pathway (42). The increased level of glucose suppresses the action of glycolytic enzymes and activates gluconeogenesis metabolism, thus reducing the pyruvate levels in the diabetic animal models (43, 44). Then the decrease in pyruvate level reduces the acetyl-CoA production and results in the reduction of TCA cycle intermediates (45). Administration of several medicinal plants can prevent metabolic disorders in diabetic rats, which was always associated with the alternations of metabolic intermediates linked to glucose metabolism and TCA cycle (46, 47). Therefore, PBDW may contribute to the antidiabetic activity through regulating the metabolites associated with glycolysis/gluconeogenesis and TCA cycle. However, the specific

metabolites linked to glucose metabolism altered by PDBW need to be further investigated by metabolomics.

CONCLUSION

To conclude, oral PDBW administration at 400 mg/kg BW prevented the decrease of body weight, reduced the levels of blood glucose and HbA1c and increased serum insulin levels in HFD-STZ induced diabetic mice. The lipid profiles, glucose tolerance and insulin sensitivity were improved after PDBW treatment. PDBW regulated gluconeogenesis by decreased the mRNA expression of PEPCK and G6Pase. PDBW also promoted glycogenesis as shown by the increase in hepatic glycogen content and GS phosphorylation and the down-regulation of GSK3β phosphorylation. Furthermore, the upstream signaling pathways, Akt and AMPK, may mediate the effects of PDBW on hepatic glucose metabolism. These findings provide evidences of PDBW in the prevention and amelioration of type 2 diabetes.

DATA AVAILABILITY STATEMENT

The raw data supporting the conclusions of this article will be made available by the authors, without undue reservation.

ETHICS STATEMENT

The animal study was reviewed and approved by China Agricultural University Animal Ethics Committee.

AUTHOR CONTRIBUTIONS

TL, RC, and XM contributed to the conception and design of the study. TL and RC conducted experiments. TL and HZ analyzed the data. TL wrote the manuscript. XM and MD revised the manuscript. All authors contributed to the article and approved the submitted version.

FUNDING

This work was supported by the National Natural Science Foundation of China (Grant no. 31871806) and the Beijing Dairy Industry Innovation Team (BAIC06-2020).

SUPPLEMENTARY MATERIAL

The Supplementary Material for this article can be found online at: https://www.frontiersin.org/articles/10.3389/fnut.2020.00161/full#supplementary-material

REFERENCES

1. Ogurtsova K, da Rocha Fernandes JD, Huang Y, Linnenkamp U, Guariguata L, Cho NH, et al. IDF diabetes atlas: global estimates for the prevalence of diabetes for 2015 and 2040. *Diabetes Res Clin Pract.* (2017) 128:40–50. doi: 10.1016/j.diabres.2017.03.024
2. Chatterjee S, Khunti K, Davies MJ. Type 2 diabetes. *Lancet.* (2017) 389:2239–51. doi: 10.1016/S0140-6736(17)30058-2
3. Levetan C. Oral antidiabetic agents in type 2 diabetes. *Curr Med Res Opin.* (2007) 23:945–52. doi: 10.1185/030079907X178766
4. Chatterjee S, Davies MJ. Current management of diabetes mellitus and future directions in care. *Postgrad Med J.* (2015) 91:612–21. doi: 10.1136/postgradmedj-2014-133200
5. Rines AK, Sharabi K, Tavares CD, Puigserver P. Targeting hepatic glucose metabolism in the treatment of type 2 diabetes. *Nat Rev Drug Discov.* (2016) 15:786–804. doi: 10.1038/nrd.2016.151
6. Bantubungi K, Hannou SA, Caron-Houde S, Vallez E, Baron M, Lucas A, et al. Cdkn2a/p16(Ink4a) regulates fasting-induced hepatic gluconeogenesis through the PKA-CREB-PGC1 alpha pathway. *Diabetes.* (2014) 63:3199–209. doi: 10.2337/db13-1921
7. Jiang G, Zhang BB. Glucagon and regulation of glucose metabolism. *Am J Physiol Endocrinol Metab.* (2003) 284:E671–8. doi: 10.1152/ajpendo.00492.2002
8. Palsamy P, Subramanian S. Modulatory effects of resveratrol on attenuating the key enzymes activities of carbohydrate metabolism in streptozotocin-nicotinamide-induced diabetic rats. *Chem Biol Interact.* (2009) 179:356–62. doi: 10.1016/j.cbi.2008.11.008
9. Liu TY, Shi CX, Gao R, Sun HJ, Xiong XQ, Ding L, et al. Irisin inhibits hepatic gluconeogenesis and increases glycogen synthesis *via* the PI3K/Akt pathway in type 2 diabetic mice and hepatocytes. *Clin Sci.* (2015) 129:839–50. doi: 10.1042/CS20150009
10. Manning BD, Toker A. AKT/PKB signaling: navigating the network. *Cell.* (2017) 169:381–405. doi: 10.1016/j.cell.2017.04.001
11. Meng F, Ning H, Sun Z, Huang F, Li Y, Chu X, et al. Ursolic acid protects hepatocytes against lipotoxicity through activating autophagy *via* an AMPK pathway. *J Funct Foods.* (2015) 17:172–82. doi: 10.1016/j.jff.2015.05.029
12. Day EA, Ford RJ, Steinberg GR. AMPK as a therapeutic target for treating metabolic diseases. *Trends Endocrinol Metab.* (2017) 28:545–60. doi: 10.1016/j.tem.2017.05.004
13. Tomczyk M, Latte KP. Potentilla–a review of its phytochemical and pharmacological profile. *J Ethnopharmacol.* (2009) 122:184–204. doi: 10.1016/j.jep.2008.12.022
14. Jin Q, Nan JX, Lian LH. Antitumor activity of leaves from *potentilla discolor* on human hepatocellular carcinoma cell line HepG-2. *Chin J Nat Med.* (2011) 9:61–4. doi: 10.1016/S1875-5364(11)60022-8
15. Yang J, Chen H, Zhang L, Wang Q, Lai MX. Anti-diabetic effect of standardized extract of *Potentilla discolor* bunge and identification of its active components. *Drug Dev Res.* (2009) 71:127–32. doi: 10.1002/ddr.20340
16. Song C, Huang L, Rong L, Zhou Z, Peng X, Yu S, et al. Anti-hyperglycemic effect of *Potentilla discolor* decoction on obese-diabetic (Ob-db) mice and its chemical composition. *Fitoterapia.* (2012) 83:1474–83. doi: 10.1016/j.fitote.2012.08.013
17. Li X, Sui Y, Li S, Xie B, Sun Z. A-type procyanidins from litchi pericarp ameliorate hyperglycaemia by regulating hepatic and muscle glucose metabolism in streptozotocin (STZ)-induced diabetic mice fed with high fat diet. *J Funct Foods.* (2016) 27:711–22. doi: 10.1016/j.jff.2016.08.010
18. Retnakaran R, Shen S, Hanley AJ, Vuksan V, Hamilton JK, Zinman B. Hyperbolic relationship between insulin secretion and sensitivity on oral glucose tolerance test. *Obesity.* (2008) 16:1901–7. doi: 10.1038/oby.2008.307
19. Chen Y, Luo J, Zhang Q, Kong L. Identification of active substances for dually modulating the renin–angiotensin system in bidens pilosa by liquid chromatography–mass spectrometry–based chemometrics. *J Funct Foods.* (2016) 21:201–11. doi: 10.1016/j.jff.2015.12.011
20. Omezzine F, Bouaziz M, Simmonds MS, Haouala R. Variation in chemical composition and allelopathic potential of mixoploid trigonella foenum-graecum L. with developmental stages. *Food Chem.* (2014) 148:188–95. doi: 10.1016/j.foodchem.2013.10.040
21. Perry RJ, Kim T, Zhang XM, Lee HY, Pesta D, Popov VB, et al. Reversal of hypertriglyceridemia, fatty liver disease, and insulin resistance by a liver-targeted mitochondrial uncoupler. *Cell Metab.* (2013) 18:740–8. doi: 10.1016/j.cmet.2013.10.004

22. Giri B, Dey S, Das T, Sarkar M, Banerjee J, Dash SK. Chronic hyperglycemia mediated physiological alteration and metabolic distortion leads to organ dysfunction, infection, cancer progression and other pathophysiological consequences: an update on glucose toxicity. *Biomed Pharmacother.* (2018) 107:306–28. doi: 10.1016/j.biopha.2018.07.157
23. Srinivasan K, Viswanad B, Asrat L, Kaul CL, Ramarao P. Combination of high-fat diet-fed and low-dose streptozotocin-treated rat: a model for type 2 diabetes and pharmacological screening. *Pharmacol Res.* (2005) 52:313–20. doi: 10.1016/j.phrs.2005.05.004
24. Nath S, Ghosh SK, Choudhury Y. A murine model of type 2 diabetes mellitus developed using a combination of high fat diet and multiple low doses of streptozotocin treatment mimics the metabolic characteristics of type 2 diabetes mellitus in humans. *J Pharmacol Toxicol Methods.* (2017) 84:20–30. doi: 10.1016/j.vascn.2016.10.007
25. Li YG, Ji DF, Zhong S, Lin TB, Lv ZQ. Hypoglycemic effect of deoxynojirimycin-polysaccharide on high fat diet and streptozotocin-induced diabetic mice *via* regulation of hepatic glucose metabolism. *Chem Biol Interact.* (2015) 225:70–9. doi: 10.1016/j.cbi.2014.11.003
26. Doerr R, Hoffmann U, Otter W, Heinemann L, Hunger-Battefeld W, Kulzer B, et al. Oral glucose tolerance test and HbA(1)c for diagnosis of diabetes in patients undergoing coronary angiography: the silent diabetes study. *Diabetologia.* (2011) 54:2923–30. doi: 10.1007/s00125-011-2253-y
27. Abdulkhaleq LA, Assi MA, Noor MHM, Abdullah R, Saad MZ, Taufiq-Yap YH. Therapeutic uses of epicatechin in diabetes and cancer. *Vet World.* (2017) 10:869–72. doi: 10.14202/vetworld.2017.869-872
28. Liu Y, Cao Y, Fang S, Wang T, Yin Z, Shang X, et al. Antidiabetic effect of cyclocarya paliurus leaves depends on the contents of antihyperglycemic flavonoids and antihyperlipidemic triterpenoids. *Molecules.* (2018) 23:1042. doi: 10.3390/molecules23051042
29. Bansal P, Paul P, Mudgal J, Nayak PG, Pannakal ST, Priyadarsini KI, et al. Antidiabetic, antihyperlipidemic and antioxidant effects of the flavonoid rich fraction of Pilea microphylla (L.) in high fat diet/streptozotocin-induced diabetes in mice. *Exp Toxicol Pathol.* (2012) 64:651–8. doi: 10.1016/j.etp.2010.12.009
30. Tan K, Tesar C, Wilton R, Jedrzejczak RP, Joachimiak A. Interaction of antidiabetic alpha-glucosidase inhibitors and gut bacteria alpha-glucosidase. *Protein Sci.* (2018) 27:1498–508. doi: 10.1002/pro.3444
31. Jia Y, Ma Y, Cheng G, Zhang Y, Cai S. Comparative study of dietary flavonoids with different structures as alpha-glucosidase inhibitors and insulin sensitizers. *J Agric Food Chem.* (2019) 67:10521–33. doi: 10.1021/acs.jafc.9b04943
32. Cheng H, Xu N, Zhao W, Su J, Liang M, Xie Z, et al. (-)-Epicatechin regulates blood lipids and attenuates hepatic steatosis in rats fed high-fat diet. *Mol Nutr Food Res.* (2017) 61:1700303. doi: 10.1002/mnfr.201700303
33. Wang L, Ma Q. Clinical benefits and pharmacology of scutellarin: a comprehensive review. *Pharmacol Ther.* (2018) 190:105–27. doi: 10.1016/j.pharmthera.2018.05.006
34. Collins QF, Liu HY, Pi J, Liu Z, Quon MJ, Cao W. Epigallocatechin-3-gallate (EGCG), a green tea polyphenol, suppresses hepatic gluconeogenesis through 5'-AMP-activated protein kinase. *J Biol Chem.* (2007) 282:30143–9. doi: 10.1074/jbc.M702390200
35. Lee J, Kim MS. The role of GSK3 in glucose homeostasis and the development of insulin resistance. *Diabetes Res Clin Pract.* (2007) 77(Suppl. 1):S49–57. doi: 10.1016/j.diabres.2007.01.033
36. Cordero-Herrera I, Martin MA, Bravo L, Goya L, Ramos S. Cocoa flavonoids improve insulin signalling and modulate glucose production via AKT and AMPK in HepG2 cells. *Mol Nutr Food Res.* (2013) 57:974–85. doi: 10.1002/mnfr.201200500
37. Babujanarthanam R, Kavitha P, Pandian MR. Quercitrin, a bioflavonoid improves glucose homeostasis in streptozotocin-induced diabetic tissues by altering glycolytic and gluconeogenic enzymes. *Fundam Clin Pharmacol.* (2010) 24:357–64. doi: 10.1111/j.1472-8206.2009.00771.x
38. Sajan MP, Ivey RA III, Farese RV. BMI-related progression of atypical PKC-dependent aberrations in insulin signaling through IRS-1, Akt, FoxO1 and PGC-1alpha in livers of obese and type 2 diabetic humans. *Metabolism.* (2015) 64:1454–65. doi: 10.1016/j.metabol.2015.08.011
39. Ha J, Guan KL, Kim J. AMPK and autophagy in glucose/glycogen metabolism. *Mol Aspects Med.* (2015) 46:46–62. doi: 10.1016/j.mam.2015.08.002
40. Guo XD, Zhang DY, Gao XJ, Parry J, Liu K, Liu BL, et al. Quercetin and quercetin-3-O-glucuronide are equally effective in ameliorating endothelial insulin resistance through inhibition of reactive oxygen species-associated inflammation. *Mol Nutr Food Res.* (2013) 57:1037–45. doi: 10.1002/mnfr.201200569
41. Yang LL, Xiao N, Liu J, Liu K, Liu B, Li P, et al. Differential regulation of baicalin and scutellarin on AMPK and Akt in promoting adipose cell glucose disposal. *Biochim Biophys Acta Mol Basis Dis.* (2017) 1863:598–606. doi: 10.1016/j.bbadis.2016.11.024
42. Hasanpour M, Iranshahy M, Iranshahi M. The application of metabolomics in investigating anti-diabetic activity of medicinal plants. *Biomed Pharmacother.* (2020) 128:110263. doi: 10.1016/j.biopha.2020.110263
43. Mediani A, Abas F, Maulidiani M, Khatib A, Tan CP, Ismail IS, et al. Metabolic and biochemical changes in streptozotocin induced obese-diabetic rats treated with phyllanthus niruri extract. *J Pharm Biomed Anal.* (2016) 128:302–12. doi: 10.1016/j.jpba.2016.06.003
44. Zhao L, Gao H, Lian F, Liu XA, Zhao YX, Lin DH. H-1-NMR-based metabonomic analysis of metabolic profiling in diabetic nephropathy rats induced by streptozotocin. *Am J Physiol-Renal.* (2011) 300:F947–56. doi: 10.1152/ajprenal.00551.2010
45. Abu Bakar MH, Sarmidi MR, Cheng KK, Khan AA, Suan CL, Huri HZ, et al. Metabolomics - the complementary field in systems biology: a review on obesity and type 2 diabetes. *Mol Biosyst.* (2015) 11:1742–74. doi: 10.1039/C5MB00158G
46. Wan W, Jiang B, Sun L, Xu LJ, Xiao PG. Metabolomics reveals that vine tea (Ampelopsis grossedentata) prevents high-fat-diet-induced metabolism disorder by improving glucose homeostasis in rats. *PLoS ONE.* (2017) 12:e0182830. doi: 10.1371/journal.pone.0182830
47. Shen X, Liu H, Xiang H, Qin XM, Du GH, Tian JS. Combining biochemical with H-1 NMR-based metabolomics approach unravels the antidiabetic activity of genipin and its possible mechanism. *J Pharmaceut Biomed.* (2016) 129:80–9. doi: 10.1016/j.jpba.2016.06.041

Conflict of Interest: The authors declare that the research was conducted in the absence of any commercial or financial relationships that could be construed as a potential conflict of interest.

frontiers in Nutrition

ORIGINAL RESEARCH
published: 22 October 2020
doi: 10.3389/fnut.2020.584900

Identification of Flavoanoids From Finger Citron and Evaluation on Their Antioxidative and Antiaging Activities

Xuguang Luo[1,2†], *Jin Wang*[1,2†], *Haiqiang Chen*[1,2], *Aimei Zhou*[1,2*], *Mingyue Song*[1], *Qingping Zhong*[1,2], *Hanmin Chen*[2] *and Yong Cao*[1]

[1] Guangdong Provincial Key Laboratory of Nutraceuticals and Functional Foods, College of Food Science, South China Agricultural University, Guangzhou, China, [2] Guangdong Zhancui Food Co., Ltd, Chaozhou, China

Finger citron (*Citrus medica* L. *var. sarcodactylis* Swingle) is a traditional Chinese herb and considered as a healthy food. Flavonoids are the major bioactive substances in Finger citron. In this study, the major flavonoids of finger citron (FFC) were purified with AB-8 macroporous resins, and then three of them were identified as diosmetin-6-8-di-*C*-glucoside, hesperidin and diosmetin-6-*C*-glucoside, and other two were preliminarily inferred as limocitrol 3-alpha-l-arabinopyranosyl-(1->3)-galactoside and scutellarein 4′-methyl ether 7-glucoside by high-performance liquid chromatography and ultraperformance liquid chromatography to quadrupole time-of-flight mass spectrometry. Further, their antioxidation and antiaging activities were determined *in vitro* and *in vivo*. *In vitro*, chemical assays revealed that the purified FFC had strong antioxidative activity as demonstrated by its strong DPPH (2,2-diphenyl-1-picrylhydrazyl) and ABTS [2,2-azinobis (3-ethyl-benzothiazoline-6-sulphonic acid) diammonium salt] radical scavenging activities and ORAC (oxygen radical absorbance capacity). *In vivo*, the purified FFC significantly increased the mean and maximum lifespan of *Caenorhabditis elegans* by 31.26 and 26.59%, respectively, and showed no side effects on their physiological functions. Under normal and oxidative stress conditions, purified FFC reduced the accumulation of reactive oxygen species (ROS) and malondialdehyde, while increased superoxide dismutase (SOD) and catalase (CAT) enzyme activities in *C. elegans*. Together, we successfully identified three major substances in purified FFC of finger citron and determined the excellent antiaging activity of FFC, which is attributed to its strong antioxidative activity and effect on homeostasis of ROS.

Keywords: finger citron, flavonoids, antioxidation, anti-aging, *Caenorhabditis elegans*

OPEN ACCESS

Edited by:
Hang Xiao,
University of Massachusetts Amherst, United States

Reviewed by:
Quancai Sun,
Jiangsu University, China
Sui Kiat Chang,
Chinese Academy of Sciences, China

***Correspondence:**
Aimei Zhou
zhouam@scau.edu.cn

†These authors have contributed equally to this work and share first authorship

Specialty section:
This article was submitted to Food Chemistry, a section of the journal Frontiers in Nutrition

Received: *18 July 2020*
Accepted: *11 September 2020*
Published: *22 October 2020*

Citation:
Luo X, Wang J, Chen H, Zhou A, Song M, Zhong Q, Chen H and Cao Y (2020) Identification of Flavoanoids From Finger Citron and Evaluation on Their Antioxidative and Antiaging Activities. Front. Nutr. 7:584900. doi: 10.3389/fnut.2020.584900

INTRODUCTION

Flavonoids are important plant secondary metabolites presented broadly in nature (1), which provide protection against foreign agents such as UV radiation, parasite, and viruses (2). Currently, more than 9,000 flavonoids have been discovered (3), and *Citrus* fruits are found to be a rich source of flavonoids (4). The biological activity of flavonoids has been widely investigated, including antioxidative (5, 6), antiaging (6), anti-inflammatory (7), anticancer (8), antidiabetic, and antibacterial (9, 10).

Finger citron (*Citrus medica* L. *var. sarcodactylis* Swingle), with a popular name "Fo-Shou" in Chinese, belongs to the variants of *Citrus medica* L. and is considered as both food and medicine in China. As a food, finger citron is widely produced into preserved fruit (11). As a traditional Chinese medicine adjuvant, finger citron is often used for the treatment of stomachache, headache, infectious hepatitis, arthritis, etc. (12). Finger citron is now widely distributed in the southwest of China, India, Vietnam, and Malaysia (13) and has been reported to contain various bioactive components including essential oil (12), flavonoids (13), polysaccharide (14), coumarin, and phenolic acids (15), etc. The essential oil of finger citron has attracted many scientific interests due to its diverse bioactivities, such as anti-inflammatory, antioxidation, and antibacterial (12, 14, 16), but finger citron flavonoids, also as the primary bioactive ingredients in finger citron, received relatively few studies. Little information about the major components and biological activities of flavonoids from finger citron is available, which limits the exploration of their potential application value.

Aging has many adverse effects on human health. It increases the risk of cancer, neurodegenerative disorders, and cardiovascular and metabolic diseases (17–21). Reactive oxygen species (ROS), produced by all aerobic cells (22), play an important role in aging. According to the free radical theory of aging, which is later called oxidative stress theory of aging, age-related functional losses are caused as the result of the accumulation of oxidative damage to biological macromolecules by ROS and NO (22). Flavonoids have been reported to show excellent antioxidative and antiaging activities (23). The flavonoids extracted from finger citron may also have these functional activities. DPPH (2,2-diphenyl-1-picrylhydrazyl), ABTS [2,2-azinobis (3-ethyl-benzothiazoline-6-sulphonic acid) diammonium salt] radical scavenging capacity and ORAC (oxygen radical absorbance capacity) assays are the most commonly used assays for determining antioxidation performance *in vitro* (24), whereas *Caenorhabditis elegans* is a well-established *in vivo* model organism that has been successfully used to study organismal aging, antioxidation, and identification of new pharmacology (25, 26) because of its advantages of facile lifespan, ease of cultivation, complete genome sequence, and so on (27). Moreover, it is demonstrated that *C. elegans* possesses 60 to 80% of human gene homologs (28).

In the present study, flavonoids of finger citron (FFC) were extracted by continuous phase-transition extraction with a novel type of extraction device developed by us, which has great advantages in extraction efficiency and yield of active compositions (29, 30). The resulted FFC were then purified and identified, and its antioxidative and antiaging were further investigated *in vitro* and *in vivo*.

Abbreviations: FFC, flavonoids of finger citron; *C. elegans*, *Caenorhabditis elegans*; *E. coli* OP50, *Escherichia coli* strain OP50; DPPH, 2,2-diphenyl-1-picrylhydrazyl; ABTS, 2,2-azinobis (3-ethyl-benzothiazoline-6-sulphonic acid) diammonium salt; AAPH, 2,2′-azobis (2-methylpropionamidine) dihydrochloride; H_2DCF-DA, 2′,7′-dichlorodihydrofluorescein diacetate; DCF, 2′,7′-dichlorofluorescein; ROS, reactive oxygen species; MDA, malondialdehyde; SOD, superoxide dismutase; CAT, catalase.

MATERIALS AND METHODS

Materials

Dry finger citron slices were supported by Guangdong Zhancui Food Co., Ltd. (Chaozhou, Guangdong, China). The samples were further dried with hot air at 40°C for 24 h to guarantee the moisture content was lower than 15%. Then the dried samples were smashed into powder with particle size of 30 mesh, which was packed immediately in vacuum polyethylene bags and frozen at −20°C for further use.

Chemicals

AB-8 macroporous resin was provided by Bengbu Tianxing Ion-Resin Co., Ltd. (BengBu, Anhui, China). DPPH and fluorescein sodium salt were purchased from Sigma Chemical Co., Ltd. (St. Louis, United States). Trolox, ABTS, and 2,2′-azobis(2-methylpropionamidine) dihydrochloride (AAPH) were purchased from Aladdin Bio-Chem Technology Co., Ltd. (Shanghai, China). *C. elegans* of wild-type N2 (var. Bristol) was obtained from the Caenorhabditis Genetics Center (University of Minnesota, Minneapolis, MN, United States). The uracil mutant *Escherichia coli* OP50 (*E. coli* OP50) was provided by the College of Resource and Environment, South China Agricultural University. 2′,7′-dichlorodihydrofluorescein diacetate (H_2DCF-DA) and paraquat (PQ) were purchased from Sigma–Aldrich Co., Ltd (St. Louis, MO, USA). SOD (superoxide dismutase), CAT (catalase), and MDA (malondialdehyde) assay kits were provided by Nanjing Jiancheng Bioengineering Institute (Nanjing, Jiangsu, China). All other chemicals were of analytical-reagent grade.

Isolation and Purification of FFC

Based on our previous study, 400 g of finger citron dry powder was used to extract crude FFC with 85% ethanol by continuous phase-transition extraction at 0.2 MPa and 90°C for 120 min. AB-8 macroporous resin was then chosen from four types of macroporous resins (AB-8, D-301, HPD-300, HPD-400) to purify the resulted crude FFC by column chromatography conducted on a glass column (2.4 × 30 cm) according to the parameters determined in advance. Briefly, 1,080 mL FFC solution (2 mg total flavonoids per mL) was loaded onto the column with AB-8 (bed volumes 135 mL) at 4 mL/min and kept at room temperature for 270 min to reach adsorption equilibrium. The saturated resin was then eluted with 1,400 mL of 60% ethanol at 0.4 mL/s. The collected fraction was concentrated by a rotary evaporator (R204B3, Shanghai Shensheng Technology Co., Ltd., Shanghai, China) at 50°C, followed by freeze-drying with a lyophilizer (FD-1PF, Beijing DETIANYOU Instrument Co., Ltd., Beijing, China) and stored at −20°C for further use. The purified FFC contain 50.5% flavonoids.

The flavonoid content in the purified FFC was determined by UV-vis spectrophotometer (UV-3010, HITACHI, Japan) at the wavelength of 420 nm according to the method of NY/Y 2010–2011 (an officially recognized Chinese criterion for the determination of total flavonoids in citrus fruits and derived products). A standard curve was established using hesperidin with the concentration range from 0.00 to 0.10 mg/mL. Briefly, 1.00 mL purified FFC liquid was diluted to 5.00 mL with a blank

solution reagent (NaOH-citric acid buffer solution, pH 6.0) and then accurately mixed with 5.00 mL of "9+1" diethylene glycol solution (900 mL diethylene glycol + 100 mL distilled water) and 0.10 mL of 160 g/L NaOH solution in 10 mL colorimetric tube. At the same time, the same amount of test solution without NaOH solution was used as absorbance of a reagent blank. The mixture was put in a water bath at 40°C for 10 min and cooled in a cold-water bath for 5 min. The content of flavonoids in the purified FFC was calculated based on the following equation:

$$\text{Purified FFC flavonoids content} = \frac{c \times \text{v} \times f}{m} \times 100\% \quad (1)$$

where c (mg/mL) was the hesperidin concentration calculated according to the standard curve; v (mL) was the sample liquid volume; f was dilution factor of the sample solution; and m (g) was the weight of the purified FFC after freeze-drying.

Chemical Analysis of Major Peak Components of FFC

High-performance liquid chromatography (HPLC) and ultraperformance liquid chromatography to quadrupole time-of-flight mass spectrometry (UPLC-Q-TOF-MS) were used for qualitative identification of the major peak components in purified FFC. For HPLC analysis, an LC-10AT VP plus system (Shimadzu, Kyoto, Japan) concentration with an Eclipse Plus C_{18}column (250 × 4.6 mm, 5 μm, Agilent) was used to analyze purified FFC. The mobile phase constituted 0.1% formic acid solution in water (A) and methanol (B), the gradient of the mobile phase was as follows: 0–40 min, 25–80% B, 40–45 min, 80–95% B, 45–70 min, 95–25% B. The flow rate was 1 mL/min. The detection wavelength was 280 nm, and the injection volume was set as 20 μL.

UPLC separation was carried out using an Eclips plus C_{18} column (100 × 2.1 mm, 1.8 μm, Agilent) with gradient solvents A and B in mobile phase, where A was 0.4% formic acid (vol/vol) in distilled water and B was acetonitrile with a gradient of 25% to 60% in 20 min at a flow rate of 1.0 mL/min. The injection volume was 10 μL, and the UV detection wavelength was 280 nm. An Agilent 6540UHD Q-TOF tandem mass spectrometer was used for MS and MS/MS detection. The operation conditions were as follows: drying gas (N_2) flow rate, 8 L/min; drying gas temperature, 300°C; nebulizer, 50 psig; sheath gas flow rate, 12 L/min; sheath gas temperature, 350°C; capillary voltages, 4,000 V; fragmentor, 130 V; skimmer, 65 V; OCT RF Vpp, 750 V. The data were acquired in negative ion mode; mass spectra were recorded across the range of m/z 105–1,100.

Antioxidant Activities of FFC Against DPPH Radical

DPPH radical-scavenging activity of the purified FFC was determined using the mothod of Najafian et al. (31) with some modifications. Blank ethanol solvents or flavonoid sample solutions (100 μL) were mixed with a 100 μL DPPH (2×10^{-4} mol/L) ethanol solution in a 96-well plate. The mixtures were incubated for 30 min at room temperature in the dark. The absorbance was read at 517 nm. Ascorbic acid was used as a positive control. The scavenging capability against DPPH radical was calculated as follows:

$$\text{DPPH radical}-\text{scavenging activity}(\%) = [1-(A_t - A_r)/A_0] \times 100 \quad (2)$$

Where A_t represents the absorbance of the sample at 517 nm, A_r was the absorbance of sample solution and A_0 was the absorbance of DPPH solution.

Antioxidant Activities of FFC Against ABTS Radical

ABTS radical-scavenging activity of the purified FFC was determined according to the method of Re et al. (32) with slight modifications. ABTS radical cation ($ABTS^+$) was produced by mixing 5 mL ABTS stock solution (7 mmol/L) with 88 μL potassium persulfate (140 mmol/L) and allowing the mixture to stand at room temperature for 12 h in the dark. Distilled water was then mixed with $ABTS^+$ to each measurement until an absorbance of 0.70 ± 0.02 was shown at 734 nm. A 100 μL of the $ABTS^+$ solution was allowed to react with 100 μL of samples at different concentrations or 75% ethanol (as a control) or ascorbic acid (as a positive control) for 10 min. Absorbance was measured at 734 nm immediately by Microplate reader (Enspire2300, PE, US). The scavenging capability against ABTS radical was calculated as follows:

$$\text{ABTS radical}-\text{scavenging activity}(\%) = [1-(A_t - A_r)/A_0] \times 100 \quad (3)$$

Where A_t represents the absorbance of the sample at 734 nm, A_r represents the absorbance of the mixtures of sample and ethanol, A_0 represents the absorbance of the control.

Measurement of ORAC

The ORAC assay was carried out following the method of Thaipong et al. (24) with a slight modification to determine the peroxy radical scavenging activity of the purified FFC. Briefly, 100 μL of fluorescein (8.4×10^{-8} mol/L) in 75 mmol/L phosphate buffer (pH 7.4) was added to the wells of a 96-well plate Fluorescein was measured to determine the background excitation at 490 nm and emission at 514 nm. After that, 50 μL of the sample, Trolox standard or blank (distilled water) was added to the wells of the 96-well plate, followed by oscillation for 3 min and incubation at 37°C for 10 min. Subsequently, 50 μL of AAPH (153 mmol/L, freshly prepared in phosphate buffer) was added to each well, and the fluorescence value was measured every 90 s in 3.5 h. The final ORAC value was calculated from the net area (between the Trolox standard curve and the blank value) and the regression equation for different concentrations of Trolox (0.02, 0.04, 0.06, 0.08, and 0.1 mmol/L). The ORAC value was expressed as the average micromolar ± SD of the Trolox equivalent (TE) per micron of compound.

Cultivation and Synchronization

Caenorhabditis elegans were cultured and assayed on NGM plates at 20°C and *E. coli* OP50 bacteria were inoculated.

Synchronized hermaphrodite population were obtained by the sodium hypochlorite treatment, which killed the adult worms and recovered the hatched L1 larvae on NGM/OP50 plate (33).

Preparation of Treatment Plates

A 5 μL of purified FFC (200 μg/mL) and control (distilled water) were filtered to remove bacteria, mixed with 95 μL *E. coli* OP50, and then inoculated onto NGM (65 mm × 10 mm) plates to feed worms.

Lifespan Assay

The lifespan studies were performed as previously described (34). Synchronized L4 larvae were further transferred to fresh NGM plates with 5 μL of purified FFC (200 μg/mL) and control (distilled water) (3 plates per group, and at least 30 L4 larvae of N2 wild type per plate). During the reproductive period, the worms were transferred to the NGM plates every day. In other periods, the worms were transferred to new plates every 2 days to ensure the concentration of the treated compounds. Surviving and dead worms (the criterion for worm death was that there was no respond to a touch-provoked) were counted every alternate day from the first day of L4 larvae until all worms had died. The worms should be excluded from the statistics, which escaped from NGM plates or suffered from hatching of embryos within the adult hermaphrodite before eggs were laid (a so-called "internal hatch").

Reproduction Assay

The reproduction assay was determined using the method of Chen et al. (35) Briefly, the L4 larvae of *C. elegans* (10 individuals, 2 worms per plate) were shifted to fresh plates every day during reproduction day until worms were basically no longer spawning. Eggs on all plates were allowed to hatch at 20°C for 24 h and the number of progenies of each worm was counted at L4 stage.

Movement Assay

This assay was performed according to the previously reported method with a slight modification (36). The worms were cultured from eggs similar to the method described in the lifespan assay. On days 5, 10, and 15 of life, 10 individuals were randomly selected and their body locomotion phenotype were measured by gently prodding them with a platinum wire. Worms that move spontaneously and smoothly in a sinusoidal and symmetrical pattern were categorized as class A. Worms that respond to touch but move slowly and uncoordinatedly were classified as class B. And worms which move their noses or tails only when prodded were classified as class C. Meanwhile, the sinusoidal locomotion of the worms was also analyzed by recording the number of worms that move in a sinusoidal manner within 1 min on the 5th, 10th, and 15th days (7 worms were selected from each plate for recording), while the head swing frequency was measured on days 2 and 6 by transferring the L4 stage worms into each set of medium and the standard of the head swing frequency was the number of times from one side to the other side within 30 s.

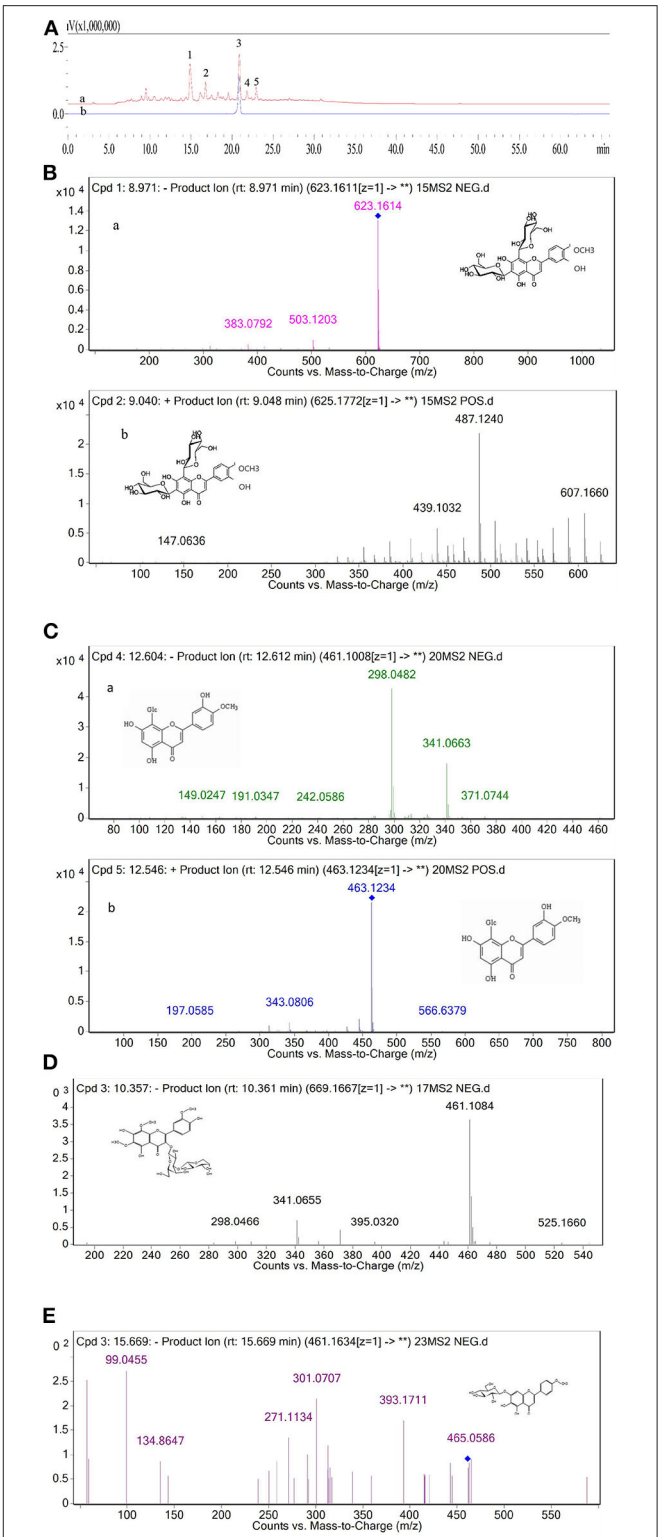

FIGURE 1 | (A) HPLC chromatogram of the purified FFC detected at 280 nm (a) and hesperidin standard detected at 280 nm (b). **(B)** The MS/MS of peak 1 in negative ionization (a) and positive ionization (b). **(C)** The MS/MS of peak 4 in negative ionization (a) and positive ionization (b). **(D)** The MS/MS of peak 2 in negative ionization. **(E)** The MS/MS of peak 5 in negative ionization.

Thermotolerance and Oxidative Stress Assays

Thermotolerance and oxidative stress assays were carried out based on the method described by Hansen et al. (37) with a slight modification. Thermotolerance assay was performed with hermaphrodites at 20°C as the aging assay. After 96-h treatment with purified FFC, the adult worms (30 worms per plate) were changed from 20 to 35°C. Survivals were scored every 4 h to draw the life curve after the temperature changed and the worms that died due to dryness on both sides of the plate were excluded. For oxidative stress assay, the worms were transferred into the newly prepared NGM/*E. coli* OP50 plates containing paraquat (25 mg/mL, M/V) after treatment with purified FFC or control for 96 h. The worm survival rate was recorded every 24 h until all of the worms died (the worms did not respond when touched with a platinum wire). In addition, ROS, SOD, CAT, and MDA were determined according to the methods described in Measurement of ROS and Measurement of SOD, CAT, and MDA after oxidative stress treatment.

Measurement of ROS

ROS detection was performed as the reported literature (35). Synchronized L4 larvae were transferred to fresh NGM plates with 5 μL of purified FFC (200 μg/mL) or control (distilled water). After treatment with purified FFC or control for 96 h, bacteria were removed by transferring the worms to the new NGM plate 3 times. Eighty worms were then transferred into a 96-well plate with 50 μL of M9 buffer. Meanwhile, 50 μL of 100 μM H_2DCF-DA solution in M9 buffer was added to the 96-well plate including a worm-free control well containing H_2DCF-DA. The fluorescence intensity was measured by an EnSpire® Multimode Plate Reader (PerkinElmer, USA) every 20 min for 20 h at a reaction temperature of 25°C, an emission wavelength of 528 nm and an excitation wavelength of 485 nm. The results were presented as relative fluorescence units (RFU).

Measurement of SOD, CAT, and MDA

SOD, CAT and MDA detection were conducted according to the method described by Liu et al. (38) with a minor modification. After treatment with purified FFC or control for 96 h, 200 worms were rinsed three times with sterile water and centrifuged at low speeds. The supernatant was then discarded and the precipitate was adjusted with 0.5 mL sterile water, followed by ultrasonically decomposition with a JY92-2D Ultrasonic cell Disruption System (Scientz, China) for 2 min (repeated twice) at low temperature. Subsequently, 0.5 mL of 1% CHAPS solution (wt/vol) was added to the worm homogenate and centrifuged for 15 min (4°C, 12,000 rpm). The supernatant was gathered and stored at 4°C until use. SOD, CAT and MDA were, respectively, detected with SOD assay kit (WST-1 method), CAT assay kit (Ultraviolet), and MDA assay kit (Colorimetric method) (Nanjing Institute of Bioengineering Institute, China). Enzyme activities were expressed in units of milligrams of protein.

Statistical Analysis

All results were presented as mean ± SD ($n = 3$). One-way analysis of variance (ANOVA) was performed using SPSS 16.0 software (SPSS Inc., Chicago, IL, United States), and different letters indicate that the values were significantly different ($p < 0.05$).

RESULTS AND DISCUSSION

Chemical Analysis of the Major Peak Components of FFC

On the basis of our previous work, crude FFC prepared by continuous phase transition extraction were first purified by AB-8 resin. Five components (1–5) of the purified FFC were found to have high UV absorption at 280 nm as shown in the HPLC spectrogram (**Figure 1A**-a). According to the reported literature (39), the major flavonoids in *Rutaceae* family were hesperidin and naringin. Therefore, peak 3 in the HPLC spectrum of the purified FFC was confirmed as hesperidin by comparing to hesperidin standard substance. Other peaks (1, 2, 4, 5) obtained by HPLC were further analyzed by UPLC-Q-TOF-MS/MS. Based on the previous study on the MS spectra of these flavonoids, these peaks were identified by generating molecular formula and the fragmentation pattern in positive and negative ionization modes as depicted in **Table 1** and **Figures 1B–E**. Peak 1 with a molecular anion at 623 and typical *C*-glycosyl fragments at m/z 503, 383 (M-H-120, M-H-240) was assigned as diosmetin 6,8-di-*C*-glucoside with a molecular formula $C_{28}H_{32}O_{16}$ (40). Peak 4 with $[M-H]^-$ ion at m/z 461 ($[M+H]^+$ ion at m/z 463) and characteristic MS^n ions at 341(343) (M-120) and 298 was identified as diosmetin 8-*C*-glucoside (orientin 4′-methyl ether) with a molecular formula $C_{22}H_{22}O_{11}$ (41). Peak 2 and 5 [$(M-H)^-$ ions at m/z 669 and 461, respectively], were preliminarily judged as limocitrol 3-alpha-L-arabinopyranosyl-(1->3)- galactoside (MS^n ions at m/z 461, 395, 341) and scutellarein 4′-methyl ether 7-glucoside (MS^n ions at m/z 393, 301, 271) by molecular structure correlation, respectively.

In vitro Antioxidant Activity of FFC

DPPH, ABTS scavenging capacity and ORAC assay are the most commonly used methods for determining antioxidation performance *in vitro* (24). The scavenging capacity of DPPH and ABTS radicals of the purified FFC were investigated at concentrations of 0.2 to 1 mg/mL and compared with ascorbic acid, which served as a control. As shown in **Figures 2A,B**, the purified FFC exhibited strong scavenging capacity for both DPPH and ABTS radicals. Interestingly, FFC showed more potent effect to scavenge ABTS radical than that to DPPH radical at the same concentration. In addition, the DPPH radical scavenging ability of the purified FFC was in a dose-dependent manner (0.2–0.8 mg/mL, $p < 0.05$), and its scavenging ability was close to that of ascorbic acid at the concentration of 0.8 mg/mL, which was 89.86% and up to 93.68% of that of ascorbic acid ($p < 0.05$). At 1.0 mg/mL, the DPPH radical scavenging ability of the purified FFC was 90.24%, which exhibited no significant difference with that of 0.8 mg/mL ($p > 0.05$) and amounted to 94.74% of that of ascorbic acid ($p < 0.05$). For ABTS radical scavenging ability, the purified FFC had a strong scavenging capacity of 87.94% at low concentration (0.2 mg/mL) and the increase of the concentration had no evident

TABLE 1 | Identification of the major compounds in the purified FFC by UPLC-Q-TOF-MS/MS.

Peak No.	Rt (min)	Formula	$[M-H]^-/[M+H]^+$ (m/z)	MS^n Inos (–/+) (m/z)	Tentative identification	Reference
1	14.875	$C_{28}H_{32}O_{16}$	623.1611/625.1767	533.1301,503.1203, 383.0792/607.1660, 487.1240,439.1032	Diosmetin-6-8-di-*C*-glucoside	(40)
2	16.775	$C_{29}H_{34}O_{18}$	669.1667/	461.1084,395.0320, 341.0655/	Limocitrol 3-alpha-L-arabinopyranosyl-(1->3)-galactoside	
3	20.884	$C_{28}H_{34}O_{15}$	–	–	Hesperidin	By hesperidin standard
4	21.816	$C_{22}H_{22}O_{11}$	461.1088/463.1236	341.0663, 298.0482/343.0811	Diosmetin-6-*C*-glucoside	(41)
5	22.933	$C_{22}H_{22}O_{11}$	461.1634/	393.1711,301.0707, 271.1134/	Scutellarein 4′-methyl ether 7-glucoside	

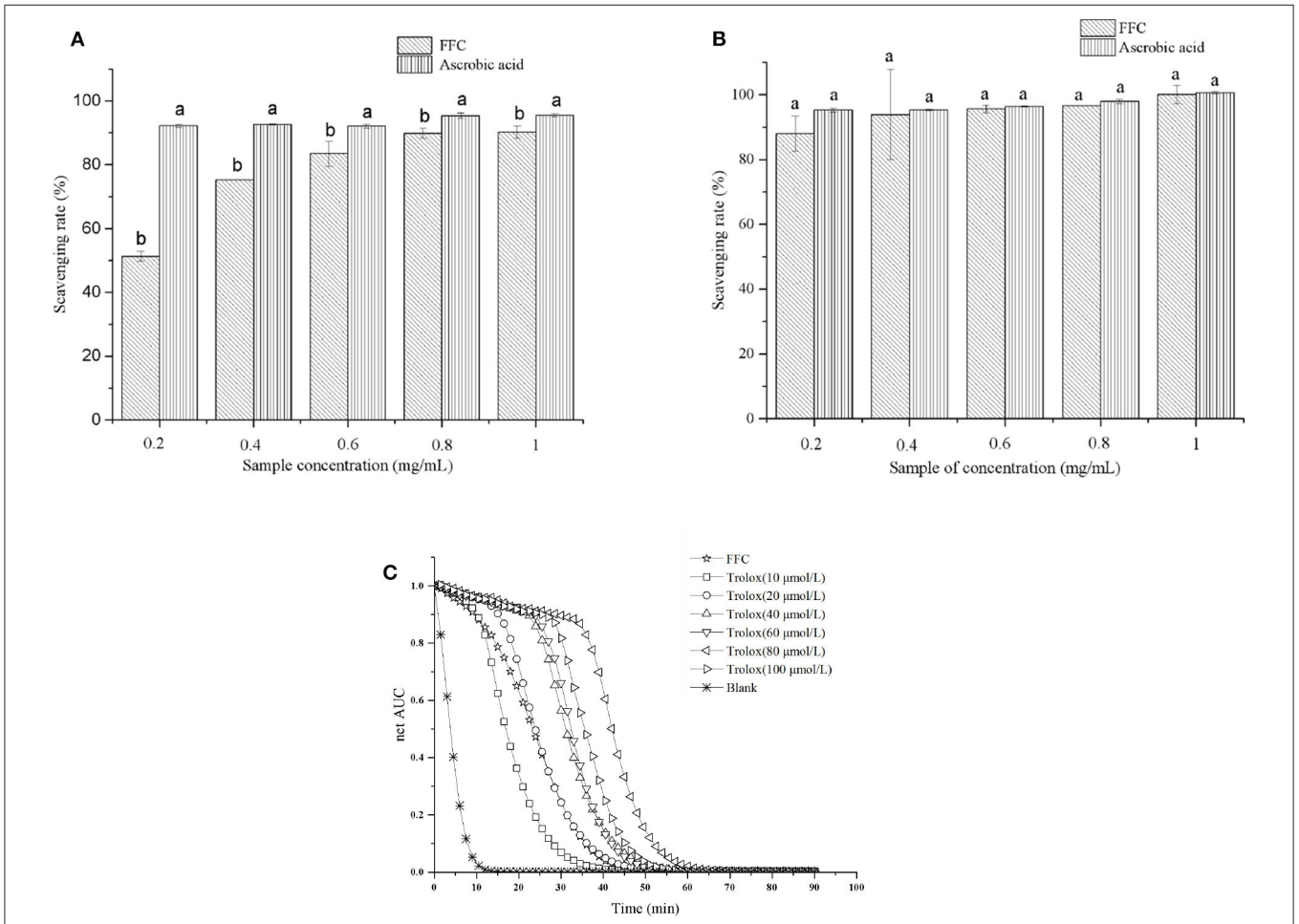

FIGURE 2 | *In vitro* antioxidant tests for the purified FFC. DPPH scavenging activity **(A)**, ABTS scavenging activity **(B)**, and fluorescence decay curves **(C)**. Different letters indicate that the values were significantly different ($p < 0.05$).

effect on its capacity ($p > 0.05$). Furthermore, the $ABTS^+$ scavenging ability of the purified FFC was not significantly different from that of ascorbic acid at concentrations of 0.2 to 1 mg/mL ($p > 0.05$). **Figure 2C** depicted the ORAC value of the purified FFC. The results demonstrated that the purified FFC exhibited strong antioxidative activity with an ORAC value of 928.64 μmol TE/g, which was equal to that of 20 μmol/L Trolox.

DPPH and ABTS assays are based on an electron transfer and involve reduction of a colored oxidant (24, 42), while ORAC assay

TABLE 2 | Effects of the purified FFC on the lifespan of *C. elegans*.

Concentration (μg/mL)	Mean of lifespan (mean ± SD) (days)	Maximum lifespan (mean ± SD) (days)	Mean fold increase (%)
Control	15.66 ± 1.35^{b}	16.96 ± 0.85^{b}	0^{b}
200 μg/mL FFC	20.56 ± 0.97^{a}	21.47 ± 0.94^{a}	$31.26 \pm 5.04\%^{a}$

Different letters in a column indicate that the values were significantly different ($p < 0.05$).

involves the transfer of a hydrogen atom, in which substrate and antioxidants compete for thermally created peroxyl radicals (43). Determination of these antioxidant capacities *in vitro* are helpful to investigate the potential health benefits of the purified FFC on oxidative stress mediated diseases (e.g., aging, inflammation) (42). Chanput et al. (44) tested the antioxidative activity of three sub groups of flavonoids at a range of concentrations by *in vitro* chemical-based assays including DPPH, ABTS, and ORAC methods and found the antioxidative activities of these flavonoids were dose-dependent and in opposite relationship with the decrease of inflammatory genes. Our results demonstrated that the purified FFC had strong antioxidative function *in vitro*, suggesting it may potentially have excellent antiaging activity.

Effects of FFC on the Lifespan of *C. elegans*

It is well-confirmed that irreversible oxidative damage accumulates during aging (45). To understand the antioxidative and antiaging effect of FFC, N2 wide-type worms were treated the purified FFC started from L4 larvae till death. Based on our previous study, 200 μg/mL purified FFC was the optimal dose on lifespan elongation of *C. elegans*, so 200 μg/mL was selected for our later experiments. As depicted in **Figure 3** and **Table 2**, purified FFC not only manifested a notable survival curve ($p < 0.001$, by the log-rank test), but also evidently increased the mean lifespan and maximum lifespan of the worms ($p < 0.05$), which were 31.26 and 26.59% greater than those of the control, respectively. The total lifespan of *C. elegans* was about three to 4 weeks, and the extension of 1 or 2 days in the lifespan is significantly different (26), so these findings indicated that supplementation with the purified FFC could significantly prolong the lifespan of *C. elegans*. As compared with the blank group, Cai et al. (46) also confirmed that the high dose *Epimedium* flavonoids group could significantly prolong the mean lifespan and maximum lifespan.

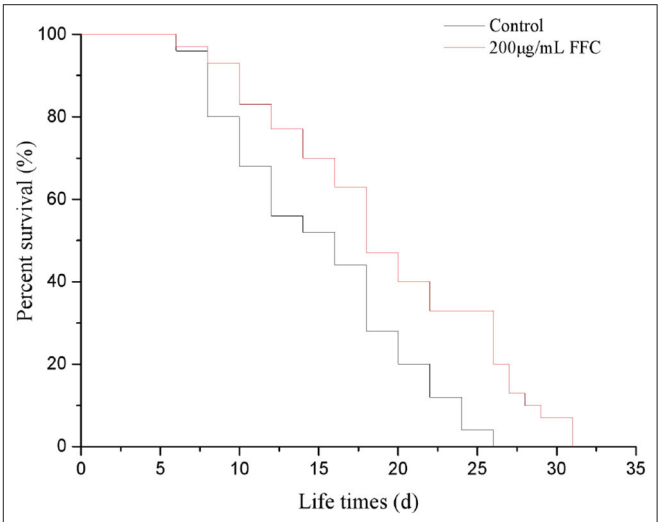

FIGURE 3 | Effects of the purified FFC on the fraction survival of *C. elegans*. Survival curves of wild-type (N_2) worms raised at 20°C on the plates containing H_2O (control) or the purified FFC (200 μg/mL). The survival curves treated with 200 μg/mL of the purified FFC were significantly different by the log-rank test ($p < 0.001$).

Effects of FFC on Physiological Functions of *C. elegans*

The aging of *C. elegans* is accompanied by a decline in physiological functions, such as reproduction, motility, and the response to external mechanical stimuli (47). Some mechanisms that extend lifespan have a side impact on their progeny production capacity (48). In our study, we recorded the effect of FFC treatment on the progeny production per day to investigate whether FFC suppressed or delayed nematode reproduction. Results showed that the purified FFC at 200 μg/mL neither slowed reproduction nor reduced total progeny production as illustrated in **Figure 4A** ($p > 0.05$). Interestingly, these findings indicated that FFC elongated the lifespan of *C. elegans* not by restraining or delaying progeny production. Similarly, Yang et al. (23) also confirmed that flavonoids from *Toona sinensis* leaf could improve the mean and maximum lifespan of *C. elegans*, but showed little effect on its reproductive capacity.

The aging of *C. elegans* is correlated with the level of muscle deterioration, which leads to the decline of move ability and response to external mechanical stimuli (47). To determine whether FFC can enhance lifespan of *C. elegans* by extending movement ability, different movement characteristics including the locomotivity, sinusoidal locomotion and head swing frequency were tested to evaluate the movement behavior at early, middle, and mid-late life stages (i.e., on the 5th, 10th, and 15th day, respectively). After treatment with 200 μg/mL of purified FFC, the movement of worms was scored using three classes of locomotion phenotypes (A, B, and C classification) as shown in **Figure 4B**. The control group appeared class B movement in early life stage (day 5), while the treatment of FFC could reduce the class B movement to keep the normal sinusoidal (A) movement. With the aging of *C. elegans*, class C began to appear in middle stage (day 10), and FFC could inhibit C-type movement, thereby improving its movement ability ($p < 0.05$). But there was no significant difference

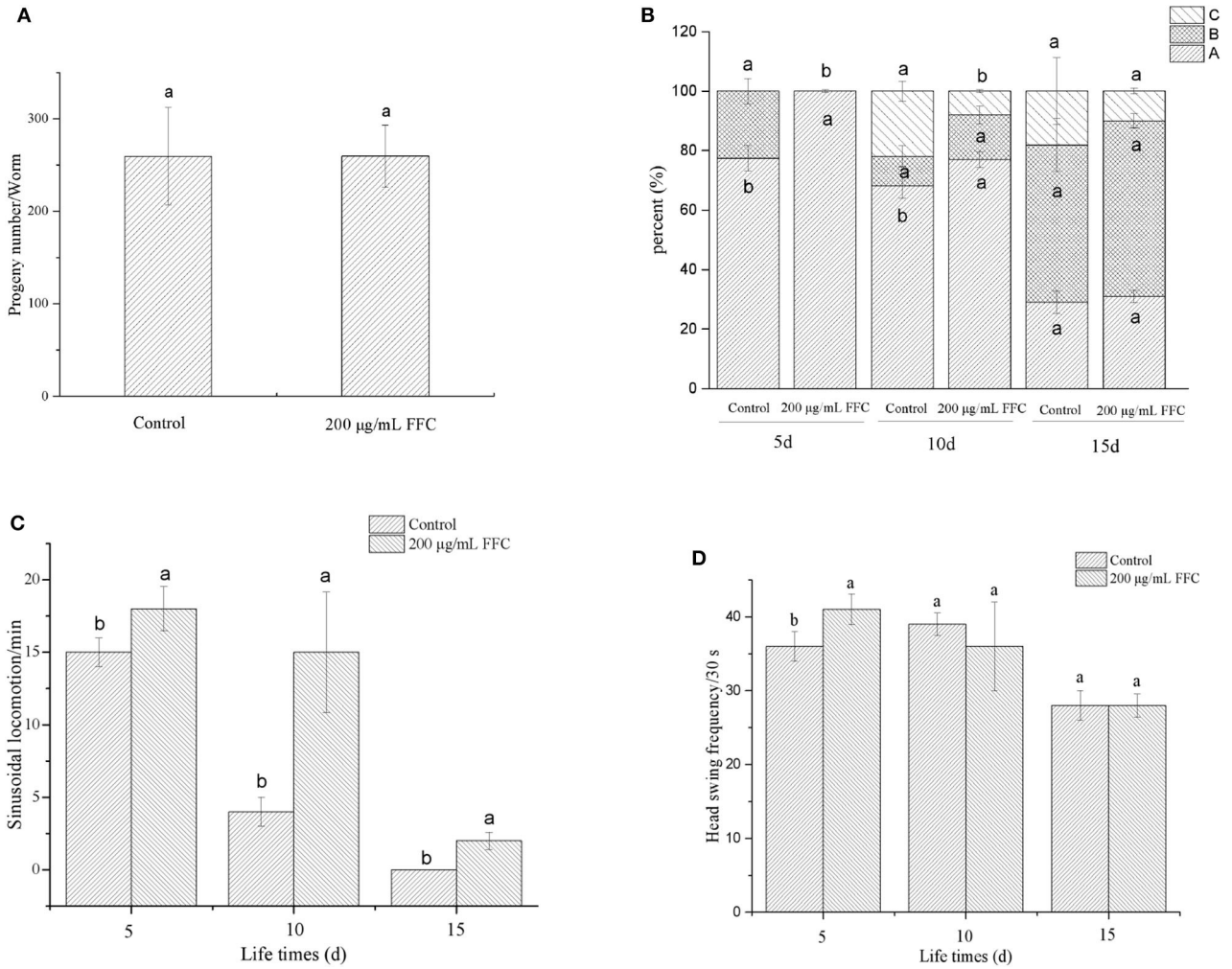

FIGURE 4 | Effects of the purified FFC on the physiological functions of *C. elegans*. **(A)** The number of progeny of each worm was counted until the parental worms were dead or stopped producing progeny. The three levels of locomotivity **(B)**, the sinusoidal locomotion **(C)**, and the frequency of the head swing **(D)** were performed under a dissecting microscope for 30 s on days 5, 10, and 15 of the worms. Different letters in these groups denote that the values were significantly different ($p < 0.05$).

between the control and FFC group on locomotion ability in mid-late stage ($p > 0.05$). **Figure 4C** demonstrated that FFC treatment could also increase the sinusoidal locomotion of the worms at three life stages ($p < 0.05$), while **Figure 4D** showed that FFC could increase the head swing frequency of the worms significantly only in early stage when compared with the non-treated control worms ($p < 0.05$). These findings indicated that FFC could increase the movement ability of *C. elegans* to some extent, primarily in the early and middle stages.

To summarize, FFC could prolong the lifespan of *C. elegans* without causing obvious defect in its physiological functions, including reproduction, exercise capacity, and respond to external mechanical stimuli. Therefore, we continued to gain insight into the related mechanisms.

Effects of FFC on the Stress Resistance of *C. elegans*

According to the previous studies, longevity extension is usually associated with increased survival under stress conditions (49). The worms treated with or without FFC were shifted from 20 to 35°C on the fourth day to determine whether FFC has the effect of extending the lifespan of the worms under heat shock. As shown in **Figure 5A**, the survival rates of the worms treated with the purified FFC increased significantly from 17% (the control) to 37% after 8 h at 35°C ($p < 0.05$). In addition, FFC-treated worms showed a significantly different survival curve compared to the control group ($p < 0.01$ by the log-rank test) (**Figure 5B**). These findings declared that FFC supplements could act protectively under the thermal stress and enhance resistance to heat shock in *C. elegans*. Cai et al. (46) also found that *Epimedium* flavonoids could significantly

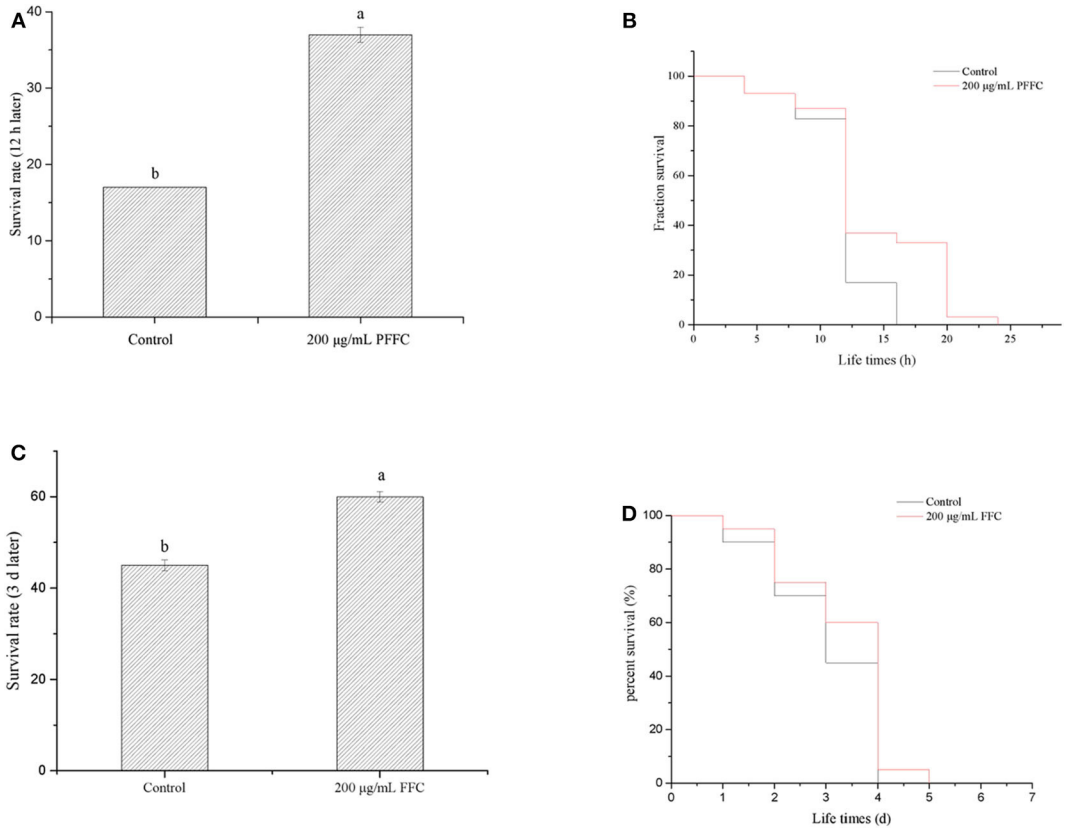

FIGURE 5 | Effects of the purified FFC on thermal and oxidative resistance of *C. elegans*. **(A)** Survival rates of worms after 12 h when they were shifted from 20 to 35°C on day 4. **(B)** Survival curve of worms after they were shifted from 20 to 35°C on day 4. The survival curves of worms treated with 200 μg/mL purified FFC were significantly different by the log-rank test ($p < 0.01$). **(C)** Survival rates of worms after they were transferred into the freshly prepared NGM/OP50 plates containing paraquat (25 mg/mL) on day 3. **(D)** Survival curve of worms after they were transferred into the freshly prepared NGM/OP50 plates containing paraquat (25 mg/mL). Different letters indicate that the values were significantly different ($p < 0.05$).

prolong the mean lifespan of *C. elegans* under heat shock at 35°C.

Moreover, to determine whether purified FFC has the ability to extend worm lifespan under oxidative stress, the worms were transferred into the freshly prepared NGM/OP50 plates containing paraquat (25 mg/mL) after 96-h treatment with purified FFC or control. Although the survival curve of the worms treated by FFC was not significantly different from that of the control group ($p > 0.05$ by the log-rank test) (**Figure 5D**), their survival rates exhibited a significantly increase after 3 d compared to the control group, which increased by 33.33% as illustrated in **Figure 5C**, suggesting FFC had protective effects against paraquat-treated worms. These results suggested that FFC supplements had protective effects on *C. elegans* against paraquat-induced oxidative stress.

Effects of FFC on Accumulation of ROS, MDA, and Enzyme Activity

Antioxidants have the potential to reduce oxidative stress levels, thereby delaying aging and age-related diseases (50). The accumulation of ROS accelerates aging and mitochondrial damage (51). In addition, the amount of MDA can reflect the degree of lipid peroxidation in the body, indirectly reflecting the degree of cell damage. Therefore, we investigated whether FFC could affect the accumulation of ROS and MDA under normal and oxidative stress. The accumulation of ROS was measured using H_2DCF-DA, and the fluorescent dye DCF (2′,7′-dichlorofluorescein) indicated the accumulation of ROS in the cells. Under normal and 25 mg/mL paraquat-induced oxidative stress conditions, the ROS accumulation of the worms fed with the purified FFC were 81.07% and 61.46% lower than those of the control, respectively (**Figure 6A**). Similarly, the purified FFC could significantly decrease the amount of MDA in the worms under normal and paraquat-induced oxidative stress conditions ($p < 0.05$), which was 56.06 and 66.18% lower than the untreated worms, respectively (**Figure 6B**). These findings indicated that lifespan extension of the worms by FFC might be partly related to its ability to scavenge intracellular ROS and MDA.

SOD plays an extremely important role in preventing aging and biomolecular damage, and the activity of the enzyme in organisms reflects the magnitude of the antioxidant capacity (52, 53). On the other hand, CAT can react with H_2O_2 in

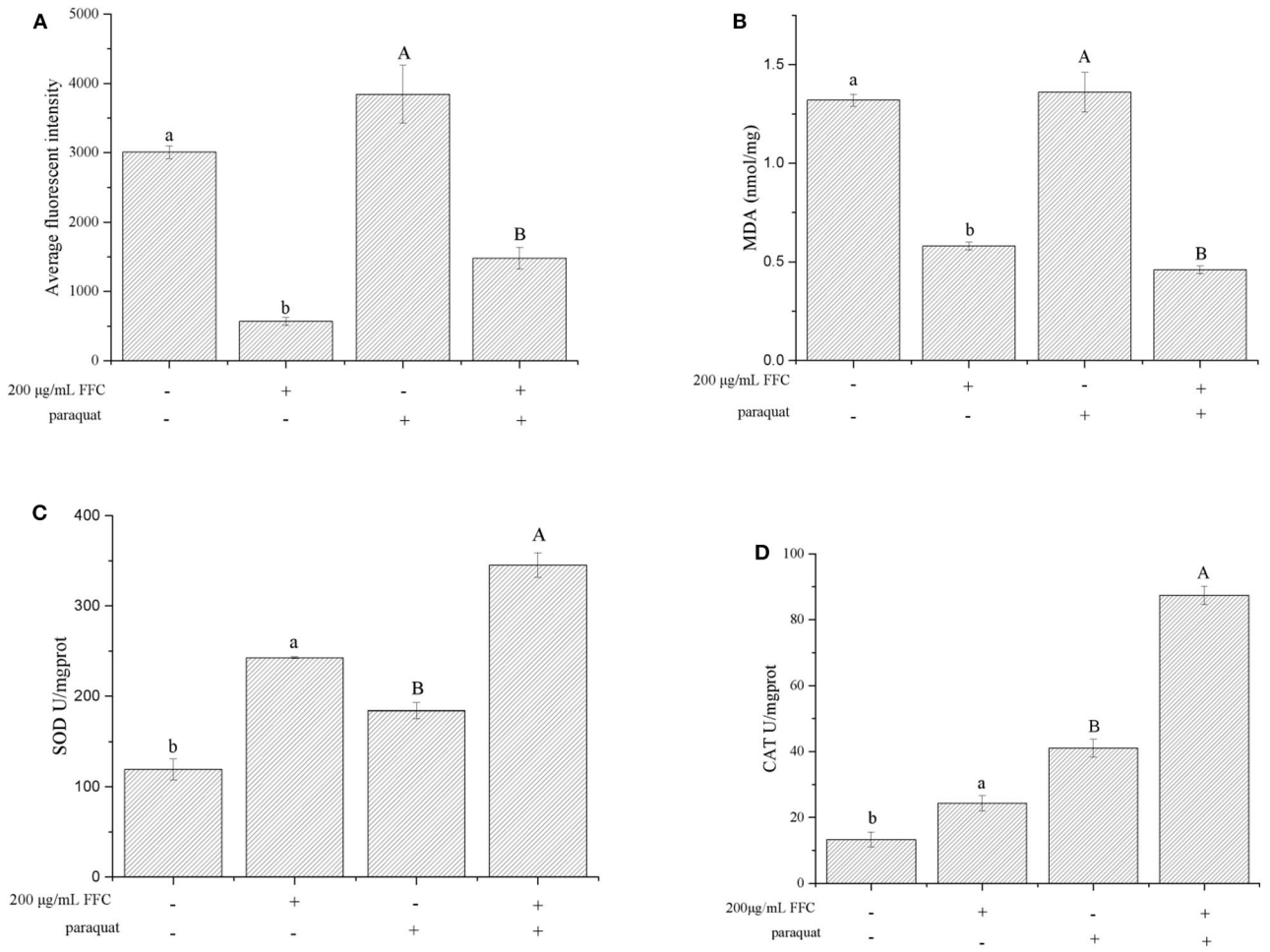

FIGURE 6 | Effects of the purified FFC on the accumulation of ROS and MDA and enzyme activity under normal and 25 mg/mL paraquat-induced oxidative stress conditions. **(A)** ROS, **(B)** MDA, **(C)** SOD, and **(D)** CAT were measured according to the methods described in Measurement of ROS and Measurement of SOD, CAT, and MDA, in which 80 or 200 worms were collected for sample preparation after treatment with the purified FFC or control for 96 h. SOD and CAT enzyme activity was expressed as units/mg of protein. Data are expressed as the mean ± SD of three independent experiments ($N = 3$). Different letters in these groups denote values that were significantly different ($p < 0.05$).

organisms and decompose it to H_2O and O_2, thereby preventing the damage to the body from oxygen metabolisms and protecting living tissues from poisoning (54). To investigate the effect of FFC on worm's antioxidant enzymes, the activity of SOD and CAT in FFC treated and untreated worms were examined under normal and oxidative stress conditions (exposure to 25 mg/mL paraquat). The activity of SOD enzyme in the worms under the presence of the purified FFC was significantly higher than that of the untreated worms ($p < 0.05$) as depicted in **Figure 6C**, which was increased by 103.14 and 87.56% respectively under normal and oxidative stress conditions compared to the control. Similarly, the CAT enzyme activity of the worms fed with the purified FFC was also evidently higher than that of the control, and was 81.91 and 113.07% higher than the control worms accordingly (**Figure 6D**). These results suggested that FFC could increase SOD and CAT enzyme activity of *C. elegans* under both normal and oxidative stress conditions, indicating that lifespan elongation of *C. elegans* exposed to FFC might attribute to the elimination effect of FFC on the excess ROS and MDA by improving the enzyme activity of SOD and CAT. Similar results were reported in the study of Zhou et al. (55), who discovered that flavonoids from the herb *Scutellariae barbatae* could delay the aging of *C. elegans* through up-regulating the activity of antioxidant enzymes like SOD and CAT.

CONCLUSION

Taken together, we analyzed five major peak components in the purified FFC and identified three of them by HPLC and UPLC-MS/MS as diosmetin-6-8-di-*C*-glucoside (peak 1), hesperidin (peak 3), and diosmetin-6-*C*- glucoside (peak 4), while Peaks 2 and 5 were preliminarily judged as limocitrol 3-alpha-L-arabinopyranosyl-(1->3)-galactoside and scutellarein 4′-methyl ether 7-glucoside by molecular structure correlation, respectively. Further, the antioxidant and antiaging activities of the purified FFC were evaluated *in vivo* and *in vitro*.

Our findings suggested that the purified FFC had excellent prospects for its antioxidant function *in vitro*. In addition, the purified FFC could increase the lifespan of *C. elegans* without causing side effects on their physiological functions including reproduction, locomotion ability, sinusoidal locomotion, and head swing frequency. Also, the purified FFC could prolong the lifespan of *C. elegans* by enhancing its resistance to thermal and oxidative stress. A further study showed that the lifespan improvement mediated by the purified FFC under normal and oxidative stress conditions was associated with the decreased ROS and MDA accumulation and the increased SOD and CAT enzyme activities. These results provided useful information for the utilization of FFC in natural antioxidant and antiaging functional foods.

DATA AVAILABILITY STATEMENT

The raw data supporting the conclusions of this article will be made available by the authors, without undue reservation.

AUTHOR CONTRIBUTIONS

XL: data curation and writing - original draft. JW: methodology and investigation. HC, MS, and QZ: writing - review and editing. AZ: conceptualization, writing - review and editing, and supervision. HC: supervision. YC: investigation and supervision. All authors contributed to the article and approved the submitted version.

FUNDING

This research was funded by Sailing Plan Guangdong Innovation and Entrepreneurship Team Project, China with the grant number of 2016YT03S056.

ACKNOWLEDGMENTS

The author is also grateful to Zhancui Food Co., Ltd. (Chaozhou, Guangdong, China) for the finger citron samples used in this work.

REFERENCES

1. Wang T, Li Q, Bi K. Bioactive flavonoids in medicinal plants: structure, activity and biological fate. *Asian J Pharm Sci.* (2018) 13:12–23. doi: 10.1016/j.ajps.2017.08.004
2. Spagnuolo C, Moccia S, Russo GL. Anti-inflammatory effects of flavonoids in neurodegenerative disorders. *Eur J Med Chem.* (2018) 153:105–15. doi: 10.1016/j.ejmech.2017.09.001
3. Zhang X, Huang H, Zhao X, Qiang L, Sun C, Xian L, et al. Effects of flavonoids-rich Chinese bayberry (Myrica rubra Sieb. et Zucc) pulp extracts on glucose consumption in human HepG2 cells. *J Funct Foods.* (2015) 14:144–53. doi: 10.1016/j.jff.2015.01.030
4. Kawaii S, Tomono Y, Katase E, Ogawa K, Yano M. Quantitation of flavonoid constituents in citrus fruits. *J Agr Food Chem.* (1999) 47:3565–71. doi: 10.1021/jf990153
5. Sun XB. The content of flavonoids and anti-oxidation in different efficient parts of euonymus alatus. *Bull Botanical Res.* (2007) 27:619–21. doi: 10.3969/j.issn.1673-5102.2007.05.025
6. Jung D, Choe T. Antioxidant activities and anti-aging effects of *Orostachys japonicus* A. Berger extracts. *J Korean Appl Sci Technol.* (2016) 33:361–73. doi: 10.12925/jkocs.2016.33.2.361
7. Chen XM, Tait AR, Kitts DD. Flavonoid composition of orange peel and its association with antioxidant and anti-inflammatory activities. *Food Chem.* (2017) 218:15–21. doi: 10.1016/j.foodchem.2016.09.016
8. Byun E, Kim H, Song H, Kim WS. Hesperidin structurally modified by gamma irradiation induces apoptosis in murine melanoma B16BL6 cells and inhibits both subcutaneous tumor growth and metastasis in C57BL/6 mice. *Food Chem Toxicol.* (2019) 127:19–30. doi: 10.1016/j.fct.2019.02.042
9. Ali MY, Zaib S, Rahman MM, Jannat S, Iqbal J, Park SK, et al. Didymin, a dietary citrus flavonoid exhibits anti-diabetic complications and promotes glucose uptake through the activation of PI3K/Akt signaling pathway in insulin-resistant HepG2 cells. *Chem Biol Interact.* (2019) 305:180–94. doi: 10.1016/j.cbi.2019.03.018
10. Zhang S, Li DD, Zeng F, Zhu ZH, Song P, Zhao M, et al. Efficient biosynthesis, analysis, solubility and anti-bacterial activities of succinylglycosylated naringenin. *Nat Prod Res.* (2018) 33:1756–60. doi: 10.1080/14786419.2018.1431633
11. Bao P, Luo Y, Hu X, Song L, Yang J. Isolation, structural characterization, and immunostimulatory activity of a new water-soluble polysaccharide and its sulfated derivative from *Citrus medica* L. *var. Sarcodactylis. Int J Biol Macromol.* (2019) 123:500–11. doi: 10.1016/j.ijbiomac.2018.11.113
12. Kim KN, Ko YJ, Yang HM, Ham YM, Roh SW, Jeon YJ, et al. Anti-inflammatory effect of essential oil and its constituents from fingered citron (*Citrus medica* L. *var. sarcodactylis*) through blocking JNK, ERK and NF-κB signaling pathways in LPS-activated RAW 264.7 cells. *Food Chem Toxicol.* (2013) 57:126–31. doi: 10.1016/j.fct.2013.03.017
13. Chan Y, Li C, Shen Y, Wu T. Anti-inflammatory principles from the stem and root barks of citrus medica. *Chem Pharm Bull.* (2010) 58:61–5. doi: 10.1248/cpb.58.61
14. He Z, Liang F, Zhang Y, Pan Y. Water-soluble polysaccharides from finger citron fruits (*Citrus medica* L. *var. sarcodactylis*). *Carbohyd Res.* (2014) 388:100–4. doi: 10.1016/j.carres.2013.12.020
15. Liu Y, Wang Z, Zhang J. *Dietary Chinese Herb*. Springer Science & Business Media (2015). p. 327–31. doi: 10.1007/978-3-211-99448-1_37
16. Lou Z, Chen J, Yu F, Wang H, Kou X, Ma C, et al. The antioxidant, antibacterial, antibiofilm activity of essential oil from *Citrus medica* L. *var. sarcodactylis* and its nanoemulsion. *LWT Food Sci Technol.* (2017) 80:371–7. doi: 10.1016/j.lwt.2017.02.037
17. Benayoun BA, Pollina EA, Brunet A. Epigenetic regulation of ageing: linking environmental inputs to genomic stability. *Nat Rev Mol Cell Bio.* (2015) 16:593–610. doi: 10.1038/nrm4048
18. Judith C. Aging, cellular senescence, and cancer. *Annu Rev Physiol.* (2013) 75:685–705. doi: 10.1146/annurev-physiol-030212-183653
19. Kudlow BA, Kennedy BK, Monnat RJ. Werner and hutchinson-gilford progeria syndromes: mechanistic basis of human progeroid diseases. *Nat Rev Mol Cell Bio.* (2007) 8:394–404. doi: 10.1038/nrm2161
20. Lópezotín C, Blasco MA, Partridge L, Serrano M, Kroemer G. The hallmarks of aging. *Cell.* (2013) 153:1194–217. doi: 10.1016/j.cell.2013.05.039
21. Geng L, Liu Z, Zhang W, Li W, Wu Z, Wang W, et al. Chemical screen identifies a geroprotective role of quercetin in premature aging. *Protein Cell.* (2019) 10:417–35. doi: 10.1007/s13238-018-0567-y
22. Ilaria L, Gennaro R, Francesco C, Giulia B, Luisa A, David D, et al. Oxidative stress, aging, and diseases. *Clin Interv Aging.* (2018) 13:757–72. doi: 10.2147/CIA.S158513
23. Yang W, Wang C, Cui G, Chen M, Wang Y, Han H. Retarding ageing effect of *Toona sinensis* leaf flavonoids on *Caenorhabditis elegans*. *Modern Food Sci Technol.* (2010) 26:932–3. doi: 10.3969/j.issn.1673-9078.2010.09.005
24. Thaipong K, Boonprakob U, Crosby K, Cisneros-Zevallos L, Byrne DH. Comparison of ABTS, DPPH, FRAP, and ORAC assays for estimating antioxidant activity from guava fruit extracts. *J Food Compos Anal.* (2012) 19:669–75. doi: 10.1016/j.jfca.2006.01.003

25. Vu TC, Chen W, Shi J, Zhang M, Yang H, Wang N, et al. The anti-oxidation and anti-aging effects of ganoderma lucidum in *Caenorhabditis elegans*. *Exp Gerontol.* (2019) 117:99–105. doi: 10.1016/j.exger.2018.11.016
26. Liu X, Luo Q, Rakariyatham K, Yong C, Goulette T, Xin L, et al. Antioxidation and anti-ageing activities of different stereoisomeric astaxanthin *in vitro* and *in vivo*. *J Funct Foods.* (2016) 25:50–61. doi: 10.1016/j.jff.2016.05.009
27. Johnson TE. Advantages and disadvantages of *Caenorhabditis elegans* for aging research. *Exp Gerontol.* (2003) 38:1329–32. doi: 10.1016/j.exger.2003.10.020
28. Titus K, Hengartner MO. Finding function in novel targets: *C. elegans* as a model organism. *Nat Rev Drug Discov.* (2006) 5:387–98. doi: 10.1038/nrd2031
29. Zhao L, Zhang Y, He L, Dai W, Lai Y, Yao X, et al. Soy sauce residue oil extracted by a novel continuous phase transition extraction under low temperature and its refining process. *J Agr Food Chem.* (2014) 62:3230–5. doi: 10.1021/jf405459v
30. Yang H, Zhou A, Xia X, Gou B, Liu X, Chen S. Study on the extract technology and component analysis of bergamot essential oil by low-temperature continuous phase transition. *Sci Technol Food Ind.* (2015) 35:289–93. doi: 10.13386/j.issn1002-0306.2015.16.050
31. Najafian L, Babji AS. Production of bioactive peptides using enzymatic hydrolysis and identification antioxidative peptides from patin (*Pangasius sutchi*) sarcoplasmic protein hydolysate. *J Funct Foods.* (2014) 9:280–9. doi: 10.1016/j.jff.2014.05.003
32. Re R, Pellegrini N, Proteggente A, Pannala A, Yang M, Rice-Evans C. Antioxidant activity applying an improved ABTS radical cation decolorization assay. *Free Radic Biol Med.* (1999) 26:1231–7. doi: 10.1016/S0891-5849(98)00315-3
33. Fabian TJ, Johnson TE. Production of age-synchronous mass cultures of *Caenorhabditis elegans*. *J Gerontol.* (1994) 49:B145–56. doi: 10.1093/geronj/49.4.B145
34. Brian O, Monica D. Metformin induces a dietary restriction-like state and the oxidative stress response to extend *C. elegans* healthspan via AMPK, LKB1, and SKN-1. *PLoS ONE.* (2010) 5:e8758. doi: 10.1371/journal.pone.0008758
35. Chen Y, Onken B, Chen H, Xiao S, Liu X, Driscoll M, et al. Mechanism of longevity extension of *Caenorhabditis elegans* induced by pentagalloyl glucose isolated from eucalyptus leaves. *J Agr Food Chem.* (2014) 62:3422–31. doi: 10.1021/jf500210p
36. Vayndorf EM, Lee SS, Rui HL. Whole apple extracts increase lifespan, healthspan and resistance to stress in *Caenorhabditis elegans*. *J Funct Foods.* (2013) 5:1235–43. doi: 10.1016/j.jff.2013.04.006
37. Hansen M, Hsu A, Dillin A, Kenyon C. New genes tied to endocrine, metabolic, and dietary regulation of lifespan from a *Caenorhabditis elegans* genomic RNAi screen. *PLoS Genet.* (2005) 1:e17. doi: 10.1371/journal.pgen.0010017
38. Liu X, Chen X, Liu H, Cao Y. Antioxidation and anti-aging activities of astaxanthin geometrical isomers and molecular mechanism involved in *Caenorhabditis elegans*. *J Funct Foods.* (2018) 44:127–36. doi: 10.1016/j.jff.2018.03.004
39. Salerno R, Casale F, Calandruccio C, Procopio A. Characterization of flavonoids in citrus bergamia (*Bergamot*) polyphenolic fraction by liquid chromatography-high resolution mass spectrometry (LC/HRMS). *Pharmanutrition.* (2016) 4:S1–7. doi: 10.1016/j.phanu.2015.10.001
40. Teresa M, Luca C, Anna Lisa P, Milagros García M, Dulce María S, Rita Patrizia A, et al. HPLC-PDA-MS and NMR characterization of a hydroalcoholic extract of Citrus aurantium L. *var. amara* peel with antiedematogenic activity. *J Agr Food Chem.* (2013) 61:1686–93. doi: 10.1021/jf302815t
41. Anghel B, Ramirez JE, Carlos A, Beatriz S, Simirgiotis MJ. HPLC-UV-MS profiles of phenolic compounds and antioxidant activity of fruits from three citrus species consumed in Northern Chile. *Molecules.* (2014) 19:17400–21. doi: 10.3390/molecules191117400
42. Floegel A, Kim D, Chung S, Koo SI, Chun OK. Comparison of ABTS/DPPH assays to measure antioxidant capacity in popular antioxidant-rich US foods. *J Food Compos Anal.* (2011) 24:1043–8. doi: 10.1016/j.jfca.2011.01.008
43. Woillez M, Me Rillon J, Coutie Re P, Dudonne SP, Vitrac X. Comparative study of antioxidant properties and total phenolic content of 30 plant extracts of industrial interest using DPPH, ABTS, FRAP, SOD, and ORAC assays. *J Agric Food Chem.* (2009) 57:1768–74. doi: 10.1021/jf803011r
44. Chanput W, Krueyos N, Ritthiruangdej P. Anti-oxidative assays as markers for anti-inflammatory activity of flavonoids. *Int Immunopharmacol.* (2016) 40:170–5. doi: 10.1016/j.intimp.2016.08.038
45. Lapointe J, Hekimi S. When a theory of aging ages badly. *Cell Mol Life Sci.* (2010) 67:1–8. doi: 10.1007/s00018-009-0138-8
46. Cai W, Zhang X, Huang J, Shen Z. Effect of Epimedium flavonoids in retarding aging of *C. elegans*. *Chin J Integrated Tradit Western Med.* (2008) 28:522–5. doi: 10.3321/j.issn:1003-5370.2008.06.011
47. Lin C, Zhang X, Xiao J, Zhong Q, Kuang Y, Cao Y, et al. Effects on longevity extension and mechanism of action of carnosic acid in caenorhabditis elegans. *Food Funct.* (2019) 10:1398–410. doi: 10.1039/C8FO02371A
48. Kim DK, Jeon H, Dong SC. 4-Hydroxybenzoic acid-mediated lifespan extension in *Caenorhabditis elegans*. *J Funct Foods.* (2014) 7:630–40. doi: 10.1016/j.jff.2013.12.022
49. Lithgow GJ, White TM, Melov S, Johnson TE. Thermotolerance and extended life-span conferred by single-gene mutations and induced by thermal stress. *Proc Natl Acad Sci USA.* (1995) 92:7540–4. doi: 10.1073/pnas.92.16.7540
50. Papaevgeniou N, Chondrogianni N. Anti-aging and anti-aggregation properties of polyphenolic compounds in *C. elegans*. *Curr Pharm Des.* (2018) 24:2107–20. doi: 10.2174/1381612824666180515145652
51. Harman D. Aging: a theory based on free radical and radiation chemistry. *J Gerontol.* (1956) 11:298–300. doi: 10.1093/geronj/11.3.298
52. Das KC, Muniyappa H. Age-dependent mitochondrial energy dynamics in the mice heart: role of superoxide dismutase-2. *Exp Gerontol.* (2013) 48:947–59. doi: 10.1016/j.exger.2013.06.002
53. Rizvi SI, Maurya PK. Alterations in antioxidant enzymes during aging in humans. *Mol Biotechnol.* (2007) 37:58–61. doi: 10.1007/s12033-007-0048-7
54. Maurya PK, Noto C, Rizzo LB, Rios AC, Nunes SO, Barbosa DS, et al. The role of oxidative and nitrosative stress in accelerated aging and major depressive disorder. *Prog Neuropsychopharmacol Biol Psychiatry.* (2016) 65:134–44. doi: 10.1016/j.pnpbp.2015.08.016
55. Zhou W, Lin J, Wang S, Lin H. Effect of *Herba Scutellariae Barbatae* flavonoids in delaying aging of *Caenorhabditis elegans* and human umbilical vein endothelial cells *in vitro*. *J Southern Med Univ.* (2017) 37:821–6. doi: 10.3969/j.issn.1673-4254.2017.06.19

Conflict of Interest: HC was employed by the company Guangdong Zhancui Food Co., Ltd.

The remaining authors declare that the research was conducted in the absence of any commercial or financial relationships that could be construed as a potential conflict of interest.

frontiers in Nutrition

ORIGINAL RESEARCH
published: 15 December 2020
doi: 10.3389/fnut.2020.543421

The Stability, Microstructure, and Microrheological Properties of *Monascus* Pigment Double Emulsions Stabilized by Polyglycerol Polyricinoleate and Soybean Protein Isolate

*Duoxia Xu, Boyan Zheng, Yixin Che, Guorong Liu, Yingmao Yuan, Shaojia Wang and Yanping Cao**

Beijing Advanced Innovation Center for Food Nutrition and Human Health (BTBU), School of Food and Health, Engineering and Technology Research Center of Food Additives, Beijing Higher Institution Engineering Research Center of Food Additives and Ingredients, Beijing Technology & Business University, Beijing, China

OPEN ACCESS

Edited by:
Jinkai Zheng,
Chinese Academy of Agricultural Sciences (CAAS), China

Reviewed by:
Fang Yuan,
China Agricultural University, China
Fuguo Liu,
Northwest A&F University, China

***Correspondence:**
Yanping Cao
xdxbtbu@126.com

Specialty section:
This article was submitted to Food Chemistry, a section of the journal Frontiers in Nutrition

Received: *17 March 2020*
Accepted: *10 November 2020*
Published: *15 December 2020*

Citation:
Xu D, Zheng B, Che Y, Liu G, Yuan Y, Wang S and Cao Y (2020) The Stability, Microstructure, and Microrheological Properties of Monascus Pigment Double Emulsions Stabilized by Polyglycerol Polyricinoleate and Soybean Protein Isolate. Front. Nutr. 7:543421. doi: 10.3389/fnut.2020.543421

Monascus pigment is a natural food pigment and is commonly used for coloring and as antiseptic of cured meat products, confectionery, cakes, and beverages. However, *Monascus* pigment is sensitive to environmental conditions. The main aim of this study was to investigate the effect of polyglycerol polyricinoleate (PGPR) and soy protein isolate (SPI) on the particle size, zeta potential, physical stability, microstructure, and microrheological properties of *Monascus* pigment double emulsions. The effects of ionic strength, heating, and freeze thawing treatment on the stabilities of *Monascus* pigment double emulsions were also characterized. It was found that the optimum PGPR and SPI concentrations for fabricating *Monascus* pigment double emulsion were 3.6 and 3.0 wt%, respectively. The fabricated *Monascus* pigment double emulsion was composed of fine particles with narrow and uniform size distributions. Microrheological property results suggested that the elastic characteristic of the *Monascus* pigment double emulsion was dominated with increasing PGPR and SPI contents. It was mainly due to the increased collision and interaction between the droplets during the movement resulting in force increasing. *Monascus* pigment double emulsions with <5 mM $CaCl_2$ prevented calcium to destroy the physical stability of emulsions, while *Monascus* pigment double emulsions with more than 10 mM $CaCl_2$ formed creaming. After freeze thawing treatment, creaming occurred in *Monascus* pigment double emulsion. However, it was stable against heating treatment due to heating leading to a dense network structure. It could be contributed to the practical applications of *Monascus* pigment double emulsions in food products.

Keywords: *Monascus* pigment, double emulsions, microrheological properties, stability, microstructure

INTRODUCTION

In recent years, people are more aware of the importance of health; these findings make natural pigments become more popular as food colorants (1). *Monascus* pigment is a natural food pigment and is commonly used for coloring and as antiseptic of cured meat products, confectionery, cakes, and beverages (2). *Monascus* has been proven to have good biological function in various fields, including lowering blood lipids, lowering blood pressure and cholesterol levels, anti-inflammatory and anti-cancer activity, anti-mutation, immunity, anti-depression, prevention of arteriosclerosis, and other biological activities (3, 4).

However, *Monascus* pigment is sensitive to environmental conditions such as heating, basic or acidic pH, light, and oxygen (5). Therefore, its application in food is limited. There are some studies about the stability of *Monascus* pigment. Vendruscolo et al. (6) reported the thermal stability of natural pigments produced by *Monascus* ruberin-submerged fermentation. Jian et al. (7) used gum arabic as a stabilizer for improving *Monascus* pigment water solubility under acidic conditions through the formation of *Monascus* pigment–gum arabic complexes. It was found that the study of improving the stability of *Monascus* pigments was limited (8). Little attention has been paid to improve the stability of *Monascus* pigments by food delivery system.

Water-in-oil-in-water (W/O/W) emulsions are complex liquid dispersion systems known also as double emulsions, in which a water-in-oil emulsion dispersed in a second continuous water phase (9–11). It is reported that double emulsions can be used to protect and control release of bioactive compounds (12, 13). Therefore, double emulsions have good prospect in the application of food, pharmacy, and cosmetic fields (14, 15). In previous studies, natural pigments such as β-carotene and curcumin were encapsulated in emulsions for stabilization studies (16, 17). In order to improve the properties of food colorants, beetroot betalains have also been encapsulated in W/O/W emulsions, leading to stable pink-colored double emulsions (14). Using the inner water phase of W/O/W emulsions for encapsulation of *Monascus* pigment could isolate them from the detrimental surrounding aqueous environment; in order to achieve this, a stable formulation needs to be developed.

Therefore, more comprehensive studies are required to fabricate *Monascus* pigment double emulsions. Hydrophobic emulsifier polyglycerol polyricinoleate (PGPR) and hydrophilic emulsifier soy protein isolate (SPI) have been shown to be effective for the fabrication of W/O/W emulsions for encapsulation of pigment (18). The main aim of this study was to investigate the effect of different concentrations of polyglycerol polyricinoleate (PGPR) and soy protein isolate (SPI) on the physical stability, microstructure, and microrheological properties of *Monascus* pigment double emulsions. The effects of ionic strength, heating, and freeze thawing treatment on the stability of *Monascus* pigment double emulsions were also characterized. The present study could demonstrate the potential of W/O/W emulsions as an effective delivery system for the stabilization of *Monascus* pigment. Ultimately, this work could be contributed to the practical applications of *Monascus* pigment double emulsions in food products.

MATERIALS AND METHODS

Materials

Monascus pigment was obtained from Guangzhou Tianyi Biologic Technology Co., Ltd (Zhanjiang, China). The hydrophilic emulsifier soy protein isolate (SPI, protein ≥ 90.0 wt%) was purchased from Shanghai Yuanye Biologic Technology Co., Ltd (Shanghai, China). The hydrophobic emulsifier polyglycerol polyricinoleate (PGPR) was purchased from Meida Food Co., Ltd (Beijing, China). Soybean oil (China Kerry Grain and Oil Co., Ltd.) was purchased from a local supermarket and used without further purification. All other chemicals were of analytical grade.

Preparation of *Monascus* Pigment Double Emulsions

Preparation of Primary Water-in-Oil (W/O) Emulsion

Monascus pigment double emulsions were made in a two-step procedure as shown in **Figure 1**. The primary W/O emulsion was formed with 10 wt% inner water phase and 90 wt% oil phase. For the inner water phase, 0.5 wt% *Monascus* pigment was dissolved in ultrapure water at 35°C for 1 h. The oil phase was prepared by dispersing different concentrations of PGPR in soybean oil and mixed it with a magnetic stirrer at 50°C for 2 h. W/O emulsions were prepared with an Ultra-Turrax homogenizer (IKA T25, Germany) at 15,000 rpm for 10 min at room temperature.

Preparation of *Monascus* Pigment Double Emulsion

For the outer water phase, different concentrations of SPI were dispersed in phosphate buffer at pH 6.8 and mixed it with a magnetic stirrer at 50°C for 2 h. The *Monascus* pigment double emulsion consists of 40 wt% W/O inner emulsion and 60 wt% aqueous phase. The primary *Monascus* pigment W/O emulsion and the external aqueous phase containing different concentrations of SPI were sheared at 11,000 rpm for 10 min, at room temperature. The coarse emulsions were subsequently homogenized using a homogenizer (GYB30-6S, Donghua factory, Shanghai, China) at an operational pressure of 50 MPa three times, respectively.

In order to investigate the effect of different contents of emulsifiers (PGPR & SPI) on the fabrication of *Monascus* pigment W/O/W emulsion, the final double emulsions with different contents of emulsifiers PGPR ranging from 0.9 to 5.4 wt% and SPI ranging from 0.15 to 3.0 wt% were designed.

Addition of Different Contents of $CaCl_2$ in the *Monascus* Pigment Double Emulsions

The influence of ionic strength on the *Monascus* pigment double-emulsion physical stability was studied. Different concentrations of $CaCl_2$ solution (0, 10, 20, 40, 100 mM) were prepared and then mixed with the *Monascus* pigment double emulsions (3.6 wt% PGPR and 3.0 wt% SPI) in a 1:1 ratio (v/v).

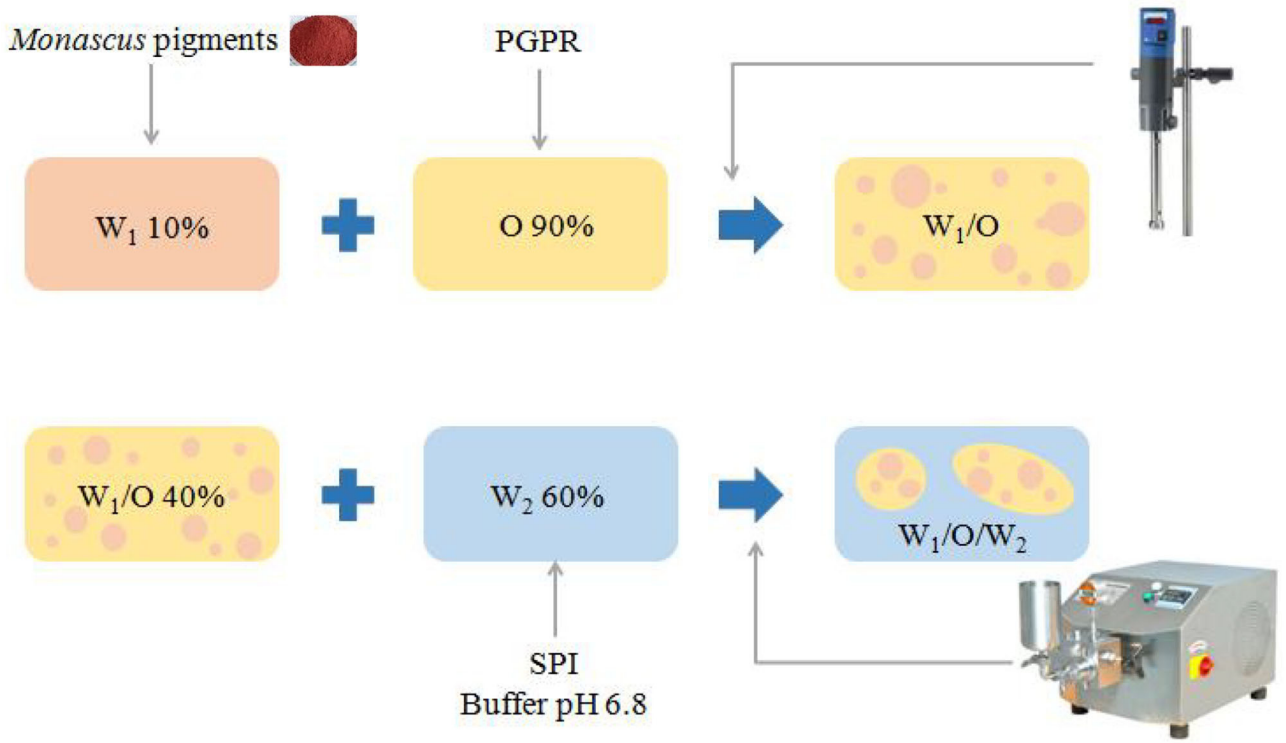

FIGURE 1 | The process of preparing *Monascus* pigment double emulsions.

Heating and Freeze Thawing Treatments on the *Monascus* Pigment Double Emulsions

To investigate the influence of temperature on the stability of *Monascus* pigment double emulsions, the *Monascus* pigment double emulsions (3.6 wt% PGPR and 3.0 wt% SPI) diluted with phosphate buffer in a 1:1 ratio (v/v) were heated at 90°C for 30 min by thermostat water bath. For the freeze thawing treatment, the *Monascus* pigment double emulsions were frozen at −18°C for 22 h then thawed at 40°C for 2 h by thermostat water bath.

Particle Size Measurement

The average droplet size of *Monascus* pigment double emulsions was determined according to the method of Wang et al. (19) by dynamic light scattering (DLS) using a Zetasizer Nano-ZS90 (Malvern Instruments, Worcestershire, UK) at a fixed detector angle of 90°. *Monascus* pigment emulsions were diluted using 1.0 mM phosphate buffer solution at pH 6.8 to minimize multiple scattering effects prior to each measurement. The measured time correlation functions were analyzed by Automatic Program equipped with the correlator. The results were described as mean particle diameter (size, nm) and particle size distribution.

Zeta Potential

The zeta potential of the *Monascus* pigment double emulsions was measured by using Zetasizer Nano-ZS90 (Malvern Instruments, Worcestershire, UK). The zeta potential was determined by measuring the direction and velocity of droplet movement in the applied electric field. All *Monascus* pigment double emulsions were diluted 50 times using 1.0 mM phosphate buffer solution at pH 6.8 to avoid multiple scattering effects. After loading the samples into the instrument, they were equilibrated for about 120 s before particle charge data was collected over 11 continuous readings (20).

Physical Stability Analyzed by LUMisizer

The physical stability of the *Monascus* pigment double emulsions with different ratios of SPI and PGPR were measured with the LUMisizer (L.U.M. GmbH, Berlin, Germany), an instrument employing centrifugal sedimentation to accelerate the occurrence of instability phenomena such as flocculation, sedimentation or creaming (21, 22). The integration graph shows the percentage of light absorbance per hour described as the "instability index." The physical stability of the *Monascus* pigment double emulsions can be reflected by the instability index, which is the integrated transmission profile against the measuring time; the higher the instability index, the lower the stability. The instrumental parameters used for the measurement were as follows: volume, 0.4 mL of dispersion; 2,500 rpm; time, 7,620 s; time interval, 30 s; temperature, 25°C (23).

Microstructure

In this experiment, the microscopic particles of the *Monascus* pigment double emulsion were directly observed by confocal

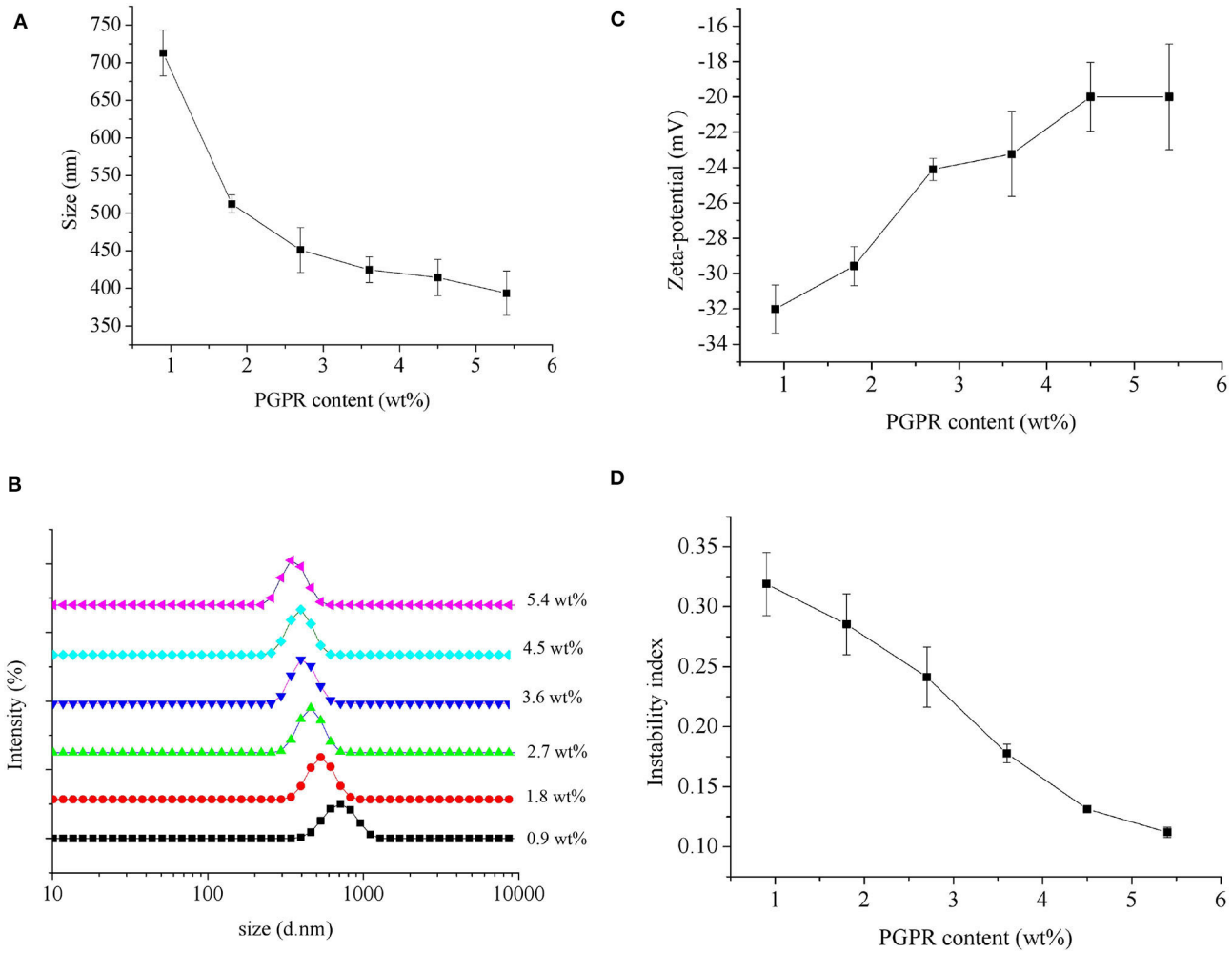

FIGURE 2 | Influence of PGPR concentrations on the mean particle size **(A)**, particle size distribution **(B)**, zeta potential **(C)**, and instability index **(D)** of *Monascus* pigment double emulsions.

laser scanning microscopy (FV1200, Olympus, Japan). The SPI in the *Monascus* pigment double emulsions was dyed with Nile blue at a ratio of 0.025% (w/w), and the soybean oil was dyed with Nile red at a ratio of 0.005% (w/w). The fluorescence signal from the Nile red and Nile blue dyes was obtained, respectively, by exciting the samples using laser sources of 488 and 637 nm, and collecting wavelengths 590–650 nm (24). All microstructures were observed with a 60 × objective lens (oil immersion).

Microrheological Property

The commercial Rheolaser Master (Formulaction, l'Union, France) used for the measurements of the microrheological property of *Monascus* pigment double emulsions is based on diffusing wave spectroscopy (DWS). The mean square displacement (MSD) curves were calculated from the dynamic speckle images, scattering by the sample as a function of time (25). The *Monascus* pigment double emulsions was placed into flat-bottomed cylindrical glass tubes (140 mm height, 16 mm diameter). The obtained data were calculated by the software Rheosoft Master 1.4.0.0 and expressed as solid-liquid balance (SLB) value.

Statistical Analysis

All *Monascus* pigment emulsions were prepared in triplicate, and all measurements were performed three times. Data were subjected to analysis of variance (ANOVA) using the software package Origin 8.5 for Windows.

RESULTS AND DISCUSSION

Effect of PGPR on the *Monascus* Pigment Double Emulsions

Particle Size

The effect of different concentrations of PGPR on the average droplet size of *Monascus* pigment double emulsion is shown in **Figure 2A**. There was a significant decrease in the average droplet size from 713.0 ± 30.7 to 451.0 ± 30.0 nm with increasing amount of PGPR from 0.9 to 2.7 wt%, after which the average

droplet size decreased from 424.8 ± 17.1 to 393.5 ± 29.6 nm with the increase of PGPR concentration from 3.6 to 5.4 wt%. The effect can also be seen in the droplet size distributions (**Figure 2B**). The *Monascus* pigment double emulsion contained a single peak at each PGPR concentration. The peak shifted to the left and decreased in intensity with increasing PGPR concentrations. For the lower PGPR concentration tested (0.9 and 1.8 wt%), the *Monascus* pigment emulsions showed a narrow size distribution, peaks corresponding to bigger sizes. Compared to *Monascus* pigment double emulsions with 2.7 wt% PGPR, the sample with 3.6 wt% PGPR was composed of fine particles with a narrow and uniform size distribution. At higher PGPR concentrations (4.5 and 5.4 wt%), the peaks of *Monascus* pigment emulsions shifted slightly to the left due to the enough adsorbing concentration of PGPR. It was in line with the findings of Marze (26) that slightly higher PGPR concentrations were sufficient for interface coverage 1.2 mg/m^2. It has even been reported that larger inner water droplets could lead to the full release of the internal droplet content into the external water phase (27). It was consistent with those previously reported by Hattrem et al. (28) and Serdaroglu et al. (29) for slightly higher PGPR concentrations with good stability of double emulsion.

Zeta Potential

The effect of different concentrations of PGPR on the zeta potential of *Monascus* pigment double emulsion is shown in **Figure 2C**. It was found that the zeta potential of all *Monascus* pigment double emulsions was negative, indicating the negatively charged emulsions droplets. The zeta potential was obviously affected by the content of PGPR used for emulsification. As shown in **Figure 2C**, the magnitude of the zeta potential of the *Monascus* pigment emulsion was decreased gradually from −32.0 to −20.0 mV with increasing PGPR concentration from 0.9 to 5.4 wt%. This might be explained by the fact that PGPR is a non-ionic surfactant; therefore, a decreased effect on zeta potential was observed by the droplets surrounded by non-ionic surfactants (30). The results suggested that emulsions showed gradual tendency of adsorption with increasing PGPR content.

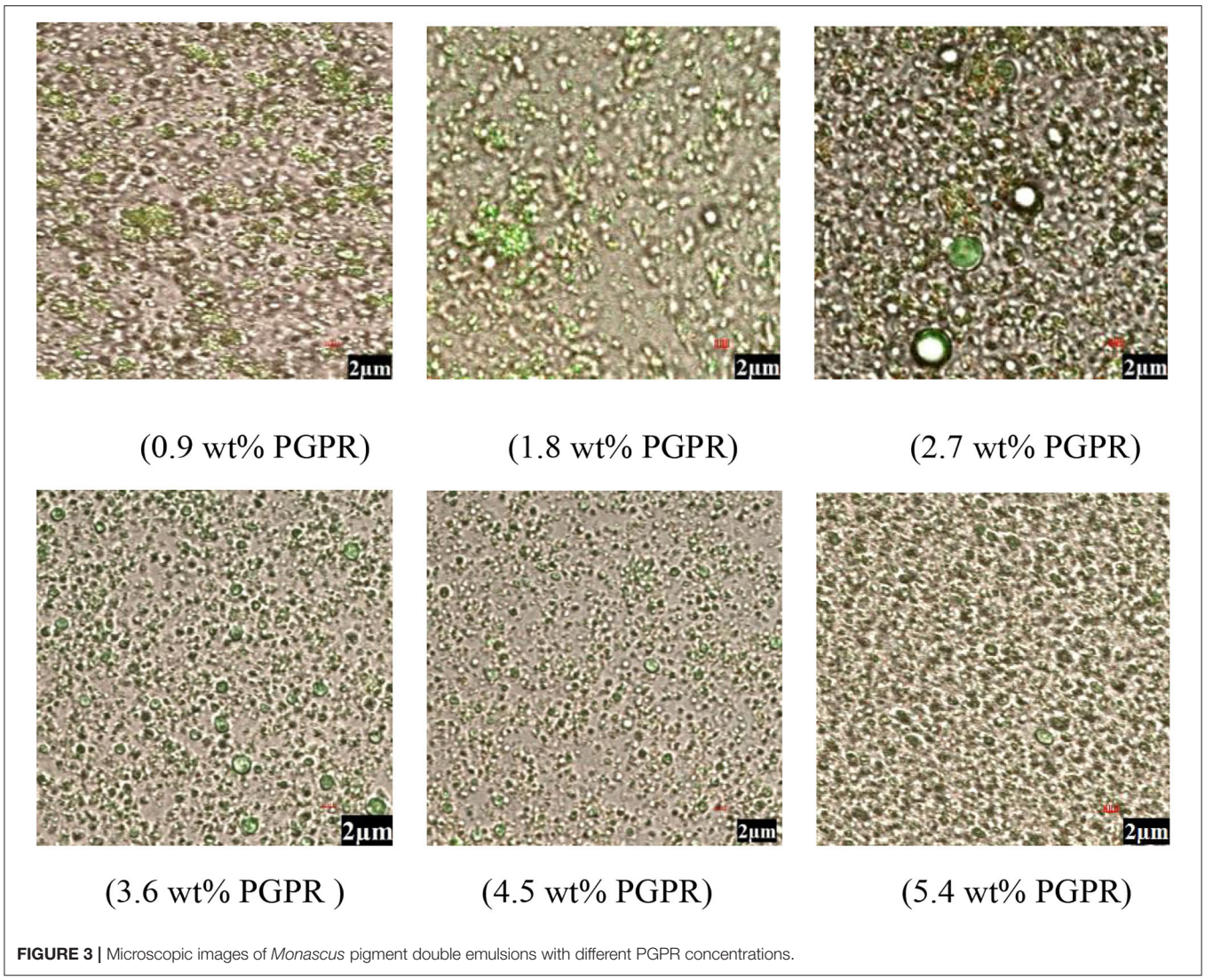

FIGURE 3 | Microscopic images of *Monascus* pigment double emulsions with different PGPR concentrations.

It was found that there was no significant difference between zeta potential of emulsions with more than 3.6 wt% PGPR. It indicated that enough concentration of PGPR for preparing *Monascus* pigment double emulsion was 3.6 wt%.

Physical Stability

To further investigate the influence of PGPR concentration on the physical stability of *Monascus* pigment double emulsions, the instability index was present (**Figure 2D**). The higher instability index exhibits the much lower stability of the emulsion. As can be seen, the instability index of *Monascus* pigment double emulsions decreased with increasing PGPR concentration. It demonstrated that preparing *Monascus* pigment double emulsions with high concentrations of PGPR could enhance the stability. The improved stability of *Monascus* pigment double emulsions with increasing content of PGPR can be attributed to the strong steric repulsion between droplets resulting from the relatively thick PGPR layer adsorbed to their surfaces. *Monascus* pigment double emulsions with high concentrations of PGPR had high initial osmotic pressure; a good physical stability could be achieved providing that the PGPR concentration is sufficient (31). On the other hand, the improved stability of the *Monascus* pigment double emulsions can also be attributed to the increased viscosity and a gel-like network. Similar results were also reported by Cofrades et al. (32) and Serdaroglu et al. (29) who proved that 6.0–6.4 wt% PGPR in the oil phase was stable on the double emulsions used as animal fat replacers in meat systems.

Microstructure

Confocal laser microscopy images of *Monascus* pigment double emulsions with different PGPR concentrations are shown in **Figure 3**. In the images, the green area represented oil phase enrichment and the red area represented the *Monascus* pigment phase region. In the microstructure observed by CLSM, *Monascus* pigment in the out water phase could be seen in the double emulsion with 0.9 wt% PGPR and some aggregated droplets were shown in the emulsions prepared with 0.9, 1.8, and 2.7 wt% PGPR. As the PGPR concentration was increased (3.6 and 4.5 wt%), aggregated droplets in the microstructure disappeared and small droplets were evenly distributed throughout the emulsion system. It was found that some droplet aggregation was also observed at relatively higher PGPR (5.4 wt%) concentrations. It can be concluded that the microstructure of *Monascus* pigment double emulsion stabilized with 3.6 and 4.5 wt% PGPR was more uniform. According to Eisinaite et al. (31), the water phase was entrapped in the PGPR formed reverse micelles. Therefore, when the content of PGPR was lower, the interfacial tension reduction and the increase of the polarity of the oil phase were not enough to prevent the aggregation of droplets (33). This phenomenon suggests that the presence of enough PGPR could improve the stability of *Monascus* pigment double emulsion against aggregation and coalescence.

Therefore, 3.6 wt% PGPR was the optimum concentration for preparing stable *Monascus* pigment double emulsions. Because

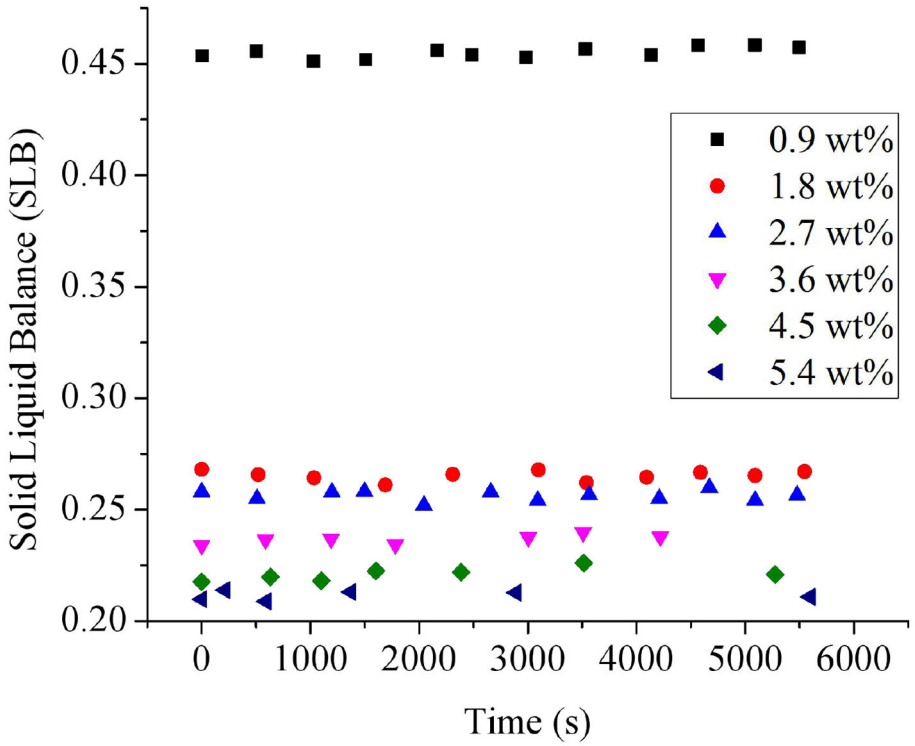

FIGURE 4 | Influence of PGPR concentrations on the solid–liquid balance (SLB) values of *Monascus* pigment double emulsions.

the droplets had a relatively smaller droplet size, high zeta potential, and a lower instability index, the *Monascus* pigment double-emulsion droplets appeared to be saturated with PGPR at this concentration.

Microrheological Properties

The influence of PGPR concentrations on the microrheological properties of *Monascus* pigment double emulsions was measured using the Rheolaser lab. The technique monitored the Brownian motion and the interactions of droplets (34). The microrheology study could also illustrate the solid and liquid characteristics of emulsion by solid–liquid Balance (SLB) value, which is a ratio between the solid-like and liquid-like behavior of the sample (23). The droplets' movement showed a more solid behavior when the SLB is <0.5, while the emulsion showed a more viscous or liquid behavior with the SLB ranging between 0.5 and 1 (35). As shown in **Figure 4**, all the SLB values of *Monascus* pigment double emulsions were <0.5, which means that the solid behavior dominated at all the PGPR concentrations. The SLB values of *Monascus* pigment double emulsions were decreased with increasing PGPR content. It suggested that the elastic characteristic of the *Monascus* pigment double emulsion was enhanced by the further addition of PGPR. It was mainly due to the increased collision and interaction between the droplets during the movement resulting in force increasing. These results could be explained in terms of a decrease in the mobility of the *Monascus* pigment double-emulsion droplets with increasing PGPR concentration. It proved that enough PGPR did adsorb to *Monascus* pigment double-emulsion droplets, leading to a

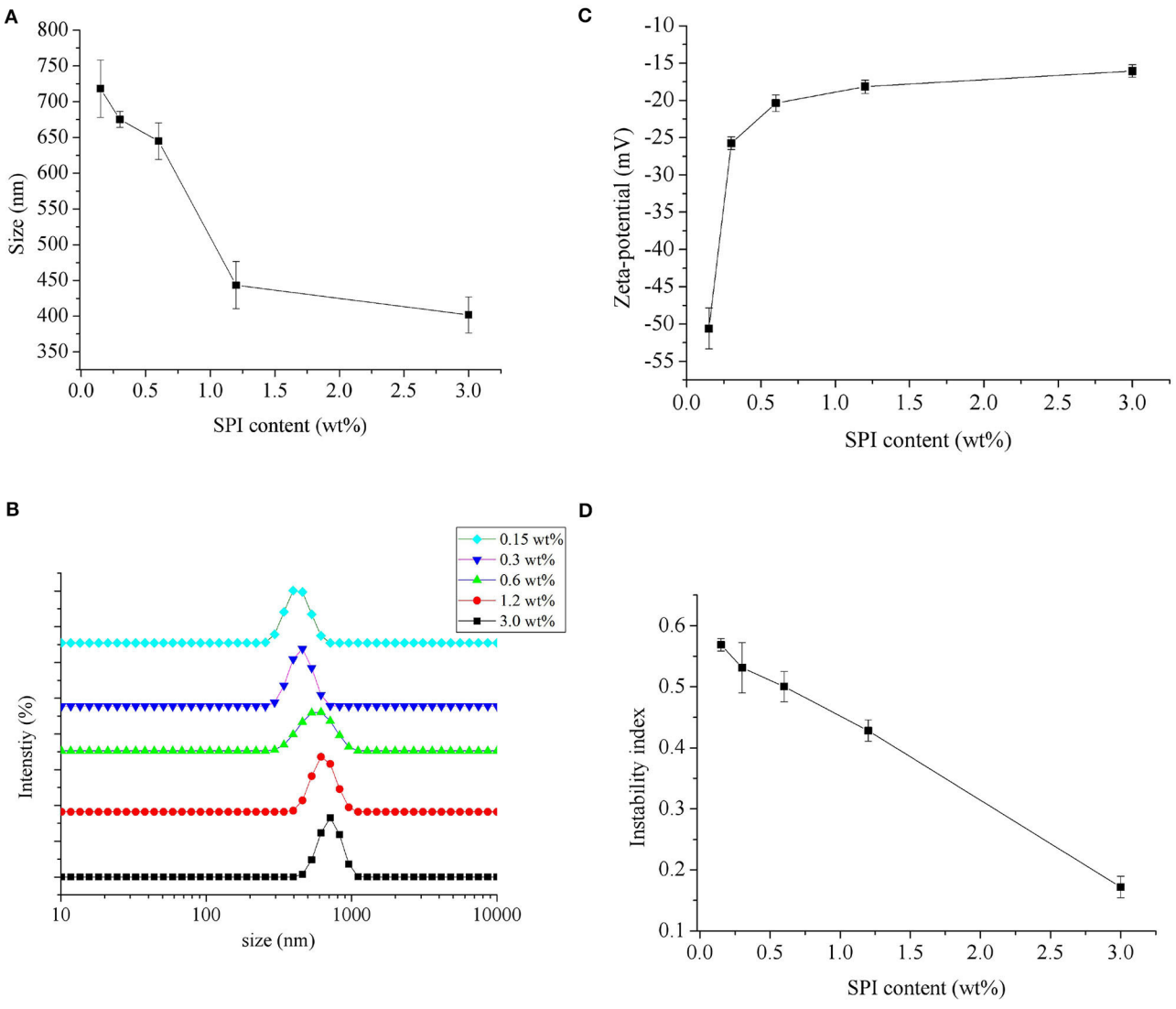

FIGURE 5 | The mean particle size **(A)**, particle size distribution **(B)**, zeta potential **(C)**, and instability index **(D)** of *Monascus* pigment double emulsions with different SPI concentrations.

dramatic decrease of droplet mobility compared with the lower content of PGPR.

Effect of SPI on the *Monascus* Pigment Double Emulsions

Particle Size and Zeta Potential

The impact of varied SPI contents on the average droplet size and droplet size distributions of *Monascus* pigment double emulsion is investigated in **Figure 5**. It was found that SPI concentration had a strong influence on the droplet size of *Monascus* pigment emulsion. With increasing SPI concentration, smaller droplets were formed, which is in accordance with conventional emulsification theory (36). The stabilizing effect of emulsifier molecules increases with its concentration. When the SPI concentration was 3.0 wt%, there was a large decrease in the mean particle size. The decrease in droplet size was a clear indication of the enough adsorption of SPI onto the *Monascus* pigment double-emulsion droplets and corresponded to the differences in the droplet charge described in **Figure 5C**. Therefore, SPI as a surfactant was adsorbed to the surface of the droplets forming a protective coating that inhibits droplet aggregation.

Zeta potential, besides size distribution, is another important parameter characterizing stability of emulsion. **Figure 5C** shows the influence of SPI concentration on the zeta potential of *Monascus* pigment double emulsions. It was found that the net charge on the *Monascus* pigment double emulsions became less negative as the SPI was increased. It is generally known that the surface charge of the protein-coated emulsion droplets is governed by the degree of ionization of amino groups ($-NH_2$) and carboxyl groups (-COOH) of the protein molecules. The decrease of zeta potential of *Monascus* pigment double-emulsion droplets with increasing SPI content was attributed to that the structure of interfacial SPI was altered due to its adsorption (37).

Physical Stability

Monascus pigment double emulsions stabilized with 0.15–3.0 wt% SPI were examined by the instability index according to the integrated transmission profiles against the measuring time

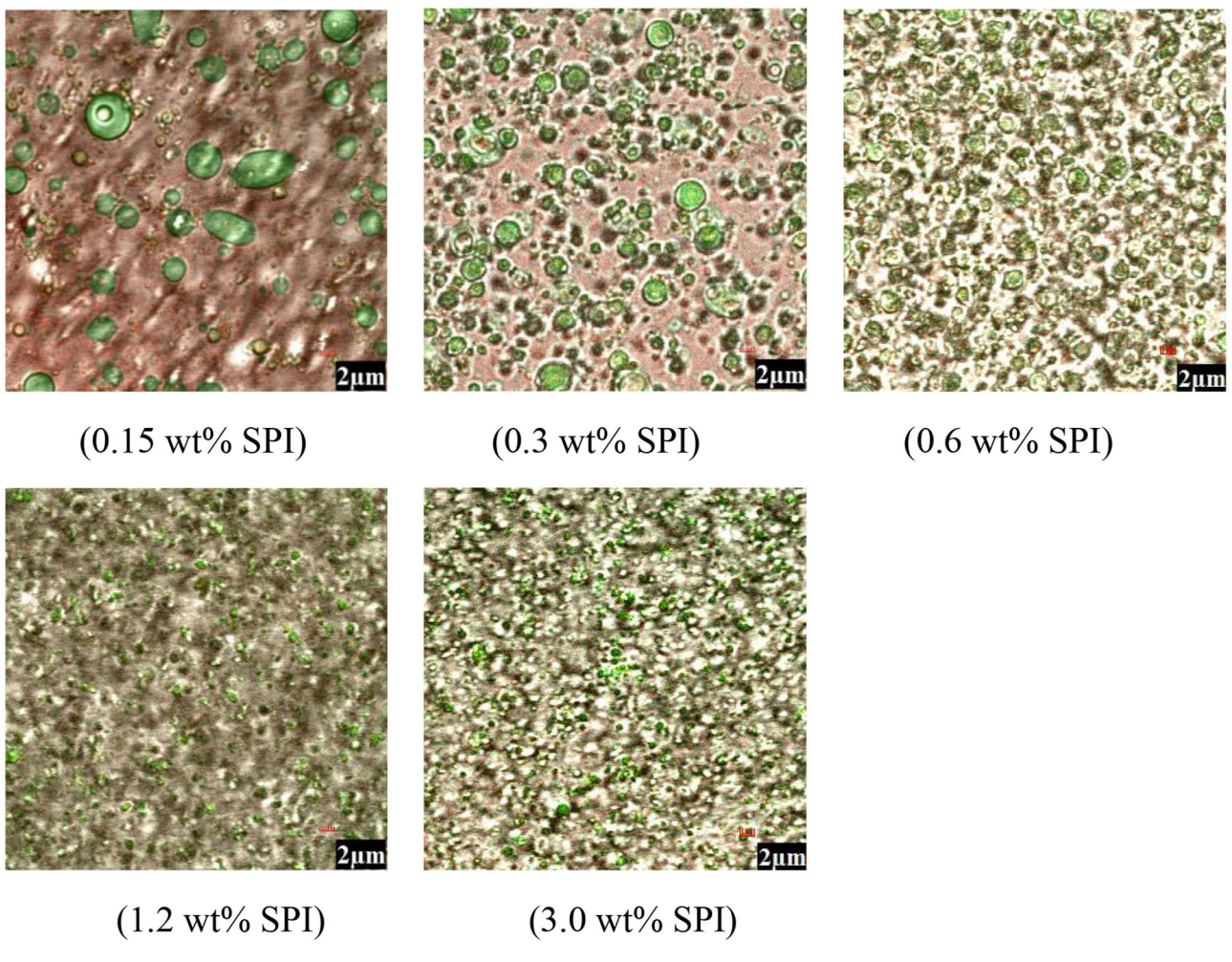

FIGURE 6 | Microscopic images of *Monascus* pigment double emulsions with different SPI concentrations.

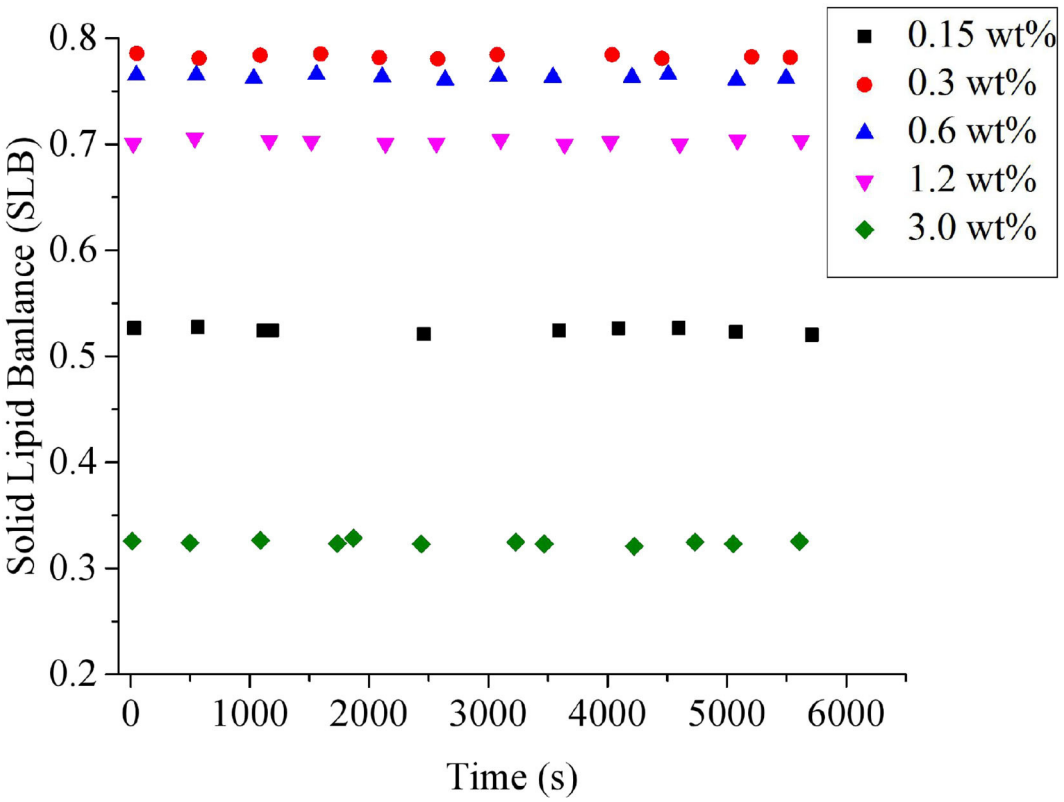

FIGURE 7 | Influence of SPI concentrations on the solid–liquid balance (SLB) values of *Monascus* pigment double emulsions.

in **Figure 5D**. As the SPI concentration increased, the instability index decreased, suggesting that SPI can protect the *Monascus* pigment emulsion from flocculation. The addition of SPI had an optimum effect on the stability for *Monascus* pigment emulsions with 3.0 wt% SPI, since the highest SPI concentration led to the lowest instability index. It was reported that the addition of biopolymers to the external phase improved physical stability by forming a coating around droplets or increasing the viscosity (38). The results could be explained by the fact that when the SPI concentration was low, it was insufficient to cover the entire droplet in the emulsion. Thus, it may lead to bridge flocculation by interacting the surfaces of the *Monascus* pigment double emulsions through attractive electrostatic interaction. With increasing concentration of SPI, it would be enough to cover the droplets and form a thick layer on the *Monascus* pigment double-emulsion droplets. Therefore, it would inhibit the flocculation by the steric hindrance repulsion.

Microstructure

The appearance of *Monascus* pigment double-emulsion droplets was observed by confocal microscopy as shown in **Figure 6**. The CLSM images confirmed the formation of *Monascus* pigment double emulsions, which consist of W/O emulsion droplets in the continuous aqueous phase. The oil droplets dyed with Nile red appeared green, the SPI molecules dyed with Nile blue appeared red, and the inner water phase without dye appeared white. When the W_2 phase was at low (0.15 and 0.3 wt%) SPI concentration, the double emulsions consisting of relatively large oil droplets without uniform sizes, with some smaller water droplets inside, gave a visual impression of inhomogeneity. The particle size of *Monascus* pigment double emulsions was decreased with SPI concentration increasing from 0.6 to 3.0 wt% leading to the reduction in coalescence of W/O emulsion droplets. It may be because SPI exhibit O/W droplets a layer with steric hindrance interaction, as confirmed by the observation of double-emulsion droplets.

Microrheological Properties

The effect of SPI concentration on the microrheological property of *Monascus* pigment double emulsion was investigated without disturbing the emulsions system by using the Rheolaser lab. The SLB value indicates the equilibrium state of the emulsion by calculating the slope of the platform area (39). In **Figure 7**, it was found that the SLB values of the double emulsions were more than 0.5 with SPI <3.0 wt%, which indicated that those emulsions were liquid behavior, while there was a sharp decrease in SLB value as the SPI concentration was increased to 3.0 wt%. The SLB of *Monascus* pigment double emulsion stabilized with 3.0 wt% SPI was <0.5. It proved that the *Monascus* pigment double emulsion with 3.0 wt% SPI and 3.6 wt% PGPR presented a solid behavior leading to loss of droplet mobility. This phenomenon

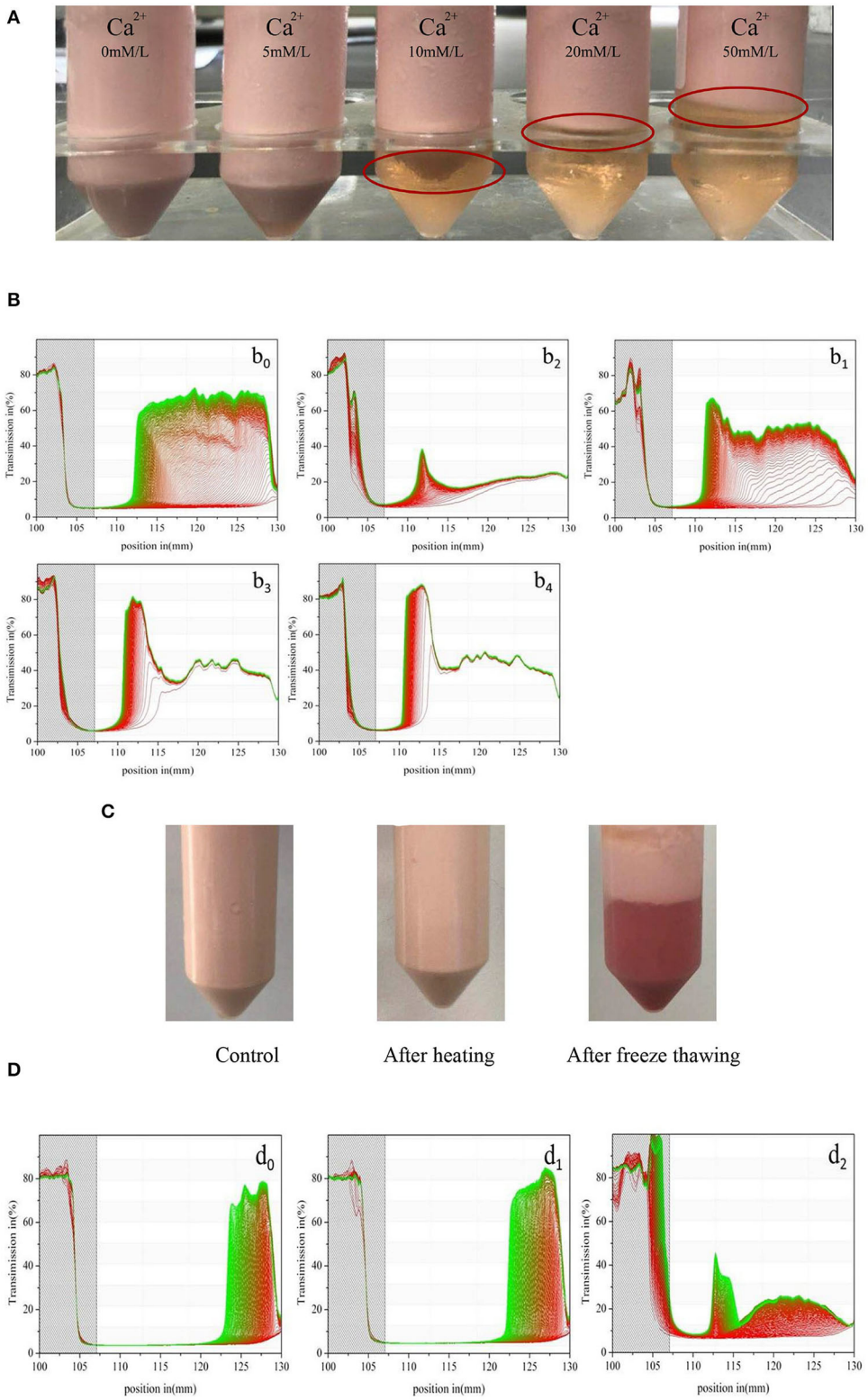

FIGURE 8 | Effect of $CaCl_2$ concentration on the visual creaming stability **(A)** and the original transmissions as a function of sample position of *Monascus* pigment double emulsions **(B)**. The stability was expressed as the slope of the integrated transmission time plots determined at 2,500 rpm during 7,650 s at 25°C (b_0: without $CaCl_2$; b_1: with 5 mM $CaCl_2$; b_2: with 10 mM $CaCl_2$; b_3: with 20 mM $CaCl_2$; b_4: with 50 mM $CaCl_2$). Effect of heating and freeze thawing treatment on the visual creaming stability **(C)** and original transmissions as a function of sample position **(D)** of *Monascus* pigment double emulsions (d_0: control; d_1: after thermal treatment; d_2: after freeze thawing treatment).

may be attributed to the colloidalization of the emulsion system as the SPI concentration was increased to a specific degree.

Effect of Ionic Strength, Heating, and Freeze Thawing Treatments on the Stability of Monascus Pigment Double Emulsion

Figure 8A shows the impact of different $CaCl_2$ concentrations on the visual creaming stability and original transmissions as a function of the sample position of *Monascus* pigment double emulsions. According to the visual creaming stability, the increase of Ca^{2+} content in the systems produced a higher extent of creaming. It exhibited that *Monascus* pigment double emulsions with <5 mM $CaCl_2$ prevented calcium to destroy the physical stability of emulsions, while *Monascus* pigment double emulsions with more than 10 mM calcium concentration were unstable.

The changes in the transmission profiles over space and time further prove that the influence of different Ca^{2+} concentrations on *Monascus* pigment double emulsions resulted in different physical stabilities. In **Figure 8B**, it was found that with increasing Ca^{2+} concentrations from 5 to 50 mM, the first profile taken after 30 s exhibited high transmissions along the sample length. A sharp front of *Monascus* pigment double emulsions with more than 10 mM moved toward the top during centrifugation. Our research group (40) reported that the sharp front means that nearly all droplets are moving as a zone creaming. The structure of the creaming was a flocculated network. With increasing concentration of the Ca^{2+} concentration more than 10 mM, the profiles were nearly spaced with a considerably smaller distance during centrifugation. It indicated that these *Monascus* pigment double emulsions with more than 10 mM Ca^{2+} were creaming easily. The profiles of *Monascus* pigment double emulsions with 20 and 50 mM Ca^{2+} were quite similar. This result can be explained by the binding of SPI by Ca^{2+}, leading to the aggregation by electrostatic screening (41). It was reported that Ca^{2+} not only contributed its nutritional property but also acted functionally by allowing the obtaining of double-emulsion systems with creamy texture without the need of addition of saturated fats. The obtained result proved that the isolated creaming *Monascus* pigment double emulsions could work as a reduced fat replacer of whipped dairy cream with important calcium contribution.

The impact of heating and freeze thawing treatment on the *Monascus* pigment double emulsion was also studied. As shown in **Figures 8C,D**, it was found that there was no creaming and the *Monascus* pigment double emulsion was stable against heating treatment. During heating, the bonds between SPI molecules were formed. Presumably, hydrophobic interactions and disulfide bridges often play major roles (42). Hydrogen bonds may also be present. Roesch and Corredig (43) reported that covalent interactions have occurred between soybean proteins during heating. Therefore, heating could result in the improved viscosity of *Monascus* pigment double emulsion, which led to a more structured network.

After freeze thawing cycling, creaming occurred in *Monascus* pigment double emulsion. It indicated that the droplets migrated to the top of the sample and promoted their coalescence. It revealed that droplet aggregation and coalescence of *Monascus* pigment double emulsion occurred after freeze thawing treatments. The destabilization was attributed to the SPI relatively thin absorbed layers of the *Monascus* pigment double-emulsion droplets. It also might be because the adsorbed SPI either underwent a conformational change or is desorbed from the droplet surfaces due to freeze-thawing treatments (44).

CONCLUSION

Monascus pigment double emulsions were fabricated in the presence of PGPR and SPI and characterized in terms of droplet size, stability, microstructure, and microrheological properties. According to the results, the droplet size as well as stability was highly dependent on the concentration of the PGPR and SPI used. Higher PGPR and SPI concentrations yielded lower droplet sizes and higher stability and more solid behaviors. It was shown that 3.6 wt% PGPR and 3.0 wt% SPI were the optimum concentrations of emulsifiers to form *Monascus* pigment double emulsion. Microstructure proved that aggregated droplets disappeared and small droplets were evenly distributed throughout the emulsion system with increasing PGPR and SPI contents. The elastic characteristic of the *Monascus* pigment double emulsion was enhanced by the addition of PGPR and SPI due to the increased collision and interaction between the droplets. *Monascus* pigment double emulsion was unstable to more than 10 mM Ca^{2+} and freeze-thawing treatment due to the weak electrostatic interaction. However, it was stable against heating treatment probably due to heating leading to a more structured network. It could be useful for a broad application of *Monascus* pigment double emulsions in food products.

DATA AVAILABILITY STATEMENT

All datasets generated for this study are included in the article/supplementary material.

AUTHOR CONTRIBUTIONS

DX, BZ, and YC: data curation, writing–original draft preparation, investigation, and validation. GL, YY, and SW: methodology, investigation, and validation. DX: writing–review and editing, project administration, and funding acquisition. YC: conceptualization, supervision, project administration, and funding acquisition. All authors contributed to the article and approved the submitted version.

FUNDING

This research was funded by the 13th Five-Year the State Key Development Program (2016YFD0400802), National Natural Science Foundation of China (31771976 & 32072216), School Level Cultivation Fund of Beijing Technology and Business University for Distinguished

and Excellent Young Scholars (BTBUYP2020), Beijing Key Laboratory of the Innovative Development of Functional Staple and the Nutritional Intervention for Chronic Disease, Beijing Science and Technology Commission (Z171100001317004), Support Project of High-level Teachers in Beijing Municipal Universities in the Period of 13th Five-year Plan (CIT & TCD201804018), Construction of Service Capability of Scientific and Technological Innovation (PXM2019_014213_000010, PXM2018_014213_000033, PXM 2018_014213_000014, 19005857058), Cultivation and Development of Innovation Base Z171100002217019), and Quality Construction of Talents Training—First-class Specialty Construction (Municipal Level),—Food Science and Engineering (PXM2019_014213_000010). The authors are grateful to Guangdong Tianyi Biological Technology Co. for providing the *Monascus* pigment.

REFERENCES

1. Downham A, Collins P. Coloring our foods in the last and next millenium. *Int J Food Sci Tech*. (2000) 35:5–22. doi: 10.1046/j.1365-2621.2000.00373.x
2. Chen W, He Y, Zhou Y, Shao Y, Feng Y, Li M, et al. Edible Filamentous fungi from the species Monascus: early traditional fermentations, modern molecular biology, and future genomics. *Compr Rev Food Sci F*. (2015) 14:555–67. doi: 10.1111/1541-4337.12145
3. Hsu WH, Lee BH, Liao TH, Hsu YW, Pan TM. Monascus-fermented metabolite monascin suppresses inflammation via PPAR-gamma regulation and JNK inactivation in THP-1 monocytes. *Food Chem Toxicol*. (2012) 50:1178–86. doi: 10.1016/j.fct.2012.02.029
4. Tseng Y, Yang J, Chang H, Lee Y, Mau J. Antioxidant properties of methanolic extracts from monascal adlay. *Food Chem*. (2006) 97:375–81. doi: 10.1016/j.foodchem.2005.04.022
5. Singh N, Goel G, Singh N, Pathak BK, Kaushik D. Modeling the red pigment production by Monascus purpureus MTCC 369 by Artificial Neural Network using rice water based medium. *Food Biosci*. (2015) 11:17–22. doi: 10.1016/j.fbio.2015.04.001
6. Vendruscolo F, Müller BL, Moritz DE, de Oliveira D, Schmidell W, Ninow JL. Thermal stability of natural pigments produced by Monascus ruber in submerged fermentation. *Biocatal Agric Biotechnol*. (2013) 2:278–84. doi: 10.1016/j.bcab.2013.03.008
7. Jian W, Sun Y, Wu JY. Improving the water solubility of Monascus pigments under acidic conditions with gum arabic. *J Sci Food Agr*. (2017) 97:2926–33 doi: 10.1002/jsfa.8130
8. Gandía-Herrero F, Jiménez-Atiénzar M, Cabanes J, García-Carmona F, Escribano J. Stabilization of the bioactive pigment of opuntia fruits through maltodextrin encapsulation. *J Agr Food Chem*. (2010) 58:10646–52. doi: 10.1021/jf101695f
9. Artiga-Artigas M, Molet-Rodríguez A, Salvia-Trujillo L, Martín-Belloso O. Formation of double (W1/O/W2) emulsions as carriers of hydrophilic and lipophilic active compounds. *Food Bioprocess Tech*. (2019) 12:422–35. doi: 10.1007/s11947-018-2221-3
10. Dickinson E. Double emulsions stabilized by food biopolymers. *Food Biophys*. (2011) 6:1–11. doi: 10.1007/s11483-010-9188-6
11. Giroux H, Robitaille G, Britten M. Controlled release of casein-derived peptides in the gastrointestinal environment by encapsulation in water-in-oil-in-water double emulsions. *LWT-Food Sci Technol*. (2016) 69:225–32. doi: 10.1016/j.lwt.2016.01.050
12. Eisinaite V, Juraite D, Schroen K, Leskauskaite D. Preparation of stable food-grade double emulsions with a hybrid premix membrane emulsification system. *Food Chem*. (2016) 206:59–66. doi: 10.1016/j.foodchem.2016.03.046
13. Lamba H, Sathish K, Sabikhi L. Double emulsions: emerging delivery system for plant bioactives. *Food Bioprocess Tech*. (2015) 8:709–28. doi: 10.1007/s11947-014-1468-6
14. Eisinaite V, Juraite D, Schroën K, Leskauskaite D. Food-grade double emulsions as effective fat replacers in meat systems. *J Food Eng*. (2017) 213:54–9. doi: 10.1016/j.jfoodeng.2017.05.022
15. Lobato-Calleros C, Recillas-Mota MT, Espinosa-Solares T, Alvarez-Ramirez J, Vernon-Carter EJ. Microstructural and rheological properties of low-fat stirred yoghurts made with skim milk and multiple emulsions. *J Texture Stud*. (2009) 40:657–75. doi: 10.1111/j.1745-4603.2009.00204.x
16. Aditya NP, Aditya S, Yang HJ, Kim HW, Park SO, Lee J, et al. Curcumin and catechin co-loaded water-in-oil-in-water emulsion and its beverage application. *J Funct Foods*. (2015) 15:35–43. doi: 10.1016/j.jff.2015.03.013
17. Akinosho HO, Wicker L. Stability of β-carotene loaded emulsions vary by viscosity of hydroxypropyl methylcellulose dispersions. *LWT-Food Sci Technol*. (2015) 63:582–9. doi: 10.1016/j.lwt.2015.02.024
18. Utama DT, Jeong H, Kim J, Lee SK. Formula optimization of a Perilla-canola oil (O/W) emulsion and its potential application as an animal fat replacer in meat emulsion. *Korean J Food ScI An*. (2018) 3:580–92. doi: 10.5851/kosfa.2018.38.3.580
19. Wang X, Li X, Xu D, Zhu Y, Cao Y, Wang J, et al. Comparision of heteroaggregation, layer-by-layer and directly mixing techniques on the physical properties and *in vitro* digestion of emulsions. *Food Hydrocolloid*. (2019) 95:228–37. doi: 10.1016/j.foodhyd.2019.04.034
20. Wang X, Li X, Xu D, Zhu Y, Cao Y, Li X, et al. Modulation of stability rheological properties, and microstructure of heteroaggregated emulsion: influence of oil content. *LWT-Food Sci Technol*. (2019) 109:457–66. doi: 10.1016/j.lwt.2019.04.031
21. Ma N, Gao Q, Li X, Xu D, Yuan Y, Cao Y. Enhancing physicochemical stability and digestibility of DHA emulsions by encapsulation of DHA droplets in caseinate/alginate honeycomb-shaped microparticles. *Food Funct*. (2020) 11:2080–93. doi: 10.1039/C9FO02947H
22. Sobisch T, Lerche D. Thickener performance traced by multisample analytical centrifugation. *Colloids Surface A*. (2008) 331:114–8. doi: 10.1016/j.colsurfa.2008.05.040
23. Wang X, Li X, Xu D, Liu G, Xiao J, Cao Y, et al. Influence of unadsorbed emulsifiers on the rheological properties and structure of heteroaggregate of whey protein isolate (WPI) coated droplets and flaxseed gum (FG) coated droplets. *Food Hydrocolloid*. (2018) 80:42–52. doi: 10.1016/j.foodhyd.2018.01.041
24. Zhang Y, Liang S, Zhang J, Chi Y, Tian B, Li L, et al. Preparation of whey protein isolate nanofibrils by microwave heating and its application as carriers of lipophilic bioactive substances. *LWT-Food Sci Technol*. (2020) 125:109123. doi: 10.1016/j.lwt.2020.109213
25. Xu D, Qi Y, Wang X, Li X, Wang S, Cao Y, et al. The influence of flaxseed gum on the microrheological property and physicochemical stability of whey protein stabilized β-carotene emulsion. *Food Funct*. (2017) 8:415–23. doi: 10.1039/C6FO01357K
26. Marze S. Relaxation processes of PGPR at the water/oil interface inferred by oscillatory or transient viscoelasticity measurements. *Langmuir*. (2009) 25:12066–72. doi: 10.1021/la9016849
27. Matsumoto S, Kohda M. The viscosity of W/O/W emulsions: an attempt to estimate the water permeation coefficient of the oil layer from the viscosity changes in diluted systems on aging under osmotic pressure gradients. *J Colloid Interf Sci*. (1980) 73:13–20. doi: 10.1016/0021-9797(80)90115-0
28. Hattrem MN, Dille MJ, Seternes T, Draget KI. Macro - vs. micromolecular stabilisation of W/O/W-emulsions. *Food Hydrocolloid*. (2014) 37:77–85. doi: 10.1016/j.foodhyd.2013.10.024
29. Serdaroglu M, Ozturk B, Urgu M. Emulsion characteristics, chemical and textural properties of meat systems produced with double emulsions as beef fat replacers. *Meat Sci*. (2016) 117:187–95. doi: 10.1016/j.meatsci.2016.03.012
30. Tamnak S, Mirhosseini H, Tan CP, Amid TB, Kazemi M, Hedayatnia S. Encapsulation properties, release behavior and physicochemical characteristics of water-in-oil-in-water (W/O/W) emulsion stabilized

with pectin-pea protein isolate conjugate and Tween 80. *Food Hydrocolloid*. (2016) 61:599–608. doi: 10.1016/j.foodhyd.2016.06.023
31. Eisinaite V, Estrada PD, Schroen K, Berton-Carabin C, Leskauskaite D. Tayloring W/O/W emulsion composition for effective encapsulation: the role of PGPR in water transfer-induced swelling. *Food Res Int*. (2018) 106:722–8. doi: 10.1016/j.foodres.2018.01.042
32. Cofrades S, Antoniou I, Solas MT, Herrero AM, Jimenez-Colmenero F. Preparation and impact of multiple (water-in-oil-in-water) emulsions in meat systems. *Food Chem*. (2013) 141:338–46. doi: 10.1016/j.foodchem.2013.02.097
33. Wen L, Papadopoulos KD. Effects of surfactants on water transport in W1/O/W2 emulsions. *Langmuir*. (2000) 16:7612–7. doi: 10.1021/la000071b
34. Corredig M, Alexander M. Food emulsions studied by DWS: recent advances. *Trends Food Sci Tech*. (2008) 19:67–75. doi: 10.1016/j.tifs.2007.07.014
35. Moschakis T. Microrheology and particle tracking in food gels and emulsions. *Curr Opin Colloid In*. (2013) 18:311–23. doi: 10.1016/j.cocis.2013.04.011
36. McClements DJ, Decker EA, Park Y, Weiss J. Structural design principles for delivery of bioactive components in nutraceuticals and functional foods. *Crit. Rev Food Sci*. (2009) 49:577–606. doi: 10.1080/10408390902841529
37. Laouini A, Jaafar-Maalej C, Sfar S, Charcosset C, Fessi H. Liposome preparation using a hollow fiber membrane contactor–application to spironolactone encapsulation. *Int J Pharmaceut*. (2011) 415:53–61. doi: 10.1016/j.ijpharm.2011.05.034
38. Panagopoulou E, Evageliou V, Kopsahelis N, Ladakis D, Koutinas A, Mandala I. Stability of double emulsions with PGPR, bacterial cellulose and whey protein isolate. *Colloid Surface A*. (2017) 522:445–52. doi: 10.1016/j.colsurfa.2017.03.020
39. Wang J, Tan Y, Xu H, Niu S, Yu J. Effect of 2, 2-azobis (2-amidinopropane) dihydrochloride oxidized casein on the microstructure and microrheology properties of emulsions. *Food Sci Biotechno*. (2016) 25:1283–90. doi: 10.1007/s10068-016-0202-8
40. Li X, Wang X, Liu J, Xu D, Cao Y, Sun B. The effect of unadsorbed proteins on the physiochemical properties of the heteroaggregates of oppositely charged lactoferrin coated lutein droplets and whey protein isolate coated DHA droplets. *Food Funct*. (2018) 9:3956–64. doi: 10.1039/C8FO00371H
41. Márquez AL, Wagner JR, Palazolo GG. Effects of calcium content and homogenization method on the microstructure, rheology, and stability of emulsions prepared with soybean flour dispersions. *Eur J Lipid Sci Tech*. (2018) 120:1700500. doi: 10.1002/ejlt.201700500
42. Chihi ML, Mession JL, Sok N, Saurel R. Heat-induced soluble protein aggregates from mixed pea globulins and beta-Lactoglobulin. *J Agr Food Chem*. (2016) 64:2780–91. doi: 10.1021/acs.jafc.6b00087
43. Roesch R, Corredig M. Heat-induced soy-whey proteins interactions: formation of soluble and insoluble protein complexes. *J Agr Food Chem*. (2005) 53:3476–82. doi: 10.1021/jf048870d
44. Xu D, Yuan F, Wang X, Li X, Hou Z, Cao Y. The effect of whey protein isolate-dextran conjugates on the freeze-thaw stability of oil-in-water emulsions. *J. Disper. Sci. Technol*. (2010) 32:77–83. doi: 10.1080/01932690903546785

Conflict of Interest: The authors declare that the research was conducted in the absence of any commercial or financial relationships that could be construed as a potential conflict of interest.

frontiers in Nutrition

ORIGINAL RESEARCH
published: 16 December 2020
doi: 10.3389/fnut.2020.587665

Effect of Kefir on Soybean Isoflavone Aglycone Content in Soymilk Kefir

*Minke Yang, Xiaojuan Yang, Xiaoqu Chen, Jie Wang, Zhenlin Liao, Li Wang, Qingping Zhong and Xiang Fang**

College of Food Science, South China Agricultural University, Guangzhou, China

Kefir is a traditional fermented milk originating in the Caucasus area and parts of Eastern Europe. In this study, the kefir culture, which is modified upon the addition of lactic acid bacteria (LAB) cells, specifically for soymilk kefir fermentation with the highest capacity of isoflavone biotransformation, was successfully produced, and the metagenomics composition of soymilk or milk fermented using these kefir cultures was investigated. The metagenome analysis showed that the microbiota of kefir in M-K (milk inoculated with kefir), SM-K (equal volumes of soymilk and milk inoculated with kefir), and S-K (pure milk inoculated with kefir) were related to the addition of soymilk or not. Furthermore, the HPLC chromatogram revealed that Guixia 2 (Guangzhou, China) may be a good source of soymilk kefir fermentation due to its high isoflavone aglycone content (90.23 ± 1.26 μg/g in daidzein, 68.20 ± 0.74 μg/g in genistein). Importantly, the starter culture created by adding 1.5 g probiotics (Biostime®, Guangzhou, China) to Chinese kefir showed a significant increase in the levels of isoflavone aglycones (72.07 ± 0.53 μg/g in isoflavone aglycones). These results provided insight into understanding the suitable soybean cultivar and starter cultures, which exhibit promising results of isoflavone biotransformation and flavor promotion during soymilk kefir fermentation.

Keywords: kefir, whole genome sequencing, soy bean cultivar, isoflavone aglycones, biotransformation, soymilk

OPEN ACCESS

Edited by:
Jinkai Zheng,
Chinese Academy of Agricultural Sciences (CAAS), China

Reviewed by:
Huaxi Yi,
Ocean University of China, China
Subrota Hati,
Anand Agricultural University, India
Sandra Garcia,
State University of Londrina, Brazil

****Correspondence:***
Xiang Fang
fxiang@scau.edu.cn

Specialty section:
This article was submitted to Food Chemistry, a section of the journal Frontiers in Nutrition

Received: *27 July 2020*
Accepted: *27 October 2020*
Published: *16 December 2020*

Citation:
Yang MK, Yang XJ, Chen XQ, Wang J, Liao ZL, Wang L, Zhong QP and Fang X (2020) Effect of Kefir on Soybean Isoflavone Aglycone Content in Soymilk Kefir. Front. Nutr. 7:587665. doi: 10.3389/fnut.2020.587665

INTRODUCTION

Kefir, a fermented dairy beverage, is characterized by an acidic, mildly alcoholic flavor and creamy consistency (1). It originated in the Caucasian region and became popular in Tibet and Mongolia (2). Traditionally, kefir grains play a natural starter culture role in the production of kefir (3). They are gelatinous, white-to-light-yellow clusters, with a small, irregular cauliflower-like shape (4). As a mixed microflora, these grains are composed of an inert polysaccharide/protein matrix containing different lactic acid bacteria (LAB), yeasts, and occasionally acetic acid bacteria (AAB) in a complex symbiotic association (5), which are responsible for lactic-alcoholic fermentation (6). In general, *Kluyveromyces, Saccharomyces, Lactobacillus, Lactococcus, Leuconostoc,* and *Acetobacter* are predominant species in starter grains (7). Historically, kefir has been considered a beneficial food, with probiotic microorganisms and functional organic substances. The consumption of this fermented beverage has been recognized for a variety of health properties, such as antibacterial, antifungal, anti-allergic, and anti-inflammatory properties (8). Furthermore, some of the bioactive compounds in the kefir, including polysaccharides (kefiran), peptides, amino acids, ethanol, CO_2, acetaldehyde, acetoin, diacetyl, folic acid, calcium, and vitamins (B_1, B_{12}, and K), may contribute to these health-promoting and antimicrobial effects (9–12).

Soybean and its derivatives, which have great potential for applications in the functional food industry, are considered rich in proteins, isoflavones, and oligosaccharides (13). However, the nutritional and phytochemical compounds of soybean may vary considerably depending on cultivar, which was significantly positively correlated with the quality of soymilk. For example, some cultivars show high contents of protein but are low in ash and total solids in seeds, which meet the quality requirements of soymilk processing. Others with removal of lipoxygenase-2 show flavor improvement (14, 15). Isoflavones, in particular, have recently received more attention due to their antioxidant and estrogenic effects. Isoflavones occurred in four different chemical structures: aglycones or the free forms (daidzein, genistein, and glycitein); 7-O-β-D-glucosides or β-glucosides (daidzin, genistin, and glycitin); 6″-O-acetyl-7-O-β-D-glucosides or acetyl glucosides (acetyl daidzin, acetyl genistin and acetyl glycitin); and 6″-O-malonyl-7-O-β-D-glucosides or malonyl glucosides (malonyl daidzin, malonyl genistin, and malonyl glycitin) (16). With the lower molecular weight, aglycone forms showed improved diffusion and absorption in the human gut, resulting in better absorption than conjugates (17). Importantly, the isoflavone content may vary because of narrow genetic diversity in wild soybean (18, 19). It is also reported that lower isoflavone concentrations are generally presented in early rather than late maturing soybean cultivars (20). In addition to the genetic factor, environmental factors also influence the isoflavone content and other components (21, 22). For instance, the malonylated isoflavone glycosides were thermally unstable and were easily converted into their corresponding isoflavone glycosides under high temperature (23).

Many studies have indicated that soymilk fermented with kefir may be beneficial to human health (24–26). After fermentation, the content of aglycone isoflavone and total phenolic in soymilk kefir multiplied *in vitro* digestive system simulation (16). The populations of probiotics in the intestinal ecosystem tended to be improved during the period of fermented soymilk intake (27). The soymilk fermented with kefir and a *Bifidobacterium longum* strain had a high rate of the desired volatile aroma compounds (acetoin, diacetyl) and a low rate of the undesired compounds (1-octen-3-ol, 2-penten-1-ol, (E)-2-heptenal, 1-hexanol) (28). However, the kefir studies showed a high number of LAB strains but a low number of species (29). Importantly, some species that are not represented or exist only in very low numbers exhibit strong probiotic activity (30, 31). This phenomenon constrains the healthy function of kefir and their byproducts. Most isoflavones exist as glycosylated forms and, to a lesser extent, as aglycones (32). β-Glucosidase, which is naturally present in soybean and considered to be the key enzyme during the hydrolysis of β-glucosides into aglycones, is produced by various microorganisms from kefir (17, 26).

The selection of suitable soybean cultivar and starter for soymilk kefir has been little investigated. In the current work, the effect of soybean cultivars on soymilk fermentation was determined by using the kefir preserved in our laboratory (Kefir C), followed by metagenomics analysis. Moreover, new kefir starters were produced by the addition of lactic acid bacteria (LAB) to kefir from three different sources, including Kefir C, Chinese kefir (Kefir A), and Caucasus kefir (Kefir B). Then, high-performance liquid chromatography (HPLC) was used to examine their effectiveness in increasing the biotransformation of isoflavone to determine the most suitable starter for soymilk kefir fermentation.

TABLE 1 | Description of the soybean materials.

Code	Cultivar name	Origin
1	Huaxia 6	Xintian, Hunan
2	Huaxia 3	Yingde, Guangdong
3	Huaxia 9	Yingde, Guangdong
4	Guixiadou 2	Yingde, Guangdong
5	Huaxia 10	Guangzhou, Guangdong
6	Huachun 2	Guangzhou, Guangdong
7	Huachun 5	Guangzhou, Guangdong
8	Huaxia 9	Guangzhou, Guangdong
9	Guixiadou 2	Guangzhou, Guangdong
10	Wayao	Guangzhou, Guangdong

MATERIALS AND METHODS

Soybean Materials

Ten different soybean cultivars, which were grown in Guangdong and Hunan, were selected for this research. The sample information is shown in **Table 1**.

Preparation of Kefir Starters

The three water kefirs used in this study are from different sources. Chinese kefir (Kefir A) and Caucasus kefir (Kefir B) were purchased from the Taobao website, and our laboratory provided the third (Kefir C). These kefirs were inoculated at the rate of 3.3% (V/V) in sterilized whole milk, which was composed of whole milk powder (Fonterra™, Auckland, New Zealand) with water (10 wt %/volume), and then incubated at 25°C for 24 h. After incubation, the product was filtrated through a sieve to remove the clotted milk and the grains were washed gently with sterile water. This activation step was repeated three times.

After the activation, three types of modified kefir were manufactured using activated kefir grains. Specifically, 5 mL of fermented milk (Bright Dairy & Food Co., Ltd., Shanghai, China), which contained mixed LAB strains of *Bifidobacterium lactis*, *Lactobacillus plantarum* ST-111, *L. bulgaricus,* and *Streptococcus thermophiles*, were added into activated kefir grains during the 10-days subculture (named Starter 1, sample S1-A, S1-B, and S1-C). Following incubation, 1/2 kefir grains were filtered through a sieve to remove the coagulated milk and then rinsed with sterile water. The remaining kefir liquid product (kefir sample 1) was freeze-dried on the 12th (sample A11, B11, C11) and 27th (sample A12, B12, C12) days of subculture, using the Freeze Drying Machine (CHRIST ALPHA, Guangxi, China). In another group, the isolated kefir grains were activated as described above with the addition of 1.5 g probiotics (Biostime®, Guangzhou, China), which contains *L. helveticus, B. bifidum, B. infantis* (named Starter 2, samples S2-A, S2-B, and S2-C), during the

10-days incubation. On day 12 (samples A21, B21, C21) and 27 (samples A22, B22, C22), the kefir filtrate was lyophilized into powder. The stock solution without addition as the control group and the sterilized whole milk were renewed daily.

Fermentation of Soymilk Kefir

The dry soybeans (1 kg) were blanched in hot water for 3 min and then soaked in 0.1% $NaHCO_3$ at room temperature for 12 h, with a bean-to-water ratio of 1:9 (w/w). The soybeans were then drained and ground with 6.5 times (w/w) distilled water using a high-speed blender (SUPOR, Zhejiang, China). The resulting slurry was filtered through a sieve to separate the soymilk from the residue.

Soymilk was sterilized in an ultra-high temperature sterilization de-fishing machine (RUIPAI, Shanghai, China) at sterilizing temperature (135–140°C), vacuum degree (0.01–0.025 mpa), and then concentrated in a three-effect evaporator (LiJie, Zhejiang, China) at the exit concentration (43–46%) and exit temperature (45°C). The drying process was performed in a lab-scale spray dryer (YaChen, Shanghai, China) under the following conditions: inlet-air temperature (170°C), outlet air temperature (93–94°C), and air pressure (10 mpa). The spray-dried soymilk powders were collected and packed in airtight bags and stored in the refrigerator until further analysis.

Kefirs C, S1, and S2 were filtered through a sieve aseptically, then inoculated at the rate of 3.3% (V/V) in sterilized whole milk (10 wt %/volume), and then incubated at 25°C for 24 h. Pure water at a temperature of 95°C was added to the soya bean flour (soya bean flour/water = 1:6.5; m/v), milk powder (milk powder/water = 1:10; m/v), and sugar (sugar/water = 1:10; m/v). Next, milk, pure soymilk, and a mixture of the two (1:1; V/V) were inoculated with Kefir C culture (1%, m/v, named samples M-K, SM-K, and S-K) for genomic sequencing after incubating at 25°C for 24 h. A starter consisting of a mixture of equal volumes of soymilk and milk was inoculated with 5% (m/v) kefir S1 and S2 culture and incubated at 25°C for 24 h. After fermentation, samples were stored at 4°C for 24 h. Fermentation was not performed in the soymilk control. The parameters mentioned above, such as inoculate percentage and fermentation temperature (unpublished work), were optimized in our previous studies, which reported that under these conditions there was a maximum conversion of β-glucoside to aglycone isoflavones, taking into account the low temperature and high altitude of the kefir birthplace, the Caucasus (17, 33).

Metagenomics Analysis

The metagenomics DNA was extracted and purified using a High Pure PCR Template Preparation Kit (Roche, Basel, Switzerland), according to the manufacturer's instructions. Specifically, 300 μL of M-K, SM-K, and S-K were centrifuged and treated with Iysozyme, chemical buffer, and proteinase K, followed by phenol/chloroform/isoproponal extraction as described previously (34). Sodium acetate/glacial acetic acid/ethanol was used to purify the 300 μL DNA eluates. The metagenomics DNA were obtained and sent to the Institute of Microbiology Epidemiology (Beijing, China) for sequencing.

Sensory Analysis

To determine the suitable starter for soymilk kefir, sensory evaluation was carried out by seven trained panelists who were familiar with soymilk fermentation sensory methodology. They were asked to score for color, smell, taste, and texture of the samples, which was based on the method reported previously (35). Before assessing the samples, ∼10 g of each soymilk kefir was loaded into plastic cups, tempered to 20°C, and coded with a random three-digit number. The evaluation was carried out under proper lighting. Panelists were given water to rinse their mouths between tests. All samples were scored from 0 (lowest) to 10 (highest) for sensory attributes.

Determination of the Contents of the Different Isoflavones in Soymilk Kefir

After soymilk kefir fermentation, samples were frozen at −40°C and subsequently lyophilized to powder. The extraction of isoflavones was prepared by weighing 0.5 g of sample and mixing with 5 mL of 80% HPLC-grade methanol in a 15-mL centrifuge tube. The mixture was allowed to stand in an ultrasonic bath for 3 h at 50°C (Kunshan Ultrasonic Instrument, Jiangsu, China), centrifuged at 12,000 *g* for 10 min at 4°C (USTC ZONKIA, Anhui, China). The resulting supernatant was passed through a 0.22-μm syringe filter (Jinteng, Tianjin, China) for HPLC analysis. Soymilk with the same preparation was used as a control. Each experiment was characterized by the mean in triplicate.

The isoflavones were separated and quantified in an HPLC system (Shimadzu, Tokyo, Japan), equipped with wavelength detector (PDA-100), and coated C18 column (250 nm × 4.6 nm, 5 μm). Then 10 μL isoflavones were eluted with a mobile phase consisting of 0.1% (v/v) formic acid in acetonitrile (solvent A) and 0.1% (v/v) formic acid in water (Solvent B), and at a flow rate of 1.000 mL/min at 34°C. Eluted isoflavones were detected by their absorbance at 260 nm. For the construction of calibration curves, the following standard isoflavones were used: acetyl- and malonyl-conjugated glucosides (Wako Pure Chemical Industries, Ltd., Osaka, Japan), β-glucosides, and aglycones (Sigma-Aldrich Co., St. Louis, MO, USA).

Statistical Analysis

Experimental results were recorded by means ± standard deviation (SD) of triplicate determinations. Statistical analysis was subjected to one-way ANOVA and *T*-test using SPSS 26.0 (SPSS Inc., Chicago, IL, USA) and Graphpad Prism 8.4.3 (Graphpad, San Diego, CA, USA).

RESULTS

Metagenomics Analysis of the Microbial Composition From M-K, SM-K, and S-K

The phylogenetic classification of bacterial sequences is summarized in **Figure 1**. The sequences were distributed among three bacterial phyla, Firmicutes, Proteobacteria, and Bacteroidetes. Notably, Firmicutes dominated in all samples, corresponding to 86.42 ± 0.007%, 89.21 ± 0.007%, 82.58 ± 0.013% in M-K, SM-K, and S-K, respectively. The

second dominated bacterial phylum was Proteobacteria, representing an average of 13.00 ± 0.009%, 9.64 ± 0.0009%, and 15.80 ± 0.016% of the population in M-K, SM-K, and S-K, respectively. The richness of Firmicutes and Proteobacteria was significantly different from three kinds of fermented beverages ($^*p < 0.05$). However, the difference in Bacteroidetes and others were not statistically significant ($p > 0.05$) among groups. It is worth noting that higher diversity in the bacterial phyla presented when soymilk was added in the fermentation matrix.

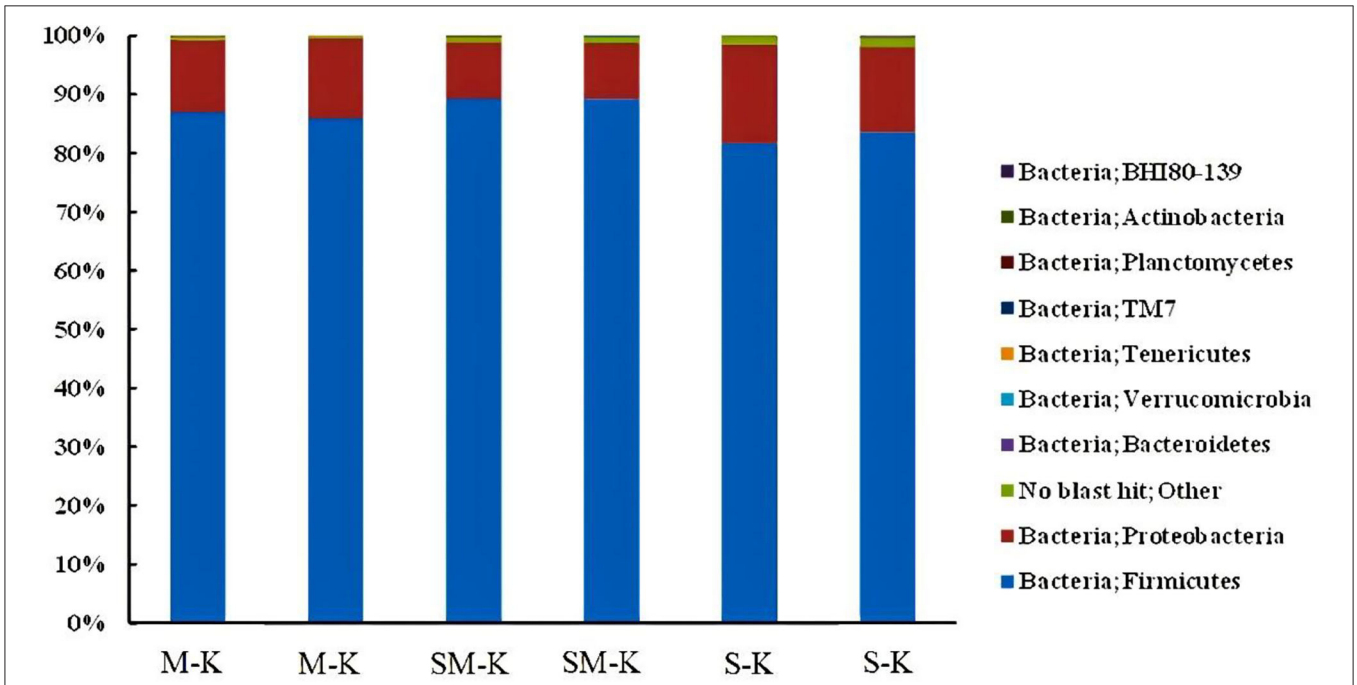

FIGURE 1 | Relative abundance (%) of metagenomes assigned to different phyla detected in M-K, SM-K, and S-K. M-K: Milk was inoculated with kefir; SM-K: equal volumes of soymilk and milk were inoculated with kefir; S-K: pure milk was inoculated with kefir.

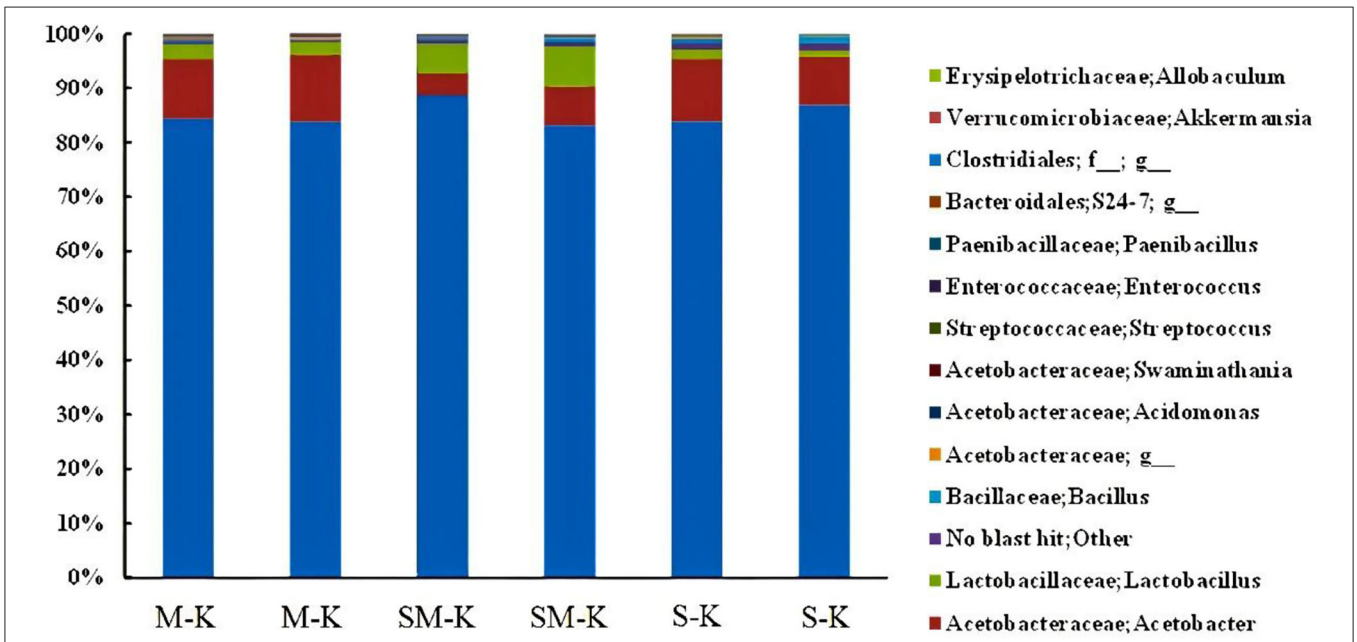

FIGURE 2 | Relative abundance (%) of metagenomes assigned to different genera detected in M-K, SM-K, and S-K. M-K: Milk was inoculated with kefir; SM-K: equal volumes of soymilk and milk were inoculated with kefir; S-K: pure milk was inoculated with kefir.

TABLE 2 | Sensory analysis of the soymilk kefir fermented with different kefir starters.

Sample	B	S1-A	S2-B	S2-A	S1-B	S1-C	A	C	S2-C
Score	54.30 ± 2.97[a]	53.57 ± 3.27[a]	52.87 ± 3.04[a]	52.27 ± 3.04[a]	52.03 ± 0.25[a]	51.77 ± 0.40[a]	50.33 ± 2.04[a]	50.50 ± 1.30[a]	49.43 ± 2.40[b]

*Mean ±standard deviation; n = 3. Different superscript letters indicate significant differences among cultivars (*p < 0.05). A: soymilk fermented with kefir A; B: soymilk fermented with kefir B; C: soymilk fermented with kefir C; S1-A: soymilk fermented with the addition of 5 mL fermented milk to kefir A; S2-A: soymilk fermented with the addition of 1.5 g probiotics to kefir A; S1-B: soymilk fermented with the addition of 5 mL fermented milk to kefir B; S2-B: soymilk fermented with the addition of 1.5 g probiotics to kefir B; S1-C: soymilk fermented with the addition of 5 mL fermented milk to kefir C. Different superscript letters (a and b) indicate significant differences in sensory score among different soymilk kefir (*p < 0.05).*

Moreover, our results showed that there were major and minor genera in every fermented beverage sample (**Figure 2**). Specifically, *Acetobacter* dominated (more than 85%), followed by *Lactobacillus* and *Streptoccus*. The richness of *Lactobacillus* varied dramatically in three fermented samples (2.50 ± 0.002% in M-K, 6.34 ± 0.015% in SM-K, 1.41 ± 0.005% in S-K). Similarly, higher diversity in the bacterial species presented when soymilk was added in the fermentation matrix.

Sensory Analysis of Soymilk Kefir

In the sensory evaluation, the five starters with the highest scores (sample Kefir B, S1-A, S2-B, S2-A, S1-B, and S1-C) were used as mixed starters for further soymilk kefir fermentation (**Table 2**). Interestingly, the soymilk kefir fermented using other starters always generated more bubbles and heavier acidity, which affected the appearance and taste of the product.

Changes in Isoflavone Contents in Soymilk Kefir With 10 Kinds of Soybean Cultivars

Table 3 shows the concentration of isoflavone aglycones in 10 soybean varieties. Importantly, we found dramatic variations in the isoflavone content in the 10 soybean cultivars. The levels of aglycone isoflavone daidzein content were 17.35–60.15 μg/g in soymilk from 10 cultivars and 23.79–91.03 μg/g in soymilk kefir. Furthermore, daidzein exhibited the highest average concentration, followed by genistein, while glycitein was not detected after fermentation. In particular, soymilk kefir from Guixia 2 (Guangzhou) and Wayao showed higher isoflavone content than soymilk kefir produced from other cultivars, with a threefold increase in aglycone isoflavone daidzein and genistein during fermentation. In contrast, the lowest levels were found in Huaxia 10 variety (23.79 μg/g) and in Huaxia 3 variety (29.21 μg/g) (**Figure 3**). Interestingly, the soymilk Guixia 2 cultivar from two locations, Yingde and Guagzhou, showed a significant difference in isoflavone content in soymilk kefir. Fermentation processes seemed to increase the concentration of free isoflavone, which might be attributed to the action of microbiota from kefir. Therefore, Guixia 2 (Guangzhou) and Wayao might be good resources for soymilk kefir fermentation because of a higher aglycone isoflavone content. The first one was selected for the next step of our research.

Changes in Aglycone Isoflavone Contents in Soymilk Kefir With Five Different Starters

Representative HPLC chromatograms of Guixia 2 soymilk (sample CK, from Guixia 2) are shown in **Figure 4**. Malonylglycitin was found to be the most predominant isoflavone. The remaining types showed different relative abundance in the following order: malonyldaidzin > glycitin > daidzin > genistein > acetylglycitin > genistin > malonylgenistin > daid-zein > glycitein > acetyldaidzin > acetylgenistin.

The isoflavone content of the conjugated daidzein and its free form are illustrated in **Figure 5a**. Notably, the abundance of malonyldaidzin and acetylglycitin in soymilk kefir decreased dramatically by fermentation, and the presence of daidzin in samples of S1-A, S1-C, and S2-A was not detected.

The concentration of the conjugated genistein was low in soymilk kefir. However, a significant increase in genistein was observed in the S1-C and S2-A samples (**Figure 5b**).

There was a significant decrease in malonylglycitin and acetylglycitin (**Figure 5c**) in all fermented samples compared to the control. However, the fermentation of soymilk showed no significant effect on the change in glycitin content except for the S1-C sample, which had a considerable reduction in the amount of glycitin. However, glycitein was not detected in soymilk kefir.

As shown in **Figure 5d** and **Table 3**, soymilk kefir showed a high concentration of isoflavone aglycone, whereas the total isoflavone had a small reduction under fermentation.

DISCUSSION

Our research indicated that Firmicutes, Proteobacteria, and Bacteroidates predominated in soymilk kefir, which was in agreement with some previous studies that confirmed the presence of the three major bacterial phyla. Firmicutes was the dominant phylum, making up 92% or more of the total sequences within the kefir milk ferment (36). Compared to the milk kefir, an increase in bacterial phyla diversity was shown in soymilk fermented with kefir. We can deduce that abundant nutrient ingredients in soymilk, such as fiber and protein, may facilitate the growth of certain microbiota in kefir. As in previous studies, soymilk kefir presented the highest *L. lactis* count value, perhaps because of its different types of protein and soy fiber in soy milk (37).

Good flavor is the most important and basic attribute of a food product. It determines the likelihood of product success in the market. In our study, the score increased from A starters to their modification samples S1-A and S2-A, suggesting that the addition of LAB in Kefir A may improve the aroma and taste of soymilk kefir. As stated above, the difference in flavor contribution during soymilk fermentation was observed in nine samples, which was influenced by their microbial composition before or after LAB modification. Thus, it appears that not all kefir samples were suitable for soymilk fermentation for flavor characteristics.

TABLE 3 | Changes in isoflavone contents in guixia 2 (guangzhou) soymilk kefir fermented with six different kefir starters.

Isoflavone	Contents of isoflavones (μg/g) in soymilk kefir fermented with six kinds of kefir starters						
	CK	S1-C	B	S1-B	S2-B	S1-A	S2-A
Total daidzein conjugates	117.18 ± 2.11^{a}	59.76 ± 2.94^{e}	101.48 ± 5.58^{b}	93.61 ± 3.44^{c}	98.66 ± 4.08^{b}	84.28 ± 2.38^{d}	80.36 ± 4.61^{e}
Total genistein conjugates	27.61 ± 1.24^{a}	23.25 ± 0.52^{bc}	23.83 ± 0.95^{b}	23.79 ± 0.76^{b}	22.70 ± 0.93^{bc}	21.95 ± 1.26^{c}	21.22 ± 0.89^{c}
Total glycitein conjugates	362.43 ± 18.07^{a}	326.64 ± 6.81^{b}	349.94 ± 15.31^{ab}	362.17 ± 15.79^{a}	348.48 ± 5.65^{ab}	340.53 ± 13.96^{ab}	333.30 ± 8.24^{b}
Total conjugated isoflavone	507.22 ± 20.63^{ab}	409.64 ± 9.85^{c}	475.25 ± 21.79^{b}	479.57 ± 19.89^{ab}	469.83 ± 10.54^{ab}	446.76 ± 17.51^{b}	434.88 ± 13.62^{b}
Total individual isoflavone	45.87 ± 3.52^{e}	68.30 ± 1.96^{b}	54.32 ± 3.14^{d}	60.32 ± 1.70^{c}	61.55 ± 1.52^{c}	63.45 ± 0.57^{c}	72.07 ± 0.53^{a}

*Mean ± standard deviation; n = 3. Means in the same row with different letters are significantly different (*p < 0.05). CK: Soymilk. B: Soymilk fermented with kefir B. S1-A: Soymilk fermented with the addition of 5 mL fermented milk to kefir A. S2-A: Soymilk fermented with the addition of 1.5 g probiotics to kefir A. S1-B: Soymilk fermented with the addition of 5 mL fermented milk to kefir B. S2-B: Soymilk fermented with the addition of 1.5 g probiotics to kefir B. S1-C: Soymilk fermented with the addition of 5 mL fermented milk to kefir C. Different superscript letters (a, b, c, d, and e) indicate significant differences in isoflavone concentration among different soybean cultivars (*p < 0.05).*

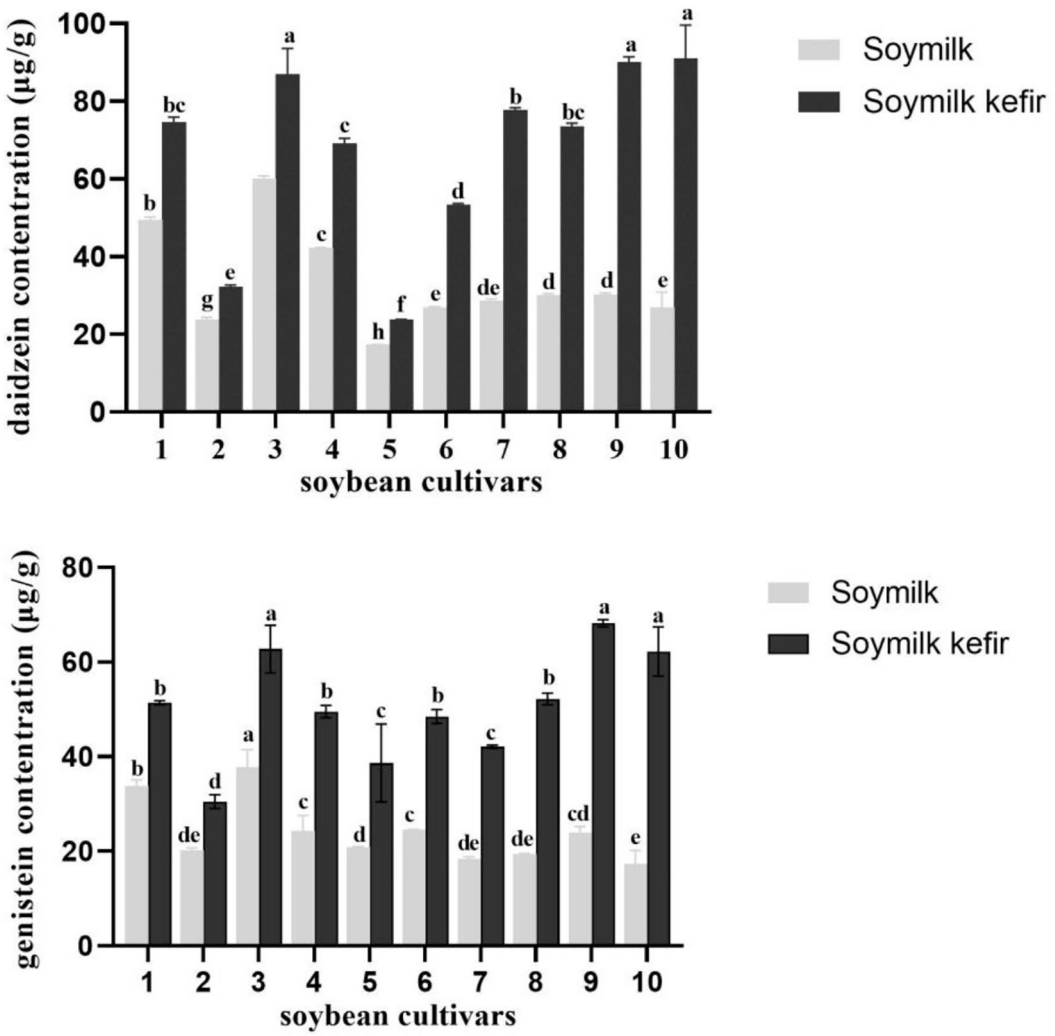

FIGURE 3 | The concentration of daidzein and genistein in soymilk kefir made from 10 soybean cultivars and kefir C. Different superscript letters indicate significant differences among cultivars (*$p < 0.05$). (1) Huaxia 6 Soybean, (2) Huaxia 3 Soybean, (3) Huaxia 9 Soybean, (4) Guixiadou 2 Soybean (Yingde, Guangdong), (5) Huaxia 10 Soybean, (6) Huachun 2 Soybean, (7) Huachun 5 Soybean, Huaxia 9 Soybean, (9) Guixiadou 2 Soybean (Guangzhou, Guangdong), (10) Wayao Soybean.

The aglycone isoflavone content of soymilk kefir varied among different soybean cultivars (**Figure 3**). In particular, the difference in aglycone isoflavone concentration in soymilk kefir was related to its original concentration in the soymilk from the 10 soybean cultivars. This is consistent with other studies, which showed that the content of aglycone isoflavone in other soymilk products,

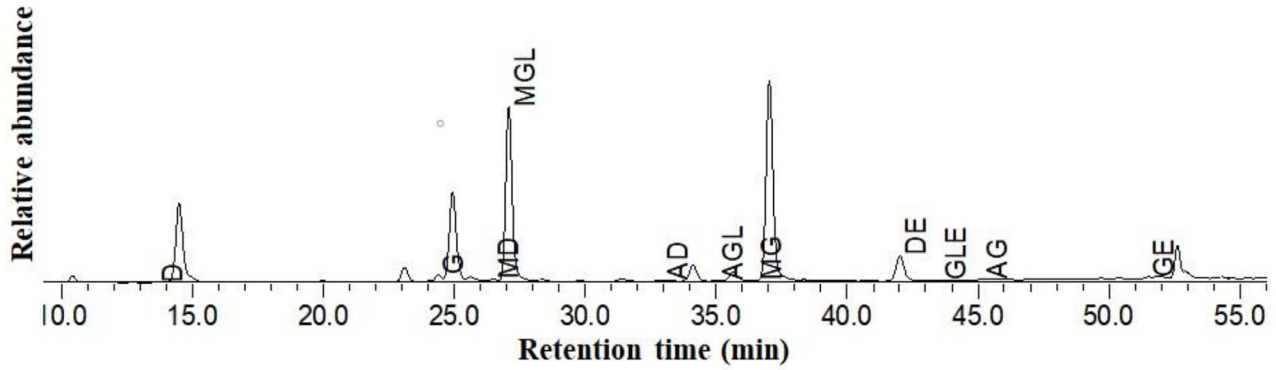

FIGURE 4 | HPLC chromatogram of isoflavones from Guixia 2 (Guangzhou) soy milk. D, Daidzin; GL, Glycitin; G, Genistin; MD, Malonyldaidzin; MGL, Malonylglycitin; AD, Acetyldaidzin; AGL, Acetylglycitin; MG, Malonylgenistin; DE, Daidzein; GLE, Glycitein; AG, Acetylgenistin; GE, Genistein.

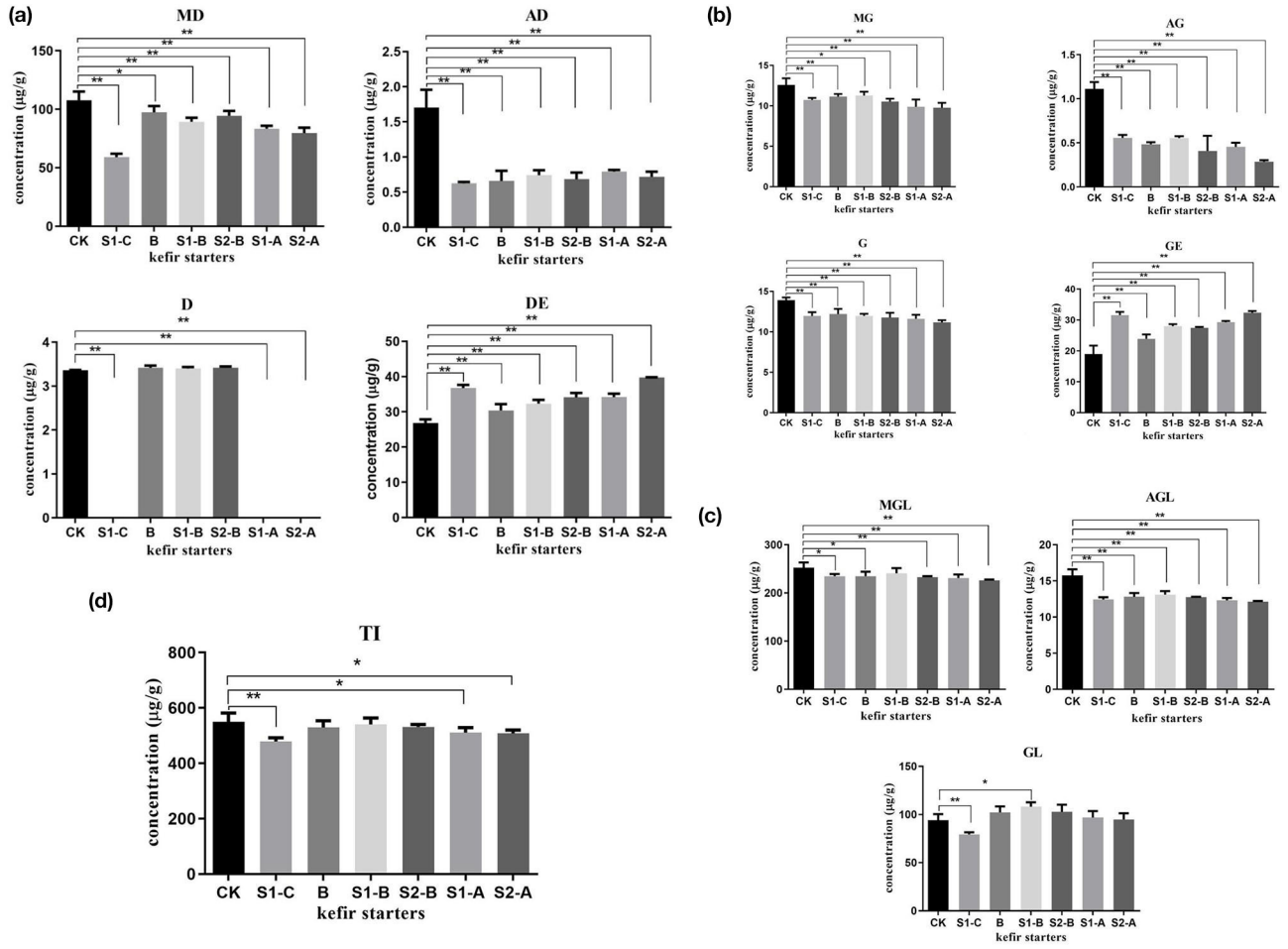

FIGURE 5 | The amounts of glycosides, genistein, glycitein and its conjugates **(a–c)**, and the total isoflavone **(d)** in Guixia 2 soymilk fermented with six different kefir starters. Data are the mean ± SD of three separate experiments performed in triplicate. One asterisk indicates a significant difference ($*p < 0.05$), and two asterisks indicate an extremely significant difference ($**p < 0.01$), with respect to Guixia 2 soymilk (the control group). TI, total isoflavone. **(A)** Soymilk fermented with kefir A. **(B)** Soymilk fermented with kefir B. **(C)** Soymilk fermented with kefir C. S1-A: Soymilk fermented with the addition of 5 mL fermented milk to kefir A. S2-A: Soymilk fermented with the addition of 1.5 g probiotics to kefir A. S1-B: Soymilk fermented with addition of 5 mL fermented milk to kefir B. S2-B: Soymilk fermented with addition of 1.5 g probiotics to kefir B. S1-C: Soymilk fermented with addition of 5 mL fermented milk to kefir C.

such as tofu, was also correlated with the soybean cultivar itself (38, 39). The proportions of the total concentrations of aglycone isoflavones varied among cultivars, especially in the malonyl-glucoside group (20), and strong correlations were observed between aglycone isoflavone content in soymilk and soybean cultivars (15). Recently, molecular genetic approaches based on QTL mapping have been conducted to promote the understanding of genome-based isoflavone content (40, 41).

During fermentation, the isoflavone (daidzin) concentrations from different samples varied, depending on the species of starter. Before fermentation, conjugated isoflavones were present in high quantities in the soymilk. After 24 h fermentation, the daidzein and genistein contents were increased more by microorganisms in Kefir A modified with probiotics than others. It was observed that, in this fermentation, β-glucosides and malonyl- and acetyl-conjugated glucoside content were reduced, likely due to the catalysis of β-glucosidase produced by this culture and degraded into aglycones. Daidzin decreased rapidly in soymilk fermented with modified Kefirs A and C but was limited in Kefir B and its modified culture fermentation. This may be due to the conversion of daidzin to daidzein by β-glucosidase produced by the microorganism from the original Kefirs A and C. In addition, the microorganism that originally exists in kefir grains, which is preferentially metabolized daidzin but in very low concentrations (accounting for <1%), proliferates rapidly and shows dominance after the LAB addition. Furthermore, glycitein was not detected in soymilk kefir, indicating that it might be vulnerable to the degradation of microorganisms in large number or it has been converted to isoflavone derivatives other than glycitein. This is consistent with the findings of Lim (42) that glycitein was the most degraded of the aglycones. Moreover, the conjugated isoflavone might convert not only to corresponding aglycones but also to other substances during fermentation, which was evidenced by the decreased total isoflavone contents. These phenomena may be explained as follows. Daidzein can be converted to equol by enzymes of bacteria (43), which is difficult to detect and quantify (44).

Our results also demonstrated that the kefir ecosystem remained quite stable with the addition of exogenous LAB, and the proliferation of these microorganisms may contribute to the particular sensory characteristics of the soymilk kefir (fizziness, acidic taste, and refreshing flavor) via the production of metabolites such as organic acids, ethanol, and aromatic compounds.

In this study, the significant bioconversion of the glucoside isoflavones into their corresponding aglycones during soymilk kefir fermentation was due to cleavage of the glycosyl bond by microbial fermentation. The discrepancy of β-glucosidase production was attributed to the differences in bacterial strains. *Lactobacillus* and *Lactococcus* from kefir may play an important role in the soymilk kefir fermentation. The greatest increase in isoflavone aglycone concentration was observed in soymilk fermented with *Lb. acidophilus* 4461, which detected the highest β-glucosidase activity at 24 h (45, 46). Choi et al. (47) reported that *Lb. delbrueckii* subsp. *delbrueckii* KCTC 1047 hydrolyzed genistin and daidzin completely in soymilk. The content of aglycone isoflavones also increased impressively in the soymilk fermented with *S. thermophiles* (48, 49). Meanwhile, isoflavone glucoside-hydrolyzing enzyme depended not only on the bacterial strain but also on the culture medium, with some lactic acid bacteria produced only in soymilk medium (47). There was no probiotic organism efficient at performing the biotransformation of all three biologically active aglycone isomers. Specifically, glycitein was the highest in soymilk inoculated with *L. paracasei*, and genistein was the highest in soymilk fermented by *L. plantarum* (50). It corresponded to our premise that the combination or facilitation of more bacteria in kefir enhanced the function of soymilk kefir.

This work is the first to consider the selection of suitable soybean cultivar and kefir starter simultaneously during the soymilk kefir fermentation. In the current study, (1) the suitable soybean cultivar was determined based on the higher levels of aglycone isoflavones in its soymilk kefir, and (2) a whole new microbial composition in kefir culture was built by the addition of exogenous LAB. The rebuilt kefir culture showed stronger ability to hydrolyze β-, malonyl-, and acetyl-conjugated glucoside than the original one, which can be reflected in the higher aglycone isoflavone concentration in soymilk kefir. Therefore, it was suitable for soymilk kefir fermentation.

In the near future it can be proposed that the suitable starter culture and soybean cultivar of soymilk kefir can be defined due to their enhancement of aglycone isoflavone contents and pleasant flavor during fermentation. Such a soymilk kefir starter can be used as a functional fermented drink, as well as an auxiliary food for menopausal women during a specific pathological period.

DATA AVAILABILITY STATEMENT

The datasets generated for this study can be found in European Nucleotide Archive, Accession No. PRJEB40909.

AUTHOR CONTRIBUTIONS

XF conceived the study conception. MY and XC performed the experiment. MY drafted the manuscript and the analysis and interpretation of data. JW, ZL, LW, and QZ revised the initial manuscript critically. All authors contributed to manuscript revision and read and approved the submitted version.

FUNDING

This study was supported by the National Natural Science Foundation of China (31671855), Key-Area Research and Development Program of Guangdong Province (2018B020205002), and the special Applied Technology Research Program of Guangdong Province (2015B020230010).

REFERENCES

1. Mitra S, Ghosh BC. Quality characteristics of kefir as a carrier for probiotic *Lactobacillus rhamnosus GG*. *Int J Dairy Technol.* (2019) 73:384–91. doi: 10.1111/1471-0307.12664
2. Kuo C, Lin C. Taiwanese kefir grains-their growth, microbial and chemical composition of fermented milk. *Aust J Dairy Technol.* (1999) 54:19.
3. de Oliveira Leite AM, Miguel MA, Peixoto RS, Rosado AS, Silva JT, Paschoalin VM. Microbiological, technological and therapeutic properties of kefir: a natural probiotic beverage. *Braz J Microbiol.* (2013) 44:341–9. doi: 10.1590/S1517-83822013000200001
4. Kabak B, Dobson AD. An introduction to the traditional fermented foods and beverages of Turkey. *Crit Rev Food Sci.* (2011) 51:248–60. doi: 10.1080/10408390903569640
5. Leite AM, Mayo B, Rachid CT, Peixoto RS, Silva JT, Paschoalin VM, et al. Assessment of the microbial diversity of Brazilian kefir grains by PCR-DGGE and pyrosequencing analysis. *Food Microbiol.* (2012) 31:215–21. doi: 10.1016/j.fm.2012.03.011
6. Bolla PA, Serradell Mde L, de Urraza PJ, de Antoni GL. Effect of freeze-drying on viability and in vitro probiotic properties of a mixture of lactic acid bacteria and yeasts isolated from kefir. *J Dairy Res.* (2011) 78:15–22. doi: 10.1017/S0022029910000610
7. Prado MR, Blandón LM, vandenberghe LP, Rodrigues C, Castro GR, Thomaz-Soccol V, et al. Milk kefir: composition, microbial cultures, biological activities, and related products. *Front Microbiol.* (2015) 6:1177. doi: 10.3389/fmicb.2015.01177
8. Sharifi M, Moridnia A, Mortazavi D, Salehi M, Bagheri M, Sheikhi A. Kefir: a powerful probiotics with anticancer properties. *Med Oncol.* (2017) 34:183. doi: 10.1007/s12032-017-1044-9
9. Garofalo C, Osimani A, Milanovic V, Aquilanti L, de Filippis F, Stellato G, et al. Bacteria and yeast microbiota in milk kefir grains from different Italian regions. *Food Microbiol.* (2015) 49:123-33. doi: 10.1016/j.fm.2015.01.017
10. de Oliveira AP, Santos GAD, Nomura CS, Naozuka J. Elemental chemical composition of products derived from kefir fermented milk. *J Food Compos Anal.* (2019) 78:86–90. doi: 10.1016/j.jfca.2019.02.005
11. Medrano M, Hamet MF, Abraham AG, Pérez PF. Kefiran protects Caco-2 cells from cytopathic effects induced by *Bacillus cereus* infection. *Antonie van Leeuwenhoek.* (2009) 96:505–13. doi: 10.1007/s10482-009-9366-z
12. Coşansu S. Survival kinetics of heat-stressed *Escherichia coli* O157:H7 and *Listeria monocytogenes* cells as post-fermentation contaminants in kefir during refrigerated storage. *Food Sci Tech.* (2018) 98:635–41. doi: 10.1016/j.lwt.2018.08.057
13. Baú TR, Garcia S, Ida EI. Evaluation of a functional soy product with addition of soy fiber and fermented with probiotic kefir culture. *Braz Arch Biol Technol.* (2014) 57:402–9. doi: 10.1590/S1516-89132014005000005
14. Jin X, Chen C, Guo S, Zhang H. Analysis on physicochemical and sensory qualities of soymilk prepared by various cultivars: application of fuzzy logic technique. *J Food Sci.* (2020) 85:1635–41. doi: 10.1111/1750-3841.15147
15. Šertovic E, Mujic I, Jokic S, Alibabic V. Effect of soybean cultivars on the content of isoflavones in soymilk. *Rom Biotechnol Lett.* (2012) 17:7151–9.
16. da Silva Fernandes M, Sanches Lima F, Rodrigues D, Handa C, Guelfi M, Garcia S, et al. Evaluation of the isoflavone and total phenolic contents of kefir-fermented soymilk storage and after the in vitro digestive system simulation. *Food Chem.* (2017) 229:373–80. doi: 10.1016/j.foodchem.2017.02.095
17. Baú TR, Garcia S, Ida EI. Changes in soymilk during fermentation with kefir culture: oligosaccharides hydrolysis and isoflavone aglycone production. *Int J Food Sci Nutr.* (2015) 66:845–50. doi: 10.3109/09637486.2015.1095861
18. Pei RL, Zhang JY, Tian L, Zhang SR, Han FX, Yan SR, et al. Identification of novel QTL associated with soybean isoflavone content. *Corp J.* (2018) 6:244–52. doi: 10.1016/j.cj.2017.10.004
19. Bi Y, Li W, Xiao J, Lin H, Liu M, Liu M, et al. Heterosis and combining ability estimates in isoflavone content using different parental soybean accessions: wild soybean, a valuable germplasm for soybean breeding. *PLoS ONE.* (2015) 10:e0114827. doi: 10.1371/journal.pone.0114827
20. Zhang J, Ge Y, Han F, Li B, Yan S, Sun J, et al. Isoflavone content of soybean cultivars from maturity group 0 to VI grown in northern and southern China. *J Am Oil Chem Soc.* (2014) 91:1019–28. doi: 10.1007/s11746-014-2440-3
21. Rasolohery CA, Berger M, Lygin AV, Lozovaya VV, Nelson RL, Daydé J. Effect of temperature and water availability during late maturation of the soybean seed on germ and cotyledon isoflavone content and composition. *J Sci Food Agr.* (2008) 88:218–28. doi: 10.1002/jsfa.3075
22. Carter A, Rajcan I, Woodrow L, Navabi A, Eskandari M. Genotype, environment, and genotype by environment interaction for seed isoflavone concentration in soybean grown in soybean cyst nematode infested and non-infested environments. *Field Crop Res.* (2018) 216:189–96. doi: 10.1016/j.fcr.2017.11.021
23. Kudou S, Fleury Y, Welti D, Magnolato D, Uchida T, kitamura K, et al. Malonyl isoflavone glycosides in soybean seeds (*Glycine max Merrill*). *Agric Biol Chem.* (1991) 55:2227–33. doi: 10.1080/00021369.1991.10870966
24. Liu JR, Chen MJ, Lin CW. Antimutagenic and antioxidant properties of milk-kefir and soymilk-kefir. *J Agr Food Chem.* (2005) 53:2467–74. doi: 10.1021/jf048934k
25. Liu J, Wang S, Chen M, Yueh P, Lin C. The anti-allergenic properties of milk kefir and soymilk kefir and their beneficial effects on the intestinal microflora. *J Sci Food Agr.* (2006) 86:2527–33. doi: 10.1002/jsfa.2649
26. McCue PP, Shetty K. Phenolic antioxidant mobilization during yogurt production from soymilk using Kefir cultures. *Process Biochem.* (2005) 40:1791–7. doi: 10.1016/j.procbio.2004.06.067
27. Cheng IC, Shang HF, Lin TF, Wang TH, Lin HS, Lin SH. Effect of fermented soy milk on the intestinal bacterial ecosystem. *World J Gastroenterol.* (2005) 11:1225–7. doi: 10.3748/wjg.v11.i8.1225
28. Karaçali R, ÖzdemIr N, Çon AH. Aromatic and functional aspects of kefir produced using soya milk and *Bifidobacterium* species. *Int J Dairy Technol.* (2018) 71:921–33. doi: 10.1111/1471-0307.12537
29. Mainville I, Robert N, Lee B, Farnworth ER. Polyphasic characterization of the lactic acid bacteria in kefir. *Syst Appl Microbiol.* (2006) 29:59–68. doi: 10.1016/j.syapm.2005.07.001
30. Cetinkaya F, Mus TE. Determination of microbiological and chemical characteristics of kefir consumed in Bursa. *Ankara Üniv Vet Fak Derg.* (2012) 59:217–21. doi: 10.1501/Vetfak_0000002528
31. Gao J, Gu F, Abdella NH, Ruan H, He G. Investigation on culturable microflora in Tibetan kefir grains from different areas of China. *J Food Sci.* (2012) 77:M425–33. doi: 10.1111/j.1750-3841.2012.02805.x
32. Hati S, Vij S, Singh BP, Mandal S. β-Glucosidase activity and bioconversion of isoflavones during fermentation of soymilk. *J Sci Food Agr.* (2015) 95:216–20. doi: 10.1002/jsfa.6743
33. Baú TR, Ida EI. Soymilk processing with higher isoflavone aglycone content. *Food Chem.* (2015) 183:161–8. doi: 10.1016/j.foodchem.2015.03.026
34. Vermote L, Verce M, de Vuyst L, Weckx S. Amplicon and shotgun metagenomics sequencing indicates that microbial ecosystems present in cheese brines reflect environmental inoculation during the cheese production process. *Int Dairy J.* (2018) 87:44–53. doi: 10.1016/j.idairyj.2018.07.010
35. Duru KC, Kovaleva E, Danilova I, Belousova A. Production and assessment of novel probiotic fermented oat flour enriched with isoflavones. *LWT Food Sci Technol.* (2019) 111:9–15. doi: 10.1016/j.lwt.2019.04.102
36. Dobson A, Sullivan O, Cotter PD, Ross P, Hill C. High-through put sequence-based analysis of the bacterial composition of kefir and an associated kefir grain. *FEMS Microbiol Lett.* (2011) 320:56–62. doi: 10.1111/j.1574-6968.2011.02290.x
37. Baú T R, Garcia S, Ida E I. Optimization of a fermented soy product formulation with a kefir culture and fiber using a simplex-centroid mixture design. *Int J Food Sci Nutr.* (2013) 64:929–35. doi: 10.3109/09637486.2013.816935
38. Palermo M, Paradiso R, de Pascale S, Fogliano V. Hydroponic cultivation improves the nutritional quality of soybean and its products. *J Agr Food Chem.* (2012) 60:250–5. doi: 10.1021/jf203275m
39. Meng S, Chang S, Gillen AM, Zhang Y. Protein and quality analyses of accessions from the USDA soybean germplasm collection. *Food Chem.* (2016) 213:31–9. doi: 10.1016/j.foodchem.2016.06.046
40. Watanabe S, Yamada R, Kanetake H, Kaga A, Anai T. Identification and characterization of a major QTL underlying soybean isoflavone malonylglycitin content. *Breeding Sci.* (2019) 69:564–72. doi: 10.1270/jsbbs.19027
41. Wang Y, Han Y, Zhao X, Li Y, Teng W, Li D, et al. Mapping isoflavone QTL with main, epistatic and QTL × environment

effects in recombinant inbred lines of soybean. *PLoS ONE.* (2015) 10:e0118447. doi: 10.1371/journal.pone.0118447
42. Lim YJ, Lim B, Kim HY, Kwon SJ, Eom SH. Deglycosylation patterns of isoflavones in soybean extracts inoculated with two enzymatically different strains of *lactobacillus* species. *Enzyme Microb Tech.* (2020) 132:109394. doi: 10.1016/j.enzmictec.2019.109394
43. Gaya P, Peirotén Á, Medina M, Landete JM. Isoflavone metabolism by a collection of lactic acid bacteria and bifidobacteria with biotechnological interest. *Int J Food Sci Nutr.* (2016) 67:117–124. doi: 10.3109/09637486.2016.1144724
44. Franke AA, Custer LJ, Wang W, Shi CY. HPLC analysis of isoflavonoids and other phenolic agents from foods and from human fluids. *Pro Soc Exp Biol Med.* (1998) 217:263–73. doi: 10.3181/00379727-217-44231
45. Donkor ON, Shah NP. Production of β-glucosidase and hydrolysis of isoflavone phytoestrogens by *Lactobacillus acidophilus*, *Bifidobacterium lactis*, and *Lactobacillus casei* in soymilk. *J Food Sci.* (2008) 1:M15–20. doi: 10.1111/j.1750-3841.2007.00547.x
46. Otieno DO, Ashton JF, Shah NP. Evaluation of enzymic potential for biotransformation of isoflavone phytoestrogen in soymilk by *Bifidobacterium animalis*, *Lactobacillus acidophilus* and *Lactobacillus casei*. *Food Res Intl.* (2006) 39:394–407. doi: 10.1016/j.foodres.2005.08.010
47. Choi YB, Kim KS, Rhee JS. Hydrolysis of soybean isoflavone glucosides by lactic acid bacteria. *Biotechnol Lett.* (2002) 24:2113–6. doi: 10.1023/A:1021390120400
48. Chien HL, Huang HY, Chou CC. Transformation of isoflavone phytoestrogens during the fermentation of soymilk with lactic acid bacteria and bifidobacteria. *Food Microbiol.* (2006) 23:772–8. doi: 10.1016/j.fm.2006.01.002
49. Lee M, Hong GE, Zhang HP, Yang CY, Han KH, et al. Production of the isoflavone aglycone and antioxidant activities in black soymilk using fermentation with *Streptococcus thermophilus* S10. *Food Sci Biotechnol.* (2015) 24:537–44. doi: 10.1007/s10068-015-0070-7
50. Ding WK, Shah NP. Enhancing the biotransformation of isoflavones in soymilk supplemented with lactose using probiotic bacteria during extended fermentation. *J Food Sci.* (2010) 75:M140–9. doi: 10.1111/j.1750-3841.2010.01526.x

Conflict of Interest: The authors declare that the research was conducted in the absence of any commercial or financial relationships that could be construed as a potential conflict of interest.

frontiers in Nutrition

ORIGINAL RESEARCH
published: 24 March 2021
doi: 10.3389/fnut.2021.647537

Flavor Characteristics of Ganpu Tea Formed During the Sun-Drying Processing and Its Antidepressant-Like Effects

Sui Xiao[1†], Jingyuan Huang[2†], Yahui Huang[3], Huiqing Lai[4], Yi Zheng[4], Dahua Liang[4], Hang Xiao[2‡] and Xu Zhang[1*‡]*

[1] Guangdong Key Laboratory for Innovative Development and Utilization of Forest Plant Germplasm, College of Forestry and Landscape Architecture, South China Agricultural University, Guangzhou, China, [2] Department of Food Science, University of Massachusetts, Amherst, MA, United States, [3] Department of Tea Science, College of Horticulture, South China Agricultural University, Guangzhou, China, [4] Yunding Ganpu Tea Industry Co., LTD, Guangzhou, China

Ganpu tea is a novel type of tea beverage with unique and pleasant flavor that encases Pu-erh tea leaves within an intact mandarin peel. However, to date, no holistic and detail studies on its chemical composition and biological activities have been reported yet. In the present study, by applying UPLC-Q-TOF and UPLC-MS technology, we systematically identified and analyzed 104 water-soluble compounds of Ganpu tea and their variation trend during the sun-drying processing. The results showed that the generation of pigments and gallic acid coincided with a dramatic decrease in catechin content, and a significant increase in alkaloid and flavonoid contents. The conversion of these compounds can contribute to the improvement of sensory attributes of Ganpu tea and maybe indispensable to its unique flavor. Moreover, the mice given orally with high dose of Ganpu tea (0.4 g/kg) showed a significantly reduced immobility duration as compared to that of the negative control group ($p < 0.01$) both in the forced swimming test and tail suspension test. Together, these results indicate that the sun-drying processing was indispensable to the formation of the unique flavor for Ganpu tea. Multiple types of compounds of Ganpu tea may collectively provide the synergistic attributes to its antidepressant-like properties.

Keywords: Ganpu tea, flavor, sun-drying processing, antidepressant-like properties, health functions

OPEN ACCESS

Edited by:
Fernando M. Nunes, University of Trás-os-Montes and Alto Douro, Portugal

Reviewed by:
Chi-Tang Ho, Rutgers, The State University of New Jersey, United States
Chuanyi Peng, Anhui Agricultural University, China

***Correspondence:**
Hang Xiao
hangxiao@foodsci.umass.edu
Xu Zhang
zhangxu919@hotmail.com

†These authors have contributed equally to this work and share first authorship

‡These authors share senior authorship

Specialty section:
This article was submitted to Food Chemistry, a section of the journal Frontiers in Nutrition

Received: *30 December 2020*
Accepted: *01 March 2021*
Published: *24 March 2021*

Citation:
Xiao S, Huang J, Huang Y, Lai H, Zheng Y, Liang D, Xiao H and Zhang X (2021) Flavor Characteristics of Ganpu Tea Formed During the Sun-Drying Processing and Its Antidepressant-Like Effects. Front. Nutr. 8:647537. doi: 10.3389/fnut.2021.647537

INTRODUCTION

Ganpu tea is a novel type of tea beverage and has gained considerable popularity in China since 2015 due to its potential health-promoting effects and unique flavor. The production value of Ganpu tea in 2016 was ∼1.6 billion RMB, almost a 3-fold increase as compared to that in 2015 (1). Due to the rapidly increasing consumption of Ganpu tea, over 2,000 new Ganpu tea enterprises have been registered in Xinhui city, Guangdong in 2017. The consumption of a combination of tea leaves and citrus peel as brewed tea can be dated back to the eighth century in Tang dynasty. It is also well-known that mandarin peel can be used as an ingredient in traditional Chinese medicine as well as functional foods (2, 3). Nowadays, the contemporary Ganpu tea product is made with both Pu-erh

tea and mandarin peel. The processing of Ganpu tea involves (a) the removal of pulp from the fruit peel while keeping the peel intact; (b) cleaning the peel and filling it with Pu-erh tea; and (c) finally sun-drying and packaging.

Pu-erh tea can be divided into Pu-erh raw tea and Pu-erh ripen tea, depending on the processing techniques and quality characteristics. For the production of Pu-erh ripen tea, the sun-dried green tea is generally used as a substrate for microbial fermentation under the high temperature and humidity conditions (4). Due to pretense of a large number of active microorganisms in this processing, such as *Aspergillus niger, Penicllium, Rhizopus,* and *Aspergillus gloucus* (5), production of Pu-erh ripen tea will face considerable risk to food safety if it is used as the ingredient for Ganpu tea. Conversely, Pu-erh raw tea is made directly from the sun-dried green tea and does not include a microbial fermentation step, and therefore, the chemical constituents and quality are more similar to those of the sun-dried green tea than to those of Pu-erh ripen tea (6). In the present study, Pu-erh raw tea was used as the ingredient for production of Ganpu tea, due to not only its relatively high food safety, but also its flavor profile being relatively well-matched with those of mandarin peel. The mandarin peel is a popular product with strong geographical indication, as the most authentic production areas are confined to the specific regions in Xinhui, Guangdong, China. Citrus peels are rich in various functional components and enzymes, which catalyze the conversion of major chemical compounds during the sun-drying processing, and provide a fruity flavor to Ganpu tea.

To date, numerous methods including hot-air drying, freeze drying, vacuum drying, and infrared drying, have been applied to dry agricultural products (7–9). Hot-air drying is the method most commonly used to dry Ganpu tea. This method has the advantages of higher efficiency, lower cost, and easier control over the external odor infiltration. However, the quality of Ganpu tea dried with this technique is questionable because the hot-air drying can impact the thermosensitive substances in the mandarin peel, causing them to crack over time. In contrast, the sun-drying method has a more suitable temperature and humidity for aging, with ample time for development and improvement of the potential flavor compounds in Ganpu tea.

In the present study, we processed Ganpu tea from both Pu-erh raw tea and mandarin peel using the sun-drying technique. Pu-erh raw tea and mandarin peel have been studied extensively in the functional drink and health product fields, respectively (4, 10–13). However, as a recently popularized commodity, to date, no holistic and detailed studies on its chemical characteristics and biological activities of Ganpu tea have been reported yet. We previously analyzed the aromatic substances of Ganpu tea and discovered a number of volatile compounds that were newly generated during the sun-drying processing (14). In this study, we systematically identified and analyzed the water-soluble compositions of Pu-erh raw tea, mandarin peel, and Ganpu tea by applying the UPLC-Q-TOF-MS and UPLC-MS technology, and investigated the conversions of potential flavor compounds of Ganpu tea during the sun-drying processing. We also conducted formal sensory evaluation to assess the final influence of these compositional changes on flavor quality criteria. Additionally, we also evaluated the preventive effects of Ganpu tea extract on depression pathology both in the FST and TST mice models. Collectively, our experiments aimed to reveal the possible chemical basis for the flavor formation of Ganpu tea and to demonstrate whether these compounds can exert antidepressant effects.

Abbreviations: GC, gallocatechin; EGC, (-)-epigallocatechin; C, catechin; EC, epicatechin; EGCG, epigallocatechin gallate; GCG, gallocatechin gallate; ECG, epicatechin gallate; CG, Catechin gallate; UPLC-Q-TOF, Ultra performance liquid chromatography coupled with Q-TOF mass spectrometry; UPLC-MS, Ultra-high performance liquid chromatography- mass spectrometry; Rt, retention time; DSA, descriptive sensory analysis; FST, forced swimming test; TST, tail suspension test.

MATERIALS AND METHODS

Plant Materials

The tea plant materials were collected from Yunding Ganpu tea industry co., LTD (Guangzhou, China). Information regarding the tea plant samples used in this study are described in **Table 1**. S1, S2, and S3 were prepared to compare the chemical compositions among Pu-erh raw tea, mandarin peel, and Ganpu tea. S4, S5, S6, and S7 were prepared for research on the variation trend of potential flavor compounds in Ganpu tea during the sun-drying processing. All samples were tested in time on the harvesting year.

Chemicals and Drugs

HPLC-grade acetonitrile, methanol, and formic acid were purchased from Fisher Scientific (Pittsburg, PA, USA). Water was purified using a Milli-Q water purification system (Millipore, Bedford, MA, USA). Clomipramine hydrochloride tablets were purchased from Beijing Novartis Pharmaceutical Co., Ltd (Beijing, China). All the other chemicals and reagents used were of the highest grade available.

Preparation of Samples

Tea plant samples were dried to constant weight using a vacuum freeze-drying machine, and the remaining weight was milled into a powder with ∼60 meshes. Approximately 2.0 g of the prepared powder sample was weighed and extracted with 100 mL of distilled water at 100°C for 45 min with shaking, and the extracts were further filtered through filter paper. The obtained supernatants were filtered through a 0.22 um membrane for subsequent UPLC-Q-TOF and UPLC-MS analysis, and then dried into powder by vacuum freeze-drying machine. The dried extract powder was subsequently used in antidepressant-like testing in mice described below (15).

UPLC-Q-TOF Analysis

An Agilent UPLC1290-6540-UHD Q-TOF system and an ACQUITY UPLC BEH C18 column (2.1 mm × 100 mm id, 1.7 μm, Waters) were used for the qualitative analysis. The mobile phase was composed of A (0.2% formic acid, v/v) and B (acetonitrile) with a gradient elution as follows: 0–15 min, 95%−95% A; 15–35 min, 95%−85% A; 35–50 min, 85%−50% A; 50–60 min, 50%−20% A; and 60–65 min, 20%−95% A. The

TABLE 1 | Sample information sheet.

Sample No.	Sample name	Description	Collection time
S1	Pu-erh raw tea	Harvested from Yunnan	2016.12
S2	Mandarin peel	Harvested from Xinhui, Guangdong	2016.12
S3	Ganpu tea	Made from S1 and S2	2016.12
S4	Ganpu tea 0 day	0 day of the full sun-drying processing	2018.09
S5	Ganpu tea 3 day	3 day of the full sun-drying processing	2018.09
S6	Ganpu tea 9 day	9 day of the full sun-drying processing	2018.09
S7	Ganpu tea 15 day	15 day of the full sun-drying processing	2018.09

column and auto-sampler temperatures were maintained at 40 and 20°C, respectively. The mobile phase was directly delivered into the electrospray ionization source at a flow rate of 0.3 mL/min. The injection volume was 5 μL. Mass spectroscopy (MS) analysis was performed in both positive and negative ion mode with the full scan mode from m/z 0 to 1,200. The capillary and cone voltages were 3.5 kV and 30 V, respectively. The collision energy was 40 eV. Nitrogen was used as desolvation gas at flow rate of 500 L/h. The temperatures of ion source and desolvation gas were set at 100 and 300°C, respectively.

UPLC-MS Analysis

An Waters ACQUITY™ QDA system coupled with PDA detector (Waters, Milford, MA, USA) were used for further research on the flavor characteristics of Ganpu tea. The chromatographic parameters, including column, mobile phase, gradient elution condition, flow rate, and injection volume, were the same as UPLC-Q-TOF-MS system described in 2.4. The UV chromatogram was monitored at 278 nm. MS analysis was performed both in positive and negative ion mode and using the full scan mode from m/z 50 to 1,200. The capillary and cone voltages were 3.5 kV and 25 V, respectively.

Analysis of Biochemical Compositions

The contents of moisture, water extract, total free amino acids and tea polyphenols were determined according to GB 5009.3-2016, GB/T 8305-2013, GB/T8314-2013, and GB/T 8313-2008, respectively. The content of tea pigment was determined using the method described in our previous work with proper modifications (15).

Descriptive Sensory Analysis (DSA)

The tea infusion was evaluated by a well-trained panel of 10 members (five males and five females, age: 20–45). Tea samples were assessed using the flavor profile method of ISO 6564 (ISO, 1985). The DSA was performed according to the procedures described previously by Kraujalyt et al. (16) and GB/T 14487-2017, with a slight modification. Briefly, 3.00 g of Ganpu tea was infused with 150 mL of freshly boiled water for 5 min in a specialized DSA tea pot, then 50 mL of tea infusion was poured into a 150 mL-cup covered with a porcelain cover, which was provided to panelists in an odor-free laboratory at 25°C. Three-digit numbers were used to code samples, and they were randomly offered to panelists after brewing for aroma and flavor assessment. Panelists agreed that the samples could be described using six attributes for aroma: stale, woody, floral, fruity, sweet, and off-flavor, as well as six attributes for flavor: bitter, silky, sweet, umami, mellow, and astringent. The intensities of the aroma and flavor attributes were scored using a scale from 0 to 10, where 0 = none or negligible perceptible intensity, and 10 = extremely high intensity. Each sample was evaluated three times by each panelist on different days. Data were expressed as a mean.

Animals

Both male and female Chinese Kun Ming (KM) mice (20 ± 2 g) were obtained from Laboratory Anima Center of Guangzhou University of Chinese Medicine (Guangzhou, Guangdong Province, China) and used in this study. The mice were housed individually in cages for 3 days to adapt to the environment under the following controlled conditions: 25 ± 2°C under a 12 h light/dark cycle and 60 ± 5% humidity with free access to water and food pellets. Each mouse was used only once. Behavioral testing was performed between 7:00 and 12:00 AM. All the procedures were conducted according to the National Institutes of Health Guide for the Care and Use of Laboratory Animals, and the animal handling and experimental procedures were approved by the Local Animal Use Committee (SCXK 2013-0020).

Measurement of Depressive-Like Behaviors

Behavior tests were performed in five groups with 12 mice in each group. The mice were given orally twice a day with the extract of Ganpu tea at 0.1 g /kg, 0.2 g /kg, and 0.4 g /kg for 15 consecutive days, respectively. Mice in positive control group were given with clomipramine hydrochloride tablets (0.02 g /kg) as the positive reference also for 15 consecutive days. The mice in negative control group were given only with the same volume of physiological saline solution for 15 consecutive days. The mice in both positive and negative control groups were tested in parallel with those receiving various doses of extract of Ganpu tea. Animal behaviors were assessed at 45 min after administration of the final dose.

Forced Swimming Test (FST)

The FST is one of the most common animal models used for examination of the depressive-like behaviors. The test was conducted as previously described (17) with slight modifications. Mice were individually inserted in an open cylinder container

(10 cm in diameter and 25 cm in height) containing 19 cm of water at 24 ± 2°C. Each mouse was judged to be immobile when it ceased struggling and remained floating motionless in the water, making only small movements necessary to keep its head above water. The duration of immobility was recorded during the last 5 min of the 7 min testing period.

Tail Suspension Test (TST)

The TST is another model commonly used for examination of depressive-like behaviors (18). The tails of mice were taped in a balance bracket at a distance of 2 cm from the tail tip, with tail straight and head being hung down 15 cm above the desktop after 45 min from the last administration. The mice were separated by cardboard just in the case when they were interfered with each other. Each mouse was treated for 7 min; the first 2 min was for adaptation. The duration of immobility (no other body movements except respiration) in the last 5 min was recorded.

Statistical Analysis

UPLC-Q-TOF-MS and UPLC-MS system were re-calibrated after analysis of every 5 samples to ensure and maintain data accuracy and stability. All the results were recorded and expressed as mean ± standard deviation (SD) of three replicates. The Heatmap analysis was carried out using the website https://software.broadinstitute.org/morpheus, and based on the relative abundances by untargeted metabolomics. The statistical analyses were performed using one-way analysis of variance (ANOVA), followed by least significant difference (LSD) test or Duncan's test. $p < 0.05$ was considered statistically significant.

RESULTS AND DISCUSSION

Comparisons of Chemical Compositions Among Pu-erh Raw Tea, Mandarin Peel and Ganpu Tea

After being extracted with boiling water, the extract was filtered and injected into the UPLC-Q-TOF system and the UPLC-MS system, respectively. Good separation was achieved after screening a series of mobile phases, UPLC columns, and gradient profiles. Meanwhile, MS conditions were optimized after testing a set of instrument parameters, as described in UPLC-Q-TOF Analysis and UPLC-MS Analysis. The total ion chromatograms (both positive and negative ion modes) and the representative UPLC chromatograms (278 nm) of Pu-erh raw tea (S1), mandarin peel (S2), and Ganpu tea (S3) were obtained by the UPLC-MS system (**Figure 1**). Peak identification of compounds in **Table 2** was performed based on the precise molecular weight and fragment ions by UPLC-Q-TOF analysis, and a comparison of them with data in the previously published literature (19–23).

The retention times (Rt), the ratio of deprotonated/protonated molecules ($[M+H]^+/[M-H]^-$), measured value, fragment ions and formula are listed in **Table 2**. Furthermore, some of the compounds in **Table 2** were identified by standard comparisons, such as gallocatechin (GC), (-)-epigallocatechin (EGC), catechin (C), epicatechin (EC), epigallocatechin gallate (EGCG), gallocatechin gallate (GCG), epicatechin gallate (ECG), catechin gallate (CG), caffeine, theobromine, theophylline, gallic acid, rutin, quercetin, and synephrine.

As shown in **Table 2**, Compounds 1–72 were detected in Pu-erh raw tea (S1) and Ganpu tea (S3, S4, S5, S6, S7) except those labeled with asterisk, which were newly generated compounds during the sun-drying processing. For example, isoleucine, threonine, arginine, and glutamine were detected only from S3 (finished product), S6 (sun-drying for 9 days), and S7 (sun-drying for 15 days), and catechin-4a-epicatechin-3-O-gallate, catechin-4a-epicatechin 3'-o-gallate, myricetin−3- locust glycoside, quercetin−3-o- rhamnoside galactoside, and vitexin were detected only from S3 (finished product), S5 (sun-drying for 3days), S6 (sun-drying for 9 days), and S7 (sun-drying for 15 days), which means these compounds were produced at different times during the sun-drying processing. Meanwhile, compounds 73-104 were detected in mandarin peel (S2) and Ganpu tea (S3, S4, S5, S6, S7) except 4H-1-Benzopyran-4-one,2,3-dihydro-5,6,7,8-tetramethoxy-2-[4-(phenylmethoxy)phenyl]- and 4H-1-Benzopyran-4-one,2-phenyl-,dihyroxy trimethoxy deriv, which were detected only from S3 (finished product), S6 (sun-drying for 9 days), and S7 (sun-drying for 15 days).

As shown in **Figure 1**, the water-soluble chemical compounds of Pu-erh raw tea (S1), mandarin peel (S2), and Ganpu tea (S3) exhibited noticeable differences and intrinsic connections in all the chromatograms. The intensities of ionization varied frequently between the positive (**Figure 1A**) and the negative ion modes (**Figure 1B**), and the mechanisms also varied between MS (**Figures 1A,B**) and UV detectors (**Figure 1C**). Still, we found similar results, i.e., water-soluble chemical compounds of Ganpu tea (S3) were more abundant and diversified as compared with those of Pu-erh raw tea (S1) and mandarin peel (S2). A total of 104 compounds were detected in Ganpu tea (S3), while only 63 and 30 compounds were detected in Pu-erh raw tea (S1) and mandarin peel (S2), respectively. Water-soluble compounds of Ganpu tea (S3) were consisted of six amino acids, 16 catechins, three alkaloids, seven pigments, 19 organic acids, and 12 flavonoids, which were also detected in the Pu-erh raw tea (S1), and 30 compounds, which were also detected in the mandarin peel (S2). Furthermore, 11 compounds labeled with asterisk and listed in **Table 2** were detected only in Ganpu tea (S3), which were newly generated during the sun-drying processing. The potential flavor compounds of Ganpu tea (S3) were shared with 59.6% compounds of Pu-erh raw tea (S1), and with 29.8% compounds of mandarin peel (S2). The remaining 10.6% potential flavor compounds in Ganpu tea were newly generated during the sun-drying processing.

Analysis of Flavor Substances From Ganpu Tea

A total of 104 potential flavor compounds were identified in Ganpu tea by UPLC-Q-TOF system. The characteristic peaks of these potential flavor compounds are classified in **Figure 2**, while other details are listed in **Table 2**. Our results showed that ten amino acids were identified in Ganpu tea. Theanine (1) is the most abundant compound, followed by pyroglutamic acid (6), threonine (8), and phenylalanine (3).

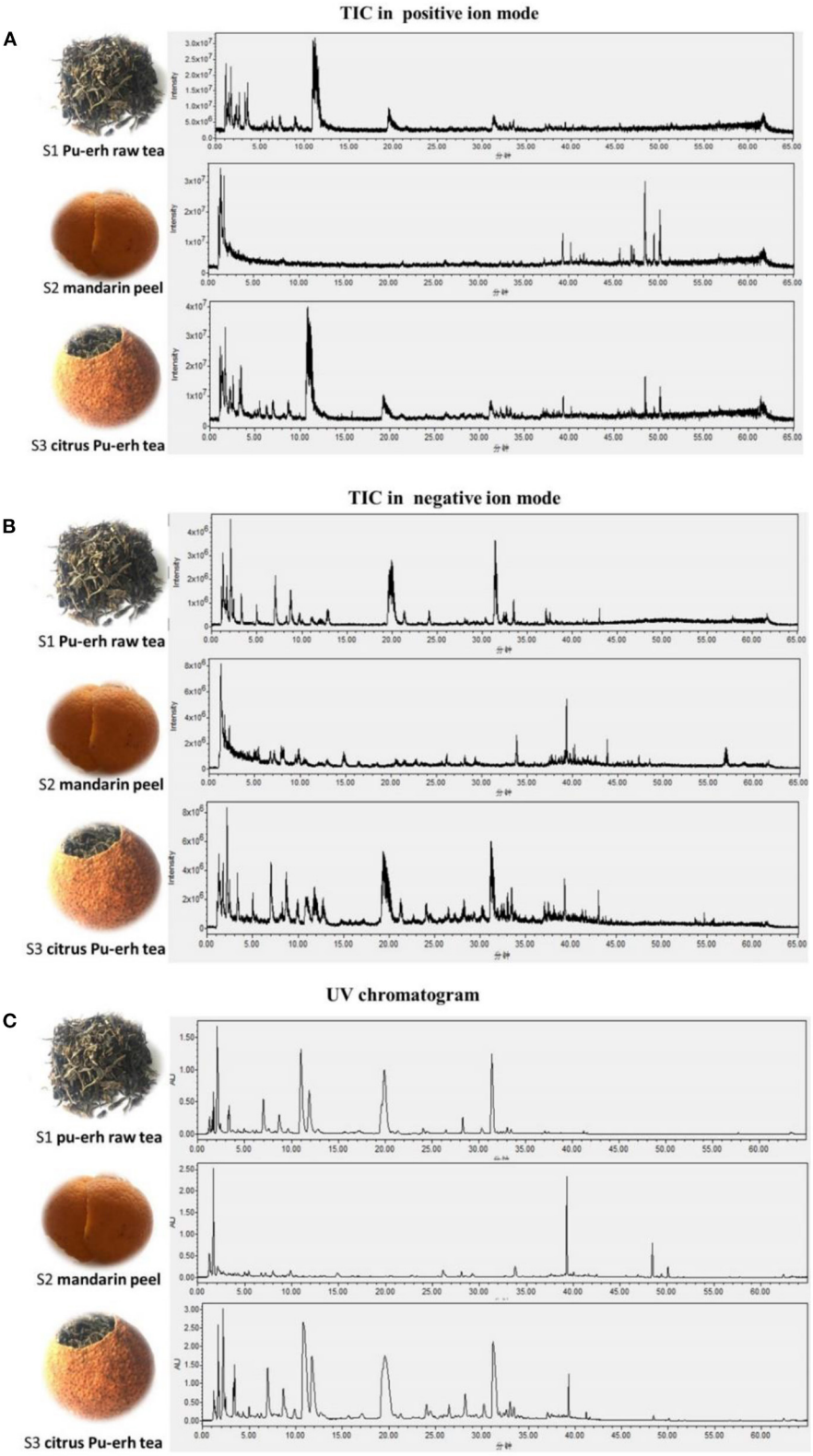

FIGURE 1 | Comparisons of the chemical compositions among Pu-erh raw tea, mandarin peel, and Ganpu tea by TIC in positive ion mode **(A)**, TIC in negative ion mode **(B)**, and UV chromatogram **(C)**, respectively. In our previous study, we investigated the source and conversion of aromatic substances of Ganpu tea. The fruity sweet aromas compounds of Ganpu tea were consisted of the main volatile components of Pu-erh raw tea and mandarin peel, in addition to the newly generated

(Continued)

FIGURE 1 | compounds during the sun-drying processing (14). Based on the data obtained from the present study, we could draw a similar conclusion that the water-soluble substances of Ganpu tea were not just a simple combination of the compounds of Pu-erh raw tea and mandarin peel. Rather, the water-soluble substances of Ganpu tea were mainly attributed to the development and transformation of the precursor ingredients that it contains and to several newly generated substances during the sun-drying processing. The final formation of the flavor of Ganpu tea may be closely related to the production and conversion of these water-soluble substances. Further researches are necessary to investigate the contribution of these compounds to the flavor characteristic of Ganpu tea.

Moreover, isoleucine (7), threonine (8), arginine (9), and glutamine (10), labeled with asterisks in **Figure 2A**, were newly generated amino acids during the full sun-drying processing, as they were identified exclusively in Ganpu tea, but not in Pu-erh raw tea or mandarin peel. In addition to the common tea catechins, such as GC (11), EGC (12), C (13), EC (14), EGCG (15), GCG (16), ECG (17), and CG (18), 10 other catechins and catechin metabolites were also identified in Ganpu tea. For example, epiafzelechin-3-O-gallate (21), gallocatechin-(4a-8)-catechin-3-O-gallate (22), and trigalloylglucose (24) all displayed a strong intensity of ionization. Notably, catechin-4a-epicatechin-3-O-gallate (25) and catechin-4a-epicatechin-3'-O-gallate (26) were newly generated during the sun-drying process, as they were discovered exclusively in Ganpu tea (**Figure 2B**). Caffeine (27) and theobromine (28) were the main alkaloids in Ganpu tea. The pigments were composed of theaflavin (29) and some anthocyanins (30–35) (**Figure 2C**). Flavonoids and their derivatives were identified in Ganpu tea and shown in **Figure 2D**. Rutin (36), kaempferol (37), myricetin-3-O-galactoside (47), quercetin (48), and their derivatives, which originated from Pu-erh raw tea were also identified in Ganpu tea. Three newly generated compounds, including myricetin−3-locust glycoside (46), quercetin−3-o- rhamnoside galactoside (49), and vitexin (53) were formed during the sun-drying processing. Meanwhile, flavonoids originating from mandarin peel are shown in **Figure 2F**. For example, naringenin (75), naringin (78), narirutin (81), hesperidin (84), poncirin (85), pentamethoxyflavanone (89), isosinensetin (91), sinensetin (92), limonin (94), nobiletin (95), and tangeretin (98) were the important chemical constituents for mandarin peel (24, 25). Nineteen organic acids and their derivatives (54–72) were identified and shown in **Figure 2E**.

As we known, catechins, pigments, amino acids, organic acids, alkaloids, and flavonoids were important for the flavor of tea drink and mandarin peel (24–26, 38). Therefore, we speculated that the unique flavor of Ganpu tea could co-attributed to these water-soluble compounds. Further researches are necessary to verify the 11 newly generated compounds whether also contribute to the flavor characteristic of Ganpu tea. The chemical compound identification of 104 metabolites of Ganpu tea was tentative in this paper. We need to positively identify major and effective compounds of Ganpu tea in our future research. Based on our previous study on the aroma of Ganpu tea (14), we predicted that potential flavor compounds would be changed considerably during the sun-drying processing due to *de novo* biosynthesis and/or enzymatic modification of the existing compounds, which were influenced by exogenous stimuli, including temperature, humidity, light, and microorganisms. To study the conversions of water-soluble compounds of Ganpu tea, we further analyzed the biochemical compositions in this study.

The Variation Trend of Potential Flavor Compounds in Ganpu Tea During the Sun-Drying Processing

Analysis of Biochemical Components

Moisture, water extract, total free amino acids, tea polyphenols, theaflavins, thearubigins, and theabrownine have respective influences on the sensory flavor and health-promoting function of Ganpu tea. These primary biochemical components and their contents were assessed within four samples with different durations of sun-drying treatment, and listed in **Table 3**. Data were expressed from three independent chemical replicates. Sun-drying treatment for 15 days could significantly decrease the moisture contents from 24.16 to 5.04% of Ganpu tea, and the 15-day-period of sunlight was necessary to reach the final moisture content. It was clear that S4 without sun-drying treatment, contained the higher moisture contents, mainly due to the fresh mandarin peel of Ganpu tea. The sun-drying processing not only reduced the moisture content but also imposed significant effect on tea polyphenols and pigments. The concentration of tea polyphenols in S7 was significantly lower than those in other samples, due to the fact that catechins had undergone a series of oxidative, condensing and degradative chemical processes to form gallic acid, theaflavins, thearubigins, and theabrownine under the sun-drying conditions (11).

As shown in **Table 3**, at the end of sun-drying processing, the contents of thearubigins and theabrownine were clearly increased. On the contrary, the content of theaflavins was clearly decreased, suggesting that theaflavins are oxidized and accumulated into thearubigins and theabrownine. The content of total free amino acids was only slightly changed during the sun-drying processing since the contents of several free amino acids, including theanine and leucine, were decreased, while other amino acids, including isoleucine, threonine, arginine, and glutamine were newly generated. The total content of water extract was increased during the sun-drying processing, suggesting that new substances are formed from oxidation, degradation, and condensation of various compounds, which collectively contribute to the unique color, taste, and aroma of the Ganpu tea.

The Variation Trend of Potential Flavor Compounds

A heatmap analysis was applied to visualize the dynamic changes of potential flavor compounds in Ganpu tea during the sun-drying processing (**Figure 3**). Each column represents a tea sample with different durations of sun-drying processing and each row represents a critical compound. A color-coded scale grading from blue to red corresponds to the content of these potential flavor compounds shifting from low to high. The sun-drying processing requires 15 days of high humidity and high

TABLE 2 | List of the identified components in tested samples.

Peak No.	Putative identification	Rt (min)	$[M+H]^+/[M-H]^-$	Measured value	Fragment ions	Formula	Detection						
							S1	S2	S3	S4	S5	S6	S7
1	Theanine	1.7	[M+H]+	175.1082	158, 129	$C_7H_{14}N_2O_3$	✓	_	✓	✓	✓	✓	✓
2	Leucine	2.1	[M+H]+	132.1012	132, 86	$C_6H_{13}NO_2$	✓	_	✓	✓	✓	✓	✓
3	Phenylalanine	3.28	[M+H]+	166.0863	120	$C_9H_{11}NO_2$	✓	_	✓	✓	✓	✓	✓
4	Tryptophan	6.3	[M+H]+	205.0974	143, 118	$C_{11}H_{12}N_2O_2$	✓	_	✓	✓	✓	✓	✓
5	Tyrosine	3.05	[M+H]+	182.0808	165, 136	$C_9H_{11}NO_3$	✓	_	✓	✓	✓	✓	✓
6	Pyroglutamic acid	2.6	[M+H]+	130.0501	_	$C_5H_7NO_3$	✓	_	✓	✓	✓	✓	✓
7	* Isoleucine	2.3	[M+H]+	132.1013	86	$C_6H_{13}NO_2$	_	_	✓	_	_	✓	✓
8	* Threonine	3.2	[M+H]+	120.0650	_	$C_4H_9NO_3$	_	_	✓	_	_	✓	✓
9	* Arginine	1.45	[M+H]+	175.1120	158, 129	$C_6H_{14}N_4O_2$	_	_	✓	_	_	✓	✓
10	* Glutamine	8.25	[M+H]+	147.0758	119, 91	$C_5H_{10}N_2O_3$	_	_	✓	_	_	✓	✓
11	Gallocatechin (GC)	3.35	[M+H]+	307.0813	_	$C_{15}H_{14}O_7$	✓	_	✓	✓	✓	✓	✓
12	(-)-Epigallocatechin (EGC)	7.00	[M+H]+	307.0814	223, 163	$C_{15}H_{14}O_7$	✓	_	✓	✓	✓	✓	✓
13	Catechin (C)	8.7	[M+H]+	291.0869	_	$C_{15}H_{14}O_6$	✓	_	✓	✓	✓	✓	✓
14	Epicatechin (EC)	19.4	[M+H]+	291.0863	165, 139	$C_{15}H_{14}O_6$	✓	_	✓	✓	✓	✓	✓
15	Epigallocatechin gallate (EGCG)	19.8	[M+H]+	459.0922	289, 139	$C_{22}H_{18}O_{11}$	✓	_	✓	✓	✓	✓	✓
16	Gallocatechin gallate (GCG)	24.0	[M+H]+	459.0924	289, 139	$C_{22}H_{18}O_{11}$	✓	_	✓	✓	✓	✓	✓
17	Epicatechin gallate (ECG)	31.3	[M+H]+	443.0972	273, 139	$C_{22}H_{18}O_{10}$	✓	_	✓	✓	✓	✓	✓
18	Catechin gallate (CG)	32.6	[M+H]+	443.0973	_	$C_{22}H_{18}O_{10}$	✓	_	✓	✓	✓	✓	✓
19	(-)-EGCG-3″-O-ME	22.6	[M-H]-	471.0920	_	$C_{23}H_{20}O_{11}$	✓	_	✓	✓	✓	✓	✓
20	Epiafzelechin	3.00	[M+H]+	275.0919	_	$C_{15}H_{14}O_5$	✓	_	✓	✓	✓	✓	✓
21	Epiafzelechin-3-O-gallate	37.2	[M-H]-	424.0795	273	$C_{22}H_{17}O_9$	✓	_	✓	✓	✓	✓	✓
22	Gallocatechin-(4a-8)-catechin-3-O-gallate	20.7	[M-H]-	745.1399	457, 423	$C_{37}H_{30}O_{17}$	✓	_	✓	✓	✓	✓	✓
23	Digallocatechin-catechin	25.9	[M-H]-	897.1869	423	$C_{45}H_{38}O_{20}$	✓	_	✓	✓	✓	✓	✓
24	*Catechin-4a-epicatechin-3-O-gallate	24.5	[M+H]+	731.1608	427, 289	$C_{37}H_{30}O_{16}$	_	_	✓	_	✓	✓	✓
25	Trigalloylglucose	28.25	[M-H]-	635.0880	423, 169	$C_{27}H_{24}O_{18}$	✓	_	✓	✓	✓	✓	✓
26	*Catechin-4a-epicatechin 3'-o-gallate	26.5	[M+H]+	731.1608	427, 289	$C_{37}H_{30}O_{16}$	_	_	✓	_	✓	✓	✓
27	Theasinesnsins A	32.00	[M+H]+	611.1395	465,303	$C_{30}H_{26}O_{14}$	✓	_	✓	✓	✓	✓	✓
28	Theasinesnsins B	33.1	[M+H]+	611.1396	465, 303	$C_{30}H_{26}O_{14}$	✓	_	✓	✓	✓	✓	✓
29	Caffeine	11.0	[M+H]+	195.0877	157	$C_8H_{10}N_4O_2$	✓	_	✓	✓	✓	✓	✓
30	Theobromine	3.45	[M+H]+	181.0721	138, 108	$C_7H_8N_4O_2$	✓	_	✓	✓	✓	✓	✓
31	Theophylline	5.3	[M+H]+	181.0718	_	$C_7H_8N_4O_2$	✓	_	✓	✓	✓	✓	✓
32	Theaflavin	30.0	[M-H]-	563.1190	_	$C_{29}H_{24}O_{12}$	✓	_	✓	✓	✓	✓	✓
33	*Procyanidin B1	15.17	[M+H]+	579.1497	409, 289	$C_{30}H_{26}O_{12}$	✓	_	✓	✓	✓	✓	✓
34	*Procyanidin B2	15.26	[M+H]+	579.1497	409, 289	$C_{30}H_{26}O_{12}$	✓	_	✓	✓	✓	✓	✓
35	*Procyanidin B3	15.7	[M+H]+	579.1495	409, 127	$C_{30}H_{26}O_{12}$	✓	_	✓	✓	✓	✓	✓
36	*Procyanidin B4	15.76	[M+H]+	579.1497	409, 289	$C_{30}H_{26}O_{12}$	✓	_	✓	✓	✓	✓	✓
37	Procyanidin B1 3-O-gallate	24.5	[M+H]+	731.1608	427, 289	$C_{37}H_{30}O_{16}$	✓	_	✓	✓	✓	✓	✓
38	Procyanidin B2 3-O-gallate	26.5	[M+H]+	731.1608	427, 289	$C_{37}H_{30}O_{16}$	✓	_	✓	✓	✓	✓	✓
39	Rutin	41.0	[M+H]+	611.1606	465, 303	$C_{27}H_{30}O_{16}$	✓	_	✓	✓	✓	✓	✓
40	Kaempferol	37.5	[M+H]+	287.0552	_	$C_{15}H_{10}O_6$	✓	_	✓	✓	✓	✓	✓
41	*Kaempferol-3-O-glucoside	35.91	[M-H]-	447.0929	284, 255	$C_{21}H_{20}O_{11}$	✓	_	✓	✓	✓	✓	✓
42	*Kaempferol-3-O-galactoside	37.56	[M-H]-	447.0925	284, 255	$C_{21}H_{20}O_{11}$	✓	_	✓	✓	✓	✓	✓
43	*Kaempferol-3- O-rutinoside	37.1	[M-H]-	593.1509	_	$C_{27}H_{30}O_{15}$	✓	_	✓	✓	✓	✓	✓
44	*Kaempferol-3- O-glucosylrutinoside	35.6	[M-H]-	755.2031	_	$C_{33}H_{40}O_{20}$	✓	_	✓	✓	✓	✓	✓
45	*Myricetin-3-O-glucoside	27.2	[M-H]-	479.0824	_	$C_{21}H_{20}O_{13}$	✓	_	✓	✓	✓	✓	✓
46	** Myricetin—3- locust glycoside	28.1	[M+H]+	625.1036	_	$C_{26}H_{24}O_{18}$	_	_	✓	_	✓	✓	✓
47	**Myricetin-3-O-galactoside	28.05	[M-H]-	479.0827	_	$C_{21}H_{20}O_{13}$	✓	_	✓	✓	✓	✓	✓
48	Quercetin	30.3	[M+H]+	303.0500	287, 257	$C_{15}H_{10}O_7$	✓	_	✓	✓	✓	✓	✓

(Continued)

TABLE 2 | Continued

Peak No.	Putative identification	Rt (min)	$[M+H]^+/[M-H]^-$	Measured value	Fragment ions	Formula	Detection						
							S1	S2	S3	S4	S5	S6	S7
49	***** Quercetin−3-o- rhamnoside galactoside	39.35	[M+H]+	611.1250	303	$C_{26}H_{26}O_{17}$	_	_	✓	_	✓	✓	✓
50	*Quercetin-**3-O-glucoside**	32.4	[M-H]-	463.0877	300, 271	$C_{21}H_{20}O_{12}$	✓	_	✓	✓	✓	✓	✓
51	*Quercetin-**3-O-galactoside**	33.5	[M-H]-	463.0878	300, 271	$C_{21}H_{20}O_{12}$	✓	_	✓	✓	✓	✓	✓
52	*Quercetin−3- O-glucosylrutinoside	31.85	[M+H]+	773.2136	303, 465	$C_{33}H_{40}O_{21}$	✓	_	✓	✓	✓	✓	✓
53	* Vitexin	49.5	[M+H]+	433.1129	395	$C_{21}H_{20}O_{10}$	_	_	✓	_	✓	✓	✓
54	Gallic acid	2.25	[M-H]-	169.0142	125	$C_7H_6O_5$	✓	_	✓	✓	✓	✓	✓
55	Quinic acid	1.3	[M-H]-	191.0560	111, 87	$C_7H_{12}O_6$	✓	_	✓	✓	✓	✓	✓
56	Caffeic acid	2.21	[M+H]+	181.0500	157	$C_9H_8O_4$	✓	_	✓	✓	✓	✓	✓
57	Malic acid	1.4	[M-H]-	133.0137	75	$C_4H_6O_5$	✓	_	✓	✓	✓	✓	✓
58	Ascorbic acid	1.9	[M-H]-	175.0240	115, 85	$C_6H_8O_6$	✓	_	✓	✓	✓	✓	✓
59	Caffeoylmalic acid	3.3	[M-H]-	295.0442	191, 113	$C_{13}H_{12}O_8$	✓	_	✓	✓	✓	✓	✓
60	*3-O-galloylquinic acid	2.15	[M-H]-	343.0662	191, 169	$C_{14}H_{16}O_{10}$	✓	_	✓	✓	✓	✓	✓
61	*5-O-galloylquinic acid	2.48	[M-H]-	343.0664	191, 169	$C_{14}H_{16}O_{10}$	✓	_	✓	✓	✓	✓	✓
62	Chlorogenic acid	5.0	[M-H]-	353.0870	191	$C_{16}H_{18}O_9$	✓	_	✓	✓	✓	✓	✓
63	*1-Caffeoylquinic acid	10.00	[M-H]-	353.0871	191	$C_{16}H_{18}O_9$	✓	_	✓	✓	✓	✓	✓
64	*3-Caffeoylquinic acid	10.09	[M-H]-	353.0869	291, 191	$C_{16}H_{18}O_9$	✓	_	✓	✓	✓	✓	✓
65	*1-p-Coumaroylquinic acid	16.01	[M-H]-	337.0915	305, 163	$C_{16}H_{18}O_8$	✓	_	✓	✓	✓	✓	✓
66	*3-p-Coumaroylquinic acid	16.3	[M-H]-	337.0917	305, 163	$C_{16}H_{18}O_8$	✓	_	✓	✓	✓	✓	✓
67	*4-p-Coumaroylquinic acid	16.87	[M-H]-	337.0918	305, 163	$C_{16}H_{18}O_8$	✓	_	✓	✓	✓	✓	✓
68	*5-p-Coumaroylquinic acid	16.92	[M-H]-	337.0918	305, 163	$C_{16}H_{18}O_8$	✓	_	✓	✓	✓	✓	✓
69	Galloylglucose	45.5	[M-H]-	331.0662	169	$C_{13}H_{16}O_{10}$	✓	_	✓	✓	✓	✓	✓
70	1,2,6-Trigalloylglucose	28.2	[M-H]-	635.0882	465, 313	$C_{27}H_{24}O_{18}$	✓	_	✓	✓	✓	✓	✓
71	3,6-Digalloylglucose	9.9	[M-H]-	483.0773	169	$C_{20}H_{20}O_{14}$	✓	_	✓	✓	✓	✓	✓
72	Strictinin	11.8	[M-H]-	633.0725	301, 275	$C_{27}H_{22}O_{18}$	✓	_	✓	✓	✓	✓	✓
73	Synephrine	1.66	[M+H]+	168.1012	150, 135	$C_9H_{13}NO_2$	_	✓	✓	✓	✓	✓	✓
74	Lucenin-2	3.691	[M+H]+	611.1609	575, 473	$C_{27}H_{30}O_{16}$	_	✓	✓	✓	✓	✓	✓
75	Naringenin	23	[M+H]+	273.0757	274, 202	$C_{15}H_{12}O_5$	_	✓	✓	✓	✓	✓	✓
76	Vicenin-2	37	[M+H]+	595.1658	457, 409	$C_{27}H_{30}O_{15}$	_	✓	✓	✓	✓	✓	✓
77	Diosmetin-6, 8-di-C-glucoside	28.1	[M+H]+	625.1762	607, 589	$C_{28}H_{32}O_{16}$	_	✓	✓	✓	✓	✓	✓
78	Naringin	37.75	[M+H]+	581.1864	_	$C_{27}H_{32}O_{14}$	_	✓	✓	✓	✓	✓	✓
79	Chysoeriol-6, 8-di-C-glucoside	29.2	[M+H]+	625.1766	409, 355	$C_{28}H_{32}O_{16}$	_	✓	✓	✓	✓	✓	✓
80	Diosmetin-6-C-glucoside	35.8	[M+H]+	463.1236	367, 343	$C_{22}H_{22}O_{11}$	_	✓	✓	✓	✓	✓	✓
81	Narirutin	37.7	[M-H]-	579.1711	271	$C_{27}H_{32}O_{14}$	_	✓	✓	✓	✓	✓	✓
82	Rhoifolin	12.0	[M+H]+	579.1709	433, 271	$C_{27}H_{30}O_{14}$	_	✓	✓	✓	✓	✓	✓
83	Diosmin	39.2	[M+H]+	609.1816	463, 301	$C_{28}H_{32}O_{15}$	_	✓	✓	✓	✓	✓	✓
84	Hesperidin	39.35	[M-H]-	609.1818	343, 301	$C_{28}H_{34}O_{15}$	_	✓	✓	✓	✓	✓	✓
85	Poncirin	26.1	[M+H]+	595.2023	463, 379	$C_{28}H_{34}O_{14}$	_	✓	✓	✓	✓	✓	✓
86	Citrusin III	43.8	[M+H]+	728.3982	700, 587	$C_{36}H_{53}N_7O_9$	_	✓	✓	✓	✓	✓	✓
87	Melitidin	44.5	[M+H]+	725.2293	419, 404	$C_{33}H_{40}O_{18}$	_	✓	✓	✓	✓	✓	✓
88	Monohydroxy-tetramethoxyflavone	48.95	[M+H]+	359.1125	329, 301	$C_{19}H_{18}O_7$	_	✓	✓	✓	✓	✓	✓
89	Pentamethoxyflavanone	50.15	[M+H]+	375.1441	211, 196	$C_{20}H_{22}O_7$	_	✓	✓	✓	✓	✓	✓
90	Monohydroxy-pentamethoxyflavone	51.2	[M+H]+	389.1231	374, 359	$C_{20}H_{20}O_8$	_	✓	✓	✓	✓	✓	✓
91	Isosinensetin	45.6	[M+H]+	373.1284	343, 153	$C_{20}H_{20}O_7$	_	✓	✓	✓	✓	✓	✓
92	Sinensetin	47	[M+H]+	373.1283	343, 153	$C_{20}H_{20}O_7$	_	✓	✓	✓	✓	✓	✓
93	Tetramethyl-O-isoscutellarein	47.2	[M+H]+	343.1176	328, 313	$C_{19}H_{18}O_6$	_	✓	✓	✓	✓	✓	✓
94	Limonin	43	[M+H]+	471.2015	425, 397	$C_{26}H_{30}O_8$	_	✓	✓	✓	✓	✓	✓
95	Nobiletin	48.5	[M+H]+	403.1386	373, 211	$C_{21}H_{22}O_8$	_	✓	✓	✓	✓	✓	✓
96	Tetramethyl-O-scutellarein	48.6	[M+H]+	343.1175	327, 313	$C_{19}H_{18}O_6$	_	✓	✓	✓	✓	✓	✓

(Continued)

TABLE 2 | Continued

Peak No.	Putative identification	Rt (min)	$[M+H]^+/[M-H]^-$	Measured value	Fragment ions	Formula	Detection						
							S1	S2	S3	S4	S5	S6	S7
97	3, 5, 6, 7, 8, 3′, 4′-Heptamethoxyflavone	49.5	[M+H]+	433.1496	403, 388	$C_{22}H_{24}O_9$	_	✓	✓	✓	✓	✓	✓
98	Tangeretin	50.2	[M+H]+	373.1285	358, 343	$C_{20}H_{20}O_7$	_	✓	✓	✓	✓	✓	✓
99	5-Hydroxy-6, 7, 8, 3′, 4′-pentamethoxyflavone	46.1	[M+H]+	389.1231	_	$C_{20}H_{20}O_8$	_	✓	✓	✓	✓	✓	✓
100	5-Hydroxy-4′- methoxy flavone-7-o-glycoside	37.5	[M+H]+	449.1440	287	$C_{22}H_{24}O_{10}$	_	✓	✓	✓	✓	✓	✓
101	*4H-1-Benzopyran-4-one,2,3-dihydro-5,6,7,8-tetramethoxy-2-[4-(phenylmethoxy)phenyl]-	44.45	[M+H]+	725.1870	_	$C_{39}H_{32}O_{14}$	_	_	✓	_	_	✓	✓
102	4H-1-Benzopyran-4-one,6,8-di-b-Dglucopyranosyl-5,7-dihydroxy-2-(4-hydroxy-3-me-thoxyphenyl)-	28.1	[M+H]+	625.1765	_	$C_{28}H_{32}O_{16}$	_	✓	✓	✓	✓	✓	✓
103	4H-1-Benzopyran-4-one,6,8-di-b-Dglucopyranosyl-5,7-dihydroxy-2-(3-hydroxy-4-me-thoxyphenyl)-	29.3	[M+H]+	625.1764	_	$C_{28}H_{32}O_{16}$	_	✓	✓	✓	✓	✓	✓
104	*4H-1-Benzopyran-4-one, 2-phenyl-,dihyroxy trimethoxy deriv	38.79	[M+H]+	343.0662	191	$C_{14}H_{14}O_{10}$	_	_	✓	_	_	✓	✓

Compounds labeled with asterisk (*) were newly generated during the sun-drying processing. Compounds labeled with star (*) means putative identification. "✓" means detected in this sample, and "_" means not detected in this sample.

temperature conditions, causing potential flavor compounds of Ganpu tea, including catechins, pigments, alkaloids, and flavonoids, to be transformed considerably.

Firstly, the contents of most catechins, particularly EGC, EGCG, GCG, and CG, were decreased by 20.2–27.2%. Meanwhile, with the exception of theaflavin, the pigments, including procyanidins and their derivatives, were clearly increased throughout the sun-drying processing. The significant reduction in catechin content from initial levels throughout the entire course of the sun-drying processing may be resulted from a series of chemical transformations of these compounds into gallic acid, pigments, and alkaloids, during the processes catalyzed by polyphenol oxidase and peroxidase enzymes (39).

Secondly, alkaloids were profoundly affected by the humid and hot sun-drying conditions. For example, the contents of caffeine, theobromine, and theophylline were increased considerably, with caffeine showing the most significant increase (28.7%). It has been proposed that extracellular enzymes produced by microorganisms, such as tannase, play a large role in catalyzing chemical reactions and promoting the transformation of the key chemical components (40).

Thirdly, organic acids showed different variation trends depending on their chemical compositions. For example, the content of 3-caffeoylquinic acid was decreased, while those of gallic acid, quinic acid, and chlorogenic acid were significantly increased with prolonging sun-drying time. Gallic acid is one of the most prominent phenolic acids in tea. The increase of its content during the sun-drying processing is likely due to the degradation of catechin gallates under high-temperature and high moisture conditions, which has been observed in a previous study (27).

Finally, a majority of the essential flavonoids identified in Ganpu tea were originated from the mandarin peel, and showed significant changes during the sun-drying processing. For instance, naringenin, naringin, narirutin, hesperidin, pentamethoxyflavanone, isosinensetin, sinensetin, limonin, nobiletin, and tangeretin were the crucial group of bioactive compounds in the mandarin peel, and they were all increased significantly during the sun-drying processing. Similarly, the contents of most common glycosidic group attached to the flavonoids in Ganpu tea were substantially increased as well. With the exception of kaempferol and its derivatives, whose contents were decreased, the contents of other flavone glycosides, including myricetin-3-O-galactoside and quercetin-3-O-galactoside, were increased significantly. Furthermore, the newly generated flavonoids, including myricetin-3-locust glycoside, quercetin-3-O-rhamnoside galactoside, and vitexin were detected starting from the third day of sun-drying processing. Biosynthesis and/or modification of constitutive flavonoids may be induced by exogenous stimuli, such as changes in sun light and temperature under the natural environments, as well as innate enzymatic activity of mandarin peel cells (28, 41). The persistent activities of enzymes involved in the flavonoid biosynthesis (chalcone flavanone isomerase, phenylalanine ammonia lyase, and cinnamate 4-hydroxylase), O-methylation enzymes (chalcone synthase, flavanone 7-O-glucosyltransferase, and flavanone 7-O-glucoside-2'-O-rhamnotransferase), methyltransferase, and chalcone-flavanone isomerase may be the important pathways for the accumulation and conversion of flavonoid compounds in Ganpu tea (29, 30, 39).

DAS With a Trained Panel

To date, the sensory characteristics of Gan*p*u tea have not been reported yet. In this study, we evaluated the influences of sun-drying processing on the sensory properties of Ganpu tea. The aroma and flavor attributes of Ganpu tea processed with different durations of sun-drying processing are presented in **Figure 4**. Six aroma attributes, including stale, woody, floral, fruity, sweet, and off-flavor, were evaluated in S4, S5, S6, and S7 (**Figure 4A**). The results showed that S7 demonstrated significantly higher intensities of sweet ($p < 0.01$) and fruity ($p < 0.01$) attributes. The 4-terpineol, thymol, and 4-isopropyl−3-

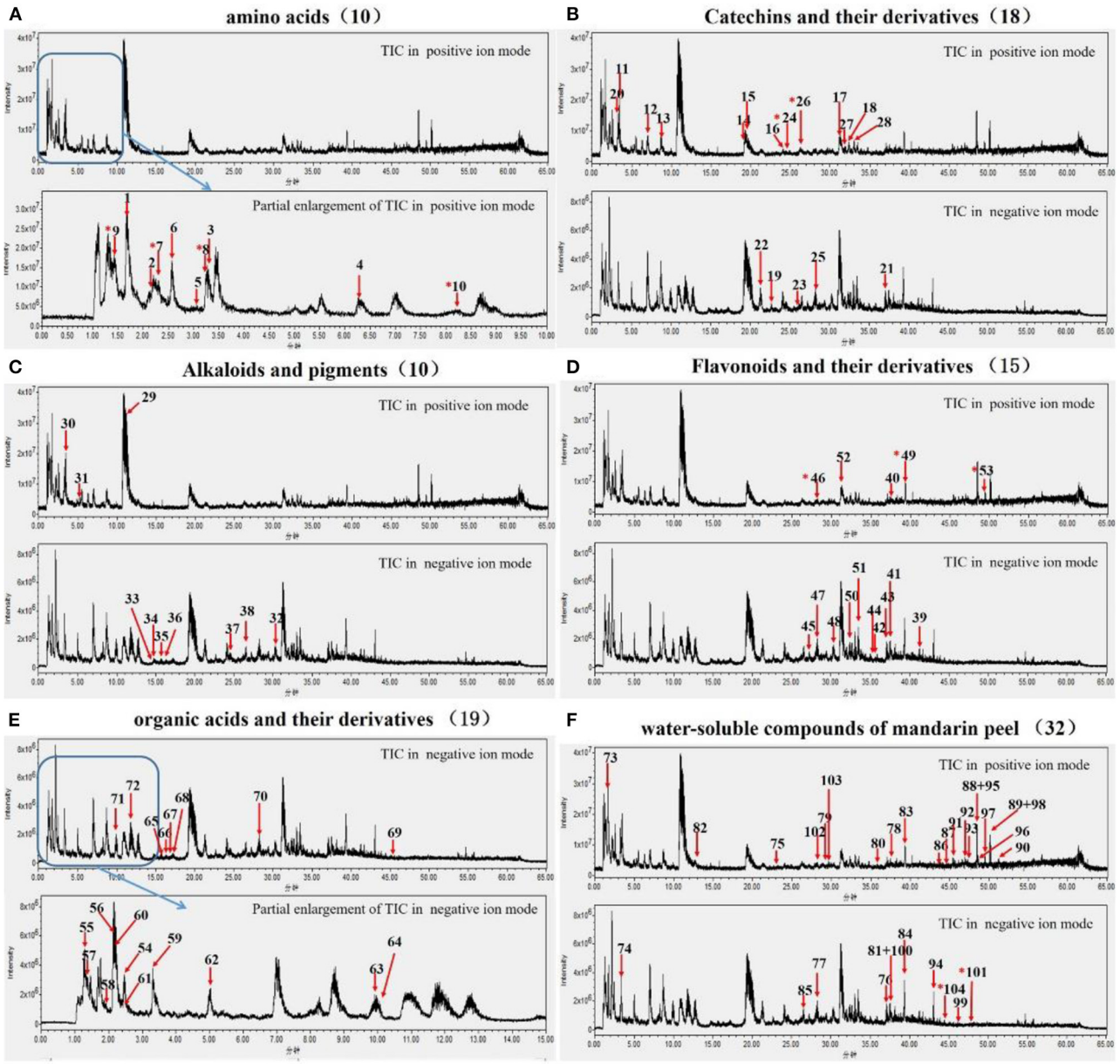

FIGURE 2 | Flavor substances of Ganpu tea were identified by UPLC-Q-TOF system in different categories, including ten amino acids **(A)**, 18 catechins and their derivatives **(B)**, three alkaloids and seven pigments **(C)**, 15 flavonoids and their derivatives **(D)**, 19 organic acids and their derivatives **(E)**, and 32 water-soluble compounds of mandarin peel **(F)**, respectively.

methyl phenol contribute to the sweet descriptor while α-ionone, β-ionone, terpinene, p-acetylanisole, and isoamyl alcohol leaf ester contribute to the fruity descriptor (16). These compounds were accumulated in significantly higher quantities in Ganpu tea with longer duration of sun-drying treatments. S7 also displayed significantly higher intensities of stale ($p < 0.05$) and floral ($p < 0.05$) descriptors. Alcohols and ketones often contribute to the floral descriptor (31), and significantly higher quantities of linalool, 4-terpineol, pinocarvone, piperitone, carvone, and carvenone were detected in S7 (14). The off-flavor was detected in S4 and S5, which may be due to a flavor resembling fermentation of Pu-erh raw tea. However, the detection of off-flavor went away with prolonging the duration of sun-drying treatment.

The flavor attributes of bitter, silky, sweet, umami, mellow, and astringent were evaluated across the four treatment groups (**Figure 4B**). Although no significant differences ($p > 0.05$) in the umami descriptor were observed, S7 did demonstrate significantly higher intensities of silky ($p < 0.01$), sweet ($p < 0.01$), and mellow ($p < 0.05$) attributes. Soluble saccharides and certain amino acids, including theanine, phenylalanine, and

TABLE 3 | Analysis of biochemical components of Ganpu tea samples with different durations of the full sun-drying processing.

Biochemical component (%)	S4 (0 day)	S5 (3 day)	S6 (9 day)	S7 (15 day)
Moisture	24.16 ± 1.38a	21.23 ± 1.04b	12.17 ± 0.76c	5.04 ± 0.98d
Water extract	30.04 ± 2.15d	31.72 ± 2.23cd	33.58 ± 2.02b	34.86 ± 1.93ab
Total free amino acids	2.37± 0.32a	2.03 ± 0.52b	2.33 ± 0.29a	2.43 ± 0.20a
Tea polyphenols	18.45 ± 1.02a	16.77±0.15b	14.10 ± 1.13c	12.12 ± 1.42d
Theaflavins	0.24 ± 0.13a	0.15 ± 0.46b	0.13 ± 0.65bc	0.10 ± 0.02c
Thearubigins	1.36 ± 0.10c	1.49 ± 0.13b	1.50 ± 0.11b	1.85 ± 0.12a
Theabrownine	1.25 ± 0.17c	1.26 ± 0.03c	1.34 ± 0.20b	1.77 ± 0.21a

Differences between samples were analyzed by Duncan's test. In each horizontal line, the mean ± SD values bearing different letters differ significantly ($p < 0.05$).

tryptophan, contribute to sweetness. Moreover, flavonoids could provide a unique taste, changing from bitter to sweet following consumption (32). Additionally, the conversions of catechins, gallic acid, and caffeine as described in the previous section may result in a softer and mellower flavor. Interestingly, S7 displayed a significantly lower intensity ($p < 0.05$) of bitter and astringent attributes, which could be attributed to the significant decrease in catechin content over the course of the sun-drying processing (33).

In general, Ganpu tea has distinctive characteristics, including bright orange liquor, silky mellow taste, and fruity sweet aroma. The sun-drying approach significantly affected the intensities of the sensory attributes of Ganpu tea. Constituents of Ganpu tea are mostly polyphenols, flavonoids, caffeine, and free amino acids, and all of them were changed continuously throughout the sun-drying processing, most probably contributing to the unique taste developed during the Ganpu tea production.

Effect of Ganpu Tea Consumption in the FST and TST

We hypothesized that tea polyphenols, flavonoids, pigments, theanine, caffeic acid, and vitexin detected in Ganpu tea in the present study would be collectively capable of conferring antidepressant-like effects through various mechanisms in animals, an effect that has been shown to take place following the regular consumption of most tea types (34). In order to test this hypothesis, we designed an *in vivo* experiment with mouse model, attempting to simulate the daily Ganpu tea consumption habits of humans. Both the FST and TST are the conventional experimental models of examining the depressive-like behaviors. The immobility times of these tests are shown in **Figure 5**. Results of the FST showed that no significant difference in immobility duration was seen between the NC group and the two oral dose groups (0.1 and 0.2 g/kg) of Ganpu tea extract ($p > 0.05$). The high oral dose group (0.4 g/kg) and PC group showed significantly reduced immobility duration as compared to that of the NC group ($p < 0.01$ and $p < 0.05$, respectively).

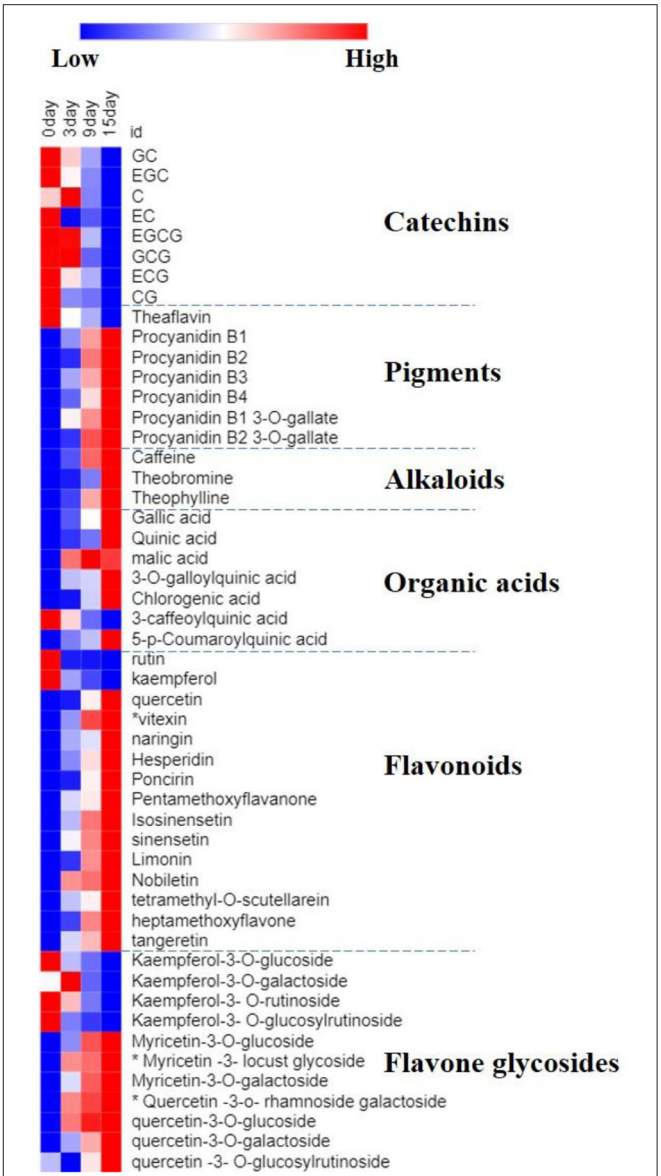

FIGURE 3 | Heatmap analysis of potential flavor compounds from Ganpu tea.

TST results showed a dose-dependent reduction in immobility duration following intake of Ganpu tea extract. The effects of oral doses at 0.1 and 0.2 g/kg of Ganpu tea extract were similar to that of the PC group, which were significantly shorter than that of the NC group ($p < 0.05$). Meanwhile, high oral dose group (0.4 g/kg) recorded an immobility time of only 26.6 s, which was significantly shorter than that of the NC group ($p < 0.01$).

The significantly reduced immobility duration of the high oral dose group (0.4 g/kg) as compared to that of the NC group ($p < 0.01$) in the FST and TST suggests that the Ganpu tea extract produced antidepressant-like effects or otherwise helps to alleviate the depressive symptoms in mice. The anti-depressive activity of Ganpu tea was likely the collective or

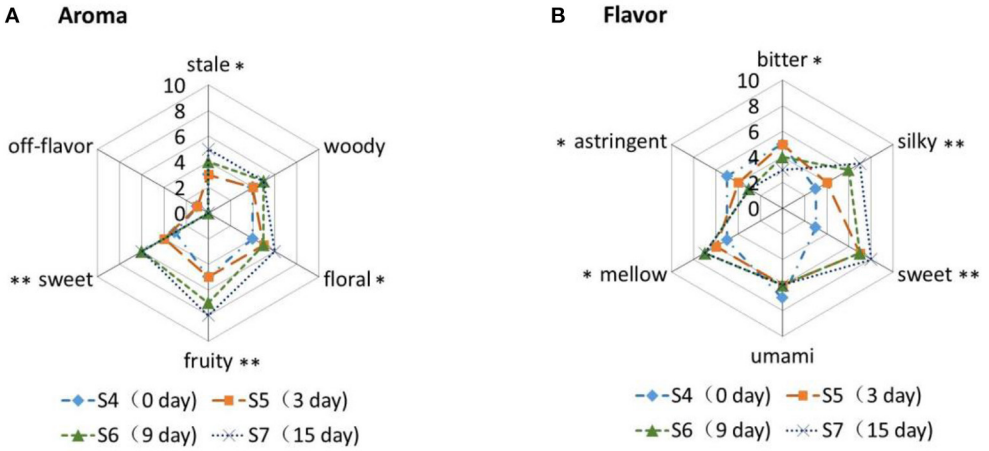

FIGURE 4 | Aroma and flavor profiles of Ganpu tea samples with different durations of sun-drying processing. The statistical analyses were performed using ANOVA, followed by LSD test (*$p < 0.05$, **$p < 0.01$).

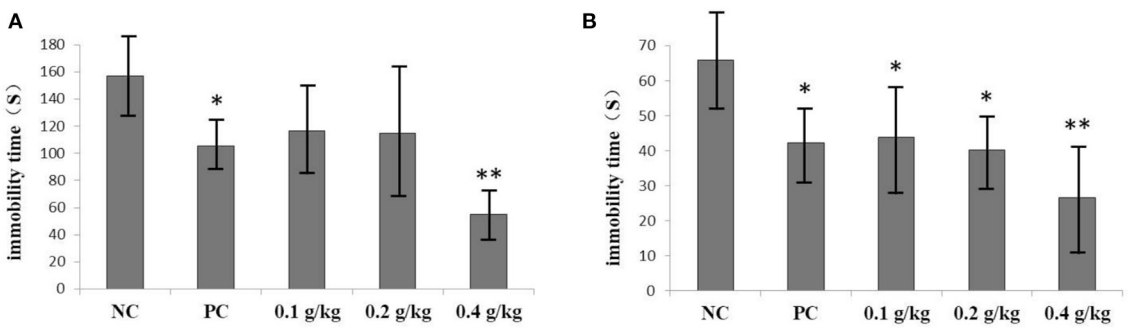

FIGURE 5 | Effects of Ganpu tea on the immobility duration of mice in the behavioral tests. **(A)** FST, and **(B)** TST. Data are expressed as mean ± SD ($n = 12$ mice per group). NC, normal control group; PC, clomipramine hydrochloride tablets group (0.02 g/kg). The statistical analyses were performed using ANOVA, followed by LSD test, *$p < 0.05$, **$p < 0.01$ as compared with that of the NC group.

synergistic result of numerous beneficial compounds present in the Ganpu tea extract. Tea polyphenols may be related to the amelioration of monoaminergic responses, antioxidant defenses, and the hypothalamic-pituitary-adrenal axis (35, 36). Flavonoids, such as quercetin, rutin, kaempferitrin, and hesperidin in Ganpu tea can attenuate the damaged monoamine neurotransmission, including that of serotonin, noradrenaline, dopamine, and 5-hydroxyindoleacetic acid, and regulate the expression levels of genes encoding neurotransmitter receptors (37). Anthocyanins were shown to regulate the activation of noradrenergic, serotonergic, and dopaminergic system (37). Caffeic acid was suggested to be active within the dopaminergic system (37). Theanine can also similarly mediate the interactions within monoaminergic systems (42). It is noteworthy that vitexin is a newly generated compound in the sun-drying processing, which was shown by Can et al. (43) to increase the catecholamine content in the synaptic cleft and to interact with serotonergic 1A, noradrenergic a2, and dopaminergic D1, D2, and D3 receptors. Further studies are necessary to determine whether other compounds in Ganpu tea are also responsible for conferring the antidepressant-like effects, and what are the underlying molecular mechanisms.

CONCLUSIONS

In the present study, we demonstrated that acquirement of the unique characteristics of high-quality Ganpu tea requires not only high-grade Pu-erh raw tea and mandarin peel, but also a full sun-drying processing for consecutive 15 days. The distinctive flavor of Ganpu tea was composed of a total of 104 water-soluble compounds, which were transformed considerably during sun-drying processing due to endogenous factors (biosynthesis or enzymatic modification of compounds within cells), as well as exogenous stimuli, including temperature, humidity, light, and microorganisms. The alterations in major chemical constituents contribute to the changes of aroma and taste of Ganpu tea. Meanwhile, tea polyphenols, flavonoids, pigments, theanine, caffeic acid, and vitexin may be also collectively responsible for the antidepressant-like effects of Ganpu tea

consumption. These findings provide a basis or understanding the chemical characteristics and health-promoting effects of Ganpu tea, and also for elucidating its value as a new flavorful beverage with potential benefit for humans suffering from the depressive symptoms.

DATA AVAILABILITY STATEMENT

The raw data supporting the conclusions of this article will be made available by the authors, without undue reservation.

ETHICS STATEMENT

All the procedures were conducted according to the National Institutes of Health Guide for the Care and Use of Laboratory Animals, and the animal handling and experimental procedures were approved by the Local Animal Use Committee (SCXK 2013-0020).

AUTHOR CONTRIBUTIONS

SX and XZ designed the concept of this study. SX, JH, HL, YZ, and DL drafted methodology and conducted formal analyses and investigation. HX and YH were project supervisors. Writing-Review and Editing were completed by HX, SX, JH, and YH. Funding Acquisition was by XZ. All authors contributed to the article and approved the submitted version.

FUNDING

This work was financially supported by the Guangdong Agricultural Science and Technology Innovation and Promotion Project (No. 2019LM1117), and Project of Strengthening Guangdong Province with Traditional Chinese Medicine (No. 20201248).

REFERENCES

1. Zhang L. The establishment of "industry standards" for the citrus Pu-erh tea has become a pressing task, China cooperation times (2017) 3:1–2.
2. Londono-Londono J, Lima VRD, Lara O, Gil A, Pasa TBC, Arango GJ, et al. Clean recovery of antioxidant flavonoids from citrus peel: optimizing an aqueous ultrasound-assisted extraction method. *Food Chem.* (2010) 119:81–7. doi: 10.1016/j.foodchem.2009.05.075
3. Zhang H, Cui J, Tian G, DiMarco-Crook C, Gao W, Zhao C, et al. Efficiency of four different dietary preparation methods in extracting functional compounds from dried tangerine peel. *Food Chem.* (2019) 289:340–50. doi: 10.1016/j.foodchem.2019.03.063
4. Lv HP, Zhang YJ, Lin Z, Liang YR. Processing and chemical constituents of Pu-erh tea: a review. *Food Res Int.* (2013) 53:608–18. doi: 10.1016/j.foodres.2013.02.043
5. Ahmed S, Unachukwu U, Stepp JR, Peters CM, Long C, Kennelly E. Pu-erh tea tasting in Yunnan, China: correlation of drinkers' perceptions to phytochemistry. *J Ethnopharmacol.* (2010) 132:176–85. doi: 10.1016/j.jep.2010.08.016
6. Wang T, Li X, Yang H, Wang F, Kong J, Qiu D, et al. Mass spectrometry-based metabolomics and chemometric analysis of Pu-erh teas of various origins. *Food Chem.* (2018) 268:271–8. doi: 10.1016/j.foodchem.2018.06.041
7. Musielak G, Kieca A. Influence of varying microwave power during microwave–vacuum drying on the drying time and quality of beetroot and carrot slices. *Dry Technol.* (2014) 32:1326–33. doi: 10.1080/07373937.2014.924135
8. Pei F, Yang WJ, Shi Y, Sun Y, Mariga AM, Zhao LY, et al. Comparison of freeze-drying with three different combinations of drying methods and their influence on colour, texture, microstructure and nutrient retention of button mushroom (*Agaricus bisporus*) slices. *Food Bioprocess Technol.* (2014) 7:702–10. doi: 10.1007/s11947-013-1058-z
9. Xu M, Tian G, Zhao C, Aftab A, Zhang H, Bi J, et al. Infrared drying as a quick preparation method for dried tangerine peel. *Int J Anal Chem.* (2017) 2017:1–11. doi: 10.1155/2017/6254793
10. Abdel-Aziz MM, Emam TM, Elsherbiny EA. Effects of mandarin (*Citrus reticulata*) peel essential oil as a natural antibiofilm agent against *Aspergillus niger* in onion bulbs. *Postharvest Biol Technol.* (2019) 156:110959. doi: 10.1016/j.postharvbio.2019.110959
11. Foo KY, Lee LK. Recent advances on the beneficial use and health implications of Pu-Erh tea. *Food Res Int.* (2013) 53:619–28. doi: 10.1016/j.foodres.2013.02.036
12. Hang X, Yang CS, Li S, Jin H, Patel T. Monodemethylated polymethoxyflavones from sweet orange (*Citrus sinensis*) peel inhibit growth of human lung cancer cells by apoptosis. *Mol Nutr Food Res.* (2009) 53:398–406. doi: 10.1002/mnfr.200800057
13. Randazzo W, Jiménez-Belenguer A, Settanni L, Perdones A, Moschetti M, Palazzolo E, et al. Antilisterial effect of citrus essential oils and their performance inedible film formulations. *Food Control.* (2016) 59:750–8. doi: 10.1016/j.foodcont.2015.06.057
14. Xiao S, Yu L-A, Lai H-Q, Cheng C, Liang D-H, Huang Y-H. Anslysis of specific aroma components in citrus Pu-erh tea by GC-MS. *Modern Food Sci Technol.* (2019) 35:1–12. doi: 10.13982/j.mfst.1673-9078.2019.11.034
15. Teng J, Zhou W, Zeng Z, Zhao W, Huang Y, Zhang X. Quality components and antidepressant-like effects of GABA green tea. *Food Funct.* (2017) 8:3311–8. doi: 10.1039/C7FO01045A
16. Kraujalyte V, Pelvan E, Alasalvar C. Volatile compounds and sensory characteristics of various instant teas produced from black tea. *Food Chem.* (2016) 194:864–72. doi: 10.1016/j.foodchem.2015.08.051
17. Lino-De-Oliveira C, Lima TCMD, Carobrez ADP. Structure of the rat behaviour in the forced swimming test. *Behav Brain Res.* (2005) 158:243–50. doi: 10.1016/j.bbr.2004.09.004
18. Steru L. The tail suspension test: a new method for screening antidepressants in mice. *Psychopharmacology.* (1985) 85:367. doi: 10.1007/BF00428203
19. Bosiljkov T, Karlović S, Brnčić M, JeŽek D, Dujmić F, Tripalo B. Extraction of bioactive compounds from tangerine peels, Eubis Cost Action, Citrus Waste Valorisation (2015) 8:23.
20. Monbaliu S, Wu A, Zhang D, Peteghem CV, Saeger SD. Multimycotoxin UPLC-MS/MS for tea, herbal infusions and the derived drinkable products. *J Agric Food Chem.* (2010) 58:12664–71. doi: 10.1021/jf1033043
21. Pongsuwan W, Bamba T, Harada K, Yonetani T, Kobayashi A, Fukusaki E. High-throughput technique for comprehensive analysis of Japanese green tea quality assessment using ultra-performance liquid chromatography with time-of-flight mass spectrometry (UPLC/TOF MS). *J Agric Food Chem.* (2008) 56:10705–8. doi: 10.1021/jf8018003
22. Yi LZ, Yuan DL, Liang YZ, Xie PS, Zhao Y. Fingerprinting alterations of secondary metabolites of tangerine peels during growth by HPLC–DAD and chemometric methods. *Anal Chim Acta.* (2009) 649:43–51. doi: 10.1016/j.aca.2009.07.009
23. Zhao Y, Chen P, Lin L, Harnly JM, Yu LL, Li Z. Tentative identification, quantitation, and principal component analysis of green pu-erh, green, and white teas using UPLC/DAD/MS. *Food Chem.* (2011) 126:1269–77. doi: 10.1016/j.foodchem.2010.11.055
24. Zhang H, Yang YF, Zhou ZQ. Phenolic and flavonoid contents of mandarin (*Citrus reticulata* Blanco) fruit tissues and their antioxidant capacity as

evaluated by DPPH and ABTS methods. *J Integr Agric.* (2018) 17:256–63. doi: 10.1016/S2095-3119(17)61664-2
25. Tumbas V, Cetkovic G, Djilas S, Canadanovic-Brunet J, Vulic J, Knez Z, et al. Antioxidant activity of mandarin (*Citrus reticulata*) peel. *J Integr Agric.* (2010) 41:256–63. doi: 10.2298/APT1041195T
26. Wang K, Ruan J. Analysis of chemical components in green tea in relation with perceived quality, a case study with Longjing teas. *Food Sci Technol.* (2009) 44:2476–84. doi: 10.1111/j.1365-2621.2009.02040.x
27. Ku KM, Kim J, Park HJ, Liu KH, Lee CH. Application of metabolomics in the analysis of manufacturing type of Pu-erh tea and composition changes with different postfermentation year. *J Agric Food Chem.* (2010) 58:345–52. doi: 10.1021/jf902818c
28. Manthey JA, Buslig BS. Flavonoids in the living system. *Q Rev Biol.* (1998) 439:1–7. doi: 10.1007/978-1-4615-5335-9_1
29. Xiao W, Li F, Zhang H, Geng Y, Yuan J, Jiang T. Preparative isolation and purification of polymethoxylated flavones from Tangerine peel using high-speed counter-current chromatography. *J Chromatogr A.* (2005) 1090:188–92. doi: 10.1016/j.chroma.2005.07.023
30. Yang Y, Zhao XJ, Pan Y, Zhou Z. Identification of the chemical compositions of Ponkan peel by ultra performance liquid chromatography coupled with quadrupole time-of-flight mass spectrometry. *Anal Methods.* (2016) 8:893–903. doi: 10.1039/C5AY02633D
31. Du L, Wang C, Zhang C, Ma L, Xu Y, Xiao D. Characterization of the volatile and sensory profile of instant Pu-erh tea using GC × GC-TOFMS and descriptive sensory analysis. *Microchem J.* (2019) 146:986–96. doi: 10.1016/j.microc.2019.02.036
32. Alasalvar C, Topal B, Serpen A, Bahar B, Pelvan E, Gökmen V. Flavor characteristics of seven grades of black tea produced in Turkey. *J Agric Food Chem.* (2012) 60:6323–32. doi: 10.1021/jf301498p
33. Wang ZH, Yue CN Tong HR. Analysis of taste characteristics and identification of key chemical components of fifteen Chinese yellow tea samples. *J Food Sci Technol.* (2020) 58:1378–88. doi: 10.1007/s13197-020-04649-2
34. Rothenberg DO, Zhang LY. Mechanisms underlying the anti-depressive effects of regular tea consumption. *Nutrients.* (2019) 11:1361. doi: 10.3390/nu11061361
35. Liu Y, Jia G, Gou L, Sun L, Yin X. Antidepressant-like effects of tea polyphenols on mouse model of chronic unpredictable mild stress. *Pharmacol Biochem Behav.* (2013) 104:27–32. doi: 10.1016/j.pbb.2012.12.024
36. Zhu WL, Shi HS, Wei YM, Wang SJ, Sun CY, Ding ZB, et al. Green tea polyphenols produce antidepressant-like effects in adult mice. *Pharmacol Res.* (2012) 65:74–80. doi: 10.1016/j.phrs.2011.09.007
37. Guan LP, Liu BY. Antidepressant-like effects and mechanisms of flavonoids and related analogues. *Eur J Med Chem.* (2016) 121:47–57. doi: 10.1016/j.ejmech.2016.05.026
38. Wang K, Liu F, Liu Z, Huang J, Xu Z, Li Y, et al. Analysis of chemical components in oolong tea in relation to perceived quality %. *J Int Food Sci Technol.* (2010) 45:913–20. doi: 10.1111/j.1365-2621.2010.02224.x
39. Zhang L, Li N, Ma Z-Z, Tu P-F. Comparison of the chemical constituents of aged pu-erh tea, ripened Pu-erh tea, and other teas using HPLC-DAD-ESI-MSn. *J Agric Food Chem.* (2011) 59:8754–60. doi: 10.1021/jf2015733
40. Zhao M, Ma Y, Wei Z-Z, Yuan W-X, Li Y-L, Zhang C-H, et al. Determination and comparison of γ-aminobutyric Acid (GABA) content in Pu-erh and other types of Chinese tea. *J Agric Food Chem.* (2011) 59:3641–8. doi: 10.1021/jf104601v
41. Min JK, John KMM, Choi JN, Lee S, Kim AJ, Kim YM, et al. Changes in secondary metabolites of green tea during fermentation by *Aspergillus oryzae* and its effect on antioxidant potential. *Food Res Int.* (2013) 53:670–7. doi: 10.1016/j.foodres.2012.12.053
42. Yin C, Gou L, Liu Y, Yin X, Zhang L, Jia G, et al. Antidepressant-like effects of L-theanine in the forced swim and tail suspension tests in mice. *Phytother Res.* (2011) 25:1636–9. doi: 10.1002/ptr.3456
43. Can ÖD, Demir Özkay Ü, Üçel UI. Anti-depressant-like effect of vitexin in BALB/c mice and evidence for the involvement of monoaminergic mechanisms. *Eur J Pharmacol.* (2013) 699:250–7. doi: 10.1016/j.ejphar.2012.10.017

Conflict of Interest: HL, YZ, and DL were employed by Yunding Ganpu Tea Company.

The remaining authors declare that the research was conducted in the absence of any conflict of interest.

frontiers in Nutrition

ORIGINAL RESEARCH
published: 31 March 2021
doi: 10.3389/fnut.2021.647782

Effect of Enzymatic Hydrolysis on the Zinc Binding Capacity and *in vitro* Gastrointestinal Stability of Peptides Derived From Pumpkin (*Cucurbita pepo L.*) Seeds

Dan Lu[1], *Mengyao Peng*[1], *Min Yu*[1], *Bo Jiang*[1], *Hong Wu*[2] *and Jingjing Chen*[1]*

[1] State Key Laboratory of Food Science and Technology, Jiangnan University, Wuxi, China, [2] Key Laboratory of Agro-Products Processing, Institute of Agro-Products Processing Science and Technology, Xinjiang Academy of Agricultural and Reclamation Science, Shihezi, China

Zinc is a crucial micronutrient for maintaining body immune system and metabolism function. However, insufficient intake from diet may lead to zinc deficiency and impair normal body function. In addition, conventional zinc salts supplementation has the disadvantage of low bioavailability since the zinc ions may be easily chelated by dietary fiber or phytate commonly found in diets rich in plants, and form precipitates that cannot be absorbed. Therefore, the objective of the present study is to prepare pumpkin seed derived peptides and to evaluate the effect of structure and surface properties on the zinc binding behavior of the pumpkin seed protein hydrolysate (PSPH), as well as their gastrointestinal stability. Briefly, different PSPHs were prepared using enzymatic hydrolysis method with bromelain, papain, flavourzyme, alcalase, and pepsin. The particle size, zeta potential, surface hydrophobicity, degree of hydrolysis, ATR-FTIR spectra, and zinc binding capacity were determined. The representative samples were chosen to characterize the binding energy and surface morphology of PSPH-Zn. At last, the *in vitro* gastrointestinal stability of PSPH and PSPH-Zn were evaluated. Our results showed that peptides hydrolyzed by papain had the largest average molecular weight, smallest particle size, highest hydrophobicity, and the greatest zinc binding capacity. Zinc showed better gastrointestinal stability in PSPHs chelates than in its salt. Meanwhile, PSPH-Zn with higher zinc binding capacity showed better stability. The result of this study indicated pumpkin seed hydrolyzed by papain may be used as a potential source for zinc fortification. The findings in this study may provide important implications for developing plant-based zinc chelating peptides.

Keywords: pumpkin seed protein, peptides, chelating, zinc, gastrointestinal stability

OPEN ACCESS

Edited by:
Jinkai Zheng,
Chinese Academy of Agricultural Sciences (CAAS), China

Reviewed by:
Lijun You,
South China University of Technology, China
Ahmed A. Zaky,
National Research Centre, Egypt

***Correspondence:**
Jingjing Chen
jingjinc@jiangnan.edu.cn

Specialty section:
This article was submitted to Food Chemistry, a section of the journal Frontiers in Nutrition

Received: *30 December 2020*
Accepted: *23 February 2021*
Published: *31 March 2021*

Citation:
Lu D, Peng M, Yu M, Jiang B, Wu H and Chen J (2021) Effect of Enzymatic Hydrolysis on the Zinc Binding Capacity and in vitro Gastrointestinal Stability of Peptides Derived From Pumpkin (Cucurbita pepo L.) Seeds. Front. Nutr. 8:647782. doi: 10.3389/fnut.2021.647782

INTRODUCTION

Zinc, as one of the essential micronutrients with important structural, immune, and regulatory functions, contributes to the synthesis of the over 300 enzymes in the human body (1). A recent study found individuals with zinc deficiency may have higher COVID-19 infection risk (2). In addition, zinc plays a crucial role in the growth of infants, children, and adolescents. Zinc

deficiency has a negative effect on growth retardation, anemia, and neuronal dysfunctions (3). Zinc deficiency is still quite common nowadays. It has been reported that about 4 to 73% of people in different countries still suffer from zinc deficiency, which may affect as many as two billion people worldwide (3).

Low dietary zinc intake and high loss of zinc during absorption can result in zinc deficiency, and may increase the risk of alopecia and skin rash (4). For this reason, different types of zinc supplements have been developed. In earlier years, zinc salts including zinc sulfate and zinc gluconate have been used as a zinc fortifier. However, phytate, a strong zinc chelator commonly existing in human diets, may form the insoluble complexes with zinc that cannot be absorbed (5). In the meantime, due to the lack of phytate-hydrolyzing enzyme, zinc could not be absorbed in the gastrointestinal tract. Furthermore, other minerals such as iron, calcium, and copper in food would compete for the non-specific divalent mineral transporters, affecting zinc absorption (6). Zinc salts supplements often have unpleasant metallic off-flavor, therefore compromising consumer acceptability.

The bioaccessibility and bioavailability of zinc are immensely affected by dietary zinc intake and absorption. Compared with inorganic zinc salts, amino acids or peptide binding can protect zinc from forming complexes with other dietary inhibitors, which will increase the digestion stability of zinc in the gastrointestinal tract and finally improving its bioavailability (4). Studies have showed that bioavailability of zinc is higher for zinc-peptide complexes than its inorganic counterparts (7). In recent years, zinc chelating peptide has been prepared from different protein sources, such as dairy (8), wheat germ protein (9), hemp (10), walnut (11), sesame (12), rapeseed (13), as well as sea cucumber (14), silver carp (15), octopus scraps (16), and tilapia bone (17).

Pumpkin (*Cucurbita pepo L.*) seed is a good source of protein (30–40%) (18). According to FAO/WHO, pumpkin seed protein is rich in all essential amino acids. It is a good source of valine, histidine, isoleucine, leucine, threonine, and methionine (19). In addition, pumpkin seeds have been recommended as a good source for obtaining dietary zinc by the World Health Organization (20). The literature findings have consistently shown that the total amount of Zn found in pumpkin seeds is about 91.2 $\mu g \cdot g^{-1}$ (20, 21). We therefore would like to explore whether the unique composition of pumpkin seed protein also makes it a good source for zinc-chelating peptides.

In this study, pumpkin seed proteins were hydrolysated by five different emzymes to prepare zinc-chelating peptides. Further, the surface hydrophobicity, zeta potential, particle size, molecular weight distribution, and amino acid composition of hydrolysis were characterized. Meanwhile, the complex of zinc and peptide were characterized by SEM, XPS, and FT-IR. The *in vitro* gastrointestianl stability of zinc was then evaluated using simulated gastrointestinal digestion. The findings of this study would be of prime importance for the utilization of pumpkin seed protein to fabrication zinc-chelating peptides, which may be used as a functional food ingredient or used in plant-based food to realize the fortification of zinc.

MATERIALS AND METHODS

Materials

Pumpkin seeds (*Cucurbita pepo L.*) were provided by Haichuansanxin Food Company (Beitun, China). Alcalase (≥200 U/mg) was purchased by Hefei Bomei Biotechnology Co., Ltd. (Hefei, China). Papain (>200 units/mg) and flavourzyme (30,000 units/g) were purchased from Solarbio Life Science (Beijing, China). Bromelain (3,000–7,000 U/mg), pepsin (1,200 U/g), pancreatin (≥4,000U/g), trypsin (≥50,000U/g), and bile salt and o-Phthalaldehyde (OPA) and dithiothreitol (DTT) were purchased from Sangon Biotech (Shanghai, China). In addition, 8-Anilino-1-naphthalenesulfonic acid (ANS) [≥97% (HPLC)] was purchased from Sigma-Aldrich. Sodium dodecyl sulfate (SDS) and L-Serine (≥BR) were purchased from Sinopharm Chemical Reagent Co., Ltd. Zinc sulfate heptahydrate, sodium hydroxide, nitric acid, n-hexane, ethyl alcohol, and other reagents were of analytical grade and purchased from Chemical Reagent Co., Ltd. (Shanghai, China). Dialysis bags (MD34-500) were purchased from Wuxi Hengkang Medical Technology Co., Ltd.

Preparation of Samples

Preparation of Pumpkin Seed Protein

The pumpkin seeds were ground into flour using a YF-1000 blender (Yongli Pharmaceutical Mechanic, Zhejiang, China). Ten volumes of hexane (w/v) were added to pumpkin seed flour to remove fat. After stirring for 2 h, the hexane was removed. This process was repeated three times to ensure complete removal of fat. The defatted pumpkin seed flour was dispersed in deionized water (w/v:1/10) and adjusted pH 10 with 1 M NaOH. Then the mixture was stirred gently for 30 min and centrifuged at 4°C and 10,000 g for 20 min. The supernatant was collected and then filtered with a filter paper. The protein dissolved in the filtrate was sedimented by adjusting pH to 5.00 with 1 M HCl. The precipitation was washed with deionized water, centrifuged at 10,000 g for 20 min to remove possible impurities. The pH of the protein was adjusted to 7 using NaOH. Then it was frozen-dried to obtain pumpkin seed protein powder. The powder was stored in −20°C for further use.

Preparation of Pumpkin Seed Protein Hydrolysates

The pumpkin seed protein powder was dissolved in deionized water (4%, w/w). Pumpkin seed protein solution was boiled in a water bath for 15 min to inactivate endogenous enzymes. After cooling, the pH was adjusted with 1 M NaOH or 1 M HCl for enzymatic hydrolysis. Thereafter, the solutions were hydrolyzed with bromelain (pH 6.5, 37°C), alcalase (pH 8.0, 50°C), papain, flavourzyme (pH 7.0, 55°C), papain (pH 7.0, 55°C), and trypsin (pH 7.5, 37°C) (2% enzyme to substrate ratio, w/w) for 3 h. Each protein solution was placed in a conical flask with sealing membrane and was hydrolyzed in constant-temperature shaker water bath using the water-bathing Constant Temperature Vibrator (THZ-82, Changzhou Guohua Electric Appliance Co. Ltd). After the enzymatic hydrolysis, the enzyme was deactivated by heating in a boiling water bath for 15 min and cooled to room temperature. The pH was adjusted to 7 by 1 M

NaOH or 1 M HCl and centrifuged at 10,000 g for 15 min. The precipitation was discarded, and the supernatant was retained. The supernatant was filtered and freeze dried. Then the pumpkin seed protein hydrolysate (PSPH) was obtained and stored in a −20°C freezer for later use.

Preparation of PSPH-Zn

Peptide-zinc complexes were prepared in reference to previous methods with some modifications (10). PSPHs were respectively dissolved in the deionized water at the concentration of 20 mg/ml. Then, 100 mM zinc sulfate solution was dripped into the peptide solution slowly to make the final concentration of peptide: zinc to 1:1 (g: mmol), and the mixtures were incubated in 60°C water shaking bath for 60 min. After that, ethanol was added into the incubates until the ethanol concentration was up to 80% to precipitate peptides and peptide-zinc (II) complexes. Left to stand for 60 min at room temperature, the intermixture was centrifuged at 10,000 g for 10 min to get the centrifugal precipitates. The white precipitates were washed three times with 80% ethanol to remove the unbound zinc. Finally, the peptide–zinc (II) complexes were collected and prepared for freeze-dried structure characterization.

Characterization of PSPH and PSPH-Zn

Degree of Hydrolysis

The degree of hydrolysis (DH) of PSPHs were determined using the o-Phthalaldehyde (OPA) method described by Nielsen et al. (22). The PSPH was dissolved in deionized water, and the 400 μl sample solutions was mixed with 3 ml OPA-reagents for 2 min precisely. Then the optical density (OD) was measured at 340 nm using an UV-Visible Spectrophotometer (MAPADA P7, Shanghai, China). Double distilled water was used as blank. The degree of hydrolysis was calculated using the following equations:

$$Serine\ NH_2 = \frac{OD_{sample} - OD_{blank}}{OD_{standard} - OD_{blank}} * \frac{0.9516 meqv}{L} * \frac{d}{c}$$

where serine-NH_2 represents meqv serine NH_2/g protein, OD_{sample} was the absorbance of each sample, the $OD_{standard}$ was the absorbance of serine standard, *d* was dilution factor, and c was protein content of pumpkin seed.

$$DH\ (\%) = \frac{h}{h_{tot}} * 100\% = \frac{\frac{Serine\ NH_2 * \beta}{\alpha}}{h_{tot}} * 100\%$$

where h was number of hydrolyzed peptide bonds, $\alpha = 1$, $\beta = 0.4$, h_{tot} is the total number of peptide bonds in the protein substrate (meqv/g protein).

Molecular Weight Distribution

The molecular weight distribution of PSPHs was determined by gel permeation chromatography (GPC) using a high performance liquid chromatography (HPLC) system (Agilent 1100, Agilent Technologies Inc., Germany). Chromatographic column: TSK gel SWXL 300 mm × 7.8 nm; 2 ml sample solution was added into a 10 mL volumetric flask, acetonitrile/water/trifluoroacetic acid (45/55/0.1: v/v/v) solution was added to bring the volume to 10 ml. The solution was then filtered and analyzed on the HPLC. The flow rate was 0.5 ml/min. The temperature of the column was 30°C and the sample was detected at 220 nm.

Zeta Potential and Average Particle Diameter Analysis

Dried PSPH (0.5%, w/v) was dissolved in deionized water and diluted 10 times for measurement. The mean particle diameter and zeta potential of PSPHs were determined using a Zetasizer (Nano-ZS, Malvern Instruments Ltd., Malvern, UK).

Surface Hydrophobicity

The surface hydrophobicity of PSPHs was analyzed using 8-Anilino-1-naphthalenesulfonic acid (ANS) as fluorescent probe. PSPH was dissolved (0.05%, w/v) in phosphate buffer (10 mM, pH 7.0). Each protein dispersion was diluted with phosphate buffer to obtain serial protein concentrations of 0.005 to 0.025% (w/v). Then, 20 μl ANS solution (8.0 mmol/L) was added into 4 ml protein solution and mixed thoroughly. The samples were measured using a Hitachi F-7000 fluorescence spectrophotometer (Hitachi Lt., Tokyo, Japan). The excitation wavelength was 390 nm and an emission wavelength was 470 nm. The fluorescence intensity was plotted on the ordinate and the protein concentration was used to the abscissa. The initial slope was used as an index of protein hydrophobicity (H_0).

Amino Acid Composition Analysis

The amino acid composition was determined in reference to reported methods (23). Dried PSPH was digested using 6 M HCl at 110°C for 24 h under nitrogen atmosphere. The composition of amino acid was measured by Sykam S433D automatic amino acid analyzer (Munich, Germany).

Zinc Binding Capacity

Zinc binding capacity was calculated according to the method published by Wang (10). The samples were digested in nitric acid using a hot plate at 150°C for 2 h and 180°C for 1 h until smoke was observed. After cooling, the digestion solution was transferred into a 10 ml or 25 ml volumetric flask and brought to volume with H_2O. After further dilution of 1,000 to 2,000-fold, the content of Zn^{2+} was measured using atomic absorption method (Atomic Absorption Spectrometer, Thermo Fisher Scientific). Zinc binding capacity was calculated as described previously using the following formula:

$$Zinc\ binding\ capacity\ (\%) = \frac{The\ amount\ of\ Zn^{2+}\ in\ the\ complex\ (mg)}{The\ amount\ of\ Zn^{2+}\ added\ (mg)} * 100\%$$

Attenuated Total Reflection Fourier Transform Infrared Spectroscopy (ATR-FTIR)

The ATR-FTIR spectra of PSPHs (PSPH-Bro, PSPH-Alc, PSPH-Fla, PSPH-Pap, PSPH-Try) were determined using a Nicolet

iS10 FTIR spectrophotometer (Thermo Fisher Scientific Corp., Waltham, USA). Each sample was placed on the crystal and the data was collected. The ATR-FTIR spectra was scanned 16 times with a spectral resolution of 2 cm^{-1} and recorded at the wavenumbers between 4,000 to 400 cm^{-1}. The data was processed with the OMNIC software (Thermo Fisher Scientific Inc., OMNIC 9.2.86).

Morphology of PSPH and PSPH-Zn Complexes

A scanning electron microscopy (SEM, S-4800, Hitachi Science Systems, Ltd., Tokyo, Japan) was used to observe detailed surface morphology of representative PSPH and PSPH-Zn complex. The powders were glutted on the plate, respectively, sprayed with gold, and then observed using the SEM at an accelerating potential of 5 kV.

X-Ray Photoelectron Spectroscopy Spectra of PSPH and PSPH-Zn Complexes

X-ray photoelectron spectroscopy measurements of representative PSPH and PSPH-Zn were carried out with an AXIS Supra by Kratos Analytical Inc. (Wharfside, Manchester, UK). The monochromatized Al Ka radiation (hv = 1,486.6 eV, 225 W) was used as an X-ray source. The base pressure is 10^{-9} torr. A pass energy of 160 eV and a 1 eV step size was used to obtain survey scan spectra. A pass energy of 40 eV and a 0.1 eV step size was used to obtain narrow region scans. The analyzed area of all XPS spectra was 300 × 700 μm^2. A charge neutralizer was used throughout as the

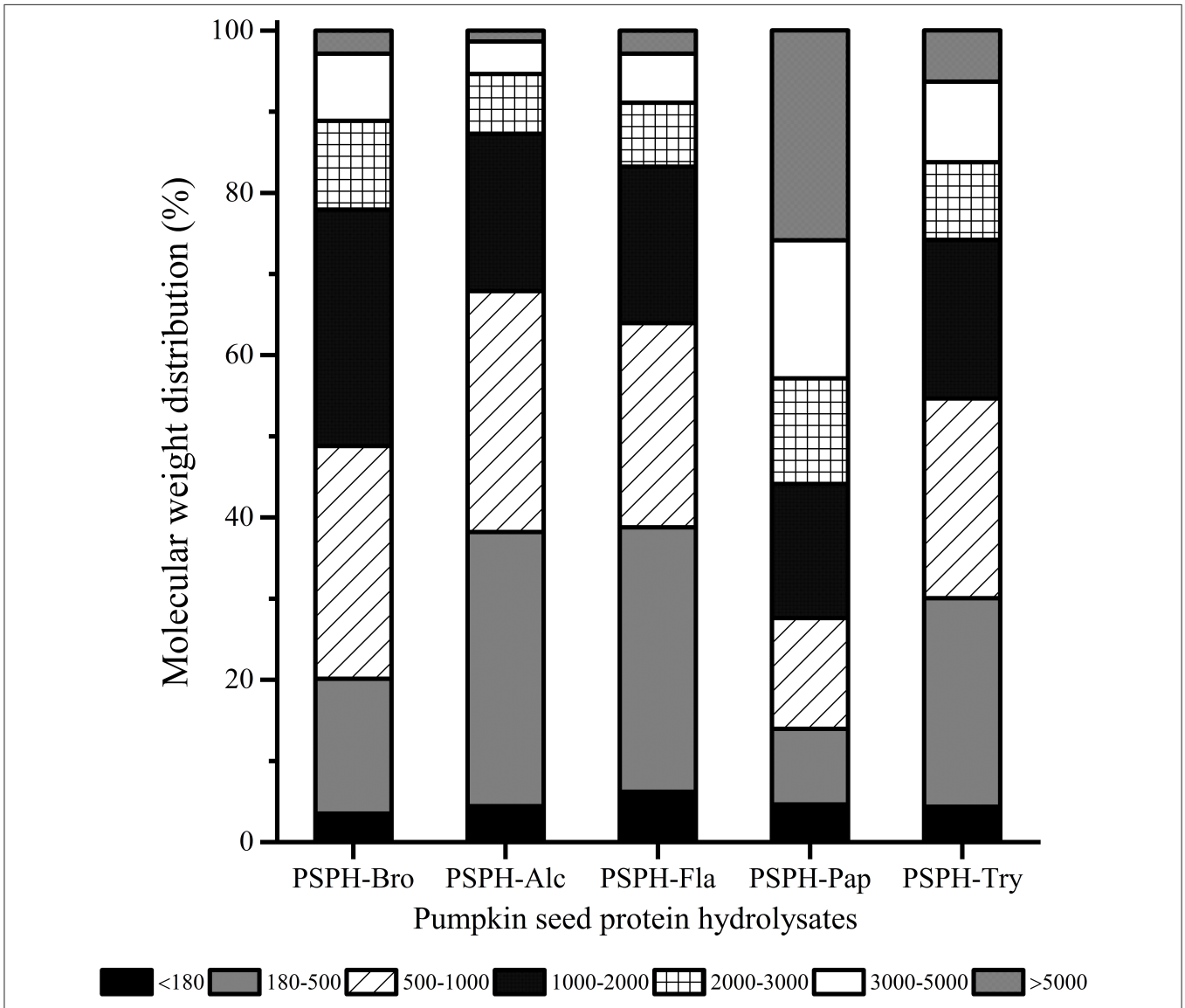

FIGURE 1 | Molecular weight distribution of pumpkin seed protein hydrolysates produced with bromelain (PSPH-Bro), alcalase (PSPH-Alc), flavourzyme (PSPH-Fla), papain (PSPH-Pap), trypsin (PSPH-Try) after hydrolysis 3 h in a 2% (w/w) enzyme to substrate ratio.

samples were mounted so that they were electrically isolated from the sample bar. All spectrums were calibrated using C 1s (284.8 eV).

Gastrointestinal Stability of PSPH and PSPH-Zn

The gastrointestinal stabilities of PSPH and PSPH-Zn were determined using the methods reported by Udechukwu et al. (8) and Liao et al. (17) with some modifications. Briefly, the simulated gastric juice was prepared by pepsin in 0.1 M hydrochloric acid. And the pancreatin and bile salts were dissolved in 0.1 M $NaHCO_3$ solution to prepare simulated intestinal juice. First, the PSPH-Zn complexes were dissolved in Milli-Q water and incubated with simulated gastric juice at pH 2.0 and 37°C for 30 min in the linear shaking bath. The pepsin-substrate ratio was 1:100 (w/w). After incubation, a part of gastric digests was withdrawn and heated for 10 min in boiling water to inactivate enzymes. Then, the solutions were dialyzed in dialysis bags (molecular weight: 34–500 Da) for 6 h. Thereafter, the contents of zinc in dialysis bags were measured by atomic absorption spectrometry. Another portion of the digests were adjusted the pH to 7.5 with 1 M NaOH and continuously reacted with intestinal juice maintained the pH at 37°C for 3 h. The intestinal digests were treated with the same operation as the gastric digests. Meantime, the PSPH were used as the control. The zinc stability (%) was expressed as the percentage of the total zinc retained after dialysis.

Statistical Analysis

The experimental results were expressed in the form of mean ± standard deviation (Means± SD). The statistical analysis was conducted using the software (IBM SPSS statistic 22). One-way variance analysis ANOVA followed by Duncan's multiple comparison test was used to detect the difference between the mean values, and the $P < 0.05$ was considered as significantly different.

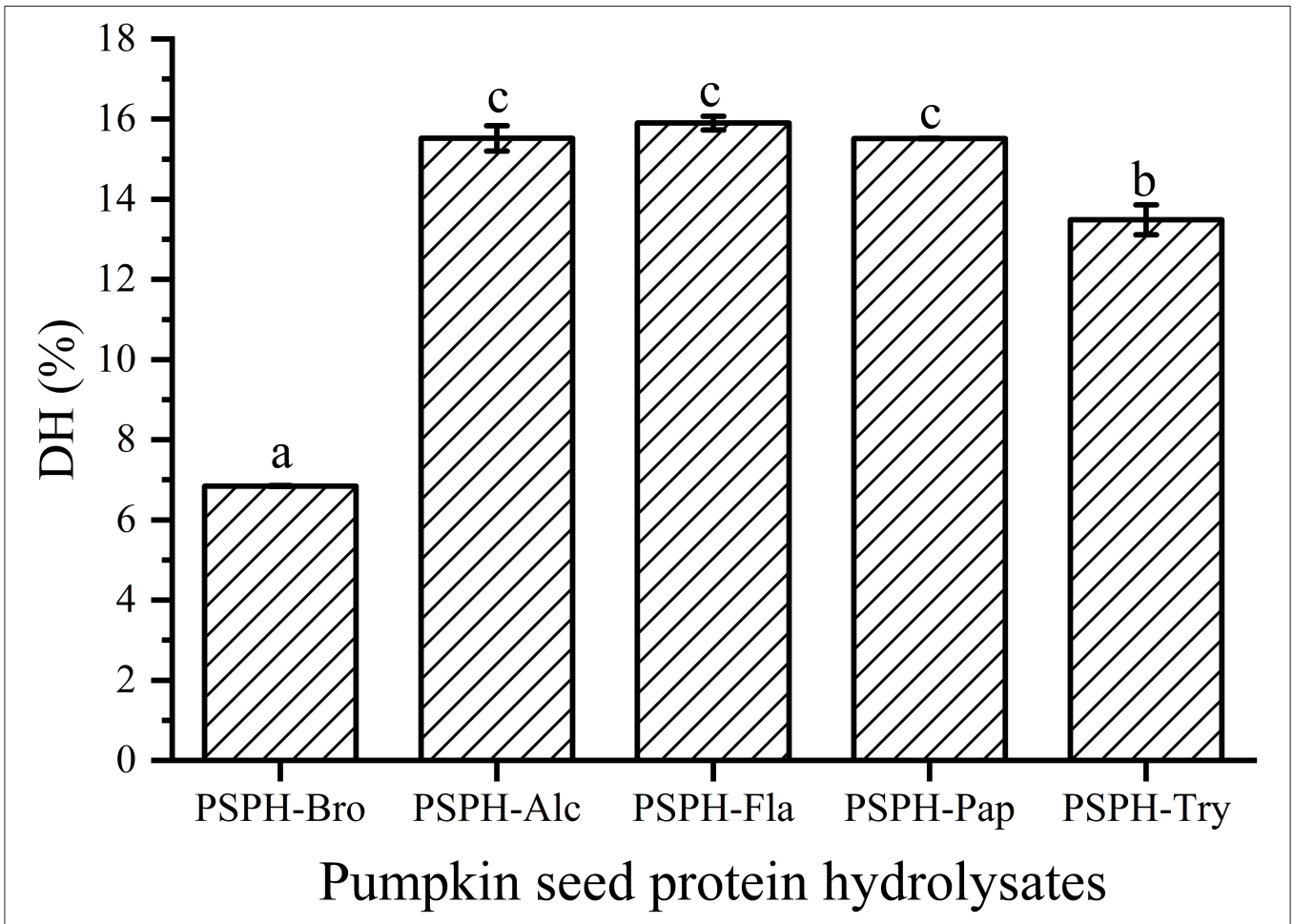

FIGURE 2 | Degree of hydrolysis (DH) of pumpkin seed protein hydrolysates produced with bromelain (PSPH-Bro), alcalase (PSPH-Alc), flavourzyme (PSPH-Fla), papain (PSPH-Pap), trypsin (PSPH-Try) after hydrolysis 3 h in a 2% (w/w) enzyme to substrate ratio. Different letters represent significantly different mean values with $P < 0.05$.

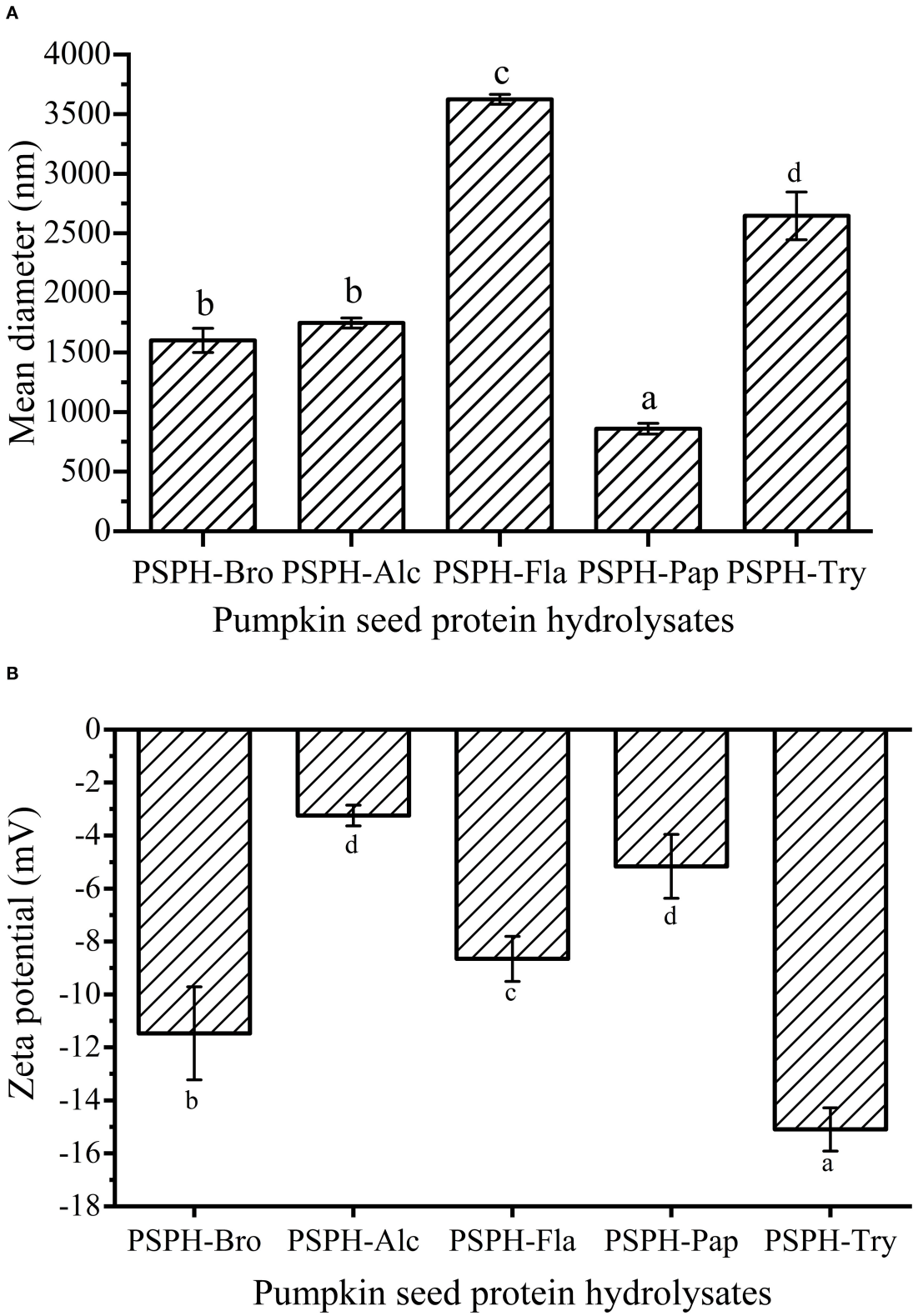

FIGURE 3 | Mean particle diameter **(A)** and Zeta potential **(B)** of pumpkin seed protein produced with bromelain (PSPH-Bro), alcalase (PSPH-Alc), flavourzyme (PSPH-Fla), papain (PSPH-Pap), trypsin (PSPH-Try) after hydrolysis 3 h in a 2% (w/w) enzyme to substrate ratio. Bars in each chart with different letters represent significantly different mean values with $P < 0.05$. Different letters represent significantly different mean values with $P < 0.05$.

RESULTS

Molecular Weight Distribution and Degree of Hydrolysis of PSPHs

The relationship between the molecular weight distribution of hydrolysates and their mental-binding properties was still not fully understood, which may differ when different peptides were derived from different sources. Chen at al. found that compared with other two peptides with different average molecular weights (P2: 2,745 Da, P3: 4,378 Da), peptide with low molecular weight (P1:1,653 Da) had stronger zinc chelation capacity and stability (24). In addition, chicken muscle peptides (>10 kDa) showed excellent chelation capacity with iron (25). The molecular weight distribution of different enzymatic hydrolysates at the same hydrolysis time (3 h) could be clearly seen from **Figure 1**. The profile of different molecular hydrolysates was divided into 6 groups (<180 Da, 180–500 Da, 500–1,000 Da, 1,000–2,000 Da, 2,000–3,000 Da, and >3,000 Da). The mean molecular weights of PSPH-Bro, PSPH-Alc, PSPH-Fla, PSPH-Pap, and PSPH-Try were 1,463 Da, 1,022 Da, 1,167 Da, 3,312 Da, and 1,582 Da, respectively. The molecular weight (Mw) of PSPH-Pap >3,000 Da accounted for more than 50%, while the percentage of molecular weight smaller than 1,000 Da was the lowest compared with other hydrolysates. And, from **Figure 5**, the PSPH-Pap has the highest zinc binding capacity compared with other hydrolysates. These results indicated that, for pumpkin seed peptides, high molecular hydrolysates can better bind with zinc ions.

DH was another factor affecting the amino acid components and sequences, which may further influence the zinc-binding capacity. There had been reports that the degree of hydrolysis was positively correlated with mental-binding capacity. Sun et al. (26) reported that sea cucumber (*Stichopus japonicus*) ovum hydrolysates produced with alcalase showed the best DH and the highest iron-binding capacity. In our study, all hydrolysates were hydrolyzed with their respective optimum pH and temperature for 3 h. Degree of hydrolysis of the five hydrolysates were 6.8 ± 0.1% for PSPH-Bro, 15.5 ± 0.3% for PSPH-Alc, 5.9 ± 0.2% for PSPH-Fla1, 15.5 ± 0.2% for PSPH-Pap, and 13.5 ± 0.4% for PSPH-Try (**Figure 2**). The DH of four hydrolysates were almost

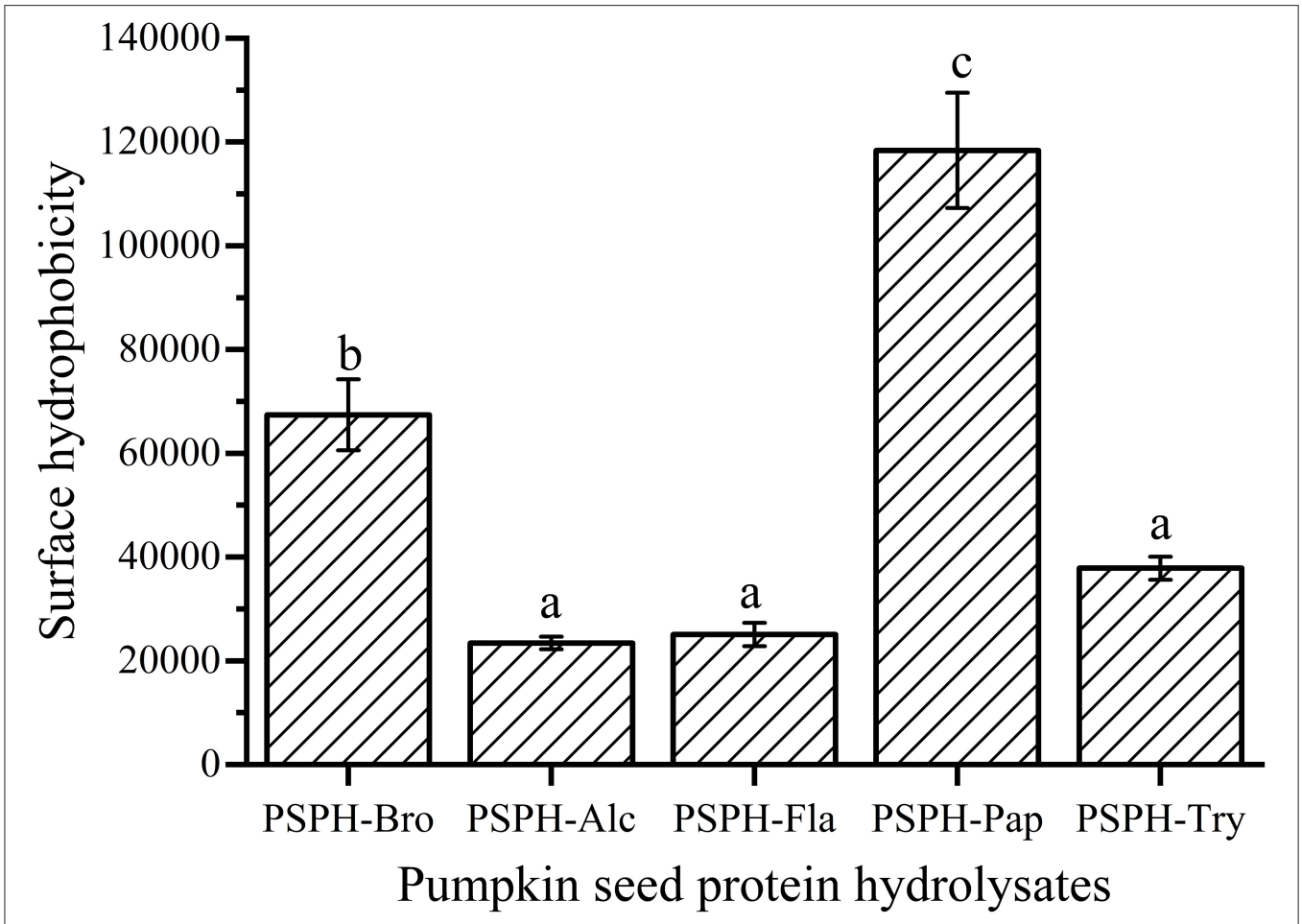

FIGURE 4 | Surface hydrophobicity of pumpkin seed protein hydrolysates produced with bromelain (PSPH-Bro), alcalase (PSPH-Alc), flavourzyme (PSPH-Fla), papain (PSPH-Pap), trypsin (PSPH-Try) after hydrolysis 3 h in a 2% (w/w) enzyme to substrate ratio. Different letters represent significantly different mean values with $P < 0.05$.

identical around 15%. The PSPH-Pap showed the greatest zinc binding capacity though the degree of hydrolysis was lower than that of alcalase and flavourzyme. The similar results can be found in the study of Wu et al. (27). DH was an influential factor affecting mental-binding capacity; a too high or too low DH is inappropriate for mental binding (28). The essential reason of the phenomenon was that proper hydrolysis was beneficial to the exposure of hydrophobic groups, which contributed to the coordination of mental and peptides (29).

Average Particle Sizes and Zeta Potential of PSPHs

Particle size of a carrier system played an important role in the bioaccessibility and bioavailability of the targeted compound it encapsulates (30). In most cases, the peptides possessing smaller sizes demonstrate better solubility and contributed to better digestibility of zinc compared with intact proteins (7). As shown in **Figure 3A**, the average particle diameters of PSPH-Bro, PSPH-Alc, PSPH-Fla, PSPH-Pap, and PSPH-Try were 1,601 ± 101 nm, 1,747 ± 42 nm, 3,624 ± 41 nm, 859 ± 45 nm, and 2,646 ± 200 nm, respectively. The PSPH-Fla and PSPH-Try had relatively larger average particle sizes, while the mean particle size of PSPH-Pap was the smallest. In most cases, the peptides possessing smaller sizes demonstrate better solubility and contributed to better digestibility of zinc compared with intact proteins (7).

The Zeta potential of the particles was defined as the electric potential at the boundary of the double layer on the particle surface (31). According to the Udechukwu report, the zinc-chelating capacity of the whey protein hydrolysates had a significantly strong negative relationship with their ζ-potential (8). The five pumpkin seed protein hydrolysates were all negatively charged, which could be observed at **Figure 3B**, and the zeta potential of PSPH-Bro, PSPH-Alc, PSPH-Fla, PSPH-Pap, and PSPH-Try were −11.47 ± 1.76 mV, −3.24 ± 0.39 mV, −8.66 ± 0.85 mV, −5.16 ± 1.21 mV, and −15.1 ± 0.82 mV. The PSPH-Alc and PSPH-Pap showed relatively low potential. The difference in zeta potential difference was caused by the specific cleavage behavior of different enzymes. For example, papain can cleave the bond between arginine/lysine and non-valine amino acid, releasing peptides with arginine/lysine as terminal amino acid, and leading to the change of zeta potential. As shown in **Figures 3A,B**, PSPH-Psp had the smallest mean particle

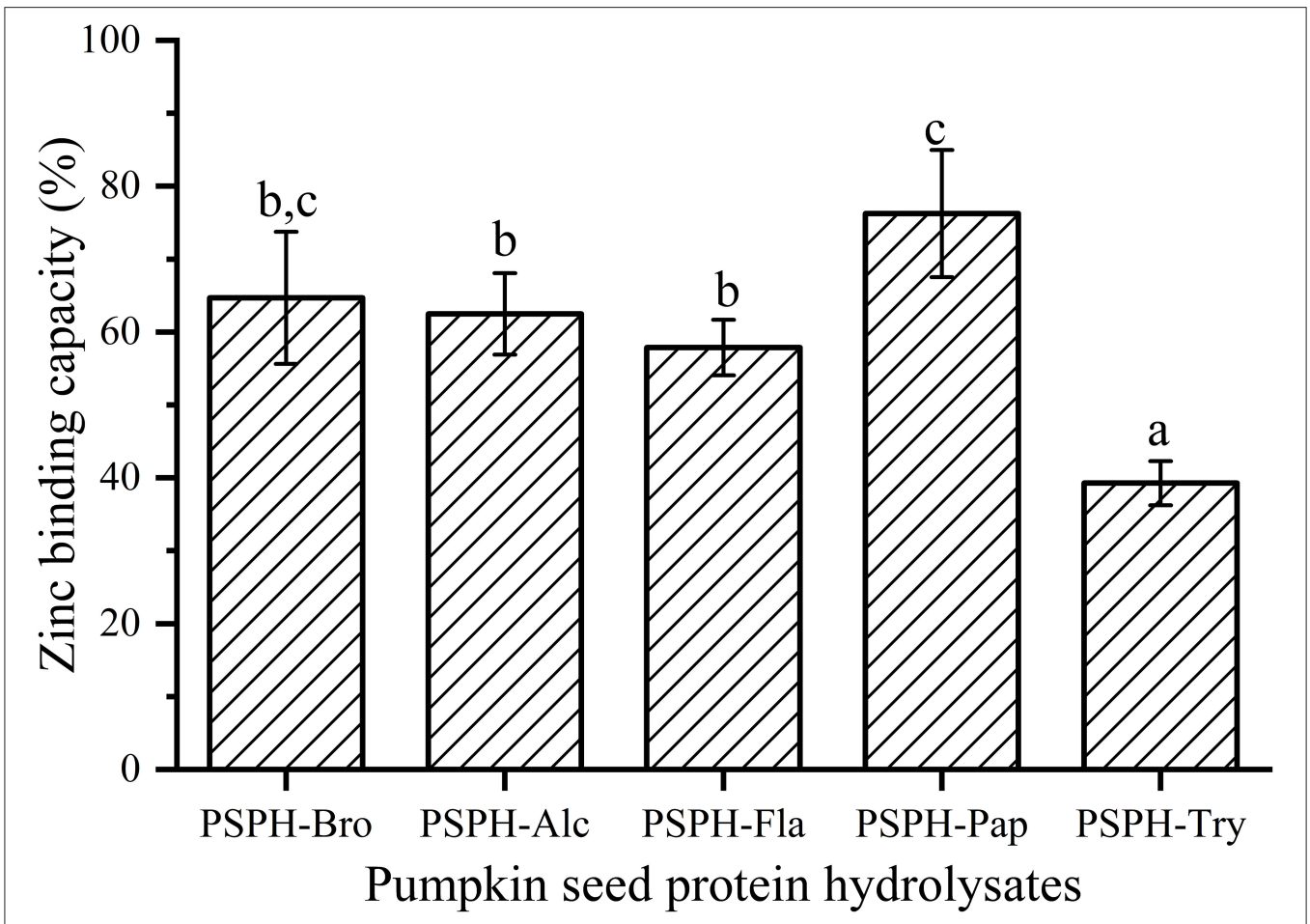

FIGURE 5 | Zinc binding capacity of pumpkin seed protein hydrolysates produced with bromelain (PSPH-Bro), alcalase (PSPH-Alc), flavourzyme (PSPH-Fla), papain (PSPH-Pap), trypsin (PSPH-Try) after hydrolysis 3 h in a 2% (w/w) enzyme to substrate ratio. Different letters represent significantly different mean values with $P < 0.05$.

TABLE 1 | Amino acid composition of pumpkin seed protein and pumpkin seed protein hydrolysates.

Amino acid	PSP	PSPH-Alc	PSPH-Tyr	PSPH-Fla	PSPH-Pap	PSPH-Bro
Asp	9.24	9.19	9.21	8.93	8.80	8.33
Glu	19.74	23.04	21.92	22.52	25.53	24.30
Ser	4.65	4.86	4.84	4.84	5.24	5.00
His	2.31	1.93	2.08	1.92	1.46	1.87
Gly	4.46	4.43	4.53	4.43	4.42	4.50
Thr	2.98	2.83	2.83	2.70	2.30	2.53
Arg	15.31	15.85	15.93	16.43	17.84	18.29
Ala	4.65	4.67	4.63	4.40	4.02	4.22
Tyr	3.74	3.37	3.31	2.94	2.50	3.13
Cys	0.49	0.52	0.56	0.52	0.48	0.56
Val	5.60	4.50	4.60	4.44	4.19	4.03
Met	2.46	2.33	2.36	2.23	1.85	2.20
Phe	5.60	5.19	5.39	5.28	4.63	4.68
Ile	4.51	4.29	4.38	4.33	3.61	3.81
Leu	7.58	7.04	7.38	7.23	6.28	6.50
Lys	3.61	3.46	3.66	3.61	3.63	3.46
Pro	3.07	2.51	2.37	3.23	3.23	2.60

PSP, pumpkin seed protein.

diameter but its net charge was not the highest, different from the theory used in colloid systems where high net negative charge will result in smaller mean particle diameter caused by electric repulsion. It was probably because each PSPH is a complicated system containing different amounts of peptides with varied compositions, chain length, and conformation.

Surface Hydrophobicity of PSPHs

The surface hydrophobicity of PSPHs was shown in **Figure 4**. The PSPH-Pap had the highest surface hydrophobicity and PSPH-Alc and PSPH-Fla had lowest surface hydrophobicity. Combined with the results in **Figure 5**, the zinc binding capacity is basically positively correlated with surface hydrophobicity. The surface hydrophobicity of proteins was caused by the exposure of some hydrophobic groups on the surface of proteins. It was the main factor affecting the intermolecular interaction and one of the key indicators to measure the functional properties of proteins.

Amino Acid Composition of PSPHs

The function of the peptide depends mainly on its composition and sequence of amino acid composition. In general, the side chain of histidine, aspartate, glutamate, cysteine, and serine can bind with minerals including Cu, Fe, and Zn through N, O, or S atoms (7). The imidazole group of histidine, the phenol ring of tyrosine, and the carboxy group of aspartate and glutamate can serve as the metal binding sites in proteins (32). Specifically, studies showed that zinc may bind to the acidic side chain of protein, phosphorylated residue, deprotonated nitrogen, and sulfur residues of amino acids and peptides. While functional groups including thiol group (cysteine, glutathione), imizadole group (hisidine), as well as asparagine and glutamine residues, phosphorylated residues, and methionine all contributed to the increased chelation capacities of zinc (33). The amino acid profiles of pumpkin seed protein and five enzymatic hydrolysates were shown in **Table 1**. PSPH-Pap contained more (45.45%) amino acids (Asp, Glu, His, Ser, Cys) that may chelate with zinc than other groups: 40.4% for native protein, 42.25% for PSPH-Bro, 42.58% for PSPH-Alc, 42.64% for PSPH-Fla, and 44% for PSPH-Try.

Zinc Binding Capacity of Different PSPHs

Zinc binding capacity or zinc chelating capacity was defined differently according to different experiments. In this study, it was defined as the percentage of zinc that was bound to PSPHs to that of total zinc added to the mixture. As shown in **Figure 5**, the zinc binding capacity of PSPHs were 64.7 ± 9.1% for PSPH-Bro, 62.5 ± 5.6% for PSPH-Alc, 57.9 ± 3.8% for PSPH-Fla, 76.3 ± 8.7% for PSPH-Pap, and 39.3 ± 3.0% for PSPH-Try, respectively. Zinc binding capacity of a certain peptide is predominately determined by the amino acid composition and arrangement of that specific peptide (33). According to the above-mentioned results, PSPH-Pap had the largest average molecular weight of 3,312 Da and contained the highest content of amino acid that tend to chelate with zinc. Udechukwu also found there was a positive correlation between zinc chelating amino acid content and zinc chelating capacity (8). In this study, each PSPH is the mixture of protein hydrolysate with different chain length as well as amino acid composition. The zinc binding capacity of PSPHs are the collective manifestation of peptide structural and chemical properties including surface hydrophobicity, average molecular weight distribution, zeta potential, as well as amino acid composition.

ATR-FTIR

In order to understand the ligand interactions between PSPH and Zn, ATR-FTIR was applied to characterize the structure of PSPH-Zn. The IR spectra of five hydrolysates of pumpkin seed protein and their zinc-binding complexes are shown in **Figures 6A–C**. The PSPH-Pap, as the peptide with the highest zinc chelation rate, was individually analyzed in detail with its zinc binding complex: PSPH-Pap-Zn.

The infrared spectra consist of two parts with no doubts: functional group region and fingerprint region. The band around 3,400 cm^{-1} represented the N-H stretching, while O-H bonds existed an absorption in the wavenumber of 2,900 cm^{-1}. Furthermore, the band around 1,600 cm^{-1} exhibited the N-H bending vibration coupled with the C=O stretching, while the absorption at 1,400 cm^{-1} was due to COO- and C-O peak occurred in 1,100 cm^{-1}. From **Figure 6A**, there were no obvious differences among the five hydrolysates.

As shown in **Figure 6B**, after binding to zinc, both transmissivity intensity and peak position were changed for peptide-zinc complex. Take PSPH-Pap with the highest zinc-chelating capacity, for example; the peaks slightly shifted from 3,272.86 cm^{-1} to 3,277.45 cm^{-1} and 2,928.39 cm^{-1} to 2,936.03 cm^{-1}, which may be caused by the stretching vibrations of N–H bonds and O-H bonds. The most apparent peak feature could be observed around 1,100 cm^{-1}, while the 1,076.96 cm^{-1}, 1,028.84 cm^{-1} shifted to the 1,102.92 cm^{-1} and 1,081.54 cm^{-1}. Moreover,

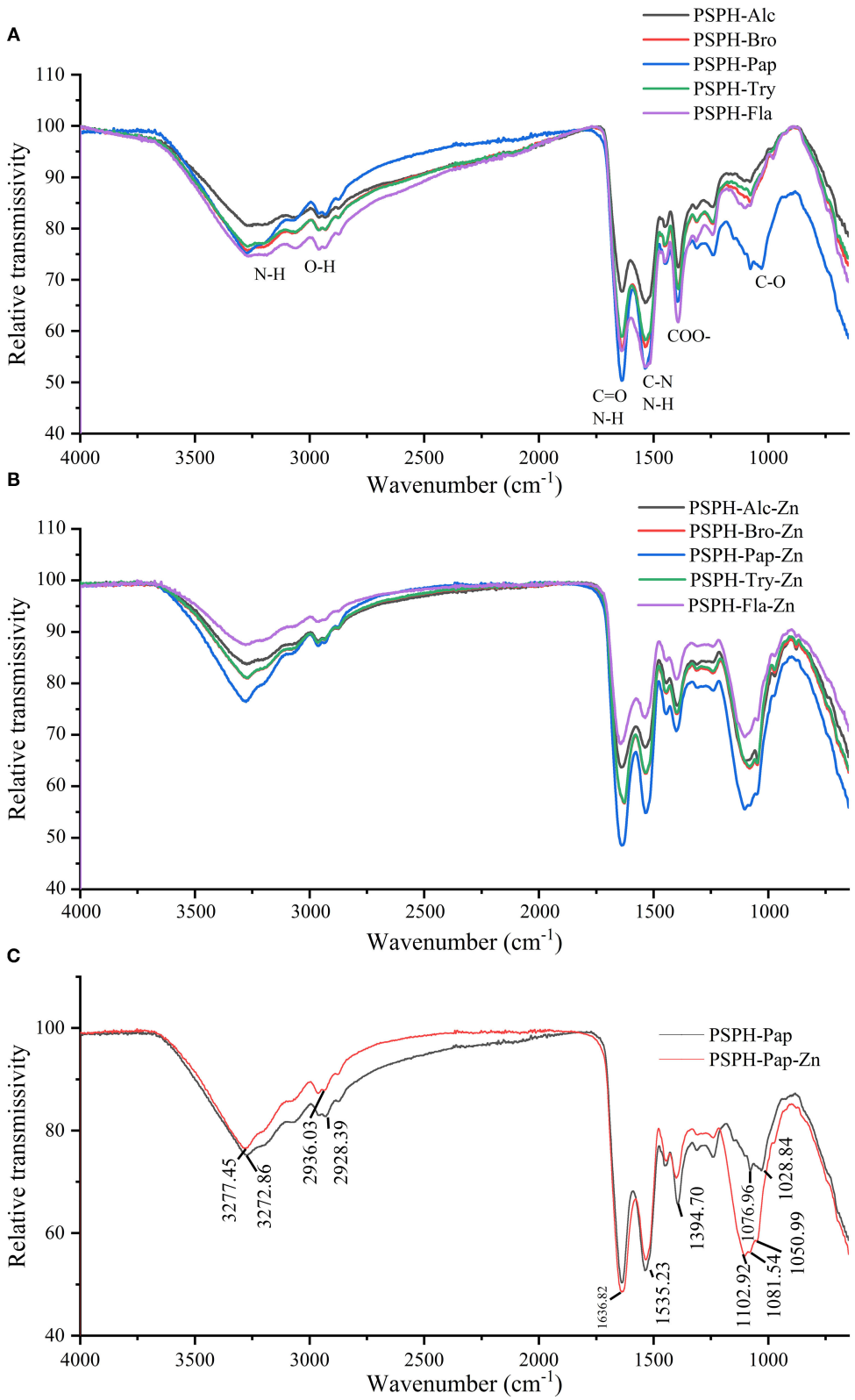

FIGURE 6 | Attenuated total reflection fourier transform infrared spectra (ATR-FTIR) of **(A)** pumpkin seed protein hydrolysates (PSPHs) in the range of 4,000 to 400 cm^{-1}; **(B)** pumpkin seed protein hydrolysates (PSPH) zinc chelates; **(C)** pumpkin seed protein hydrolysate hydrolyzed by papain (PSPH-Pap, black line) and its zinc complex (PSPH-Pap-Zn, red line).

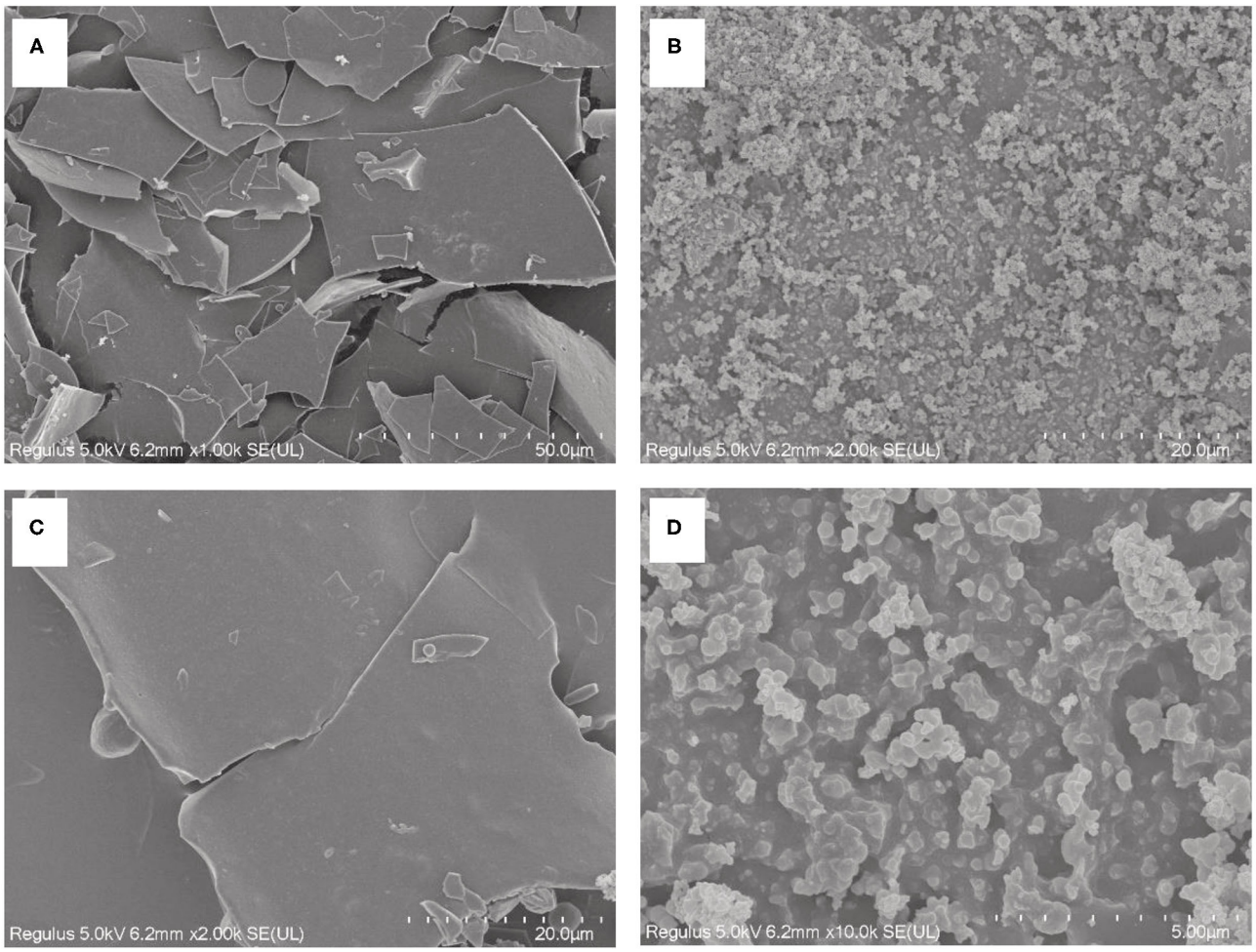

FIGURE 7 | Scanning electron microscopy (SEM) photograph of pumpkin seed protein hydrolysates produced by papain after hydrolysis 3 h in a 2% (w/w) enzyme to substrate ratio PSPH-Pap **(A, C)** and its zinc complex PSPH-Pap-Zn complex **(B, D)**.

the new absorption peaks appeared in 1,050.69 cm^{-1}. The sharp peak observed around 1,400 cm^{-1} may be attributed to the stretch of C-O. In conclusion, oxygen atoms from C-O bonds and nitrogen-atoms from the N-H bonds were the main binding sites of PSPH and zinc.

SEM

Binding to zinc has an influence on both the chemical structure and microstructure of PSPHs. **Figure 7** showed the microstructures of pumpkin seed protein hydrolysate (PSPH), PSPH-Zn, respectively. The PSPH showed a laminar structure with smooth surface (**Figures 7A,C**). However, the morphology of PSPH-Pap-Zn seemed to be the loose globular structure (**Figures 7B,D**), which could be explained as the aggregation of peptide due to the existence of zinc. In the presence of zinc, the spatial conformation of the peptides may rearrange or fold where different ligands from the amino acid side chains forms complex with zinc through coordination (34). A similar phenomenon has also been observed in the oyster-derived peptide zinc-binding complex (35), cucumber seed peptide-calcium chelate (36). Zhang et al. (37) reported that the peptide could fold and aggregate when the oyster protein hydrolysis and zinc form the compound. A detailed understanding on the molecular conformation change after zinc chelation could be obtained through molecular modeling.

X-Ray Photoelectron Spectroscopy Spectra of PSPH and PSPH-Zn

XPS is a method used to analyze the surface chemistry of a material. XPS instrument measures the kinetic energy emitted from surface elements upon X-ray exposure. It has been used to characterize the binding of iron to an Antarctic krill derived peptide (38). Since each of our PSPH samples is a mixture of peptides with different molecular weights, the XPS was only used quantitatively to identify the PSPH-Zn. As shown in **Figure 8**, there were three peaks of C1s, N1s, O1s at 284.8 eV, 399.7 eV, and 531.3 eV for both PSPH-Pap and PSPH-Pap-Zn. In the

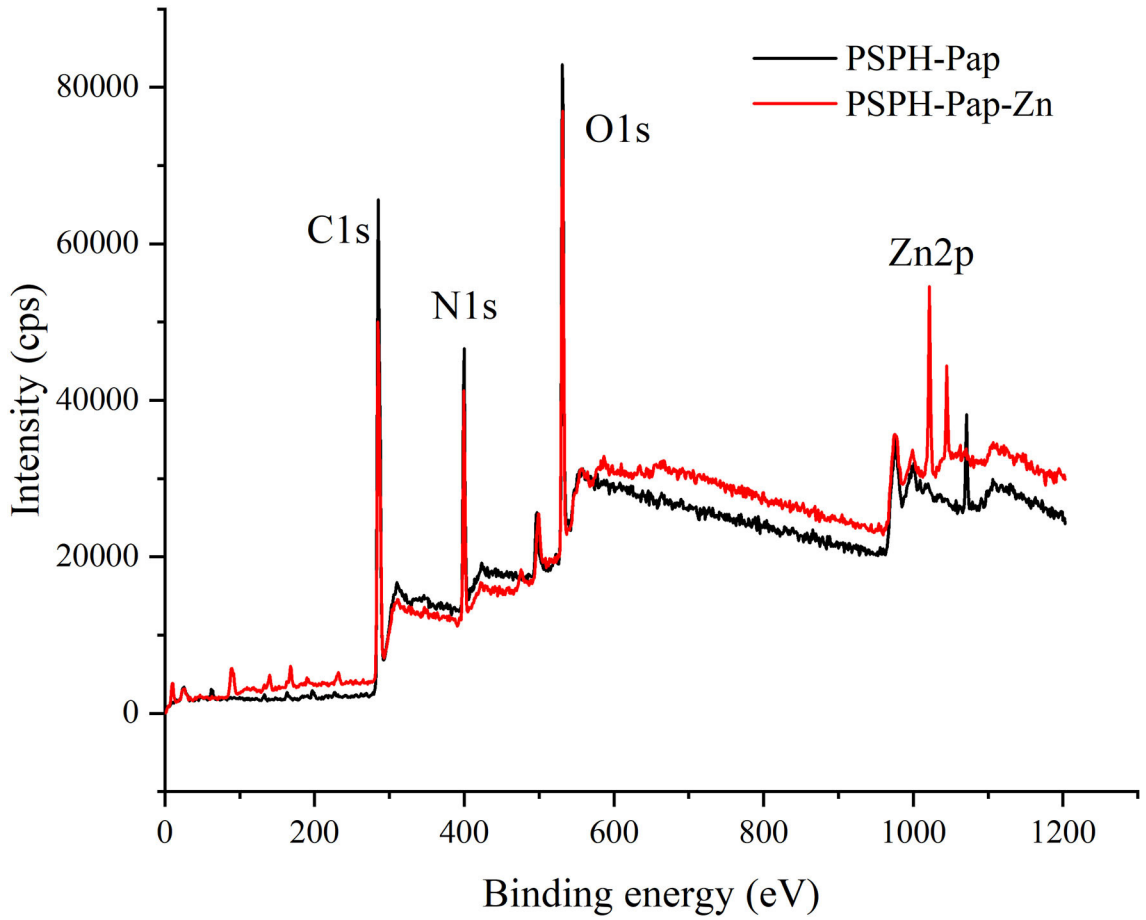

FIGURE 8 | X-ray Photoelectron Spectroscopy (XPS) spectra of pumpkin seed protein hydrolysates produced by papain after hydrolysis 3 h in a 2% (w/w) enzyme to substrate ratio (PSPH-Pap, black line) and its zinc complex (PSPH-Pap-Zn, red line).

TABLE 2 | The *in vitro* gastrointestinal stability of PAPH-Pap, PSPH-Try, and $ZnSO_4 \cdot 7H_2O$.

	Gastric digestion stability (%)	Gastrointestinal digestion stability (%)
PSPH-Pap	90.06 ± 1.64^c	52.99 ± 1.46^c
PSPH-Try	83.23 ± 1.21^b	33.23 ± 6.71^b
$ZnSO_4 \cdot 7H_20$	71.09 ± 2.63^a	17.40 ± 5.15^a

Data with different letters represent significantly different mean values with $P < 0.05$.

meantime, in the XPS spectra of PSPH-Pap-Zn, there is a strong Zn2p binding energy peak at 1,021.7 eV. This result confirmed the binding between PSPH-Pap and zinc.

In vitro Gastrointestinal Stability of PSPH and PSPH-Zn

The binding between zinc and peptides is reversible. The existence of acidic groups such as -OH, -COOH, -SH, and -NOH may induce the dissociation between zinc and peptides. The human stomach has a low pH around 0.9–1.5. Hence, it is of prime importance to evaluate the gastric stability PSPH-Zn. A desirable zinc chelating peptide should be relatively resistant to the cleavage during gastric digestion, avoiding the release of zinc to form precipitates with phytates or dietary fiber in diets. In the small intestine, minerals such as zinc are transported by transcellular or paracellular pathways. Some non-specific transporters may carry any mineral presented. Hence this transport may be affected by the presence of other metal ions. Minerals supplemented in peptide complexes can be transported differently without potential competition from other metal ions. As shown in **Table 2**, the gastric digestion stability of PSPH-Pap-Zn was 90.06 ± 1.64%, higher than that of PSPH-Try-Zn 83.23 ± 1.21%. The stabilities of zinc after both gastric and intestinal digestion were 52.99 ± 1.46% for PSPH-Pap-Zn, 33.23 ± 6.71% for PSPH-Try-Zn, both higher than 17.40 ± 5.15% for zinc salts. This may be caused by higher binding capacity of PSPH-Pap than that of PSPH-Try, preventing zinc from dissociating from the complex and dissolving in gastric juice. Overall, our result showed that PSPH derived zinc chelating peptides had better gastrointestinal stability than zinc sulfate and may be used as potential zinc fortifier.

CONCLUSIONS

In this study, five enzymes were used to prepare PSPHs. The PSPHs were characterized for their molecular weight distribution, average particle size, zeta potential, amino acid composition, and zinc binding capacity. Representative samples were analyzed using ATR-FTIR, SEM, and XPS to quantitatively characterize the binding between zinc and PSPH. Our result showed that papain may be used as an enzyme to prepare PSPH. The obtained PSPH-Pap had the average molecular weight around 3,312 Da. It has the highest zinc binding amino acid content and showed the highest zinc binding capacity. PSPH-Pap can retain more than 50% of zinc after *in vitro* gastrointestinal digestion. This study can provide a preliminary knowledge on the application of pumpkin seed in zinc fortification. Future studies should focus on the purification and identification of individual peptide that binds to zinc, while at the same time showing excellent stability in gastrointestinal tract. Efforts should also be made to elucidate the specific binding mode between zinc and this particular peptide, which will enable further developing of zinc supplements with high bioavailability.

DATA AVAILABILITY STATEMENT

The raw data supporting the conclusions of this article will be made available by the authors, without undue reservation.

AUTHOR CONTRIBUTIONS

DL: conceptualization, Investigation, Methodology, Software, Data curation, writing—original draft, writing—review & editing. MP and MY: investigation. BJ: formal analysis, writing—review & editing. HW: writing—review & editing. JC: project administration, funding acquisition, writing—review & editing. All authors contributed to the article and approved the submitted version.

FUNDING

This study was supported by Xinjiang Production and Construction Crop Scientific Research Project (2019AB027).

REFERENCES

1. Prasad AS. Zinc is an antioxidant and anti-inflammatory agent: its role in human health. *Front Nutr.* (2014) 1:14. doi: 10.3389/fnut.2014.00014
2. Wessels I, Rolles B, Rink L. The potential impact of zinc supplementation on COVID-19 pathogenesis. *Front Immunol.* (2020) 11:1712. doi: 10.3389/fimmu.2020.01712
3. Choi S, Liu X, Pan Z. Zinc deficiency and cellular oxidative stress: prognostic implications in cardiovascular diseases. *Acta Pharmacol Sin.* (2018) 39:1120–32. doi: 10.1038/aps.2018.25
4. Guo L, Harnedy PA, Li B, Hou H, Zhang Z, Zhao X, et al. Food protein-derived chelating peptides: biofunctional ingredients for dietary mineral bioavailability enhancement. *Trends Food Sci Technol.* (2014) 37:92–105. doi: 10.1016/j.tifs.2014.02.007
5. Stone B, Morell MK. CHAPTER 9—Carbohydrates. In: Khan K, Shewry PR, editors. *Wheat*. 4th ed. St. Paul, MN: AACC International Press (2009). p. 299–362. doi: 10.1094/9781891127557.009
6. Camara F, Amaro MA. Nutritional aspect of zinc availability. *Int J Food Sci Nutr.* (2003) 54:143–51. doi: 10.1080/0963748031000084098
7. Udechukwu MC, Collins SA, Udenigwe CC. Prospects of enhancing dietary zinc bioavailability with food-derived zinc-chelating peptides. *Food Funct.* (2016) 7:4137–44. doi: 10.1039/C6FO00706F
8. Udechukwu MC, Downey B, Udenigwe CC. Influence of structural and surface properties of whey-derived peptides on zinc-chelating capacity, and *in vitro* gastric stability and bioaccessibility of the zinc-peptide complexes. *Food Chem.* (2018) 240:1227–32. doi: 10.1016/j.foodchem.2017.08.063
9. Zhu K-X, Wang X-P, Guo X-N. Isolation and characterization of zinc-chelating peptides from wheat germ protein hydrolysates. *J Funct Foods.* (2015) 12:23–32. doi: 10.1016/j.jff.2014.10.030
10. Wang Q, Xiong YL. Zinc-binding behavior of hemp protein hydrolysates: soluble versus insoluble zinc-peptide complexes. *J Funct Foods.* (2018) 49:105–12. doi: 10.1016/j.jff.2018.08.019
11. Liao W, Lai T, Chen L, Fu J, Sreenivasan ST, Yu Z, et al. Synthesis and Characterization of a Walnut Peptides-Zinc Complex and Its Antiproliferative Activity against Human Breast Carcinoma Cells through the Induction of Apoptosis. *J Agric Food Chem.* (2016) 64:1509–19. doi: 10.1021/acs.jafc.5b04924
12. Wang C, Li B, Ao J. Separation and identification of zinc-chelating peptides from sesame protein hydrolysate using IMAC-Zn(2)(+) and LC-MS/MS. *Food Chem.* (2012) 134:1231–8. doi: 10.1016/j.foodchem.2012.02.204
13. Xie N, Huang J, Li B, Cheng J, Wang Z, Yin J, et al. Affinity purification and characterisation of zinc chelating peptides from rapeseed protein hydrolysates: possible contribution of characteristic amino acid residues. *Food Chem.* (2015) 173:210–7. doi: 10.1016/j.foodchem.2014.10.030
14. Liu X, Wang Z, Zhang J, Song L, Li D, Wu Z, et al. Isolation and identification of zinc-chelating peptides from sea cucumber (Stichopus japonicus) protein hydrolysate. *J Sci Food Agric.* (2019) 99:6400–7. doi: 10.1002/jsfa.9919
15. Jiang L, Wang B, Li B, Wang C, Luo Y. Preparation and identification of peptides and their zinc complexes with antimicrobial activities from silver carp (Hypophthalmichthys molitrix) protein hydrolysates. *Food Res Int.* (2014) 64:91–8. doi: 10.1016/j.foodres.2014.06.008
16. Lin Y, Tang X, Xu L, Wang S. Antibacterial properties and possible action mechanism of chelating peptides-zinc nanocomposite against Escherichia coli. *Food Control.* (2019) 106:106675. doi: 10.1016/j.foodcont.2019.06.001
17. Liao W, Chen H, Jin W, Yang Z, Cao Y, Miao J. Three Newly isolated calcium-chelating peptides from tilapia bone collagen hydrolysate enhance calcium absorption activity in intestinal caco-2 cells. *J Agric Food Chem.* (2020) 68:2091–8. doi: 10.1021/acs.jafc.9b07602
18. Nourmohammadi E, Sadeghimahoonak A, Alami M, Ghorbani, M. Amino acid composition and antioxidative properties of hydrolysed pumpkin (Cucurbita pepo L.) oil cake protein. *Int J Food Properties.* (2017) 20:3244–55. doi: 10.1080/10942912.2017.1283516
19. Rezig L, Chibani F, Chouaibi M, Dalgalarrondo M, Hessini K, Gueguen J, et al. Pumpkin (Cucurbita maxima) seed proteins: sequential extraction processing and fraction characterization. *J Agric Food Chem.* (2013) 61:7715–21. doi: 10.1021/jf402323u
20. Ovca A, Van Elteren JT, Falnoga I, Šelih VS. Speciation of zinc in pumpkin seeds (Cucurbita pepo) and degradation of its species in the human digestive tract. *Food Chem.* (2011) 128:839–46. doi: 10.1016/j.foodchem.2011.03.102
21. Juranovic I, Breinhoelder P, Steffan I. Determination of trace elements in pumpkin seed oils and pumpkin seeds by ICP-AES. *J Anal Atomic Spectrom.* (2003) 18:54–8. doi: 10.1039/b209308c
22. Nielsen PM, Petersen D, Dambmann C. Improved method for determining food protein degree of hydrolysis. *J Food Sci.* (2001) 66:642–6. doi: 10.1111/j.1365-2621.2001.tb04614.x
23. Li Y, Jiang B, Zhang T, Mu W, Liu J. Antioxidant and free radical-scavenging activities of chickpea protein hydrolysate (CPH). *Food Chem.* (2008) 106:444–50. doi: 10.1016/j.foodchem.2007.04.067
24. Chen L, Shen X, Xia G. Effect of molecular weight of tilapia (oreochromis niloticus) skin collagen peptide fractions on zinc-chelating capacity and

bioaccessibility of the zinc-peptide fractions complexes *in vitro* digestion. *Appl Sci.* (2020) 10. doi: 10.3390/app10062041
25. Seth A, Mahoney R. Binding of iron by chicken muscle protein digests: the size of the iron-binding peptides. *J Sci Food Agric.* (2000) 80:1595–600. doi: 10.1002/1097-0010(20000901)80:11<1595::AID-JSFA684>3.0.CO;2-Y
26. Sun N, Cui P, Jin Z, Wu H, Wang Y, Lin S. Contributions of molecular size, charge distribution, and specific amino acids to the iron-binding capacity of sea cucumber (Stichopus japonicus) ovum hydrolysates. *Food Chem.* (2017) 230:627–36. doi: 10.1016/j.foodchem.2017.03.077
27. Wu W, He L, Liang Y, Yue L, Peng W, Jin G, et al. Preparation process optimization of pig bone collagen peptide-calcium chelate using response surface methodology and its structural characterization and stability analysis. *Food Chem.* (2019) 284:80–9. doi: 10.1016/j.foodchem.2019.01.103
28. Wang L, Ding Y, Zhang X, Li Y, Wang R, Luo X, et al. Isolation of a novel calcium-binding peptide from wheat germ protein hydrolysates and the prediction for its mechanism of combination. *Food Chem.* (2018) 239:416–26. doi: 10.1016/j.foodchem.2017.06.090
29. Chen D, Mu X, Huang H, Nie R, Liu Z, Zeng M. Isolation of a calcium-binding peptide from tilapia scale protein hydrolysate and its calcium bioavailability in rats. *J Funct Foods.* (2014) 6:575–84. doi: 10.1016/j.jff.2013.12.001
30. Yao M, Mcclements DJ, Xiao H. Improving oral bioavailability of nutraceuticals by engineered nanoparticle-based delivery systems. *Curr Opin Food Sci.* (2015) 2:14–9. doi: 10.1016/j.cofs.2014.12.005
31. Shah MR, Imran M, Ullah S. Chapter 5—Nanosuspensions. In: Shah MR, Imran M, Ullah S, editors. *Lipid-Based Nanocarriers for Drug Delivery and Diagnosis*. Norwich, NY: William Andrew Publishing (2017). p. 139–72. doi: 10.1016/B978-0-323-52729-3.00005-6
32. Yamauchi O, Odani A, Takani M. Metal–amino acid chemistry. Weak interactions and related functions of side chain groups. *J Chem Soc Dalton Trans.* (2002) 3411–3421. doi: 10.1039/B202385G
33. Zhang YY, Stockmann R, Ng K, Ajlouni S. Opportunities for plant-derived enhancers for iron, zinc, and calcium bioavailability: a review. *Compr Rev Food Sci Food Saf.* (2020) 20:652–85. doi: 10.1111/1541-4337.12669
34. Yiannikouris A, Connolly C, Power R, Lobinski R. Characterization of metal-peptide complexes in feed supplements of essential trace elements. *Metallomics.* (2009) 1:235–48. doi: 10.1039/b901406c
35. Li J, Gong C, Wang Z, Gao R, Ren J, Zhou X, et al. Oyster-derived zinc-binding peptide modified by plastein reaction via zinc chelation promotes the intestinal absorption of zinc. *Mar Drugs.* (2019) 17:341. doi: 10.3390/md17060341
36. Wang X, Gao A, Chen Y, Zhang X, Li S, Chen Y. Preparation of cucumber seed peptide-calcium chelate by liquid state fermentation and its characterization. *Food Chem.* (2017) 229:487–94. doi: 10.1016/j.foodchem.2017.02.121
37. Zhang Z, Zhou F, Liu X, Zhao M. Particulate nanocomposite from oyster (Crassostrea rivularis) hydrolysates via zinc chelation improves zinc solubility and peptide activity. *Food Chem.* (2018) 258:269–77. doi: 10.1016/j.foodchem.2018.03.030
38. Sun N, Wang TT, Wang D, Cui PB, Hu SJ, Jiang PF, et al. Antarctic krill derived nonapeptide as an effective iron-binding ligand for facilitating iron absorption via the small intestine. *J Agric Food Chem.* (2020) 68:11290–300. doi: 10.1021/acs.jafc.0c03223

Conflict of Interest: The authors declare that the research was conducted in the absence of any commercial or financial relationships that could be construed as a potential conflict of interest.

frontiers in Nutrition

ORIGINAL RESEARCH
published: 07 April 2021
doi: 10.3389/fnut.2021.648973

Protective Effect of *Chrysanthemum morifolium* cv. Fubaiju Hot-Water Extracts Against ARPE-19 Cell Oxidative Damage by Activating PI3K/Akt-Mediated Nrf2/HO-1 Signaling Pathway

Yiming Hao[1†], Yanfang Li[2†], Jie Liu[1], Ziyuan Wang[1], Boyan Gao[2], Yaqiong Zhang[2] and Jing Wang[1*]*

[1] China-Canada Joint Lab of Food Nutrition and Health (Beijing), Beijing Technology & Business University (BTBU), Beijing, China, [2] Institute of Food and Nutraceutical Science, School of Agriculture and Biology, Shanghai Jiao Tong University, Shanghai, China

Chrysanthemum morifolium cv. Fubaiju is a kind of widely consumed herb tea with multiple health benefits. The present study was aimed to evaluate the protective capacity of *C. morifolium* cv. Fubaiju hot-water extracts (CMs) against ARPE-19 cell oxidative damage. The results showed that pretreatment with 100 μg/mL CM could significantly reduce cell oxidative damage and apoptosis. Proapoptotic protein expression such as Bax, cleaved caspase-3, and cleaved poly(ADP-ribose) polymerase (PARP) was significantly decreased after CM addition, while the expression level of antioxidant enzymes including catalase, glutamate-cysteine ligase catalytic subunit (GCLc), superoxide dismutase 2 (SOD2), and NAD(P)H:quinone oxidoreductase 1 (NQO-1) was significantly promoted. Meanwhile, CM treatment upregulated Akt phosphorylation, nuclear factor erythroid 2-related factor 2 (Nrf2) nuclear translocation, and the expression level of antioxidant gene heme oxygenase-1 (HO-1) in a dose-dependent manner under oxidative stress. Knockdown of Nrf2 by targeted small interfering RNA (siRNA) alleviated CM-mediated HO-1 transcription and almost abolished CM-mediated protection against hydrogen peroxide (H_2O_2)-induced cell damage. Correspondingly, the protective effect of CM was dramatically blocked after interference with phosphatidylinositol 3-kinase (PI3K)/Akt inhibitor LY294002, indicating that the protective effect of CM on cell oxidative damage was attributed to PI3K/Akt-mediated Nrf2/HO-1 signaling pathway.

Keywords: *Chrysanthemum morifolium*, Fubaiju hot-water extracts, ARPE-19 cell, oxidative damage, PI3K/AKT, Nrf2/HO-1

OPEN ACCESS

Edited by:
Jinkai Zheng,
Chinese Academy of Agricultural Sciences (CAAS), China

Reviewed by:
Yashi Mi,
University of Arizona, United States
Sun Young Park,
Pusan National University, South Korea
Xuebo Liu,
Northwest A&F University, China

****Correspondence:***
Jie Liu
liu_jie@btbu.edu.cn
Jing Wang
wangjing@th.btbu.edu.cn

[†]These authors have contributed equally to this work

Specialty section:
This article was submitted to Food Chemistry, a section of the journal Frontiers in Nutrition

Received: *03 January 2021*
Accepted: *22 February 2021*
Published: *07 April 2021*

Citation:
Hao Y, Li Y, Liu J, Wang Z, Gao B, Zhang Y and Wang J (2021) Protective Effect of Chrysanthemum morifolium cv. Fubaiju Hot-Water Extracts Against ARPE-19 Cell Oxidative Damage by Activating PI3K/Akt-Mediated Nrf2/HO-1 Signaling Pathway. Front. Nutr. 8:648973. doi: 10.3389/fnut.2021.648973

INTRODUCTION

Age-associated macular degeneration (AMD) is the major cause of blindness among the elderly (1–3). Previous literature has indicated that early dietary intervention of natural antioxidants may be an effective and safe way to prevent AMD (4–6). For instance, it was reported that dietary enrichment with natural antioxidants from grape extracts prevented retinal pigment epithelium (RPE) oxidation, cytoskeletal damage, and vision loss in $\beta5^{-/-}$ mouse (6). And it was found that grape extracts rich in polyphenols could restore the structure and visual function among pathologic visual decline patients (4, 5). AMD has been proven to be associated with oxidative damage, among which nuclear factor erythroid 2-related factor 2 (Nrf2) pathway has been involved to combat oxidative stress (7–10). After activation, Nrf2 translocates to the nucleus and binds with the antioxidant response element (ARE) to activate phase II antioxidant enzyme transcription, including catalase, glutamate-cysteine ligase catalytic subunit (GCLc), superoxide dismutase 2 (SOD2), NAD(P)H:quinone oxidoreductase 1 (NQO-1), and heme oxygenase-1 (HO-1). It has been found that wheat alkylresorcinols could protect ARPE-19 cells against hydrogen peroxide (H_2O_2)-induced oxidative damage *via* activation of Akt-dependent Nrf2/HO-1 signaling (10). And zeaxanthin was reported to increase Nrf2-mediated phase II enzyme expression through phosphatidylinositol 3-kinase (PI3K)/Akt activation for the prevention of ARPE-19 cell apoptosis induced by oxidative stress (11). On the contrary, Nrf2 deficiency could magnify the oxidative damage in RPE cells (12). Inhibition of Akt phosphorylation was reported to increase RPE cell oxidative damage and apoptosis (3, 10, 11). Thus, Akt-dependent Nrf2 signaling pathway activation might be a key target for the treatment of oxidative stress-induced retinal diseases.

Chrysanthemum morifolium Ramat. is a well-known food-medicine homologous flower tea that is rich in bioactive components such as flavonoids and phenolic acids (13–17). It has been reported that *C. morifolium* possesses many biological activities, including cardiovascular protection (18), antiallergy (19), gut microbiota modulation (20), anti-inflammation (14, 15), and antioxidant properties (14, 15). For instance, the hot-water extracts of *C. morifolium* could suppress lipopolysaccharide (LPS)-induced RAW 264.7 macrophage pro-inflammatory cytokine expression, such as interleukin-6 (IL-6), IL-1β, and cyclooxygenase-2 (COX-2) (14, 15). Our previous study also showed that different cultivars of chrysanthemums could protect ARPE-19 cell through depressing the increment of H_2O_2-induced intercellular reactive oxygen species (ROS) production (15). However, the mechanism of the protection of RPE cells from oxidative damage by chrysanthemum is still unclear at present. *C. morifolium* cv. Fubaiju was selected in the present study for its excellent bioactivity, great sensory quality, and large-scale production (15). The cytoprotective effects of *C. morifolium* cv. Fubaiju hot-water extracts (CMs) on H_2O_2-induced oxidative stress in ARPE-19 cells, along with the underlying mechanism, were investigated. Results of this study could provide a theoretical basis for the application of Fubaiju as bioactive ingredients in dietary supplements for the potential treatment of AMD and promote the local economy.

MATERIALS AND METHODS

Chemicals and Reagents

C. morifolium cv. Fubaiju samples were obtained from Hubei Mingmu Health Technology Co. Ltd., China. The 2′,7′-dichlorofluorescin diacetate (DCFH-DA) and H_2O_2 were obtained from Sigma-Aldrich (St. Louis, MO, USA). LY294002 and the antibodies against α-tubulin, Nrf2, HO-1, Akt, p-Akt, catalase, GCLc, NQO-1, cleaved caspase-3, cleaved poly(ADP-ribose) polymerase (PARP), Bax, Bcl-2, and Histone H3 were purchased from Abcam (Cambridge, UK). SOD2 was ordered

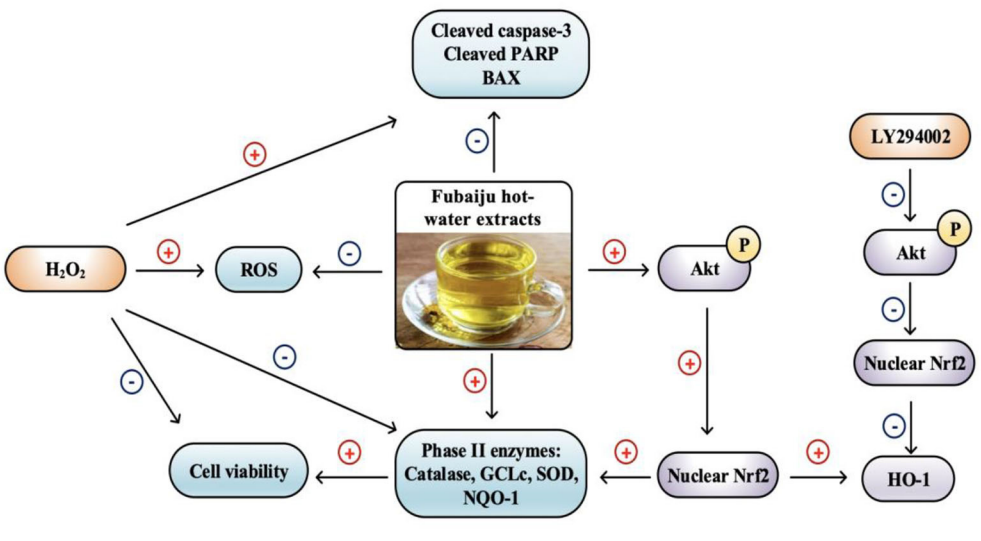

GRAPHICAL ABSTRACT | Fubaiju protected ARPE-19 cells oxidative damage by activating PI3K/Akt mediated Nrf2/HO-1 signaling pathway.

from CST (MA, USA). Control and Nrf2 small interfering RNA (siRNA) (sc-37007 and sc-37030) were ordered from Santa Cruz Biotechnology (Dallas, TX). Milli-Q purification system (Millipore Laboratory, Bedford, MA) was applied for ultrapure water preparation.

Preparation of Fubaiju Hot-Water Extracts

CMs were prepared following a reported procedure (15). Ground Fubaiju sample (2 g) was added into boiling water (20 mL) and left at room temperature overnight prior to centrifugation. Then, supernatant (5 mL) was collected and dried by freeze-dryer, and the residue was separated and weighed, followed by redissolving in H_2O (5 mL) and 10 times dilution with H_2O. The diluent was injected to ultra-performance liquid chromatography combined with a quadrupole time-of-flight mass spectrometer (UPLC/Q-TOF-MS) to investigate its chemical composition. The chemical composition of CM was composed of 26 compounds including 21 flavonoids and five phenolic acids, in which apigenin-7-O-glucoside, kaempferol-3-O-acetyl-glucoside, and apigenin-7-O-acetylglucoside were the three major components (14).

Cell Culture

Human retinal pigment epithelial cell line (ARPE-19 cells) was obtained from ATCC and cultured as previously reported (21). Briefly, ARPE-19 cells were cultured in Dulbecco's modified Eagle's medium (DMEM)/F12 medium supplemented with 10% fetal bovine serum, 100 U/mL penicillin, and 100 μg/mL streptomycin (Gibco, Madison, USA) at 37°C containing 5% CO_2. Before hydrogen peroxide treatment, cells were cultured in serum-free DMEM/F12 medium for 30 min.

Cell Viability Assay

The ARPE-19 cell viability was evaluated with the 3-(4,5-dimethylthiazol-2-yl)-2,5-diphenyltetrazolium bromide (MTT) assay as previously reported (22). ARPE-19 cells (1×10^4 cells/well) were seeded in 96-well plates and cultured for 24 h, followed by incubation with CM for 12 h, then treated with H_2O_2 for another 24 h. After MTT treatment (0.5 mg/mL, Sigma Aldrich, St. Louis, MO, USA) for another 4 h, crystal violet was dissolved in dimethyl sulfoxide (DMSO) and the absorbance at 490 nm was measured by Tecan microplate spectrophotometer (Spark 10M, Tecan, Männedorf, Switzerland).

Intracellular Reactive Oxygen Species Measurement

Intracellular ROS was measured according to the laboratory protocol (15). Briefly, the ARPE-19 cells (1×10^4 cells/well) were seeded in 96-well black plates for 24 h followed by pretreatment

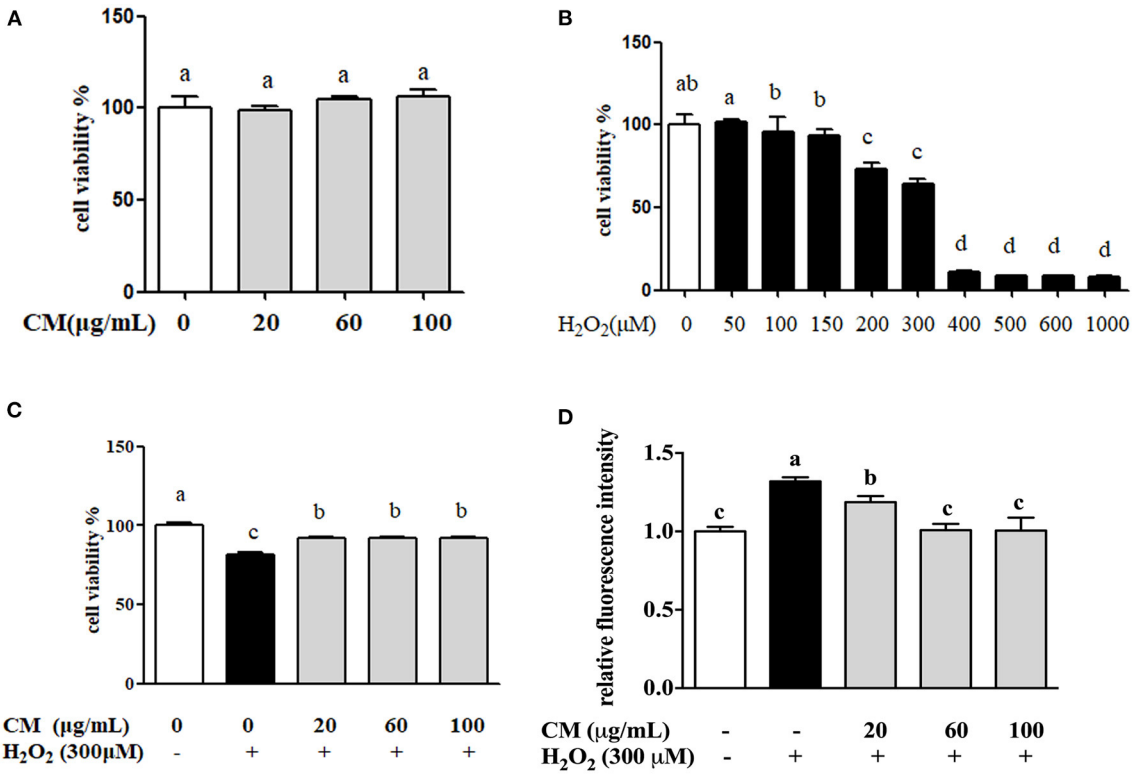

FIGURE 1 | The protective effects of Fubaiju hot-water extracts (CMs) on hydrogen peroxide (H_2O_2)-induced ARPE-19 cell oxidative damage and reactive oxygen species (ROS) generation. **(A)** The cytotoxicity of CM on ARPE-19 cells. **(B)** The cell viability of ARPE-19 cells induced by different doses of H_2O_2. **(C)** CM treatment inhibited H_2O_2-induced ARPE-19 cell damage. **(D)** The suppression of CM on ROS production in ARPE-19 cells. The results are mean ± SD ($n = 3$). Columns with different letters are significantly different ($P < 0.05$).

with CM for another 24 h. Then, cells were rinsed with Hanks' balanced salt solution (HBSS) and treated with DCFH-DA (10 μM) for 30 min at 37°C, followed by 24-h incubation with H_2O_2 (300 μM) in serum-free medium. Fluorescence intensity was examined using microplate reader with excitation at 475 nm and emission at 530 nm.

Western Blotting

Western blotting was performed as reported before (23). Briefly, to prepare the whole cell protein, ARPE-19 cells from different treatment groups were harvested and extracted with ice-cold radioimmunoprecipitation assay (RIPA) buffer mixed with phosphatase inhibitors and protease inhibitor cocktail. To extract nuclear and cytoplasmic protein, relevant nuclear and cytoplasmic protein extraction kits (Beyotime, Shanghai, China) were applied. Bicinchoninic acid (BCA) protein assay kit (Thermo Fisher, Madison, USA) was used for protein concentration determination. To separate the target proteins, protein samples (40 μg) were subjected to 12% polyacrylamide gel electrophoresis and electro-transferred to polyvinylidene fluoride (PVDF) membranes (Bio-Rad Laboratories, Hercules, USA) at 1 A, 25 V conditions for 30 min. Skim milk (5% v/v) in Tris-buffered saline containing 0.05% Tween-20 (TBST) was used for blocking at room temperature for 1.5 h. Then, target proteins were detected by incubation with corresponding primary antibodies overnight at 4°C following incubation (2 h) with horseradish peroxidase-linked secondary antibodies at ambient temperature. The protein bands were visualized using chemiluminescence reagent (Bio-Rad Laboratories, Hercules, USA). In addition, α-tubulin and Histone H3 were selected as loading control for total protein and nuclear protein, respectively.

Nrf2 SiRNA Knockdown

ARPE-19 cells (1×10^5 cells/well) were plated in 12-well plates for 24 h, following transfection with 100 nM of control siRNA or Nrf2 siRNA for 12 h (Lipofectamine 2000, Thermo Fisher, Madison, USA). Subsequently, the cells were incubated with 100 μg/mL CM for another 12 h prior to treatment with 400 μM H_2O_2. The cytoprotective effects of different treatments were evaluated by MTT assay.

Statistical Analysis

Data were indicated as means ± SD ($n = 3$). The comparisons between different groups were conducted by one-way ANOVA and analyzed by Duncan's test using SPSS 19.0 software. The value of $P \leq 0.05$ was statistical significance.

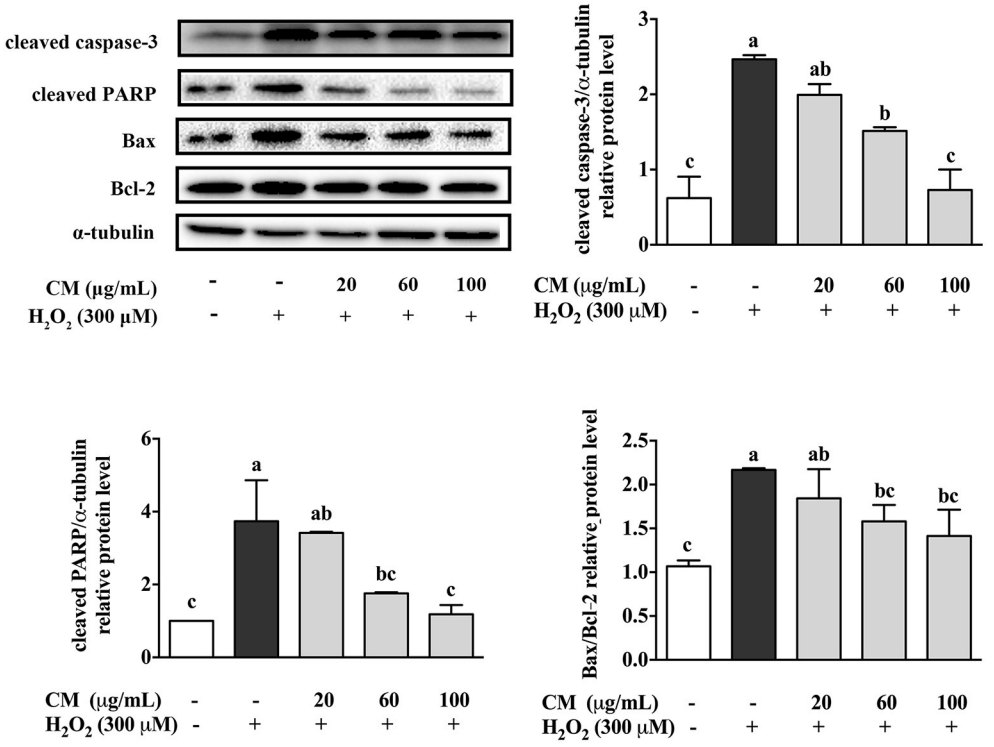

FIGURE 2 | Effects of Fubaiju hot-water extracts (CMs) on apoptosis-related protein expression induced by hydrogen peroxide (H_2O_2) in ARPE-19 cells. After pretreatment with 20, 60, and 100 μg/mL CM for 24 h, the cells were then co-treated with 300 μM H_2O_2 for another 4 h. The protein expression levels of cleaved caspase-3, cleaved poly(ADP-ribose) polymerase (PARP), Bax, Bcl-2, and α-tubulin were determined by Western blotting. Here, α-tubulin was used as a loading control. The protein levels of the bands were quantified by densitometry. The results are mean ± SD ($n = 3$). Columns with different letters are significantly different ($P < 0.05$).

RESULTS

Chrysanthemum morifolium cv. Fubaiju Hot-Water Extracts Prevented H_2O_2-Induced ARPE-19 Cell Oxidative Damage and Intracellular Reactive Oxygen Species Production

MTT results showed that there was no significant difference of cell viability between the cells treated with different doses of CM (20, 60, and 100 μg/mL) and the control group (**Figure 1A**). The cell viability of ARPE-19 cells was significantly decreased in a dose-dependent manner after incubation with H_2O_2, and 300 μM H_2O_2 was chosen to use in subsequent experiments (**Figure 1B**). As shown in **Figure 1C**, pretreatment with different concentrations of CM could attenuate 300 μM H_2O_2-induced decrease of cell viability. Iloki-Assanga et al. (24) reported that excessive intracellular ROS generation could induce severe oxidative damage and lead to chronic degenerative and ocular diseases. Meanwhile, different concentrations of CM (20, 60, and 100 μg/mL) showed a dose-dependent inhibitive effect on intracellular ROS production (**Figure 1D**). Here, 300 μM H_2O_2 treatment significantly increased the intracellular ROS production by 31.9% compared to that of the control group, while ROS generation was significantly decreased by 10.0, 23.5, and 23.8% after 20, 60, and 100 μg/mL CM treatment, respectively (**Figure 1D**; $P < 0.05$). These results suggested that the CM-mediated cytoprotective activity might be related to the inhibition of ROS generation.

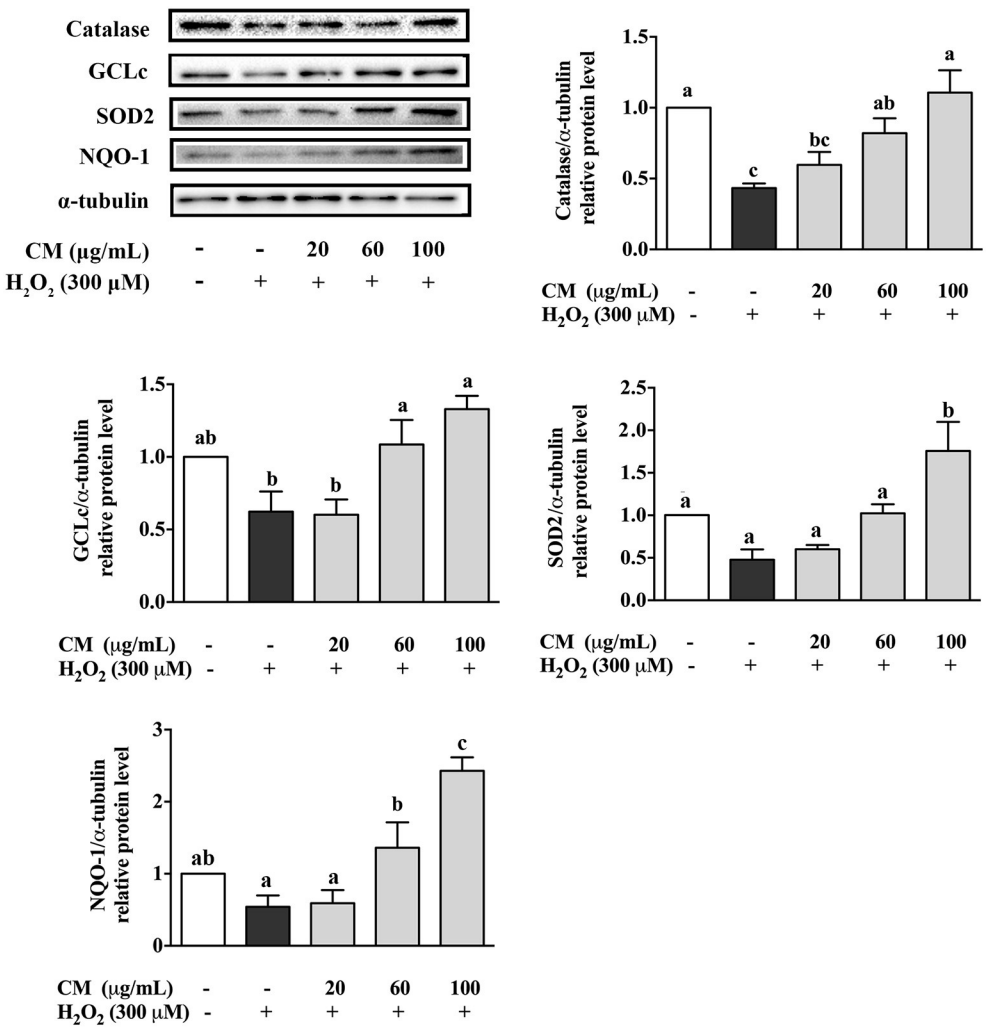

FIGURE 3 | Effects of Fubaiju hot-water extracts (CMs) on antioxidant enzyme protein expression induced by hydrogen peroxide (H_2O_2) in ARPE-19 cells. After pretreatment with 20, 60, and 100 μg/mL CM for 24 h, the ARPE-19 cells were then co-treated with 300 μM H_2O_2 for another 4 h. The protein levels of catalase, glutamate-cysteine ligase catalytic subunit (GCLc), superoxide dismutase (SOD), and NAD(P)H:quinone oxidoreductase 1 (NQO-1) were determined by Western blotting using the corresponding antibodies. Here, α-tubulin was used as a loading control. The protein levels of the bands were quantified by densitometry. The results are mean ± SD ($n = 3$). Columns with different letters are significantly different ($P < 0.05$).

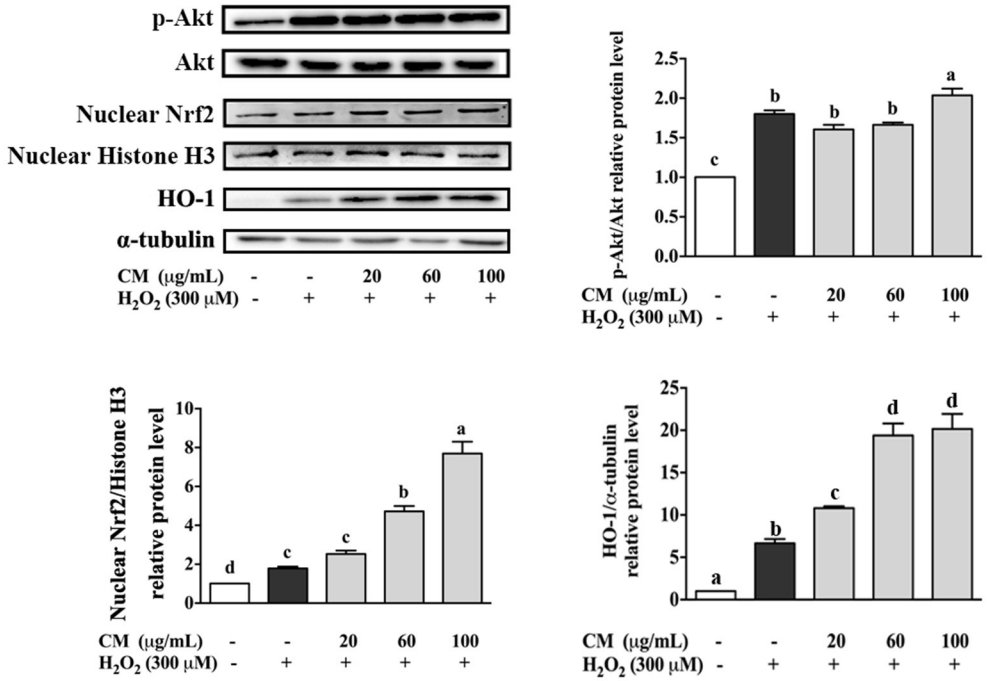

FIGURE 4 | Effects of Fubaiju hot-water extracts (CMs) on Akt/nuclear factor erythroid 2-related factor 2 (Nrf2) signaling pathway-related protein expression induced by H_2O_2 on ARPE-19 cells. After pretreatment with 20, 60, and 100 μg/mL CM for 24 h, the cells were then treated with 300 μM H_2O_2 for another 0.5 h. The protein levels of phosphor (*p*) or total (*t*) Akt, nuclear Nrf2, nuclear Histone H3, heme oxygenase-1 (HO-1), and α-tubulin were determined by Western blotting. The results are mean ± SD ($n = 3$). Columns with different letters are significantly different ($P < 0.05$).

Chrysanthemum morifolium cv. Fubaiju Hot-Water Extracts Decreased Proapoptotic Related Protein Expression

The apoptosis-related protein expression of cleaved caspase-3, cleaved PARP, Bax, and Bcl-2 was evaluated through Western blotting. Cleaved caspase-3 and cleaved PARP are major biomarkers in apoptosis (25, 26). Bax was evidenced to increase the release of cytochrome *c* from mitochondria to trigger apoptosis, while Bcl-2 reversed these effects *via* stabilizing the mitochondrial membrane to block cytochrome *c* release (27). Compared with the control group, treatment with 300 μM H_2O_2 notably increased the expression level of cleaved caspase-3 and cleaved PARP and the ratio of Bax/Bcl-2 (**Figure 2**; $P < 0.05$). In contrast, after pretreatment with CM, the increased expression of these proapoptotic related proteins was markedly suppressed in a dose-dependent manner (**Figure 2**; $P < 0.05$). The ratio of Bax/Bcl-2 was an important predictive indicator of cell apoptosis, which was positively associated with apoptosis (27). Pretreatment with CM significantly decreased the H_2O_2-induced upregulation of cleaved caspase-3, cleaved PARP, and Bax/Bcl-2 ratio, indicating that CM could prevent ARPE-19 cells from H_2O_2-induced apoptosis. Considering that cell apoptosis could be induced by the accumulation of ROS under oxidative stress (28), the antiapoptotic effect of CM could be closely related to its antioxidant capacity against oxidative stress.

Chrysanthemum morifolium cv. Fubaiju Hot-Water Extracts Increased Antioxidant Enzyme Protein Expression

To investigate the antioxidative mechanisms of CM against H_2O_2-induced cell damage, the protein expression levels of antioxidant enzymes including catalase, GCLc, SOD2, and NQO-1 were detected by Western blot. H_2O_2 treatment notably decreased the expression of catalase, GCLc, SOD2, and NQO-1 (**Figure 3**; $P < 0.05$). However, compared to the H_2O_2 group, pretreatment with 100 μg/mL CM remarkably enhanced the expression of catalase, GCLc, SOD2, and NQO-1 by 155.2, 113.4, 267.6, and 347.8%, respectively (**Figure 3**; $P < 0.05$). The results indicated that catalase, GCLc, SOD2, and NQO-1 might be involved in the protective role of CM against H_2O_2-induced oxidative stress.

Chrysanthemum morifolium cv. Fubaiju Hot-Water Extracts Attenuated H_2O_2-Induced Oxidative Damage Through the Nrf2/HO-1 Signaling Pathway

The effects of CM on the expression of Akt and nuclear Nrf2 and HO-1 were detected by Western blot. In our present study, the phosphorylation of Akt was markedly increased by pretreatment with 100 μg/mL CM compared with the group treated with 300 μM H_2O_2 (**Figure 4**; $P < 0.05$). PI3K/Akt

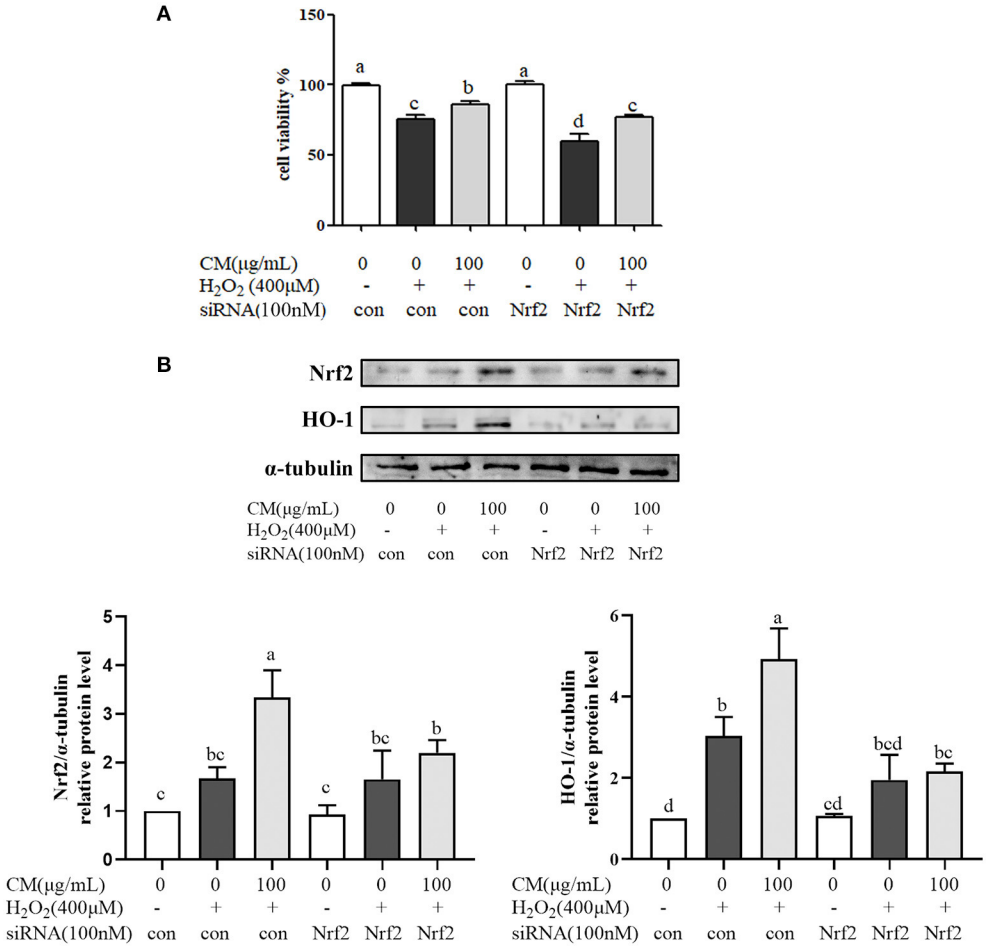

FIGURE 5 | Fubaiju hot-water extracts (CMs) protected against hydrogen peroxide (H_2O_2)-induced ARPE-19 cell oxidative damage *via* activating the nuclear factor erythroid 2-related factor 2 (Nrf2)/heme oxygenase-1 (HO-1) pathway. ARPE-19 cells were transfected with or without 100 nM Nrf2 small interfering RNA (siRNA) for 12 h and then treated with or without 100 μg/mL CM for another 12 h before incubation with 400 μM H_2O_2. **(A)** The cytoprotective effect of CM on ARPE-19 cells induced by H_2O_2 with control or Nrf2 siRNA. **(B)** The protein levels of Nrf2, HO-1, and α-tubulin were determined by Western blotting. Here, α-tubulin was used as a loading control. The protein levels of the bands were quantified by densitometry. The results are mean ± SD ($n = 3$). Columns with different letters are significantly different ($P < 0.05$).

signaling pathway is important for the activation and nuclear translocation of Nrf2 (7, 8, 29). The transcription factor Nrf2 regulates the expression of important cytoprotective enzymes, such as HO-1 (28). CM treatment elevated the expression of nuclear translocated Nrf2 and its downstream HO-1 in a dose-dependent manner (**Figure 4**). To verify whether Nrf2 was required for the protective function of CM, Nrf2 was silenced using siRNA interference (**Figure 5A**). Cell viability decreased significantly after incubation with 400 μM H_2O_2 compared to the untreated group (**Figure 5A**; $P < 0.05$), while 100 μg/mL CM remarkably reversed the decrement, which was consistent with the abovementioned results (**Figure 1C**). Treatment with 100 nM Nrf2 siRNA showed no effect on cell viability in comparison to the untreated group. However, pretreatment with 100 nM Nrf2 siRNA could aggravate H_2O_2-induced cell damage and weaken the cytoprotective effects of CM compared to the counterpart groups without Nrf2 siRNA treatment (**Figure 5A**). In addition, preincubation with 100 nM Nrf2 siRNA significantly abolished CM-mediated upregulation of Nrf2 and HO-1 at the protein level (**Figure 5B**; $P < 0.05$), suggesting that Nrf2 was required for the protection of CM on ARPE-19 cell oxidative damage.

Chrysanthemum morifolium cv. Fubaiju Hot-Water Extracts Suppressed ARPE-19 Cell Damage Through the PI3K/Akt-Mediated Nrf2/HO-1 Signaling Pathway

Nrf2/HO-1 signaling pathway could be activated *via* activation of PI3K/Akt pathway (30). PI3K inhibitor (LY294002) was used to identify whether PI3K/Akt pathway was activated for the protection of CM on ARPE-19 cells (**Figure 6**). Treatment with LY294002 alone had no effect on the cell viability compared with the non-treatment group; however, pretreatment with

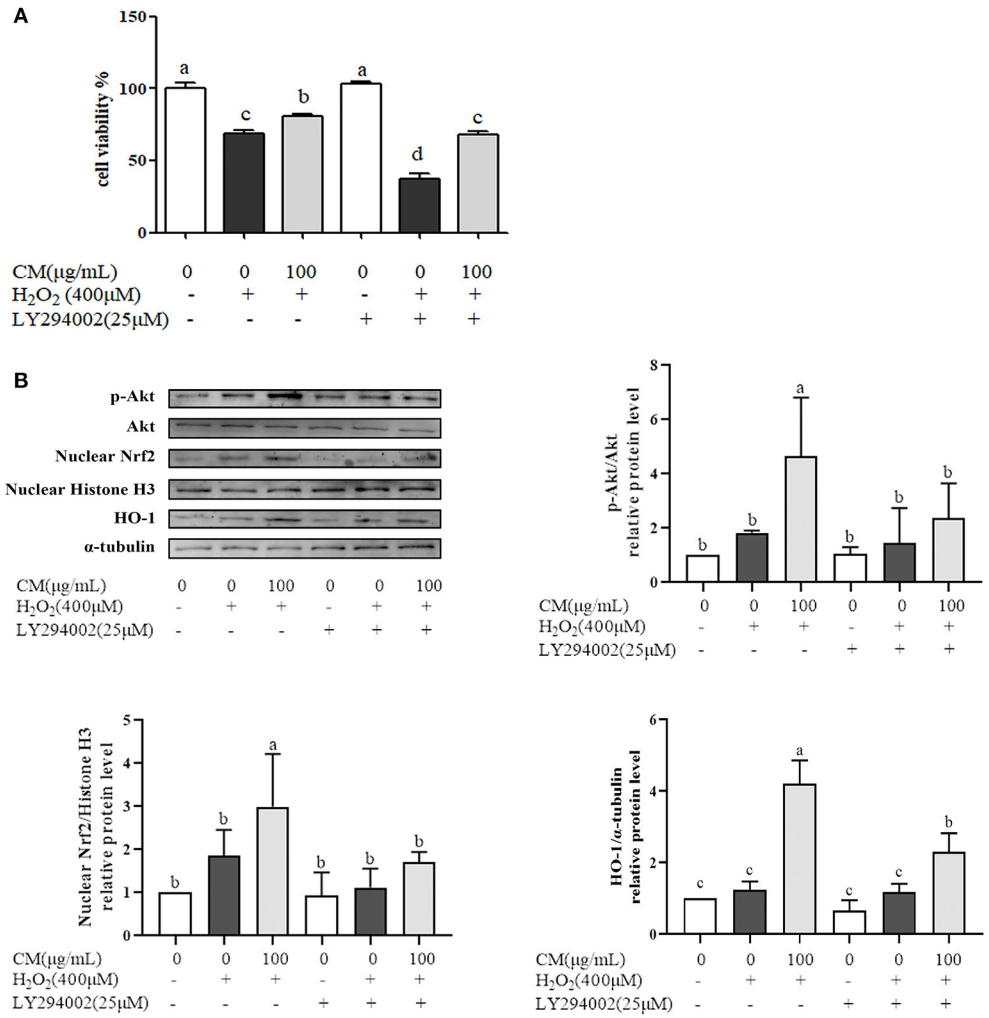

FIGURE 6 | Fubaiju hot-water extracts (CMs) protected against hydrogen peroxide (H_2O_2)-induced ARPE-19 cell oxidative damage by activating the Akt-dependent nuclear factor erythroid 2-related factor 2 (Nrf2)/heme oxygenase-1 (HO-1) pathway. ARPE-19 cells were cultured with 100 μg/mL CM for 24 h and then transfected with or without 25 μM phosphatidylinositol 3-kinase (PI3K) inhibitor LY294002 for 4 h before incubation with or without 400 μM H_2O_2. **(A)** The cytoprotective effect of CM on ARPE-19 cells induced by H_2O_2 with or without LY294002. **(B)** The protein levels of phosphor (*p*) or total (*t*) Akt, nuclear Nrf2, nuclear Histone H3, HO-1, and α-tubulin were determined by Western blotting. The protein levels of the bands were quantified by densitometry. The results are mean ± SD ($n = 3$). Columns with different letters are significantly different ($P < 0.05$).

LY294002 could aggravate cell damage caused by H_2O_2 and impair the protective effects of CM compared to the counterpart group without LY294002 treatment (**Figure 6A**; $P < 0.05$). Moreover, LY294002 remarkably blocked the CM-mediated phosphorylation of Akt and decreased its downstream gene expression, such as nuclear translocated Nrf2 and HO-1 at the protein level (**Figure 6B**), implying the involvement of PI3K/Akt pathway in the protection of CM against H_2O_2-induced ARPE-19 cell oxidative damage.

DISCUSSION

This study revealed the underlying mechanism of the cytoprotection of CM on H_2O_2-induced oxidative stress in ARPE-19 cells. Oxidative stress induces RPE cell apoptosis, which is the major contributor to the onset and development of many age-related degenerative diseases (29, 31). Our results suggested that CM treatment could reduce intracellular ROS production and promote phase II enzyme expression such as catalase, GCLc, SOD2, NQO-1, and HO-1, causing the reduction of ARPE-19 cell apoptosis. Previous study also indicated CMs were able to scavenge DPPH·, $ABTS^{\cdot+}$, and oxygen radicals; depress the increment of H_2O_2-induced intercellular ROS production; and inhibit the expression of LPS-induced inflammatory cytokines (14, 15). The possible reason for the protective effects of CM against oxidative stress in ARPE-19 cells may be because it is rich in natural antioxidants. A total of 26 compounds including 21 flavonoids and five phenolic acids were identified from

CM, in which apigenin-7-O-glucoside, kaempferol-3-O-acetyl-glucoside, and apigenin-7-O-acetylglucoside were the three major components (14–16).

To further reveal the underlying mechanism of the cytoprotective activity of CM, Nrf2 activation and the expression of downstream antioxidant enzymes were investigated. Nrf2 is a redox-sensitive transcription factor that regulates many phase II antioxidant enzyme expression, and activation of Nrf2 is evidenced to be one of the critical defensive mechanisms against oxidative stress (32). Our results demonstrated that transfecting ARPE-19 cells with Nrf2 siRNA accelerated H_2O_2-induced oxidative damage and depressed the protective effects of CM against oxidative stress. In line with the above results, apigenin could attenuate the tert-butyl hydroperoxide (t-BHP)-induced oxidative damage in ARPE-19 cells *via* the Nrf2 pathway (33). The activities of SOD, catalase, glutathione peroxidase (GSH-PX), and the total antioxidant capacity (T-AOC) were notably increased after apigenin intervention (33). Natural bioactive compounds in food ingredients could promote Nrf2 activation and protect the retina from oxidative stress causing retinal diseases. For example, it was found that kaempferol prevented ARPE-19 cells from H_2O_2-induced oxidative damage and apoptosis *via* reducing ROS production and decreasing the expression of Bax/Bcl-2, caspase-3, and vascular endothelial growth factor (VEGF) (34). Weng et al. (35) reported that quercetin restored the H_2O_2-reduced cell viability decrement and increased Nrf2, NQO-1, and HO-1 expression at the protein level. The phytochemicals of CM included many multi-bioactive compounds such as aglycone and glycoside of kaempferol, quercetin, and apigenin, which might partly explain that the possible mechanism of CM against oxidative stress in ARPE-19 cells was through Nrf2 signaling activation and its downstream antioxidant enzyme expression. However, whether any synergistic interaction occurs between these compounds is still unclear, which requires more research in the future. Moreover, previous research has demonstrated that PI3K/Akt pathway plays a critical role in modulating Nrf2/HO-1 protein expression as an upstream signaling, which is crucial for the cytoprotection of RPE cells (7). PI3K/Akt could make Nrf2 dissociate from Keap1 and facilitate subsequent signal transduction to induce the activation of antioxidant enzymes (36). There are many studies demonstrating that continuous oxidative stress will lead to cell damage *via* the downregulation of PI3K/Akt signaling pathway (37). Thus, upregulation of PI3K/Akt might play an important role against RPE cell oxidative damage. For example, piceatannol could protect ARPE-19 cells against H_2O_2-induced oxidative stress and apoptosis through modulating PI3K/Akt/Nrf2/HO-1 signaling pathway (7). Our present study indicated that PI3K inhibitor (LY294002) counteracted CM-mediated increase of Akt phosphorylation, Nrf2 nuclear translocation, HO-1 expression, and cytoprotective activity, which was in accordance with other published studies (3, 10, 11), suggesting that CM activated Akt-dependent Nrf2 signaling to protect ARPE-19 cells from oxidative stress.

CONCLUSIONS

In conclusion, we found that CMs were non-toxic for ARPE-19 cells and could significantly reduce H_2O_2-induced oxidative damage and apoptosis. The cytoprotective effects of CM against oxidative stress were *via* activating the PI3K/Akt-mediated Nrf2/HO-1 pathway. These results could offer an extended window for the utilization and consumption of Fubaiju as food-medicine homologous functional flower tea in functional foods/beverages to minimize the risk of AMD. However, the identification and characterization of the specific bioactive substance in Fubaiju that plays the vital role still need further study.

DATA AVAILABILITY STATEMENT

The original contributions generated for this study are included in the article/supplementary material, further inquiries can be directed to the corresponding author/s.

AUTHOR CONTRIBUTIONS

YH contributed to writing the original draft preparation, data curation and analysis, and software and investigation. YL contributed to writing the original draft preparation, data curation, and analysis. JL contributed to writing, reviewing, and editing, supervision, and project administration. ZW contributed to writing, reviewing, and editing. BG and YZ contributed to the conceptualization and methodology. JW contributed to the supervision and project administration. All authors contributed to the article and approved the submitted version.

FUNDING

This research was financially supported by the National Natural Science Foundation of China (Grant No. 32001704), the National Key Research and Development Program of China (Grant No. 2018YFC1602400), the General Project of Beijing Municipal Commission of Education (Grant No. KM202110011004), and the School Level Cultivation Fund of Beijing Technology and Business University for Distinguished and Excellent Young Scholars.

REFERENCES

1. Boujbiha MA, Hamden K, Guermazi F, Bouslama A, Omezzine A, Kammoun A, et al. Testicular toxicity in mercuric chloride treated rats: association with oxidative stress. *Reprod Toxicol.* (2009) 28:81–9. doi: 10.1016/j.reprotox.2009.03.011
2. Fang Y, Su T, Qiu X, Mao P, Xu Y, Hu Z, et al. Protective effect of alpha-mangostin against oxidative stress induced-retinal

cell death. *Sci Rer-UK*. (2016) 6:1–15. doi: 10.1038/srep 21018
3. Li Z, Dong X, Liu H, Chen X, Shi H, Fan Y, et al. Astaxanthin protects ARPE-19 cells from oxidative stress via upregulation of Nrf2-regulated phase II enzymes through activation of PI3K/Akt. *Mol Vis*. (2013) 19:1656–66.
4. Richer S, Stiles W, Thomas C. Molecular medicine in ophthalmic care. *Optometry*. (2009) 80:695–701. doi: 10.1016/j.optm.2009. 03.018
5. Richer S, Stiles W, Ulanski L, Carroll D, Podella C. Observation of human retinal remodeling in octogenarians with a resveratrol based nutritional supplement. *Nutrients*. (2013) 5:1989–2005. doi: 10.3390/nu50 61989
6. Yu C, Nandrot E, Dun Y, Finnemann S. Dietary antioxidants prevent age-related retinal pigment epithelium actin damage and blindness in mice lacking αvβ5 integrin. *Free Radical Bio Med*. (2012) 52:660–70. doi: 10.1016/j.freeradbiomed.2011.11.021
7. Hao Y, Liu J, Wang Z, Yu L, Wang J. Piceatannol protects human retinal pigment epithelial cells against hydrogen peroxide induced oxidative stress and apoptosis through modulating PI3K/Akt signaling pathway. *Nutrients*. (2019) 11:1515–27. doi: 10.3390/nu11071515
8. Lu B, Sun T, Li W, Sun X, Yao X, Sun X. Piceatannol protects ARPE-19 cells against vitamin A dimer-mediated photo-oxidative damage through activation of Nrf2/NQO1 signalling. *J Funct Foods*. (2016) 26:739–49. doi: 10.1016/j.jff.2016.08.046
9. Takayama K, Kaneko H, Kataoka K, Kimoto R, Hwang S-J, Ye F, et al. Nuclear factor (erythroid-derived)-related factor 2-associated retinal pigment epithelial cell protection under blue light-induced oxidative stress. *Oxid Med Cell Longev*. (2016) 2016:1on. doi: 10.1155/2016/86 94641
10. Wang Z, Hao Y, Wang Y, Liu J, Yuan X, Sun B, et al. Wheat alkylresorcinols protect human retinal pigment epithelial cells against H2O2-induced oxidative damage through Akt-dependent Nrf2/HO-1 signaling. *Food Funct*. (2019) 10:2797HO-1. doi: 10.1039/C8FO0 2564A
11. Zou X, Gao J, Zheng Y, Wang X, Chen C, Cao K, et al. Zeaxanthin induces Nrf2-mediated phase II enzymes in protection of cell death. *Cell Death Dis*. (2014) 5:e1218hin. doi: 10.1038/cddis.2014.190
12. Wang L, Kondo N, Cano M, Ebrahimi K, Handa J. Nrf2 signaling modulates cigarette smoke-induced complement activation in retinal pigmented epithelial cells. *Free Radical Bio Med*. (2014) 70:155–66. doi: 10.1016/j.freeradbiomed.2014.01.015
13. Lai JP, Lim YH, Su J, Shen HM, Ong CN. Identification and characterization of major flavonoids and caffeoylquinic acids in three Compositae plants by LC/DAD-APCI/MS. *J Chromatogr B*. (2007) 848:215–25. doi: 10.1016/j.jchromb.2006.10.028
14. Li Y, Hao Y, Gao B, Geng P, Huang H, Yu L, et al. Chemical profile and in vitro gut microbiota modulatory, anti-inflammatory and free radical scavenging properties of *Chrysanthemum morifolium* cv. Fubaiju. *J Funct Foods*. (2019) 58:114al. doi: 10.1016/j.jff.2019.04.053
15. Li Y, Yang P, Luo Y, Gao B, Sun J, Lu W, et al. Chemical compositions of chrysanthemum teas and their anti-inflammatory and antioxidant properties. *Food Chem*. (2019) 286:8sit. doi: 10.1016/j.foodchem.2019. 02.013
16. Lin L, Harnly J. Identification of the phenolic components of chrysanthemum flower (*Chrysanthemum morifolium* Ramat). *Food Chem*. (2010) 120:319rif. doi: 10.1016/j.foodchem.2009.09.083
17. Wang S, Hao LJ, Zhu JJ, Zhang QW, Wang ZM, Zhang X, et al. Study on the effects of sulfur fumigation on chemical constituents and antioxidant activity of *Chrysanthemum morifolium* cv. Hang-ju. *Phytomedicine*. (2014) 21:773–9. doi: 10.1016/j.phymed.2013.10.019
18. Hua B, Lv G, Zhang Y. Progress in studies on cardiac effects of *Chrysanthemum morifolium* Ramat's flavonoids. *Chin J Pract Chin With Mod Med*. (2006) 19:1868–9.
19. Xie YY, Qu JL, Wang QL, Wang Y, Yoshikawa M, Yuan D. Comparative evaluation of cultivars of *Chrysanthemum morifolium* flowers by HPLC-DAD-ESI/MS analysis and antiallergic assay. *J Agr Food Chem*. (2012) 60:12574–83. doi: 10.1021/jf304080v
20. Tao J, Duan J, Qian Y, Qian D, Guo J. Investigation of the interactions between *Chrysanthemum morifolium* flowers extract and intestinal bacteria from human and rat. *Biomed Chromatogr*. (2016) 30:1807–19. doi: 10.1002/bmc.3756
21. Feng J, Chen X, Sun X, Wang F, Sun X. Expression of endoplasmic reticulum stress markers GRP78 and CHOP induced by oxidative stress in blue light-mediated damage of A2E-containing retinal pigment epithelium cells. *Ophthalmic Res*. (2014) 52:224–33. doi: 10.1159/000 363387
22. Liu J, Wang Y, Hao Y, Wang Z, Yang Z, Wang Z, et al. 5-Heptadecylresorcinol attenuates oxidative damage and mitochondria-mediated apoptosis through activation of the SIRT3/FOXO3a signaling pathway in neurocytes. *Food Funct*. (2020) 11:2535–42. doi: 10.1039/C9FO03028J
23. Liu J, Wang Y, Wang Z, Hao Y, Bai W, Wang Z, et al. 5-heptadecylresorcinol, a biomarker for whole grain rye consumption, ameliorates cognitive impairments and neuroinflammation in APP/PS1 transgenic mice. *Mol Nutr Food Res*. (2020) 64:1–10. doi: 10.1002/mnfr.201 901218
24. Iloki-Assanga SB, Lewis-Luján LM, Fernández-Angulo D, Gil-Salido AA, Lara-Espinoza CL, Rubio-Pino JL. Retino-protective effect of Bucida buceras against oxidative stress induced by H_2O_2 in human retinal pigment epithelial cells line. *BMC Complem Altern M*. (2015) 15:254–75. doi: 10.1186/s12906-015-0765-6
25. Boulares AH, Yakovlev AG, Ivanova V, Stoica BA, Wang G, Iyer S, et al. Role of poly (ADP-ribose) polymerase (PARP) cleavage in apoptosis Caspase 3-resistant PARP mutant increases rates of apoptosis in transfected cells. *J Biol Chem*. (1999) 274:22932–40. doi: 10.1074/jbc.274.33. 22932
26. Porter AG, Jänicke RU. Emerging roles of caspase-3 in apoptosis. *Cell Death Differ*. (1999) 6:99–104. doi: 10.1038/sj.cdd.4400476
27. Nakamura H, Kumei Y, Morita S, Shimokawa H, Ohya K, Shinomiya K. Antagonism between apoptotic (Bax/Bcl-2) and anti-apoptotic (IAP) signals in human osteoblastic cells under vector-averaged gravity condition. *Ann NY Acad Sci*. (2003) 1010:143–7. doi: 10.1196/annals.1299.023
28. Bellezza I. Oxidative stress in age-related macular degeneration: Nrf2 as therapeutic target. *Front Pharmacol*. (2018) 9:1280–6. doi: 10.3389/fphar.2018.01280
29. Zhang H, Liu Y, Jiang Q, Li K, Zhao Y, Cao C, et al. Salvianolic acid A protects RPE cells against oxidative stress through activation of Nrf2/HO-1 signaling. *Free Radical Bio Med*. (2014) 69: 219–28. doi: 10.1016/j.freeradbiomed.2014.01.025
30. Martin D, Rojo A, Salinas M, Diaz R, Gallardo G, Alam J, et al. Regulation of heme oxygenase-1 expression through the phosphatidylinositol 3-kinase/Akt pathway and the Nrf2 transcription factor in response to the antioxidant phytochemical carnosol. *J Biol Chem*. (2004) 279:8919–29. doi: 10.1074/jbc.M309660200
31. Campagne MVL, LeCouter J, Yaspan BL, Ye W. Mechanisms of age-related macular degeneration and therapeutic opportunities. *J Pathol*. (2014) 232:151–64. doi: 10.1002/path.4266
32. Nakagami Y. Nrf2 Is an attractive therapeutic target for retinal diseases. *Oxidative Oxid Med Cell Longev*. (2016) 2016:1–9. doi: 10.1155/2016/7469326
33. Xu X, Li M, Chen W, Yu H, Yang Y, Hang L. Apigenin attenuates oxidative injury in ARPE-19 cells thorough activation of Nrf2 pathway. *Oxid Med Cell Longev*. (2016) 2016:1–10. doi: 10.1155/2016/43 78461
34. Du W, An Y, He X, Zhang D, He W. Protection of kaempferol on oxidative stress-induced retinal pigment epithelial cell damage. *Oxid Med Cell Longev*. (2018) 2018:1–14. doi: 10.1155/2018/1610751
35. Weng S, Mao L, Gong Y, Sun T, Gu Q. Role of quercetin in protecting ARPE-19 cells against H2O2-induced injury via nuclear factor erythroid 2 like 2 pathway activation and endoplasmic reticulum stress inhibition. *Mol Med Rep*. (2017) 16:3461–68. doi: 10.3892/mmr.2017.6964
36. Zhuang Y, Wu H, Wang X, He J, He S, Yin Y. Resveratrol attenuates oxidative stress-induced intestinal barrier injury through PI3K/Akt-mediated Nrf2 signaling pathway. *Oxid Med Cell Longev*. (2019) 2019:1–14. doi: 10.1155/2019/7591840
37. Rajendran P, Ammar RB, Al-Saeedi FJ, Mohamed ME, ElNaggar MA, Al-Ramadan SY, et al. Kaempferol inhibits zearalenone-induced oxidative stress

and apoptosis via the PI3K/Akt-mediated Nrf2 signaling pathway: *in vitro* and *in vivo* studies. *Int J Mol Sci*. (2021) 22:217–34. doi: 10.3390/ijms22010217

Conflict of Interest: The authors declare that the research was conducted in the absence of any commercial or financial relationships that could be construed as a potential conflict of interest.

frontiers in Nutrition

ORIGINAL RESEARCH
published: 05 May 2021
doi: 10.3389/fnut.2021.647748

Effects of High-Pressure Homogenization on Pectin Structure and Cloud Stability of Not-From-Concentrate Orange Juice

Wantong Yu[1,2], *Jiefen Cui*[2], *Shaojie Zhao*[2], *Liping Feng*[2], *Yanqi Wang*[2], *Junmei Liu*[1]* and *Jinkai Zheng*[2]*

[1] College of Food Science and Engineering, Jilin Agricultural University, Changchun, China, [2] Institute of Food Science and Technology, Chinese Academy of Agricultural Sciences, Beijing, China

OPEN ACCESS

Edited by:
Michael Rychlik,
Technical University of Munich, Germany

Reviewed by:
Ashish Rawson,
Indian Institute of Food Processing Technology, India
Yun Ping Neo,
Taylor's University, Malaysia

***Correspondence:**
Junmei Liu
liujunmei@jlau.edu.cn
Jinkai Zheng
zhengjinkai@caas.cn

Specialty section:
This article was submitted to Food Chemistry, a section of the journal Frontiers in Nutrition

Received: 30 December 2020
Accepted: 07 April 2021
Published: 05 May 2021

Citation:
Yu W, Cui J, Zhao S, Feng L, Wang Y, Liu J and Zheng J (2021) Effects of High-Pressure Homogenization on Pectin Structure and Cloud Stability of Not-From-Concentrate Orange Juice. Front. Nutr. 8:647748. doi: 10.3389/fnut.2021.647748

Not-from-concentrate (NFC) juice is popular with consumers due to its similarity to fresh fruit juice in taste, flavor, and beneficial nutrients. As a commonly used technology in fruit juice production, high-pressure homogenization (HPH) can enhance the commercial value of juice by improving the color, flavor, taste, and nutrient contents. In this study, the effects of HPH on the pectin structural properties and stability of NFC orange juice were investigated. The correlations between HPH-induced changes in the structure of pectin and the stability of orange juice were revealed. Compared with non-homogenized orange juice, HPH increased the galacturonic acid (GalA) content and the linearity of pectin, while decreasing the molecular weight (Mw), pectin branching, and rhamnogalacturonan (RG) contribution, and cracks and pores of different sizes formed on the surface of pectin, implying depolymerization. Meanwhile, with increasing pressure and number homogenization of passes, HPH effectively improved the stability of NFC orange juice. HPH can effectively prevent the stratification of orange juice, thereby promoting consumer acceptance and endowing a higher commercial value. The improvement of the stability of NFC orange juice by HPH was related to the structural properties of pectin. Turbidity was significantly ($P < 0.01$) positively correlated with GalA and pectin linearity, but was significantly ($P < 0.01$) negatively correlated with Mw, RG contribution, and pectin branching. Modification of pectin structure can improve the stability of NFC orange juice. In this work, the relationship between the pectin structure and stability of NFC orange juice is elucidated, providing a path toward improving consumer acceptance and enhancing the palatability and nutritional and functional qualities of orange juice. Manufacturers can use this relationship to modify pectin directionally and produce high-quality NFC orange juice beverages.

Keywords: high-pressure homogenization, NFC orange juice, pectin, structure, stability

INTRODUCTION

The orange is one of the most important agricultural products, with high annual yield worldwide (73.3 million tons in 2019), much of which is used to produce orange juice (1). In recent years, not-from-concentrate (NFC) orange juice has become increasingly popular among consumers because its flavor is closer to that of freshly squeezed orange juice (2, 3). More importantly, NFC orange juice is rich in various nutrients (pectin, vitamin C, carotenoids, and flavanones) and exhibits several biological activities (4), including antioxidant (5), anti-inflammatory (6), and anticarcinogenic effects (7). It is processed from fresh oranges by washing, squeezing, homogenizing, and sterilizing. It is not concentrated during its production process and no chemical preservatives are added (3). The endocarp cells are ruptured during the process of mechanical squeezing, and the membrane as well as many components (pectin, protein, cellulose, hemicelluloses, and hesperidin) are suspended in the orange juice (8, 9). These suspensions lead to the cloudy and turbid appearance of NFC orange juice and affect its cloud stability. Due to containing particles of different sizes and the existence of pectin and pectin methylesterase (PME), orange juice is easily delaminated (10), which destroys its stability and thus reduces its sensory and nutritional properties, ultimately affecting consumer acceptance and the market value of orange juice. Therefore, cloud stability is an important indicator of the food, nutritional, and functional qualities of orange juice.

Pectin is part of the cloud material and plays a vital role in cloud stability. Pectin in orange juice is transformed by PME from high-methoxyl pectin to low-methoxyl pectin and pectic acid, which forms insoluble complexes with calcium ions and leads to decreased cloud stability (11), which in turn affects the sensory and nutritional properties of orange juice. Pectin is a complex polysaccharide, and its structure is mainly composed of three domains: homogalacturonan (HG), rhamnogalacturonan-I (RG-I), and rhamnogalacturonan-II (RG-II) (12, 13). HG, also known as the "smooth zone," is composed of 1,4-linked α-D-galacturonic acid (α-D-GalA) residues, which are considered the backbone of pectin, with some C-6 carboxyl groups being methylated. The functional properties of pectin in fruit-based products depend to a large extent on the properties of the HG region. RG-I comprises a backbone of alternating α-L-rhamnose and α-D-GalA residues. To most of rhamnose (Rha) residues side chains at C4 are attached that consist mainly of arabinose (Ara) and galactose (Gal) (4). RG-II has a short 1,4-linked α-D-GalA backbone, and its side chain is composed of 12 different types of sugars (12). Generally, the properties of pectin are influenced by galacturonic acid (GalA), molecular weight (Mw), and neutral sugars (14, 15). The proportion of esterified GalA residues and the distribution of esterified residues in the HG region strongly affect the solubility, thickening, gelling, and hydration properties of pectin (12). The Mw distribution of pectin is a major parameter that directly affects the apparent viscosity and other physicochemical properties (16). Notably, the structural characteristics of pectin are easily affected by the processing process, which further affects its physicochemical properties, functions, and applications (17).

High-pressure homogenization (HPH) is an important component of juice processing that can improve the stability and quality of the juice and release bioactive substances, thereby enhancing the nutritional and functional properties of the juice. HPH is realized by a piston forcing fluid through small holes. When the fluid passes through the valve, the rapid change of velocity and pressure produce turbulence and cavitation, fragmenting the polymer, particles, or cells in the system (11). HPH can enhance the turbidity and overall color of orange juice, reduce particle size, and increase the nutrient accessibility (total carotenoids, flavonoids, and vitamin C) and functional properties (antioxidant activity) in orange juice (18–20), which in turn increases consumer acceptance and improves the market value. For mixed juice (carrot, apple, and peach), HPH can increase the linearity of pectin and reduce the branches, Mw, and GalA content of pectin, indicating that pectin is depolymerised by HPH. Meanwhile, HPH can effectively improve the stability and increase nutrient contents in mixed juice (21, 22). Moreover, for carrot juice, HPH enhances the cloud stability, juice stability, and GalA content of pectin, and decreases the acetylation and Mw of pectin compared to non-homogenized (NH) juice. The effect of HPH on the structure of pectin further improves the bioavailability of carotenoids in carrot juice and the nutritional quality of the juice (13). HPH can also depolymerise commercial citrus pectin, as evidenced by a decrease in Mw (23). HPH can change the structure of pectin and improve the cloud stability of the juice, which in turn affects the sensory, nutritional, and functional properties of the juice and increases its commercial value.

However, the mechanism by which HPH modifies the pectin structure of NFC orange juice and the correlation between the stability of NFC juice and pectin structure remain unclear. Here, the effects of HPH treatments on the pectin structural properties and stability of NFC orange juice were investigated. Furthermore, the correlation between the modification of pectin structure and the stability of NFC orange juice was also elucidated. This work will provide theoretical guidance for the production of NFC orange juice of high nutritional and organoleptic quality, thereby improving the commercial value of orange juice.

MATERIALS AND METHODS

Materials

Sunkist navel oranges (*Citrus sinensis* Osb. var. *brasliliensis* Tanaka) were obtained from the local market (Beijing, China), and were stored at 4°C until experiments. Sodium hydroxide, hydrochloric acid, 95% ethanol and trifluoroacetic acid (TFA) were bought from Shanghai Aladdin Biochemical Technology Co., Ltd. (Shanghai, China). Proteinase K was purchased from Beijing Solarbio Technology Co., Ltd. (Beijing, China). Monosaccharide standards and galacturonic acid (GalA) were purchased from Sigma–Aldrich (Shanghai, China). All the other chemicals and reagents were analytical grade.

Preparation for NFC Orange Juice and High-Pressure Treatment

The oranges were washed, peeled and the pulp was squeezed into an electric juicer (MJ-WJS1222F, Midea, China) to crush the oranges. The pectin was extracted from the peel and added to the juice using the acid-extraction method to reduce the waste of resources. The crude juice was preliminarily refined by a high-speed homogenization (ULTRA-TURRAX T25 digital, IKA, Germany) and immediately filtered through a 100-mesh sieve to remove the impurities. Immediately after filtration, the orange juice was subjected to HPH.

HPH was carried out in a high-pressure homogenizer (APV-2000, SPX, Germany). Non-homogenized (NH) orange juice was used as the control group. The orange juice was divided into two equal parts. One part was subjected to HPH treatment at pressures of 30, 50, 100, and 150 MPa. The other part was subjected to 1, 2, and 3 homogenization passes at 100 MPa. The homogenizer was connected to the cooling circulation system. The temperature was kept constant at 25°C.

Pectin Analysis

Pectin Extraction

To investigate the effects of HPH on the structural characteristics of pectin in NFC orange juice, pectin extracted from NH orange juice was used as the control group, and pectin extracted from orange juice treated with different HPH (homogenization pressure: 30 MPa, 50 MPa, 100 MPa and 150 MPa; homogenization passes: 1pass, 2 passes and 3 passes) was used as the experimental group. Pectin in NFC orange juice was extracted by slightly modified acid extraction and alcohol precipitation method (24). Briefly, NFC orange juice was adjusted to pH 2 with hydrochloric acid. The solution was heated at 90°C for 1 h with continuous stirring. The slurry was then centrifuged, and the obtained supernatant was precipitated with 95% ethanol (1:2, v/v). The precipitate was re-suspended in deionized water, enzymatically purified with proteinase K (Solarbio, Beijing, China), incubated, centrifuged, and dialyzed in the supernatant (MWCO: 6,000–8,000 Da). The dialysis process lasted for 24 h and the deionized water was replaced every 6 h. After dialysis, the supernatant was precipitated by the addition of three volumes of 95% ethanol, and the resulting precipitate was dried overnight at 40°C, and then ground to a powder.

Determination of Mw

High-performance size-exclusion chromatography coupled to multiangle laser light scattering (Dawn Heleos II; Wyatt Technology, Goleta, CA, USA), reflective index (RI) detector (Optilab rEX, WyAtt, USA) and ultraviolet (UV) detector (L-2400, Hitachi, Japan) were combined to determine the Mw of the extracted pectin. In detail, pectin (10 mg) was dissolved in eluent (0.1 M NaCl) overnight, then filtered through a 0.45-μm filter membrane before analysis. Samples (200 μL) were injected into a TSKgel column (TSKgel G4000PWxl; Tosoh Bioscience, King of Prussia, PA, USA). Elution was performed with 0.1 M NaCl solution at a flow rate of 0.5 mL/min for 30 min and the column was maintained at 35°C. The refractive index increment dn/dc was set to 0.135 mL/g.

Determination of Monosaccharide Composition

High-performance anion-exchange chromatography was achieved using an ICS-3000 Ion Chromatography System (Dionex, Sunnyvale, CA, USA) equipped with a CarboPac™ PA20 column and a pulsed amperometric detector. Pectin (10 mg) was hydrolyzed using 2 M trifluoroacetic acid for 1 h at 120°C. After cooling and nitrogen drying, samples were adjusted to 5 mL, diluted, and filtered through a 0.2-μm membrane. Mixtures of GalA, Gal, Ara, Rha, xylose, and glucose at different concentrations (0.01–5 mg/L) were used as standards. 10 μL samples were injected into ultra-pure water (A), 0.25 M NaOH (B) and 1 M NaAC (C) at a flow rate of 0.5 mL/min through a gradient elution procedure. The gradient elution procedure was as follows: 0–20 min: 94% A and 6% B; 20–20.1 min: 89% A, 6% B and 5% C; 20.1–35 min: 74% A, 6% B and 20% C; 35.1–45 min: 20% A and 80% B; 45.1–55 min: 94% A and 6% B.

Determination of the Degree of Methylation (DM)

The DM of pectin was determined by titration (25). Extracted pectin (0.2 g) was dissolved in 20 mL of distilled water and stirred at room temperature for 2 h. Three drops of phenolphthalein indicator were added, and the mixture was titrated with 0.1 M NaOH until the color of the indicator changed to pink, and then the volume (V_1) was recorded. Next, 2 mL 0.25 mol/L NaOH was added to the solution, and 2 mL 0.25 mol/L hydrochloric acid solution was added after stirring at 25°C for 30 min to neutralize the excess NaOH. The solution was titrated with 0.1 M NaOH until the color of the indicator changed back to pink, then the volume (V_2) was recorded. The DM of pectin was obtained according to Equation (1).

$$\mathrm{DM}\ (\%) = \frac{V_2}{V_1 + V_2} \times 100 \quad (1)$$

Scanning Electron Microscopy (SEM) Analysis

SEM (SU8010; Hitachi, Tokyo, Japan) was used to observe the surface morphology of pectin extracted from orange juice after different treatments (homogenization pressure: 30, 50, 100, and 150 MPa; homogenization passes: 1pass, 2 passes, and 3 passes). Pectin powder samples (5 mg) were fixed to the sample table with double-sided tape, and each sample was coated with gold powder under vacuum conditions (26). Images were taken at an acceleration voltage of 10 kV at 3000× magnification.

Stability Analysis of NFC Orange Juice

Turbidity and Pulp Sedimentation

The turbidity of raw NFC orange juice was determined after centrifugation at 25°C and 3,000 × g for 10 min.

NFC orange juice (10 mL) was stored at 4°C for 6 days for the determination of the pulp sedimentation (27). The sedimentation index (IS) of NFC orange juice was estimated using Equation (2). Where V_s was the sedimentation volume of juice (mL); V_t was the total volume of juice (mL).

$$\mathrm{IS}\ (\%) = \left(\frac{V_s}{V_t}\right) \times 100 \quad (2)$$

Particle Size Determination

The particle size parameters were determined using a Mastersizer 2000 (Malvern Instruments, Malvern, UK). Laser diffraction was used to measure particles from 0.02 μm to 2,000 μm. The median particle diameter (D_{50}, μm), volume-based diameter (D[4,3], μm), and area-based diameter (D[3,2], μm) were calculated using the software (Microtrac-Bluewave, Montgomeryville, PA, USA) provided with the equipment.

Viscosity Curves

Viscosity measurements of NFC orange juice samples were carried out using a rheometer (Physica MCR 301; Anton Paar, Graz, Austria) equipped with parallel plates (50-mm diameter) with a gap size of 1 mm. The temperature was maintained constant at 25°C using a Peltier system. In a steady-state shear mode, NFC orange juice samples (2.3 mL) were placed between the two plates and the shear rate was increased from 0.01 to 300 s^{-1} (28).

PME Activity

NFC orange juice (20 mL) was added to 40 mL of 2 M NaCl solution containing 1% pectin. The pH of the pectin–juice mixture was adjusted to 7 using 1 M NaOH. After pH stabilization, 1 mL of 0.05 M NaOH was added, and the time required to restore the pH to 7 was measured. Enzyme activity was calculated according to equation 3. Values were converted to percent residual activity relative to the untreated control sample. The NH orange juice represented 100% PME activity.

$$\text{PME activity (unit/mL)} = \frac{(\text{mL NaOH}) \times (\text{NaOH normality}) \times 10^3}{(\text{minutes}) \times (\text{mL NFC orange juice})} \quad (3)$$

Simulation Verification Experiment

Oranges were washed, peeled, juiced, and immediately filtered through a 100-mesh sieve to remove pulp using an electric juicer. The filtered orange juice was not treated with HPH. Instead, pectin solution was treated with 100 MPa of HPH, then the homogenized pectin was added to the NFC orange juice at different concentrations (0, 0.015, 0.075, 0.375, and 1.875%). In addition, the Mw and monosaccharide composition of the pectin solution (0.075%) after homogenization were determined according to the methods in sections Determination of Mw and Determination of Monosaccharide Composition, respectively.

Statistical Analysis

Data were analyzed using a one-way analysis of variance (ANOVA) following by LSD multiple comparisons or correlation analysis (SPSS 19.0 software) at the significance level of $P < 0.05$. The results were expressed as the average ± standard deviation. All assays were performed in triplicate. The figures were plotted using Origin 8.0 software.

RESULTS AND DISCUSSION

Effect of HPH on the Pectin Structure

Mw and DM

To determine the mechanisms by which HPH improves the stability of NFC orange juice, pectin was extracted from homogenized orange juice, and the structural properties were determined. The Mw and DM results for pectin were shown in **Table 1**. The Mw of homogenized pectin (185–593 kDa) was considerably less than that of NH pectin (931 kDa). The Mw decreased from 593 to 250 kDa with increasing homogenization pressure. By increasing the number of homogenization passes, the Mw decreased from 262 to 185 kDa. Depolymerisation is the main change in polysaccharides during the HPH process (16). Compared with the homogenization pressure treatment, the number of homogenization passes had a more obvious effect on the depolymerization of pectin. Citrus pectin is poor in neutral sugar side chains. High pressure disrupts neutral sugar side chains of pectin, leading to a decrease in Mw (23, 29). The results were consistent with those of water-soluble pectin extracted from carrot juice as well as those of pectin extracted from potato, both of which showed a lower Mw of HPH-treated pectin compared to untreated pectin (13, 30). The relatively low Mw may improve water solubility, which in turn may promote biological activity and thus increase the nutritional quality of orange juice (4). It has been shown that high-pressure treatment leads to a decrease in pectin Mw and viscosity, thus indicating that the decrease in viscosity of NFC orange juice is associated with a decrease in pectin Mw (31). Compared to NH pectin, the DM gradually decreased with increasing homogenization pressure and the number of passes. Relatively low-DM pectin can improve the accessibility of carotenoids in juices (13). The DM ranged from 75.8 to 78.2%, with little change under different homogenization pressures or numbers of passes. This result shows that the DM of pectin in NFC orange juice is not affected by HPH. The DM values of HPH-treated citrus pectin and apple pectin were similarly unaffected (23). Thus, the changes in Mw after homogenization were not caused by the net change in electrostatic repulsion between the pectin molecules, which may improve total carotenoid bioaccessibility in NFC orange juice.

Monosaccharide Composition

The monosaccharide compositions of pectin after different HPH treatments are shown in **Table 1**. The monosaccharide composition of pectin in NFC orange juice mainly consisted of GalA (63.0–76.2%), followed by Gal (9.7–21.2%), Ara (8.3–10.2%), and Rha (2.1–2.4%). Among them, GalA was derived from the HG and RG-I main chains. Rha was derived from the RG-I main chain, while Gal and Ara were derived from the RG-I side chain (32). The molecular structure of pectin in NFC orange juice is further characterized by the ratio of neutral sugars. GalA/(Gal+Ara+Rha) represents the linearity of the pectin. Rha/GalA represents the contribution of the RG region to the overall pectin. (Ara+Gal)/Rha is a measure of the degree of RG-I branching by comparing the amounts of RG-I side chain sugars (Ara and Gal) and Rha (33). The GalA content of homogenized pectin was higher than that of NH pectin and

TABLE 1 | Characteristic indicators of pectin in NFC orange juice.

	Homogenization press (1 pass)					Homogenization pass (100 MPa)			
	NH	30 Mpa	50 Mpa	100 Mpa	150 Mpa	NH	1	2	3
GalA (mol%)	62.97 ± 0.48^{e}	66.25 ± 0.61^{d}	67.71 ± 0.87^{d}	72.86 ± 0.41^{c}	75.07 ± 1.01^{ab}	62.97 ± 0.48^{e}	72.86 ± 0.41^{c}	74.45 ± 0.01^{b}	76.23 ± 0.74^{a}
DM (%)	86.67 ± 0.71^{a}	78.24 ± 1.10^{b}	76.33 ± 0.17^{b}	76.24 ± 0.13^{b}	75.67 ± 0.04^{b}	86.67 ± 0.71^{a}	76.24 ± 0.13^{b}	75.82 ± 0.44^{b}	76.99 ± 0.72^{b}
Fuc (mol%)	0.20 ± 0.03^{dc}	0.41 ± 0.06^{a}	0.40 ± 0.07^{a}	0.24 ± 0.04^{b}	0.12 ± 0.03^{c}	0.20 ± 0.03^{dc}	0.24 ± 0.04^{b}	0.20 ± 0.01^{bc}	0.35 ± 0.02^{ab}
Rha (mol%)	2.12 ± 0.03^{b}	2.15 ± 0.05^{b}	2.16 ± 0.04^{b}	2.14 ± 0.06^{b}	2.08 ± 0.08^{b}	2.12 ± 0.03^{b}	2.14 ± 0.06^{b}	2.07 ± 0.03^{b}	2.38 ± 0.01^{a}
Ara (mol%)	10.18 ± 0.18^{a}	9.80 ± 0.22^{ab}	9.49 ± 0.07^{b}	8.26 ± 0.14^{c}	7.55 ± 0.07^{d}	10.18 ± 0.18^{a}	8.26 ± 0.14^{c}	8.58 ± 0.25^{c}	9.59 ± 0.21^{b}
Gal (mol%)	21.16 ± 0.43^{a}	18.81 ± 0.31^{b}	16.69 ± 0.27^{c}	13.83 ± 0.31^{d}	13.17 ± 0.29^{e}	21.16 ± 0.43^{a}	13.83 ± 0.31^{c}	12.59 ± 0.47^{e}	9.72 ± 0.53^{f}
Glc (mol%)	2.95 ± 0.12^{a}	2.14 ± 0.07^{b}	3.05 ± 0.06^{a}	2.27 ± 0.04^{b}	1.44 ± 0.03^{d}	2.95 ± 0.12^{a}	2.27 ± 0.04^{b}	1.65 ± 0.01^{c}	1.11 ± 0.08^{e}
Xyl (mol%)	0.42 ± 0.01^{c}	0.44 ± 0.06^{bc}	0.50 ± 0.07^{b}	0.42 ± 0.01^{c}	0.47 ± 0.02^{bc}	0.42 ± 0.01^{c}	0.42 ± 0.01^{c}	0.46 ± 0.02^{bc}	0.6 ± 0.01^{a}
GalA/(Gal+Ara+Rha)	1.88 ± 0.03^{f}	2.15 ± 0.09^{e}	2.39 ± 0.01^{d}	3.01 ± 0.05^{c}	3.29 ± 0.10^{b}	1.88 ± 0.03^{f}	3.01 ± 0.05^{c}	3.20 ± 0.06^{b}	3.51 ± 0.07^{a}
Rha/GalA	0.0337 ± 0.0001^{a}	0.0325 ± 0.0002^{b}	0.0312 ± 0.0007^{c}	0.0293 ± 0.0006^{d}	0.0277 ± 0.0010^{e}	0.0337 ± 0.0001^{a}	0.0293 ± 0.0006^{d}	0.0278 ± 0.0001^{e}	0.0264 ± 0.0003^{f}
(Gal+Ara)/Rha	14.75 ± 0.04^{a}	13.29 ± 0.01^{b}	12.13 ± 0.03^{c}	10.34 ± 0.02^{d}	9.97 ± 0.07^{e}	14.75 ± 0.04^{a}	10.34 ± 0.09^{d}	10.24 ± 0.01^{d}	8.11 ± 0.01^{f}
Mw (×10^{5} Da)	9.31 ± 0.01^{a}	5.93 ± 0.07^{b}	3.95 ± 0.02^{c}	2.62 ± 0.04^{d}	2.50 ± 0.02^{e}	9.31 ± 0.01^{a}	2.62 ± 0.04^{d}	2.25 ± 0.09^{f}	1.85 ± 0.03^{g}

Different superscript letters indicate significant differences among groups ($P < 0.05$).

increased with pressure. Increasing the homogenizing pressure and the number of passes increased GalA/(Gal+Ara+Rha) and decreased Rha/GalA and (Gal+Ara)/Rha contents of the pectin. Compared with the homogenization pressure treatment, the number of homogenization passes resulted in more depolymerization of pectin side chains in NFC orange juice. The results show that HPH treatment enhanced the linearity of the pectin in NFC orange juice, reduced the contribution of RG to the overall pectin, and depolymerized the RG-I side chains. Therefore, it can be further clarified that the decrease in pectin Mw caused by HPH treatment is attributable to glycosidic bond cleavage. Higher linearity and lower branching of the pectin facilitate non-covalent hydrophobic interactions of the serum phase, thus improving the stability of orange juice (22).

SEM Analysis

The surface structure of pectin was examined by SEM. SEM micrographs of pectin treated with different HPH parameters are shown in **Figure 1**. The NH pectin was relatively tidy, with a lamella structure, and the surface was relatively smooth and compact. By increasing the number of homogenization passes from 1 to 3, the degree of surface cracking and pore size of pectin gradually increased (**Figure 1A**). After HPH under different pressures, the surface of pectin began to gradually become rough, and became extremely uneven at 50 MPa. When the pressure was further increased (100–150 MPa), cracks and pores began to appear on the surface of pectin, and the pores increased with increasing pressure (**Figure 1B**). Sugar beet pectin had a roughened pectin surface under a pressure of 350 MPa and was cracked or even destroyed when the pressure was 550 MPa, indicating that high pressure can degrade pectin (30). These results may be due to the decrease in Mw after different HPH treatments, resulting in the disruption of the nanostructure on the pectin surface (31).

Effect of HPH on the Stability of NFC Orange Juice

Turbidity

Turbidity is an evaluation index of cloud stability (13), and high turbidity indicates good stability of the orange juice. As shown in **Figure 2A**, the turbidity of the homogenized orange juices [optical density at 660 nm (OD_{660}), 0.65–0.82] was significantly ($P < 0.05$) higher than that of NH orange juice (OD_{660}, 0.24). This is due to the enhancement of cavitation and the increase of shear rate caused by the increasing pressure, which caused stronger disruption of the NFC orange juice particles, making them more homogeneous (27). Turbidity increased from 0.78 to 0.82 when the number of passes was increased from 2 to 3 (**Figure 2B**). Subsequent homogenization passes caused further particle fragmentation (34). Interactions between the small particles and the serum phase may inhibit the production of precipitates (35, 36). Smaller particles tended to remain in suspension after centrifugation (which was always carried out at the same acceleration), increasing the absorbance values and turbidity (28). A previous report indicated that the increase of the OD_{660} value of orange juice after HPH was associated with improved stability of the orange juice (10, 37, 38). This

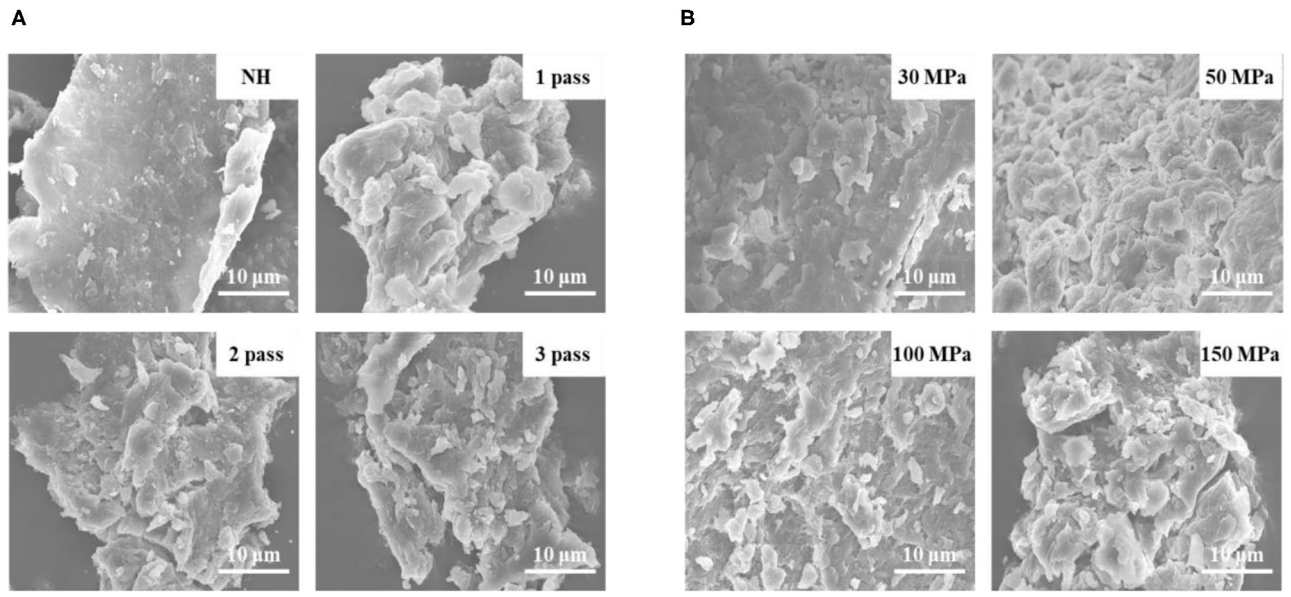

FIGURE 1 | SEM images of NFC orange juice pectin after different HPH treatments (3000× magnification). **(A)** Homogenization pass; **(B)** Homogenization pressure.

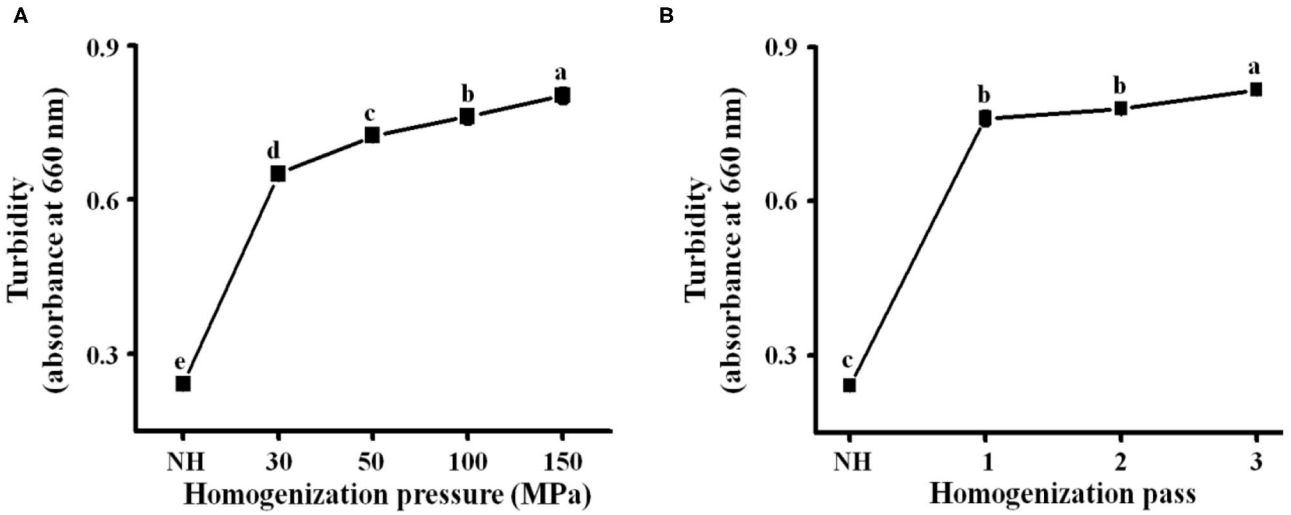

FIGURE 2 | NFC orange juice was treated with different homogenization pressures (30, 50, 100, and 150 MPa) and numbers of homogenization passes (1, 2, and 3) to study the effect of HPH on the turbidity of NFC orange juice. **(A)** Homogenization pressure; **(B)** Homogenization pass.

confirms that the turbidity increases with increasing pressure and that HPH can effectively improve the stability of orange juice. Both homogenization pressure and homogenization pass treatments significantly increased the turbidity of orange juice ($P < 0.05$). Thus, HPH not only destroys particles but also binds them by altering the pectin structure in the serum phase, thereby increasing the turbidity and stability of NFC orange juice.

Pulp Sedimentation

Pulp sedimentation is a decisive factor in the cloud stability of NFC orange juice. A relatively high IS value represents a slow settling of particles in the orange juice, which provides better stability. Compared with homogenized orange juices (IS: 100% to 71–99%), NH orange juice (IS, 100% to 47%) showed faster sedimentation after 6 days (**Figure 3**), indicating that HPH can effectively inhibit the stratification of orange juice and improve its sensory characteristics. Compared with the homogenization pressure treatment, the number of homogenization passes made the particles in the orange juice more difficult to precipitate. The same phenomenon was observed in carrot juice, where higher pressure and more homogenization passes led to smaller changes in IS values, indicating that the juice became more stable. Stokes

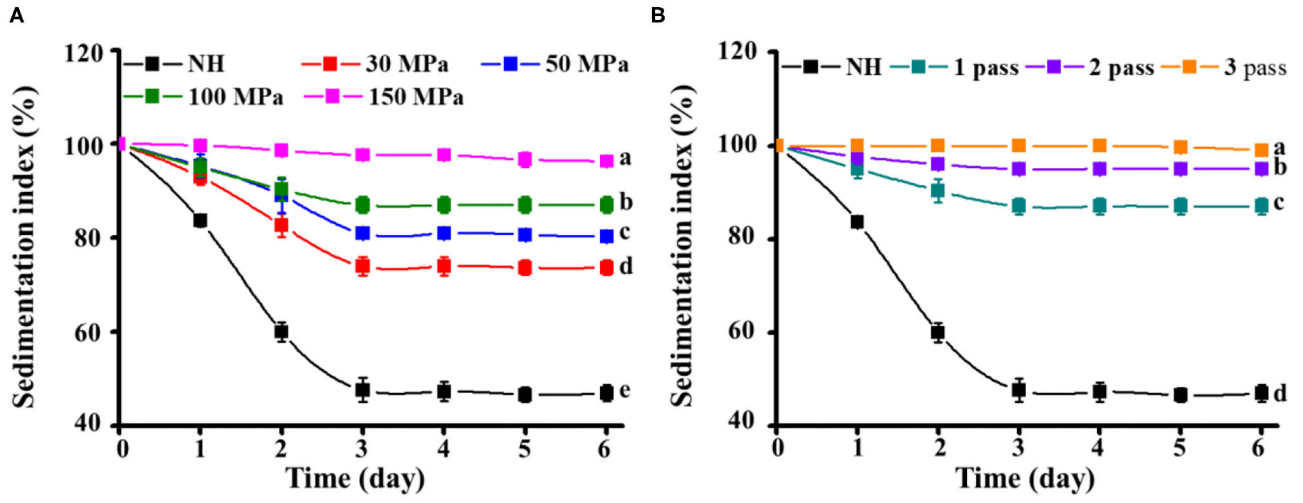

FIGURE 3 | Effect of HPH treatments on the sedimentation index of NFC orange juice. **(A)** Homogenization pressure; **(B)** Homogenization pass.

law describes the sedimentation velocity of spheres as a function of the properties of the particles and the dispersed medium (13). According to Stokes law, the particle sedimentation velocity is proportional to the particle size (diameter) and the difference between the densities of the particles and the dispersed medium (27). With relatively high pressure and more homogenization passes, NFC orange juice has more homogeneous particles. Therefore, the increased stability of homogenized orange juices may be related to the slower sedimentation due to the reduction in particle size during homogenization. In addition, due to the uniform size of the particles and large surface area, the resulting structure is quickly stabilized. Their settling was more difficult due to the drag of the opposing forces; therefore, the homogenized orange juices showed little change in IS values over 6 days. The stability of mixed juices (apple and kiwi) is influenced by particle size and interaction with the serum phase (39). HPH processing can release and alter serum phases, such as serum pectin, which binds to suspended solids and prevents precipitation, thereby increasing the stability of the cloud (40). Therefore, the combination of these particles and serum pectin also leads to minimal changes in IS values in homogenized orange juice. HPH is an important means of preventing pulp sedimentation.

Particle Size

The particle diameters (D[4,3], D[3,2], and D_{50}) of NH orange juice and homogenized orange juices are shown in **Figure 4**. D[4,3] is mainly influenced by large particles, while D[3,2] is more sensitive to small particles. These two indicators provide a complete picture of the system particle size (41). With increasing homogenization pressure and number of passes, D[4,3] and D[3,2] decreased simultaneously. These large and small particles had a similar effect on the HPH process. HPH reduced the particle diameter, which was consistent with previous observations for orange juice (10, 37) and other vegetable products such as tomato (36) and apple juices (42). At 30–50 MPa, D[4,3] decreased significantly ($P < 0.05$) from 49.9 μm to 39.6 μm, but the change of D[3,2] was not significant ($P > 0.05$) (**Figure 4A**). This indicates that in this pressure range, mainly the large particles were broken. When the pressure was further increased, D[4,3] did not change significantly ($P > 0.05$), but D[3,2] decreased significantly ($P < 0.05$) from 7.7 μm to 6.6 μm. High pressure was required to break up small-sized particles. The change in particle diameter between 100 MPa and 150 MPa was not distinct from that between 0 MPa and 50 MPa. The destructive effect of homogenizing pressure on suspended particles seemed to show an asymptotic behavior, with an increase in homogenizing pressure leading to smaller changes in particle size at higher pressures. This asymptotic behavior could be related to gap dimensions and shear stress since the stress required for disrupting smaller size particles becomes greater (20). When the number of passes increased from 2 to 3, the change in D[4,3] was not significant ($P > 0.05$), but D[3,2] decreased significantly ($P < 0.05$) from 6.1 to 5.0 μm (**Figure 4B**). This phenomenon indicated that there were no obvious changes in large-sized particles, but mainly an increase in small-sized particles. Furthermore, particle reduction can increase the brightness and improve the total color value of orange juice (19), in addition to increasing the accessibility of carotenoids and improving the sensory and nutritional properties of orange juice (43). The D_{50} of homogenized orange juices (3.7–12.1 μm) was significantly ($P < 0.05$) lower than that of NH orange juice (67.2 μm). The D_{50} tended to decrease with increasing pressure, but HPH treatment between 30 MPa and 50 MPa had no significant ($P > 0.05$) effect on D_{50}. As the pressure continued to increase, the D_{50} decreased significantly ($P < 0.05$) from 22.8 to 12.1 μm, but continued pressure increases had no significant ($P > 0.05$) effect on D_{50}. Further reduction of the cumulative particle size cannot be achieved by increasing the pressure beyond 100 MPa. As the number of passes increased, the D_{50} decreased significantly ($P < 0.05$) from 11.0 to 3.7 μm. HPH reduced the particle size in NFC orange juice, making it

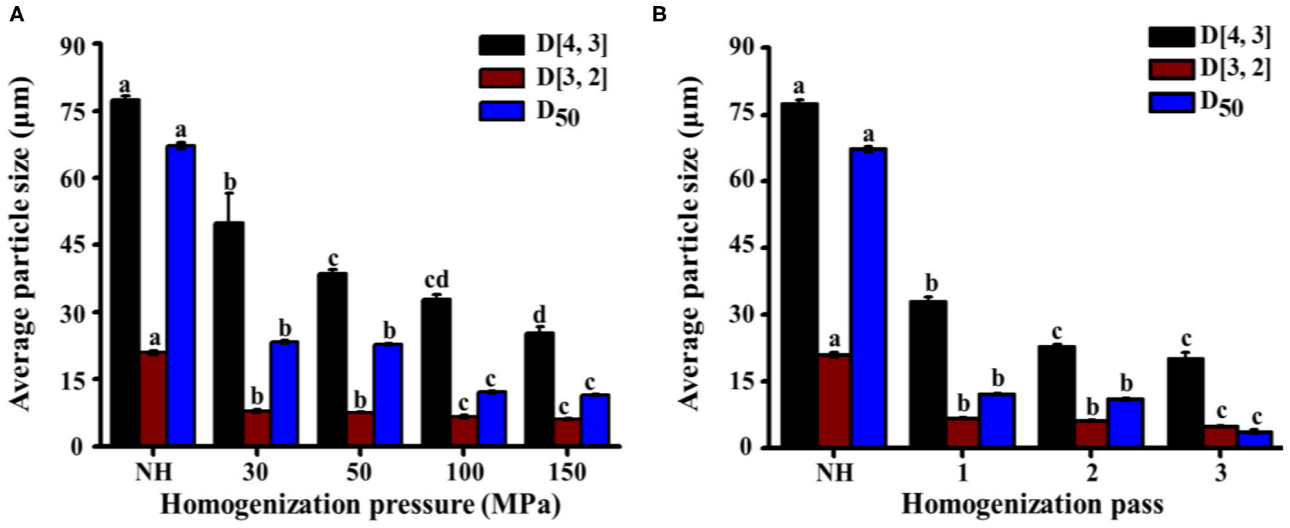

FIGURE 4 | Effect of HPH treatments on the volume average particle size (D[4,3]), surface average particle size (D[3,2]), and average particle size (D_{50}) of NFC orange juice. **(A)** Homogenization pressure; **(B)** Homogenization pass.

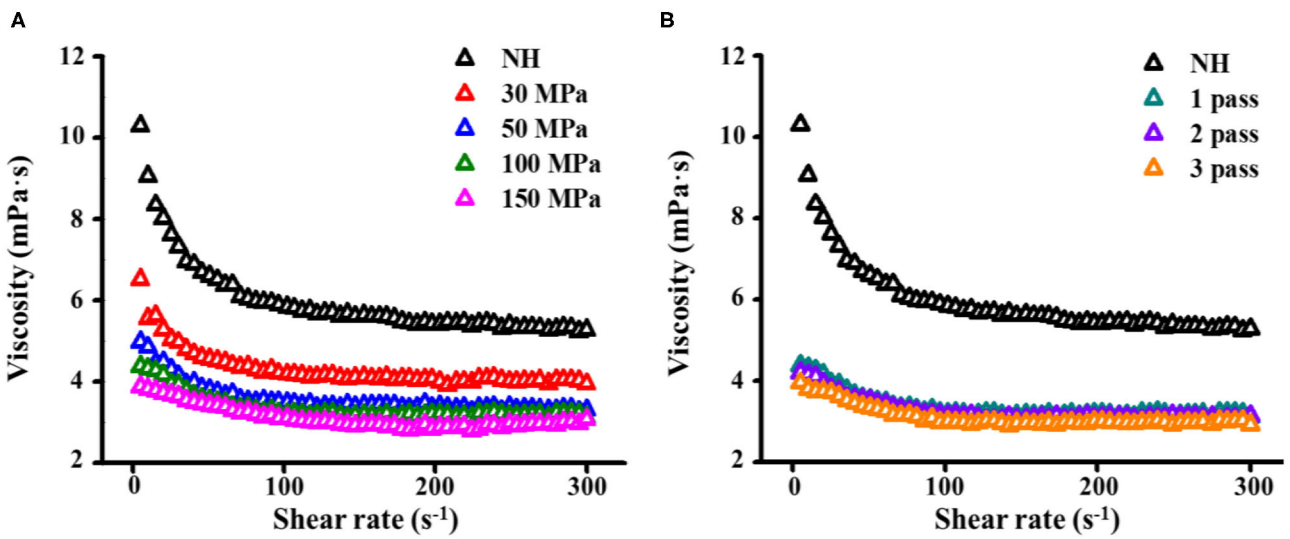

FIGURE 5 | Effect of HPH treatments on viscosity curves of NFC orange juice. **(A)** Homogenization pressure; **(B)** Homogenization pass.

more homogeneous. This in turn increased the turbidity of the NFC orange juice and delayed pulp sedimentation, increasing the stability of the orange juice and slowing precipitation. It also improved the sensory and nutritional properties of orange juice and enhanced consumer acceptance.

Viscosity Curves

The apparent viscosity represents the resistance of the fluid to flow (18). With increasing shear rate, the shear stress of NFC orange juice increased and exhibited shear-thinning behavior, independent of treatment conditions (**Figure 5**). In contrast to NH orange juice, the viscosity of homogenized orange juices decreased gradually with increasing pressure and number of passes (**Figure 5**). The homogenization pressure treatment induced more viscosity decrease than the homogenization passes, and thereby reduced more resistance and energy consumption. These results were due to a reduction in particle size. The pectin solution treated with HPH showed reduced fluid viscosity (31). Increasing the pressure and number of passes depolymerizes the pectin side chains, thereby reducing their Mw and viscosity (44), which also reduces the viscosity of the orange juice. HPH alters the rheology of NFC orange juice by altering the size of macromolecules in the serum phase (45). Similarly, a decrease in juice viscosity after HPH has been reported in blended juice

(21) and tomato puree (46). Since the viscosity of the fluid is related to frictional losses during processing, a reduction in the viscosity of NFC orange juice is desirable (18). HPH can reduce the viscosity of NFC orange juice by reducing the particle size and changing the size of the pectin molecules in the serum phase, thereby reducing fluid resistance and energy consumption in the processing industry.

PME Activity

PME activity can promote orange juice clarification, negatively affect the quality of orange juice, and reduce consumer acceptability. Compared to NH orange juice, the PME activity of the homogenized orange juices decreased with increasing pressure, reaching a minimum value of 79% at 150 MPa (**Figure 6A**). When the number of passes increased from 1 to 3, there was no significant ($P > 0.05$) effect on the PME activity (77–82%) of the homogenized orange juices (**Figure 6B**). Compared with the homogenization pressure treatment, the activity of pectin methylesterase in orange juice was lower after more homogenization passes (**Figure 6**). The inactivation of PME activity prevents the loss of turbidity, increasing the commercial value of the orange juice. PME activity in orange juice decreased by only 20% after ultra-high-pressure homogenization (UHPH) for five passes at 170 MPa (47). After UHPH at 250 MPa with different inlet temperatures, the PME activity of the orange juice decreased by up to 38%, and the samples required five homogenization passes to achieve an 80% reduction (48). Although the PME activity of orange juice treated by HPH and UHPH was still residual, its stability was improved. This result may be due to the change of pectin structure, which made it easier to interact with particles in the serum phase, and thus inhibited precipitation. It is also possible that the particle size decreases due to HPH, thus improving stability. Therefore, it is necessary to further study the effect of HPH on pectin structure modification in NFC orange juice to explain how HPH improves the stability of NFC orange juice.

Simulation Verification Experiment

Based on the above experiments, it was hypothesized that HPH could improve the stability of NFC orange juice by modifying the structural properties of pectin in NFC orange juice. The squeezed orange juice was directly filtered without HPH treatment, and the filtered orange juice was retained. At the same time, a pectin solution with a concentration of 0.075% was subjected to HPH treatment at 100 MPa, and different concentrations of pectin solution were added to the filtered NFC orange juice. The structure of the pectin used for backfilling was characterized, and its Mw and monosaccharide composition were determined to verify the consistency with previous results. The intuitive stability indicators such as turbidity, pulp sedimentation, and viscosity were measured to verify the effect of the structure-altered pectin on the stability of NFC orange juice. The Mw, linearity, and branching of pectin after 100 MPa treatment were similar those of pectin extracted from NFC orange juice under the same pressure treatment (**Table 2**). Compared with the non-pressure-treated pectin, the linearity increased and the RG contribution and branching decreased, which was consistent with our previous results. The stability of NFC orange juice was determined by adding different concentrations of homogenized pectin solution. With increasing pectin concentration, the OD_{660} value of NFC orange juice increased significantly ($P < 0.05$) from 0.25 to 2.24 (**Figure 7A**). As the pectin concentration increased, the sedimentation of particles was inhibited and the IS value of NFC orange juice increased from 39.6 to 99.9% after 6 days (**Figure 7B**). When the pectin concentration increased from 0 to 1.875%, the viscosity of NFC orange juice also increased (**Figure 7C**). The stability of NFC orange juice is improved by

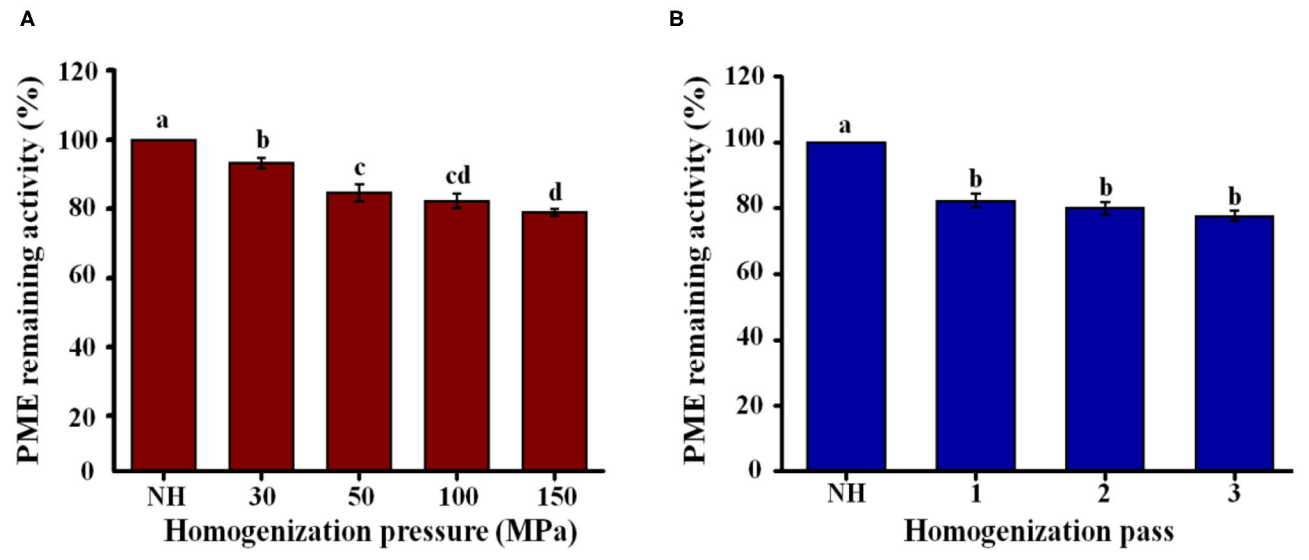

FIGURE 6 | Effect of HPH treatments on PME activity of NFC orange juice. **(A)** Homogenization pressure; **(B)** Homogenization pass.

TABLE 2 | Pectin structure properties (Mw and monosaccharide composition) after homogenization (100 MPa).

	Before homogenization	After homogenization	In NFC orange juice before homogenization
GalA (mol %)	60.57 ± 0.23^{b}	71.63 ± 0.66^{a}	72.86 ± 0.41^{a}
Fuc (mol %)	0.10 ± 0.01^{b}	0.18 ± 0.02^{b}	0.24 ± 0.04^{a}
Rha (mol %)	2.75 ± 0.36^{a}	2.28 ± 0.24^{b}	2.14 ± 0.06^{b}
Ara (mol %)	13.48 ± 1.48^{a}	6.87 ± 0.86^{b}	8.26 ± 0.14^{b}
Gal (mol %)	17.00 ± 0.49^{a}	16.57 ± 0.34^{a}	13.83 ± 0.31^{b}
Glc (mol %)	5.31 ± 0.05^{a}	1.83 ± 0.01^{c}	2.27 ± 0.04^{b}
Xyl (mol %)	0.79 ± 0.03^{a}	0.64 ± 0.06^{b}	0.42 ± 0.01^{c}
GalA/(Gal+Ara+Rha)	1.82 ± 0.15^{b}	2.79 ± 0.12^{a}	3.01 ± 0.05^{a}
Rha/GalA	0.0455 ± 0.0006^{a}	0.0318 ± 0.0002^{b}	0.0293 ± 0.0020^{b}
(Gal+Ara)/Rha	11.08 ± 0.88^{a}	10.29 ± 0.06^{b}	10.34 ± 0.01^{b}
Mw (×10^{5} Da)	9.17 ± 0.06^{a}	2.54 ± 0.09^{b}	2.62 ± 0.02^{b}

Different superscript letters indicate significant differences among groups ($P < 0.05$).

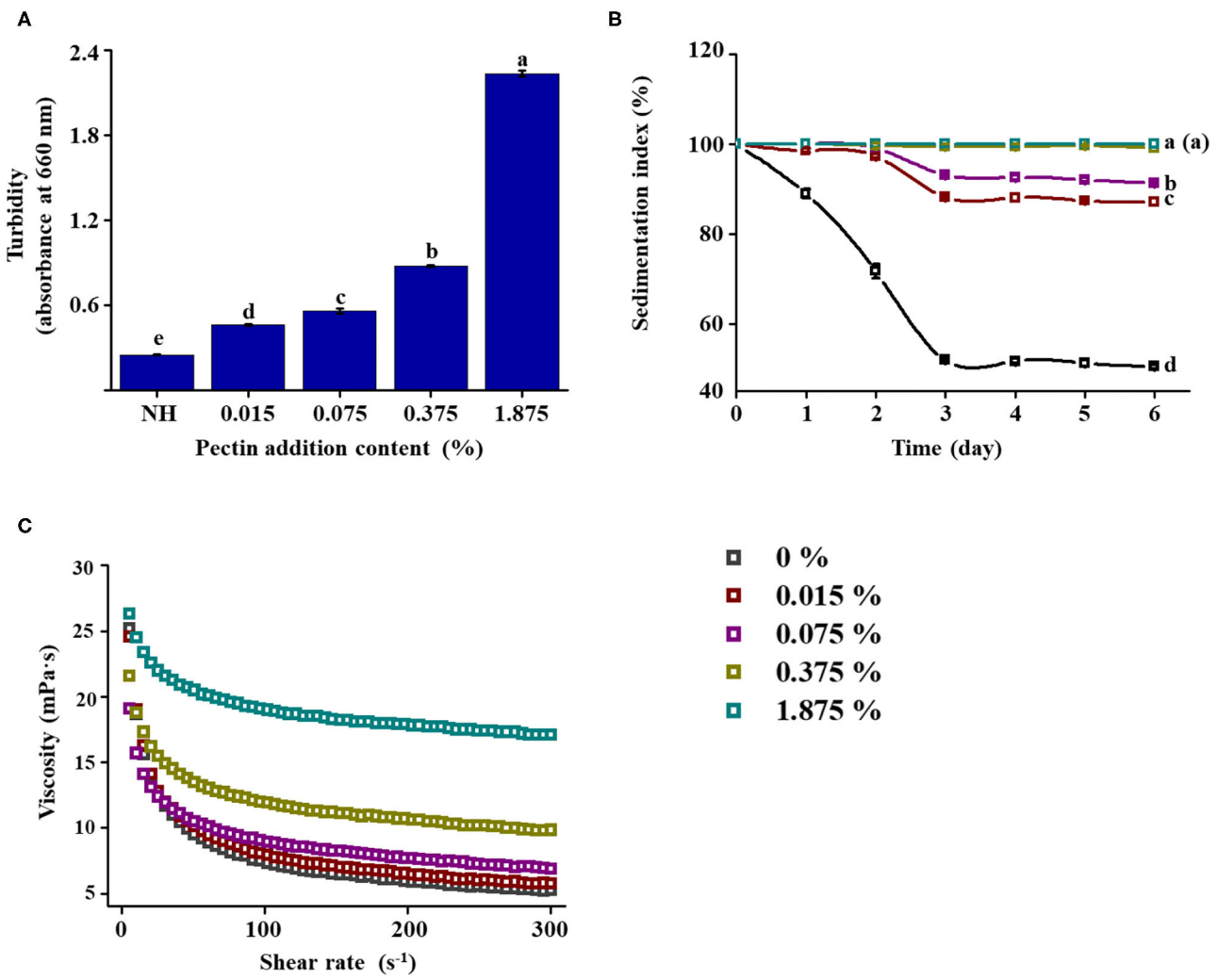

FIGURE 7 | Effect of addition of pectin (after HPH) at various concentrations on the stability of NFC orange juice. **(A)** Turbidity; **(B)** Sedimentation index; **(C)** Viscosity curves.

TABLE 3 | Correlation matrix between stability and pectin characteristics in NFC orange juice.

	Mw	GalA	GalA/(Gal+Ara+Rha)	Rha/GalA	(Gal+Ara)/Rha
Turbidity	−0.967**	0.843**	0.958**	−0.959**	−0.941**
IS	−0.935**	0.953 **	0.968**	−0.978**	−0.931**
D[4,3]	0.940**	−0.936**	−0.942**	0.958 **	0.913**
D[3,2]	0.871**	−0.791**	−0.952**	0.961**	0.966**
D_{50}	0.893**	−0.870**	−0.971**	0.962**	0.979**
Viscosity	0.953**	−0.859**	−0.912**	0.909**	0.887**

***Indicates the significant correlations ($P < 0.01$).*

adding different concentrations of homogenized pectin. This further confirmed that the modification of the pectin structure affected the stability of NFC orange juice.

Correlation Matrix Analysis

Correlations were used to describe the main variables of NFC orange juice stability and pectin structural properties after HPH treatment. Validation was performed by calculating the Pearson correlation coefficient [r] for each pairwise comparison (**Table 3**). The turbidity and IS of NFC orange juice were significantly positively ($P < 0.01$) correlated with the GalA content and linearity of pectin. The particle size and viscosity of NFC orange juice were significantly positively ($P < 0.01$) correlated with the Mw, RG contribution rate, and branching degree of pectin. Turbidity and IS were significantly ($P < 0.01$) negatively correlated with the RG contribution rate, branching degree, and Mw. There was a significant ($P < 0.01$) negative correlation between particle size and viscosity and pectin linearity. These relationships corroborate previous reports indicating that the improvement of NFC orange juice results from changes in pectin structure.

CONCLUSIONS

This work mainly investigated the effects of HPH on the structural modification of pectin, the cloud stability of NFC orange juice and their existing correlation relationship. The results showed that HPH could modify the structure of pectin in NFC orange juice and thus improve its stability. The improved stability could improve the sensory and nutritional properties of orange juice. With the increase of homogenization pressure and homogenization pass, HPH increased the GalA contents and linearity of pectin in NFC orange juice, while decreased the Mw, branching and RG contribution. At the same time, the smooth and compact surface of pectin appeared pores and cracks of different sizes, which also implied depolymerization of pectin. In addition, HPH reduced the particle sizes of orange juice and inhibited the sedimentation. Although the PME activity of NFC orange juice was still strong after HPH treatment, the cloud stability of NFC orange juice was improved. This was because the homogenized pectin interacted more easily with the particles in orange juice, thus effectively improving the stability of NFC orange juice. The stability index of NFC orange juice was strongly correlated with the structural properties of pectin, indicating that pectin directly or indirectly influenced the sensory qualities of orange juice. In this research, the relationship between pectin structure and stability of NFC orange juice was elucidated, which improved the sensory quality and market value of NFC orange juice, and improved the sensory and nutritional quality of NFC orange juice, increased consumer acceptance and commercial value, and provided theoretical guidance for the production of high-quality NFC orange juice.

DATA AVAILABILITY STATEMENT

All datasets generated for this study are included in the article material.

AUTHOR CONTRIBUTIONS

WY: methodology, investigation, conducting experiments, and writing—original draft. JC: methodology and formal analysis. SZ: validation and formal analysis. LF: formal analysis. YW: investigation. JL: supervision and writing—review and editing, and funding access and support. JZ: formal analysis, conceptualization, supervision, writing—review and editing, and funding access and support. All authors contributed to manuscript revision and read and approved the submitted version.

FUNDING

The authors would like to acknowledge the financial support provided by National Natural Science Foundation of China (Nos. 32072181, 31901681, and 31901656), CHENGUANG Biotech Group Co., Ltd., NESTLE R&D Ltd. (China), and FRUITOPS Co., Ltd.

ACKNOWLEDGMENTS

The authors would like to acknowledge the support of Elite Youth Program from Chinese Academy of Agricultural Sciences.

REFERENCES

1. De Ancos B, Rodrigo MJ, Sánchez-Moreno C, Pilar Cano M, Zacarías L. Effect of high-pressure processing applied as pretreatment on carotenoids, flavonoids and vitamin C in juice of the sweet oranges 'Navel' and the red-fleshed 'Cara Cara'. *Food Res Int*. (2020) 132:109105. doi: 10.1016/j.foodres.2020.109105
2. Xu L, Xu Z, Kelly S, Liao X. Integrating untargeted metabolomics and targeted analysis for not from concentrate and from concentrate orange juices discrimination and authentication. *Food Chem*. (2020) 329:127130. doi: 10.1016/j.foodchem.2020.127130
3. Sellami I, Mall V, Schieberle P. Changes in the key odorants and aroma profiles of Hamlin and Valencia orange juices not from concentrate (NFC) during chilled storage. *J Agr Food Chem*. (2018) 66:7428–40. doi: 10.1021/acs.jafc.8b02257
4. Cui J, Lian Y, Zhao C, Du H, Han Y, Gao W, Xiao H, Zheng J. Dietary fibers from fruits and vegetables and their health benefits via modulation of gut microbiota. *Compr Rev Food Sci F*. (2019) 18:1514–32. doi: 10.1111/1541-4337.12489
5. Zhao C, Wang F, Lian Y, Xiao H, Zheng J. Biosynthesis of citrus flavonoids and their health effects. *Crit Rev Food Sci*. (2018) 60:566–83. doi: 10.1080/10408398.2018.1544885
6. Coelho RCLA, Hermsdorff HHM, Bressan J. Anti-inflammatory properties of orange juice: possible favorable molecular and metabolic effects. *Plant Food Hum Nutr*. (2013) 68:1–10. doi: 10.1007/s11130-013-0343-3
7. Alves LDL, Santos RL, Bayer BL, Devens ALM, Cichoski AJ, Mendonça CRB. Thermosonication of tangerine juice: effects on quality characteristics, bioactive compounds, and antioxidant activity. *J Food Process Pres*. (2020) 44:e14914. doi: 10.1111/jfpp.14914
8. Aghajanzadeh S, Ziaiifar AM, Kashaninejad M, Maghsoudlou Y, Esmailzadeh E. Thermal inactivation kinetic of pectin methylesterase and cloud stability in sour orange juice. *J Food Eng*. (2016) 185:72–7. doi: 10.1016/j.jfoodeng.2016.04.004
9. Aghajanzadeh S, Ziaiifar AM. A review of pectin methylesterase inactivation in citrus juice during pasteurization. *Trends Food Sci Tech*. (2018) 71:1–12. doi: 10.1016/j.tifs.2017.10.013
10. Sentandreu E, Gurrea MDC, Betoret N, Navarro JL. Changes in orange juice characteristics due to homogenization and centrifugation. *J Food Eng*. (2011) 105:241–5. doi: 10.1016/j.jfoodeng.2011.02.027
11. Velázquez-Estrada RM, Hernández-Herrero MM, Guamis-López B, Roig-Sagués AX. Impact of ultra high pressure homogenization on pectin methylesterase activity and microbial characteristics of orange juice: a comparative study against conventional heat pasteurization. *Innov Food Sci Emerg*. (2012) 13:100–6. doi: 10.1016/j.ifset.2011.09.001
12. Liu J, Bi J, McClements DJ, Liu X, Yi J, Lyu J, et al. Impacts of thermal and non-thermal processing on structure and functionality of pectin in fruit- and vegetable- based products: a review. *Carbohyd Polym*. (2020) 250:116890. doi: 10.1016/j.carbpol.2020.116890
13. Liu X, Liu J, Bi J, Yi J, Peng J, Ning C, et al. Effects of high pressure homogenization on pectin structural characteristics and carotenoid bioaccessibility of carrot juice. *Carbohyd Polym*. (2019) 203:176–84. doi: 10.1016/j.carbpol.2018.09.055
14. Einhorn-Stoll U, Kastner H, Drusch S. Thermally induced degradation of citrus pectins during storage – alterations in molecular structure, color and thermal analysis. *Food Hydydrocolloid*. (2014) 35:565–75. doi: 10.1016/j.foodhyd.2013.07.020
15. Cuevas-Bernardino JC, Lobato-Calleros C, Román-Guerrero A, Alvarez-Ramirez J, Vernon-Carter EJ. Physicochemical characterisation of hawthorn pectins and their performing in stabilising oil-in-water emulsions. *React Funct Polym*. (2016) 103:63–71. doi: 10.1016/j.reactfunctpolym.2016.03.024
16. Villay A, Lakkis De Filippis F, Picton L, Le Cerf D, Vial C, Michaud P. Comparison of polysaccharide degradations by dynamic high-pressure homogenization. *Food Hydrocolloid*. (2012) 27:278–86. doi: 10.1016/j.foodhyd.2011.10.003
17. Zhang Y, Liao J, Qi J. Functional and structural properties of dietary fiber from citrus peel affected by the alkali combined with high-speed homogenization treatment. *LWT-Food Sci Technol*. (2020) 128:109397. doi: 10.1016/j.lwt.2020.109397
18. Leite TS, Augusto PED, Cristianini M. The use of high pressure homogenization (HPH) to reduce consistency of concentrated orange juice (COJ). *Innov Food Sci Emerg*. (2014) 26:124–33. doi: 10.1016/j.ifset.2014.08.005
19. Velázquez Estrada RM, Hernández Herrero MM, Guamis López B, Roig Saguès AX. Influence of ultra-high pressure homogenization on physicochemical and sensorial properties of orange juice in comparison with conventional thermal processing. *Int J Food Sci Technol*. (2019) 54:1858–64. doi: 10.1111/ijfs.14089
20. Carbonell JV, Navarro JL, Izquierdo L, Sentandreu E. Influence of high pressure homogenization and pulp reduction on residual pectinmethylesterase activity, cloud stability and acceptability of lane late orange juice: a study to obtain high quality orange juice with extended shelf life. *J Food Eng*. (2013) 119:696–700. doi: 10.1016/j.jfoodeng.2013.06.041
21. Wellala CKD, Bi J, Liu X, Liu J, Lyu J, Zhou M. Effect of high pressure homogenization on mixed juice stability, rheology, physicochemical properties and microorganism reduction. *J Food Sci Tech Mys*. (2020) 57:1944–53. doi: 10.1007/s13197-019-04230-6
22. Wellala CKD, Bi J, Liu X, Liu J, Lyu J, Zhou M, et al. Effect of high pressure homogenization combined with juice ratio on water-soluble pectin characteristics, functional properties and bioactive compounds in mixed juices. *Innov Food Sci Emerg*. (2020) 60:102279. doi: 10.1016/j.ifset.2019.102279
23. Shpigelman A, Kyomugasho C, Christiaens S, Van Loey AM, Hendrickx ME. The effect of high pressure homogenization on pectin: importance of pectin source and pH. *Food Hydrocolloid*. (2015) 43:189–98. doi: 10.1016/j.foodhyd.2014.05.019
24. Galant AL, Widmer WW, Luzio GA, Cameron RG. Characterization of molecular structural changes in pectin during juice cloud destabilization in frozen concentrated orange juice. *Food Hydrocolloid*. (2014) 41:10–8. doi: 10.1016/j.foodhyd.2014.03.013
25. Lyu J, Bi J, Liu X, Zhou M, Chen Q. Characterization of water status and water soluble pectin from peaches under the combined drying processing. *Int J Biol Macromol*. (2019) 123:1172–9. doi: 10.1016/j.ijbiomac.2018.11.033
26. Yang J, Mu T, Ma M. Optimization of ultrasound-microwave assisted acid extraction of pectin from potato pulp by response surface methodology and its characterization. *Food Chem*. (2019) 289:351–9. doi: 10.1016/j.foodchem.2019.03.027
27. Kubo MTK, Augusto PED, Cristianini M. Effect of high pressure homogenization (HPH) on the physical stability of tomato juice. *Food Res Int*. (2013) 51:170–9. doi: 10.1016/j.foodres.2012.12.004
28. Liu F, Wang Y, Li R, Bi X, Liao X. Effects of high hydrostatic pressure and high temperature short time on antioxidant activity, antioxidant compounds and color of mango nectars. *Innov Food Sci Emerg*. (2013) 21:35–43. doi: 10.1016/j.ifset.2013.09.015
29. Peng X, Mu T, Zhang M, Sun H, Chen J, Yu M. Effects of pH and high hydrostatic pressure on the structural and rheological properties of sugar beet pectin. *Food Hydrocolloid*. (2016) 60:161–9. doi: 10.1016/j.foodhyd.2016.03.025
30. Xie F, Zhang W, Lan X, Gong S, Wu J, Wang Z. Effects of high hydrostatic pressure and high pressure homogenization processing on characteristics of potato peel waste pectin. *Carbohyd Polym*. (2018) 196:474–82. doi: 10.1016/j.carbpol.2018.05.061
31. Chen J, Liang R, Liu W, Liu C, Li T, Tu Z, et al. Degradation of high-methoxyl pectin by dynamic high pressure microfluidization and its mechanism. *Food Hydrocolloid*. (2012) 28:121–9. doi: 10.1016/j.foodhyd.2011.12.018
32. Ma X, Wang W, Wang D, Ding T, Ye X, Liu D. Degradation kinetics and structural characteristics of pectin under simultaneous sonochemical-enzymatic functions. *Carbohyd Polym*. (2016) 154:176–85. doi: 10.1016/j.carbpol.2016.08.010
33. Houben K, Jolie RP, Fraeye I, Van Loey AM, Hendrickx ME. Comparative study of the cell wall composition of broccoli, carrot, and tomato: structural characterization of the extractable pectins and hemicelluloses. *Carbohyd Res*. (2011) 346:1105–11. doi: 10.1016/j.carres.2011.04.014

34. Van Buggenhout S, Wallecan J, Christiaens S, Debon SJJ, Desmet C, Van Loey A, et al. Influence of high-pressure homogenization on functional properties of orange pulp. *Innov Food Sci Emerg*. (2015) 30:51–60. doi: 10.1016/j.ifset.2015.05.004
35. Santiago JSJ, Jamsazzadeh Kermani Z, Xu F, Van Loey AM, Hendrickx ME. The effect of high pressure homogenization and endogenous pectin-related enzymes on tomato purée consistency and serum pectin structure. *Innov Food Sci Emerg*. (2017) 43:35–44. doi: 10.1016/j.ifset.2017.07.028
36. Augusto PED, Ibarz A, Cristianini M. Effect of high pressure homogenization (HPH) on the rheological properties of tomato juice: time-dependent and steady-state shear. *J Food Eng*. (2012) 111:570–9. doi: 10.1016/j.jfoodeng.2012.03.015
37. Betoret E, Betoret N, Carbonell JV, Fito P. Effects of pressure homogenization on particle size and the functional properties of citrus juices. *J Food Eng*. (2009) 92:18-23. doi: 10.1016/j.jfoodeng.2008.10.028
38. Betoret E, Sentandreu E, Betoret N, Fito P. Homogenization pressures applied to citrus juice manufacturing. Functional properties and application. *J Food Eng*. (2012) 111:28-33. doi: 10.1016/j.jfoodeng.2012.01.035
39. Yi J, Kebede B, Kristiani K, Grauwet T, Van Loey A, Hendrickx M. Minimizing quality changes of cloudy apple juice: the use of kiwifruit puree and high pressure homogenization. *Food Chem*. (2018) 249:202–12. doi: 10.1016/j.foodchem.2017.12.088
40. Moelants KRN, Cardinaels R, Jolie RP, Verrijssen TAJ, Van Buggenhout S, Van Loey AM, et al. Rheology of concentrated tomato-derived suspensions: effects of particle characteristics. *Food Bioprocess Tech*. (2014) 7:248–64. doi: 10.1007/s11947-013-1070-3
41. Lopez-Sanchez P, Nijsse J, Blonk HCG, Bialek L, Schumm S, Langton M. Effect of mechanical and thermal treatments on the microstructure and rheological properties of carrot, broccoli and tomato dispersions. *J Sci Food Agr*. (2011) 91:207–17. doi: 10.1002/jsfa.4168
42. Donsì F, Esposito L, Lenza E, Senatore B, Ferrari G. Production of shelf-stable annurca apple juice with pulp by high pressure homogenization. *Int J Food Eng*. (2009) 5:64–7. doi: 10.2202/1556-3758.1602
43. Stinco CM, Sentandreu E, Mapelli-Brahm P, Navarro JL, Vicario IM, Meléndez-Martínez AJ. Influence of high pressure homogenization and pasteurization on the *in vitro* bioaccessibility of carotenoids and flavonoids in orange juice. *Food Chem*. (2020) 331:127259. doi: 10.1016/j.foodchem.2020.127259
44. Santiago JSJ, Salvia-Trujillo L, Zucca R, Van Loey AM, Grauwet T, Hendrickx ME. *In vitro* digestibility kinetics of oil-in-water emulsions structured by water-soluble pectin-protein mixtures from vegetable purées. *Food Hydrocolloid*. (2018) 80:231–44. doi: 10.1016/j.foodhyd.2018.02.007
45. Augusto PED, Ibarz A, Cristianini M. Effect of high pressure homogenization (HPH) on the rheological properties of a fruit juice serum model. *J Food Eng*. (2012) 111:474–7. doi: 10.1016/j.jfoodeng.2012.02.033
46. Tan J, Kerr WL. Rheological properties and microstructure of tomato puree subject to continuous high pressure homogenization. *J Food Eng*. (2015) 166:45–54. doi: 10.1016/j.jfoodeng.2015.05.025
47. Lacroix N, Fliss I, Makhlouf J. Inactivation of pectin methylesterase and stabilization of opalescence in orange juice by dynamic high pressure. *Food Res Int*. (2005) 38:569–76. doi: 10.1016/j.foodres.2004.11.010
48. Welti-Chanes J, Ochoa-Velasco CE, Guerrero-Beltrán JÁ. High-pressure homogenization of orange juice to inactivate pectinmethylesterase. *Innov Food Sci Emerg*. (2009) 10:457–62. doi: 10.1016/j.ifset.2009.05.012

Conflict of Interest: The authors declare that this study received funding from CHENGUANG Biotech Group Co., Ltd., NESTLE R&D Ltd. (China), and FRUITOPS Co., Ltd. The funders were not involved in the study design, collection, analysis, interpretation of data, the writing of this article and the decision to submit it for publication.

frontiers in Nutrition

ORIGINAL RESEARCH
published: 19 May 2021
doi: 10.3389/fnut.2021.647750

Thermal and Acidic Treatments of Gluten Epitopes Affect Their Recognition by HLA-DQ2 *in silico*

Jihui Gao[1†], Haolan Du[2†], Zekun Zhou[1†], Zhongxin Liang[1], Hongrui Liang[1], PeiAo Zhang[1], Xue Wei[2], Shujun Liu[2], Linglin Fu[3], Yanbo Wang[3], Huilian Che[1], Wentong Xue[1], Fengjiao Xin[2] and Dong Yang[1]**

[1] Beijing Key Laboratory of Functional Food From Plant Resources, College of Food Science and Nutritional Engineering, China Agricultural University, Beijing, China, [2] Institute of Food Science and Technology, Chinese Academy of Agricultural Sciences, Beijing, China, [3] Food Safety Key Laboratory of Zhejiang Province, School of Food Science and Biotechnology, Zhejiang Gongshang University, Hangzhou, China

OPEN ACCESS

Edited by:
Hang Xiao,
University of Massachusetts Amherst, United States

Reviewed by:
Carmen Gianfrani,
National Research Council (CNR), Italy
Fernando M. Nunes,
University of Trás-os-Montes and Alto Douro, Portugal

***Correspondence:**
Dong Yang
dyang@cau.edu.cn
Fengjiao Xin
2002hongzhi30@163.com

[†] These authors have contributed equally to this work

Specialty section:
This article was submitted to Food Chemistry, a section of the journal Frontiers in Nutrition

Received: 30 December 2020
Accepted: 08 April 2021
Published: 19 May 2021

Citation:
Gao J, Du H, Zhou Z, Liang Z, Liang H, Zhang P, Wei X, Liu S, Fu L, Wang Y, Che H, Xue W, Xin F and Yang D (2021) Thermal and Acidic Treatments of Gluten Epitopes Affect Their Recognition by HLA-DQ2 in silico. Front. Nutr. 8:647750. doi: 10.3389/fnut.2021.647750

Celiac disease (CD) is a prevalent disorder with autoimmune features. Dietary exposure of wheat gluten (including gliadins and glutenins) to the small intestine activates the gluten-reactive $CD4^+$ T cells and controls the disease development. While the human leukocyte antigen (HLA) is the single most important genetic factor of this polygenic disorder, HLA-DQ2 recognition of gluten is the major biological step among patients with CD. Gluten epitopes are often rich in Pro and share similar primary sequences. Here, we simulated the solution structures changes of a variety of gluten epitopes under different pH and temperatures, to mimic the fermentation and baking/cooking processes. Based on the crystal structure of HLA-DQ2, binding of differently processed gluten epitopes to DQ2 was studied *in silico*. This study revealed that heating and pH change during the fermentation process impact the solution structure of gluten epitope. However, binding of differently treated gluten epitope peptide (GEP) to HLA-DQ2 mainly depended on its primary amino acid sequence, especially acidic amino acid residues that play a pivotal role in their recognition by HLA-DQ2.

Keywords: gluten, epitope, immunogenecity, peptide, HLA-DQ2

INTRODUCTION

Wheat is one of the most widely grown cereal crop, and bread made with wheat flour is one of the oldest staple food since the Neolithic era of human history (1, 2). Flour-based staple food supplies not only carbohydrates but also proteins, which takes 8–15% of the wheat kernel weight, to human diet (3). Among wheat proteins, 85–90% is gluten, and intolerance to it leads to an autoimmune disease called celiac sprue (4). Gluten includes glutenins and gliadins, and glutenins are catalyzed by related enzymes and/or oxidants to form a cohesive network as the structural basis of dough (5). Besides gluten from wheat, similar prolamin proteins such as hordeins from rye and secalins from barley could also trigger this inflammation (6). Celiac disease (CD) affects ∼1% of the world's population, and it has been suggested that the increasing prevalence of CD over the past decades is partially due to the inadvertently changed immunoreactivity of wheat during breeding (7–10). Undiagnosed disease and poor diet compliance often lead to increased morbidity and mortality (11, 12). However, studies of wheat cultivars over 120 years found no trends in relative or absolute CD-active peptides, indicating a relatively evolutional stability of the CD epitopes (13).

As suggested by its name, prolamin proteins are rich in the amino acid residues proline and glutamine. For example, glutenins often contain repetitive sequences in its central domain, such as the GQQ repeat, the PGQGQQ repeat, and the GYYPTSL(P)QQ repeat (14). The ineffective cleavage of gastrointestinal enzymes to prolamin proteins at sites before and after proline or glutamine often ends up with large CD active peptides, which were absorbed into the lamina propria (15). And they are often resistant to processing by the luminal and brush-border enzymes. As a result, they are transported to the mucosal epithelium in the form of polypeptides, deamidated by tissue transglutaminase (TG2), and recognized predominately by the $CD4^+$ T-cells. T-cell recognition is relying mostly by the HLA-DQ2 molecule, preferentially of negatively charged residues at the anchor positions of P4, P6, and P7 and controls the CD development (16–18).

Different processing changes the epitope conformation, which in turn may alter their recognition by HLA-DQ2 (19). To review the post-harvest journey of prolamin proteins, they go through different treatments with various combinations of pH and temperatures depending on the food to make. During the sourdough fermentation process in leavened dough preparation, microbial acidification could bring the pH down to ∼3.0–4.5 (20). After being endowed with a certain shape, the dough is then usually steamed/baked at temperatures of 100°C or higher (5). In some cases, the dough is boiled (at 100°C) without fermentation during the cooking of dumplings, spaghettis, and noodles. Eventually, all these deli would be consumed and delivered to the fasted stomach, where the pH is ∼2 (21). Considering that the prolamins deep in the deli could enter the gut without sufficient digestion in the stomach, it is possible that the conformation of an epitope at pH 3.0–4.5 is maintained even after passing through the stomach (22). Thus, there are typically two thermal conditions and three pH conditions among different treatment scenarios that a gluten epitope could possibly undergo. It would be enlightening to determine which factor, or combination of them, impact the epitope conformation and subsequent allergenicity more profoundly with a possible molecular mechanism provided.

MATERIALS AND METHODS

Homology Comparison and Structure Generation

The six gluten epitope homologous comparison was conducted with the Multiple Sequence Alignment tool-Clustalw Omega in the European Bioinformatics Institute of the European Molecular Biology Laboratory (EMBL-EBI) (23). And the three-dimensional structures of these peptides were generated with PyMol (24).

Different Thermal and pH Treatments of the Gluten Epitope Peptides

Different pH and acidic treatments of each of the above gluten epitope peptides (GEPs) were performed with the BIOVIA Discovery Studio software V16.1.0. Based on the CHARMm36 molecular mechanics and molecular dynamics (MD) force field engine, MD was performed in the DS standard dynamics cascade. All systems were solvated in an $\sim 33 \times 28 \times 59$ $Å^3$ orthorhombic box with a minimum clearance of 7 Å using the explicit periodic boundary water model and neutralized by the addition of sodium cation and chloride anion to an ionic concentration of 0.3326 (unpublished data). For the acidic treatment, the pH was set at 2.0 and 4.5, respectively. Initially, the system underwent two energy minimization steps: 1,000 steps of steepest descent minimization and 2,000 steps of conjugate gradient minimization with the adopted Newton–Raphson algorithm (25). The following three steps of heating, equilibration, and production were performed afterwards. The whole system was heated from 50 K to target temperature in 4 ps without constraints, and then the equilibrium step was run at target temperature for 20 ps without constraints. The following production step was run at different target temperature and pressure of 1.0 for 200 ps with typed NPT and no constraints. As for the native state, acidic treatment simulations, the target temperature was set at 298.15 K, and the pH was set at 7.5. As for the thermal treatment, and thermal treatment simultaneously combined with acidic treatment, the target temperature was set at 373.15 K. The electrostatic parameter was set to automatic, which recognizes the periodic environment and used the particle mesh Ewald (PME) electrostatic calculation (26). Among the 100 conformations generated, the one in the solvation boundary with the lowest total energy was selected for the subsequent study.

Immunogenicity Assessment as Recognition by HLA-DQ2

The selected conformation of each GEP after different treatments was applied to molecular docking to the epitope presenting groove of the HLA-DQ2 X-ray crystal structure (PDB ID: 1S9V) where the original GEP1 in the published structure was removed (27). The HLA-DQ2 receptor was further prepared in an $\sim 72 \times 60 \times 97$ $Å^3$ orthorhombic box with a minimum clearance of 7 Å *via* the aforementioned MD simulation protocols, except that the pH for protonation was set at pH 7.5, the ionic strength was set at 0.2, and the target temperature for MD production step was set at 310.15 K (28, 29). To evaluate the HLA-DQ2 recognition of differently treated GEPs, molecular docking was performed with the DS CDOCKER module between the native, differently treated GEPs and HLA-DQ2. Both the GEP and DQ2 were prepared at pH 7.5 and ionic strength of 0.2, and the epitope presenting groove was selected as the binding site with the radius set at 22.6 Å. CDOCKER is a grid-based docking mechanism operated by the CDOCKER algorithm (30). Of over 1,000 dynamic steps, 10 random conformations were generated for the initial ligand conformation at a temperature of 1,000 K accompanied with 10 orientations. The following simulated annealing was performed with 2,000 steps heating to a target temperature of 700 K and 5,000 steps cooling to a target temperature of 300 K. Among the 10 GEP-DQ2 binding conformations generated, the complex with the lowest CDOCKER energy was subjected to the Calculate Binding Energies module equipped in the DS, and subsequent association constant calculation was performed. For

the GEP-DQ2 interaction analysis, LigPlot was used to analyze the hydrophobic interactions, and PyMol was used to analyze the hydrogen bonding (31).

RESULTS

Gluten Epitope Diversity and Rationale in This Study

Most of the gluten epitope identified so far are sequences in the gliadins, and among the 61 identified gluten epitopes summarized in this study, 42 of them are recognized by the HLA-DQ2 molecule (**Supplementary Table 1**). The minimal length required for T-cell recognition is nine amino acids (4). Thus, we selected five peptides (GEP2–6) ranging from 11 to 12 amino acids long, which maximally represent the sequence diversity among all the gluten epitopes summarized (**Figure 1**). Most of these peptides are the common fragments of gluten epitopes identified previously, and epitopes with the most similar amino acid sequences are listed (32). Additionally, another peptide (LQPFPQPELPY, GEP1), which has been reported to bind to DQ2, was studied in parallel as an indicator of the computational accuracy (27). GEP2–6 are very diversified in their primary sequences except GEP1. Among these six GEPs, GEP1, GEP2, GEP3, and GEP5 have been identified as recognized by DQ2 (33). GEP4, GEP5, and GEP6 are identified as recognized by DQ8 (34, 35). So far, GEP4 and GEP6 are identified as solely recognized by HLA-DQ8. Studying their *in silico* recognition by DQ2 may reveal the molecular basis of recognition specificity. There is an acidic glutamic acid (E) in GEP1 and a basic lysine (K) in GEP6, while the rest of the amino acid residues are either aromatic or aliphatic. Specifically, glutamine (Q) and proline (P) are always present in these epitopes, while glutamine takes up 16.7–50% and proline takes up 8.3–45.5% of the total amino acid residues.

In this study, we simulated the conformation of each above GEP under different pH and temperature treatments to mimic the fermentation, cooking, and digestion processes in reality in a simplified module. GEP1 has been co-crystallized with HLA-DQ2 at a pH of buffer mixture (2 μl of 25 mM Tris–HCl pH 8.0 with 2 μl of 50 mM sodium acetate, pH 3.5) and room temperature in previous studies (27). The same GEP1–DQ2 complex was simulated at pH 7.5 and 25°C. Results show that the DQ2 conformations between the one obtained from X-ray diffraction and *in silico* simulation were nearly the same with a root mean square deviation (RMSD) of 1.292 Å. This suggested a relatively robust computational result that sufficiently reflected the experimental one. The RMSD between the GEP1 in the crystal structure and the simulated structure is 2.315 Å; this slight difference in structure is probably due to the change in pH during crystallization (8.0 vs. 7.5) and the difference of "room temperature" and 25°C.

FIGURE 1 | Sequence alignment of the selected gluten epitope peptides (GEPs). The six selected GEPs were chosen among the reported gluten epitopes with maximum primary sequence diversity, and aligned with the European Bioinformatics Institute of the European Molecular Biology Laboratory (EMBL-EBI) multiple sequence alignment tool for sequence comparison. The leftmost lane is the number of the GEP, the middle is its sequence, and the rightmost lane is the number of the amino acid residues in each corresponding GEP. The rightmost lane is the epitope with the most similar amino acid sequences. Red indicates amino acid residues L, P, F, and A; green indicates amino acid residues Q, Y, G, S, N, and C; blue indicates amino acid residue E; magenta indicates amino acid residue K.

As mentioned above, for different pH conditions, these situations could be (1) the untreated/unleavened dough at physiological pH 7.5; (2) the microbial leavened dough at pH 4.5; and (3) prolamins in the stomach treated at pH 2.0. For different temperature conditions, the scenarios are simplified into two cases: (1) the uncooked dough at room temperature of 25°C and (2) the cooked dough at 100°C (baking temperatures above 100°C are simplified to this temperature). In this theoretical study, the pH and temperature conditions were simplified and systemized. Three different pH values were applied in this study: pH 7.5 represents the native structure of untreated GEPs, pH 4.5 represents mild acidic treatment where the sourdough fermentation potentially affects the recognition of GEPs, and pH 2.0 represents intensified acid treatment where the gluten was digested in a fasted stomach before entering the small intestine. Two temperatures were applied in this study: 25°C represents the GEPs at their native temperature, and 100°C represents the heat treatment. Different combinations of these pH and temperatures represent scenarios of eating different food (wheat flour based). For example, treatment at pH 4.5 and 100°C simplifies the situation where the steamed bread (fermented) was consumed, while treatment at pH 7.5 and 100°C simplifies the situation where an unleavened bread was cooked and consumed (**Figure 2**). Additionally, the treatment of pH 7.5 and 100°C, followed by treatment of pH 2.0 and 25°C, was studied to investigate the gastric digestion (pH 2.0) of a cooked dough with GEP in it (**Figure 2**, dashed line).

Following different combinations of treatment, each GEP was applied to the recognition by HLA-DQ2 *in silico*. Their recognition, specifically at the peptide-presenting groove of the DQ2 heterodimer interface as previously reported, triggers the presentation of these GEPs to T-cells in the small intestine (4). Thus, it is an indicator to evaluate the immunogenicity of a GEP conformation by measuring its recognition by HLA-DQ2.

Heat Treatment to the Conformation of Gluten Epitopes and Their Recognition by HLA-DQ2

Generally, heat treatment at 100°C substantially influenced the conformation of each GEP (**Figure 3**). For GEP1, recognition by DQ2 rendered a conformational change of this peptide by an RMSD of 2.833 Å (**Figure 3A**). The binding energy

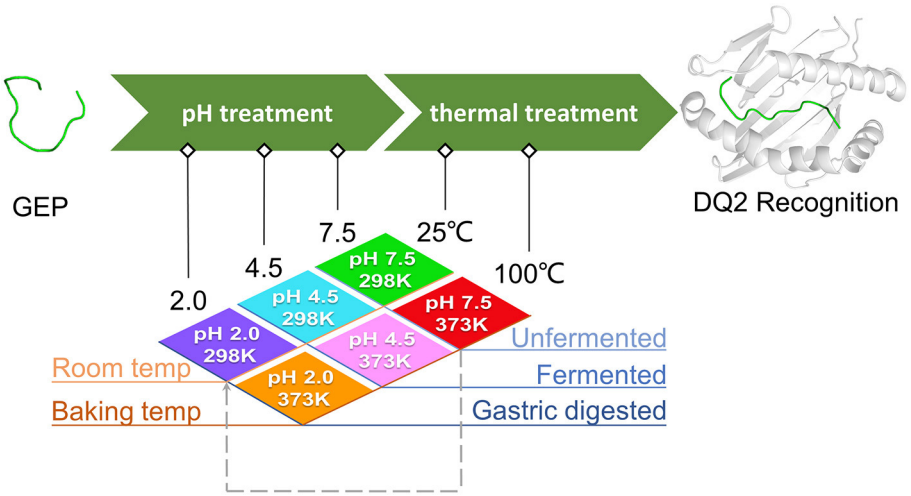

FIGURE 2 | Study rationale and scheme of different treatments on the gluten epitope peptides (GEPs). The native gluten protein (pH 7.5 at 25°C), with GEP sequences on it, went through low pH treatment (pH 4.5 during bacterial fermentation and pH 2.0 during gastric digestion in the fasted stomach) and thermal treatment (100°C during boiling/steaming) under different circumstances. The pH and temperature conditions in all scenarios were simplified into a combination of temperatures (298.15 and 373.15 K) and pH (2.0, 4.5, and 7.5). Each GEP went through a treatment of one of the above combinations. The dashed arrow represents the case where the dough was treated at pH 7.5 and 100°C before taken in the diet (pH 2.0 and 25°C). The conformation of GEPs after the above seven treatments was applied for recognition by HLA-DQ2, and the molecular docking parameters generated served as indicators for their immunogenicity.

calculated from the CDOCK pose with the best score was −18.06 kJ/mol. Heat treatment deviated this structure from its native conformation by 3.519 Å, and binding to DQ2 further deviated its conformation from the heat-treated one for 2.918 Å (**Table 1**). Compared with the native DQ2, the number of hydrogen bonds that formed between GEP1 and DQ2 did not change, while the number of amino acid residues involved in their hydrophobic interactions increased from eight to nine in GEP1 and from 16 to 20 in DQ2 (**Table 1**). Binding energy of the heat-treated GEP1–DQ2 complex was calculated as 25.70 kJ/mol that leads to an $\sim 10^{-8}$-fold decrease in the binding affinity.

For GEP2, its recognition by DQ2 rendered a structural change of 2.49 Å. Heat treatment deviated its conformation from the native one for 4.473 Å, and the DQ2 bound conformation was greatly compressed compared with that of the native one with an RMSD of 3.865 Å (**Figure 3B**). The number of hydrogen bonds that formed between GEP2 and DQ2 decreased from eight to seven, while there are more (eight compared with seven) amino acid residues in GEP2 and more (16 compared with 12) amino acid residues in DQ2 involved in their hydrophobic interactions (**Table 1**). The binding energy calculated from the best CDOCKER pose was −35.801 kJ/mol for native GEP2 binding to DQ2 and −37.520 kJ/mol for the thermal denatured, and this subsequently led to an increase of binding affinity of ∼2-fold.

For GEP3, binding to DQ2 dramatically altered the conformation of this peptide with an RMSD of 7.464 Å (**Figure 3C**), and heat treatment changed its conformation with an RMSD of 3.317 Å (**Table 1**). The heat-treated GEP3 was recognized by DQ2 with structural adjustment of 2.632 Å. The GEP3–DQ2 interaction was enhanced as the hydrogen bonds increased from four to nine between them, and one more amino acid residue in GEP3 and four more amino acid residues in DQ2 are involved in the hydrophobic interactions between them. The binding energy calculated was −107.90 kJ/mol for the native GEP3 binding to DQ2 and −83.39 kJ/mol for the heat-treated one, and this caused an $\sim 10^{-5}$-fold decrease in binding affinity.

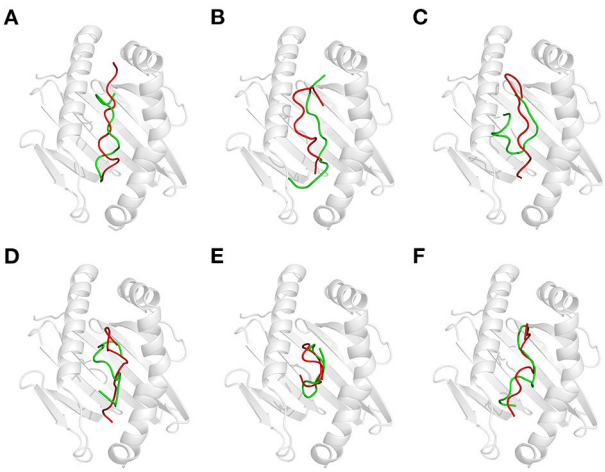

FIGURE 3 | Effect of thermal treatment on the recognition of gluten epitope peptides (GEPs). In each panel, the white cartoon representation presents the HLA-DQ2 with the epitope presenting groove facing outwards. The ribbon diagram represents each GEP. The green ones represent native GEPs at pH 7.5 and 25°C, and the red ones represent the thermal treated one at pH 7.5 and 100°C. **(A–F)** GEP1–GEP6, respectively.

TABLE 1 | Binding parameters of differently treated GEP to HLA-DQ2.

GEP	Treatment[a]	RMSD[b] (Å)		H-bond[c]	Hydrophobic interactions[d]		-CDOCKER_Energy (kJ/mol)	Binding energy (kJ/mol)	Fold change[e]
		Apo-	Complex		GEP	DQ2			
GEP1	Native	-	2.833	6	8	16	91.417	−18.06	1
	Thermal	3.519	2.918	6	9	20	91.991	25.704	− − −
	Acidic	3.412	5.013	5	8	15	91.523	−32.917	+
	Thermal→acidic	3.036	2.187	7	9	15	77.441	−71.362	+ + +
	Thermal + acidic	4.948	6.751	8	7	12	100.05	−110.197	+ + + + +
GEP2	Native	-	2.49	8	7	12	97.661	−35.801	1
	Thermal	4.473	3.865	7	8	16	103.333	−37.52	+
	Acidic	2.922	4.599	8	8	13	93.062	−146.546	+ + + + ++
	Thermal→acidic	3.666	5.046	12	5	13	97.45	−114.467	+ + + + +
	Thermal + acidic	4.717	2.439	5	11	11	90.677	−36.869	+
GEP3	Native	-	7.464	4	8	9	105.68	−107.904	1
	Thermal	3.317	2.632	9	9	13	105.278	−83.393	− −
	Acidic	2.49	4.413	12	8	16	89.354	−100.185	−
	Thermal→acidic	4.118	5.554	9	8	12	90.234	−146.7	++
	Thermal + acidic	3.221	3.889	10	11	16	95.405	−110.683	+
GEP4	Native	-	6.021	6	5	7	130.191	−15.707	1
	Thermal	1.31	5.877	13	8	11	136.997	−109.147	+ + + + +
	Acidic	3.41	3.543	4	9	19	124.675	−18.95	+
	Thermal→acidic	1.499	4.285	8	9	13	119.475	−77.955	+ + ++
	Thermal + acidic	3.534	5.23	6	9	13	126.646	−51.78	++
GEP5	Native	-	6.981	5	8	11	89.723	−168.754	1
	Thermal	4.268	5.808	7	10	11	88.878	−87.384	− − − − −
	Acidic	3.185	2.751	5	10	14	76.625	−2.767	− − − − − − − − − −
	Thermal→acidic	3.286	5.543	5	8	12	77.887	−122.648	− − −
	Thermal + acidic	2.049	6.827	6	9	9	79.793	−105.359	− − − −
GEP6	Native	-	6.593	5	10	17	154.2	56.631	1
	Thermal	4.301	5.436	6	8	13	148.007	−77.677	+ + + + + + + ++
	Acidic	3.853	4.018	4	8	14	144.691	46.745	+
	Thermal→acidic	5.459	4.883	10	9	11	144.543	−25.624	+ + + + +
	Thermal + acidic	4.011	5.576	7	7	13	143.858	−26.142	+ + + + +

[a] *Treatment conditions, native stands for the gluten epitope peptide (GEP) conformation at pH 7.5 and 25°C; thermal treatment stands for the GEP conformation at pH 7.5 and 100°C; acidic treatment stands for the GEP conformation at pH 2 and 25°C; thermal→acidic treatment stands for the GEP conformation at pH 7.5 and 100°C and then simulated at pH 2.0 and 25°C; thermal + acidic treatment stands for the GEP conformation at pH 2.0 and 100°C.*

[b] *RMSD is the root mean square deviation; apo- is the RMSD between conformations of differently treated GEPs and the corresponding native GEP; DQ2 complex is the RMSD between the conformations of differently treated GEPs in the GEP-DQ2 complex and the corresponding native apo-GEPs.*

[c] *Number of hydrogen bonds is the number of hydrogen bonds that formed between native and differently treated GEPs and the DQ2.*

[d] *Number of residues involved in hydrophobic interactions represents the numbers of amino acid residues in GEP/DQ2 involved in their interactions after different treatments.*

[e] *Fold change is the change of association constant of one particular treated GEP binding to DQ2 compared with that of the corresponding native GEP binding to DQ2. + indicates a fold increase < 10^3; ++ indicates a fold increase between 10^3 and 10^7; + + + indicates a fold increase between 10^7 and 10^{10}; + + ++ indicates a fold increase between 10^{10} and 10^{13}, and so on. − indicates a fold decrease with the same magnitude as the + sign.*

For GEP5, DQ2 recognition leads to an intensive structural change with an RMSD of 6.981 Å (**Figure 3E**). Heat treatment changed the unbound GEP5 structure with an RMSD of 4.268 Å, and binding of the heat-treated GEP5 bound to DQ2 deviated from its unbound conformation with an RMSD of 5.808 Å. The number of hydrogen bonds that formed in the GEP5–DQ2 complex increased from five to seven, and the number of amino acid residues in GEP5 involved in hydrophobic interactions increased from 8 to 10, while the number of amino acid residues in DQ2 involve in their hydrophobic interactions did not change (**Table 1**). The binding energy was calculated as −168.75 kJ/mol and decreased to −87.38 kJ/mol as the GEP5 was thermal treated. This led to a very significant decrease in their binding affinity.

Although right now GEP4 and GEP6 are only reported to bind to HLA-DQ8, they are still recognized by HLA-DQ2 here *in silico* with structural adjustment (RMSD of 6.021 and 6.593 Å, respectively) to fit the peptide-presenting groove (**Figures 3D,F**). Heat treatment changed the conformation of GEP6 more significantly (RMSD of 4.301 Å) than GEP4 (RMSD of 1.310 Å), and subsequent binding to DQ2 leads to conformational

rearrangement of 5.877 and 5.436 Å, respectively. After heat treatment, GEP4 increased its interaction with DQ2, as seven more hydrogen bonds were formed and seven more amino acid residues were involved in their hydrophobic interactions. On the other hand, GEP6 formed one more hydrogen bond with DQ2, but six less amino acid residues were involved in their hydrophobic interactions (**Table 1**). For both GEP4 and GEP6, thermal treatment caused a significant decrease in their binding energy and consequently a large increase in their binding affinity to DQ2.

Acidic Treatment to the Conformation of Gluten Epitopes and Their Recognition by HLA-DQ2

Acidic treatment mimics the bacterial fermentation in the dough at pH 4.5 and gastric digestion in a fasted stomach at pH 2.0. It is found that the conformation of all GEPs at pH 4.5 is identical with that at pH 7.5 (**Supplementary Table 2**). Each GEP was compared with its folding at pH 4.5 and pH 2.0, while the former was noted as the native and the latter does impact the structure of all GEPs (**Figure 4**). For GEP1, acidic treatment rendered a structural change with an RMSD of 3.412 Å, and recognition by HLA-DQ2 deviated its structure with an RMSD of 5.013 Å (**Figure 4A**). The number of both the hydrogen bonds and the amino acid residues involved in their hydrophobic interactions between GEP1 and DQ2 decreased slightly (**Table 1**). However, the binding energy after acidic treatment decreased to −32.92 kJ/mol, indicating an $\sim 10^2$-fold increased binding affinity.

For GEP2, acidic treatment deviated its structure with an RMSD of 2.922 Å. When this acid-treated peptide bound to DQ2, its conformation was changed with an RMSD of 4.599 Å (**Figure 4B**). Compared with that of the native one, the interaction between the acid-treated GEP2 and DQ2 was merely more intensive by only one more amino acid residue, in both GEP2 and DQ2, involved in their hydrophobic interaction (**Table 1**). The binding energy dramatically decreased to −146.55 kJ/mol, suggesting an astounding increase of $\sim 10^{18}$-fold in binding affinity.

For GEP3, acidic treatment changed its conformation by an RMSD of 2.490 Å, and further binding to HLA-DQ2 changed its structure by another RMSD of 4.413 Å (**Figure 4C**). Acid-treated GEP3 binds with DQ2 with eight more hydrogen bonds, and seven more amino acid residues in DQ2 are involved in their hydrophobic interactions (**Table 1**). The binding energy of acid-treated GEP3 to DQ2 slightly increased to −100.19 kJ/mol, which leads to a slight decrease of binding affinity.

For GEP5, acidic treatment changed the peptide conformation by an RMSD of 3.185 Å (**Figure 4E**), and binding to DQ2 leads to a structural adjustment with an RMSD of 2.751 Å (**Table 1**). Compared with the native structure, acidic treatment strengthened the interaction between GEP5 and HLA-DQ2 by increasing their hydrophobic interactions where two more amino acid residues in GEP5 and three more amino acid residues in DQ2 are involved in their recognition. The binding energy of acid-treated GEP5 to DQ2 dramatically increased to −2.77 kJ/mol, which led to a significant decrease of $\sim 10^{-28}$-fold.

For GEP4 and GEP6, acidic treatment deviated their structures from each corresponding one with RMSD of 3.410 and 3.853 Å, while DQ2 binding changed their structures from the apo-one for 3.543 and 4.018 Å, respectively (**Figures 4D,F**). For GEP4, less hydrogen bonds were formed while significantly more hydrophobic interactions were involved after acidic treatment. For GEP6, hydrogen bonding and hydrophobic interactions were both weakened in acid-treated GEP6–DQ2 complex (**Table 1**). For both GEP4 and GEP6, there is a slight decrease in their binding energies to DQ2, which leads to an increase in their binding affinities.

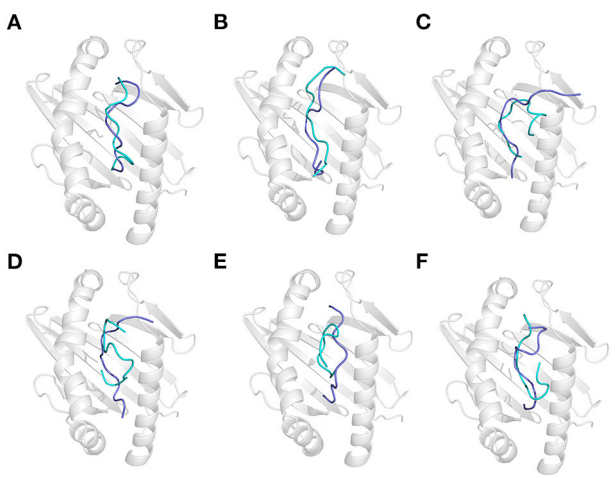

FIGURE 4 | Effect of acidic treatment on the recognition of gluten epitope peptides (GEPs). In each panel, the white cartoon representation presents the HLA-DQ2 with the epitope presenting groove facing outwards. The ribbon diagram represents each GEP. The cyan ones represent native GEPs at pH 4.5 and 25°C, and the slate ones represent the thermal treated one at pH 2.0 and 25°C. **(A–F)** GEP1–GEP6, respectively.

Combination of Thermal and Acidic Treatment to the Conformation of Gluten Epitopes and Their Recognition by HLA-DQ2

To mimic the combination of thermal and acidic treatment, the thermal treatment at 100°C (cooking) was followed by acidic treatment at pH 2.0 (gastric digestion). As a theoretical study, the situation where the GEPs were treated at pH 2.0 and 100°C was also investigated. That is, the thermal and acidic treatments were undertaken simultaneously. For GEP1, thermal treatment followed by acidic treatment leads to a structural change from the native one with an RMSD of 3.036 Å, and recognition by DQ2 leads to a change with an RMSD of 2.187 Å (**Figure 5A**). Thermal treatment followed by acidic treatment altered the GEP1–DQ2 interaction by increasing one hydrogen bond. One more amino acid residue in GEP1 and one less amino acid residue in DQ2 were involved in their hydrophobic interactions. The binding energy between GEP1 and DQ2 after such treatment decreased to −71.36 kJ/mol, which subsequently leads to a large increase of their binding affinity of $\sim 10^8$-fold. Once the thermal and

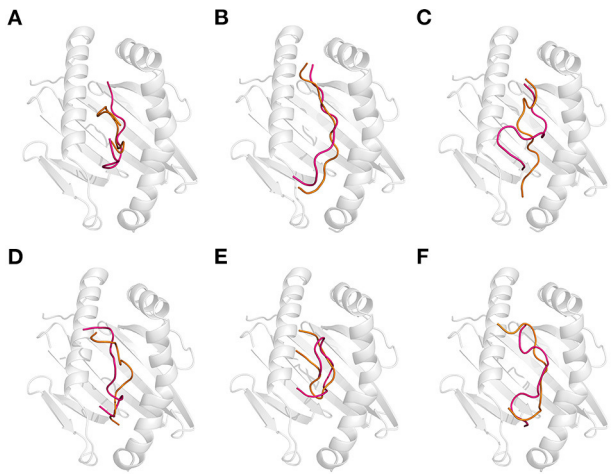

FIGURE 5 | Effect of the combination of thermal and acidic treatments on the recognition of gluten epitope peptides (GEPs). In each panel, the white cartoon representation presents the HLA-DQ2 with the epitope presenting groove facing outwards. The ribbon diagram represents each GEP. The hot pink ones represent the thermal treated one at pH 7.5 and 100°C followed by acidic treatment at pH 2.0 and 25°C. The orange ones represent the simultaneous thermal and acid-treated ones at pH 2.0 and 100°C. **(A–F)** GEP1–GEP6, respectively.

acidic treatments were applied simultaneously, the apo-GEP1 structure deviated more severely with an RMSD of 4.948 Å, and docking to the DQ2 peptide-presenting groove resulted in a severe compressed structural change of 6.751 Å. There are two more hydrogen bonds that formed, while one less amino acid residue in GEP1 and four less amino acid residue in DQ2 were involved in their hydrophobic interactions (**Table 1**). And the corresponding binding energy decreased to −110.19 kJ/mol, which led to a very large increase of their binding affinity of $\sim 10^{15}$-fold.

For GEP2, thermal treatment followed by acidic treatment changed its structure with an RMSD of 3.666 Å, and binding to DQ2 leads to a structural change of 5.046 Å (**Figure 5B**). There were four more hydrogen bonds that formed, and two less amino acid residues in GEP2 and one more amino acid residue in DQ2 were involved in their hydrophobic interactions. This led to a large decrease of their binding energy to −114.47 kJ/mol, which corresponds to an $\sim 10^{13}$-fold increase of their binding affinity. When the thermal and acidic treatments were applied simultaneously, there is a structural change with an RMSD of 4.717 Å, and recognition by DQ2 changed its conformation by 2.439 Å. There are three less hydrogen bonds that formed, while four more amino acid residues in GEP2 and one less amino acid residue in DQ2 were involved in their hydrophobic interactions (**Table 1**). The corresponding binding energy only slightly decreased to −36.87 kJ/mol, and the binding affinity almost did not change.

For GEP3, thermal treatment followed by acidic treatment deviated the peptide structure from its native form with an RMSD of 4.118 Å, and binding to DQ2 leads to a structural change with an RMSD of 5.554 Å (**Figure 5C**). The GEP3–DQ2 interaction was intensified by forming five more hydrogen bonds, and three more amino acid residues in DQ2 were involved in their hydrophobic interactions. This treatment leads to a decrease of their binding energy to −146.70 kJ/mol that caused an $\sim 10^{6}$-fold increase of their binding affinity. Simultaneous thermal and acidic treatments deviated the peptide from its native structure with an RMSD of 3.221 Å, and subsequent binding to DQ2 leads to a conformational change with an RMSD of 3.889 Å. The GEP3–DQ2 interaction was strengthened by six more hydrogen bonds, while three more amino acid residues in GEP3 and seven more amino acid residues in DQ2 were involved in their hydrophobic interactions. This treatment also leads to a decrease of binding energy to −110.68 kJ/mol that translated to a slight increase of their binding affinity.

For GEP5, acidic treatment after thermal treatment of this peptide changed it structure with an RMSD of 3.286 Å, and subsequent binding to DQ2 leads to a structural change of 5.543 Å (**Figure 5E**). There is little enhancement of the GEP5–DQ2 interactions by one more amino acid residue in DQ2 involved in their interactions after such treatment. This treatment led to an increase to their binding energy to −122.65 kJ/mol that translated to an $\sim 10^{-8}$-fold decrease of binding affinity. Once the thermal and acidic treatments were applied at the same time, the peptide structure was changed with an RMSD of 2.049 Å, and subsequent binding to DQ2 leads to a structural change of 6.827 Å. The number of hydrogen bonds that formed in between them increased by one. One more amino acid residue in GEP5 and two less amino acid residues in DQ2 were involved in their interactions. This treatment caused an increase in their binding energy to −105.36 kJ/mol, which corresponds to a 10^{-11}-fold decrease in their binding affinity.

For GEP4 and GEP6, acid treatment following thermal treatment deviated these epitopes from their native structures with RMSD of 1.499 and 5.459 Å, respectively. Subsequent binding to DQ2 adjusted their conformations with RMSD of 4.285 and 4.883 Å, respectively (**Figures 5D,F**). There is a significant enhancement of GEP4–DQ2 interaction with the hydrogen bonds increased by two, and the number of amino acid residues increased by 10 in the GEP4–DQ2 complex. And the binding energy increased to −77.96 kJ/mol, which corresponded to an $\sim 10^{10}$-fold increase in their binding affinity. There are five more hydrogen bonds that formed in the GEP6–DQ2 complex, while one less amino acid residue in GEP6 and six less amino acid residues in DQ2 were involved in their hydrophobic interactions. The binding energy decreased to −25.62 kJ/mol, which corresponded to an $\sim 10^{13}$-fold increase in their binding affinity.

When the thermal and acidic treatments were applied simultaneously, the conformations of these peptides were deviated from their native forms with RMSD of 3.534 and 4.011 Å, and recognition of these treated peptides by DQ2 changed their structures with RMSD of 5.230 and 5.576 Å (**Figures 5D,F**). For GEP4, the hydrogen bonding remained the same, while the hydrophobic interactions were enhanced by four more amino acid residues in GEP4 and six more amino acid residues in DQ2. This treatment leads to a decrease of the binding energy to −51.78 kJ/mol that corresponded to an $\sim 10^{6}$-fold increase

in their binding affinity. For GEP6, two more hydrogen bonds formed, while a total of seven less amino acid residues were involved in the GEP6–DQ2 hydrophobic interactions. And this led to a decrease of binding energy to −26.14 kJ/mol, which corresponded to an $\sim 10^{13}$-fold increase in their binding affinity.

DISCUSSION

Heat treatment, which almost certainly undermines the native structure of a protein, does not necessarily decrease the allergenicity of a protein allergen (36). For example, roasting decreased the allergenicity of hazelnut while increasing the IgE binding of two major allergens, Ara h 1 and Ara h 2, in peanuts (37, 38). Even in the same food, heat treatment exerts different allergenicity effects depending on the protein component. For example, boiling treatment lowered the IgE binding to shrimp extracts but enhanced the IgE binding to the purified TM from boiled shrimps (39). It is consistent in this study that different GEPs responded differently to heat treatment in exhibiting their binding to HLA-DQ2.

For GEP1 and GEP2, there is one extra Q in the N-terminus of GEP2, and the E8 is changed into Q in GEP2. Thus, these two epitopes exhibited a similar binding behavior to HLA-DQ2 after acidic treatment: thermal treatment followed by acidic treatment and simultaneously thermal and acidic treatments. The difference is that they corresponded differently to the thermal treatment at physiological pH. For both GEP1 and GEP2, one more amino acid residue in the peptide and four more amino acid residues in the DQ2 are involved in the hydrophobic interaction after thermal treatment, indicating an exposure of hydrophobic residues after thermal treatment of these epitopes. However, the conformation of exposed GEP1 and GEP3 is obviously different. The thermal treated and DQ2 bound GEP1 peptide is compressed compared with its native one, while that of the GEP2 is more severely compressed. Consistent with previous studies, this result indicated that the pivotal role of one acidic amino acid residue in the gluten epitope could profoundly impact its immunogenicity during food processing (17, 18).

For these six GEPs studied here, GEP1, GEP2, GEP3, and GEP5 are known to be recognized by DQ2. Their responses to different treatments on exhibiting DQ2-mediated immunogenicity are vastly different. For GEP1 and GEP3, some treatments decrease their binding to HLA-DQ2, while other treatments increase their binding. For GEP2 and GEP4, all treatments increased their binding. On the other hand, all treatments decreased the binding of GEP5. Considering the sequence similarity between GEP2 and GEP5, a little variance in primary sequence does lead to dramatically different DQ2 recognition.

GEP4 and GEP6 are reported to be only recognized by DQ8. It is not clear that the uncertainty of recognition of these two epitopes by HLA-DQ2 is due to the lack of evidence or not. However, *in silico* study here not only revealed that they are recognized by HLA-DQ2 but also indicated that thermal and acidic treatments both sensitized their recognition. Interestingly, thermal treatment alone intensified the recognition of these two GEPs most, while any form of acidic treatment, following the thermal treatment or in a simultaneous combination with thermal treatment, weakened this effect. It is noticed the FxxxQxN sequence is in both GEP4 and GEP6 that formed an intra-chain kink structure. Neither thermal treatment nor acidic treatment disrupted this structure. For GEP4 and GEP6, all treatments increased their binding, and this suggested a possible role of kink structures in the HLA-DQ2-induced immunogenicity.

Of course, this study was performed by placing all the GEPs in an infinitely diluted solution. In reality, the GEPs are in the cellular conditions and the molecular crowding effect, chaperons, and pH buffering that survive the GEPs from the thermal and acidic treatments (40–42). What could happen *in silico* does not necessarily mean it could happen in reality. However, a theoretical study like this offers a structural and mechanistic insight into what could happen as the molecular basis of different food processing methods to decrease the allergenicity. This is potentially helpful in the *in vitro* mutagenesis and breeding strategies to obtain wheat species with reduced amount of gluten epitopes for the prevention of CD. For example, breeding between the diploid *Triticum monococcum* and hexaploid wheat could potentially generate a cultivar with reduced immune response due to the higher digestibility of gluten proteins in the former (43).

CONCLUSIONS

In this study, computational simulation of thermal, acidic, and thermal treatment followed by further acidic treatment, and simultaneous thermal and acidic treatment of GEPs with each subsequent binding to HLA-DQ2 were performed. Results show that the amino acid sequences of each GEP profoundly impact their recognition by HLA-DQ2, especially the acidic amino acid residues dramatically change the binding characteristics of a GEP. The peptide conformation, such as a kink, is stable and conserved during different treatments and binding to DQ2. Our results indicated GEP4 and GEP6 still bind to HLA-DQ2; however, this kink structure might be structurally characteristic of HLA-DQ8 recognized gluten epitopes.

DATA AVAILABILITY STATEMENT

The raw data supporting the conclusions of this article will be made available by the authors, without undue reservation.

AUTHOR CONTRIBUTIONS

DY and FX designed the study. JG, HD, ZZ, ZL, HL, and PZ performed the experiment. HD, JG, XW, SL, LF, YW, HC, WX, FX, and DY analyzed the data. DY wrote the paper. ZZ, HD, and JG contributed equally to this work. All authors read and approved the final manuscript.

FUNDING

This research was funded by the National Key Research and Development Program of China, Grant Number

2019YFC1605000; the National Natural Science Foundation of China, Grant Number 31801482; and the Central Public-interest Scientific Institution Basal Research Fund, Grant Number S2020JBKY-13.

ACKNOWLEDGMENTS

The authors are grateful to Prof. Zhanhui Wang for help in molecular simulation software and Prof. Chih-chen Wang in the Institute of Biophysics, Chinese Academy of Sciences, for her support and encouragement in our research.

SUPPLEMENTARY MATERIAL

The Supplementary Material for this article can be found online at: https://www.frontiersin.org/articles/10.3389/fnut.2021.647750/full#supplementary-material

REFERENCES

1. Guo Y, Zhao C, Yu P, Gao J, Liang Z, Ji R, et al. Molecular basis of sodium chloride dominated glutenin interaction and bread properties. *LWT*. (2021) 142:111011. doi: 10.1016/j.lwt.2021.111011
2. Joye IJ, Lagrain B, Delcour JA. Endogenous redox agents and enzymes that affect protein network formation during breadmaking—a review. *J Cereal Sci*. (2009) 50:1–10. doi: 10.1016/j.jcs.2009.04.002
3. Biesiekierski JR. What is gluten? *J Gastroenterol Hepatol*. (2017) 32:78–81. doi: 10.1111/jgh.13703
4. Sollid LM. Coeliac disease: dissecting a complex inflammatory disorder. *Nat Rev Immunol*. (2002) 2:647–55. doi: 10.1038/nri885
5. Zhao C, Luo Z, Li M, Gao J, Liang Z, Sun S, et al. Wheat protein disulfide isomerase improves bread properties *via* different mechanisms. *Food Chem*. (2020) 315:126242. doi: 10.1016/j.foodchem.2020.126242
6. Trier JS. Celiac sprue. *N Engl J Med*. (1991) 325:1709–19. doi: 10.1056/NEJM199112123252406
7. Caio G, Volta U, Sapone A, Leffler DA, De Giorgio R, Catassi C, et al. Celiac disease: a comprehensive current review. *BMC Med*. (2019) 17:142. doi: 10.1186/s12916-019-1380-z
8. Gatti S, Lionetti E, Balanzoni L, Verma AK, Galeazzi T, Gesuita R, et al. Celiac screening: increased prevalence of celiac disease in school-age children in Italy. *Clin Gastroenterol Hepatol*. (2020) 18:596–603. doi: 10.1016/j.cgh.2019.06.013
9. Singh P, Arora A, Strand TA, Leffler DA, Catassi C, Green PH, et al. Global prevalence of celiac disease: systematic review and meta-analysis. *Clin Gastroenterol Hepatol*. (2018) 16:823–36.e2. doi: 10.1016/j.cgh.2017.06.037
10. van den Broeck HC, de Jong HC, Salentijn EMJ, Dekking L, Bosch D, Hamer RJ, et al. Presence of celiac disease epitopes in modern and old hexaploid wheat varieties: wheat breeding may have contributed to increased prevalence of celiac disease. *Theor Appl Genet*. (2010) 121:1527–39. doi: 10.1007/s00122-010-1408-4
11. Fasano A, Catassi C. Current approaches to diagnosis and treatment of celiac disease: an evolving spectrum. *Gastroenterology*. (2001) 120:636–51. doi: 10.1053/gast.2001.22123
12. Corrao G, Corazza GR, Bagnardi V, Brusco G, Ciacci C, Cottone M, et al. Club del Tenue Study: mortality in patients with coeliac disease and their relatives: a cohort study. *Lancet*. (2001) 358:356–61. doi: 10.1016/s0140-6736(01)05554-4
13. Pronin D, Börner A, Scherf KA. Old and modern wheat (*Triticum aestivum* L.) cultivars and their potential to elicit celiac disease. *Food Chem*. (2021) 339:127952. doi: 10.1016/j.foodchem.2020.127952
14. Gao J, Yu P, Liang H, Fu J, Luo Z, Yang D. The wPDI redox cycle coupled conformational change of the repetitive domain of the HMW-GS 1Dx5-A computational study. *Molecules*. (2020) 25:4393. doi: 10.3390/molecules25194393
15. Plugis NM, Khosla C. Therapeutic approaches for celiac disease. *Best Pract Res Clin Gastroenterol*. (2015) 29:503–21. doi: 10.1016/j.bpg.2015.04.005
16. Johansen BH, Vartdal F, Eriksen JA, Thorsby E, Sollid LM. Identification of a putative motif for binding of peptides to HLA-DQ2. *Int Immunol*. (1996) 8:177–82. doi: 10.1093/intimm/8.2.177
17. van de Wal Y, Kooy YM, Drijfhout JW, Amons R, Koning F. Peptide binding characteristics of the coeliac disease-associated DQ(alpha1*0501, beta1*0201) molecule. *Immunogenetics*. (1996) 44:246–53. doi: 10.1007/BF02602553
18. Vartdal F, Johansen BH, Friede T, Thorpe CJ, Stevanovic S, Eriksen JE, et al. The peptide binding motif of the disease associated HLA-DQ (alpha 1* 0501, beta 1* 0201) molecule. *Eur J Immunol*. (1996) 26:2764–72. doi: 10.1002/eji.1830261132
19. Rahaman T, Vasiljevic T, Ramchandran L. Effect of processing on conformational changes of food proteins related to allergenicity. *Trends Food Sci Technol*. (2016) 49:24–34. doi: 10.1016/j.tifs.2016.01.001
20. Gänzle MG, Loponen J, Gobbetti M. Proteolysis in sourdough fermentations: mechanisms and potential for improved bread quality. *Trends Food Sci Technol*. (2008) 19:513–21. doi: 10.1016/j.tifs.2008.04.002
21. Dressman JB, Berardi RR, Dermentzoglou LC, Russell TL, Schmaltz SP, Barnett JL, et al. Upper gastrointestinal (GI) pH in young, healthy men and women. *Pharm Res*. (1990) 7:756–61. doi: 10.1023/A:1015827908309
22. Shan L, Molberg O, Parrot I, Hausch F, Filiz F, Gray GM, et al. Structural basis for gluten intolerance in celiac sprue. *Science*. (2002) 297:2275–9. doi: 10.1126/science.1074129
23. Madeira F, Park YM, Lee J, Buso N, Gur T, Madhusoodanan N, et al. The EMBL-EBI search and sequence analysis tools APIs in 2019. *Nucleic Acids Res*. (2019) 47:W636–41. doi: 10.1093/nar/gkz268
24. *The PyMOL Molecular Graphics System*. In: New York, NY: Schrodinger, LLC (2015).
25. Sarkar TK, Yang X. Application of the conjugate gradient and steepest descent for computing the eigenvalues of an operator. *Signal Process*. (1989) 17:31–8. doi: 10.1016/0165-1684(89)90070-4
26. Darden T, York D, Pedersen L. Particle Mesh Ewald—an N.Log(N) method for Ewald sums in large systems. *J Chem Phys*. (1993) 98:10089–92. doi: 10.1063/1.464397
27. Kim CY, Quarsten H, Bergseng E, Khosla C, Sollid LM. Structural basis for HLA-DQ2-mediated presentation of gluten epitopes in celiac disease. *Proc Natl Acad Sci USA*. (2004) 101:4175–9. doi: 10.1073/pnas.0306885101
28. Porcelli AM, Ghelli A, Zanna C, Pinton P, Rizzuto R, Rugolo M. pH difference across the outer mitochondrial membrane measured with a green fluorescent protein mutant. *Biochem Biophys Res Commun*. (2005) 326:799–804. doi: 10.1016/j.bbrc.2004.11.105
29. Haraldsdottir HS, Thiele I, Fleming RM. Quantitative assignment of reaction directionality in a multicompartmental human metabolic reconstruction. *Biophys J*. (2012) 102:1703–11. doi: 10.1016/j.bpj.2012.02.032
30. Wu G, Robertson DH, Brooks CL, III, Vieth M. Detailed analysis of grid-based molecular docking: a case study of CDOCKER-A CHARMm-based MD docking algorithm. *J Comput Chem*. (2003) 24:1549–62. doi: 10.1002/jcc.10306
31. Yu P, Zhou F, Yang D. Curdlan conformation change during its hydrolysis by multi-domain beta-1,3-glucanases. *Food Chem*. (2019) 287:20–7. doi: 10.1016/j.foodchem.2019.02.070
32. Sollid LM, Tye-Din JA, Qiao SW, Anderson RP, Gianfrani C, Koning F. Update 2020: nomenclature and listing of celiac disease-relevant gluten epitopes recognized by CD4(+) T cells. *Immunogenetics*. (2020) 72:85–8. doi: 10.1007/s00251-019-01141-w
33. Arentz-Hansen H, McAdam SN, Molberg O, Fleckenstein B, Lundin KE, Jorgensen TJ, et al. Celiac lesion T cells recognize epitopes that cluster in regions of gliadins rich in proline residues. *Gastroenterology*. (2002) 123:803–9. doi: 10.1053/gast.2002.35381

34. Tollefsen S, Arentz-Hansen H, Fleckenstein B, Molberg O, Raki M, Kwok WW, et al. HLA-DQ2 and -DQ8 signatures of gluten T cell epitopes in celiac disease. *J Clin Invest*. (2006) 116:2226–36. doi: 10.1172/JCI27620
35. van de Wal Y, Kooy YM, van Veelen PA, Pena SA, Mearin LM, Molberg O, et al. Small intestinal T cells of celiac disease patients recognize a natural pepsin fragment of gliadin. *Proc Natl Acad Sci USA*. (1998) 95:10050–4. doi: 10.1073/pnas.95.17.10050
36. Kilara A, Sharkasi TY. Effects of temperature on food proteins and its implications on functional properties. *Crit Rev Food Sci Nutr*. (1986) 23:323–95. doi: 10.1080/10408398609527429
37. Hansen KS, Ballmer-Weber BK, Luttkopf D, Skov PS, Wuthrich B, Bindslev-Jensen C, et al. Roasted hazelnuts—allergenic activity evaluated by double-blind, placebo-controlled food challenge. *Allergy*. (2003) 58:132–8. doi: 10.1034/j.1398-9995.2003.23959.x
38. Maleki SJ, Chung SY, Champagne ET, Raufman JP. The effects of roasting on the allergenic properties of peanut proteins. *J Allergy Clin Immunol*. (2000) 106:763–8. doi: 10.1067/mai.2000.109620
39. Liu GM, Cheng H, Nesbit JB, Su WJ, Cao MJ, Maleki SJ. Effects of boiling on the IgE-binding properties of tropomyosin of shrimp (*Litopenaeus vannamei*). *J Food Sci*. (2010) 75:T1–5. doi: 10.1111/j.1750-3841.2009.01391.x
40. Cheung MS, Klimov D, Thirumalai D. Molecular crowding enhances native state stability and refolding rates of globular proteins. *Proc Natl Acad Sci USA*. (2005) 102:4753–8. doi: 10.1073/pnas.0409630102
41. Horwich AL. Chaperoned protein disaggregation–the ClpB ring uses its central channel. *Cell*. (2004) 119:579–81. doi: 10.1016/j.cell.2004.11.018
42. Zhan X, Yi X, Yue L, Fan X, Xu G, Xing B. Cytoplasmic pH-stat during phenanthrene uptake by wheat roots: a mechanistic consideration. *Environ Sci Technol*. (2015) 49:6037–44. doi: 10.1021/acs.est.5b00697
43. Picascia S, Camarca A, Malamisura M, Mandile R, Galatola M, Cielo D, et al. In celiac disease patients the *in vivo* challenge with the diploid *Triticum monococcum* elicits a reduced immune response compared to hexaploid wheat. *Mol Nutr Food Res*. (2020) 64:e1901032. doi: 10.1002/mnfr.201901032

Conflict of Interest: The authors declare that the research was conducted in the absence of any commercial or financial relationships that could be construed as a potential conflict of interest.

frontiers in Nutrition

ORIGINAL RESEARCH
published: 21 May 2021
doi: 10.3389/fnut.2021.645416

Effects of Anaerobic Fermentation on Black Garlic Extract by *Lactobacillus*: Changes in Flavor and Functional Components

Li Ma[1,2], *Chengying Zhao*[2], *Jifeng Chen*[1]* *and Jinkai Zheng*[2]*

[1] School of Life Sciences, Zhengzhou University, Zhengzhou, China, [2] Institute of Food Science and Technology, Chinese Academy of Agricultural Sciences, Beijing, China

The purpose of this study is to investigate the potential application of probiotics in the development of novel functional foods based on black garlic. The single-factor analysis (extraction temperatures, solid-to-liquid ratios, and extraction times) and the response surface methodology were firstly used to optimize hot water extraction of soluble solids from black garlic. The optimal extraction conditions were temperature 99.96°C, solid-to-liquid ratio 1:4.38 g/ml, and extracting 2.72 h. The effects of *Lactobacillus* (*Lactobacillus plantarum*, *Lactobacillus rhamnosus*, and co-culture of them) fermentation on the physicochemical properties of black garlic extract broth were studied for the first time. Artificial and electronic sensory evaluations demonstrated that fermentation significantly influenced the sensory characteristics. The variations of metabolites in different broth samples (S1, unfermented; S2, 1-day fermentation by *L. plantarum*; S3, 2-day fermentation by *L. rhamnosus*; and S4, 1-day fermentation by co-cultured *Lactobacillus*) were further investigated by gas chromatography-mass spectrometry and liquid chromatography-mass spectrometry/mass spectrometry analysis. As a result, *Lactobacillus* fermentation significantly reduced the pH; increased the contents of the total acid, amino nitrogen, total polyphenol, and total flavonoid; and reduced the content of 5-hydroxymethylfurfural (a carcinogenic component) by 25.10–40.81% in the black garlic extract. The contents of several components with unpleasant baking flavors (e.g., furfural, 2-acetylfuran, and 5-methyl furfural) were reduced, whereas the contents of components with green grass, floral, and fruit aromas were increased. More importantly, the contents of several functional components including lactic acid, Gly-Pro-Glu, sorbose, and α-CEHC (3,4-dihydro-6-hydroxy-2,5,7,8-tetramethyl-2H-1-benzopyran-2-propanoic acid) were increased after *Lactobacillus* fermentation. The results demonstrated the potential of probiotic fermentation to improve the quality of black garlic. This work will provide an insight into the strategic design of novel black garlic products and facilitate the application of black garlic in functional foods.

Keywords: black garlic extract, fermentation, *Lactobacillus*, sensory, functional components

OPEN ACCESS

Edited by:
Michael Rychlik, Technical University of Munich, Germany

Reviewed by:
Michael Erich Netzel, The University of Queensland, Australia
Xianjun Yuan, Nanjing Agricultural University, China

***Correspondence:**
Jinkai Zheng
jinkai8212@163.com
Jifeng Chen
chenjifeng@zzu.edu.cn

Specialty section:
This article was submitted to Food Chemistry, a section of the journal Frontiers in Nutrition

Received: *23 December 2020*
Accepted: *06 April 2021*
Published: *21 May 2021*

Citation:
Ma L, Zhao C, Chen J and Zheng J (2021) Effects of Anaerobic Fermentation on Black Garlic Extract by Lactobacillus: Changes in Flavor and Functional Components. Front. Nutr. 8:645416. doi: 10.3389/fnut.2021.645416

INTRODUCTION

Black garlic (*Allium sativum* L.) is an emerging processed food obtained by fresh garlic under high temperature (60–90°C) and high humidity (60–80%) for 60–90 days (1, 2). In recent years, black garlic has been highly relished, especially by consumers in Asian countries such as Japan, Singapore, and China (2, 3). Unlike fresh garlic, the pungent tasting allicin is easily decomposed and converted into antioxidants during the production of black garlic (3, 4). At the same time, the depolymerization of garlic polysaccharide significantly increases the reducing sugar content, and organic acids are produced by a series of reactions that endow black garlic with a sweet and sour taste (1). In addition, cell wall polysaccharides degrade under high-temperature conditions, resulting in tissue softening and a chewy, jelly-like texture (1, 3). Moreover, evidence suggests that black garlic has many remarkable nutritional and health benefits, including anti-oxidative, anti-allergic, anti-diabetic, anti-inflammatory, and anti-cancer effects (5–7). Therefore, research on black garlic has attracted extensive attention, especially on its development and application in functional foods.

An investigation on the components of black garlic is of particular importance, as they determine its physicochemical and sensory properties. The functional components of black garlic are composed mainly of sulfur compounds, carbohydrates, amino acids, melanoidin (MLD), polyphenols, and 5-hydroxymethylfurfural (5-HMF) (7). Sulfides endow black garlic with its unique flavor and play an important role in its anti-cancer bioactivity (8, 9). At high temperatures, carbohydrates and amino acids can be transferred to antioxidant compounds (e.g., MLD) by a series of Maillard reactions of non-enzymatic browning (10–12). MLD plays a key role in the changes in physical, chemical, and sensory properties as well as the biological effects of food, including antioxidant, antitumor, antibacterial, anti-inflammatory, hypoglycemic, and antihypertensive activities (11, 13, 14). In addition, the content of polyphenols, flavonoids, and phenolic acids in black garlic can be increased by 7–11-, 1–5-, and 4–8-fold in comparison with fresh garlic, respectively, which could significantly increase its antioxidant effects (9). A higher temperature has been used to shorten the processing time of black garlic, which results inserious declines in the taste, flavor, and health value of black garlic in the market and even serious accumulation of harmful substances (e.g., 5-HMF).

Probiotics, defined as living microorganisms that can bring health benefits to the host when used in an appropriate amount, have been used to produce fruit and vegetable juice products in the market with a pleasant taste and flavor, as well as functional foods (15, 16). Probiotic fermentation is widely used in the food industry. For example, *Lactobacillus plantarum*-fermented garlic can increase the content of diallyl trisulfide to retain H_2S-releasing activity, which can regulate cardiovascular functions and anti-cancer activities (17). In RAW 264.7 cells, a blend of *Leuconostoc mesenteroides*-fermented garlic and *Cirsium setidens* Nakai can promote antioxidant and immune activities (18). In animal studies, *L. plantarum* BL2-fermented garlic extract promotes weight loss in diet-induced obese mice (19); *Saccharomyces cerevisiae* (KCTC7910)-fermented black garlic can increase antioxidant activity, protect the liver and kidneys, lower blood lipid levels, and promote weight loss (20). Currently, there are few reports on the fermentation and extraction of black garlic using the *L. plantarum*- and *Lactobacillus rhamnosus*-fermented extracts on the market. Black garlic contains a high level of reducing sugar, which can provide energy for probiotic metabolism. Conversely, the fermentation process may also affect the flavor and functional components of black garlic.

Herein, we aimed to investigate the effects of *Lactobacillus* (*L. plantarum* and *L. rhamnosus*) fermentation on black garlic extract, especially the changes in flavor and functional components. The conditions of soluble solid extraction from black garlic were optimized by a single-factor analysis and the response surface methodology. The variations in physicochemical properties as well as in artificial and electronic sensory characteristics were analyzed systematically. To reveal the mechanisms of these variations, gas chromatography–mass spectrometry (GC-MS) and liquid chromatography–mass spectrometry (LC-MS) were used to investigate the effects of probiotic fermentation on the components of black garlic, especially flavor and functional components.

MATERIALS AND METHODS

Materials and Reagents

L. plantarum (BNCC336421) and *L. rhamnosus* (BNCC185356) were purchased from Beijing Be Na Culture Collection Technology Co. (Beijing, China). Processed black garlic was provided by Heze Tianhong Fruits and Vegetables Co. (Shandong, China).

Optimization of Black Garlic Extraction Conditions

Single-factor and response surface optimization experiments were used to optimize the hot water extraction of soluble solids from black garlic (21). In the single-factor experiments, samples (50 g) of peeled and cleaned black garlic were soaked in ultrapure water for extraction at various temperatures (60, 70, 80, 90, and 100°C), solid-to-liquid ratios (1:4, 1:5, 1:6, 1:7, and 1:8 g/ml), and extraction times (1.0, 1.5, 2.0, 2.5, and 3.0 h). The black garlic mixture was vacuum-filtered through a 300-mesh nylon cloth to obtain the black garlic extraction solution. The soluble solid content was measured using a portable Abbe refractometer (WAY-2S, Yice, Shanghai, China).

After preliminary screening, the optimal extraction conditions were determined, then a three-factor, three-level Box–Behnken design was performed to optimize the extraction conditions. The extraction temperature, solid-to-liquid ratio, and extraction time were selected as the three main variables, and the soluble solid content of the extract was defined as the response of the combined independent variables. The soluble solid content (Y) was calculated according to Equation 1 (22):

$$Y = \beta_0 + \sum_{i=1}^{n} \beta_i X_i + \sum_{i=1}^{n} \beta_{ii} {X_i}^2 + \sum_{j=i+1}^{n} \beta_{ij} X_j$$

where Y is the predicted response (soluble solid content); β_0 is a constant; β_i, β_{ii}, and β_{ij} represent the coefficients of the linear, quadratic, and interaction effects, respectively; and X_i and X_j are the independent variables. The fit of the model was evaluated by coefficients of determination (R^2), P-values, lack-of-fit test, and root mean square errors. The validation of the model was performed by applying the optimized extraction conditions of the independent variables and comparing them with the predicted values.

Fermentation of Black Garlic Extract by *Lactobacillus*

Under anaerobic conditions (95% N_2 and 5% CO_2), 1 g freeze-dried powder of *L. plantarum* or *L. rhamnosus* was inoculated on de man rogosa and sharpe (MRS) agar medium and cultured for 48 h. Vigorous colonies were activated twice in succession, inoculated with vigorous growth in ring 2 into 100 ml MRS broth, and cultured at 0.5% dissolved oxygen and 37°C for 24 h. The above processes were all carried out in an anaerobic incubator (YQX-1, Yuejin, Shanghai, China). Then, 10 ml of rejuvenation culture solution was centrifuged at 5,000*g* for 10 min at 4°C, and the precipitate was used for the fermentation of black garlic extract broth.

Black garlic extract broth was pasteurized at 100°C for 10 min. Under anaerobic conditions, rejuvenated probiotics were diluted to 10^{10} colony-forming units (CFUs)/ml. The sterilized black garlic extract broth was fermented with 1% *L. plantarum* dilution, *L. rhamnosus* dilution, or a 1:1 mixture of the two for 0–4 days. Subsequently, the fermented black garlic extract broths were stored at −80°C until used.

Measurement of pH and Viable Bacterial Counts in Black Garlic Fermentation Broth

pH

At room temperature (25°C), a pH meter was used to measure the pH of the black garlic fermentation broth.

Viable Bacterial Counts

The viable bacterial counts were determined according to previous studies with minor modifications (23). After *Lactobacillus* was fermented for 1 day, 10 ml of fermentation broth was centrifuged at 5,000 *g* for 10 min at 4°C. The supernatant was discarded, and 10 ml sterilized PBS (pH 7.2) was added, which was diluted in a 10-fold series. Then, 50 μl of a different dilution was coated on MRS agar medium and cultured upside down at 37°C for 24 h, respectively. When the number of CFUs on the culture medium counted to 30–100, it was used to calculate the number of viable bacteria in the fermentation broth.

Measurement of Total Acid and Amino Nitrogen Contents of Black Garlic Fermentation Broth

Black garlic fermentation broth (20.00 ml, 1:10 dilution) was transferred to a beaker and stirred. The solution was titrated with 0.05 mol/l NaOH solution to pH 8.20, and the consumed volume of NaOH solution was recorded. Then, 2.50 ml formaldehyde was added to the mixture, which was titrated with 0.05 mol/l NaOH to pH 9.20, and the amount of NaOH solution consumed was recorded. Distilled water (20.00 ml) was used as the blank group. The consumed volumes of NaOH solution were used to calculate the total acid content and the amino nitrogen (amino-N) content (20).

Measurement of the Total Polyphenol Content of Black Garlic Fermentation Broth

The total polyphenol content was determined according to previous studies with minor modifications (18, 24). We added 1.25 ml 10% Folin–Ciocalteu reagent (*v*/*v*) and 1 ml 7.50% sodium carbonate solution (*w*/*v*) to 0.50 ml black garlic fermentation broth (1:50 dilution). The mixture was incubated in a 45°C water bath for 40 min. The absorbance was measured at 765 nm, and the total polyphenol content was measured using gallic acid equivalents as the calibration curve standard.

Measurement of Total Flavonoid Content of Black Garlic Fermentation Broth

The total flavonoid content was determined according to a previous report with minor modifications (18). First, 5.00 ml black garlic fermentation broth (1:20 dilution) was added to 0.30 ml 5% $NaNO_2$ solution (*w*/*v*) and incubated for 5 min. Then, 0.30 ml 10% aluminum chloride solution (*m*/*v*) was added, followed by incubation for 6 min. Next, 2.00 ml NaOH solution (1 M) was added, and the mixture was adjusted to a volume of 10 ml by addition of distilled water and incubated for 15 min. The absorbance at 510 nm was measured using a microplate reader. The absorbance of quercetin equivalents was used as the standard curve to calculate the total flavonoid content.

Measurement of the Reducing Sugar Content of Black Garlic Fermentation Broth

Determination of the reducing sugar content was performed using the DNS method (25). First, 750 μl DNS reagent was added to 1.00 ml black garlic fermentation broth (1:400 dilution) and mixed evenly by vortexing. Then, 100.00 μl 10% sodium hydroxide solution (*w*/*v*) was added to the mixture and mixed well. The samples were incubated at 100°C for 15 min and then cooled rapidly, and the absorbance was measured at 540 nm using a microplate reader. The absorbance of glucose sugar was measured as the standard curve to calculate the reducing sugar content.

Measurement of the 5-HMF Content of Black Garlic Fermentation Broth by High-Performance Liquid Chromatography

The content of 5-HMF in black garlic fermentation broth was determined according to previous studies with slight modification (26). The black garlic fermentation broth was diluted (1:100) and filtered through a 0.22-μm aqueous phase filter membrane. The 5-HMF content was determined by a high-performance liquid chromatography (HPLC) device equipped with a photodiode array detector (L2455; Hitachi, Tokyo, Japan). The detection wavelength was 284 nm, and the column was

a ZORBAX Eclipse Plus-C18 (50 × 2.1 mm, 1.8 μm; Agilent Technologies, Santa Clara, CA, USA). The mobile phase was distilled water and acetonitrile (88:12, *v*/*v*), the flow rate was 1.0 ml/min, the column temperature was 25°C, and the injection volume was 20 μl.

Sensory Evaluation of Black Garlic Fermentation Broth

Artificial Sensory Evaluation

After fermentation of the black garlic broth, an artificial sensory evaluation was performed by a well-trained food evaluation team composed of 15 members in the sensory room assigned by the Institute of Agricultural Products Processing. The black garlic fermentation broth samples were numbered and randomly provided to each team member individually. The same individuals participated in all evaluations, and all were blinded to the samples tested, while water and salt-free biscuits were provided between samples for palate cleansing. Fifteen attributes related to appearance, smell, taste, and touch were scored on the unstructured evaluation form. The scoring standard was an 8-cm hedonic scale with intensity descriptors. The direction extends from the center to the outside, and the intensity increases (1: low and 8: high). The additional attributes about the overall sensory preferences of each sample were given on the same scale, defining the overall assessment (27).

Electronic Sensory Evaluation

The electronic eye, electronic nose, and electronic tongue were used to analyze the color, aroma, and taste of the black garlic fermentation broth using a bionic system to analyze the sensory attributes (28). Color was expressed as L^* (luminance), a^* (red-green), and b^* (yellow-blue). The color difference (ΔE) was calculated according to Equation 2:

$$\Delta E = \sqrt{(L^* - {L_0}^*)^2 + (a^* - {a_0}^*)^2 + (b^* - {b_0}^*)^2}$$

where L^*, a^*, and b^* represent the test group and L_0^*, a_0^*, and b_0^* represent the control group. The electronic nose distinguishes the difference in sample aroma based on 10 gas sensors with different selection modes. Specifically, W1C, W5S, W3C, W6S, W5C, W1S, W1W, W2S, W2W, and W3S are sensitive to aromatic compounds, nitrogen oxides, ammonia and aromatic compounds, hydrogen, alkanes and aromatic compounds, methane, sulfur compounds, ethanol, aromatic and organic sulfur compounds, and alkanes. A principal component analysis (PCA) was used to identify the fragrance based on the sensor response value signal. The electronic tongue was based on five sensors that are sensitive to acid, sweet, bitter, salty, and fresh to identify samples, and we used PCA to identify taste based on the sensor response signal.

Headspace Solid-Phase Microextraction–GC–MS Analysis of Black Garlic Fermentation Broth

Headspace solid-phase microextraction (HS-SPME) was used to separate and concentrate the volatile components in the black garlic fermentation broth, which were then analyzed by GC-MS (QP 2010 Plus; Shimadzu, Japan) (21, 29). The SPME procedure was as follows: 2.00 ml black garlic extract and 100 μl (0.38 μg/ml) cyclohexanone were transferred into a 20-ml headspace bottle with a 20-mm aluminum cap and a 20-mm silicon/polytetrafluoroethylene diaphragm. The sample vial was incubated at 50°C for 30 min in the dark. The SPME needle (75-μm divinylbenzene/carboxen/polydimethylsiloxane) was aged for 3 min at 250°C until no residue was observed, inserted into the headspace bottle at 50°C for 30 min, and immediately retracted and inserted into the GC inlet. The desorption temperature and time were 250°C and 5 min, respectively. The GC oven temperature was programmed as follows: 40°C for 3 min, increase to 160°C at a rate of 4°C/min, hold for 3 min, then increase to 250°C at a rate of 7°C/min, and hold for 5 min. GC conditions were as follows: carrier gas, high-purity nitrogen; split, 1:30; flow rate, 1.00 ml/min; inlet temperature, 230°C; and flame ionization detector temperature, 250°C. A DB-WAX capillary column (100 mm × 0.25 mm i.d., 0.25 μm, Agilent Technologies, Santa Clara, CA, USA) was used. The MS conditions were as follows: ionization mode, electron bombardment (electron ionization source); ion source temperature, 230°C; transmission line temperature, 250°C; electron energy, 70 eV; and scanning range, *m*/*z* 30–600. The volatile compounds of the black garlic fermentation broth were identified by comparing their retention time, CAS number, linear retention indices (Kovats indices), serial number, mass spectra, and principal fragments with those in the NIST 11 standard library. Based on the GC peak area of the internal standard (cyclohexanone), the relative contents of each volatile compound in the four samples were calculated.

LC–Quadrupole Time-of-Flight–MS/MS Analysis of Black Garlic Fermentation Broth

LC–quadrupole time-of-flight (Q-TOF)–MS/MS (1200 LC, 6540 UHD Q-TOF; Agilent Technologies) was used to initially identify the polar metabolites in the broth. The method for LC–Q-TOF–MS/MS analysis was slightly modified according to previous reports (30). The fermentation broth was diluted (1:100) with ultrapure water, mixed with an equal volume of methanol, filtered through a 0.25-μm organic phase membrane, and stored at −20°C until used. The mobile phases were 0.10% (*v*/*v*) formic acid in ultrapure water (phase A) and 0.1% (*v*/*v*) formic acid in methanol (phase B) at a flow rate of 0.4 ml/min. The gradient was as follows: start at 5% B, increase from 5 to 10% B over 5 min, increase from 10 to 100% B over 25 min, and hold at 100% B for 5 min. The setup was as follows: chromatographic column, ZORBAX Eclipse Plus-C18 (50 × 2.1 mm i.d., 1.8 μm, Agilent Technologies); column temperature, 40°C; and injection volume, 10 μl. The parameters of the dual electrospray ionization source and mass spectrometer were as follows: capillary, skimmer, and Q1 voltages set to 3,500 V, 60 eV, and 120 V, respectively; N_2 atomizing gas flow rate, 40 psi; drying gas flow rate, 10 ml/min; temperature, 325°C; and octopole radiofrequency voltage, 750 V. Two values of collision energy, 20 and 40 eV, were combined with MS/MS data at two fragmentation levels. The *m*/*z* range

of 30–1,700 was used for MS and MS/MS; data were collected at a rate of one spectrum per second in the extended dynamic range mode. The auto MS/MS mode was configured with two maximum precursors per cycle and an exclusion window of 1 min after two consecutive selections of the same precursor. To ensure the expected mass accuracy of the recorded ions, *m*/*z* 121.0509 (protonated purine), *m*/*z* 922.0098 [protonic hexakis (1H, 1H, 3H-tetrafluoropropoxy) phosphazene (HP) at *m*/*z* 921], and the signals at *m*/*z* 112.9856 (trifluoroacetic acid anion) and *m*/*z* 1,033.9881 (HP at *m*/*z* 921) in a negative ionization mode were continuously calibrated internally.

The MassHunter workstation software (version B 08.00 qualitative analysis; Agilent Technologies) was used to extract potential molecular features (MFs) from all datasets. All ions with a single charge count exceeding 1,500 were taken into account in the extraction algorithm. The isotope distribution of MF inclusions should be defined by at least two ions (peak spacing *m*/*z* tolerance = 0.0025 and mass accuracy = 10.0 ppm). In addition to $[M + H]^+$ and $[M - H]^-$ ions, there were also adducts in positive ionization mode (+Na, +K, and $+NH_4$), negative ionization mode (+Cl and +HCOO), and neutral loss caused by dehydration to identify MFs corresponding to the same potential metabolite. The raw data were filtered with a minimum count level of 3,000 for samples analyzed in positive ionization mode and 2,500 in negative ionization mode. The resulting MFs were tentatively identified by searching MS and MS/MS information in the METLIN Metabolite and Chemical Entity Database (http://metlin.scripps.edu/), and an accuracy error limit of 5 ppm was set for identification.

Statistical Analysis

All experiments were conducted in triplicate, and the data were expressed as mean ± standard deviation (SD). The statistical methods of this study mainly used the analysis of variance (ANOVA) and a *post-hoc* least significant difference (LSD) test to calculate the difference between the treatments. The difference was significant at $P < 0.05$. IBM Statistical SPSS 25 (IBM Corporation, Chicago, IL, USA) was used for the statistical analysis of data. Design Expert 10 (Stat-Ease, Minneapolis, MN, USA) was used for the analysis in response surface optimization experiment. Origin 2019 software (OriginLab Corporation, Hampton, MA, USA) was used to draw graphics.

RESULTS AND DISCUSSION

Effects of Extraction Conditions on Soluble Solids and Response Surface Optimization

Hot water extraction is economical, convenient, and simple and is commonly used for dietary preparation in daily life. Here, we firstly assessed the effects of the extraction temperature, solid-to-liquid ratio, and extraction time on the soluble solid contents of black garlic using single-factor experiments. As shown in **Figure 1A**, as the extraction temperature increased (especially above 80°C), the content of soluble solids increased significantly ($P < 0.05$), which might be due the destruction of plant cell walls by high temperatures (31). The effect of the solid-to-liquid ratio was subsequently investigated at 100°C (**Figure 1B**). When the soluble solids in the solvent extraction were not saturated, the concentration of soluble solids decreased as the solid-to-liquid ratio increased (31). With prolongation of the extraction time, the soluble solid content increased from 1 to 2.5 h and then remained constant (**Figure 1C**). As a result, the parameters selected for the following studies were as follows: extraction temperature of 100°C, solid-to-liquid ratio of 1:4, and extraction time of 2.5 h.

To further increase the extraction rate of soluble solids, the response surface method was used to optimize the extraction conditions based on the above results from single-factor experiments. The experiments were performed based on a three-level Box–Behnken design (**Table 1**). The obtained regression model of the relationship between soluble solids in black garlic extract and extraction conditions was fitted using a second-order equation:

$$\begin{aligned} y = {} & +22.36250 - 0.53938 \times A - 0.38125 \times B - 0.62500 \\ & \times C + 0.005438 \times A^2 + 0.21875 \times B^2 + 0.05000 \\ & \times C^2 - 0.036250 \times AB + 0.03375 \times AC - 0.21250 \times BC \end{aligned}$$

where y was the content of soluble solids in the black garlic extract, and A, B, and C are the extraction temperature, solid-to-liquid ratio, and extraction time, respectively. The analysis results of the model were significant ($P < 0.05$), with an F-value of 114.384, demonstrating that the measured and predicted values of the model had high consistency. The coefficient of determination ($R^2 = 0.9932$) indicated the high degree of fit. Only 0.0068% of the variation could not be explained by the model. The adjusted coefficient of determination (0.9846) was close to the coefficient of determination, and the comprehensive evaluation model had good statistical significance.

A comprehensive evaluation of the effects of each independent extraction variable and their interactions on soluble solids in black garlic extract was conducted using a three-dimensional response surface diagram to obtain the best extraction conditions (**Figure 2**). In **Figure 2A**, when the extraction time was 1 h, the high temperature and low solid-to-liquid ratio increased the soluble solid content, and it was the highest at 99.96°C with a solid-to-liquid ratio of 1:4.4 (**Figure 2D**). When the solid-to-liquid ratio was 1:4 g/ml, long-term and high-temperature extraction was better than short-term and low-temperature extraction. However, with further extension of the extraction time, the soluble solid content no longer significantly increased (**Figure 2B**). When the extraction temperature was fixed at 100°C, the soluble solids first increased as the extraction time increased and then decreased at a high solid-to-liquid ratio. The highest soluble solid content was obtained at an extraction time of ∼3 h and a solid-to-liquid ratio of ∼1:4 g/ml (**Figure 2C**). According to the prediction of the corresponding surface, the best black garlic extraction conditions were an extraction temperature of 99.96°C, a solid-to-liquid ratio of 1:4.38 g/ml, and extraction of 2.72 h. A verification experiment was performed under the optimal conditions, and the comprehensive evaluation value was 19.04%, which was close to the predicted value of 19.28%,

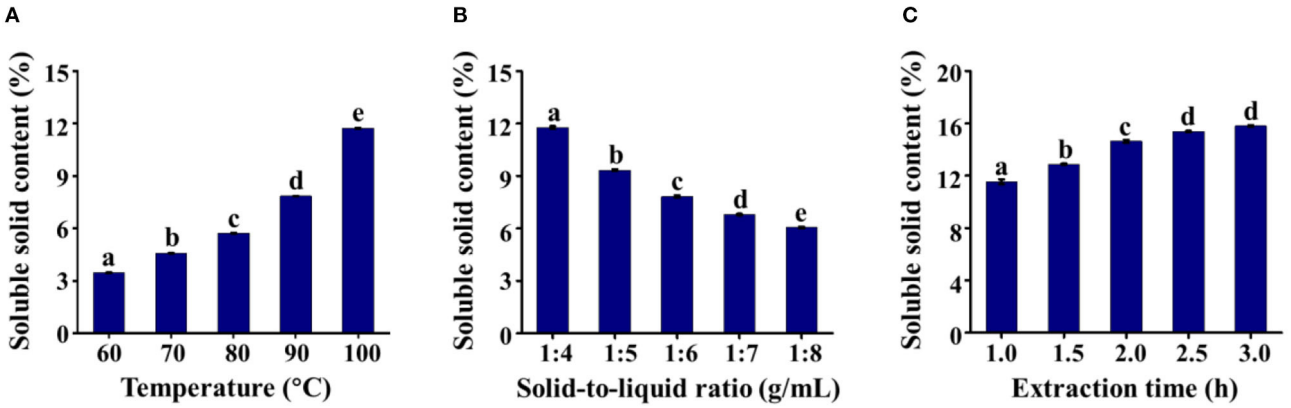

FIGURE 1 | The soluble solid contents of black garlic extracts under different **(A)** extraction temperatures, **(B)** solid-to-liquid ratios, and **(C)** extraction times. Data are means ± SD ($n = 3$).

indicating that the model optimization of the black garlic extraction process was reliable (21).

Effects of Fermentation on the Physicochemical Properties of Black Garlic Broth

During fermentation, probiotics transform certain components to obtain energy, which can change the composition of the fermentation broth and thus influence the physicochemical and sensory properties. In this study, the number of viable bacteria; pH variation; and contents of total acid, amino-N, reducing sugars, total polyphenols, total flavonoids, and 5-HMF in the fermentation broth were investigated. The number of viable bacteria in the fermented black garlic extract first increased and then decreased with the extension of fermentation time and was highest on day 2 (**Figure 3A**). The viable counts of *L. plantarum* and the mixture of *L. plantarum* and *L. rhamnosus* reached $\sim 10^{15}$ CFU/ml, whereas viable counts of *L. rhamnosus* reached 10^{13} CFU/ml, indicating that black garlic broth might be more suitable for survival of *L. plantarum* than *L. rhamnosus*. As shown in **Figure 3B**, the pH decreased significantly from 4.30 to 3.60 (*L. plantarum*), 3.93 (*L. rhamnosus*), and 3.60 (mixed *L. plantarum* and *L. rhamnosus*) after probiotic fermentation, possibly due to acids produced by *L. rhamnosus* and *L. plantarum* during fermentation. Therefore, the total acid content of the three fermentation broths was further evaluated. **Figure 3C** shows that the total acid content of the three fermentation broths increased with the extension of fermentation time, among which the total acid content of the bacteria fermentation mixture was the strongest, especially after day 1. After 4 days of fermentation, the total acid content in fermentation broths of *L. plantarum*, *L. rhamnosus*, and the mixture of *L. plantarum* and *L. rhamnosus* reached to 1.92 ± 0.01, 1.63 ± 0.01, and 2.04 ± 0.01 mg/ml, respectively. As shown in **Figure 3D**, when the black garlic extract was fermented by *L. rhamnosus* or the mixture of the two bacteria for 0–2 days, the amino-N content increased due to the destruction of protein structures. After 2 days, the amino-N content remained more or less stable. However, during fermentation by *L. plantarum*, the amino-N content first increased significantly to 8.69 ± 0.12 mg/ml from 0 to 1 day and then decreased linearly to 7.21 ± 0.12 mg/ml, possibly because the amino-N was further utilized by *L. plantarum*.

During the production of black garlic, the high temperature disrupts the glycosidic bonds of polysaccharides, which are converted into reducing sugars and oligosaccharides (25). As shown in **Figure 3E**, the reducing sugar content of the black garlic extract before fermentation was 109.05 ± 0.90 mg/ml. In the *L. plantarum* fermentation broth, the reducing sugar content decreased continuously. During *L. rhamnosus* fermentation, reducing sugars decreased sharply in the early stage (0–1 day) and then increased significantly with the extension of fermentation time. A possible reason is that the reducing sugars may be the preferred carbon source compared with sources such as polysaccharides. Therefore, the reducing sugars would be used first during the early fermentation stages until they are relatively low in abundance, at which point the probiotics may begin to consume other carbon sources (e.g., polysaccharides), which could produce high levels of reducing sugars (25, 32, 33).

Phenols and flavonoids are important plant components and, as free radical scavengers, provide significant benefits to human health (34). As shown in **Figures 3F,G**, in general, the total polyphenol and flavonoid contents increased significantly in the black garlic extract after fermentation by the three probiotics. The total polyphenol content was increased on day 1 of fermentation by *L. plantarum* or the mixture of the two bacteria and was decreased slightly thereafter. During fermentation by *L. rhamnosus*, there was a slight decrease in the total polyphenol content on day 1, possibly because the rate of free polyphenol and flavonoid production was lower than the oxidation rate of oxygen or other oxides in the air. Then, the polyphenol and flavonoid contents increased significantly to 2.69 ± 0.01 and 1.79 ± 0.08 mg/ml, respectively, which were markedly higher than those produced by fermentation by *L. plantarum* or the mixture of the two bacteria. These results were consistent with an earlier study (35). In plants, some polyphenols and flavonoids

TABLE 1 | Box–Behnken experimental design and the effects of time, temperature, and solid-to-liquid ratio on hot water extraction of soluble solids from black garlic.

No.	*A* temperature (°C)	*B* solid/liquid ratio (g/ml)	*C* time (h)	*Y* content of soluble solids (%)
1	80	4	3	8.4
2	80	4	1	5.7
3	80	6	2	4.0
4	100	6	3	11.2
5	100	8	2	7.4
6	80	6	2	4.0
7	60	4	2	3.8
8	100	4	2	14.7
9	60	6	1	2.6
10	60	8	2	2.3
11	80	6	2	4.0
12	60	6	3	3.4
13	100	6	1	7.7
14	80	8	3	3.3
15	80	6	2	4.0
16	80	6	2	4.0
17	80	8	1	2.3

Source	Sum of squares	Degree of freedom	Mean square	*F*-value	*P*-value
Model	185.02	9	20.56	114.44	<0.0001
A	104.40	1	104.40	581.16	<0.0001
B	37.41	1	37.41	208.25	<0.0001
C	8.00	1	8.00	44.53	0.0003
AB	8.41	1	8.41	46.82	0.0002
AC	1.82	1	1.82	10.15	0.0154
BC	0.72	1	0.72	4.02	0.0849
A^2	19.92	1	19.92	110.88	<0.0001
B^2	3.22	1	3.22	17.94	0.0039
C^2	0.01	1	0.011	0.06	0.8157
Residual	1.26	7	0.18		
Lack of fit	1.26	3	0.42		
R^2	0.9932				
Adj R^2	0.9846				
Regression equation	$y = +22.36250–0.53938 \times A–0.38125 \times B–0.62500 \times C + 0.005438 \times A^2 + 0.21875 \times B^2 + 0.05000 \times C^2$-$0.036250 \times AB + 0.03375 \times AC–0.21250 \times BC$				

are usually combined or bound with polysaccharides, which are unable to be extracted. Probiotic fermentation would destroy the plant cell wall and release β-glucosidase or proteolytic enzyme, which may hydrolyze polyphenols and flavonoids into free and soluble forms, resulting in an increase in the overall contents of total polyphenols and total flavonoids (35–37).

The 5-HMF is a furan compound with aldehyde and hydroxymethyl functional groups formed mainly via the Maillard reaction and dehydration of sugars during the production of black garlic (9). In recent years, 5-HMF has been classified as a pollutant that may be carcinogenic. Moreover, 5-HMF has been reported to have effects such as liver and juvenile toxicity, DNA damage, and tumor transformation (38, 39). Therefore, the variation in 5-HMF content during fermentation was further investigated. As shown in **Figure 3H**, the 5-HMF content of black garlic extracts fermented by different probiotics for 4 days decreased significantly. The probiotic fermentation significantly reduced the 5-HMF content ($P < 0.05$). Compared with unfermented broth, the 5-HMF contents in the fermentation broth of *L. plantarum*, *L. rhamnosus*, and bacterial mixture were reduced by 37.66, 25.10, and 40.81%, respectively, demonstrating the more potent ability of *L. plantarum* to reduce 5-HMF compared with *L. rhamnosus*. Notably, for all physicochemical properties, the effects of fermentation by the bacterial mixture were similar to those of *L. plantarum* fermentation and differed significantly from those of *L. rhamnosus* fermentation. The main reason might be that black garlic was more suitable for the growth of *L. plantarum* than *L. rhamnosus*. Therefore, *L. plantarum*

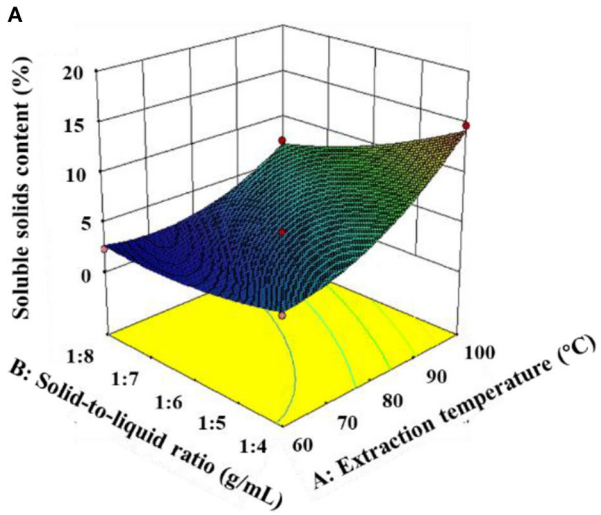

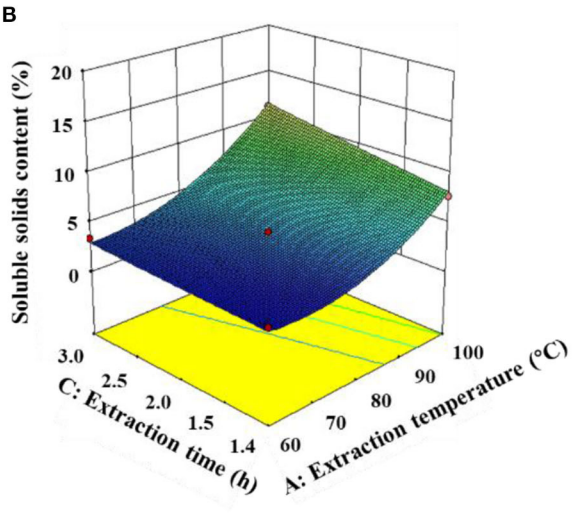

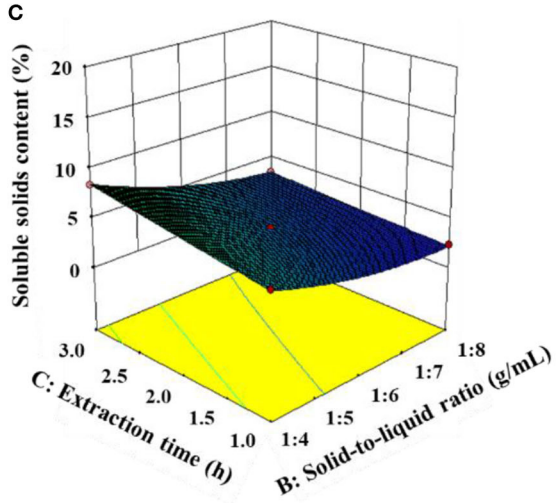

D

Factors	The optimun conductions
A: Extraction temperature (°C), B: Solid-to-liquid ratio (g/mL)	99.96, 1:4.38
A: Extraction temperature (°C), C: Extraction time (h)	99.96, 2.72
B: Solid-to-liquid ratio (g/mL), C: Extraction time (h)	1:4.38, 2.72

FIGURE 2 | Three-dimensional response surface methodology to evaluate the effects of the **(A)** solid-to-liquid ratio/extraction temperature, **(B)** extraction time/extraction temperature, and **(C)** extraction time/solid-to-liquid ratio on the soluble solid content of black garlic extract. **(D)** The optimal extraction conditions determined by the response surface methodology. Data are means ± SD ($n = 3$).

would gradually be the dominant strain, which played a major role in fermentation.

Artificial and Electronic Sensory Evaluations of Fermented Black Garlic Broth

Color, aroma, and taste are generally considered important characteristics that determine consumer evaluation of food (40). Artificial sensory evaluation is the most direct method for comprehensive analysis of food quality. Artificial sensory evaluation is based on the normal organs and processes of the human body, with advantages of simplicity, speed, economy, and practicality. Artificial sensory evaluation was conducted on the fermented black garlic broth extracts within 4 days of fermentation. The sensory characteristic scores are shown in **Figure 4**. The three fermentation products were sampled at 0, 1, 2, 3, and 4 days of fermentation. For fermentation by the same probiotic, the number of fermentation days did not largely affect the sweetness, spoilage, or sourness ($P < 0.05$). Compared with the unfermented black garlic extract (S1), the probiotic samples were slightly more acidic but were not considered unpleasant. The best overall sensory evaluations were obtained in fermentation broth samples from day 1 of fermentation by *L. plantarum* (S2), day 2 of fermentation by *L. rhamnosus* (S3), and day 1 of fermentation by co-cultured *Lactobacillus* (S4).

The artificial sensory evaluation is susceptible to human subjectivity, which results in significant differences and difficulty in reflecting the actual sensory characteristics. Electronic sensory evaluations (electronic eye, electronic nose, and electronic

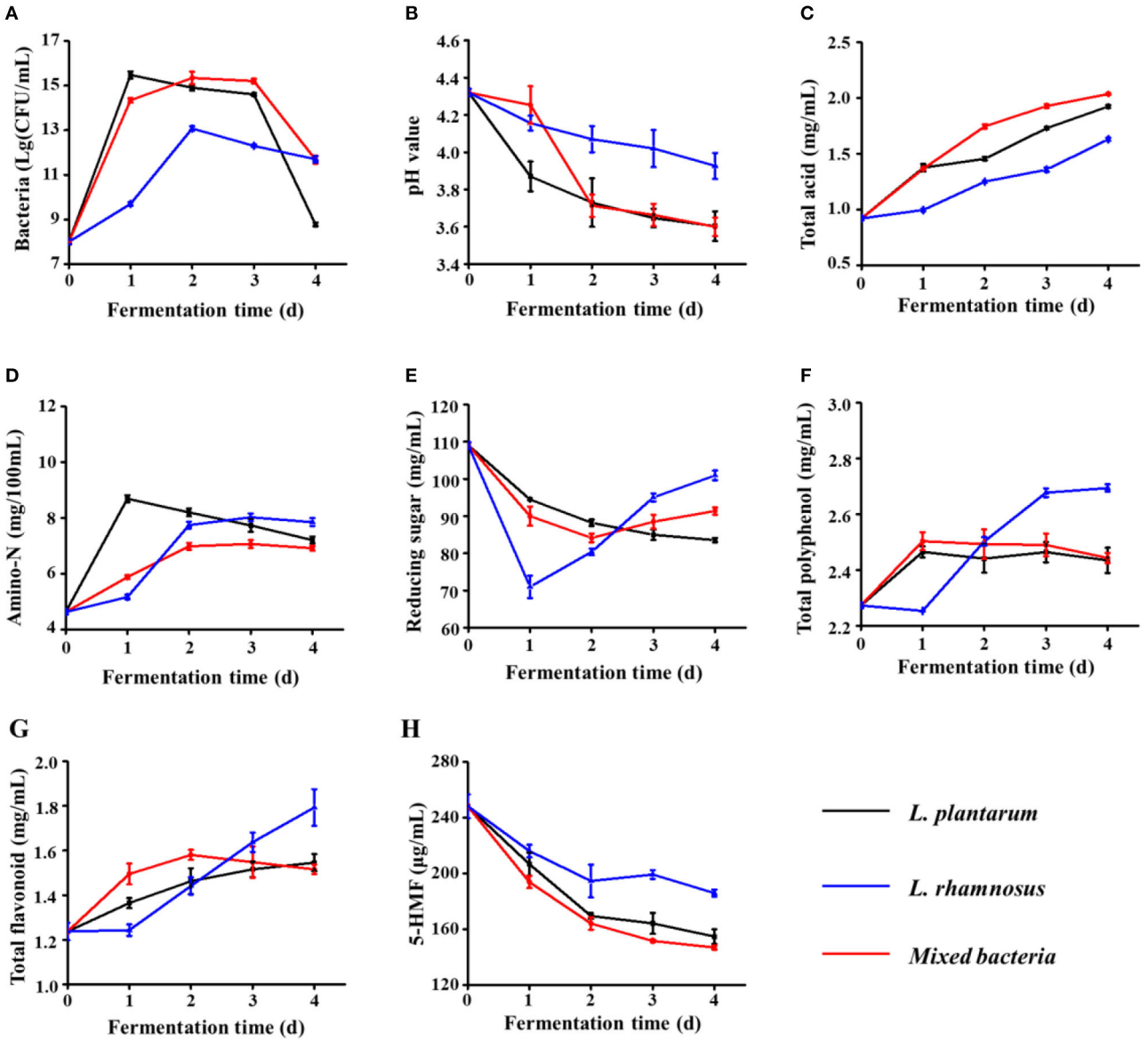

FIGURE 3 | The **(A)** viable bacterial counts, **(B)** pH, **(C)** total acid contents, **(D)** amino nitrogen (amino-N) contents, **(E)** total polyphenol contents, **(F)** total flavonoid contents, **(G)** reducing sugar contents, and **(H)** 5-hydroxymethylfurfural (5-HMF) contents of fermented black garlic extracts obtained using different probiotics and different fermentation times. Data are means ± SD ($n = 3$).

tongue) can simulate human body organs (eyes, nose, and tongue) in objective sensory evaluations of food, which are more convenient, effective, and accurate. To investigate the effects of probiotic fermentation on the sensory characteristics of black garlic, the differences between S1 and the three fermentation broths with the highest artificial sensory evaluation scores in appearance, flavor, and taste were characterized by the electronic eye, electronic nose, and electronic tongue, respectively.

Food color has been shown to affect taste perception and is also one of the main determinants of food choice (41). The analysis results of the electronic eye are shown in **Figure 5A**. Compared with S1, the L^* values of S2, S3, and S4 did not change significantly, indicating that fermentation by the three probiotics did not significantly change the black color of the black garlic extract. The a^* and b^* values of S2 and S4 were decreased significantly ($P < 0.05$), whereas those of S3 were not decreased significantly, compared with S1. These indicated that fermentation by *L. plantarum* and a mixture of the two bacteria for 1 day significantly reduced the redness and yellowness of the fermentation broth, whereas fermentation by *L. rhamnosus* for 2 days did not change the fermentation broth color. The fermentation of *L. rhamnosus* had more effect on color appearance of black garlic broth. In fact, ΔE reflects the overall difference among the samples. Based on S1, the ΔE

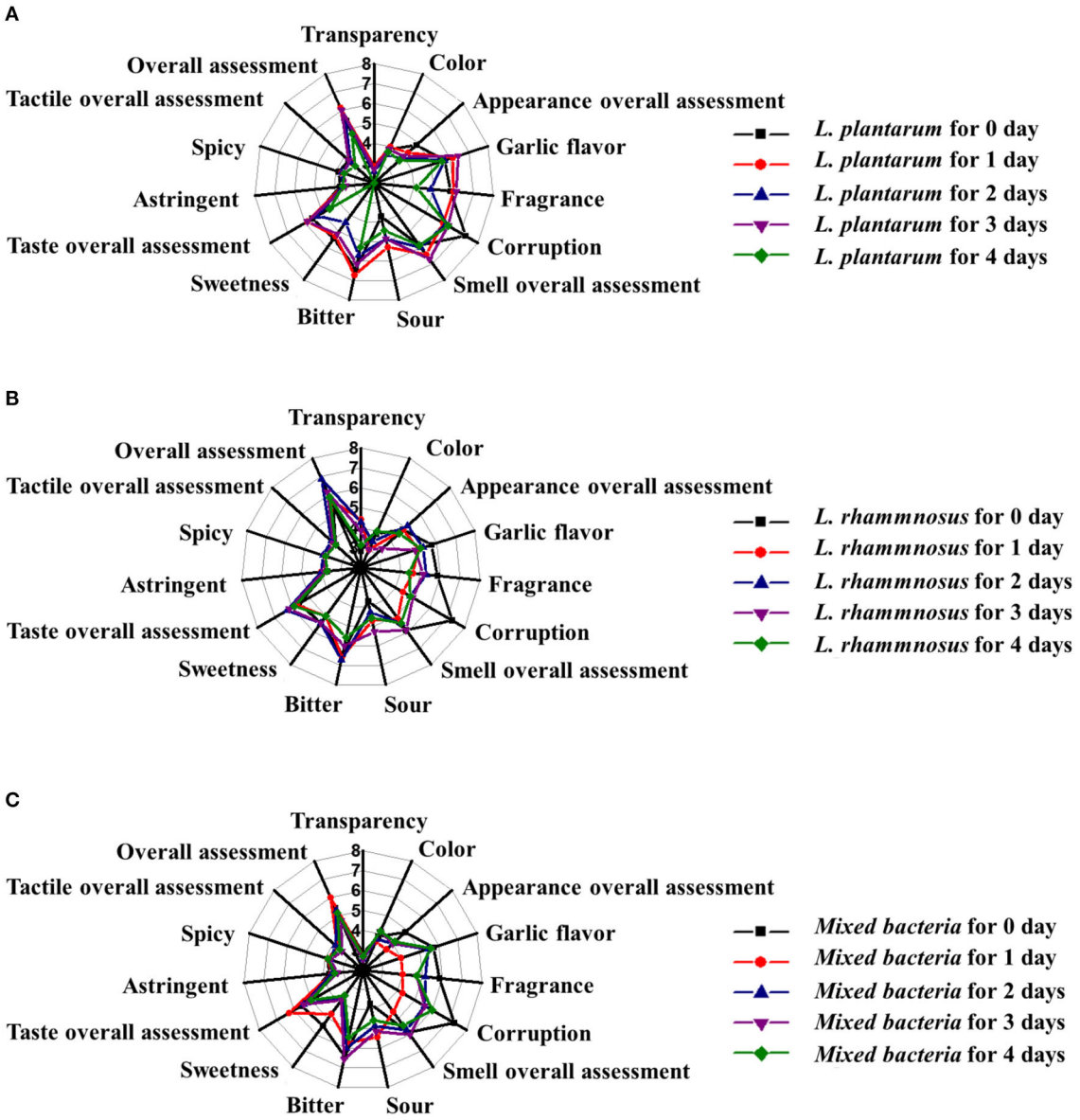

FIGURE 4 | Artificial sensory evaluation of black garlic broths fermented by **(A)** *L. plantarum*, **(B)** *L. rhamnosus*, and **(C)** a mixture of the two bacteria at different times (0, 1, 2, 3, and 4 days). Data are means ± SD ($n = 15$).

values of the three fermented samples had significant differences. These results demonstrate that the electronic eye can distinguish color changes among samples. **Figures 5B,C** shows the PCA results for the electronic nose and electronic tongue. In the two analyses, the cumulative contribution of the first two factors to the variance was above 99%, indicating significant differences among different samples. For the electronic nose analysis, the output of the 10 gas sensors showed that the response values of W5S, W1S, W1W, and W2W were critical for the four samples. The difference in aroma between unfermented and fermented products was derived mainly from nitrogen oxides, methane, sulfur compounds, and aromatic compounds. For the electronic tongue analysis, data from the seven sensors indicated that sourness, sweetness, and freshness were the key factors contributing to the PCA differences. The differences were related to the metabolites produced by probiotic fermentation. Therefore, the electronic eye, electronic nose, and electronic tongue were sufficient to distinguish samples of black garlic extract fermented by probiotics.

Effects of Fermentation on Metabolites in Black Garlic Broth

The physicochemical properties and sensory characteristics of food are determined by the components therein. The variations of metabolites in S1, S2, S3, and S4 were further investigated by HS-SPME–GC-MS and LC–Q-TOF–MS/MS analyses. As

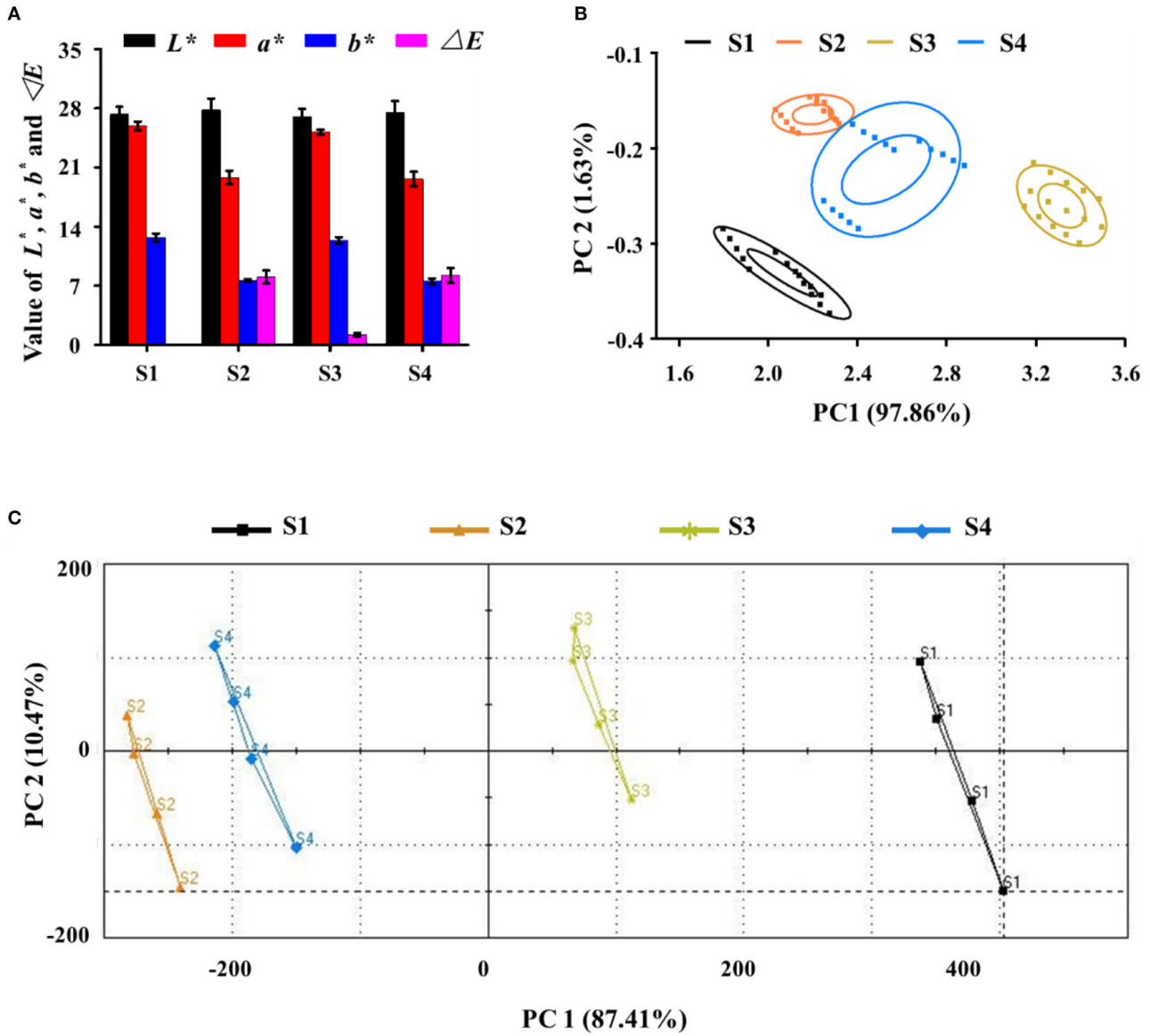

FIGURE 5 | Electronic sensory evaluation of black garlic fermentation broths by **(A)** the electronic eye, **(B)** electronic nose (PCA), and **(C)** electronic tongue (PCA). Data are means ± SD ($n = 4$).

a result, a total of 49 volatile metabolites were identified by HS-SPME–GC-MS and were divided into volatile sulfur compounds, flavor compounds, and three additional categories (**Supplementary Table 1**). The total sulfide content tended to decrease during fermentation, possibly due to the strong volatility. However, multiple sulfides could be detected in the four samples, and several with potent beneficial health effects, including diallyl sulfide, dimethyl trisulfide, 1-ethylthio-2-methyl-1-propene, 3-[(1-ethylthio) thio]-propanoic acid, 3-acetyl thio-2-methyl propanoic acid, and methyl allylthioacetate, were identified as the main sulfur compounds (**Figure 6**). **Table 2** lists 24 flavor substances identified that may contribute to the flavor of the fermentation broth, and these substances were divided mainly into grass and flower, roast, fruit, acid, and other flavors. Among them, the roast flavor was the most prominent, mainly including furfural, 2-acetylfuran, and 5-methyl furfural, which accounted for ∼3.80% of the relative total peak area. Both 2-acetylfuran and 5-methylfurfural are furfural derivatives, which are produced by the Maillard reaction. After fermentation, the contents of baking-flavored substances in S2 and S4 were decreased most significantly, indicating the potential effect of *L. plantarum*. The unfermented extract contained small amounts of green grass, floral, and fruity aroma substances. After the probiotics were fermented, they produced green grass, floral, and fruit aromas, such as benzaldehyde, phenethyl alcohol, and eugenol acetate, that improved the smell of the fermentation

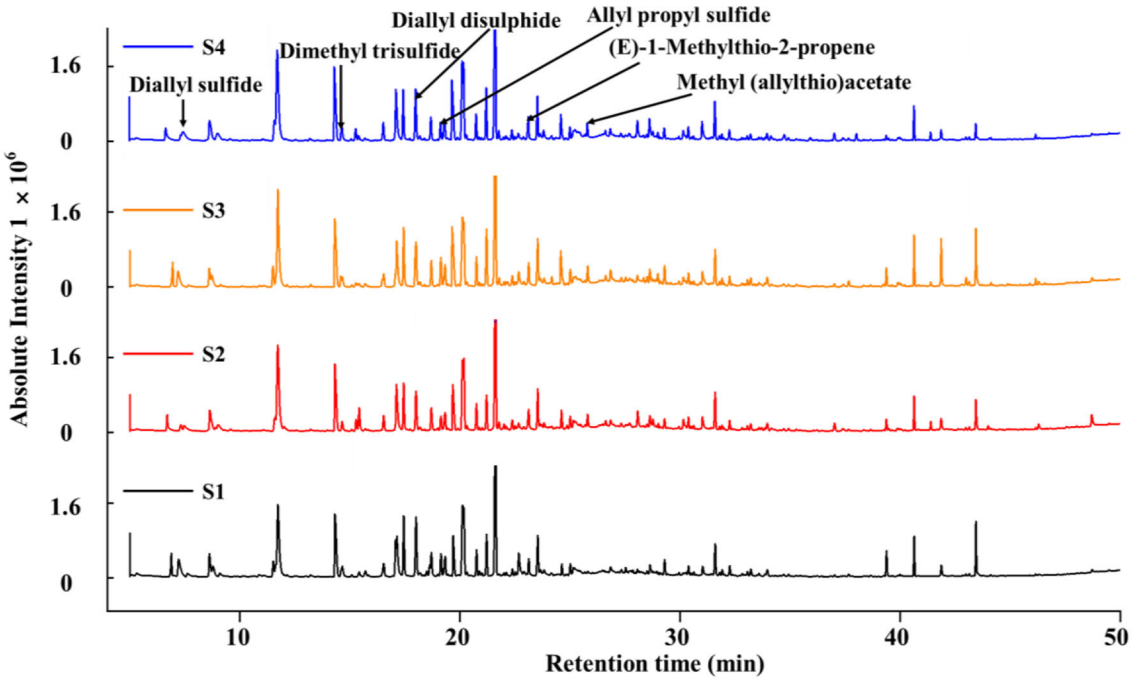

FIGURE 6 | Gas chromatography–mass spectrometry (GC-MS) profiles of volatile compounds in black garlic fermentation broth.

broth. Notably, the 5-HMF contents of the fermented samples (S2, S3, and S4) were 0.73, 1.24, and 0.26%, respectively (**Table 2**), which were lower than those of S1. This is consistent with the results shown in **Figure 3H**. *Lactobacillus* fermentation may be a new reliable method for reducing the content of 5-HMF.

Furthermore, 105, 94, 94, and 87 metabolites were identified by LC–QTOF–MS/MS in samples S1–S4, respectively, and were divided mainly into organic acids, amino acids, saccharides, organic sulfides, lipids, vitamins, etc. (**Supplementary Table 2**). *Lactobacillus* fermentation produced a large number of organic acids, which have potent antibacterial, anti-cholera, anti-inflammatory, hypoglycemic, antioxidant, and immune properties. Twenty-one organic acids were identified in the four samples (**Table 3**). The relative contents of several organic acids were enhanced in the three fermentation broths, including sinapoyl malate, isocitrate, lactic acid, cinnamic acid, creatine A, and 2,4-dimethyl-2-pentadecenoic acid. In particular, the newly produced lactic acid was relatively high in content in the three fermented samples: 14.13, 7.73, and 13.53% in samples S2, S3, and S4, respectively. The isocitrate content was increased dramatically in the probiotic fermentation broths, and this increased isocitrate content can enhance the tricarboxylic acid cycle and accelerate metabolic processes. Sinapoyl malate and cinnamic acid have also been shown to possess antioxidant and antimicrobial activities (42, 43). Notably, among the three fermentation broths, *L. plantarum* fermentation increased the organic acid content the most significantly. The total relative content of organic acids was as high as 60.60%, which is 1.7 times that in the unfermented broth. In comparison with the unfermented sample (S1), the relative content of 13,13-dimethyl-tetradecanoic acid, which exhibits a potent anti-cancer activity (44), was increased only in the *L. plantarum* fermentation broth, whereas it was almost undetectable in the other two fermentation samples. The total relative contents of amino acids and their derivatives were the highest in S2 (7.03%), followed by S3 (6.84%), S1 (3.36%), and S4 (2.65%), which was similar to the trend of the relative amino-N content. Peptides are amino acid chains smaller than proteins that play dominant roles in biological growth, development, reproduction, metabolism, and other life processes. Gly-Pro-Glu (GPE) has been identified as a neuroprotective peptide that can prevent glutamate from binding to the N-methyl-D-aspartate receptor. The relative contents of GPE in S2 (0.11%) and S3 (0.16%) were increased in comparison with S1 but were not detected in S4 (**Table 3**). Therefore, the fermentation of black garlic extracts by *L. plantarum* and *L. rhamnosus* may enhance their neuroprotective effects. Fermentation by *Lactobacillus* can also alter the composition of saccharides in black garlic broth. Notably, the relative content of sorbose was increased by 14.38-, 1.40-, and 26.6-fold in S2, S3, and S4, respectively, compared with S1; sorbose is an ideal sweetener for improving the taste of black garlic broth. Organic sulfides are the main functional ingredients involved in the health benefits of garlic. Here, N-γ-glutamyl-S-(1-propenyl) sulfide, γ-glutamyl-SAC, SAC, sulfoxide, and thiosulfate were identified as the main organic sulfides (**Table 3**). **Figure 7** shows a heat map of the relative peak area changes of the main sulfides

TABLE 2 | HS-SPME–GC-MS identification of the main functional volatile substances in black garlic broth.

Compounds	RT (min)	CAS	Mass (Da)	Serial number	Formula	Retention index	Principal fragments	S1 (%)	S2 (%)	S3 (%)	S4 (%)
Green/floral flavor											
2-Nonanone	15.290	821–55–6	142	7,667	$C_9H_{18}O$	1,052	43, 59, 99, 142	–	0.353	–	0.327
Nonanal	15.425	124–19–6	142	7,630	$C_9H_{18}O$	1,104	41, 70, 98, 124	–	0.738	–	–
Benzaldehyde	19.145	100–52–7	106	2,661	C_7H_6O	982	51, 77, 106	–	0.380	0.798	0.451
2-Undecanone	21.785	112–12–9	170	12,783	$C_{11}H_{22}O$	1,251	43, 58, 112, 127	–	0.157	–	0.191
Benzeneacetaldehyde	22.670	122–78–1	120	4,077	C_8H_8O	1,081	39, 65, 91, 120	0.968	0.149	0.381	–
Phenylethyl alcohol	30.160	1,960–12–8	122	5,604	$C_8H_{10}O$	1,136	39, 65, 91, 122	–	0.171	0.111	0.180
Eugenolacetate (6Cl)	37.020	93–28–7	206	18,320	$C_{12}H_{14}O_3$	1,552	43, 77, 91, 131	–	0.239	–	0.199
1-Dodecanol	37.670	112–53–8	186	15,467	$C_{12}H_{26}O$	1,457	55, 69, 97, 140	–	–	0.135	–
5-Hydroxymethylfurfural	43.445	67–47–0	126	6,369	$C_6H_6O_3$	1,163	41, 69, 97, 126	1.242	0.727	1.237	0.260
Fruity flavor											
Limonene	8.785	138–86–3	136	6,614	$C_{10}H_{16}$	1,018	39, 68, 93, 136	0.633	–	0.478	–
Methyl 2-furoate	32.255	611–13–2	126	6,367	$C_6H_6O_3$	909	39, 67, 95, 126	0.320	0.220	0.209	0.210
Farnesyl alcohol	41.395	4,602–84–0	222	59,386	$C_{15}H_{26}O$	1,710	41, 69, 93, 136	–	0.187	0.074	0.141
1-Tridecanol	41.870	112–70–9	200	17,566	$C_{13}H_{28}O$	1,556	56, 69, 97, 125	–	–	0.997	0.186
Roasted flavor											
Furfural	17.450	1,998–01–1	96	1,382	$C_5H_4O_2$	831	38, 39, 67, 96	2.060	1.316	1.617	1.252
2-Acetylfuran	18.700	1,192–62–7	110	3,062	$C_6H_6O_2$	878	39, 67, 95, 110	0.853	0.684	0.670	0.582
5-Methyl furfural	20.755	620–02–0	110	2,680	$C_6H_6O_2$	920	53, 81, 109, 110	0.802	0.649	0.711	0.595
2-Acetyl pyrrole	31.595	1,072–83–9	109	2,603	C_6H_7NO	1,035	39, 66, 94, 109	0.145	0.087	0.138	0.091
Sour flavor											
Acetic acid	17.115	64–19–7	60	139	$C_2H_4O_2$	576	43, 45, 60	1.729	1.905	1.610	1.900
Isovaleric acid	23.820	503–74–2	102	2,266	$C_5H_{10}O_2$	811	43, 60, 87	–	–	–	0.219
Tetramethoxy ethane	27.535	1,069–12–1	148	14,322	C_6H_{124}	883	59, 105, 133, 148	0.139	–	–	–
Other flavors											
Cyclohexanone* (earthy)	11.735	108–94–1	98	1,559	$C_6H_{10}O$	891	42, 55, 69, 98	4.750	4.750	4.750	4.750
2-Furanmethanol (bitter and spicy)	23.540	98–00–0	98	1,497	$C_5H_6O_2$	885	41, 53, 81, 98	1.333	0.969	1.169	1.041
Hexanoic acid (sweaty)	28.625	142–62–1	116	3,619	$C_6H_{12}O_2$	974	41, 60, 73, 88	0.294	0.339	0.357	0.515
1,4-Butanediol (bitterness)	30.630	110–63–4	90	1,176	$C_4H_{10}O_2$	904	31, 42, 44, 71	–	–	0.067	–
6-Heptenoic acid (fatty)	31.015	1,119–60–4	128	7,106	$C_7H_{12}O_2$	1,064	41, 68, 110, 128	0.298	0.345	0.239	0.515

**Identification of compounds confirmed by analysis of standards. An en dash (–) indicates the compound was not detected.*

TABLE 3 | Main substances identified in black garlic broth by LC–Q-TOF–MS/MS.

Compounds	RT (min)	Formula	*m/z*	Mass (Da)	Adduct	S1 (%)	S2 (%)	S3 (%)	S4 (%)
Organic acids and derivatives									
Sinapoyl malate	0.327	$C_{15}H_{16}O_9$	363.068	340.079	$[M + H]^+$	0.14	0.2	0.25	0.22
Isocitrate	0.368	$C_6H_8O_7$	191.020	192.027	$[M–H]^–$	13.98	25.04	15.31	14.91
L-Malic acid	0.397	$C_4H_6O_5$	133.014	134.021	$[M–H]^–$	1.35	–	–	–
Lactic acid	0.474	$C_3H_6O_3$	89.024	90.032	$[M–H]^–$	–	14.13	7.73	13.53
Cinnamic acid	0.713	$C_9H_8O_2$	166.086	148.053	$[M + H]^+$	0.06	0.14	0.19	0.15
Isohydrosorbic acid	0.566	$C_6H_{10}O_2$	132.102	114.068	$[M + H]^+$	1.17	0.98	1.67	1.27
Succinic acid	0.627	$C_4H_6O_4$	117.019	118.027	$[M–H]^–$	–	–	–	0.71
Cinnamic acid	0.713	$C_9H_8O_2$	166.086	148.053	$[M + H]^+$	0.06	0.14	0.19	0.15
Amino acids and derivatives									
Gly-Pro-Glu	0.353	$C_{12}H_{19}N_3O_6$	302.135	301.127	$[M + H]^+$	0.08	0.11	0.16	–
Thr-Pro-Lys	7.380	$C_{15}H_{28}N_4O_5$	362.241	344.207	$[M + NH_4]^+$	–	–	–	0.22
Lys-Ile-Gln	8.245	$C_{17}H_{33}N_5O_5$	388.254	387.247	$[M + H]^+$	–	–	–	0.15
Arg-Gln-Arg	9.254	$C_{17}H_{34}N_{10}O_5$	481.262	458.273	$[M + H]^+$	0.22	0.2	–	0.16
Thr-Leu-Pro	13.150	$C_{15}H_{27}N_3O_5$	347.230	329.197	$[M + NH_4]^+$	–	–	–	0.2
Trp-Val-Trp	22.858	$C_{27}H_{31}N_5O_4$	507.272	489.238	$[M + NH_4]^+$	–	0.1	0.13	0.14
Saccharides and derivatives									
2-O-α-D-galactopyranuronosyl-L-rhamnose	0.315	$C_{12}H_{22}O_{11}$	377.086	342.117	$[M–H]^–$	0.52	0.39	0.24	1.04
Sorbose	0.362	$C_6H_{12}O_6$	215.033	180.064	$[M–H]^–$	0.07	1.01	0.10	1.86
3-Hydroxy-2H-pyran-2-one	0.370	$C_5H_4O_3$	111.009	112.016	$[M + H]^+$	0.79	0.9	0.95	–
α-L-arabinofuranosyl-(1-3)-β-D-xylopyranosyl-(1-4)-D-xylose	0.423	$C_{15}H_{26}O_{13}$	413.130	414.137	$[M–H]^–$	–	0.31	–	0.35
Tetrahydro-6-(2-hydroxy-16,19-dimethylhexacosyl)-4-methyl-2H-pyran-2-one	24.268	$C_{34}H_{66}O_3$	540.535	522.501	$M + NH_4]^+$	–	0.29	–	0.47
Organosulfur compounds									
Cycloalliin	0.367	$C_6H_{11}NO_3S$	178.053	177.046	$[M + H]^+$	0.07	–	–	–
S-allyl-L-cysteine	0.425	$C_6H_{11}NO_2S$	162.058	161.049	$[M + H]^+$	0.47	0.34	0.40	0.27
N-γ-glutamyl-S-(1-propenyl) cysteine	1.962	$C_{11}H_{18}N_2O_5S$	289.087	290.094	$[M – H]^–$	0.93	0.56	0.80	0.38
γ-Glutamyl-S-allyl-L-cysteine	2.077	$C_{11}H_{18}N_2O_5S$	291.101	290.094	$[M + H]^+$	0.85	0.75	0.24	0.66
Lipids and derivatives									
C16 sphingosine	15.014	C16H35NO2	274.274	273.266	$[M + H]^+$	0.99	1.07	10.48	11.66
Phytosphingosine	15.463	C18H39NO3	318.300	317.292	$[M + H]^+$	6.32	9.42	8.55	9.55
C17 sphingosine	16.725	$C_{17}H_{37}NO_2$	288.290	287.282	$[M + H]^+$	0.13	–	–	–
Sphingosine	17.611	$C_{18}H_{39}NO_2$	302.305	301.298	$[M + H]^+$	0.44	0.48	1.59	0.55
Vitamins and derivatives									
α-CEHC	19.659	$C_{16}H_{22}O_4$	301.141	278.151	$[M + H]^+$	0.78	2.01	1.84	1.66
γ-Tocotrienol	19.853	$C_{28}H_{42}O_2$	409.310	410.318	$[M – H]^–$	1.48	1.49	1.49	1.46

An en dash (–) indicates that the compound was not detected; α-CEHC, 3,4-dihydro-6-hydroxy-2,5,7,8-tetramethyl-2H-1-benzopyran-2-propanoic acid.

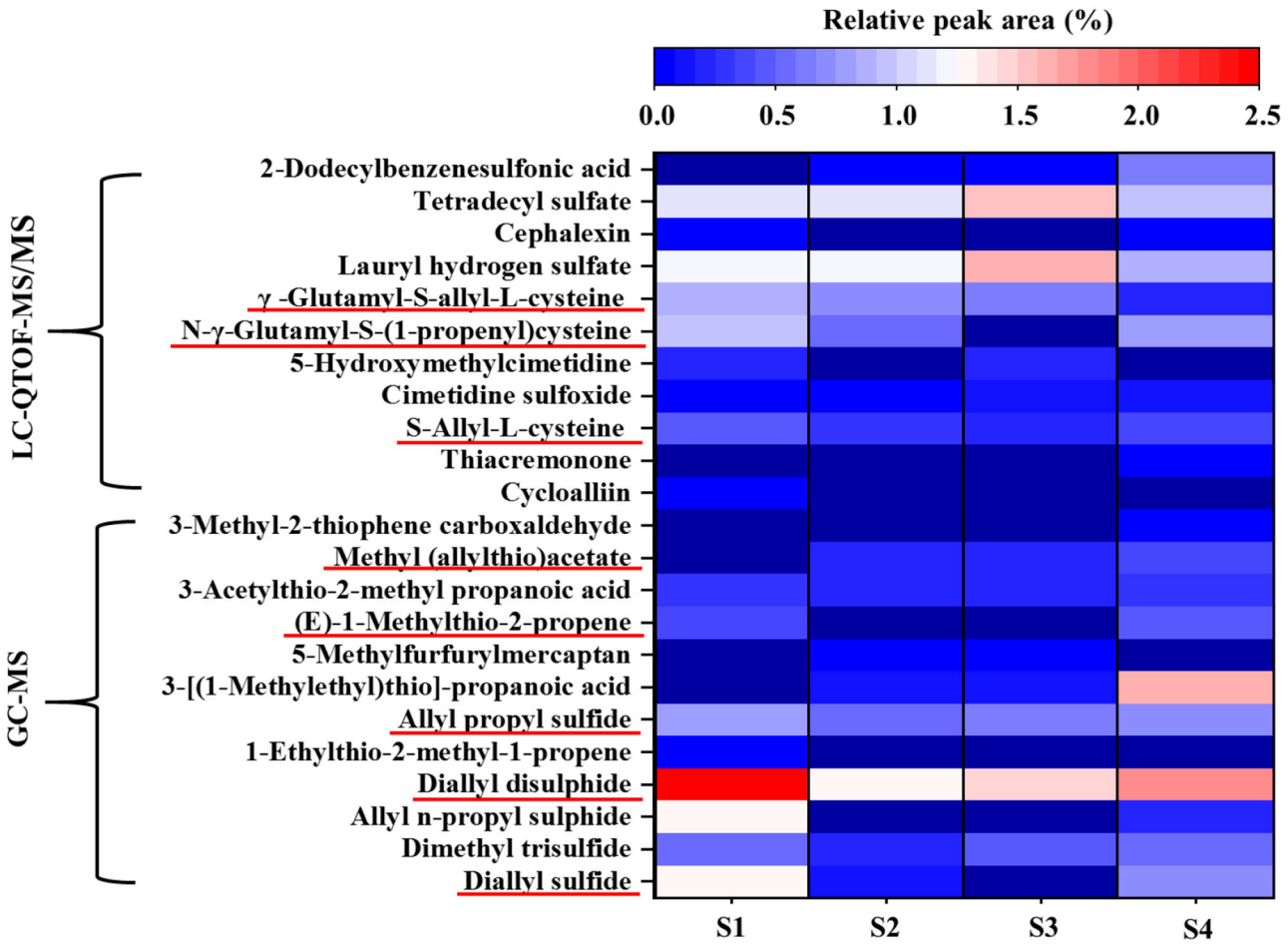

FIGURE 7 | Heat map of relative peak area changes in the main sulfides of different black garlic broth extracts based on GC-MS and liquid chromatography–quadrupole time-of-flight–tandem mass spectrometry (LC–Q-TOF–MS/MS) analyses. The colors from blue to red indicate that the sulfide content gradually increased; dark blue indicates that sulfide was not detected.

in the four samples. The relative contents of SAC in the S1, S2, S3, and S4 broths were 0.47, 0.34, 0.40, and 0.27%, respectively. SAC is a biologically active compound used in nutraceutical and medical applications for its antioxidant, anti-carcinogenic, and anti-hepatopathic activities (45). In addition, cycloalliin (0.07%) could not be detected after probiotic fermentation, which reduced the pungent odor. Sphingolipids are an important structural component of biofilms, as well as important functional molecules that participate in many signal transduction pathways and play important roles in programmed cell death and autophagy. Sphingosine is the simplest sphingolipid and a constituent of other sphingolipids together with fatty acids and the polar head group. The main sphingosines identified in the four samples (S1–S4) were phytosphingosine, C16 sphingosine, and sphingosine. The relative peak areas of phytosphingosine in samples S1–S4 were 6.32, 9.42, 8.55, and 9.55%, respectively, and a high phytosphingosine content helps maintain skin moisture and increases anti-inflammatory function. *L. rhamnosus* fermentation induced the most obvious increase in phytosphingosine content. The 3,4-dihydro-6-hydroxy-2,5,7,8-tetramethyl-2H-1-benzopyran-2-propanoic acid (α-CEHC) and γ-tocotrienol are important vitamins with antioxidant, anti-inflammatory, and reproductive functions. After probiotic fermentation, the α-CEHC content increased by at least twofold, with *L. plantarum* fermentation (S2) inducing a 2.72-fold increase, which may increase the antioxidant capacity of the probiotic fermentation broth. However, there was no obvious change in the content of γ-tocotrienol (**Table 3**). The results demonstrated that *Lactobacillus* could significantly influence the quality of black garlic by regulating the flavor and functional components. However, in actual consumption, various factors would affect the health benefits of food, including dietary habits, actual consumption (quantity/volume)/day of functional compounds, bioavailability, and metabolism *in vivo*). Therefore, the health effects of probiotic fermented black garlic broth *in vivo* need further investigation.

CONCLUSION

In this study, single-factor analysis and the response surface methodology were used to optimize the hot water extraction of soluble solids from black garlic. The optimal extraction conditions were found to be an extraction temperature of 99.96°C, a solid-to-liquid ratio of 1:4.38 g/ml, and an extraction time of 2.72 h. To obtain black garlic broth with more health-promoting effects, the effects of single-strain and mixed-strain fermentation by *L. plantarum* and *L. rhamnosus* on the physicochemical properties and flavor of black garlic extract broth were further investigated. The results showed that *L. plantarum* and *L. rhamnosus* reduced the pH of black garlic extract by increasing the total acid content, as well as increased the contents of amino-N, total polyphenols, and total flavonoids and reduced the 5-HMF content. Notably, for all physicochemical properties, the effects of fermentation by *L. plantarum* and *L. plantarum* plus *L. rhamnosus* were similar and differed significantly from the effects of fermentation by *L. rhamnosus*. Typically, fermentation by *L. plantarum* or mixed bacteria exhibited greater acid production and reduced 5-HMF content, while fermentation by *L. rhamnosus* resulted in higher total polyphenol and total flavonoid contents. Artificial sensory results demonstrated that the broths from S1, S2, and S4 received the best overall sensory evaluations. The contents of several components with unpleasant baking flavors such as furfural, 2-acetylfuran, and 5-methyl furfural were reduced, whereas those of components with green grass, floral, and fruit aromas were increased. More importantly, fermentation by *Lactobacillus* probiotics could significantly increase the contents of several functional components, including organic acids (e.g., lactic acid), amino acids (e.g., GPE), saccharides (e.g., sorbose), and vitamins (e.g., α-CEHC). *Lactobacillus* (*L. plantarum* and *L. plantarum*) could significantly influence the composition of flavor and functional components in black garlic extract. The health-promoting effects of black garlic may be consequently changed, which need a more comprehensive investigation, especially *in vivo* studies. This work will provide novel insights into the strategic design of new black garlic products and will facilitate the application of black garlic in functional foods.

DATA AVAILABILITY STATEMENT

The raw data supporting the conclusions of this article will be made available by the authors, without undue reservation.

AUTHOR CONTRIBUTIONS

LM made substantial contributions in the methodology, investigation, and writing of the original draft. CZ made substantial contributions in the validation, formal analysis, and writing of the manuscript. JC and JZ made substantial contributions in the conceptualization, supervision, writing, review, and editing of the manuscript, project administration, and funding acquisition. All authors contributed to the article and approved the submitted version.

FUNDING

The authors would like to acknowledge the financial support provided by the National Natural Science Foundation of China (Grant Nos. 32072181, 31901681, and 31901656), Weifang Young Talents Program of Institute of Food Science and Technology, Chinese Academy of Agricultural Sciences (CAAS-IFST-SN2020-02), Heze Tianhong Fruits & Vegetables Co., Ltd., CHENGUANG Biotech Group Co., Ltd., and Hunan FRUITOPS Co., Ltd.

ACKNOWLEDGMENTS

We also appreciate the Elite Youth Program of Chinese Academy of Agricultural Sciences (JZ).

SUPPLEMENTARY MATERIAL

The Supplementary Material for this article can be found online at: https://www.frontiersin.org/articles/10.3389/fnut.2021.645416/full#supplementary-material

REFERENCES

1. Martínez-Casas L, Lage-Yusty M, López-Hernández J. Changes in the aromatic profile, sugars, and bioactive compounds when purple garlic is transformed into black garlic. *J Agric Food Chem.* (2017) 65:10804–11. doi: 10.1021/acs.jafc.7b04423
2. Yang P, Song H, Wang L, Jing H. Characterization of key aroma-active compounds in black garlic by sensory-directed flavor analysis. *J Agric Food Chem.* (2019) 67:7926–34. doi: 10.1021/acs.jafc.9b03269
3. Kimura S, Tung YC, Pan MH, Su NW, Lai YJ, Cheng KC. Black garlic: a critical review of its production, bioactivity, and application. *J Food Drug Anal.* (2017) 25:62–70. doi: 10.1016/j.jfda.2016.11.003
4. Yuan H, Sun L, Chen M, Wang J. The comparison of the contents of sugar, amadori, and heyns compounds in fresh and black garlic. *J Food Sci.* (2016) 81:C1662–1668. doi: 10.1111/1750-3841.13365
5. Purev U, Chung MJ, Oh DH. Individual differences on immunostimulatory activity of raw and black garlic extract in human primary immune cells. *Immunopharmacol Immunotoxicol.* (2012) 34:651–60. doi: 10.3109/08923973.2011.649288
6. Kim MJ, Yoo YC, Kim HJ, Shin SK, Sohn EJ, Min AY, et al. Aged black garlic exerts anti-inflammatory effects by decreasing no and proinflammatory cytokine production with less cytoxicity in LPS-stimulated RAW 264.7 macrophages and LPS-induced septicemia mice. *J Med Food.* (2014) 17:1057–63. doi: 10.1089/jmf.2013.3043
7. Jeong YY, Ryu JH, Shin JH, Kang MJ, Kang JR, Han J, et al. Comparison of anti-oxidant and anti-inflammatory effects between fresh and aged black garlic extracts. *Molecules.* (2016) 21:430. doi: 10.3390/molecules21040430
8. Lanzotti V. The analysis of onion and garlic. *J Chromatogr A.* (2006) 1112:3–22. doi: 10.1016/j.chroma.2005.12.016
9. Qiu Z, Zheng Z, Zhang B, Sun-Waterhouse D, Qiao X. Formation, nutritional value, and enhancement of characteristic components in black garlic: a review for maximizing the goodness to humans. *Compr Rev Food Sci Food Saf.* (2020) 19:801–834. doi: 10.1111/1541-4337.12529
10. Santhosha SG, Jamuna P, Prabhavathi SN. Bioactive components of garlic and their physiological role in health maintenance: a review. *Food Biosci.* (2013) 3:59–74. doi: 10.1016/j.fbio.2013.07.001

11. Wu J, Jin Y, Zhang M. Evaluation on the physicochemical and digestive properties of melanoidin from black garlic and their antioxidant activities *in vitro*. *Food Chem.* (2020) 340:127934. doi: 10.1016/j.foodchem.2020.127934
12. Zhao Y, Ding Y, Wang D, Deng Y, Zhao Y. Effect of high hydrostatic pressure conditions on the composition, morphology, rheology, thermal behavior, color, and stability of black garlic melanoidins. *Food Chem.* (2021) 337:127790. doi: 10.1016/j.foodchem.2020.127790
13. Delgado-Andrade C, Rufián-Henares JA, Morales FJ. Assessing the antioxidant activity of melanoidins from coffee brews by different antioxidant methods. *J Agric Food Chem.* (2005) 53:7832–6. doi: 10.1021/jf0512353
14. Wang HY, Qian H, Yao WR. Melanoidins produced by the Maillard reaction: Structure and biological activity. *Food Chem.* (2011) 128:573–84. doi: 10.1016/j.foodchem.2011.03.075
15. Wang CY, Ng CC, Su H, Tzeng WS, Shyu YT. Probiotic potential of noni juice fermented with lactic acid bacteria and bifidobacteria. *Int J Food Sci Nutr.* (2009) 60 (Suppl. 6):98–106. doi: 10.1080/09637480902755095
16. Ejtahed H-S, Angoorani P, Soroush A-R, Atlasi R, Hasani-Ranjbar S, Mortazavian AM, et al. Probiotics supplementation for the obesity management; a systematic review of animal studies and clinical trials. *J Funct Foods.* (2019) 52:228–242. doi: 10.1016/j.jff.2018.10.039
17. Tocmo R, Lai AN, Wu Y, Liang D, Fogliano V, Huang D. Organosulphide profile and hydrogen sulphide-releasing activity of garlic fermented by *Lactobacillus plantarum*. *J Funct Foods.* (2017) 30:254–9. doi: 10.1016/j.jff.2017.01.001
18. Daliri EBM, Choi SI, Cho BY, Jo HY, Kim SH, Chelliah R, et al. Biological activities of a garlic–*Cirsium setidens* nakai blend fermented with *Leuconostoc mesenteroides*. *Food Sci Nutr.* (2019) 6:1032–9. doi: 10.1002/fsn3.1032
19. Lee HS, Lim WC, Lee SJ, Lee SH, Lee JH, Cho HY. Antiobesity effect of garlic extract fermented by *Lactobacillus plantarum* BL2 in diet-induced obese mice. *J Med Food.* (2016) 19:823–9. doi: 10.1089/jmf.2016.3674
20. Jung YM, Lee SH, Lee DS, You MJ, Chung IK, Cheon WH, et al. Fermented garlic protects diabetic, obese mice when fed a high-fat diet by antioxidant effects. *Nutr Res.* (2011) 31:387–96. doi: 10.1016/j.nutres.2011.04.005
21. Zhang H, Cui J, Tian G, DiMarco-Crook C, Gao W, Zhao C, et al. Efficiency of four different dietary preparation methods in extracting functional compounds from dried tangerine peel. *Food Chem.* (2019) 289:340–50. doi: 10.1016/j.foodchem.2019.03.063
22. Candioti LV, De Zan MM, Camara MS, Goicoechea HC. Experimental design and multiple response optimization. Using the desirability function in analytical methods development. *Talanta.* (2014) 124:123–38. doi: 10.1016/j.talanta.2014.01.034
23. Mosso AL, LeBlanc JG, Motta C, Castanheira I, Ribotta P, Sammán N. Effect of fermentation in nutritional, textural and sensorial parameters of vegan-spread products using a probiotic folate-producing *Lactobacillus sakei* strain. *LWT Food Sci Technol.* (2020) 127:109339. doi: 10.1016/j.lwt.2020.109339
24. Kim JS, Kang OJ, Gweon OC. Comparison of phenolic acids and flavonoids in black garlic at different thermal processing steps. *J Funct Foods.* (2013) 5:80–6. doi: 10.1016/j.jff.2012.08.006
25. Lu X, Li N, Qiao X, Qiu Z, Liu P. Effects of thermal treatment on polysaccharide degradation during black garlic processing. *LWT Food Sci Technol.* (2018) 95:223–9. doi: 10.1016/j.lwt.2018.04.059
26. Lee C-H, Chen Y-T, Hsieh H-J, Chen K-T, Chen Y-A, Wu J-T, et al. Exploring epigallocatechin gallate impregnation to inhibit 5-hydroxymethylfurfural formation and the effect on antioxidant ability of black garlic. *LWT–Food Sci Technol.* (2020) 117:108628. doi: 10.1016/j.lwt.2019.108628
27. Pavli FG, Argyri AA, Chorianopoulos NG, Nychas G-JE, Tassou CC. Effect of *Lactobacillus plantarum* L125 strain with probiotic potential on physicochemical, microbiological and sensorial characteristics of dry-fermented sausages. *LWT Food Sci Technol.* (2020) 118:108810. doi: 10.1016/j.lwt.2019.108810
28. Yang Y, Zhao C, Tian G, Lu C, Li C, Bao Y, et al. Characterization of physical properties and electronic sensory analyses of citrus oil-based nanoemulsions. *Food Res Int.* (2018) 109:149–58. doi: 10.1016/j.foodres.2018.04.025
29. Liu J, Guo W, Yang M, Liu L, Huang S, Tao L, et al. Investigation of the dynamic changes in the chemical constituents of Chinese "Laba" garlic during traditional processing. *RSC Adv.* (2018) 8:41872–83. doi: 10.1039/c8ra09657k
30. Molina-Calle M, de Medina VS, Priego-Capote F, de Castro MDL. Establishing compositional differences between fresh and black garlic by a metabolomics approach based on LC–QTOF MS/MS analysis. *J Food Compos Anal.* (2017) 62:155–63. doi: 10.1016/j.jfca.2017.05.004
31. Papoutsis K, Pristijono P, Golding JB, Stathopoulos CE, Bowyer MC, Scarlett CJ, et al. Optimizing a sustainable ultrasound-assisted extraction method for the recovery of polyphenols from lemon by-products: comparison with hot water and organic solvent extractions. *Eur Food Res Technol.* (2018) 244:1353–65. doi: 10.1007/s00217-018-3049-9
32. Polak-Berecka M, Choma A, Wasko A, Gorska S, Gamian A, Cybulska J. Physicochemical characterization of exopolysaccharides produced by *Lactobacillus rhamnosus* on various carbon sources. *Carbohydr Polym.* (2015) 117:501–9. doi: 10.1016/j.carbpol.2014.10.006
33. Liu P, Lu X, Li N, Zheng Z, Zhao R, Tang X, et al. Effects and mechanism of free amino acids on browning in the processing of black garlic. *J Sci Food Agric.* (2019) 99:4670–6. doi: 10.1002/jsfa.9707
34. Daliri EB, Kim SH, Park BJ, Kim HS, Kim JM, Kim HS, et al. Effects of different processing methods on the antioxidant and immune stimulating abilities of garlic. *Food Sci Nutr.* (2019) 7:1222–9. doi: 10.1002/fsn3.942
35. Adetuyi FO, Ibrahim TA. Effect of fermentation time on the phenolic, flavonoid and vitamin C contents and antioxidant activities of okra (*Abelmoschus esculentus*) seeds. *Niger Food J.* (2014) 32:128–37. doi: 10.1016/s0189-7241(15)30128-4
36. Demir N, Yildiz O, Alpaslan M, Hayaloglu AA. Evaluation of volatiles, phenolic compounds and antioxidant activities of rose hip (*Rosa L.*) fruits in Turkey. *LWT Food Sci Technol.* (2014) 57:126–33. doi: 10.1016/j.lwt.2013.12.038
37. Lee YG, Cho JY, Kim YM, Moon JH. Change in flavonoid composition and antioxidative activity during fermentation of onion (*Allium cepaL.*) by *Leuconostoc mesenteroides* with different salt concentrations. *J Food Sci.* (2016) 81:C1385–93. doi: 10.1111/1750-3841.13329
38. Zhang X, Li N, Lu X, Liu P, Qiao X. Effects of temperature on the quality of black garlic. *J Sci Food Agric.* (2016) 96:2366–72. doi: 10.1002/jsfa.7351
39. Shapla UM, Solayman M, Alam N, Khalil MI, Gan SH. 5-Hydroxymethylfurfural (HMF) levels in honey and other food products: effects on bees and human health. *Chem Cent J.* (2018) 12:35. doi: 10.1186/s13065-018-0408-3
40. Gotow N, Kobayashi T, Kobayakawa T. Retronasal aroma allows feature extraction from taste of a traditional Japanese confection. *Flavour.* (2013) 2:1–9. doi: 10.1186/2044-7248-2-26
41. Spence C, Levitan CA, Shankar MU, Zampini M. Does food color influence taste and flavor perception in humans? *Chemosens Percept.* (2010) 3:68–84. doi: 10.1007/s12078-010-9067-z
42. Sova M. Antioxidant and antimicrobial activities of cinnamic acid derivatives. *Mini-Rev Med Chem.* (2012) 12:749–67. doi: 10.2174/138955712801264792
43. Mention MM, Flourat AL, Peyrot C, Allais F. Biomimetic regioselective and high-yielding Cu(i)-catalyzed dimerization of sinapate esters in green solvent Cyrene^{TM}: towards sustainable antioxidant and anti-UV ingredients. *Green Chem.* (2020) 22:2077–85. doi: 10.1039/d0gc00122h
44. Lin T, Yin X, Cai Q, Fan X, Xu K, Huang L, et al. 13-Methyltetradecanoic acid induces mitochondrial-mediated apoptosis in human bladder cancer cells. *Urol Oncol.* (2012) 30:339–45. doi: 10.1016/j.urolonc.2010.04.011
45. Kim JH, Nam SH, Rico CW, Kang MY. A comparative study on the antioxidative and anti-allergic activities of fresh and aged black garlic extracts. *Int J Food Sci Technol.* (2012) 47:1176–82. doi: 10.1111/j.1365-2621.2012.02957.x

Conflict of Interest: The authors declare that the research was conducted in the absence of any commercial or financial relationships that could be construed as a potential conflict of interest.

frontiers in Nutrition

CORRECTION
published: 23 September 2021
doi: 10.3389/fnut.2021.745272

Corrigendum: Effects of Anaerobic Fermentation on Black Garlic Extract by *Lactobacillus*: Changes in Flavor and Functional Components

Li Ma[1,2], *Chengying Zhao*[2], *Jifeng Chen*[1*] and *Jinkai Zheng*[2*]

[1] School of Life Sciences, Zhengzhou University, Zhengzhou, China, [2] Institute of Food Science and Technology, Chinese Academy of Agricultural Sciences, Beijing, China

OPEN ACCESS

Approved by:
Frontiers Editorial Office,
Frontiers Media SA, Switzerland

***Correspondence:**
Jinkai Zheng
jinkai8212@163.com
Jifeng Chen
chenjifeng@zzu.edu.cn

Specialty section:
This article was submitted to Food Chemistry, a section of the journal Frontiers in Nutrition

Received: 21 July 2021
Accepted: 22 July 2021
Published: 23 September 2021

Citation:
Ma L, Zhao C, Chen J and Zheng J (2021) Corrigendum: Effects of Anaerobic Fermentation on Black Garlic Extract by Lactobacillus: Changes in Flavor and Functional Components. Front. Nutr. 8:745272. doi: 10.3389/fnut.2021.745272

Keywords: black garlic extract, fermentation, *Lactobacillus*, sensory, functional components

A Corrigendum on

Effects of Anaerobic Fermentation on Black Garlic Extract by *Lactobacillus*: Changes in Flavor and Functional Components

by Ma, L., Zhao, C., Chen, J., and Zheng, J. (2021). Front. Nutr. 8:645416. doi: 10.3389/fnut.2021.645416

In the published article, there was an error in the author's name Jinkai Zheng. Instead of "Jinkai Zheng," it should be the corresponding author name "Jinkai Zheng[2]*".

The authors apologize for this error and state that this does not change the scientific conclusions of the article in any way. The original article has been updated.

frontiers in Nutrition

ORIGINAL RESEARCH
published: 29 July 2021
doi: 10.3389/fnut.2021.694936

Fermented and Germinated Processing Improved the Protective Effects of Foxtail Millet Whole Grain Against Dextran Sulfate Sodium-Induced Acute Ulcerative Colitis and Gut Microbiota Dysbiosis in C57BL/6 Mice

Yuhan Zhang[1,2,3], *Wei Liu*[2]*, *Di Zhang*[3], *Yanbing Yang*[2], *Xianshu Wang*[2] and *Lingfei Li*[1]*

[1] College of Food Science and Technology, Yunnan Agricultural University, Kunming, China, [2] Institute of Agro-Food Science and Technology, Shandong Academy of Agricultural Sciences, Jinan, China, [3] Qilu Hospital, Shandong University, Jinan, China

OPEN ACCESS

Edited by:
Jinkai Zheng,
Chinese Academy of Agricultural Sciences (CAAS), China

Reviewed by:
Ashok Kumar Pandurangan,
B. S. Abdur Rahman Crescent Institute of Science and Technology, India
Guodong Zhang,
University of Massachusetts Amherst, United States
Parmanand Malvi,
Yale University, United States
Zhigang Liu,
Northwest A and F University, China

***Correspondence:**
Wei Liu
980701611@qq.com
Lingfei Li
lingfeili@163.com

Specialty section:
This article was submitted to Food Chemistry, a section of the journal Frontiers in Nutrition

Received: 14 April 2021
Accepted: 07 July 2021
Published: 29 July 2021

Citation:
Zhang Y, Liu W, Zhang D, Yang Y, Wang X and Li L (2021) Fermented and Germinated Processing Improved the Protective Effects of Foxtail Millet Whole Grain Against Dextran Sulfate Sodium-Induced Acute Ulcerative Colitis and Gut Microbiota Dysbiosis in C57BL/6 Mice. Front. Nutr. 8:694936. doi: 10.3389/fnut.2021.694936

This study investigated the effects of foxtail millet whole grain flours obtained through different processing methods on alleviating symptoms and gut microbiota dysbiosis in a dextran sulfate sodium (DSS)-induced murine colitis model. Sixty C57BL/6 mice were divided into six groups (n = 10 in each group), including one control group (CTRL) without DSS treatment and five DSS-treated groups receiving one of the following diets: AIN-93M standard diet (93MD), whole grain foxtail millet flour (FM), fermented (F-FM), germinated (G-FM), and fermented-germinated foxtail millet flour (FG-FM). A comparison of the disease activity index (DAI) demonstrated that foxtail millet whole grain-based diets could alleviate the symptoms of enteritis to varying degrees. In addition, 16S rRNA gene sequencing revealed that FG-FM almost completely alleviated DSS-induced dysbiosis. Mice on the FG-FM diet also had the lowest plasma IL-6 levels and *claudin2* expression levels in the colon, indicating reduced systemic inflammation and improved gut barrier function. This study suggested that foxtail millet whole grain is an attractive choice for the intervention of IBD and gut microbiota dysbiosis, and its prebiotic properties are highly affected by the processing methods.

Keywords: foxtail millet, fermentation, germination, gut microbiota, inflammatory bowel disease, mouse colitis model

INTRODUCTION

Inflammatory bowel disease (IBD) is a chronic and incurable inflammatory disease that has two major entities: Crohn's disease (CD) and ulcerative colitis (UC) (1). Patients with IBD suffer from multiple clinical symptoms, including abdominal pain, diarrhea, blood in stools, and weight loss, as well as having a higher risk of developing colorectal carcinoma (CRC) (2). In this century, IBD has become a global health concern because of its high disease burden in Western countries and increasing prevalence in newly industrialized countries in Asia, Africa, and South America (3).

At present, IBD is widely accepted to be a multifactor disease driven by complex interactions among genetics, environmental factors, and the host immune system (4). The precise etiology of IBD is still unclear, which is a major problem for the prevention and medical therapy of IBD (5).

The gut microbiota is a collective term for microorganisms that live in the intestine of humans and other animals. The gut microbiota is primarily made up of bacteria, but it also includes viruses, archaea, and fungi inhabiting the gastrointestinal tract (6). It is the largest independent organ of the human body, performing indispensable functions such as digestion, absorption, metabolism, and immunity (7). There has been increasing evidence indicating that dysbiosis of the gut microbiota, which is usually manifested as a decrease in gut microbial diversity or a shift in the balance between commensal and potentially pathogenic bacteria (1), plays an important role in IBD and IBD-associated CRC (6). The reduction in gut microbial diversity, as well as differences in the composition of gut microbiota between IBD patients and healthy controls, have previously been demonstrated (8). For instance, several species of the phylum *Proteobacteria* have been reported as microbial signatures for gut microbiota in IBD patients (9). The most studied member of the *Proteobacteria*, *Escherichia coli*, was found to be excessively proliferated in IBD patients, playing a non-eligible role in the development of IBD (10). Along with an increase in the relative abundance of species from the phylum *Proteobacteria*, the abundance of the phyla *Firmicutes* and *Bacteroidetes*, which are the dominant phyla in the gut microbiota of healthy individuals, was significantly decreased in IBD patients (11).

The key factors for the pathogenesis of IBD have been highlighted. Therefore, the gut microbiota has emerged as a promising new target for the prevention and clinical treatment of IBD. In clinical practice, the application of fecal microbiota transplantation (FMT) has been proven to be effective in alleviating clinical symptoms in IBD patients (12). However, the potential hazards of FMT remain controversial, making the possibility of its widespread application unclear (13). Probiotic therapy has also been shown to be effective in both murine colitis models and IBD patients (14). In addition, due to the direct impact on the gut microbiota (15), dietary ingredients can also be used as promising strategies for the prevention and therapy of IBD due to their direct impact on the gut microbiota (15). Several food polyphenols and specific carbohydrates, for example, are effective in relieving the clinical symptoms of IBD (16, 17).

Cereals are at the bottom of the nutrition pyramid and make up a large percentage of the daily diet. Foxtail millet (*Setaria italica Beauv.*) is an old staple crop in Europe and Asia and is still one of the main food crops in northern China (18). Foxtail millet has superior nutritional properties among cereals, containing high amounts of proteins, minerals, and vitamins (19). In addition to being a daily nutritional source, small millets, including foxtail millet, have anti-inflammatory properties and can therefore be used for the prevention of related chronic diseases, such as atherosclerosis and diabetes (20, 21). Along with its superior nutritional properties and documented anti-inflammatory function, foxtail millet is also rich in non-nutrient prebiotics, such as polyphenols and dietary fibers (22), suggesting its possible positive effects on the gut microbiota and IBD. Bond polyphenols and peroxidase of foxtail millet bran have also been reported to inhibit colitis-induced carcinogenesis in a mouse model (23, 24).

In daily life, the foxtail millet is usually peeled and refined rather than the whole grain. The dehulling process results in a significant decrease in antinutrients and an increase in the bioavailability of foxtail millet, reducing the burden on the digestive system (19). However, the cereal bran, which is lost during the peeling process, contains abundant prebiotics that can effectively promote the growth of probiotics, modulate the bacterial composition of gut microbiota, and increase the production of short-chain fatty acids (SCFAs) (25). In addition to dehulling, germination and fermentation have also been reported to decrease the contents of anti-nutrients and improve the digestibility of whole grains, such as millets (26). Germination induces a significant increase in free amino acids, as well as significant beneficial effects on the availability of polyphenolic components, minerals, and γ-aminobutyrate (GABA) in foxtail millet (27, 28). On the other hand, the fermentation process causes the degradation of cellulose and hemicellulose in the cereal bran, resulting in the formation of more porous and loose structures and polysaccharides, which significantly improves the digestibility and prebiotic properties of foxtail millet (26).

In order to develop cost-effective dietary strategies for the prevention of IBD, this study investigated the alleviation of gut microbiota dysbiosis and the reduction in the symptoms of DSS-induced murine colitis models using foxtail millet flours obtained through different processing methods. Based on the hypothesis that different pretreatment methods will affect the function of millet in the prevention of colon colitis, four foxtail millet whole-grain cereal flours were studied: foxtail millet whole grain flour (FM), fermented foxtail millet whole grain flour (F-FM), germinated foxtail millet whole grain flour (G-FM), and fermented-germinated foxtail millet flour (FG-FM). This study used a traditional staple food in daily life as a dietary intervention for IBD to provide a new perspective for the prevention and treatment of IBD.

MATERIALS AND METHODS

Preparation of Foxtail Millet Cereal Flours and Animal Diets

The foxtail millet used in this study was provided by the Crop Institute, Shandong Academy of Agricultural Science (Jinan, China). Both FM and G-FM were prepared using foxtail millet whole grains and germinated foxtail millet whole grains, respectively. F-FM and FG-FM were prepared by fermenting foxtail millet whole grains or germinated foxtail millet whole grains by fermentation using *Lactobacillus plantarum* NBRC 15,891 (29), respectively. The following are the preparation details:

FM: The foxtail millet whole grain seeds were ground and screened using an 80-mesh sieve to prepare the foxtail millet whole grain flour (FM).

F-FM: The FM flour was mixed with tap water (1:3) and heated for 10 minutes in a 75±5°C water bath to gelatinize the starch. After that, it was inoculated with *L. plantarum* NBRC 15,891 at a concentration of 10^6 CFU per 100 g FM flour and incubated at 37°C until the pH dropped to 4.0 ± 0.2. The resulting slurry was dried at 55°C, ground and screened using an 80-mesh sieve to produce fermented polished foxtail millet flour (F-PFM).

G-FM: The germinated foxtail millet was prepared as described previously (30). The foxtail millet seeds were soaked in tap water overnight at room temperature. After draining the water, the seeds were spread out on a moist muslin cloth and covered with moist absorbent gauze. The seeds were left to sprout at room temperature for 48 h. After sprouting, the germinated seeds were dried at 55°C before being ground and screened using an 80-mesh sieve to prepare the germinated whole-grain foxtail millet flour (G-FM).

FG-FM: FG-FM flour was prepared using G-FM flour following the same preparation procedure that was used for F-FM.

The contents of starch, total proteins, crude fats, ashes, dietary fibers, and the moisture of cereal flours are provided in (**Supplementary Table 1**). Cereal flour-based animal diets were designed based on the AIN-93M standard rodent formula. The foxtail millet test diets contained 50% cereal flours, with the remaining 50% supplemented with standard nutrients according to the AIN-93M formula. The animal diets were prepared by Nantong Troffe Technology Co., Ltd. (Jiangsu, China). The detailed compositions of the experimental diets are provided in (**Supplementary Table 2**).

Detection of the Main Compounds in Foxtail Millet Cereal Flours With LC/MS Analysis

The detailed method of sample preparation has been previously described (31). A total of 50 mg sample was weighted, and a 1,000 μL extract solution (methanol: water = 3:1 with isotopically labeled internal standard mixture) was added. The samples were then homogenized at 35 Hz for 4 min and sonicated for 5 min in an ice-water bath. Both the homogenization and sonication cycles were repeated three times. After that, the samples were incubated for 1 h at −40 °C and centrifuged at 12,000 rpm for 15 min at 4 °C. The resulting supernatant was transferred to a new glass vial for analysis. The quality control (QC) sample was prepared by mixing an equal aliquot of the supernatants from each sample.

The LC-MS/MS analyses were performed using a UHPLC system (Vanquish, Thermo Fisher Scientific) with a UPLC HSS T3 column (2.1 × 100 mm, 1.8 μm) coupled to a Q Exactive HFX mass spectrometer (Orbitrap MS, Thermo). The mobile phase consisted of 5 mmol/L ammonium acetate and 5 mmol/L acetic acid in water (A) and acetonitrile (B). The auto-sampler temperature was 4 °C, and the injection volume was 3 μL. The QE HFX mass spectrometer was used to acquire MS/MS spectra using the information-dependent acquisition (IDA) mode in the control of the acquisition software (Xcalibur, Thermo). In this mode, the acquisition software continuously evaluates the full scan MS spectrum. The following ESI source parameters were used: sheath gas flow rate at 30 Arb, Aux gas flow rate at 10 Arb, capillary temperature at 350 °C, full MS resolution at 60,000, MS/MS resolution at 7,500, collision energy at 10/30/60 in NCE mode, and spray Voltage at 4.0 kV (positive) or −3.8 kV (negative), respectively. The resulting raw data were converted to the mzXML format using ProteoWizard and processed with an in-house program, which was developed using R and based on XCMS, for peak detection, extraction, alignment, and integration. Then, metabolite annotation was performed using an in-house MS2 database (BiotreeDB). The cutoff for annotation was set at 0.3.

Animals Experiments Design

Preparation of foxtail millet-based animal diets and animal experimental protocols are shown in **Figures 1A,B**. Sixty male C57BL/6 mice (6 weeks old) were purchased from the Model Animal Research Center of Nanjing University (Nanjing, China) and housed in a specific pathogen-free facility with ad libitum access to food and water. After two weeks of acclimation, the mice were randomly assigned to one of the following six experimental diet groups (n = 10 per diet, 5 mice per cage): CTRL group (control group; mice fed an AIN-93M standard diet, without being exposed to DSS); 93MD group (mice fed an AIN-93M standard diet); FM group (mice fed an FM flour diet); F-FM group (mice fed an F-FM flour diet); G-FM group (mice fed a G-FM flour diet) and FG-FM group (mice fed an FG-FM flour diet).

After one week of experimental diet supplementation, all mice (except mice from the CTRL group) were exposed to DSS treatment (molecular weight 36–50 kDa; MP Biomedicals) in their drinking water (2.5%) for five consecutive days, with the first day of DSS treatment was designated as day 0. The DSS solution was freshly prepared and replaced every day. After five days of DSS treatments, the mice were anesthetized with isoflurane, and blood was collected with a capillary tube containing 1% heparin sodium solution by orbital puncture. Following that, the blood was centrifuged at 6,000 rpm for 10 minutes to obtain plasma. After the mice were sacrificed by cervical dislocation, their abdomens were opened and cecal contents were collected, snap-frozen in liquid nitrogen, then stored at −80°C for further analysis. The length of the mouse colon was measured from the colon-cecal junction to the anus. A 2-cm section of the mouse colon was fixed for histological analysis, and then the rest was collected and snap-frozen in liquid nitrogen for further analysis. The spleen and liver weights of the mice were recorded. The animals were cared for according to the Guide for P.R. China Legislation on the Use and Care of Laboratory Animals. All experimental procedures were approved by the Animal Care and Use Ethics Committee of the Institute of Agro-food Science and Technology at Shandong Academy of Agricultural Sciences (Jinan, China) (Approval ID: SDAA-IAFST-2018003).

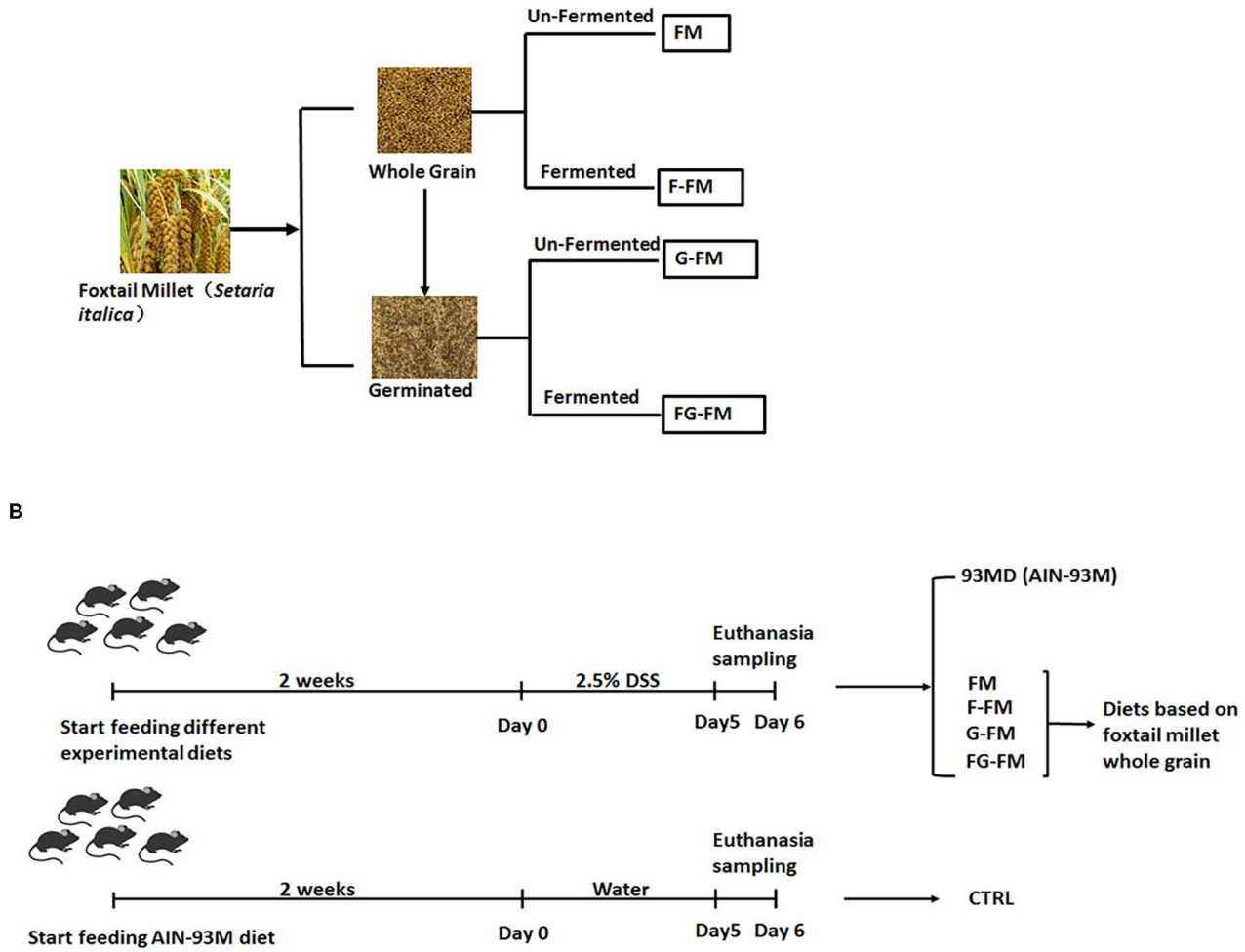

FIGURE 1 | Experimental design illustration: **(A)** preparation of foxtail millet-based animal diets and **(B)** animal experimental protocol.

Evaluation of Disease Activity Index (DAI)

During induction, disease progression was evaluated by recording body weight, stool characteristics and rectal bleeding every day. The DAI was determined by combining the measured scores of body weight (0–4), stool consistency (0–3), and rectal bleeding (0–3) as previously described (32, 33). The measured score ranges were as follows: body weight loss (0 = ≤1%; 1 = 1–5%; 2 = 5–10%; 3 = 10–20%; and 4 = >20%), stool consistency (0 = normal; 1 = soft stools; 2 = loose stools; and 3 = diarrhea), and rectal bleeding (0 = negative hemoccult; 1 = hemoccult; 3 = traces of blood; and 4 = visible rectal bleeding).

Histopathological Scores

For histopathological observations, the colon tissues were fixed in 10% formalin for more than 48 h, sectioned at 5 μm, and stained with hematoxylin-eosin. Eight fields were randomly selected in each section and were scored for colonic epithelial damage (0–6), inflammatory infiltrate in the mucosa (0–3), submucosa (0–2) and muscularis/serosa (0–1) as previously described (34). The given scores were described as follows: colonic epithelial damage (0 = normal; 1= hyperproliferation, irregular crypts, and goblet cell loss; 2 = 10–50% crypt loss; 3 = 50–90% crypt loss; 4 = complete crypt loss, surface epithelium intact; 5 = small- to medium-sized ulcer, <10 crypt width; 6 = large-scale ulcer, < 10 crypt width), inflammatory infiltrate in the mucosa (0 = normal; 1 = mild; 2 = modest; 3 = severe), submucosa (0 = normal; 1 = mild to modest; 2 = severe), and muscularis/serosa (0 = normal; 1 = moderate to severe). The average scores of eight randomly selected fields for all four individual scores were added, which resulted in a total scoring range of 0–12 per colon.

Analysis of Gut Microbiota Using 16S rRNA Gene Sequencing

The 16S rRNA gene sequencing method has been previously described (33). Total bacterial DNA was extracted from frozen cecal content, the V3-V4 region of the 16S rRNA gene was amplified, and a DNA library was constructed. Paired-end sequencing with a read length of 2 × 150 bp was performed using the Illumina HiSeq platform (Illumina, Inc., San Diego, California). The demultiplexed paired-end reads were joined using the FLASH v1.2.7 software (35), quality filtered (36), and the chimerism was removed (37). The resulting tags were then assigned to OTUs (38) with a 97% threshold of pairwise identity and aligned using the Silva reference database (Release 128, http://www.arb-silva.de) (39).

Quantification of Inflammatory Cytokines in Mouse Plasma

Mouse plasma samples were centrifuged at 3,000 rpm for 10 minutes at 4°C, then the supernatant was collected and diluted 2-fold using the diluent provided in the Proinflammatory Panel 1 (mouse) V-PLEXTM Kit. The concentrations of IL-6 and IL-1β were measured using the V-PLEXTM mouse IL-6 Kit and V-PLEXTM mouse IL-1β Kit on a MESO QuickPlex SQ 120 (Mesoscale Discovery, Rockville, MD) according to the manufacturers' instructions.

Gene Expression Analysis by qRT-PCR

The relative expression levels of genes related to intestinal barrier function (*Claudin1*, *Claudin2*, *ZO-1*, and *Occludin*) in the colon were determined using qRT-PCR. Total RNA was extracted from a 1-cm-long colon segment following the cecum using the TRIzol RNA extraction method (Invitrogen, Carlsbad, CA, USA) and quantified using a NanoDrop 2,000 spectrophotometer. The total quantified RNA was then reverse transcribed to cDNA using a QuantiTect Reverse Transcription Kit (Qiagen, USA). The relative expression levels of the selected genes were determined using the ViiA™ 7 Real-Time PCR System (Applied Biosystems, USA). The Ct values of each gene were first normalized to the housekeeping gene *GAPDH* (ΔCt value), and the fold-change in the same gene in the control sample (mice from the CTRL group) was calculated using the $2^{-\Delta\Delta Ct}$ method for mRNA quantification. The primer sequences for all the genes (*GAPDH*, *claudin 1*, *claudin 2*, *ZO-1*, and *occludin*) are provided in (**Supplementary Table 3**).

TABLE 1 | The significantly differential compounds in FM flour vs. F-FM flour.

Name	FM (Mean ± SD)	F-FM (Mean ± SD)	Fold change	*P*-Value
Phosphoric acid	0.027 ± 0.0021	0.016 ± 0.0016	0.61	0.0022
Cytosine	0.0073 ± 0.00094	0.27 ± 0.021	37.40	0.0020
Hypoxanthine	0.19 ± 0.00099	0.34 ± 0.0072	1.82	<0.0001
Niacinamide	0.071 ± 0.0046	0.23 ± 0.0099	3.32	<0.0001
Adenosine	1.30 ± 0.029	0.21 ± 0.0043	0.16	0.00018
Choline	3.59 ± 0.59	8.29 ± 0.31	2.31	0.00025
D-Proline	0.71 ± 0.033	0.98 ± 0.013	1.37	0.00021
Pyrrolidine	0.0069 ± 0.0019	0.041 ± 0.00036	5.95	<0.0001
Yuccaol C	0.15 ± 0.013	0.28 ± 0.012	1.89	0.00022
2,5-Dihydro-2,4-dimethyloxazole	0.36± 0.016	0.52 ± 0.083	1.44	0.032
L-Serine	0.071 ± 0.0060	0.014 ± 0.0034	0.20	0.00014
Guanine	0.16 ± 0.012	2.55 ± 0.055	16.27	<0.0001
N2,N2-Dimethylguanosine	0.0063 ± 0.00036	0.018 ± 0.00066	2.83	<0.0001
Putrescine	0.016 ± 0.00037	0.019 ± 0.00052	1.19	0.0011
6-Angeloylfuranofukinol	0.0043 ± 0.00039	0.13 ± 0.0038	31.14	0.00025
N-Methyltyramine	2.09 ± 0.17	4.32 ± 0.093	2.06	<0.0001
(Â±)-erythro-Isoleucine	1.70 ± 0.051	0.089 ± 0.0078	0.052	0.00025
ent-Epiafzelechin(2a->7,4a->8)epiafzelechin 3-(4-hydroxybenzoic acid)	0.019 ± 0.00031	0.0090 ± 0.00053	0.48	<0.0001
11-Hydroxyeicosatetraenoate glyceryl ester	0.00090 ± 0.00014	0.00015 ± 0.000065	0.17	0.0012
L-Phenylalanine	1.11 ± 0.077	0.13 ± 0.011	0.12	0.0017
2-Furancarboxaldehyde	2.09 ± 0.072	0.15 ± 0.0054	0.072	0.00042
p-Aminobenzoic acid	0.40 ± 0.0085	0.35 ± 0.015	0.86	0.0052
Prostaglandin H2 2-glyceryl Ester	0.021 ± 0.0014	0.012 ± 0.00026	0.59	0.00049
Benzyl gentiobioside	0.0010 ± 0.00016	0.00054 ± 0.000040	0.51	0.0060
L-Threonine	0.034 ± 0.0034	0.026 ± 0.0027	0.75	0.027
Guanosine	0.087 ± 0.0019	0.007 8± 0.00050	0.090	<0.0001
13,14-Dihydro-15-keto PGF2a	0.0034 ± 0.00036	0.0051 ± 0.00029	1.50	0.0029

Statistics

Data sets involving more than two groups were assessed using one-way ANOVA, followed by Fisher's LSD *post hoc* tests using GraphPad Prism version 6.00 for Windows (GraphPad Software Inc., USA). A value of $P < 0.05$ was considered to be statistically significant and presented as the mean ± SD. A heatmap was created based on transformed z-score values using the HemI software.

RESULTS

Comparison of the Main Compounds of Differential Pre-treated Foxtail Millet Flours

The main compounds of Foxtail millet flours were identified using LC/MS. Comparisons with accurate mass and MS/MS data of natural products in MS2 databases revealed more than 1,000 main compounds in foxtail millet flours; In order to accurately identify more compounds influenced by different pre-treated methods, a strict filter condition was set (MS score > 0.99; VIP > 1). After filtering, the changes of the main compounds across the groups were compared, and compounds that significantly changed ($P < 0.05$) were listed in **Tables 1–3**.

As shown in **Tables 1–3**, when comparing the effects of differential pre-treatment methods (fermentation, germination, or both) on the main compounds in foxtail millet whole grain (F-FM vs. FM; G-FM vs. FM; FG-FM vs. FM), 27 deferentially expressed compounds were identified in F-FM (compared to FM); 29 deferentially expressed compounds were identified in G-FM (compared to FM); 29 deferentially expressed compounds were identified in FG-FM (compared to FM). It was worth noting that 19 compounds had significant changes in all three comparisons (F-FM vs. FM; G-FM vs. FM; FG-FM vs. FM). Out of these 19 compounds, 8 of them, including Niacinamide, D-Proline, Pyrrolidine, Yuccaol C, Putrescine, N-Methyltyramine, 2-[4-(3-Hydroxypropyl)-2-methoxyphenoxy]-1,3-propanediol 1-xyloside, and Benzyl gentiobioside were up-regulated in all three pre-treated foxtail millets (F-FM, G-FM, FG-FM) when compared to un-treated foxtail millet whole grain (FM).

TABLE 2 | The significantly differential compounds in FM flour vs. G-FM flour.

Name	FM (Mean ± SD)	G-FM (Mean ± SD)	Fold change	*P*-Value
Phosphoric acid	0.027 ± 0.0021	0.054 ± 0.0029	2.03	0.00018
Niacinamide	0.071 ± 0.0046	0.23 ± 0.0076	3.29	<0.0001
Adenosine	1.30 ± 0.029	1.48 ± 0.058	1.14	0.0087
Choline	3.59 ± 0.59	8.90 ± 1.70	2.48	0.0070
D-Proline	0.71 ± 0.033	5.39 ± 0.54	7.56	0.0042
Pyrrolidine	0.0069 ± 0.0019	0.22 ± 0.083	32.51	0.045
Yuccaol C	0.15 ± 0.013	0.24 ± 0.024	1.67	0.0035
2,5-Dihydro-2,4-dimethyloxazole	0.36 ± 0.016	0.53 ± 0.10	1.47	0.044
L-Serine	0.071 ± ± 0.0060	0.24 ± 0.046	3.47	0.021
N2,N2-Dimethylguanosine	0.0063 ± 0.00036	0.0019 ± 0.00064	0.30	0.00049
Avocadyne	0.022 ± 0.00029	0.013 ± 0.000081	5.67	<0.0001
2-Pyrrolidinone	0.051 ± 0.0021	0.060 ± 0.0052	1.18	0.044
Putrescine	0.016 ± 0.00037	0.10 ± 0.021	6.38	0.020
6-Angeloylfuranofukinol	0.0043 ± 0.00039	0.012 ± 0.00055	2.71	<0.0001
N-Methyltyramine	2.09 ± 0.17	4.09 ± 0.063	1.95	<0.0001
(Â±)-erythro-Isoleucine	1.70 ± 0.051	18.47 ± 1.69	10.85	0.0034
ent-Epiafzelechin(2a->7,4a->8)epiafzelechin 3-(4-hydroxybenzoic acid)	0.019 ± 0.00031	0.0092 ± 0.0025	0.49	0.021
2-[4-(3-Hydroxypropyl)-2-methoxyphenoxy]-1,3-propanediol 1-xyloside	0.0012 ± 0.00011	0.0016 ± 0.00013	1.41	0.0084
11-Hydroxyeicosatetraenoate glyceryl ester	0.00090 ± 0.00014	0.0063 ± 0.00060	7.06	0.00011
Quinoline	0.0079 ± 0.0011	0.033 ± 0.0020	4.21	<0.0001
Oxolan-3-one	0.043 ± 0.0023	0.050 ± 0.00082	1.16	0.0071
L-Phenylalanine	1.11 ± 0.077	14.44 ± 0.44	13.01	<0.0001
2-Furancarboxaldehyde	2.09 ± 0.072	3.59 ± 0.31	1.72	0.0012
Maltotetraose	0.00056 ± 0.00012	0.0025 ± 0.000031	4.53	0.00050
Piperidine	0.016 ± 0.0018	0.023 ± 0.0020	1.45	0.010
Benzyl gentiobioside	0.0010 ± 0.00016	0.046 ± 0.0048	43.46	0.0038
L-Threonine	0.034 ± 0.0034	0.46 ± 0.042	13.48	0.0031
Guanosine	0.087 ± 0.0019	0.17 ± 0.0038	1.91	<0.0001
13,14-Dihydro-15-keto PGF2a	0.0034 ± 0.00036	0.0016 ± 0.00011	0.48	0.0012

TABLE 3 | The significantly differential compounds in FM flour vs. FG-FM flour.

Name	FM (Mean ± SD)	FG-FM (Mean ± SD)	Fold change	*P*-Value
Phosphoric acid	0.027 ± 0.0021	0.12 ± 0.0058	4.41	<0.0001
Cytosine	0.0073 ± 0.00094	0.63 ± 0.030	87.18	0.00078
Hypoxanthine	0.19 ± 0.00099	1.12 ± 0.016	5.95	<0.0001
Niacinamide	0.071 ± 0.0046	0.55 ± 0.010	7.75	<0.0001
Adenosine	1.30 ± 0.029	0.50 ± 0.014	0.38	<0.0001
Thiamine	0.086 ± 0.027	0.036 ± 0.0025	0.42	0.088
Etonogestrel	0.0042 ± 0.00069	0.019 ± 0.0011	4.55	<0.0001
D-Proline	0.71 ± 0.033	6.46 ± 0.27	9.07	0.00064
Pyrrolidine	0.0069 ± 0.0019	0.22 ± 0.054	31.50	0.021
Yuccaol C	0.15 ± 0.013	0.35 ± 0.092	2.43	0.056
L-Serine	0.071 ± 0.0060	0.0012 ± 0.00031	0.017	0.0024
Guanine	0.16 ± 0.012	6.81 ± 0.18	43.46	0.00024
N2,N2-Dimethylguanosine	0.0063 ± 0.00036	0.020 ± 0.00074	3.13	<0.0001
Avocadyne	0.022 ± 0.00029	0.0093 ± 0.00078	4.12	0.00013
Putrescine	0.016 ± 0.00037	0.070 ± 0.014	4.35	0.021
6-Angeloylfuranofukinol	0.0043 ± 0.00039	0.093 ± 0.0024	21.54	0.00018
N-Methyltyramine	2.09 ± 0.17	5.17 ± 0.097	2.47	<0.0001
(Â±)-erythro-Isoleucine	1.70 ± 0.051	8.24 ± 0.66	4.84	0.0033
ent-Epiafzelechin(2a->7,4a->8)epiafzelechin 3-(4-hydroxybenzoic acid)	0.019 ± 0.00031	0.0014 ± 0.00036	0.074	<0.0001
2-[4-(3-Hydroxypropyl)-2-methoxyphenoxy]-1,3-propanediol 1-xyloside	0.0012 ± 0.00011	0.0015 ± 0.000083	1.30	0.012
Quinoline	0.0079 ± 0.0011	0.020 ± 0.0014	2.58	0.00027
L-Phenylalanine	1.11 ± 0.077	5.18 ± 0.12	4.67	<0.0001
2-Furancarboxaldehyde	2.09 ± 0.072	4.08 ± 0.20	1.96	<0.0001
Maltotetraose	0.00056 ± 0.00012	0.0085 ± 0.00035	15.10	<0.0001
Benzyl gentiobioside	0.0010 ± 0.00016	0.032 ± 0.00057	31.02	<0.0001
L-Threonine	0.034 ± 0.0034	0.083 ± 0.010	2.43	0.0015
Guanosine	0.087 ± 0.0019	0.032 ± 0.00086	0.37	<0.0001
13,14-Dihydro-15-keto PGF2a	0.0034 ± 0.00036	0.0014 ± 0.00017	0.40	0.00082
L-Valine	0.21 ± 0.0083	0.13 ± 0.0029	0.62	<0.0001

Body Weight Loss and DAI

After five days of exposure to DSS, all mice exposed to DSS developed certain symptoms of enteritis in comparison to the untreated CTRL group, manifested by significant weight loss, severe diarrhea, and rectal bleeding (**Figure 2**). As shown in **Figure 2A**, disease progression in the 93MD group was obviously faster than in the foxtail millet-based diet groups. At the end of DSS induction (Day 5), mice that were fed millet-based diets had a DAI index that was significantly lower than that of the 93MD group, indicating that the four different pre-treated foxtail millet whole grains could relieve the symptoms of enteritis to varying degrees (**Figure 2A**). From a numerical point of view, the disease index of the two groups fed fermented foxtail millet diets (F-FM and FG-FM) was significantly lower compared to the mice fed unfermented foxtail millet diets (FM and G-FM), although the difference was not significant due to individual variation. In comparison to the 93MD group, the body weight loss of mice from the F-FM, G-FM, and FG-FM groups was alleviated significantly, while the body weight loss of FM showed no significant differences from that of the 93MD group (**Figure 2B**). These results indicated that both fermentation and germination treatments were effective in alleviating body weight loss during the induction of enteritis in a mouse model.

Moreover, three of the 93MD group mice died at day 5 post-induction due to severe enteritis symptoms. DSS exposure was stopped by the end of day 5 to obtain more data, and the mice were fasted overnight and then dissected the next day. None of the mice in any other groups died during the colitis induction process.

Pathological Characteristics and Histopathological Scores

All groups exposed to DSS displayed typical symptoms of enteritis, such as significant shortening of the colon (**Figure 3A**) and enlarged spleen (**Figure 3B**), when compared to the control group without DSS treatment. Among the groups exposed to DSS, the shortening of the colon in the 93MD group was the most significant, while in the other groups that were fed foxtail millet-based diets, it was relieved to vary degrees. The shortening

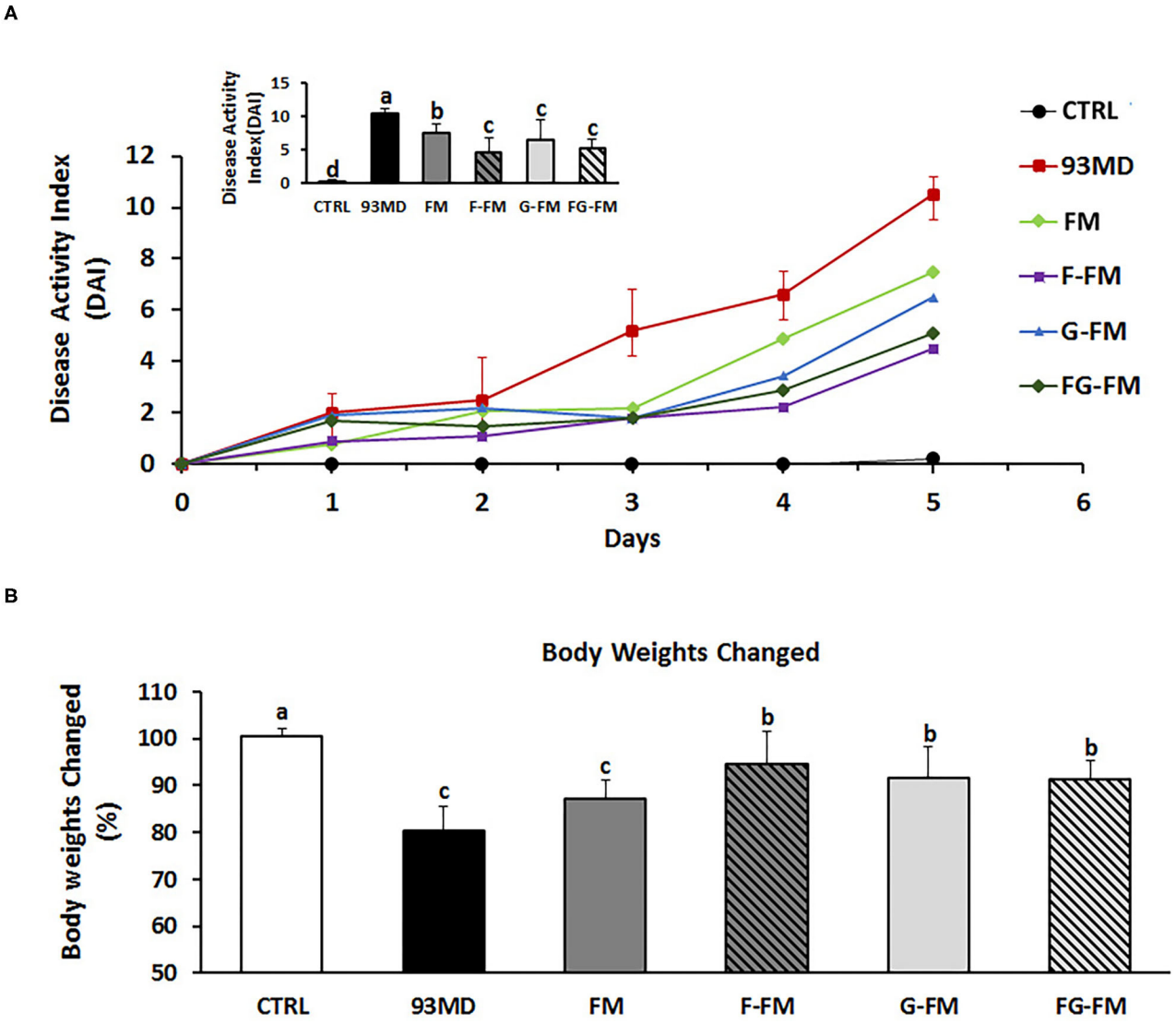

FIGURE 2 | Body physiological: **(A)** DAI (disease activity index) scores monitored every day over the 5 days of DSS exposure; **(B)** relative changes in body weights on day 5 post-induction; comparisons of various anatomical measurements among five groups using one-way analysis of variance (ANOVA), followed by Fisher's LSD *post hoc* tests. Bars with the same letter indicate a non-significant difference ($P > 0.05$). Data are expressed as the mean ±SD. Sample size: $n = 7$ in 93MD group, $n = 10$ in other groups.

of the colon in the FM group was not relieved as well as in the other foxtail millet-based diet groups. There were no significant differences in the spleen weights of the DSS-treated groups fed different diets.

Histopathological examination (**Figures 3C,D**) of the colon revealed that DSS treatment induced epithelial injury in all eight DSS-treated groups. According to histopathological scores (**Figure 3D**), mice in the F-FM and FG-FM groups had significantly less intestinal damage than mice in the 93MD group, indicating that the fermentation process was essential to improve the ability of foxtail millet whole grains to protect mice from intestinal injury induced by DSS exposure. When combined with the histological scores of colon tissue damage, DAI, and other indicators, it was concluded that FG-FM was more effective in preventing or alleviating symptoms of colitis.

Gut Microbial Diversity Indices

The Chao1 index (**Figure 4A**) and Shannon diversity index (**Figure 4B**) were calculated to determine the effects of foxtail millet-based diets on the richness and diversity of bacterial species, respectively. Exposure to DSS induction significantly decreased both the Chao1 index and Shannon diversity index (CTRL vs. 93MD). The FM, F-FM, G-FM, and FG-FM groups had significantly higher Chao1 indices than the 93MD group, indicating that diets made from foxtail millet whole grains significantly restored the bacterial richness of gut microbiota.

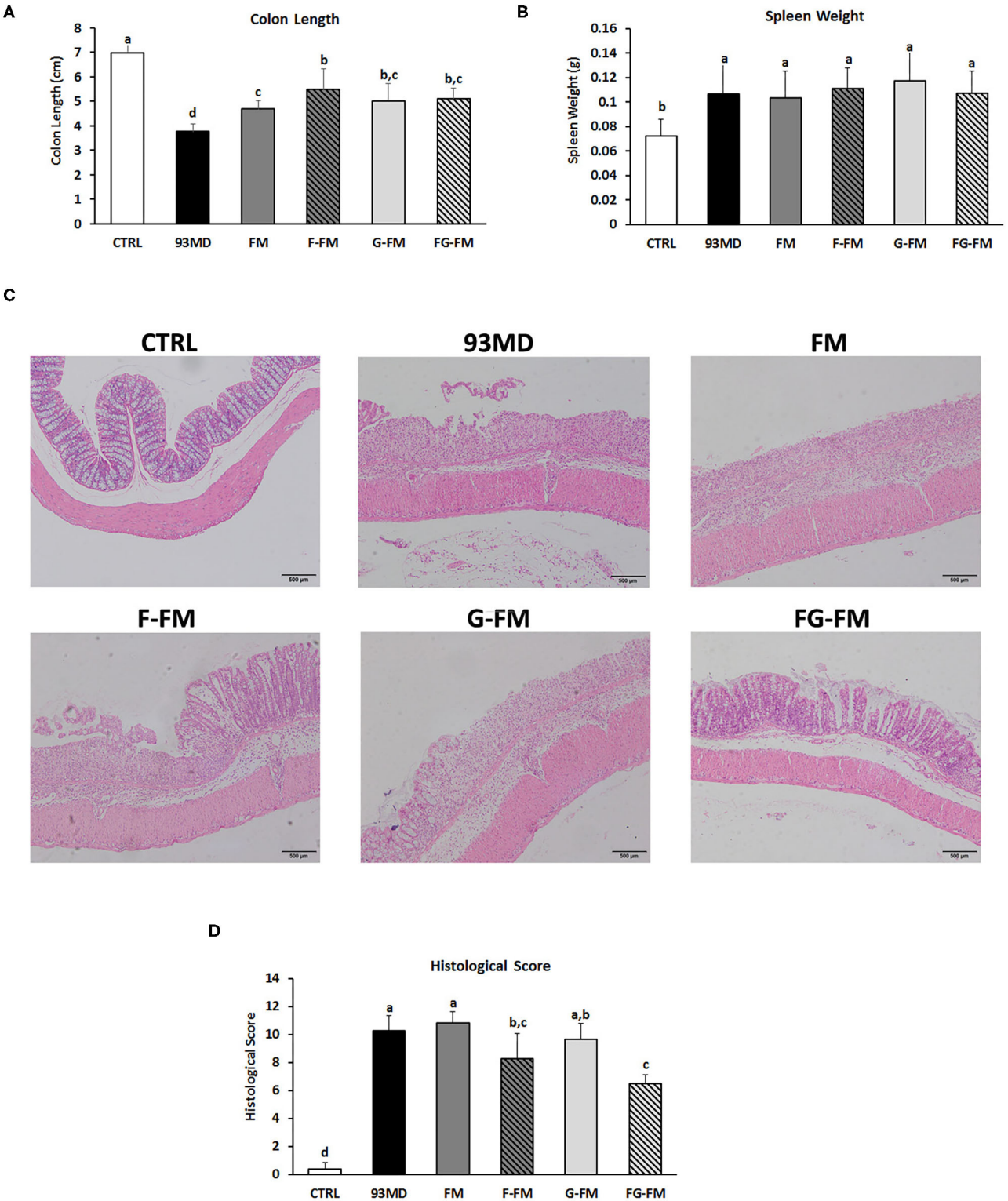

FIGURE 3 | Pathological and histopathological characteristics in different groups: **(A)** lengths of colon from different diet groups; **(B)** spleen weights of the different groups; **(C)** histological analysis and **(D)** histological severity scores of the different treatment mice. Comparisons of various anatomical measurements among six groups using one-way analysis of variance (ANOVA), followed by Fisher's LSD *post hoc* tests. Data are expressed as the mean ± SD. Bars with the same letter indicate a non-significant difference ($P > 0.05$). Sample size: $n = 7$ in 93MD group, $n = 10$ in other groups.

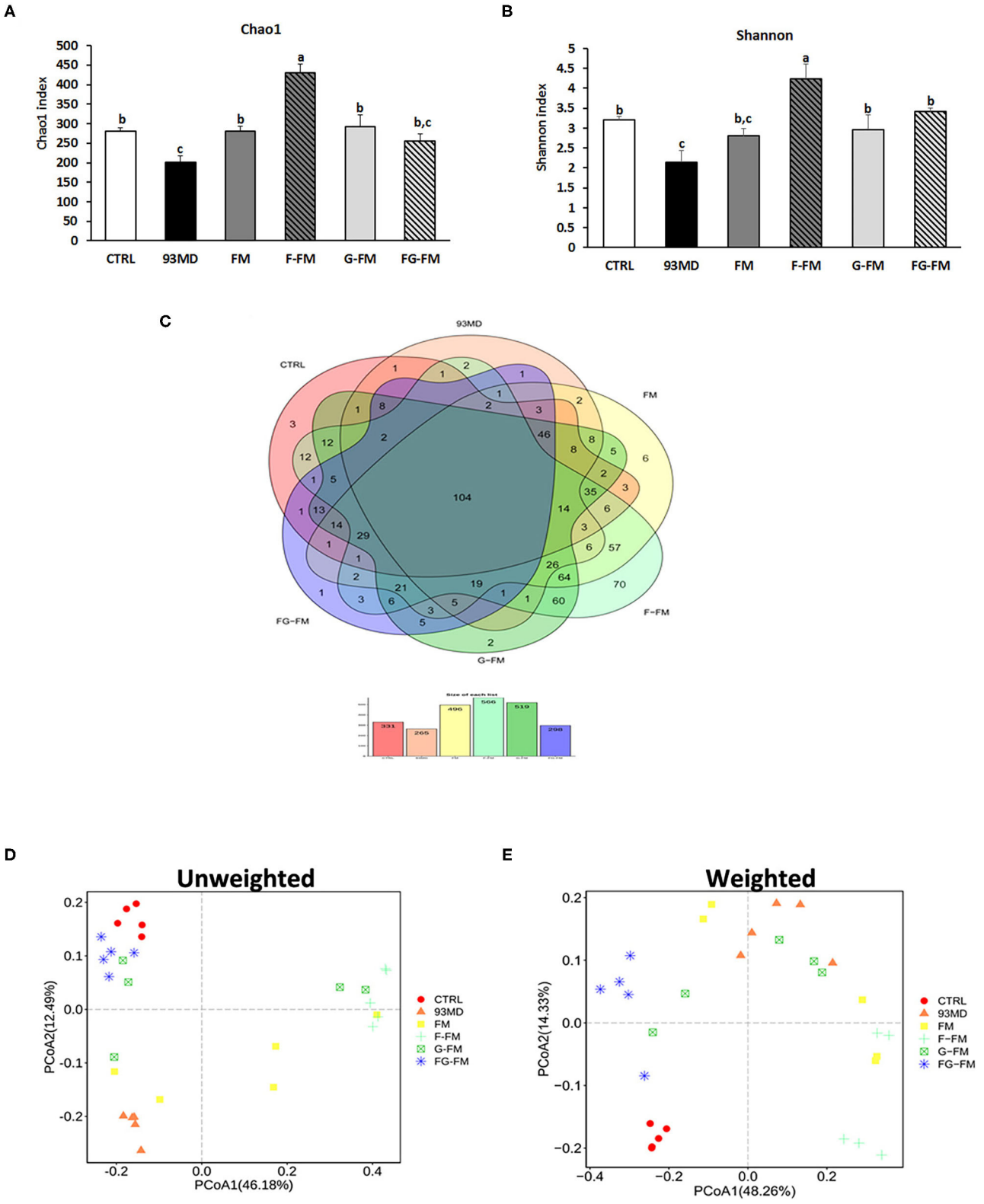

FIGURE 4 | Microbiota diversity indices of the different groups: **(A)** the bacterial richness of microbiota communities estimated by the Chao1 value. **(B)** The bacterial diversity of the microbiota communities estimated by the Shannon index; **(C)** Venn diagrams that illustrated the observed overlap of OTUs; **(D)** PCoA plot of unweighted UniFrac distance values and **(E)** weighted UniFrac distance values. All groups of α diversity indices (Chao1 and Shannon) were analyzed by one-way analysis of variance (ANOVA) followed by Fisher's LSD *post hoc* tests. Bars with the same letter indicate a non-significant difference ($P > 0.05$). Five samples per group were randomly selected for microbiota analysis.

Shannon indices were similar to Chao 1 indices in terms of details, except that the index of the FM group was not significantly higher than the 93MD group, indicating that foxtail millet whole grains pretreated by germination and fermentation had a stronger ability to restore intestinal microbial diversity than untreated foxtail millet whole grain. The shared and specific OTUs among different groups are represented by Venn diagrams in **Figure 4C**. A total of 106 OTUs were shared by all six groups, with the F-FM group having the largest number of unique OTUs (seventy). This was consistent with the results of the Chao1 and Shannon indices, which showed that the F-FM group had the highest scores. The improvement of these two indices in the foxtail millet whole grain-based diet group indicated that the foxtail millet whole grain (especially pretreated forms) had a positive effect on the intestinal flora ecosystem. There are reductions in bacterial species richness and diversity in IBD patients (40) and animal models of enteritis (33). Therefore, the promotion of microbial diversity benefits from foxtail millet whole grains may be attributed to the prevention of colitis-related symptoms.

The principal coordinates analysis (PCoA) of weighted and unweighted UniFrac distance matrix of gut microbiota is shown in **Figure 4D**, (unweighted) **Figure 4E** (weighted). In both the weighted and unweighted UniFrac plots, the CTRL group showed a significant difference from the 93MD group, as well as clear aggregation with the FG-FM group. In the unweighted UniFrac matrices, neither principal coordinate 1 (PC1, 38.48%) nor PC2 (15.27%) could separate the CTRL group from the FG-FM group; in the weighted UniFrac matrices, the CTRL and FG-FM groups did not separate in PC1 (41.81%) but were barely separated in PC2 (14.15%). This result demonstrated that intake of the FG-FM diet restored the disturbance in gut microbiota composition caused by enteritis to the greatest extent in mouse models. This positive reaction of the structure of gut microbiota communities to FG-FM diets provides important information for further research and development of functional foods for IBD.

Composition of Gut Microbiota in Different Groups

As illustrated in **Figures 5A,B**, the composition of gut microbiota varied significantly in mice from different treatment groups. **Figure 5A** shows the significant variation in the composition of gut microbiota in mice from different groups at the phylum level. In the CTRL group, *Firmicutes* was the most dominant bacterial community (36.1%), followed by *Proteobacteria* (32.5%) and *Bacteroidetes* (22.5%). On the other hand, in the 93MD group, there was a significant reduction in the relative abundance of *Firmicutes* and *Bacteroidetes* (*Firmicutes* = 26.4%; *Bacteroidetes* = 4.1%) and a significant increase in the relative abundance of *Proteobacteria*, which were the most dominant (40.3%). This finding was consistent with the literature, which reported that the unusual expansion of *Proteobacteria* could be considered a "signature" of dysbiosis in gut microbiota (10, 41, 42). It was worth noting that in the four groups that were fed foxtail millet whole grain-based diets, the gut microbiota composition of the mice from the FG-FM group (*Firmicutes,* 51.7%; *Bacteroidetes,* 30.8%; *Proteobacteria,* 8.3%) was close to the 'normal' state of the CTRL group, which was also consistent with the PCoA results.

The composition analysis of the gut microbiota at the genus level (**Figure 5B**) revealed dramatic blooms of the genera *Escherichia-Shigella* and *Helicobacter* in the 93MD group (*Escherichia-Shigella*, 36.1%; *Helicobacter,* 26.4%), which were almost undetectable in the CTRL group. *Escherichia-Shigella* even occupied a predominant position in the gut microbiota of the 93MD group. However, the overexpansion of *Escherichia-Shigella* and *Helicobacter* was almost completely suppressed in the gut microbiota of mice from the F-FM and FG-FM groups.

The significant OTUs (operational taxonomic units) associated with DSS induction and diet intervention were also analyzed (**Figure 5C**). The corresponding detailed data, statistical results, and classification information are presented in **Supplementary Material**. As shown in **Figure 5C**, the numbers of OTU2, OTU1, OTU48, OUT20, OTU2, OTU2009, OTU180, and OTU31 increased in the 93MD group (compared to the CTRL group), whereas the increasing trend was inhibited to varying degrees in the foxtail millet whole-grain diet groups. These OTUs were classified as uncultured bacteria from the genera OTU2 *Helicobacter* (OTU2), *Escherichia-Shigella* (OTU1), *Allobaculum* (OTU48), *Coriobacteriaceae_UCG-002* (OTU20), *Mucispirillum* (OTU2009 and OTU180), and *Dubosiella* (OTU31). Unlike *Helicobacter* and *Escherichia-Shigella,* the genera *Allobaculum*, *Coriobacteriaceae_UCG-002*, *Mucispirillum*, and *Dubosiella* could not be classified as either pro-inflammatory or anti-inflammatory bacteria. Taking the genus *Mucispirillum* as an example, it was identified to be associated with inflammatory bowel disease (43) or other inflammatory diseases (44), whereas it was also reported to be related to a healthier state of gut microbiota (45). These seemingly contradictory conclusions also reflect the complexity of gut microbiota structure and function.

According to **Figure 5C**, there were 16 OTUs that obviously decreased in the 93MD group compared to the CTRL group, and six of these OTUs (including OTUs 56, 22, 54, 76, 99 and 106) showed the same characteristics; that is, the numbers of these six OTUs showed an obvious rebond in the FG-FM group. These six OTUs were classified into uncultured bacterial strains from the genus *Lachnoclostridium* (OTU106), genus *Desufovibrio* (OTU22), and *Lachnospiraceae NK4A136* group (OTU76) and three uncultured bacterial strains from the family *Muribaculaceae* (OUT54, OTU56, and OTU99). Moreover, there were 5 OTUs significantly higher in the FG-FM group than in the other five groups, which were classified as species *Mucispirillum schaedleri* ASF457 (OTU25), uncultured bacteria from the genus *Lactobacillus* (OTU45), genus *Alistipes* (OTU50), and family *Muribaculaceae* (OTU49 and OTU86). Five OTUs classified to the family *Muribaculaceae* were significantly higher in the FG-FM group, which was consistent with the predominant position of *Muribaculaceae* in the gut microbiota of the FG-FM group (demonstrated in **Figure 5B**).

Plasma Levels of Inflammatory Cytokines and Colonic Barrier Function

The levels of the inflammatory cytokines IL-6 and IL-1β in the plasma are shown in **Figure 6**. DSS exposure increased the

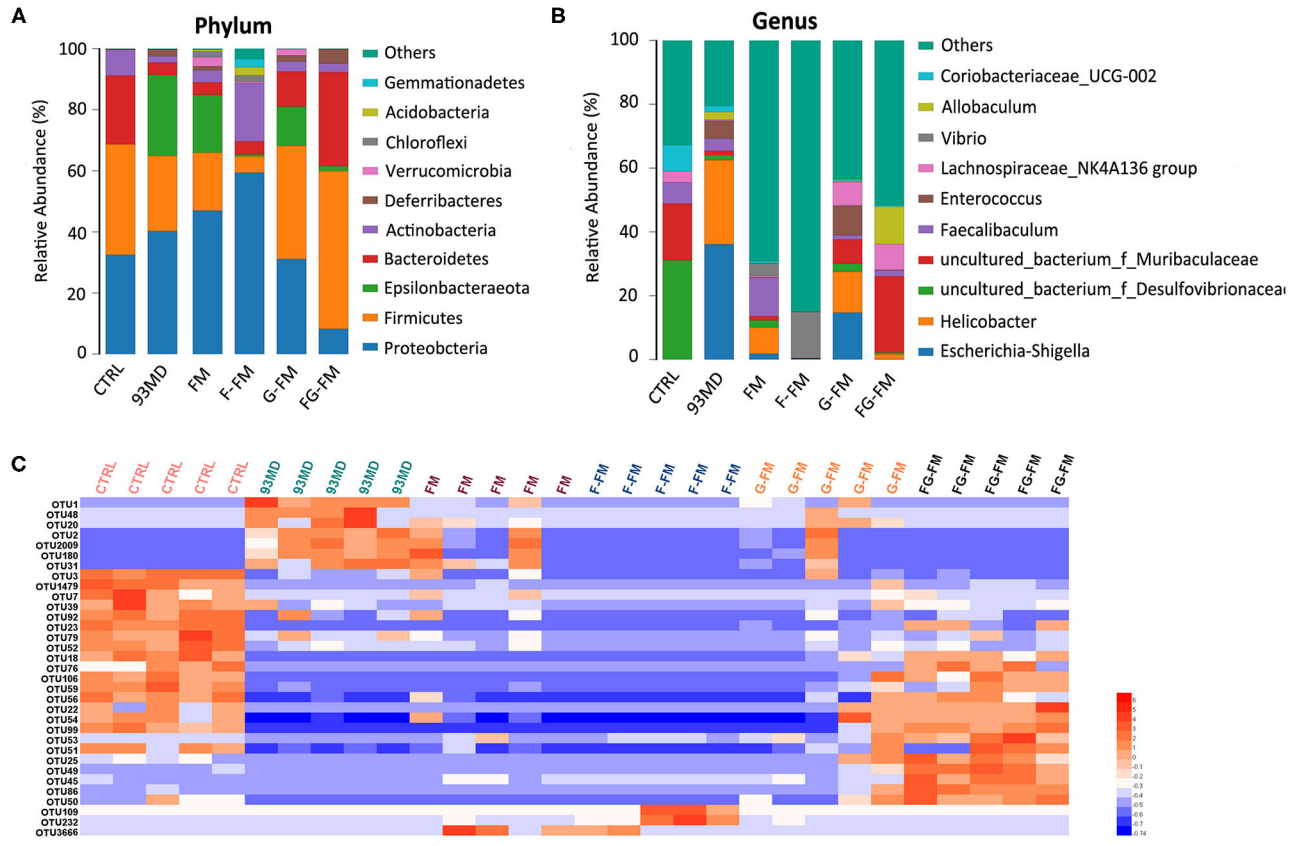

FIGURE 5 | Compositions of gut microbiota in mice at the **(A)** phylum level and **(B)** genus level in all experimental groups and **(C)** heatmap of OTUs (average OTU numbers >100) with significant differences in the gut microbiota of mice ($n = 5$/group).

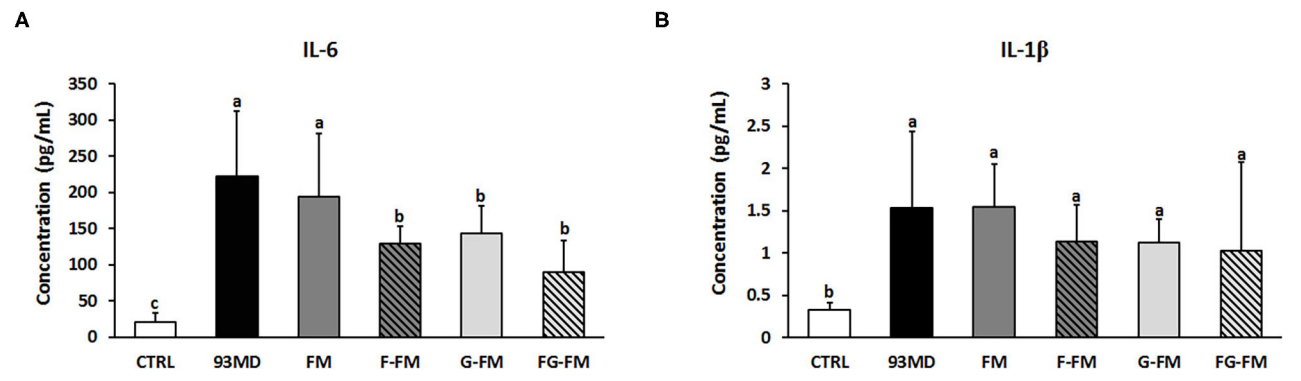

FIGURE 6 | Levels of inflammatory cytokines in the plasma of mice, **(A)** IL-6; **(B)** IL-1β. All data were analyzed by one-way analysis of variance (ANOVA) followed by Fisher's LSD *post-hoc* tests. Bars with the same letter indicate a non-significant difference ($P > 0.05$). Sample size: $n = 7$ in 93 MD group, $n = 10$ in other groups.

circulating levels of IL-6 and IL-1β compared to the untreated CTRL group. Certain foxtail millet whole grain-based diets reduced the levels of IL-6, with the FG-FM group showing the most potent anti-inflammatory effects.

As demonstrated in **Table 4**, the expression levels of two key tight junction proteins, *ZO-1* and *occludin*, were dramatically decreased in the DSS-induced colitis mice compared to the CTRL group. The loss of *ZO-1* and *occludin* genes has been reported in DSS-induced colitis mouse models (46, 47). The expression of *ZO-1* and *occludin* was also below the detection level in the 93MD group. However, it was partially restored in the foxtail millet-based diet-fed mice, especially *ZO-1* in the FG-FM group. Unlike *ZO-1* and *occludin*, the expression of *claudin 1* and *claudin 2* was significantly upregulated in the majority of

TABLE 4 | Expression levels of genes related to gut barrier function in the mouse colon.

Groups	*Claudin1*	*Claudin2*	*ZO-1*	*Occludin*
CTRL	1.00 ± 0.43 **(b)**	1.00 ± 0.44 **(b, c)**	1.00 ± 0.27 **(a)**	1.00 ± 0.079 **(a)**
93MD	10.97 ± 8.16 **(a)**	1.53 ± 0.23 **(a)**	ND*	ND*
FM	8.49 ± 3.31 **(a)**	1.29 ± 0.61 **(a, b)**	0.020 ± 0.025 **(b)**	0.0052 ± 0.0043 **(b)**
F-FM	7.69 ± 2.92 **(a)**	1.19 ± 0.39 **(a, b)**	0.29 ± 0.37 **(b)**	0.016 ± 0.022 **(b)**
G-FM	8.03 ± 4.62 **(a)**	1.21 ± 0.27 **(a, b)**	0.25 ± 0.44 **(b)**	0.0017 ± 0.0015 **(b)**
FG-FM	6.49 ± 2.71 **(a)**	0.69 ± 0.12 **(c)**	0.52 ± 0.88 **(a)**	0.018 ± 0.011 **(b)**

The data are expressed as the relative fold change compared to the CTRL group.
Data were expressed as Mean ± SD.
The same letter (Bold) indicates a non-significant difference ($P > 0.05$).
**Indicated below the detection limit (non-detectable).*

DSS-induced colitis mice when compared to the CTRL group without DSS treatment. This observation was consistent with previous studies that reported the upregulation of *claudin 1* and *claudin 2* increased intestinal permeability and aggravated inflammation (48, 49). The intake of the FG-FM diet significantly inhibited the overexpression of *claudin2*, which also indicated the maintenance of gut barrier function in this group.

DISCUSSION

Despite continuous efforts, the existing drugs and treatments are still not completely effective for the treatment and prevention of IBD, and pharmacological side effects of drugs are usually inevitable (50). Therefore, there is an increasing demand for the development of effective prevention strategies for IBD. Dietary strategies are very attractive in the prevention of chronic inflammation-related diseases, especially IBD, due to their low cost and safety (51). Foxtail millet is a traditional staple food in the northern areas of China and is mainly consumed as porridge. In this study, it was demonstrated that foxtail millet whole grain supplementary diets were suitable for dietary intervention in IBD. The germination or fermentation process optimized the disease suppression ability of whole-grain foxtail millet. Furthermore, whole grain foxtail millet that had undergone dual processing of germination and fermentation showed excellent anti-inflammatory properties and prebiotic characteristics, which makes it not only effective for IBD patients but also has the potential to be used as an approach to treat or prevent other intestinal diseases.

When the foxtail millet was consumed as whole grain without debranning and polishing, the fermentation process significantly enhanced its prebiotic characteristics and function to alleviate the symptoms of colitis. When consumed as a whole grain, it introduced higher dietary fiber to the diet. Although dietary fibers have been reported to possess clinical benefits for IBD patients (52), the untreated whole grain foxtail millet had no effect on relieving the symptoms of colitis in this study. However, whole grain foxtail millet that had been germinated or fermented, especially those that had undergone both the germination and fermentation processes (FG-FM group), could relieve the symptoms of enteritis to varying degrees.

The analysis of compounds in different pre-treated foxtail millet could also partially explain why the fermentation or germination process could significantly improve colitis symptoms relief and its prebiotic abilities. Despite the availability of various compounds and that most of them have not been extensively studied, the relationships between several compounds and IBD have been established. For example, nicotinamide, which was up-regulated via both fermentation and germination process, have been proved to contribute to the amelioration of experimental colitis (53). A similar case is the compound N-methyltyramine (54), although there is no direct evidence to prove its beneficial effect on IBD, a recent study has begun to focus on its role in intestinal health. Due to the complexity of the changes in the chemical composition of foxtail millet whole grain caused by fermentation or germination, the more attention should focus on this area.

The FG-FM flour displayed excellent prebiotic characteristics, including restoration of the overall composition of the intestinal flora to near-normal levels, inhibition of the proliferation of the conditional pathogenic bacteria, and promotion of beneficial bacteria growth.Although the underlying mechanism is far to be fully understood, there is no doubt that the gut microbiota plays a vital role in the pathogenesis and development of IBD (6, 10). This can also explain why FG-FM was effective in relieving the symptoms of colitis to a certain extent. For instance, *Escherichia-Shigella*, which was prevalent in the IBD patients (55), and also had higher relative abundance in the DSS-induced colitis model (56), was almost completely suppressed in the FG-WFM diet-fed mice. The predominant position of *Muribaculaceae* in the gut microbiota of the FG-FM group was also observed. In most studies, *Muribaculaceae* (also known as S24-7 clade or *Candidatus Homeothermaceae*) was significantly decreased in disease models (such as obesity, diabetes, and intestinal colitis) and rebonded fowllowing effective treatment or dietary intervention (57–59). Therefore, an increase in *Muribaculaceae* should be considered as a marker of the recovery of gut microbiota. In addition, the growth stimulation of probiotics, such as *Lactobacillus* (56), may be associated with the alleviation of colitis symptoms in the FG-FM group. This evidence indicated that the prebiotic characteristics of FG-FM might contribute to the alleviation of the symptoms of colitis in mouse models.

The foxtail millet whole grain-based diet (FG-FM) also displayed efficient anti-inflammatory activity in DSS-induced colitis mouse models. The rebalancing ability of FG-FM on gut microbiota contributed to its excellent anti-inflammatory activity based on the reported role of gut microbiota in inflammation (6). Functional loss of the gut barrier and a decrease in gut permeability are also characteristics of IBD. The upregulation of *ZO-1* and *occludin* expressions, as well as the downregulation of *claudin 2* expression, indicated that FG-FM consumption significantly increased the function of the gut barrier. Furthermore, a study reported that IL-6 monoclonal antibody treatment using DSS-induced colitis mouse models effectively suppressed the expression of *claudin 2* and attenuated gut permeability (60). This finding suggested that in FG-FM diet-fed mice, a decrease in inflammatory cytokine levels is correlated with an improved gut barrier function.

In summary, this study demonstrated that the foxtail millet supplementary diets are suitable for dietary intervention in IBD patients based on a mouse model. The germination or fermentation process optimizes the disease suppression ability of whole-grain foxtail millet. Moreover, whole grain foxtail millet that has undergone dual processing of germination and fermentation had excellent pro-inflammatory activity and prebiotic characteristics, making it effective not only for IBD patients but also for the treatment or prevention of other intestinal diseases.

DATA AVAILABILITY STATEMENT

The datasets presented in this study can be found in online repositories. The names of the repository/repositories and accession number(s) can be found below: https://www.ncbi.nlm.nih.gov/, PRJNA719303.

ETHICS STATEMENT

The animal study was reviewed and approved by Ethics Committee of the Institute of Agro-food Science and Technology at Shandong Academy of Agricultural Sciences (Jinan, Shandong, China).

AUTHOR CONTRIBUTIONS

WL: conceptualization, supervision, formal analysis, writing-original draft, and writing-review and editing. LL: conceptualization and writing-review and editing. YZ: investigation and writing-original draft preparation. DZ: supervision and investigation. XW: investigation. YY: resources. All authors contributed to the article and approved the submitted version.

FUNDING

This study was supported by the Key Research and Development Plan of Shandong Province (Grant Number: 2018YYSP010), the Special Foundation for Taishan Scholars (Grant Number: tsqn20161067), and the Key Project of Yunnan Provincial Agricultural Union (Grant Number: 2017FG001-015).

SUPPLEMENTARY MATERIAL

The Supplementary Material for this article can be found online at: https://www.frontiersin.org/articles/10.3389/fnut.2021.694936/full#supplementary-material

REFERENCES

1. Ni J, Wu GD, Albenberg L, Tomov VT. Gut microbiota and IBD: causation or correlation? *Nat Rev Gastroenterol Hepatol*. (2017) 14:573–84. doi: 10.1038/nrgastro.2017.88
2. Rhodes JM, Campbell BJ. Inflammation and colorectal cancer: IBD-associated and sporadic cancer compared. *Trends Mol Med*. (2002) 8:10–6. doi: 10.1016/S1471-4914(01)02194-3
3. Ng SC, Shi HY, Hamidi N, Underwood FE, Tang W, Benchimol EI, et al. Worldwide incidence and prevalence of inflammatory bowel disease in the 21st century: a systematic review of population-based studies. *Lancet*. (2018) 390:2769–78. doi: 10.1016/S0140-6736(17)32448-0
4. Nishida A, Inoue R, Inatomi O, Bamba S, Naito Y, Andoh A. Gut microbiota in the pathogenesis of inflammatory bowel disease. *Clin J Gastroenterol*. (2018) 11:1–10. doi: 10.1007/s12328-017-0813-5
5. Guan Q. A comprehensive review and update on the pathogenesis of inflammatory bowel disease. *J Immunol Res*. (2019) 2019:7247238. doi: 10.1155/2019/7247238
6. Yu LC. Microbiota dysbiosis and barrier dysfunction in inflammatory bowel disease and colorectal cancers: exploring a common ground hypothesis. *J Biomed Sci*. (2018) 25:79. doi: 10.1186/s12929-018-0483-8
7. Rowland I, Gibson G, Heinken A, Scott K, Swann J, Thiele I, et al. Gut microbiota functions: metabolism of nutrients and other food components. *Eur J Nutr*. (2018) 57:1–24. doi: 10.1007/s00394-017-1445-8
8. Nagalingam NA, Kao JY, Young VB. Microbial ecology of the murine gut associated with the development of dextran sodium sulfate-induced colitis. *Inflamm Bowel Dis*. (2011) 17:917–26. doi: 10.1002/ibd.21462
9. Mukhopadhya I, Hansen R, El-Omar EM, Hold GL. IBD-what role do Proteobacteria play? *Nat Rev Gastroenterol Hepatol*. (2012) 9:219–30. doi: 10.1038/nrgastro.2012.14
10. Palmela C, Chevarin C, Xu Z, Torres J, Sevrin G, Hirten R, et al. Adherent-invasive Escherichia coli in inflammatory bowel disease. *Gut*. (2018) 67:574–87. doi: 10.1136/gutjnl-2017-314903
11. Frank DN, St Amand AL, Feldman RA, Boedeker EC, Harpaz N, Pace NR. Molecular-phylogenetic characterization of microbial community imbalances in human inflammatory bowel diseases. *Proc Natl Acad Sci USA*. (2007) 104:13780–5. doi: 10.1073/pnas.0706625104
12. You JHS, Jiang X, Lee WH, Chan PKS, Ng SC. Cost-effectiveness analysis of fecal microbiota transplantation for recurrent Clostridium difficile infection in patients with inflammatory bowel disease. *J Gastroenterol Hepatol*. (2020) 35:1515–23. doi: 10.1111/jgh.15002
13. DuPont HL, Jiang ZD, DuPont AW, Utay NS. Abnormal intestinal microbiome in medical disorders and potential reversibility by fecal microbiota transplantation. *Dig Dis Sci*. (2020) 65:741–56. doi: 10.1007/s10620-020-06102-y

14. Isaacs K, Herfarth H. Role of probiotic therapy in IBD. *Inflamm Bowel Dis*. (2008) 14:1597–605. doi: 10.1002/ibd.20465
15. Bibbo S, Ianiro G, Giorgio V, Scaldaferri F, Masucci L, Gasbarrini A, et al. The role of diet on gut microbiota composition. *Eur Rev Med Pharmacol Sci*. (2016) 20:4742−9.
16. Santino A, Scarano A, De Santis S, De Benedictis M, Giovinazzo G, Chieppa M. Gut microbiota modulation and anti-inflammatory properties of dietary polyphenols in IBD: new and consolidated perspectives. *Curr Pharm Des*. (2017) 23:2344–51. doi: 10.2174/1381612823666170207145420
17. Obih C, Wahbeh G, Lee D, Braly K, Giefer M, Shaffer ML, et al. Specific carbohydrate diet for pediatric inflammatory bowel disease in clinical practice within an academic IBD center. *Nutrition*. (2016) 32:418–25. doi: 10.1016/j.nut.2015.08.025
18. Chen J, Duan W, Ren X, Wang C, Pan Z, Diao X, et al. Effect of foxtail millet protein hydrolysates on lowering blood pressure in spontaneously hypertensive rats. *Eur J Nutr*. (2017) 56:2129–38. doi: 10.1007/s00394-016-1252-7
19. Verma S, Srivastava S, Tiwari N. Comparative study on nutritional and sensory quality of barnyard and foxtail millet food products with traditional rice products. *J Food Sci Technol*. (2015) 52:5147–55. doi: 10.1007/s13197-014-1617-y
20. Kam J, Puranik S, Yadav R, Manwaring HR, Pierre S, Srivastava RK, et al. Dietary interventions for type 2 diabetes: how millet comes to help. *Front Plant Sci*. (2016) 7:1454. doi: 10.3389/fpls.2016.01454
21. Liu F, Shan S, Li H, Li Z. Treatment of peroxidase derived from foxtail millet bran attenuates atherosclerosis by inhibition of CD36 and STAT3 *in Vitro* and *in Vivo*. *J Agric Food Chem*. (2020) 68:1276–85. doi: 10.1021/acs.jafc.9b06963
22. Dong JL, Wang L, Lu J, Zhu YY, Shen RL. Structural, antioxidant and adsorption properties of dietary fiber from foxtail millet (Setaria italica) bran. *J Sci Food Agric*. (2019) 99:3886–94. doi: 10.1002/jsfa.9611
23. Yang R, Shan S, Zhang C, Shi J, Li H, Li Z. Inhibitory effects of bound polyphenol from foxtail millet bran on colitis-associated carcinogenesis by the restoration of gut microbiota in a mice model. *J Agric Food Chem*. (2020) 68:3506–17. doi: 10.1021/acs.jafc.0c00370
24. Shan S, Wu C, Shi J, Zhang X, Niu J, Li H, et al. Inhibitory effects of peroxidase from foxtail millet bran on colitis-associated colorectal carcinogenesis by the blockage of glycerophospholipid metabolism. *J Agric Food Chem*. (2020) 68:8295–307. doi: 10.1021/acs.jafc.0c03257
25. Kumar A, Henderson A, Forster GM, Goodyear AW, Weir TL, Leach JE, et al. Dietary rice bran promotes resistance to Salmonella enterica serovar Typhimurium colonization in mice. *BMC Microbiol*. (2012) 12:71. doi: 10.1186/1471-2180-12-71
26. Chu J, Zhao H, Lu Z, Lu F, Bie X, Zhang C. Improved physicochemical and functional properties of dietary fiber from millet bran fermented by Bacillus natto. *Food Chem*. (2019) 294:79–86. doi: 10.1016/j.foodchem.2019.05.035
27. Sharma N, Alam T, Goyal SK, Fatma S, Pathania S, Niranajan K. Effect of different storage conditions on analytical and sensory quality of thermally processed, milk-based germinated foxtail millet porridge. *J Food Sci*. (2018) 83:3076–84. doi: 10.1111/1750-3841.14371
28. Sharma S, Saxena DC, Riar CS. Changes in the GABA and polyphenols contents of foxtail millet on germination and their relationship with in vitro antioxidant activity. *Food Chem*. (2018) 245:863–70. doi: 10.1016/j.foodchem.2017.11.093
29. Pranotoa Y, Anggrahinia S, Efendib Z. Effect of natural and Lactobacillus plantarum fermentation on *in-vitro* protein and starch digestibilities of sorghum flour. *Food Biosci*. (2013) 2:46–52. doi: 10.1016/j.fbio.2013.04.001
30. Suma PF, Urooj A. Influence of germination on bioaccessible iron and calcium in pearl millet (Pennisetum typhoideum). *J Food Sci Technol*. (2014) 51:976–81. doi: 10.1007/s13197-011-0585-8
31. Doppler M, Kluger B, Bueschl C, Schneider C, Krska R, Delcambre S, et al. Stable isotope-assisted evaluation of different extraction solvents for untargeted metabolomics of plants. *Int J Mol Sci*. (2016) 17. doi: 10.3390/ijms17071017
32. Xiao HT, Lin CY, Ho DH, Peng J, Chen Y, Tsang SW, et al. Inhibitory effect of the gallotannin corilagin on dextran sulfate sodium-induced murine ulcerative colitis. *J Nat Prod*. (2013) 76:2120–5. doi: 10.1021/np4006772
33. Liu W, Zhang Y, Qiu B, Fan S, Ding H, Liu Z. Quinoa whole grain diet compromises the changes of gut microbiota and colonic colitis induced by dextran Sulfate sodium in C57BL/6 mice. *Sci Rep*. (2018) 8:14916. doi: 10.1038/s41598-018-33092-9
34. Katakura K, Lee J, Rachmilewitz D, Li G, Eckmann L, Raz E. Toll-like receptor 9-induced type I IFN protects mice from experimental colitis. *J Clin Invest*. (2005) 115:695–702. doi: 10.1172/JCI22996
35. Magoc T, Salzberg SL. FLASH: fast length adjustment of short reads to improve genome assemblies. *Bioinformatics*. (2011) 27:2957–63. doi: 10.1093/bioinformatics/btr507
36. Bolger AM, Lohse M, Usadel B. Trimmomatic: a flexible trimmer for Illumina sequence data. *Bioinformatics*. (2014) 30:2114–20. doi: 10.1093/bioinformatics/btu170
37. Edgar RC, Haas BJ, Clemente JC, Quince C, Knight R. UCHIME improves sensitivity and speed of chimera detection. *Bioinformatics*. (2011) 27:2194–200. doi: 10.1093/bioinformatics/btr381
38. Edgar RC. Search and clustering orders of magnitude faster than BLAST. *Bioinformatics*. (2010) 26:2460–1. doi: 10.1093/bioinformatics/btq461
39. Quast C, Pruesse E, Yilmaz P, Gerken J, Schweer T, Yarza P, et al. The SILVA ribosomal RNA gene database project: improved data processing and web-based tools. *Nucleic Acids Res*. (2013) 41:D590–6. doi: 10.1093/nar/gks1219
40. Pascal V, Pozuelo M, Borruel N, Casellas F, Campos D, Santiago A, et al. A microbial signature for Crohn's disease. *Gut*. (2017) 66:813–22. doi: 10.1136/gutjnl-2016-313235
41. Humbel F, Rieder JH, Franc Y, Juillerat P, Scharl M, Misselwitz B, et al. Association of alterations in intestinal microbiota with impaired psychological function in patients with inflammatory bowel diseases in remission. *Clin Gastroenterol Hepatol*. (2019) 18:2019–29. doi: 10.1016/j.cgh.2019.09.022
42. Dheer R, Davies JM, Quintero MA, Damas OM, Deshpande AR, Kerman DH, et al. Microbial signatures and innate immune gene expression in lamina propria phagocytes of inflammatory bowel disease patients. *Cell Mol Gastroenterol Hepatol*. (2019) 9:387–402. doi: 10.1016/j.jcmgh.2019.10.013
43. Shao X, Sun C, Tang X, Zhang X, Han D, Liang S, et al. Anti-inflammatory and intestinal microbiota modulation properties of jinxiang garlic (Allium sativum L.) polysaccharides toward dextran sodium sulfate-induced colitis. *J Agric Food Chem*. (2020) 68:12295–309. doi: 10.1021/acs.jafc.0c04773
44. Zhang X, Coker OO, Chu ES, Fu K, Lau HCH, Wang YX, et al. Dietary cholesterol drives fatty liver-associated liver cancer by modulating gut microbiota and metabolites. *Gut*. (2020) 70:761–74. doi: 10.1136/gutjnl-2019-319664
45. Kong H, Yu L, Gu Z, Li C, Ban X, Cheng L, et al. Novel short-clustered maltodextrin as a dietary starch substitute attenuates metabolic dysregulation and restructures gut microbiota in db/db mice. *J Agric Food Chem*. (2020) 68:12400–12. doi: 10.1021/acs.jafc.0c05798
46. Poritz LS, Garver KI, Green C, Fitzpatrick L, Ruggiero F, Koltun WA. Loss of the tight junction protein ZO-1 in dextran sulfate sodium induced colitis. *J Surg Res*. (2007) 140:12–9. doi: 10.1016/j.jss.2006.07.050
47. Kuo WT, Shen L, Zuo L, Shashikanth N, Ong M, Wu L, et al. Inflammation-induced occludin downregulation limits epithelial apoptosis by suppressing caspase-3 expression. *Gastroenterology*. (2019) 157:1323–37. doi: 10.1053/j.gastro.2019.07.058
48. Pope JL, Bhat AA, Sharma A, Ahmad R, Krishnan M, Washington MK, et al. Claudin-1 regulates intestinal epithelial homeostasis through the modulation of Notch-signalling. *Gut*. (2014) 63:622–34. doi: 10.1136/gutjnl-2012-304241
49. Barrett KE. Claudin-2 pore causes leak that breaches the dam in intestinal inflammation. *J Clin Invest*. (2020) 130:5100–1. doi: 10.1172/JCI140528
50. Connell WR, Kamm MA, Dickson M, Balkwill AM, Ritchie JK, Lennard-Jones JE. Long-term neoplasia risk after azathioprine treatment in inflammatory bowel disease. *Lancet*. (1994) 343:1249–52. doi: 10.1016/S0140-6736(94)92150-4
51. Halmos EP, Gibson PR. Dietary management of IBD–insights and advice. *Nat Rev Gastroenterol Hepatol*. (2015) 12:133–46. doi: 10.1038/nrgastro.2015.11
52. Galvez J, Rodriguez-Cabezas ME, Zarzuelo A. Effects of dietary fiber on inflammatory bowel disease. *Mol Nutr Food Res*. (2005) 49:601–8. doi: 10.1002/mnfr.200500013
53. Bettenworth D, Nowacki TM, Ross M, Kyme P, Schwammbach D, Kerstiens L, et al. Nicotinamide treatment ameliorates the course of experimental colitis

mediated by enhanced neutrophil-specific antibacterial clearance. *Mol Nutr Food Res*. (2014) 58:1474–90. doi: 10.1002/mnfr.201300818
54. Ni J, Guo Y, Chang N, Cheng D, Yan M, Jiang M, et al. Effect of N-methyltyramine on the regulation of adrenergic receptors via enzymatic epinephrine synthesis for the treatment of gastrointestinal disorders. *Biomed Pharmacother*. (2019) 111:1393–8. doi: 10.1016/j.biopha.2018.12.145
55. Chen L, Wang W, Zhou R, Ng SC, Li J, Huang M, et al. Characteristics of fecal and mucosa-associated microbiota in Chinese patients with inflammatory bowel disease. *Medicine*. (2014) 93:e51. doi: 10.1097/MD.0000000000000051
56. Zhu X, Xiang S, Feng X, Wang H, Tian S, Xu Y, et al. Impact of cyanocobalamin and methylcobalamin on inflammatory bowel disease and the intestinal microbiota composition. *J Agric Food Chem*. (2019) 67:916–26. doi: 10.1021/acs.jafc.8b05730
57. Lagkouvardos I, Lesker TR, Hitch TCA, Galvez EJC, Smit N, Neuhaus K, et al. Sequence and cultivation study of Muribaculaceae reveals novel species, host preference, and functional potential of this yet undescribed family. *Microbiome*. (2019) 7:28. doi: 10.1186/s40168-019-0637-2
58. Chen KJ, Chen YL, Ueng SH, Hwang TL, Kuo LM, Hsieh PW. Neutrophil elastase inhibitor (MPH-966) improves intestinal mucosal damage and gut microbiota in a mouse model of 5-fluorouracil-induced intestinal mucositis. *Biomed Pharmacother*. (2021) 134:111152. doi: 10.1016/j.biopha.2020.111152
59. Li ZR, Jia RB, Wu J, Lin L, Ou ZR, Liao B, et al. Sargassum fusiforme polysaccharide partly replaces acarbose against type 2 diabetes in rats. *Int J Biol Macromol*. (2021) 170:447–58. doi: 10.1016/j.ijbiomac.2020.12.126
60. Xiao YT, Yan WH, Cao Y, Yan JK, Cai W. Neutralization of IL-6 and TNF-alpha ameliorates intestinal permeability in DSS-induced colitis. *Cytokine*. (2016) 83:189–92. doi: 10.1016/j.cyto.2016.04.012

Conflict of Interest: The authors declare that the research was conducted in the absence of any commercial or financial relationships that could be construed as a potential conflict of interest.

Publisher's Note: All claims expressed in this article are solely those of the authors and do not necessarily represent those of their affiliated organizations, or those of the publisher, the editors and the reviewers. Any product that may be evaluated in this article, or claim that may be made by its manufacturer, is not guaranteed or endorsed by the publisher.

frontiers in Nutrition

ORIGINAL RESEARCH
published: 01 September 2021
doi: 10.3389/fnut.2021.731724

Effects of Molecular Distillation on the Chemical Components, Cleaning, and Antibacterial Abilities of Four Different Citrus Oils

Feilong Yang[1†], *Huijuan Zhang*[1†], *Guifang Tian*[1,2], *Wenbo Ren*[1], *Juan Li*[1], *Hang Xiao*[2*] and *Jinkai Zheng*[1*]

[1] *Institute of Food Science and Technology, Chinese Academy of Agricultural Sciences, Beijing, China,* [2] *Department of Food Science, University of Massachusetts, Amherst, MA, United States*

Essential oils (EOs) from citrus fruits are excellent aromatic resources that are used in food, cosmetics, perfume, and cleaning products. EOs extracted from four citrus varieties, sweet orange, grapefruit, mandarin, and lemon, were separated into two fractions by molecular distillation. The composition, physicochemical properties, cleaning ability, and antimicrobial activity of each EO were then systematically evaluated. The relationships between each of the aforementioned characteristics are also discussed. In keeping with the principle of "*like dissolves like*," most citrus EOs show better cleaning ability than acetone and all tend to dissolve the fat-soluble pigment. The key components of citrus EOs are 1-Decanol, α-terpineol, geraniol, and linalool for the inhibition of *Staphylococcus aureus*, *Escherichia coli*, *Candida albicans*, and *Vibrio parahaemolyticus*, respectively. The findings of this study will be of significant importance for the effective utilization of citrus peel resources and in the development of future applications for citrus EOs.

Chemical Compounds Studied in This Article: (+)-α-Pinene (PubChem CID: 6654); β-Phellandrene (PubChem CID: 11142); 3-Carene (PubChem CID: 26049); β-Myrcene (PubChem CID: 31253); D-Limonene (PubChem CID: 440917); γ-Terpinene (PubChem CID: 7461); Octanal (PubChem CID: 454); Decanal (PubChem CID: 8175); Linalool (PubChem CID: 6549); 1-Octanol (PubChem CID: 957); β-Citral (PubChem CID: 643779); α-Terpineol (PubChem CID: 17100); Hedycaryol (PubChem CID: 5365392); α-Citral (PubChem CID: 638011); 1-Decanol (PubChem CID: 8174); Geraniol (PubChem CID: 637566).

Keywords: citrus oil, components, physicochemical properties, cleaning ability, antimicrobial activity, molecular distillation

OPEN ACCESS

Edited by:
Dharini Sivakumar,
Tshwane University of Technology, South Africa

Reviewed by:
Fatih Öz,
Atatürk University, Turkey
Marcin Szymanski,
Adam Mickiewicz University, Poland

***Correspondence:**
Jinkai Zheng
zhengjinkai@caas.cn
Hang Xiao
hangxiao@foodsci.umass.edu

[†] *These authors have contributed equally to this work*

Specialty section:
This article was submitted to Food Chemistry, a section of the journal Frontiers in Nutrition

Received: *28 June 2021*
Accepted: *04 August 2021*
Published: *01 September 2021*

Citation:
Yang F, Zhang H, Tian G, Ren W, Li J, Xiao H and Zheng J (2021) Effects of Molecular Distillation on the Chemical Components, Cleaning, and Antibacterial Abilities of Four Different Citrus Oils. Front. Nutr. 8:731724. doi: 10.3389/fnut.2021.731724

INTRODUCTION

Citrus, a genus in the *Rutaceae* family, is an important fruit tree crop widely cultivated in tropical and subtropical regions of the world (1). Most cultivated citrus species are developed by interbreeding the basic taxa (2). Among those species, sweet orange (*Citrus sinensis* L.), grapefruit (*Citrus paradisi* Mac.), mandarin (*Citrus deliciosa* Ten.), and lemon (*Citrus limon* [L.] Burm.) are commercially available worldwide (3). Owing to their pleasant aroma and sweet-sour flavor, citrus

fruits are widely consumed as fresh foods or processed into juices, jams, wines, and innumerable other kinds of food (4). The attractive aroma of citrus fruits comes from essential oils (EOs), which are found primarily in the oil sacs or oil glands in the flavedo layer of the citrus peel (5). Citrus EOs are colorless or yellow transparent liquids that are soluble in ether, chloroform, anhydrous ethanol, and petroleum ether, with a density of 0.84–0.87 g/cm^3 and refractive index of 1.46–1.47. Citrus EOs also have optical rotation because of the rich chiral compositions. These volatile citrus EOs are susceptible to the outside environment as they are sensitive to oxygen, heat, and UV (6). In recent years, citrus EOs have been widely utilized in foods, perfumes, medicine, and cosmetics due to their high yield, attractive aroma, and antimicrobial and antioxidant properties (7, 8).

There are ∼200 volatile components in citrus EOs, which can be divided into three major categories: monoterpenes, sesquiterpenes, and their oxygen-containing derivatives (9). Among them, D-limonene is a major component, accounting for 25–97% in the EO of different citrus varieties (10). Although of relatively low content, oxygen-containing mono- and sesquiterpenes are the main aroma-producing components that determine the flavor of citrus EOs (11). Unsaturated straight-chain aldehydes, ranging in length from C_8 to C_{14}, such as citral, citronellal, geraniol, linalool, linalyl acetate, and geranyl acetate, are the primary odiferous components of citrus EOs (12). The physicochemical properties and chemical composition of citrus EOs are affected by their extraction and separation methods. These methods include cold pressing, distillation, and solvent extraction (13). Cold pressing is an economical and effective way to extract citrus EOs with few adverse effects on the quality of the product (14). Molecular distillation is an effective technique for the fractionation of citrus EOs (15–17).

The properties and activities of the volatile components of citrus EOs are determined by their composition and the chemical structures of key components. Many of the volatile components of citrus EOs have proven to be powerful cleaning and degreasing agents. For example, D-limonene can be used in place of noxious organic solvents, such as chlorinated hydrocarbons and n-hexane, as a "green" solvent both for degreasing or for natural products extraction (18, 19). Terpenes in particular are associated with degreasing ability (20, 21). Citrus EOs have also exhibited potent antimicrobial activities. Mandarin EO is shown to inhibit the growth of *Candida albicans*, *Escherichia coli*, *Listeria innocua*, and *Staphylococcus aureus*, with inhibition zones ranging from 9.2 to 27.6 mm (22). Terpenes such as γ-terpinene, β-pinene, ρ-cymene, α-terpinolene, and α-thujene in mandarin EO are considered the main contributors to its antimicrobial activity (22). In addition, linalool, citral, geraniol, and decanal play major roles in the activity of citrus EOs against pathogenic microorganisms (7, 23). Citrus EOs also exhibit high fumigant toxicity on insects (24). The characteristics of citrus EOs and their biological activities are affected by the citrus variety, and the extraction and separation methods used to obtain the EOs. However, the relationships among these factors have not been clearly elucidated, limiting the widespread industrial application of citrus EOs.

In this study, crude EOs were extracted by cold pressing from four varieties of citrus fruit, which are sweet orange, grapefruit, mandarin, and lemon. Each oil was then separated into two fractions by molecular distillation. The composition, physicochemical properties, aroma characteristics, cleaning ability, and antimicrobial activity of each fraction were evaluated to reveal any potential relationships among these features. Our findings provide a scientific basis for the practical utilization of citrus EOs in food, perfume, medicine, and other fields.

MATERIALS AND METHODS

Materials

Sweet orange (*C. sinensis* L.), grapefruit (*C. paradisi* Mac.), mandarin (*C. deliciosa* Ten.), and lemon (*C. limon* [L.] Burm.) were grown in Jiangxi province of China and used in this study. High performance liquid chromatography (HPLC) grade ethanol and 6-methyl-5-hepten-2-one were obtained from Fisher Scientific (Shanghai, China). Tween 80 and calcium chloride were purchased from Sinopharm Chemical Reagent Co., Ltd. (Beijing, China). Commercial detergent, corn oil, and machine oil were purchased from a local supermarket in Beijing. Liquid nitrogen was provided by Beijing Shangtong Hong Chemical Co., Ltd. (Beijing, China). Standard strains of *E. coli* (ATCC 43888), *S. aureus* (ATCC 22004), *Vibrio parahaemolyticus* (ATCC 17802), *C. albicans* (CMCC (F) 98001), *Salmonella typhi* (ATCC 14028), and *Pseudomonas aeruginosa* (ATCC 27853) were obtained from Beijing Solarbio Science & Technology Co., Ltd. (Beijing, China). Solid and liquid media for each microbial strain were provided by Beijing Aoboxing Biotechnology Co. Ltd. (Beijing, China). Gentamicin and ketoconazole and phosphate buffer solution (PBS, pH = 7.02, 0.0067 M) were purchased from Sigma-Aldrich (Shanghai, China). Ultrapure water was prepared by a Milli-Q system (Millipore, Bedford, USA).

Crude Citrus EOs Extraction by Cold Pressing

Crude EOs from four citrus varieties was extracted by the cold press method as described in our previous report with some modifications (25). Citrus peel of each variety (25 kg) was collected from fresh and ripe citrus fruits after cleaning. Then they were soaked in a calcium chloride solution (0.8%) for 5 h at room temperature. Cold pressing of these treated citrus EOs was performed on a Pressofiner (6YL-70, Nanyang Qifeng Machinery Co. Ltd., Henan, China), giving a mixture of citrus EO and water which was immediately centrifuged at 12,000 rpm for 10 min at 4°C (5810R, Eppendorf, USA) to get the separated EO layer. Finally, 500, 480, 455, and 510 ml of EO were obtained from sweet orange, grapefruit, mandarin, and lemon peel, respectively. Afterwards, they were stored in the dark at −20°C before further separation and analysis.

EO Fractions Preparation by Molecular Distillation

Separation of fractions 1 and fractions 2 from citrus crude EOs was performed on a lab-modified wiped-film molecular

distillation apparatus as shown in **Figure 1A**. The citrus crude oils were separated more effectively with filtration, vacuum, and stirring devices configured on our feeding system of molecular distillation. Specifically, 300 ml of the crude EO was fed with the rate at 2.5 ml/min and the operating pressure at 6×10^{-3} mbar. The uniformity and unity of the EO film were achieved by setting the film-forming system at 250 rpm of its rotational speed, keeping evaporation temperature and condensation temperature at 65 and 5°C, respectively. Finally, the fractions of citrus EOs were stored in the dark at −20°C before analysis.

GC-MS Analysis

Analysis of the composition of citrus EO samples was carried through Shimadzu QP 2010 plus gas chromatography coupled with a mass spectrometer detector (GC-MS, Shimadzu Co. Ltd., Kyoto, Japan) which was equipped with DB-WAX capillary column (100 m × 0.25 mm i.d., film thickness, 0.25 μm) and flame ionization detector (FID). Specifically, 1 ml of 30-fold diluted citrus EO samples (dilution with ethanol) and 1 μL of 6-methyl-5-hepten-2-one (99%, internal standard) were mixed in a vial to be delivered to GC-MS. During the analysis process, the GC oven temperature was programmed as that in our previous study (25). Lastly, the retention time of the volatile standards, the Kovats indices, and mass spectra in the NIST 11 databases were all used to identify the components of the four crude EOs and their fractions. The relative content of each component in the citrus EOs was expressed in the form of 6-methyl-5-hepten-2-one equivalents by comparing the concentration-peak area ratios relative to that of the internal standard (6-methyl-5-hepten-2-one).

Physical Properties

The physical properties, i.e., chromatism, density, viscosity, refractive index, optical rotation, solubility in 90% ethanol, and surface tension, of citrus EO samples were characterized at 20°C according to reported methods with slight modifications (6, 25). Digital Imaging System (Digieye, Verivide, England) was employed to analyze the chromaticity of those samples. Chromatism (ΔE) was calculated quantitatively according to the following equation based on the measured L^* (luminosity), a^* (red–green), and b^* (yellow–blue) values of the samples (**Equation 1**).

$$\Delta E = \sqrt{(L^* - L_0^*)^2 + (a^* - a_0^*)^2 + (b^* - b_0^*)^2} \quad (1)$$

Where L^*, a^*, and b^* belong to the test groups (citrus EOs), while L_0^*, a_0^*, and b_0^* are from the control group (ultrapure water). The density of the citrus EO was measured by the weighing method with an electronic balance (ME204E, Mettler-Toledo, Shanghai, China) involved. The viscosity, refractive index, and surface tension data of the samples were directly measured by a dynamic shear rheometer (Physia MCR 301, Anton Paar, Austria), a digital refractometer (DR102, TO YOU OPTICAL Instrument Co., Shandong, China), and an Attention theta tensiometer (Biolin Scientific, Finland), respectively. Optical rotation determination was achieved by a Polarimeter (341, Perkin Elmer, Shanghai, China). Specific optical rotation ([α]) was calculated as follow (**Equation 2**):

$$[\alpha] = \frac{\alpha}{l \times \rho} \quad (2)$$

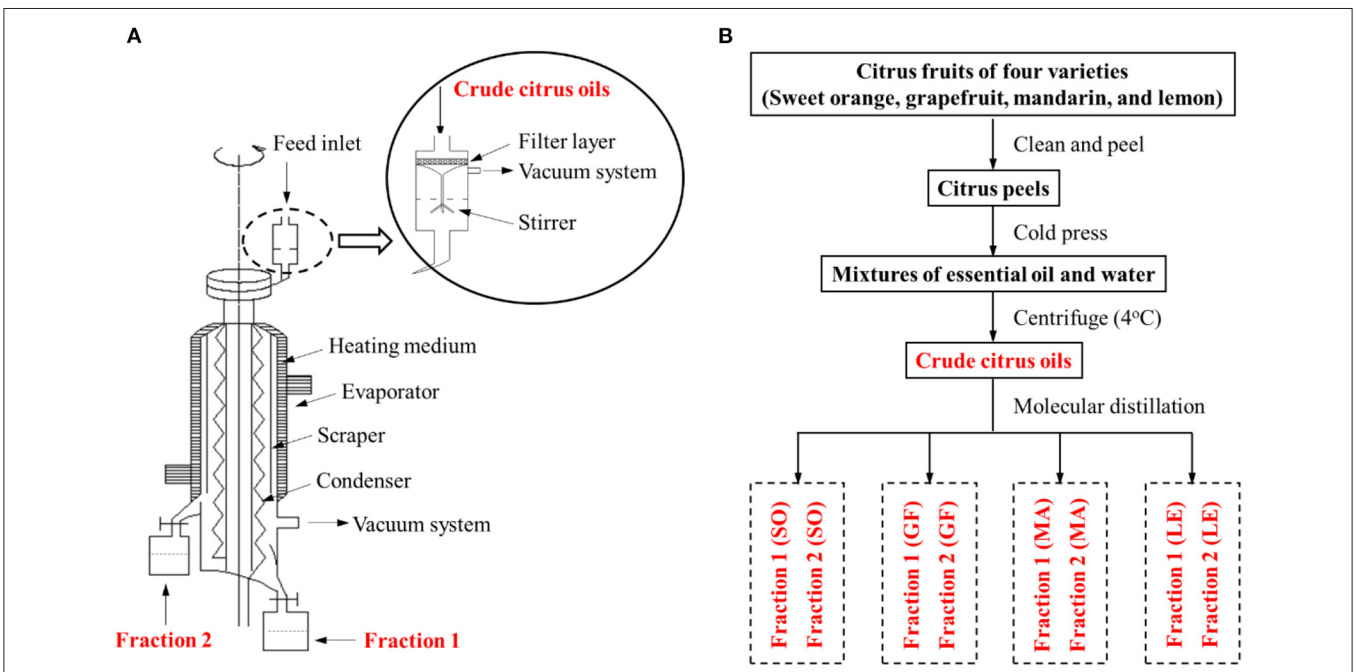

FIGURE 1 | (A) Schematic diagram of our molecular distillation apparatus. **(B)** Flow chart of the extraction and separation of citrus essential oils (EOs) from sweet orange (SO), grapefruit (GF), mandarin (MA), and lemon (LE).

Where α represents the optical rotation of the citrus EOs, l represents the length of the rotator tube (dm), and ρ represents the density value of the citrus EO (g/cm^3).

Electronic Nose Analysis

Electronic nose (AIRSENSE Analytics, GmBH, Schwerin, Germany) was used to identify and discriminate aroma characteristics of citrus EO samples by simulating human olfaction (26). Ten gas sensors (W1C, W5S, W3C, W6S, W5C, W1S, W1W, W2S, W2W, and W3S) with a specific signal response for selective components are the key elements of this test instrument (27). The raw data of this electronic sensory apparatus was preprocessed by principal component analysis (PCA) to distinguish the flavor characteristics of the EO samples extracted from different citrus varieties.

Determination of Cleaning Ability

The cleaning property of the citrus EOs was determined to develop a new type of cleaning agent for industry and household application. A measurement of 2 ml of cooking and machine oil were used to leave representative oil stains on a square white gauze (4 × 4 cm). Additionally, 4 ml of citrus EO samples, acetone, and commercial detergent was used as the agent to clean the stain in the gauze, respectively (only commercial detergent cleaned oil stain with the help of water and a rub). The photos of the degreasing results demonstrate the discrepancy in cleaning effects of the citrus EOs visually.

Solubility Determination of Pigments With Different Polarities in Citrus EO Samples

The solubility of some common pigments (β-carotene, curcumin, and carmine) in citrus essential oils, n-hexane, acetone, and 95% ethanol were determined. Specifically, these pigments were added to 1 ml of EO samples, n-hexane, and 95% ethanol until they became insoluble. Then the solutions were filtered, 20 μL of which were diluted with dimethyl sulfoxide (DMSO) (200 μL). The absorbance of the dilutions was measured in a 96-well plate under 470 nm (for β-carotene and curcumin) and 512 nm (for carmine), respectively. The essential oils, n-hexane, and 95% ethanol with no pigments, undergoing the same dilution with DMSO, were used as blank controls. The corresponding absorbance serves as a parameter for comparing the ability of the pigments to dissolve in different essential oils, n-hexane, and 95% ethanol.

The Calculation of Contribution Scores

Based on the principle "*like dissolves like*," the contribution scores of components were made to roughly explain the degree of their assistance with pigments' solubility in EO samples. First, the optimal log P for samples to dissolve each pigment was found as following steps. Found from Scifinder Inc., the log P of all the components (shown in **Table 1**) were used to roughly estimate that of each EOs and control samples; the log P of each sample would be equivalent with the sum of products of component percentages and their log P. Then plotting the solubility of each pigment in samples on the Y-axis to the ranked log P of samples on the X-axis, the relationship between the

TABLE 1 | Major components in the citrus essential oils (Eos) determined by gas chromatography with a mass spectrometer (GC-MS).

No.	Rt (min)	Components	Log P (25°C)	Sweet orange oil (mg/L)			Grapefruit oil (mg/L)			Mandarin oil (mg/L)			Lemon oil (mg/L)		
				Crude oil	Fraction 1	Fraction 2	Crude oil	Fraction 1	Fraction 2	Crude oil	Fraction 1	Fraction 2	Crude oil	Fraction 1	Fraction 2
1	4.20	(+)-α-Pinene	4.321	300	320	254	350	368	222	310	341	228	393	390	340
2	6.88	β-Phellandrene	4.386	432	459	389	523	546	390	623	647	472	550	593	557
3	7.86	3-Carene	4.321	106	118	100	82	86	59	126	130	94	87	96	90
4	8.68	β-Myrcene	4.252	1,093	1,120	979	1,244	1,264	900	1,181	1,263	912	1,294	1,381	1,291
5	10.43	D-Limonene	4.552	19,301	20,258	18,089	22,672	22,292	17,578	20,538	22,168	17,020	22,580	22,698	22,430
6	12.10	γ-Terpinene	4.386	–	–	–	26	26	–	260	251	203	28	29	29
7	14.46	Octanal	4.418	168	166	163	100	62	112	73	65	60	107	92	151
8	26.21	Decanal	3.970	229	191	292	210	74	291	163	101	173	220	154	398
9	29.82	Linalool	2.795	385	359	412	5,856	4,269	6,366	312	256	281	607	558	747
10	30.45	1-Octanol	2.876	–	–	34	248	132	319	104	94	83	255	201	309
11	36.18	β-Citral	3.100	–	–	69	114	–	156	103	55	118	1,860	1,551	2,642
12	37.63	α-Terpineol	2.708	–	–	–	299	96	405	260	124	–	298	214	–
13	37.62	Hedycaryol	4.886	–	–	–	–	–	–	–	–	325	–	–	502
14	39.02	α-Citral	3.127	62	46	90	94	112	136	–	58	135	2,112	1,646	3,207
15	41.73	1-Decanol	3.895	–	–	–	95	–	148	45	–	62	102	45	219
16	46.24	Geraniol	2.942	–	–	–	6,233	1,926	8,239	–	–	–	36	–	90

solubility of pigments and log *P* of samples was found. The figures were analyzed by averaging the solubility values which had insignificant log *P* ($p > 0.05$) and comparing them with other solubility values to find the highest one, whose corresponding log *P* would be the optimal log *P* for the pigment to dissolve in a solvent. Finally, the contribution scores would be calculated as the following equation.

$$\text{Contribution Score} = 1 - \left| \frac{\log P_{component} - \log P_{optimal}}{\log P_{component} + \log P_{optimal}} \right|$$

Log $P_{\text{component}}$ represented log *P* of each component of EO samples; log P_{optimal} represented the relatively optimal log *P* for a solvent to dissolve the corresponding pigment.

Screening of Antimicrobial Activity

The screening of antimicrobial activity of the citrus EO samples was achieved by the disc diffusion test (Kirby–Bauer test) (23, 28, 29). Firstly, 100 μL suspension of the dilute microorganisms (10^6-10^7 CFU/mL, diluted with sterile PBS) was seeded into the specific solid medium in Petri dishes (90 mm). Subsequently, a sterile filter paper disk with a diameter of 6 mm was placed onto the surface of the solid medium, soaked with 5 μL of each undiluted citrus EO sample. Gentamicin and ketoconazole were used as positive controls for anti-bacteria and anti-fungi, respectively. The plates were inoculated with strains under their standard culture conditions. Finally, the inhibition zone diameter for each EO sample was measured using a standard millimeter ruler (Deli, Shanghai, China).

Determination of Minimum Inhibitory Concentration of Antimicrobial Activity

The minimum inhibitory concentration (MIC) of citrus EO samples was measured by the double dilution method with specific liquid culture media in a 96-well plate (30). Using 0.5% tween 80 as emulsifier, the citrus EOs were tested at series of concentrations: 10, 5, 2.5, 1.25, 0.625, 0.313, 0.156, and 0.078% (v/v). Microbial growth was indicated by turbidity readings at 600 nm measured by a microplate reader (Varioskan Flash, Thermo Fisher Scientific, Waltham, MA, USA) after incubation. The lowest concentration of citrus EOs inhibiting microbial growth in the culture medium was considered as their MIC.

The Calculation of Linear Correlation Coefficient

A linear correlation coefficient was used to indicate the relationship between antimicrobial activity and component content of EO samples. According to antibacterial ability, the EO samples were sorted from weak to strong. Then plotting the percentage of the component in EOs samples on the Y-axis to the corresponding order number (1, 2, 3, …) on the X-axis, the linear correlation coefficient between antimicrobial activity and component was calculated by Excel (Microsoft Inc., USA).

Statistical Analysis

All individual experimental operations and measurements were performed in triplicates. The data of the results were presented as means ± standard deviation calculations. A one-way analysis of variance (ANOVA) and Duncan's multiple range test ($p < 0.05$) were applied to determine the significance of the difference between the data of different citrus EOs by using SPSS 22 (IBM SPSS Inc., Chicago, IL, USA). Principal component analysis, orthogonal partial least squares discriminant analysis (OPLS-DA) models, and the corresponding contribution scores production were performed on SIMCA 14.1 (Sartorius Stedim Biotech Inc., Malmö, Sweden).

RESULTS AND DISCUSSION

Chemical Composition of Crude Citrus EOs and Fractions Thereof

A flow chart describing the extraction and separation of EOs from sweet orange, grapefruit, mandarin, and lemon is shown in **Figure 1B**. Each crude citrus EO was divided into two fractions using a lab-modified molecular distillation apparatus. Colorless, low molecular weight volatiles with a longer free path reached the condenser plate while heated under vacuum. These collected in the distillate stream were named Fraction 1. High molecular weight components with shorter free paths returned to the heating plate, resulting in an enriched residue stream, which was named Fraction 2 (**Figure 2A**). The chemical compositions of the crude EOs and their fractions were determined using GC-MS with full dissociation and identified by matching GC peak retention times, Kovats indices, and the MS spectra of the detected compounds with corresponding standards. The results are presented in **Table 1**. A total of 37 components were identified and divided into seven subcategories: monoterpenes, sesquiterpenes, aldehydes, esters, alcohols, ethers, and phenols. Sixteen major volatiles, accounting for over 99% of the total detected essential oil components, were identified as (+)-α-pinene, β-phellandrene, 3-carene, β-myrcene, D-limonene, γ-terpinene, octanal, decanal, linalool, 1-octanol, β-citral, α-terpineol, hedycaryol, α-citral, 1-decanol, and geraniol. The chemical structures of the 16 components are shown in **Figure 2B**. Note that the first six volatiles to elute were terpenes, followed by oxygen-containing components primarily consisting of fatty aldehydes and alcohols. Although the composition of volatile components in the investigated EOs varied, D-limonene (49.78–87.94%, with a concentration over 17,020 mg/L, shown in **Table 1**) was the most abundant component of all the crude EOs and their fractions, in agreement with previous reports (31).

Principal component analysis and OPLS-DA models were applied to the GC-MS data to reveal content discrepancies between samples. The chemical compositions of mandarin and sweet orange were similar, but lemon and grapefruit each exhibited unique chemical compositions (**Figure 3A**). More than 93% of the sweet orange and mandarin EOs were

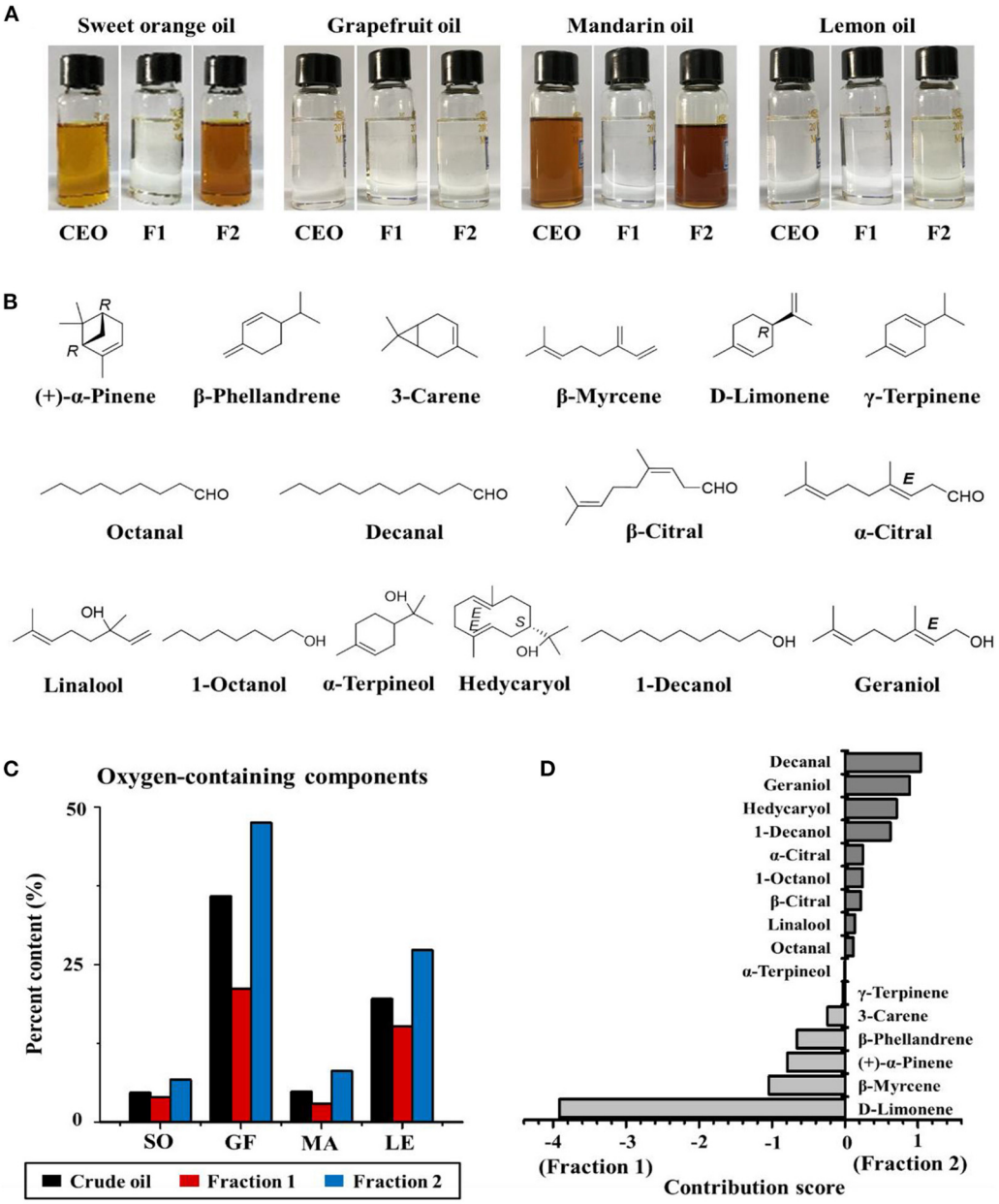

FIGURE 2 | (A) The appearance of sweet orange, grapefruit, mandarin, and lemon essential oils (CEO, F1, and F2 represent crude essential oil, Fractions 1 and 2, respectively). **(B)** Chemical structures of the major components of citrus EOs. **(C)** Percentage of oxygen-containing components in crude EOs and Fractions 1 and 2 of sweet orange (SO), grapefruit (GF), mandarin (MA), and lemon (LE). **(D)** Contribution score of each component to the difference between Fractions 1 and 2.

terpenes, including D-limonene, β-myrcene, and β-phellandrene, whereas grapefruit and lemon EOs contained significantly more oxygen-containing components at 35.87 and 19.15%, respectively (**Figure 2C**). These results indicate that citrus variety strongly affects the composition and concentration of volatile components in citrus EOs. **Figure 3B** shows the significant differences between Fraction 1 and Fraction 2. Note that D-limonene contributed most of the content discrepancy, although other discrepancies were also evident. Furthermore, components with a higher content in Fraction 1 were denoted with negative values, while those with a higher content in fraction 2 are denoted with positive values (**Figure 2D**). Generally, the highest amounts of oxygen-containing components were found in Fraction 2 samples, followed by crude EOs, and Fraction 1 samples. These results suggest that the effective separation of Fraction 1 and Fraction 2 from the citrus crude EOs was achieved by the separation method and the relatively large free path components were enriched in Fraction 2.

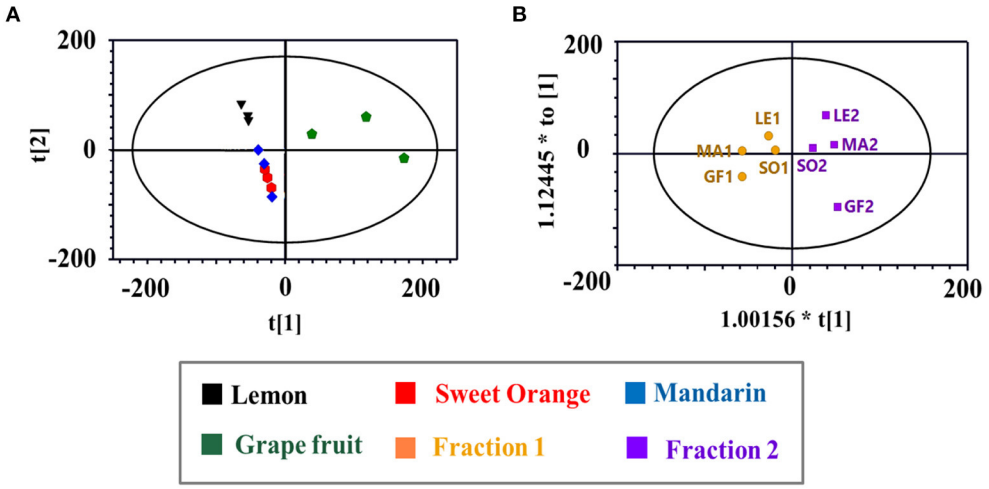

FIGURE 3 | (A) The principal component analysis (PCA) scores plot of citrus EOs samples; **(B)** The orthogonal partial least squares discriminant analysis (OPLS-DA) scores plot of the two fractions of citrus EOs samples. Each point represented an individual EOs sample. Compositions were labeled in the loading plot.

Differences in Physical Properties and Aroma Profiles Between Citrus EO Samples

Physical properties of each citrus EO were characterized, including color, optical rotation, solubility in 90% ethanol, viscosity, density, refractive index, surface tension, and the aroma profile (**Figures 4A–I**). Color differences between the EOs were quantified in terms of ΔE (**Figure 4A**). In general, the ΔE of sweet orange and mandarin oils were significantly higher than those of grapefruit and lemon oil crude oils ($p < 0.05$), except for Fraction 1. This indicated that the former contained more natural pigments, such as carotenoids (5, 32). The total carotenoid content of mandarin EO was the highest, followed by those of orange and grapefruit. In contrast, all fractions of grapefruit and lemon EOs and Fraction 1 samples of sweet orange and mandarin oils were colorless. The order of ΔE for sweet orange and mandarin oils was Fraction 2 > crude EO > Fraction 1. The above results indicated that all Fraction 1 samples and lemon and grapefruit oils contained smaller amounts of natural pigments, whereas the crude oils and Fraction 2 samples of sweet orange and mandarin contained greater amounts of colored substances. The color of citrus essential oils was related to natural pigments that were enriched in Fraction 2 following molecular distillation.

The solubility of each EO and fraction in 90% ethanol was also evaluated (**Figure 4C**). The solubility of different subgroups differed significantly, with Fraction 2 > crude EOs > Fraction 1. This may be because Fraction 2 contained more oxygen-containing compounds (mainly alcohols and aldehydes) with polarities similar to that of ethanol. In contrast, Fraction 1 contained more hydrocarbon compounds such as D-Limonene. These results were consistent with the "*like dissolves like*" concept. The trend in viscosity was similar to that of solubility, but no differences were observed between the viscosities of sweet orange and lemon oils (**Figure 4D**). The result reflected differences in composition among the three subgroups, i.e., Fraction 1, Fraction 2, and crude oils, because the viscosity of a mixture is often determined by the viscosity of its contents. Comparing the density, surface tension, and refractive index of the three subgroups, all the data followed a similar trend that was Fraction 2 > crude EOs > Fraction 1 (shown in **Figures 4E–G**). Overall, this series of experiments showed that the physical properties of EOs were affected by the composition. Density, viscosity, refractive power, surface tension, and solubility in 90% ethanol increased with higher concentrations of oxygenated species such as geraniol and decanal.

The aroma of citrus EOs is often used to create a romantic atmosphere, alleviate stress, and enhance communication (33, 34). Here, the characteristic aroma profiles of citrus EOs were determined using an electronic nose. The raw data were collected by 10 sensors (W1C, W5S, W3C, W6S, W5C, W1S, W1W, W2S, W2W, and W3S) and further analyzed using PCA in WinMuster software (Version 1.6.2, Airsense Analytics Inc., Germany). Original variables were obtained by classifying the principal components of citrus EOs. The odor characteristics of crude EOs and their fractions were shown in **Figures 4H,I**. The cumulative variance contributions of principal component 1 (PC1) and principal component 2 (PC2) were more than 99.9%, which showed that the aroma profiles of both crude EOs and their fractions, and for each of the four citrus varieties, were easily differentiated by PCA. Data points corresponding to each oil and fraction clustered in separate regions, indicating significant differences in the odors of EOs of different citrus varieties. These data also showed that EOs were well-separated by molecular distillation. Mandarin EO was tested as a representative sample. Furthermore, comparisons between EOs and fractions from the four citrus varieties show clear differences in aroma, particularly in Fraction 2. Taken together with component analyses, which showed enriched levels of geraniol, decanal, 1-decanol, hedycaryol, 1-octanol, octanal, citral, and linalool in Fraction 2, it can be deduced that these components were

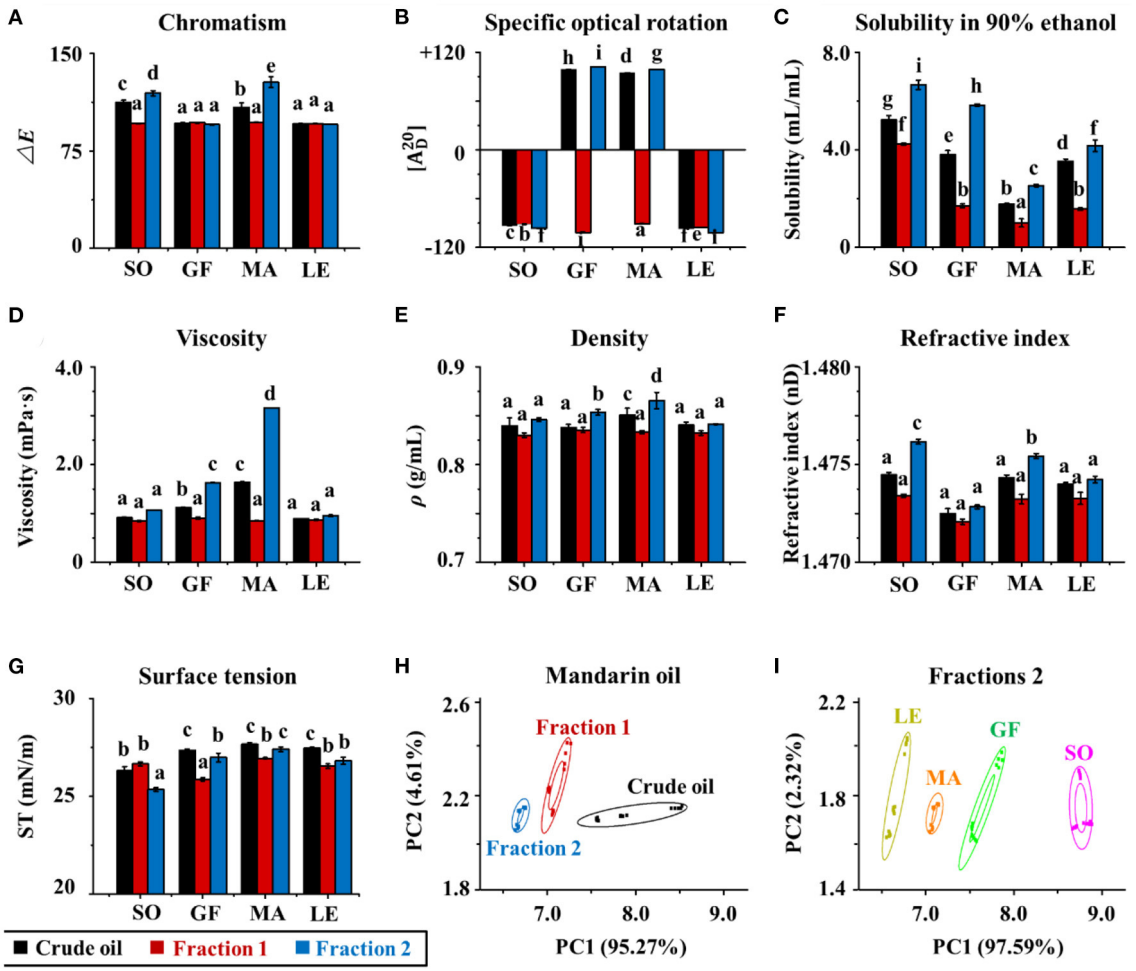

FIGURE 4 | (A) Color, specific, **(B)** optical rotation, **(C)** solubility in 90% ethanol, **(D)** viscosity, **(E)** density, **(F)** refractive index, and **(G)** surface tension of crude essential oils (CEOs) and Fractions 1 (F1) and 2 (F2) of SO, GF, MA, and LE. **(H)** Electronic nose analyses (PCA) of crude EOs and Fractions 1 and 2 of MA oil. **(I)** Electronic nose analyses of Fractions 2 of SO, GF, MA, and LE.

primarily responsible for the unique aroma of each EO. The particularly strong responses of sensors W1S, W5S, and W2W also suggested that odor differences were strongly influenced by levels of ethanol, oxynitride, and aromatic and organic sulfur-containing compounds, as well as some oxygen-containing volatiles like linalool and geraniol (35).

Cleaning Abilities of Citrus EO and Common Detergents

The cleaning and degreasing properties of each EO and fraction thereof were evaluated against commercial corn oil and machine oil. The data in **Figure 5A** showed that our EO samples were more effective than detergent and acetone in removing grease. Comparisons between different EO samples showed that the colorless oils, i.e., all the Fraction 1 samples and lemon and mandarin oils, exhibited better degreasing abilities than crude EOs and Fraction 2 samples of sweet orange and mandarin, which were yellow or dark yellow. The order of degreasing ability for citrus EOs was opposite to that of ΔE. In addition, non-volatile substances, such as pigments in the EOs, can be retained in the material being cleaned. The real cleaning and degreasing effects of citrus EOs may be masked by the color of these pigments to some extent. The data in **Table 1** shows that the high level of terpenes and low polarity of aldehydes and alcohols, especially D-limonene with a 49.78–87.94% share, were closely related to the cleaning ability of a given citrus EO (20, 21).

We then evaluated the solubility of common pigments in citrus EOs and traditional organic cleaning agents like 95% ethanol or acetone to assess their relative cleaning abilities. Higher solubility for a given pigment would suggest that it could be more easily removed from a piece of fabric or substrate. The results in **Figure 5B** show that, compared with 95% ethanol and acetone, citrus EOs had better solubility for β-carotene, the pigment which has less polarity. For curcumin with relatively higher polarity, Fraction 1 appeared low solubility to it while Fraction 2 can have the most dissolved. All EO samples had

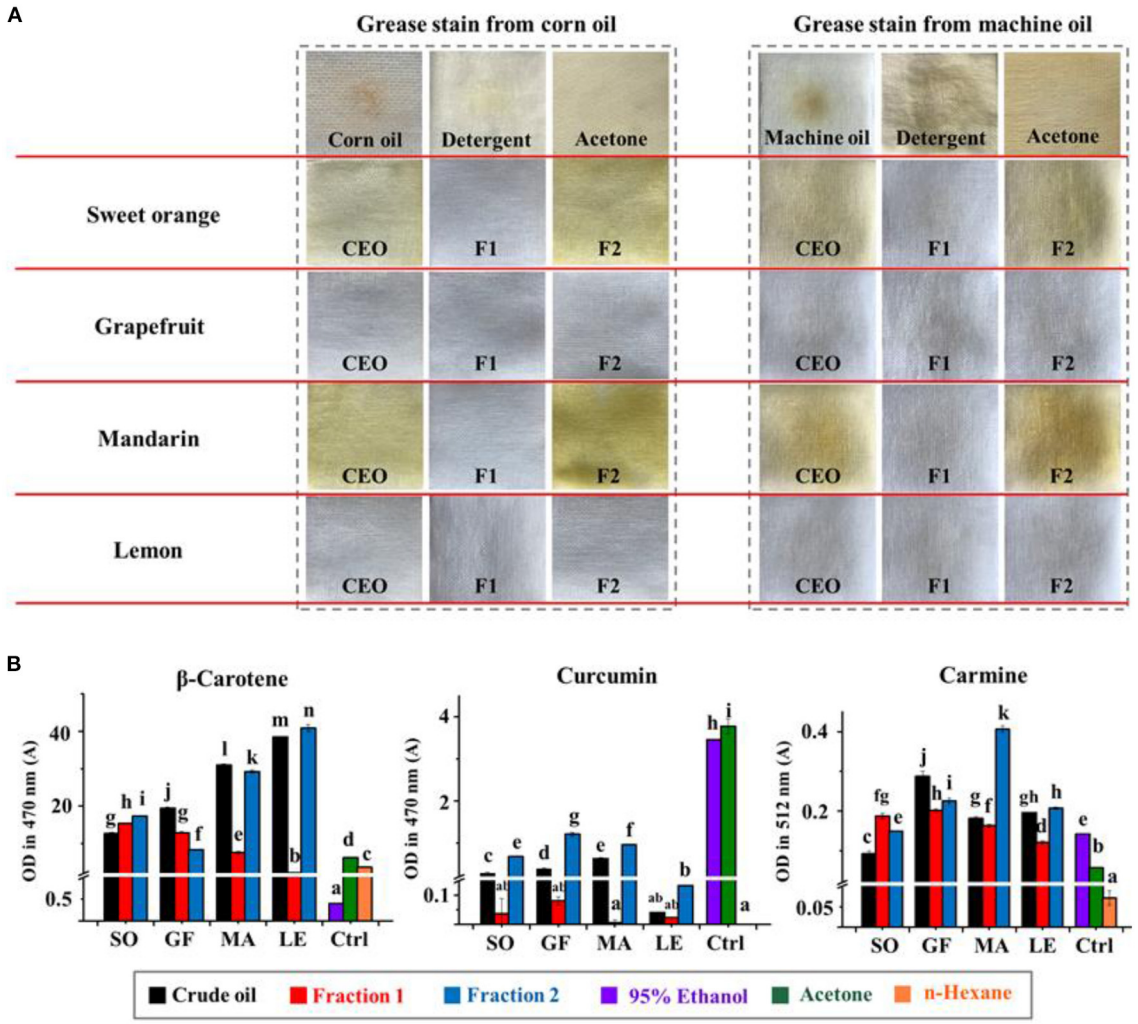

FIGURE 5 | (A) The degreasing abilities (corn oil and machine oil) of crude essential oils (CEOs) and Fractions 1 (F1) and 2 (F2) of SO, GF, MA, and LE. **(B)** The solubility of curcumin, β-carotene, and carmine in citrus EO samples. Ctrl indicates the control group, including 95% ethanol, acetone, and n-hexane.

little solubility for hydrophilic carmine. These results conformed to the trend of EO samples to dissolve low polarity substances (oil stain). A solvent with low polarity, namely n-hexane, has shown a solubility trend to dissolve more fat-compatible β-carotene and the least of water-soluble carmine while 95% ethanol as well as acetone, the medium polar solvents, dissolved the most of curcumin with medium polarity, the empirical rule "like dissolves like" seems feasible in this test. Therefore, based on this principle and the order of solubility for pigments of the EO samples, a kind of index was designed to suggest the degree of contribution of the solvents to dissolving pigments (**Table 2**). Generally, hydrocarbons [(+)-α-pinene, phellandrene, carene, myrcene, limonene, terpinene, octanal, and decanal] contributed more to the dissolving ability of EOs than oxygen-containing components (linalool, 1-octanol, β-citral, α-terpineol, hedycaryol, α-citral, 1-decanol, and geraniol). This is especially when the polarity of solutes gets lower, as inferred from the comparison between β-carotene and curcumin. For carmine, all citrus EO samples have shown little dissolving ability to it, hence the contribution scores of their components were around zero. Together with the content of low polar components in citrus EOs, the above results can prove that it was low polar components that gave citrus EOs the ability to clean oil stains, especially highly contained D-limonene.

The Antimicrobial Activities of Citrus EOs

Preliminary screening of the antimicrobial activities of undiluted citrus EOs was performed using disc diffusion assays with filter paper discs 0.6 cm in diameter (**Figure 6**). Significant differences ($p < 0.05$) were observed among the 12 citrus EO samples in their antimicrobial activities against a gram-positive bacterium (*S. aureus* ATCC 22004), gram-negative bacteria (*E.*

TABLE 2 | Contribution scores for the cleaning ability of pigments and linear correlation coefficients between the antimicrobial activity and citrus oil components.

Component	Cleaning ability (contribution scores)*			Antimicrobial activity (correlation coefficients)**			
	β-carotene	Curcumin	Carmine	*S. aureus*	*E. coli*	*V. parahaemolyticus*	*C. albicans*
(+)-α-Pinene	0.9872	0.9572	−0.0196	–	–	–	–
Phellandrene	0.9798	0.9497	−0.0193	–	–	–	–
Carene	0.9872	0.9572	−0.0196	–	–	–	–
Myrcene	0.9953	0.9652	−0.0200	–	–	–	–
Limonene	0.9612	0.9312	−0.0186	–	–	–	–
Terpinene	0.9798	0.9497	−0.0193	–	–	–	–
Octanal	0.9761	0.9461	−0.0192	0.3292	0.1121	–	0.0382
Decanal	0.9704	0.9995	−0.0214	0.6151 (s)	0.3257	0.0019	0.2279
Linalool	0.7978	0.8268	−0.0305	0.0652	0.1933	0.6318 (s)	0.3664
1-Octanol	0.8115	0.8407	−0.0296	0.6719 (s)	0.4386	0.3206	0.2692
β-Citral	0.8479	0.8774	−0.0275	0.0048	–	0.0495	–
α-Terpineol	0.7827	0.8115	−0.0315	0.0339	0.5611 (s)	–	0.6386 (s)
Hedycaryol	0.9259	0.8961	−0.0173	0.1543	0.0171	–	0.0171
α-Citral	0.8522	0.8817	−0.0272	0.0056	–	0.0588	0.0945
1-Decanol	0.9609	0.9910	−0.0218	0.6837 (s)	0.4011	0.1833	0.3158
Geraniol	0.8225	0.8518	−0.0290	0.3065	0.5279 (s)	0.524 (s)	0.6287 (s)

**The higher contribution scores the components have, the greater they promote pigments to dissolve in EO samples.*

***s (strongly relative, $r^2 > 0.5$); m (medium relative, $0.2 < r^2 < 0.5$). For Antimicrobial activity, only positive correlations are flagged.*

coli ATCC 43888, *V. parahaemolyticus* ATCC 17802, *S. typhi* ATCC 14028, and *P. aeruginosa* ATCC 27853), and fungi (*C. albicans* CMCC [F] 98001). The data in **Table 3** shows that grapefruit and lemon oils had inhibitory effects on four kinds of microbes, namely *S. aureus*, *E. coli*, *V. parahaemolyticus*, and *C. albicans*, whereas mandarin and sweet orange oils only inhibited *V. parahaemolyticus*. None of the tested oils inhibited *S. typhi* or *P. aeruginosa*. These results suggest that the antimicrobial activity of citrus EOs is strain-dependent and not determined by the Gram characteristics of the bacteria. Grapefruit oil had the strongest inhibitory effects against those bacteria except *V. parahaemolyticus*. For *V. parahaemolyticus*, the order of inhibition ability was lemon oil > grapefruit oil > mandarin oil > sweet orange oil. In addition, Fraction 2 samples consistently outperformed Fraction 1 samples and crude EOs in terms of antimicrobial activity. Not surprisingly, the minimum inhibitory concentration (MIC) results were generally consistent with those of disc diffusion assays. However, MIC analyses indicated that grapefruit oil was more effective against *V. parahaemolyticus* than lemon oil, whereas sweet orange oil exhibited the lowest antimicrobial activity.

The data in **Table 2** further demonstrates the relationship between EO composition and antimicrobial activity. For *S. aureus*, a strong correlation with the inhibition effect was shown by 1-octanol (0.6719), 1-decanol (0.6837), and decanal (0.6151). As sweet orange and mandarin oils also contained a similar content of decanal but processed no inhibition effect on *S. aureus*, decanal were obviously not the contributor to the inhibition of EOs on *S. aureus*. Furthermore, few inhibition effects of decanal on *S. aureus* are also reported (36). On the other hand, 1-octanol has been reported to inhibit *E. coli* instead of *S. aureus* (37, 38), which also excluded 1-octanol from the contributor list. Thus, grapefruit and lemon oils inhibited *S. aureus* mainly under the influence of 1-decanol. Considering the reported excellent inhibition ability of geraniol and α-terpineol on *E. coli* (39, 40), geraniol and α-terpineol with a strong correlation (0.5279 and 0.5611, respectively) may be the decisive factor for grapefruit and lemon essential oils to inhibit *E. coli*. Likewise, geraniol and α-terpineol with strong correlation (0.6287 and 0.6386, respectively) may be the main contributor to the inhibition effect of grapefruit and lemon EO samples on *C. albicans* while linalool (0.6318) and geraniol (0.524) may be the key factor for all the citrus EO samples to inhibit *V. parahaemolyticus*. As for some compounds which linked their content and antibacterial activity with a medium correlation, such as geraniol for *S. aureus* (0.3065), 1-octanol and 1-dectanol for *E. coli* (0.4386 and 0.4011), 1-octanol for *V. parahaemolyticus* (0.3206), and linalool, 1-octanol, and 1-dectanol for *C. albicans* (0.3664, 0.2692, and 0.3158), it has already been reported that they exerted inhibition effects on some microorganism in previous publications (10, 37, 38, 41, 42). This means that they may also contribute to the antibacterial activity of citrus essential oil. Most of the above antibacterial components of component inhibited the growth of microorganisms by damaging cell membranes probably through the massive accumulation of reactive oxygen species (43–45). Although the above-mentioned compounds have been reported to have related antibacterial activity, no article reported which bioactive may play a leading role in inhibiting a certain organism in citrus essential oils. In this paper, it has been concluded that 1-decanol had the major responsibility for the inhibition effects of citrus EOs on *S. aureus*. α-Terpineol and geraniol were the main factors in inhibiting

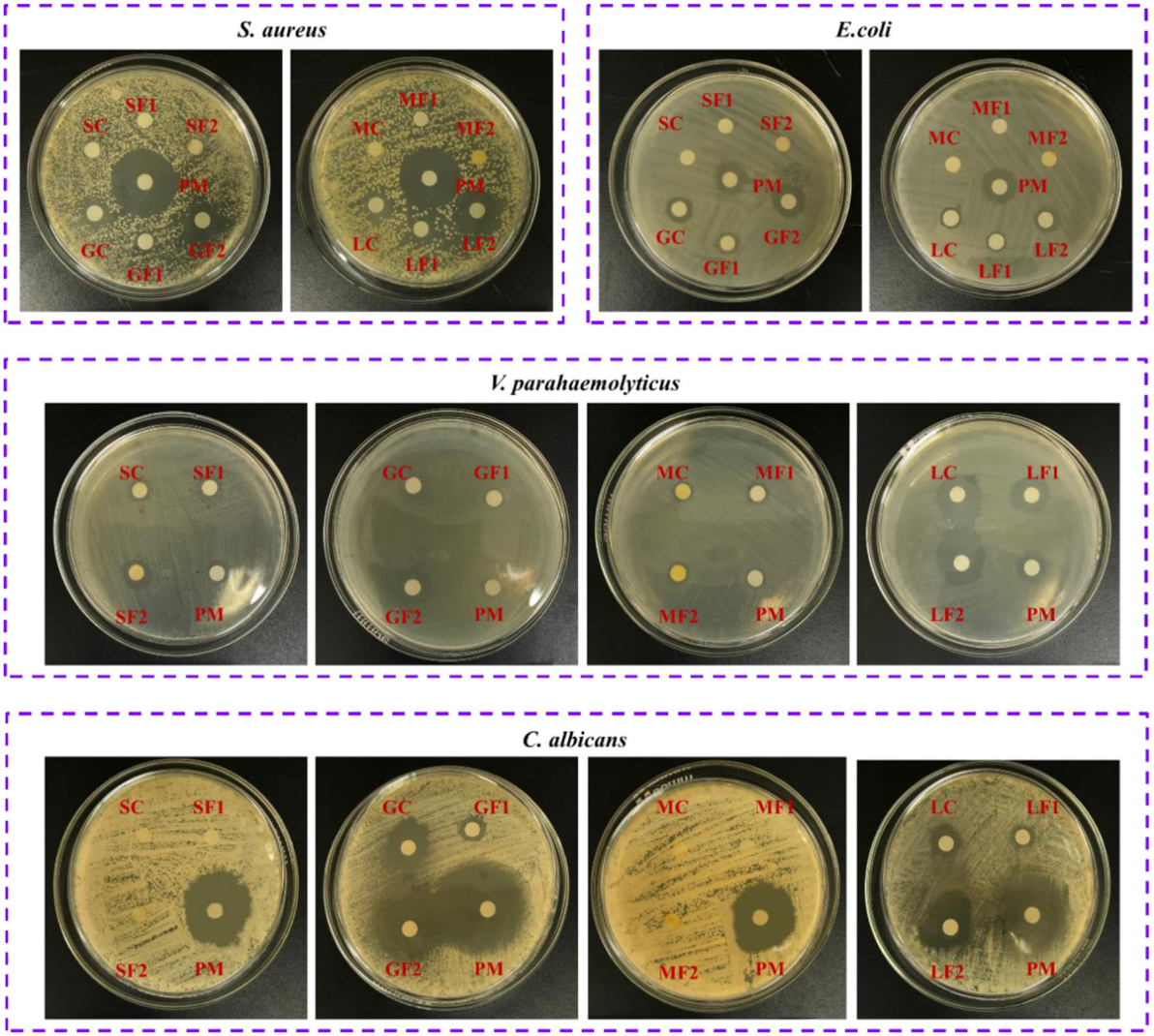

FIGURE 6 | The inhibition effects of citrus EOs against *S. aureus*, *E. coli*, *V. parrahaemolyticus*, and *C. albicans* (SOC, sweet orange crude oil; SOF1, fraction 1 of sweet orange oil; SOF2, fraction 2 of sweet orange oil; GFC, grapefruit crude oil; GFF1, fraction 1 of grapefruit oil; GFF2, fraction 2 of grapefruit oil; MAC, mandarin crude oil; MAF1, fraction 1 of mandarin oil; MAF2, fraction 2 of mandarin oil; LEC, lemon crude oil; LEF1, fraction 1 of lemon oil; LEF2, fraction 2 of lemon oil; PM, positive medicine).

E. coli and *C. albicans*. Linalool and geraniol exerted the most anti-*V. parahaemolyticus* effect in citrus EOs.

CONCLUSIONS

Crude EOs were extracted from sweet orange, grapefruit, mandarin, and lemon and successfully separated into fractions using a molecular distillation apparatus. The physicochemical characteristics, cleaning ability, and antimicrobial activity of each EO and fraction were systematically evaluated, showing significant differences in chemical composition, molecular structures, and concentrations of components. Sweet orange and mandarin oils consisted largely of terpenes (>93%), including D-limonene, β-myrcene, and β-phellandrene, whereas grapefruit and lemon oils contained more oxygen-containing components like linalool, geraniol, α-citral, and β-citral (15.25–47.53%). The highest levels of oxygen-containing components were found in Fractions 2 samples, whereas Fraction 1 samples contained more terpenes. The color, density, viscosity, refractive index, optical rotation, and solubility in 95% ethanol of each citrus EO were closely related to the composition and relative concentrations of components. Aroma profiles depended on the contents of geraniol, decanal, 1-decanol, hedycaryol, 1-octanol, octanal, citral, and linalool. In keeping with the principle of "like dissolves like," citrus EOs showed better cleaning ability than acetone and all tended to dissolve fat-soluble pigments. The key components in the inhibition of *S. aureus*, *E. coli*, *C. albicans*, and *V. parahaemolyticus* were 1-Decanol, α-terpineol, geranio, l and linalool, respectively. The findings of this study will help

TABLE 3 | The inhibition zone diameters and minimum inhibitory concentrations of citrus EOs against *Staphylococcus aureus*, *Escherichia coli*, *Vibrio parahaemolyticus*, and *Candida albicans*.

Citrus oil		The inhibition zone diameters (cm)				The minimum inhibitory concentration (%, v/v)			
		S. aureus	*E. coli*	*V. parahaemolyticus*	*C. albicans*	*S. aureus*	*E. coli*	*V. parahaemolyticus*	*C. albicans*
Sweet orange oil	Crude oil	–	–	0.83 ± 0.11*b*	–	–	–	0.313	–
	Fraction 1	–	–	0.73 ± 0.04*ab*	–	–	–	0.313	–
	Fraction 2	–	–	0.93 ± 0.25*bc*	–	–	–	0.156	–
Grapefruit oil	Crude oil	1.40 ± 0.10*c*	1.13 ± 0.13*c*	1.13 ± 0.04*c*	1.90 ± 0.14*d*	2.5	0.625	0.156	0.625
	Fraction 1	0.82 ± 0.08*b*	0.75 ± 0.05*b*	0.93 ± 0.04*bc*	0.95 ± 0.07*bc*	>10	10	0.156	>10
	Fraction 2	1.73 ± 0.25*d*	1.93 ± 0.31*d*	1.30 ± 0.07*c*	2.65 ± 0.21*e*	5	0.313	0.156	0.156
Mandarin oil	Crude oil	–	–	1.05 ± 0.21*c*	–	–	–	1.25	–
	Fraction 1	–	–	0.93 ± 0.04*bc*	–	–	–	1.25	–
	Fraction 2	–	–	1.10 ± 0.14*c*	–	–	–	1.25	–
Lemon oil	Crude oil	1.17 ± 0.12*c*	0.77 ± 0.03*b*	1.75 ± 0.07*d*	1.25 ± 0.07*c*	5	2.5	0.156	>10
	Fraction 1	0.97 ± 0.06*bc*	0.67 ± 0.03*a*	1.50 ± 0.14*c*	0.90 ± 0.14*bc*	5	5	0.313	>10
	Fraction 2	1.63 ± 0.15*d*	0.85 ± 0.09*b*	1.95 ± 0.07*d*	1.65 ± 0.21*d*	5	2.5	0.156	>10
0.1 mg/mL positive medicine (Gentamicin or ketoconazole)	2.75 , 0.22e	1.11 ± 0.07*c*	0.99 ± 0.09*bc*	2.95 ± 0.44*e*					

'a, b, c, d' denote statistically difference. The data with the same letter means they are not statistically different.

optimize the utilization of citrus peel resources and expand future applications of citrus EOs.

DATA AVAILABILITY STATEMENT

The original contributions presented in the study are included in the article/supplementary material, further inquiries can be directed to the corresponding author/s.

AUTHOR CONTRIBUTIONS

FY and HZ: methodology, investigation, conducting experiments, and writing—original draft. GT: methodology and formal analysis. WR: validation and formal analysis. JL: investigation. HX: formal analysis, supervision, and writing—review and editing. JZ: formal analysis, conceptualization, supervision, writing—review and editing, funding access, and support. All authors contributed to manuscript revision and read and approved the submitted version.

ACKNOWLEDGMENTS

The authors would like to acknowledge the financial support provided by the National Natural Science Foundation of China (No. 32072181).

REFERENCES

1. Patsalou M, Menikea KK, Makri E, Vasquez MI, Drouza C, Koutinas M. Development of a citrus peel-based biorefinery strategy for the production of succinic acid. *J Clean Prod.* (2017) 166:706–16. doi: 10.1016/j.jclepro.2017.08.039
2. Ollitrault P, Navarro L. Citrus. *Fruit Breed.* (2012) 2012:623–62. doi: 10.1007/978-1-4419-0763-9_16
3. Cuenca J, Garcia-Lor A, Navarro L, Aleza P. Citrus genetics and breeding. *Adv Plant Breed Strateg Fruits.* (2018) 2018:403–36. doi: 10.1007/978-3-319-91944-7_11
4. Zhou Y, He W, Zheng W, Tan Q, Xie Z, Zheng C, et al. Fruit sugar and organic acid were significantly related to fruit Mg of six citrus cultivars. *Food Chem.* (2018) 259:278–85. doi: 10.1016/j.foodchem.2018.03.102
5. Yang Y, Wang X, Zhao C, Tian G, Zhang H, Xiao H, et al. Chemical mapping of essential oils, flavonoids and carotenoids in citrus peels by Raman microscopy. *J Food Sci.* (2017) 82:2840–6. doi: 10.1111/1750-3841.13952
6. Ahmad M, Rehman SU, Anjum FM, Bajwa EE. Comparative physical examination of various citrus peel essential oils. *Int J Agric Biol.* (2006) 8:186–90.
7. Yi F, Jin R, Sun J, Ma B, Bao X. Evaluation of mechanical-pressed essential oil from Nanfeng mandarin (*Citrus reticulata* Blanco cv. Kinokuni) as a food preservative based on antimicrobial and antioxidant activities. *LWT Food Sci Technol.* (2018) 95:346–53. doi: 10.1016/j.lwt.2018.05.011
8. Calo JR, Crandall PG, O'Bryan CA, Ricke SC. Essential oils as antimicrobials in food systems–a review. *Food Control.* (2015) 54:111–9. doi: 10.1016/j.foodcont.2014.12.040
9. Nannapaneni R, Chalova VI, Crandall PG, Ricke SC, Johnson MG, O'Bryan CA. Campylobacter and Arcobacter species sensitivity to commercial orange oil fractions. *Int J Food Microbiol.* (2009) 129:43–9. doi: 10.1016/j.ijfoodmicro.2008.11.008
10. Jing L, Lei Z, Li L, Xie R, Xi W, Guan Y, et al. Antifungal activity of citrus essential oils. *J Agric Food Chem.* (2014) 62:3011–33. doi: 10.1021/jf5006148
11. Strano MC, Calandra M, Aloisi V, Rapisarda P, Strano T, Ruberto G. Hot water dipping treatments on Tarocco orange fruit and their effects on peel essential oil. *Postharvest Biol Tec.* (2014) 94:26–34. doi: 10.1016/j.postharvbio.2014.01.026
12. Gonçalves D, Costa P, Bejar CL, Bocquet A, Rodrigues CE, Rodrigues AE. Air diffusion of aroma-active components from crude citrus essential oils and

their extract phases obtained by solvent extraction. *Ind Eng Chem Res.* (2018) 57:5670–9. doi: 10.1021/acs.iecr.7b05203
13. González-Mas MC, Rambla JL, López-Gresa MP, Blázquez MA, Granell A. Volatile compounds in citrus essential oils: a comprehensive review. *Front Plant Sci.* (2019) 10:1–18. doi: 10.3389/fpls.2019.00012
14. Ferhat MA, Meklati BY, Chemat F. Comparison of different isolation methods of essential oil from Citrus fruits: cold pressing, hydrodistillation and microwave 'dry'distillation. *Flavour Frag J.* (2007) 22:494–504. doi: 10.1002/ffj.1829
15. Guo Q, Liu K, Deng W, Zhong B, Yang W, Chun J. Chemical composition and antimicrobial activity of Gannan navel orange (*Citrus sinensis* Osbeck cv. Newhall) peel essential oils. *Food Sci Nutr.* (2018) 6:1431–7. doi: 10.1002/fsn3.688
16. Perini J, Silvestre W, Agostini F, Toss D, Pauletti G. Fractioning of orange (*Citrus sinensis* L.) essential oil using vacuum fractional distillation. *Sep Sci Technol.* (2017) 52:1397–403. doi: 10.1080/01496395.2017.1290108
17. Silvestre WP, Agostini F, Muniz LA, Pauletti GF. Fractionating of green mandarin (*Citrus deliciosa* Tenore) essential oil by vacuum fractional distillation. *J Food Eng.* (2016) 178:90–4. doi: 10.1016/j.jfoodeng.2016.01.011
18. Ravichandran C, Badgujar PC, Gundev P, Upadhyay A. Review of toxicological assessment of d-limonene, a food and cosmetics additive. *Food Chem Toxicol.* (2018) 120:668–80. doi: 10.1016/j.fct.2018.07.052
19. Sahad N, Som AM, Baharuddin AS, Mokhtar MN, Busu Z, Sulaiman A. Recovery of residual crude palm oil (RCPO) from oil palm decanter cake (OPDC) using d-limonene. *Adv Mater Res*. (2015) 1113:405–10. doi: 10.4028/www.scientific.net/AMR.1113.405
20. Huang Y, Ho SSH, Ho KF, Lee SC, Gao Y, Cheng Y, et al. Characterization of biogenic volatile organic compounds (BVOCs) in cleaning reagents and air fresheners in Hong Kong. *Atmos Environ.* (2011) 45:6191–6. doi: 10.1016/j.atmosenv.2011.08.012
21. Moran RE, Bennett DH, Tancredi DJ, Ritz B, Hertz-Picciotto I. Frequency and longitudinal trends of household care product use. *Atmos Environ.* (2012) 55:417–24. doi: 10.1016/j.atmosenv.2012.03.021
22. Boudries H, Loupassaki S, Ladjal Ettoumi Y, Souagui S, Bachir Bey M, Nabet N, et al. Chemical profile, antimicrobial and antioxidant activities of *Citrus reticulata* and *Citrus clementina* (L.) essential oils. *Int Food Res J.* (2017) 24:1782–92.
23. Giteru SG, Coorey R, Bertolatti D, Watkin E, Johnson S, Fang Z. Physicochemical and antimicrobial properties of citral and quercetin incorporated kafirin-based bioactive films. *Food Chem.* (2015) 168:341–7. doi: 10.1016/j.foodchem.2014.07.077
24. Hu W, Zhang N, Chen H, Zhong B, Yang A, Kuang F, et al. Fumigant activity of sweet orange essential oil fractions against red imported fire ants (Hymenoptera: Formicidae). *J Econ Entomol.* (2017) 110:1556–62. doi: 10.1093/jee/tox120
25. Yang Y, Zhao C, Chen J, Tian G, McClements DJ, Xiao H, et al. Encapsulation of polymethoxyflavones in citrus oil emulsion-based delivery systems. *J Agric Food Chem.* (2017) 65:1732–9. doi: 10.1021/acs.jafc.7b00147
26. Yang Y, Zhao C, Tian G, Lu C, Zhao S, Bao Y, et al. Effects of preheating and storage temperatures on aroma profile and physical properties of citrus-oil emulsions. *J Agric Food Chem.* (2017) 65:7781–9. doi: 10.1021/acs.jafc.7b03270
27. Zhang H, Cui J, Tian G, DiMarco-Crook C, Gao W, Zhao C, et al. Efficiency of four different dietary preparation methods in extracting functional compounds from dried tangerine peel. *Food Chem.* (2019) 289:340–50. doi: 10.1016/j.foodchem.2019.03.063
28. Randazzo W, Jiménez-Belenguer A, Settanni L, Perdones A, Moschetti M, Palazzolo E, et al. Antilisterial effect of citrus essential oils and their performance in edible film formulations. *Food Control.* (2016) 59:750–8. doi: 10.1016/j.foodcont.2015.06.057
29. Wu H, Lei Y, Zhu R, Zhao M, Lu J, Xiao D, et al. Preparation and characterization of bioactive edible packaging films based on pomelo peel flours incorporating tea polyphenol. *Food Hydrocolloid.* (2019) 90:41–9. doi: 10.1016/j.foodhyd.2018.12.016
30. Radünz M, Trindade MLM, Camargo TM, Radünz AL, Borges CD, Gandra EA, et al. Antimicrobial and antioxidant activity of unencapsulated and encapsulated clove (*Syzygium aromaticum*, L.) essential oil. *Food Chem.* (2019) 276:180–6. doi: 10.1016/j.foodchem.2018.09.173
31. Hosni K, Zahed N, Chrif R, Abid I, Medfei W, Kallel M, et al. Composition of peel essential oils from four selected Tunisian Citrus species: evidence for the genotypic influence. *Food Chem.* (2010) 123:1098–104. doi: 10.1016/j.foodchem.2010.05.068
32. López-Muñoz GA, Antonio-Pérez A, Diaz-Reyes J. Quantification of total pigments in citrus essential oils by thermal wave resonant cavity photopyroelectric spectroscopy. *Food chem.* (2015) 174:104–9. doi: 10.1016/j.foodchem.2014.11.039
33. Mahato N, Sharma K, Koteswararao R, Sinha M, Baral E, Cho MH. Citrus essential oils: extraction, authentication and application in food preservation. *Crit Rev Food Sci.* (2019) 59:611–25. doi: 10.1080/10408398.2017.1384716
34. Xiao Z, Ma S, Niu Y, Chen F, Yu D. Characterization of odour-active compounds of sweet orange essential oils of different regions by gas chromatography-mass spectrometry, gas chromatography-olfactometry and their correlation with sensory attributes. *Flavour Frag J.* (2016) 31:41–50. doi: 10.1002/ffj.3268
35. Zellner BdA, Dugo P, Dugo G, Mondello L. Gas chromatography–olfactometry in food flavour analysis. *J Chromatogr A.* (2008) 1186:123–43. doi: 10.1016/j.chroma.2007.09.006
36. Federman C, Ma C, Biswas D. Major components of orange oil inhibit *Staphylococcus aureus* growth and biofilm formation, and alter its virulence factors. *J Med Microbiol.* (2016) 65:688–95. doi: 10.1099/jmm.0.000286
37. Togashi N, Shiraishi A, Nishizaka M, Matsuoka K, Endo K, Hamashima H, et al. Antibacterial activity of long-chain fatty alcohols against *Staphylococcus aureus*. *Molecules*. (2007) 12:139–48. doi: 10.3390/12020139
38. Skalicka-Wozniak K, Grzegorczyk A, Swiatek Ł, Walasek M, Widelski J, Rajtar B, et al. Biological activity and safety profile of the essential oil from fruits of Heracleum mantegazzianum Sommier & Levier (Apiaceae). *Food Chem Toxicol.* (2017) 109:820–6. doi: 10.1016/j.fct.2017.05.033
39. Guimarães AC, Meireles LM, Lemos MF, Guimarães MCC, Endringer DC, Fronza M, et al. Antibacterial activity of terpenes and terpenoids present in essential oils. *Molecules.* (2019) 24:2471–83. doi: 10.3390/molecules24132471
40. Badawy ME, Marei GIK, Rabea EI, Taktak NE. Antimicrobial and antioxidant activities of hydrocarbon and oxygenated monoterpenes against some foodborne pathogens through *in vitro* and *in silico* studies. *Pestic Biochem Phys.* (2019) 158:185–200. doi: 10.1016/j.pestbp.2019.05.008
41. Ghosh T, Srivastava SK, Gaurav A, Kumar A, Kumar P, Yadav AS, et al. A combination of linalool, vitamin C, and copper synergistically triggers reactive oxygen species and DNA damage and inhibits Salmonella enterica subsp. enterica Serovar Typhi and Vibrio fluvialis. *Appl Environ Microb.* (2019) 85:e02487–18. doi: 10.1128/AEM.02487-18
42. Porfírio EM, Melo HM, Pereira AMG, Cavalcante TTA, Gomes GA, Carvalho MGd, et al. *In vitro* antibacterial and antibiofilm activity of Lippia alba essential oil, citral, and carvone against *Staphylococcus aureus*. *Sci World J.* (2017) 2017:4962707. doi: 10.1155/2017/4962707
43. Arunachalam K, Ramar M, Ramanathan S, Govindaraju A, Shunmugiah KP, Kandasamy R, et al. *In vivo* protective effect of geraniol on colonization of *Staphylococcus epidermidis* in rat jugular vein catheter model. *Pathog Dis.* (2018) 76:fty055. doi: 10.1093/femspd/fty055
44. OuYang Q, Tao N, Zhang M. A damaged oxidative phosphorylation mechanism is involved in the antifungal activity of citral against *Penicillium digitatum*. *Front Microbiol.* (2018) 9:239–52. doi: 10.3389/fmicb.2018.00239
45. Yan G, Zhu B-R, Tian F-L, Hui X, Li H, Li Y-M, et al. Inhibitory activity of plant essential oils against *E. coli* 1-deoxy-d-xylulose-5-phosphate reductoisomerase. *Molecules.* (2019) 24:2518–27. doi: 10.3390/molecules24142518

Conflict of Interest: The authors declare that the research was conducted in the absence of any commercial or financial relationships that could be construed as a potential conflict of interest.

Publisher's Note: All claims expressed in this article are solely those of the authors and do not necessarily represent those of their affiliated organizations, or those of the publisher, the editors and the reviewers. Any product that may be evaluated in this article, or claim that may be made by its manufacturer, is not guaranteed or endorsed by the publisher.

frontiers in Nutrition

ORIGINAL RESEARCH
published: 17 September 2021
doi: 10.3389/fnut.2021.714869

Effect of Heat Treatment on the Property, Structure, and Aggregation of Skim Milk Proteins

Hongbo Li[1,2], *Tingting Zhao*[2], *Hongjuan Li*[2] *and Jinghua Yu*[2]*

[1] Beijing Advanced Innovation Center for Food Nutrition and Human Health, Beijing Technology and Business University (BTBU), Beijing, China, [2] State Key Laboratory of Food Nutrition and Safety, Key Laboratory of Food Nutrition and Safety, Ministry of Education, College of Food Engineering and Biotechnology, Tianjin University of Science and Technology, Tianjin, China

To study the mechanism of heat-induced protein aggregates, skim milk was heated at 55, 65, 75, 85, and 95°C for 30 s. Then, the sulfhydryl content, surface hydrophobicity, and secondary structure of heat-treated skim milk were studied. Treating skim milk at different temperatures induced a decrease in sulfhydryl content (75.9% at 95°C) and an increase in surface hydrophobicity (44% at 95°C) with a disrupted secondary structure containing random coil, β-sheet, and β-turn of skim milk proteins. The change in these properties facilitated aggregate formation through disulfide bonds and hydrophobicity interaction. Microstructural observation also showed a higher degree of aggregation when skim milk was heated at 85 and 95°C. The result of two-dimensional polyacrylamide gel electrophoresis demonstrated that the aggregates consisted of a high proportion of κ-casein, β-lactoglobulin, and other whey proteins.

Keywords: heat treatment, skim milk, property, protein aggregation, 2D-PAGE

OPEN ACCESS

Edited by:
Hang Xiao,
University of Massachusetts Amherst, United States

Reviewed by:
Miryam Amigo-Benavent, University of Limerick, Ireland
Joana Costa, University of Porto, Portugal

***Correspondence:**
Jinghua Yu
yujinghuamail@163.com

Specialty section:
This article was submitted to Food Chemistry, a section of the journal Frontiers in Nutrition

Received: *02 June 2021*
Accepted: *19 August 2021*
Published: *17 September 2021*

Citation:
Li H, Zhao T, Li H and Yu J (2021) Effect of Heat Treatment on the Property, Structure, and Aggregation of Skim Milk Proteins. Front. Nutr. 8:714869. doi: 10.3389/fnut.2021.714869

INTRODUCTION

Milk derived from domesticated mammalian animals has a long history of being a part of the human diet. The current milk and milk products for human consumption are mainly from cows, followed by buffaloes, goats, horses, yaks, and camels (1). In the processing of these dairy products, heat treatment is an essential step to reduce the potential risk of survival of pathogenic microorganisms and extend the shelf life of final products. It can also improve the functional properties of some specific dairy products, such as yogurt and cheese (2, 3). Heat treatment has a significant effect on the protein network of dairy product (4). It is well-known that heat-treated milk can form a gel network with better strength and firmness in a shorter time (5). The application of heat leads to different reactions among milk proteins, contributing to the denaturation and/or aggregation of whey proteins and formation of complexes between caseins and whey proteins (6–9).

In dairy proteins, caseins with molecular weight ranging from 19 to 25.2 kDa account for about 80% of total proteins, while whey proteins represent 20%. The main components in whey proteins are β-lactoglobulin (β-LG) and α-lactalbumin (α-LA), representing 50 and 25%, respectively, followed by minor constituents, such as bovine serum albumin (BSA), lactoferrin, and immune globulin (10). In these proteins, caseins are relatively stable at a high temperature, and whey proteins are more susceptible to heat treatment (11). The denaturation of β-LG and α-LA occurs at temperatures above 70–75°C, but the other whey proteins such as BSA and lactoferrin begin to denature

at a lower temperature of about 65°C (12, 13). Considerable research studies have been conducted to study the composition of complexes and reactions between proteins (14, 15). Results showed that non-covalent interactions between whey proteins and casein micelles, and the formation of disulfide bond are the most important reactions in the process of heat treatment (16). During the heat treatment of milk, β-LG/κ-casein complexes are formed with the exchange of thiol-disulfide (17). It has been reported that β-LG containing a free sulfhydryl group and two disulfide bonds plays an important role in the formation of β-LG/κ-casein complexes (18, 19).

At present, the effect of heat treatment on milk proteins is mainly focused on the interaction between the proteins, but there are few studies on the properties and structure of total milk proteins. According to the temperature range of whey protein denaturation, 55, 65, 75, 85, and 95°C are selected as the heat treatment temperature on skim milk. The goal of this study is to explore the mechanism of heat-induced protein aggregates after heat treatment on skim milk, and the interaction of different denatured milk proteins.

MATERIALS AND METHODS

Sample Preparation

Fresh cow milk was purchased from a local dairy plant, and 0.02% (w/v) sodium azide was added to prevent bacterial growth. Total protein was determined by the Association of Official Analytical Chemists (20) Method Nos. 991.20 with a conversion factor of 6.38. Cow milk was centrifuged at 2,000 × g for 20 min at 4°C to remove the cream, then the skim milk was heated at 55, 65, 75, 85, and 95°C for 30 s in a recirculating tubular heat exchanger made in the laboratory. This heat exchanger contained a tubular coil (1 mm inner diameter) located in a thermostatic water bath and controlled with a constant-flow pump. After heat treatment, the skim milk was rapidly cooled in an ice water bath.

Sulfhydryl Determination

The sulfhydryl content of the heat-treated samples was determined using the 5,5′-dithiobis (2-nitrobenzoic acid) (DNTB) method. Three hundred microliters of the samples were mixed with 5 ml urea (8 mol L^{-1}) and 20 μl DNTB (4 m ml^{-1}) (Borunlaite Co., Ltd., Beijing, China) and incubated for 15 min at room temperature. Then, the mixture was immediately measured at 412 nm with a UV-752 UV-vis spectrophotometer (Sunnu Hengping Co., Ltd., Shanghai, China). The mixture without DNTB as a blank control and sulfhydryl content was expressed as micromoles sulfhydryl per milliliter milk.

Surface Hydrophobicity

The surface hydrophobicity of the heat-treated samples was estimated using the 8-anilino-1-naphthalene sulphonic acid (ANS)-binding fluorimetric assay method. A solution of 8 mmol L^{-1} ANS (Sigma, Shanghai, China) was prepared in a 0.01 mol/L PBS buffer (pH 6.7). The heat-treated samples were also diluted using the PBS buffer to 0.0025, 0.005, 0.01, and 0.02% (w/v), respectively. For each sample, 20 μl ANS was added and equilibrated for 1 h. The fluorescence intensity was measured with a RF-5301 fluorescence spectrophotometer (Shimadu, Shanghai, China), with the excitation wavelength set at 390 nm and the emission wavelength at 470 nm (Ex 390/Em 470). The excitation and emission slits were both set at a bandwidth of 5 nm.

Fourier Transform Infrared Measurement

The secondary structure of the heat-treated samples was analyzed using a Vector22 FTIR (Bruker, Karlsruhe, Germany) spectrometer with a distributed temperature gradient sensing (DTGS) detector. All spectra were recorded within the range of 4,000–650 cm^{-1} with a 4 cm^{-1} resolution and 32 scans. The measurements were performed in a dry atmosphere at room temperature. In order to reduce the influence of steam absorption in the measurements, dry nitrogen was constantly used.

Scanning Electron Microscopy

The microstructure of the heat-treated samples was determined using SEM SU1510 (Hitachi, Tokyo, Japan). The heat-treated samples were fixed in 2.5% glutaraldehyde for 3 h at 4°C, and washed three times using a 0.1 mol L^{-1} PBS buffer (pH 7.2). After washing, the samples were dehydrated using 50, 70, 90, and 100% ethanol. Then, ethanol was replaced by isoamyl acetate, and the samples were dried at room temperature. The dried samples were coated with a 4-nm gold layer and observed.

PAGE Analysis

The aggregates and interactions of proteins in the heat-treated skim milk samples were characterized with the two-dimensional sodium dodecyl sulfate–polyacrylamide gel electrophoresis (2D-PAGE) method. For the first dimension (non-reduced SDS-PAGE), 20-μl samples were loaded and run on 5–15% home-made Tris-HCl gel. The gel strip including aggregates was cut and soaked in a β-mercaptoethanol (β-ME) buffer for 2 h and then placed on top of 5–15% gel for the second dimension (reduced SDS-PAGE). Electrophoresis was carried out in a Tris-glycine electrophoresis buffer. The gel was stained with Coomassie Brilliant Blue R250 and scanned using a Gel Doc XR system (Bio-Rad Laboratories Inc., Hercules, CA, United States). An unstained protein molecular weight marker (14.3–97.2 KDa; ComWin Biotech, Beijing, China) was used in all gels to identify skim milk proteins.

Statistical Analysis

Data were analyzed with SPSS 14.0 (SPSS Inc, Chicago, IL, United States) and one-way analysis of variance with Duncan's *post-test* was applied. The level of significance was established at $p < 0.05$. All the assays were carried out in triplicate, and data were expressed as mean values ± standard deviation (SD).

RESULT AND DISCUSSION

Sulfhydryl Determination

The sulfhydryl content of the heat-treated skim milk samples was studied. As shown in **Figure 1**, there is no significant change in sulfhydryl content at the lower temperature treatment (55 and 65°C) compared with the sample without heat treatment, but

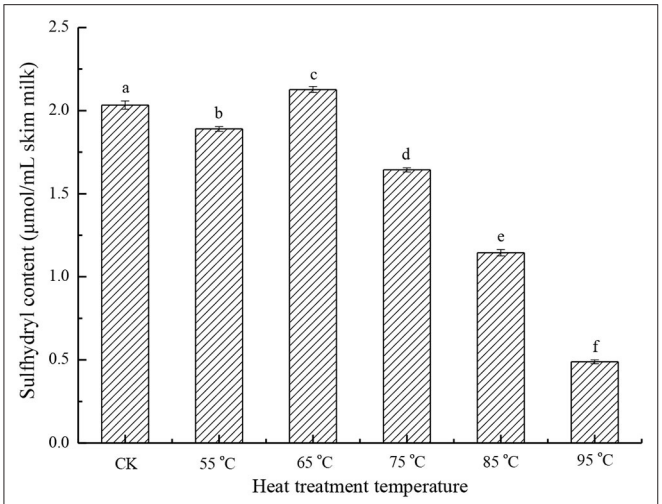

FIGURE 1 | Sulfhydryl content of different heat-treated skim milk. CK, skim milk without heat treatment.

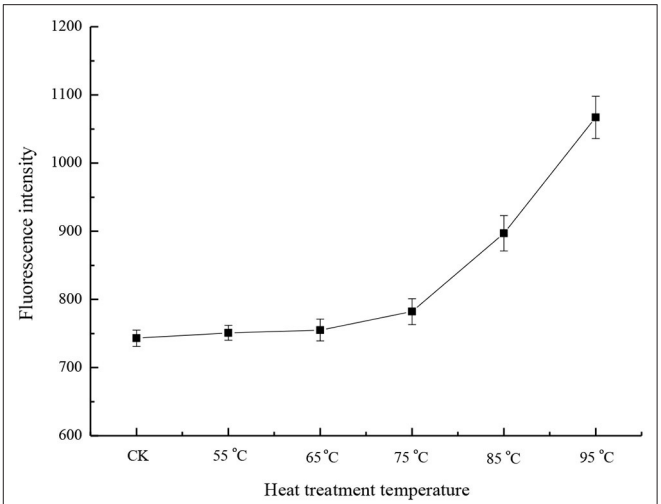

FIGURE 2 | Surface hydrophobicity of different heat-treated skim milk. CK, skim milk without heat treatment.

with the increasing of heat treatment temperature, the sulfhydryl content drops significantly ($p < 0.05$). When the treatment temperature reached 95°C, sulfhydryl content was only 24.1% of the control sample. This indicated that heat treatment induced the formation of aggregates through thiol-disulfide exchange. Sulfhydryl is one of the important functional groups in proteins, and it mainly exists in cysteine residues. In milk proteins, sulfhydryl exists in the form of a free thiol group and disulfide bond, and it is important for the maintenance of the native structure of proteins (12). Since heat treatment can cause protein aggregation through thiol-disulfide exchange, and then result in further aggregation *via* hydrophobic association, sulfhydryl content can be used to characterize the aggregation degree of protein samples (17, 21).

In milk proteins, only β-LG has a free thiol group, so the effect of heat treatment on sulfhydryl is mainly focused on β-LG (12). After heat treatment, the free thiol group of β-LG was exposed and involved in the thiol-disulfide exchange reaction, so this free thiol group has the potential to react with other proteins, such as κ-casein and BSA (5, 22). Cho et al. have reported that disulfide bonds and the free thiol group present in β-LG play a very important role in the formation of the β-LG /κ-casein complex by SH/S-S interchange (18). Another possibility to reduce the sulfhydryl content is by the interaction of two β-LG molecules to form a disulfide-bonded dimer (19).

Surface Hydrophobicity Analysis

Hydrophobicity is a property that affects the functionalities of proteins, and is mainly determined by the amino acid composition of proteins. The surface hydrophobicity of the heated samples increased in the heat temperature range of 75 to 95°C (**Figure 2**). At 95°C, the surface hydrophobicity was 1.44 times that of the control sample. This was consistent with the previous results (23, 24). Hiller and Lorenzen (25) studied the surface hydrophobicity of heat-treated milk proteins such as whey protein isolate, micellar casein, and BSA. The results showed that heat treatment increased the surface hydrophobicity of whey protein isolate and decreased the surface hydrophobicity of BSA, and that the treatment had a little effect on casein. Since BSA accounts for only 1.2% of milk proteins (26), the change in surface hydrophobicity mainly depends on other whey proteins. During heat treatment, β-LG is denatured first, followed by α-LA. When milk was heated at temperatures above 65°C, whey proteins, such as β-LG, α-LA, BSA, and lactoferrin unfolded and exposed previously buried hydrophobic groups, so the surface hydrophobicity was increased at a higher temperature (26). Moreover, the denaturation of whey proteins is reversible at a temperature range of 55 to 65°C, and irreversible at a higher temperature (5, 23).

FTIR Analysis

Fourier transform infrared spectroscopy was selected to obtain the spectrum of skim milk proteins, which illustrated protein conformation. The FTIR spectra of the samples with different heat treatments are shown in **Figure 3**. Generally, the FTIR spectra of proteins have a strong absorption band in the 1,700–1,600 cm^{-1} region (amide I), which indicates the C = O stretching mode of the peptide chain. In the amide I region, the band that appears at 1,660–1,640 cm^{-1} represents α-helix and random coil, and the band that appears at 1,640–1,620 cm^{-1} represents β-sheet. **Figure 3** shows that amide I peak positions have changed slightly in the different samples. Position altering in amide I revealed the change in the secondary structure of milk proteins. In order to obtain further information on secondary structural changes, the OMNIC analysis procedure was used to calculate the proportions of α-helix, β-sheet, β-turn, and random coil in skim milk proteins (**Table 1**). Random coil was increased, and β-turn was decreased as the heat temperature increased, suggesting the direct conversion of regular β-turn into an irregular random coil with the reduction of the intramolecular

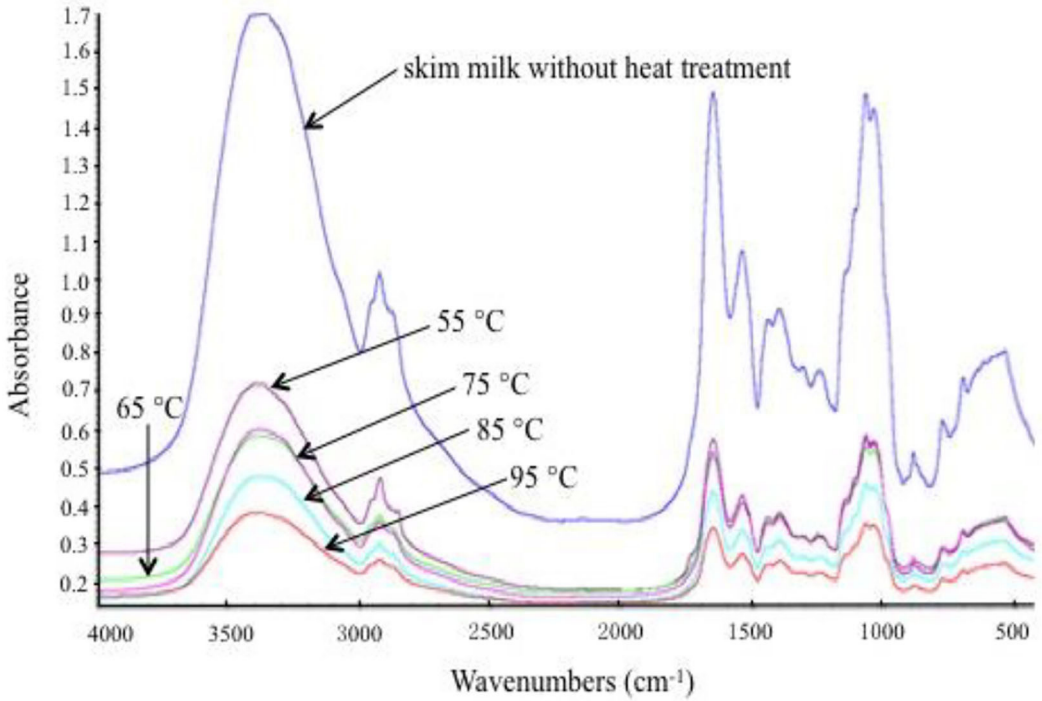

FIGURE 3 | Fourier transform infrared (FTIR) spectra of different heat-treated skim milk.

TABLE 1 | Percentage of secondary structures of skim milk heat-treated at different temperatures.

Heat treat temperature	β-sheet	Random coil	α-helix	β-turn
Skim milk	30.8	9.4	10.3	49.5
55°C	31.9	9.5	10.1	48.5
65°C	33.3	9.6	10.1	47.0
75°C	32.2	10.7	10.0	47.1
85°C	30.4	12.3	10.3	46.9
95°C	32.0	12.5	9.5	46.0

hydrogen bond. The reduction of α-helix at 95°C might correspond to the partial unfolding of the α-helix region. The increase in β-sheet might be due to the exposure of hydrophobic regions of milk proteins, which is consistent with the surface hydrophobicity results. Although heat treatment affected the secondary structure of skim milk proteins, this change was not obvious. This might be because caseins, as the main protein in skim milk, mainly existed in casein micelles, and this structure was relatively stable at the above heat treatment temperature (9). Moreover, the subtle change in secondary structure related to the whey proteins. Studies have shown that the content of β-sheet in β-LG is increased when heated above 60°C (12), and that the formation of β-sheet in BSA is irreversible on heating above 70°C (27). The heat treatment of whey proteins caused an abrupt loss in some secondary structures such as disrupted random coil, β-sheet, and β-turn, resulting in the exposure of the free thiol group and, thus, increasing the exposure of inner hydrophobic amino acids (28). This further accelerated the aggregation between milk proteins through disulfide bond and hydrophobic interaction.

Microstructure of Heat-Treated Skim Milk

Scanning electron microscopy micrographs were obtained from the skim milk samples treated with different temperatures (**Figure 4**). The SEM images indicated that the morphology of the skim milk proteins heated at 55°C had little change compared with that of the control sample (**Figures 4A,B**). Caseins (big particles) and whey proteins (small particles) separately dispersed, and no aggregation was formed. The image of samples heated at 65 and 75°C (**Figures 4C,D**) showed that some proteins aggregated to form casein micellar particles with relatively small whey protein complexes present. The heat treatment of skim milk at 85°C (**Figure 4E**) showed a higher degree of aggregation between caseins, but also

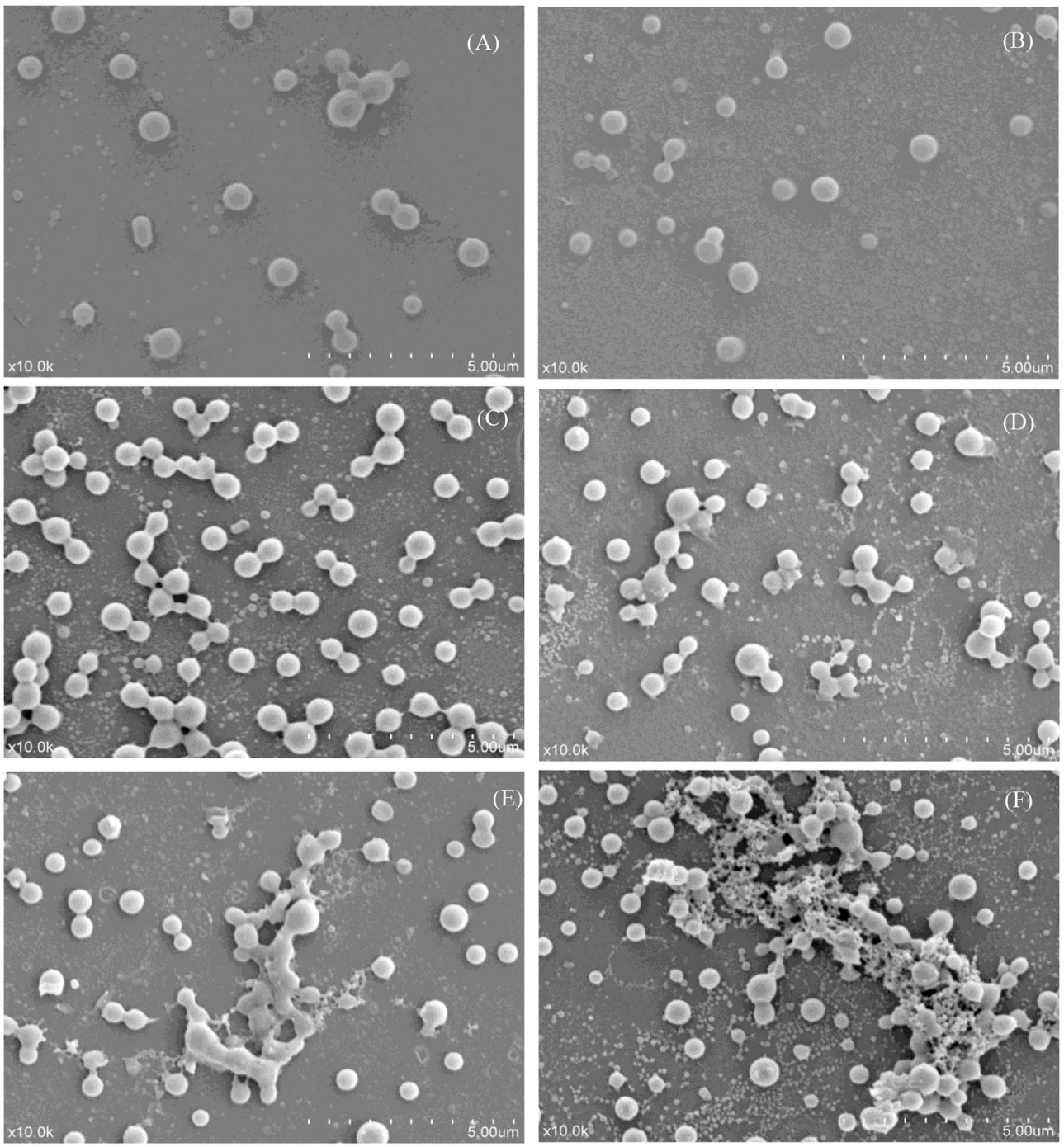

FIGURE 4 | Scanning electron micrographs of different heat-treated skim milk. **(A)** Skim milk without heat treatment; **(B–F)** skim milk heat treated at 55, 65, 75, 85, and 95°C, respectively. All the micrographs were originally taken at a magnification of 10,000 ×. The scale bar represents 5 μm.

demonstrated the presence of smaller whey protein complexes. The heat temperature of the sample reached 95°C and resulted in a rather loose and reticular structure, with the interaction between casein and whey protein. It was obvious that the aggregation was a large casein cluster aggregated by small whey protein particles (**Figure 4F**). This aggregation had been demonstrated by disulfide bonds (29) and, to a much lesser extent, by non-covalent bonds (4). Unfortunately, it could not determine which casein and whey protein participated in the aggregation through SEM, so a 2D-PAGE analysis was performed to study the interaction between milk proteins.

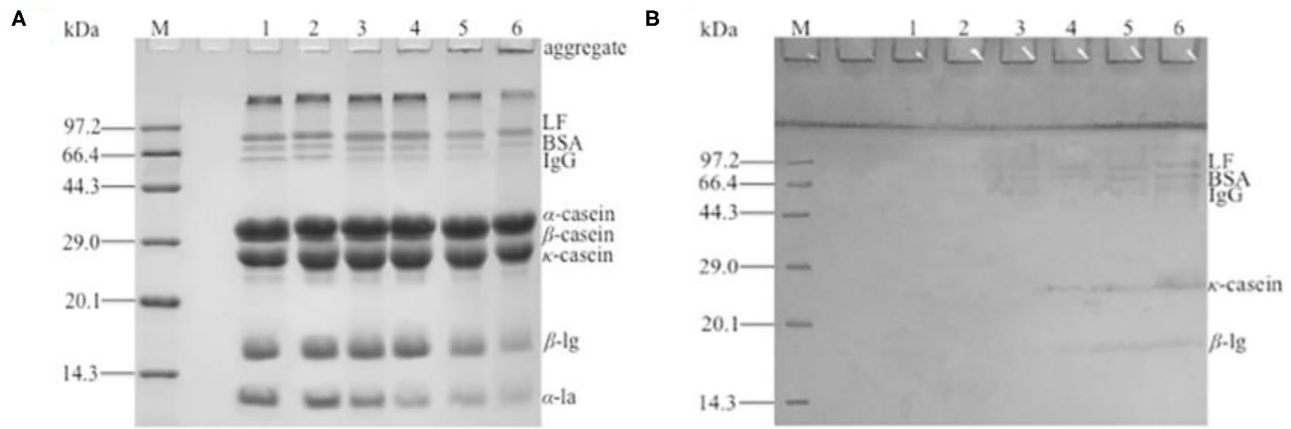

FIGURE 5 | Two-dimensional (2D) sodium dodecyl sulfate–polyacrylamide gel electrophoresis (SDS-PAGE) of different heat-treated skim milk. **(A)** Non-reduced SDS-PAGE of heat-treated samples; **(B)** reduced SDS-PAGE of protein aggregates excised from non-reduced gel. Lane M, protein marker; lane 1, skim milk without heat treatment; lanes 2–6, skim milk heat treatment at 55, 65, 75, 85, and 95°C, respectively.

PAGE Analysis

The heat-treated samples were analyzed by non-reduced SDS-PAGE (**Figure 5A**) and, after reduction with β-ME, by reduced SDS-PAGE (**Figure 5B**). As seen in **Figure 5A**, the intensity of bands corresponding to β-LG and α-LA are markedly reduced with the increase in heat temperature. It can be noted that the lower heat treatment temperatures (55 and 65°C) limited the denaturation and aggregation of β-LG and α-LA, with more than 95% of the above proteins remaining in its native form, similar to the sample without heat treatment, while heat treatment at 95°C promoted the denaturation of most β-LG and α-LA with the rearrangement of the spatial structure. Other minor whey proteins such as BSA, lactoferrin, and immune globulin were very unstable, and the lower intensities of bands that correspond to these three proteins were observed in the samples heat-treated at 65°C. The immune globulin G and BSA bands were essentially absent in the severely heat-treated sample (95°C). Furthermore, large protein aggregates were present in the loading well-indicating molecular weights well-above 200 kDa. The density of the aggregates was enhanced with the increase in heat temperature. By comparison, the SDS-PAGE of reduced samples appeared to be similar (data not shown), indicating that no irreducible covalent bonds formed and that no polypeptide bond was cleaved by the heat treatment (19, 30).

The protein aggregates were excised from the non-reduced gel for the second dimension (**Figure 5B**). The result showed that a series of bands were present in the SDS-PAGE gel and that the molecular weight was identical to the immune globulin G, BSA, lactoferrin, κ-casein, and β-LG, indicating that the aggregates were formed by the polymerization of the referred proteins. Because immune globulin G, BSA, and lactoferrin were denatured at a lower temperature (13), the aggregates formed at 65°C were mainly these three proteins. With the increase in heat treatment temperature, κ-casein and β-LG participated in the polymerization. A polymerization experiment of α-LA, β-LG, κ-casein, and BSA by dissolving two of them in simulated milk ultrafiltrate was done (data not shown). The result showed that β-LG could react with other β-LG or κ-casein and accelerate the denaturation and aggregation of α-LA. BSA responded to the heat treatment similarly to β-LG, except that BSA reacted at a lower temperature. This result further demonstrated that the heat-induced aggregates mainly composed by β-LG, κ-casein and BSA. This was similar with the previous reports (5, 19, 31). It was generally considered that β-LG could react with other β-LG or κ-casein through disulfide bonds (17, 18). The result of sulfhydryl content showed that the free thiol group was used to form disulfide bond with other milk protein, so the sulfhydryl content dropped significantly with the increase in heat treatment temperature. In general, reactivity of free thiol group is dependent on the protein unfolding degree, as well as disulfide interchange occurring at high temperature (29). In the SDS-PAGE, monomer structure of κ-casein and β-LG were observed after aggregates were reduced by β-ME. This indicated that the new disulfide bond existed in the aggregates, and this result was consistent with the decrease in sulfhydryl content. However, α-LA was not observed in the SDS-PAGE, and this might be because of the intensity of aggregates containing α-LA was too low to observe. Although α_{s2}-casein, which had two Cys residues, did not react with β-LG, it was present as a dimer with intermolecular disulfide bonds (32). This was because α_{s2}-casein was not located at the surface of the micelle, and the disulfide bonds were not accessible to the denaturing or denatured β-LG (30). The aggregates of the other two caseins, α_{s1}-casein and β-casein (12), were formed by hydrophobic interaction, so α_{s1}-casein and β-casein were absent from the SDS-PAGE gel.

CONCLUSION

In this study, the mechanism of heat-induced milk protein aggregates was investigated in detail. The result showed that heat treatment decreased sulfhydryl content, increased surface

hydrophobicity, and disrupted the secondary structure of milk proteins. The change in these properties accelerated the denaturation of milk proteins and the formation of aggregates linked by disulfide bonds and hydrophobicity interaction. Moreover, the aggregates were formed at high heat temperature mainly composed of κ-casein, β-LG, and other whey proteins.

DATA AVAILABILITY STATEMENT

The original contributions presented in the study are included in the article/**Supplementary Material**, further inquiries can be directed to the corresponding author.

AUTHOR CONTRIBUTIONS

This study was conceived, designed, and written by HongbL. TZ performed the experiments and analyzed the data. HongjL improved the manuscript. JY provided experimental technical support. All authors contributed to the article and approved the submitted version.

FUNDING

This study was financially supported by the National Key Research and Development Program of China (Grant No. 2017YFE0131800), and Tianjin Municipal Education Commission (Grant No. 2018KJ092).

SUPPLEMENTARY MATERIAL

The Supplementary Material for this article can be found online at: https://www.frontiersin.org/articles/10.3389/fnut.2021.714869/full#supplementary-material

REFERENCES

1. Goff HD. Introduction to dairy science and technology: milk history, consumption, production, and composition. In: *The Dairy Science and Technology eBook*. Guelph, ON: University of Guelph. Available online at: https://www.uoguelph.ca/foodscience/book-page/dairy-science-and-technology-ebook
2. Wang W, Zhang L, Li Y, Feng Z. Heat-induced protein aggregates and difference in the textural properties of whole milk gel. *J Food Qual.* (2012) 35:247–54. doi: 10.1111/j.1745-4557.2012.00444.x
3. Osman M, Abdalla M, Mohammed H, Salih A. Effect of heat treatment of milk on the physicochemical, microbiological and sensory characteristics of white cheese (*Gibna bayda*). *GSC Adv Res Rev.* (2020) 3:20–8. doi: 10.30574/gscarr.2020.3.3.0044
4. Zhao X, Cheng M, Zhang X, Li X, Wang C. The effect of heat treatment on the microstructure and functional properties of whey protein from goat milk. *J Dairy Sci.* (2019) 103:1289–302. doi: 10.3168/jds.2019-17221
5. Wagner J, Biliaderis CG, Moschakis T. Whey proteins: musings on denaturation, aggregate formation and gelation. *Cri Rev Food Sci Nutri.* (2020) 60:3793–806. doi: 10.1080/10408398.2019.1708263
6. Guyomarc'h F, Nono M, Nicolai T, Durand D. Heat-induced aggregation of whey proteins in the presence of κ-casein or sodium caseinate. *Food Hydrocoll.* (2009) 23:1103–10. doi: 10.1016/j.foodhyd.2008.07.001
7. Wijayanti HB, Bansal N, Deeth HC. Stability of whey proteins during thermal processing: a review. *Compre Rev Food Sci Food Safety.* (2014) 13:1235–51. doi: 10.1111/1541-4337.12105
8. Akkerman M, Rauh VM, Christensen M, Johansen LB, Hammershoj M, Larsen LB. Effect of heating strategies on whey protein denaturation-revisited by liquid chromatography quadrupole time-of-flight mass spectrometry. *J Dairy Sci.* (2016) 99:152–66. doi: 10.3168/jds.2015-9924
9. Halabi A, Deglaire A, Hamon P, Bouhallab S, Dupont D, Croguennec T. Kinetics of heat-induced denaturation of proteins in model infant milk formulas as a function of whey protein composition. *Food Chem.* (2019) 302:125296. doi: 10.1016/j.foodchem.2019.125296
10. Villa C, Costa J, Oliveira M, Mafra I. Bovine milk allergens: a comprehensive review. *Compr Rev Food Sci Food Saf.* (2018) 17:137–64. doi: 10.1111/1541-4337.12318
11. Donato L, Guyomarc'h F, Amiot S, Dalgleish DG. Formation of whey protein/κ-casein complexes in heated milk: preferential reaction of whey protein with κ-casein in the casein micelles. *Int Dairy J.* (2007) 17:1161–7. doi: 10.1016/j.idairyj.2007.03.011
12. Considine T, Patel HA, Anema SG, Singh H, Creamer LK. Interactions of milk proteins during heat and high hydrostatic pressure treatments - a review. *Innov Food Sci Emerge Technol.* (2007) 8:1–23. doi: 10.1016/j.ifset.2006.08.003
13. Xiong L, Boeren S, Vervoort J, Hettinga K. Effect of milk serum proteins on aggregation, bacteriostatic activity and digestion of lactoferrin after heat treatment. *Food Chem.* (2021) 337:127973–83. doi: 10.1016/j.foodchem.2020.127973
14. Peram MR, Loveday SM, Ye A, Singh H. *In vitro* gastric digestion of heat-induced aggregates of β-lactoglobulin. *J. Dairy Sci.* (2013) 96:63–74. doi: 10.3168/jds.2012-5896
15. Li Q, Zhao Z. Interaction between lactoferrin and whey proteins and its influence on the heat-induced gelation of whey proteins. *Food Chem.* (2018) 252:92–8. doi: 10.1016/j.foodchem.2018.01.114
16. Chevalier F, Kelly AL. Proteomic quantification of disulfide-linked polymers in raw and heated bovine milk. *J Agr Food Chem.* (2010) 58:7437–44. doi: 10.1021/jf1010879
17. Xiong L, Li C, Boeren S, Vervoort J, Hettinga K. Effect of heat treatment on bacteriostatic activity and protein profile of bovine whey proteins. *Food Res Int.* (2019) 127:108688. doi: 10.1016/j.foodres.2019.108688
18. Cho Y, Singh H, Creamer LK. Heat-induced interactions of β-lactoglobulin A and κ-casein B in a model system. *J Dairy Res.* (2003) 70:61–71. doi: 10.1017/S0022029902005642
19. Xu W, He S, Ying M, Zhang Y, Wang R. Effect of the heat-induced whey proteins/κ-casein complex on the acid gelation of yak milk. *Res Adv.* (2015) 5:8952–6. doi: 10.1039/C4RA14432E
20. AOAC. *Official Methods of Analysis of AOAC International.* 18th ed. Arlington: AOAC (2016).
21. Havea P, Carr AJ, Creamer LK. The roles of disulphide and non-covalent bonding in the functional properties of heat-induced whey protein gels. *J Dairy Res.* (2004) 71:330–9. doi: 10.1017/S002202990400024X
22. Creamer LK, Bienvenie A, Nilsson H, Paulsson M, Wanroij MV, Lowe EK, et al. Heat-induced redistribution of disulfide bonds in milk proteins. 1. bovine β-Lactoglobulin. *J Agr Food Chem.* (2004) 52:7660–8. doi: 10.1021/jf049388y
23. Moro A, Gatti C, Delorenzi N. Hydrophobicity of whey protein concentrates measured by fluorescence quenching and its relation with surface functional properties. *J Agric Food Chem.* (2001) 49:4784–9. doi: 10.1021/jf001132e
24. Kim DA, Cornec M, Narsimhan G. Effect of thermal treatment on interfacial properties of β-lactoglobulin. *Colloid J Interface Sci.* (2005) 285:100–9. doi: 10.1016/j.jcis.2004.10.044
25. Hiller B, Lorenzen PC. Surface hydrophobicity of physicochemically and enzymatically treated milk proteins in relation to techno-functional properties. *J Agric Food Chem.* (2008) 56:461–8. doi: 10.1021/jf072400c

26. Raikos V. Effect of heat treatment on milk protein functionality at emulsion interfaces. A review. *Food Hydrocoll.* (2010) 24:259–65. doi: 10.1016/j.foodhyd.2009.10.014
27. Murayama K, Tomida M. Heat-induced secondary structure and conformation change of bovine serum albumin investigated by fourier transform infrared spectroscopy. *Biochemistry.* (2004) 43:11526–32. doi: 10.1021/bi0489154
28. Croguennec T, O'Kennedy BT, Mehra R. Heat-induced denaturation/aggregation of β-lactoglobulin A and B: kinetics of the first intermediates formed. *Int Dairy J.* (2004) 14:399–409. doi: 10.1016/j.idairyj.2003.09.005
29. Pereira,1 RN, Costa J, Rodrigues RM, Villa C, Machado L, Mafra I, et al. Effects of ohmic heating on the immunoreactivity of β-lactoglobulin - a relationship towards structural aspects. *Food Funct.* (2020) 5:4002–13. doi: 10.1039/C9FO02834J
30. Patel HA, Singh H, Anema SG, Creamer LK. Effects of heat and high hydrostatic pressure treatments on disulfide bonding interchanges among the proteins in skim milk. *J Agric Food Chem.* (2006) 54:3409–20. doi: 10.1021/jf052834c
31. Hong YH, Creamer LK. Changed protein structures of bovine β-lactoglobulin B and α-lactalbumin as a consequence of heat treatment. *Int. Dairy J.* (2002) 12:345–59. doi: 10.1016/S0958-6946(02)00030-4
32. Rasmussen LK, Højrup P, Petersen TE. Localization of two interchain disulfide bridges in dimers of bovine αs2-casein. *Eur J Biochem.* (1992) 203:381–6. doi: 10.1111/j.1432-1033.1992.tb16561.x

Conflict of Interest: The authors declare that the research was conducted in the absence of any commercial or financial relationships that could be construed as a potential conflict of interest.

Publisher's Note: All claims expressed in this article are solely those of the authors and do not necessarily represent those of their affiliated organizations, or those of the publisher, the editors and the reviewers. Any product that may be evaluated in this article, or claim that may be made by its manufacturer, is not guaranteed or endorsed by the publisher.

frontiers in Nutrition

ORIGINAL RESEARCH
published: 16 November 2021
doi: 10.3389/fnut.2021.769463

Effect of Aqueous Enzymatic Extraction of Deer Oil on Its Components and Its Protective Effect on Gastric Mucosa Injury

Yun-Shi Xia[1,2], Yin-shi Sun[1,2], Chang Liu[3], Zhi-Man Li[2], Duo-Duo Ren[1,2], Rui Mu[1,2], Yan-Ting Zhang[2], Pan-Pan Bo[1,2], Li-juan Zhao[2] and Zi Wang[1]**

[1] College of Chinese Medicinal Materials, Jilin Agricultural University, Changchun, China, [2] Institute of Special Wild Economic Animals and Plants, Chinese Academy of Agricultural Sciences, Changchun, China, [3] College of Food Science and Engineering, Changchun University, Changchun, China

In this study, deer suet fat was used as a raw material to study the effects of aqueous enzymatic extraction of deer oil on its components, followed by studies into the potential protective activity, and related molecular mechanisms of deer oil on ethanol-induced acute gastric mucosal injury in rats. The results show that aqueous enzymatic extraction of deer oil not only has a high extraction yield and has a small effect on the content of active ingredients. Deer oil can reduce total stomach injury. Without affecting the blood lipid level, it can reduce the oxidative stress, which is manifested by reducing the content of myeloperoxidase (MPO) and enhancing the activity level of superoxide dismutase (SOD) and glutathione peroxidase (GSH-Px). It also enhances the expression of defense factors prostaglandin (E2), epidermal growth factor (EGF), and somatostatin (SS), it inhibits apoptosis evidenced by the enhanced of Bcl-2 and decreased expression of cleavage of caspase-3 and Bax. At the same time, it reduces inflammation, which is manifested by reducing the expression of IL-1β, interleukin 6 (IL-6), and tumor necrosis factor alpha (TNF-α) gastric tissue pro-inflammatory cytokines, and enhancing the expression of anti-inflammatory factors IL-4 and IL-10, and inhibiting the mitogen-activated protein kinase/nuclear factor kappa B (MAPK/NF-κB) signaling pathway in gastric tissue.

Keywords: deer oil, aqueous enzymatic extraction, ethanol, gastric mucosal injury, MAPK pathway, NF-κB pathway

OPEN ACCESS

Edited by:
Jinkai Zheng,
Institute of Food Science and Technology, Chinese Academy of Agricultural Sciences (CAAS), China

Reviewed by:
Yueliang Zhao,
Shanghai Ocean University, China
Jiangning Hu,
Dalian Polytechnic University, China
Wei Li,
Jilin Agricultural University, China

***Correspondence:**
Yin-shi Sun
sunyinshi2015@163.com
Zi Wang
wangzi8020@126.com

Specialty section:
This article was submitted to Food Chemistry, a section of the journal Frontiers in Nutrition

Received: *02 September 2021*
Accepted: *26 October 2021*
Published: *16 November 2021*

Citation:
Xia Y-S, Sun Y-s, Liu C, Li Z-M, Ren D-D, Mu R, Zhang Y-T, Bo P-P, Zhao L-j and Wang Z (2021) Effect of Aqueous Enzymatic Extraction of Deer Oil on Its Components and Its Protective Effect on Gastric Mucosa Injury. Front. Nutr. 8:769463. doi: 10.3389/fnut.2021.769463

INTRODUCTION

A gastric ulcer is a peptic ulcer that occurs in the corners of the stomach, gastric antrum, cardia, and hiatal hernia (1). It is one of the most common diseases worldwide. There are many factors that cause gastric ulcers, such as *Helicobacter pylori* infection, drugs, dietary factors, stress, and abnormal gastric motility, which are more common in middle-aged and elderly people due to chronic exposure to risk factors irregular eating, mental stress, etc. (2). Severe gastric ulcers have complications such as upper gastrointestinal bleeding, ulcer perforation, pyloric obstruction, and even cancer (3).

The most intuitive manifestation of gastric ulcers is gastric mucosal damage. Alcoholism is one of the most important inducing factors. The direct contact of ethanol and mucosa can

induce many metabolic and functional changes leading to mucosal damage, with symptoms such as acute gastrointestinal bleeding and diarrhea. It can also cause gastric mucosal necrosis due to acute hemorrhagic lesions, mucosal edema, epithelial dissection, and inflammatory cell infiltration. The pathogenesis of ethanol-triggered gastric ulcers is multifactorial and includes mucosal inflammation, oxidative stress, and epithelial cell apoptosis. The influx of activated neutrophils into gastric tissues triggers the release of diverse proinflammatory cytokines that amplify the inflammatory process in gastric mucosa (4). In the context of mucosal inflammation, the nuclear factor kappa B (NF-κB) pathway is considered a core participant in the inflammatory environment. Driven by proinflammatory cytokines and reactive oxygen species (ROS), activated NF-κB increases. The transcription of various inflammatory signals can enhance the occurrence of inflammation. In addition, the mitogen-activated protein kinase (MAPK) pathway involves p38MAPK, extracellular signal-regulated kinase (ERK) and cJun N-terminal kinase (JNK), which are transduction pathways that express various protoinflammatory mediators and apoptosis signals (5). Currently, the main clinical treatment of gastric ulcers includes the use of synthetic anti-secretory drugs, such as H2 receptor antagonists (cimetidine) or proton pump inhibitors (omeprazole), antibiotics (clarithromycin), and antacids. Although these synthetic drugs have high purity, their long-term use may also cause a variety of side effects (6). Therefore, it is necessary to find safe and effective drugs from nature (7).

Deer oil is the fatty oil of the sika deer (*Cervus nippon*) or red deer (*Cervus elaphus*). It is also called deer fat. It is a widely sourced natural biological resource with easy access. The extraction of deer oil mainly adopts the boiling method, and the aqueous enzymatic method of extracting oil has mild conditions, and the enzyme-related degradation products do not react with the oil, which can effectively protect the oil, protein, and secondary degradation products, etc. The obtained oil has high purity and good quality (8). Current research into the composition of deer oil has focused on fatty acids and amino acids, which are easily absorbed by the skin to prevent water loss and delay aging. Deer oil has a certain antioxidant activity, so it has a certain development prospect in cosmetics and health products industry. According to research of lard and other animal fats, deer oil has a significant protective effect on acute gastric mucosal injury caused by ethanol (9). However, the protective mechanism of deer oil on gastric mucosal damage is still not understood. Based on the known protective effect of deer oil against gastric mucosal injury, the protective effect of deer oil form on alcohol-induced gastric mucosal injury and its possible mechanism were explored.

MATERIALS AND METHODS

Materials and Animals

Animals and reagents were procured as follows: 8-week-old SD rats, weighing 170–180 g, were purchased from Liaoning Changsheng Biotechnology Co., Ltd., certificate number SCXK (Liao) 2015-0001; deer oil: unprocessed fresh suet fat from Changchun Shilu Deer Industry Co., Ltd.; neutral protease and alkaline protease: Solarbio; superoxide dismutase (SOD) and glutathione peroxidase (GSH-Px) kits: Nanjing Jiancheng Institute of Biological Engineering; myeloperoxidase (MPO), rat tumor necrosis factor alpha (TNF-α), rat interleukin 6 (IL-6), rat interleukin 4 (IL-4), rat interleukin 10 (IL-10), prostaglandin (E2), epidermal growth factor (EGF), and somatostatin (SS) kits: Shanghai Enzyme-Linked Biotechnology Co., Ltd. (MLBIO); anhydrous ethanol: Sinopharm Chemical Reagent Co., Ltd.; physiological saline: Kunming Nanjiang Pharmaceutical Co., Ltd.; sodium pentobarbital and 10% neutral formalin: Beijing Coolaibo Technology Co., Ltd.; IκBα(H-4), NFκB, p38α/β MAPK(A-12), ERK(D-2), JNK(D-2), p-NFκB p65(27.Ser 536), p-JNK(G-7), p-p38 MAPK(D-8), p-ERK(E-4), p-IκBα, IKKα/β, GAPDH: Santa Cruz Biotechnology, Int; caspase-3, Bcl-2, Bax: abcam.

Water Extraction of Deer Oil

The deer oil was extracted in the laboratory according to the optimal extraction process determined in literature (10). Accurately weigh 200 g of washed and drained frozen deer suet oil, and use a blender to chop it into small pieces. Under the conditions of solid-liquid ratio 1:1, compound enzyme ratio (neutral protease and alkaline protease) 1:3, compound enzyme dosage 2%, extraction temperature 55°C, extraction time 2.5 h, pH 7.0. Then use the vacuum drying method to remove excess water, deer oil was obtained.

Determination of Basic Indicators

Determination of the Yield

Record the weight of the initial fresh deer suet oil before extraction and the quality of the deer oil extracted after filtration (11).

Yield = The quality of filtered deer oil/Weight of initial fresh Luer Suet before extraction × 100%.

Moisture Determination

Determined according to China GB5009.3-2016.

Composition Determination

Protein

Weigh 2–5 g of sample (approximately equivalent to 30–40 mg nitrogen), accurate to 0.001 g, detected on a fast nitrogen analyzer. The CR temperature is above 1,030°C, and the RR temperature is above 650°C.

Phospholipids

Refer to the molybdenum blue colorimetric method in the China standard SN/T 3851-2014.

Cholesterol

Weigh 250 mg deer oil (accurate to 1 mg) into a 25 ml flask, add 1.0 ml betulin internal standard solution. Add 5 ml of potassium hydroxide-ethanol solution, heat to keep it boiling for 15 min, add 5 ml of ethanol and shake well. Pipette 5 ml of the above liquid into the prepared alumina column, collect the eluent, first eluting with 5 ml of ethanol, then eluting with 30 ml of ether, and remove the solvent in the flask with a rotary evaporator.

Gas chromatographic conditions: Stationary phase: SE-54, length 50 m, inner diameter 0.25 mm, film thickness 0.10 μm; Carrier gas: helium, carrier gas flow rate: 36 cm/s, split ratio 1:20; Detector temperature and inlet temperature: 320°C; The column temperature adopts the programmed heating method, which is increased from 240 to 255°C at a rate of 4°C/min; injection volume: 1 μl.

Fatty Acids

Methyl Ester Treatment

Weigh 150 mg deer oil, add 8 ml of 2% NaOH-methanol solution, and reflux at 80 ± 1°C until the oil droplets disappear. Cool down to room temperature, add 7 ml of 15% BF_3-methanol solution, reflux at 80 ± 1°C for 3 min, take it out, and quickly cool to room temperature. Accurately add 15 ml of n-heptane, vortex for 2 min, add saturated NaCl aqueous solution, and stand to separate layers. Pipette about 5 ml of the upper n-heptane solution into a 50 ml centrifuge tube containing 3–5 g of anhydrous sodium sulfate, vortex for 1 min, centrifuge, and dilute the supernatant by 10 times or 100 times for injection.

GC/MS Instrument Conditions Chromatographic Column

DB-23 60 m × 0.25 × 0.25 μm; Carrier gas: high purity He; Carrier gas flow: 1.0 ml/min; Inlet: 220°C; EI source: 230°C; Program temperature rise conditions: the initial temperature is 60°C, keep for 1 min, 10°C/min, increase to 180°C, then 3°C/min to 220°C, hold for 2 min.

Gastric Mucosal Injury Caused by Ethanol

Rat Body Weight and Organ Index

Thirty healthy male SD rats were selected and kept in an environment with a temperature of 22–25°C and a relative humidity of 45–65%. They were free to drink and eat. After 1 week of adaptive feeding, they were randomly divided into five groups with six rats in each group: indicated as the normal group, model group, positive control drug (0.1 g/kg cimetidine) group, low-dose deer oil group (0.50 g/kg, L-Deer oil), high-dose deer oil group (0.85 g/kg, H-Deer oil). Weights were recorded for the predose period (before dosing on the 1st day), midterm (before dosing on the 15th day), and final period (before the 30th day of dosing). The normal group and the model group were given normal saline; the deer oil groups were given 10 ml/(kg·bw) once a day for 30 consecutive days. After the last administration, food and water were withheld for 24 h. Except for the normal group, rats in the other groups were given 1.0 ml of absolute ethanol per rat. After 1 h, the rats were anesthetized with sodium pentobarbital, and the heart was sacrificed. The gastric tissue was taken and weighed (12–14).

Histopathological Examination of Rat Gastric Mucosa

After blood was collected and the rat was sacrificed, whole gastric tissue was collected, the pylorus was ligated, and 10% formalin was perfused. After fixation for 20 min, the stomach was cut along its greater curvature. The gastric surface contents were washed with normal saline, and the gastric mucosa was unfolded with a Vernier caliper. The length and width of the bleeding zone and the number of bleeding points were recorded, and the score was determined according to the bleeding of the gastric mucosa in **Table 1**, according to the scoring method in Xia et al. (8). After observation, the most severely injured part of the gastric mucosa was selected, fixed in 10% neutral formalin, washed with water, dehydrated, and immersed in wax, which was sliced continuously at a thickness of 5 μm followed by deparaffinization to water. After H&E staining, pathological changes in rat stomach tissues were observed under a microscope (15, 16).

TABLE 1 | Criteria for visual observation of ethanol in acute gastric mucosal injury in rats.

Scoring	1	2	3	4
Blood point	1			
Length of bleeding zone (mm)	1∼5	5∼10	10∼15	>15
Width of bleeding zone (mm)	1∼2	>2	–	–

Each bleeding point on the gastric mucosa is assigned one point, meaning that a bleeding band with width >2 will be assigned two points.

Determination of Cytokines

Determination of Blood Biochemical Indicators

The blood of the rat was centrifuged at 2,000 rpm/min for 20 min at 4°C, serum was drawn, and triglyceride (TG), total cholesterol (T-CHO), high-density lipoprotein (HDL-C), and low-density lipoprotein (LDL-C) contents were measured.

Analysis of SOD, GSH-Px, and MPO Levels in Gastric Tissue

Approximately 15 mg of gastric tissue was homogenized in physiological saline, centrifuged at 12,000 rpm/min for 10 min at 4°C, and the supernatant was stored at −80°C after collection. The protein content of the homogenate was determined by the BCA protein determination method, and the levels of SOD, GSH-Px, and MPO in the gastric tissue were determined according to the kit-supplied method.

Determination of Inflammatory and Defensive Factors in Gastric Tissue

The levels of IL-4, IL-6, IL-10, TNF-α, E2, EGF, and SS were measured according to the manufacturers' protocols, and the absorbance was measured at 450 nm with a microplate reader.

mRNA Expression in Gastric Tissue

Total RNA in the stomach tissue was extracted with the Easystep Super Total RNA Extraction Kit. After the RNA concentration was detected by a Quick Drop, the integrity was verified by 1% agarose gel electrophoresis. The isolated RNA was reverse transcribed into cDNA according to the BioRT cDNA synthesis kit method, and reverse transcription-PCR (RT-PCR) was performed using the gene-specific primers described in **Table 2**, with the expression level of GAPDH mRNA as a built-in parameter. Finally, agarose gel electrophoresis containing ethidium bromide was used to observe the PCR-amplified products with visualization using a computer image analysis system for semiquantitative analysis.

Western Blot Analysis

Protein was extracted from gastric homogenates with lysis buffer, and protein concentration was measured using the BCA method. Proteins were separated on a 10–15% SDS-PAGE gel and transferred to membrane at constant current of 200 mA. The membrane was then incubated with milk powder for 2 h, washed with PBST for 30 min, incubated with the primary antibody at 4°C overnight, washed again with PBST, and the corresponding secondary antibody was added and incubated with slow shaking at room temperature for 2 h. After the secondary antibody was washed away, HRP chemiluminescence detection was used for visualization and Image G image analysis. The net gray value of the band was compared with the measurement of the internal reference GAPDH, the ratio was calculated, and the differences between the groups were compared.

Statistical Analysis

All data are expressed as the means ± standard deviation (SD) and analyzed with GraphPad Prism 5.0. One-way analysis of variance (one-way ANOVA) was used to test the differences between groups, and $P < 0.05$ indicated significant differences.

RESULTS

The Influence of Aqueous Enzymatic Extraction of Deer Oil on Basic Indicators

The deer oil extracted by the aqueous enzymatic method is a light yellow transparent liquid, which may be because the low temperature extraction has little effect on the appearance and color of the deer oil. The aqueous enzymatic method uses related enzymes to degrade the oil cells and release the oil from the oil cells. In this experiment, the compound enzymes screened in the laboratory were used to extract deer oil, so that the enzymatic hydrolysis reaction proceeded more completely, so the yield of deer oil was higher. In **Table 3**, The water content of deer oil extracted by hydroenzymatic method was 4.33 ± 0.55%, the protein content was 0.12 ± 0.01%, the phospholipid content was 0.48 ± 0.01 mg/100 g, and the cholesterol content was 44.40 ± 0.96 mg/100 g. Life Science Identifiers.

TABLE 2 | Sequences of primers for RT-PCR amplification.

Target gene	Primer sequence (5′–3′)	Length (bp)
IL-1β	TGCTGATGTACCAGTTGGGG CTCCATGAGCTTTGTACAAG	245
IL-6	GCCCTTCAGGAACAGCTATG CAGAATTGCCATTGCACAAC	240
TNF-α	TGATCGGTCCCAACAAGGA TGCTTGGTGGTTTGCTACGA	140
EPO	ACCACTCCCAACCCTCATCAA CGTCCAGCACCCCGTAAATAG	325
EPOR	TGGATGAATGGTTGCGAC TTTGAAGCCAAGTCAGAG	127
GAPDH	AGGTCGGTGTGAACGGATTTG TGTAGACCATGTAGTTGAGGTCA	123

Influence of Aqueous Enzymatic Extraction of Deer Oil on Fatty Acid

It can be seen from **Table 4** that a total of 20 fatty acids were detected in the deer oil extracted by the aqueous enzymatic method. Among them, there are five kinds of fatty acids with content >5%, which are palmitic acid (C16:0), oleic acid (C18:1n9C), stearic acid (C18:0), palmitoleic acid (C16:1n7), and linoleic acid. Acid (C18:2n6). Nine kinds of saturated fatty acids, mainly including palmitic acid, stearic acid, myristic acid, etc., accounting for 57.44% of the total fatty acid; four types of monounsaturated fatty acids, including oleic acid, palmitoleic acid, etc., account for 28.87% of the total fatty acids; seven types of polyunsaturated fatty acids, including linoleic acid, linolenic acid, etc., account for 6.00% of the total fatty acids.

The Effect of Deer Oil on Gastric Mucosal Injury Induced by Ethanol in Rats

In **Table 5**, during the test period, the rats in each group continued to increase their body weight, and there was no significant difference compared with the normal group ($P > 0.05$). Compared with the normal group, the organ index of the model group was significantly higher than that of the normal group ($P < 0.001$), with evidence such as bleeding and edema apparent, indicating success of the model; the organ index, gastric mucosal congestion area, and injury score index of rats in each administration group were reduced to a certain extent compared with the model group ($P < 0.001$, $P < 0.01$, $P < 0.05$).

As shown in **Figure 1A**, the gastric mucosa of rats in the normal group was intact and smooth, without bleeding points or bands; the gastric mucosal surface of rats in the model group was severely congested and swollen, with darker and thicker bleeding bands; the gastric mucosa of rats in the positive drug group had a small amount of slight bleeding on the surface of the gastric mucosa, and the color was lighter; the rats in the deer oil group had slight local bleeding on the gastric mucosa, with small bleeding bands and bleeding spots on the surface.

The results of H&E staining showed that the gastric mucosal cells of the normal group were tightly arranged and ordered, the cells were darker in blue and purple, and the overall gastric mucosal morphology was complete, with clear and obvious boundaries; the gastric mucosal cells of the model group were

TABLE 3 | The effect of aqueous enzymatic extraction of deer oil on basic indicators.

Appearance characteristics	Yield (%)	Water content (%)	Protein (%)	Phospholipids (mg/100 g)	Cholesterol (mg/100 g)
Light yellow transparent liquid	85.63 ± 7.39	4.33 ± 0.55	0.12 ± 0.01	0.48 ± 0.01	44.40 ± 0.96

loosely arranged, disordered, and hollow. Cells aggregated into pieces, with inflammatory infiltration and swelling of the gastric mucosa; the cells of the deer oil group was arranged in an orderly manner, and the fragmented cells were significantly reduced. In addition, the deer oil treatment groups showed dose-dependent protection of gastric mucosal morphology (**Figure 1B**).

The Effect of Deer Oil on Cytokines in Rats

As shown in **Figure 2**, compared with the normal group, the blood lipid levels of rats in each administration group increased to a certain extent, but there was no significant difference ($P > 0.05$). Compared with the normal group, the GSH-Px activity of the model group decreased ($P < 0.001$), the MPO level increased ($P < 0.05$), and the activity of E2, EGF, and SS decreased ($P < 0.05$, $P < 0.001$), indicating that absolute ethanol caused oxidative stress in rats and a decrease in the level of defensive factors. Compared with the model group, pretreatment in the positive drug group increased the activity of E2 and SS ($P < 0.05$); pretreatment with deer oil effectively increased the activity of SOD and GSH-Px ($P < 0.01$, $P < 0.001$) and reduced the MPO level ($P < 0.05$), increased the activity of EGF and SS ($P < 0.05$, $P < 0.01$), and was dose-dependent.

TABLE 4 | Fatty acid content of deer oil extracted by aqueous enzymatic method.

Category	Fatty acid composition	Absolute content (g/100 g)
	C10:0	0.02
	C12:0	0.15
	C13:0	0.06
	C14:0	2.79
Saturated Fat Acid	C15:0	0.81
(SFA)	C16:0	33.90
	C17:0	0.82
	C18:0	18.80
	C20:0	0.09
	Total	57.44
	C14:1n5	0.61
	C16:1n7	6.28
Monounsaturated fatty acids	C18:1n9C	21.70
(MUFA)	C20:1	0.28
	Total	28.87
	C15:1n5	0.01
	C18:2n6	5.55
	C18:3n3	0.23
Polyunsaturated fatty acids	C20:2n6	0.08
(PUMA)	C20:3n6	0.04
	C20:3n3	0.01
	C20:4n6	0.08
	Total	6.00
Total fatty acid(TFA)	Total	92.31

The Effect of Deer Oil on Cell Apoptosis and Inflammation

As shown in **Figure 3A**, compared with the normal group, the cleavage of caspase-3 increased ($P < 0.001$), the expression of Bax increased ($P < 0.001$), and the expression of Bcl-2 decreased ($P < 0.001$) in the model group. Ethanol induced apoptosis of gastric mucosal cells. Compared with the model group, deer oil inhibited the protein expression of cleaved caspase-3 and Bax ($P < 0.001$) and increased the expression of Bcl-2 ($P < 0.001$), thereby reducing the occurrence of cell apoptosis. This shows that the protective effect of deer oil on gastric mucosal damage is related to the inhibition of cell apoptosis, and the effect is better than that of the positive drug group.

ELISA kits were used to determine the levels of proinflammatory cytokines and anti-inflammatory cytokines in gastric tissue. As shown in **Figure 3C**, compared with the normal group, the IL-6 and TNF-α levels of the model group were increased ($P < 0.05$, $P < 0.001$), and the anti-inflammatory cytokines IL-4 and IL-10 were not obviously changed or decreased significantly ($P < 0.001$). Compared with the model group, the deer oil pretreatment groups had decreased proinflammatory cytokine contents and increased anti-inflammatory cytokine contents ($P < 0.05$, $P < 0.01$). Based on the above experimental results, to further evaluate the role of inflammation in ethanol-induced gastric mucosal damage, RT-PCR was performed on the deer oil group to detect the changes in IL-1β, IL-6, TNF-α, EPO, and EPOR mRNA in gastric tissue. As shown in **Figure 3B**, compared with the normal group of rats, the mRNA expression levels of inflammatory factors EPO and EPOR in the gastric tissue of the model group was significantly increased ($P < 0.001$); the mRNA expression levels of each index in the deer oil were significantly reduced ($P <$

TABLE 5 | Effect of deer oil on acute gastric mucosal injury indices in rats (x ± S).

Group	Dose (g/kg)	Initial body weight (g)	15 days body weight (g)	30 days body weight (g)	Viscera index	Congestion area (mm)	Injury integral index
Normal	0	168.42 ± 7.33	272.81 ± 10.90	319.98 ± 18.34	0.0055	–	–
Model	0	168.37 ± 5.43	287.95 ± 12.18	334.65 ± 18.66	0.0079$^{###}$	75.56 ± 11.40	39.76 ± 3.41
Cimetidine	0.10	167.37 ± 6.21	289.32 ± 9.86	329.64 ± 11.53	0.0061***	25.94 ± 4.95***	18.13 ± 4.22*
L-deer oil	0.50	170.53 ± 6.03	294.97 ± 9.64	371.54 ± 15.07	0.0064***	17.11 ± 4.91***	13.40 ± 3.65**
H-deer oil	0.85	173.53 ± 4.98	299.12 ± 8.64	382.72 ± 10.56	0.0059***	13.40 ± 4.16***	10.65 ± 5.27***

$^{###}P < 0.001$ *vs. ethanol-induced ulcer model group,* $^{*}P < 0.05$, $^{**}P < 0.01$, $^{***}P < 0.001$ *vs. normal control group.*

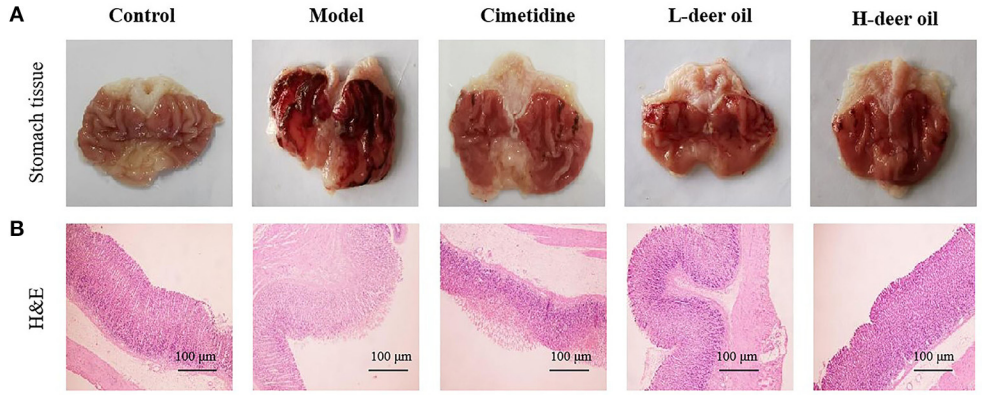

FIGURE 1 | Effects of deer oil on gastric mucosal injury induced by alcohol in rats. **(A)** Representative photos showing macroscopic gastric injury. **(B)** Deer oil alleviate ethanol-induced gastric histopathological damage. Representative photomicrographs of gastric tissues harvested 1 h after ethanol administration (H & E, 40×).

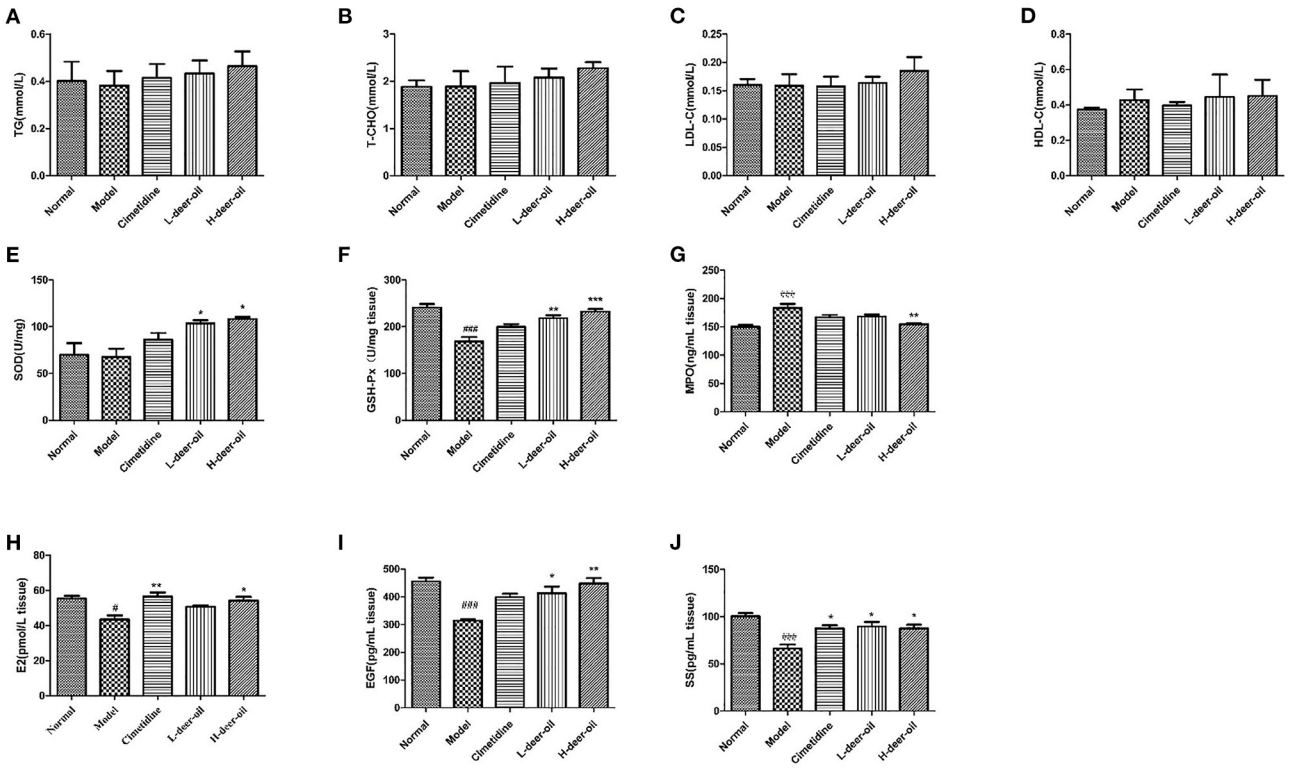

FIGURE 2 | Effects of deer oil on cytokines in rats. **(A)** Gastric TG; **(B)** Gastric T-CHO; **(C)** Gastric LDL-C; **(D)** Gastric HDL-C; **(E)** Gastric SOD; **(F)** Gastric GSH-Px; **(G)** Gastric MPO; **(H)** Gastric E2; **(I)** Gastric EGF; **(J)** Gastric SS. Data are presented as the means ± SD ($n = 6$). $^{\#\#\#}p < 0.001$ vs. Normal group, $^{\#}p < 0.05$ vs. Normal group,$^{***}p < 0.001$ vs. Model group, $^{**}p < 0.01$ vs. Model group,$^{*}p < 0.05$ vs. Model group.

0.001). These data show that after ethanol intake in the model group, a large amount of proinflammatory factors are secreted, leading to the increase of EPO and EPOR levels; the deer oil pretreatment groups secreted less inflammatory factors, the inflammatory factors IL-1β, IL-6, TNF-α, EPO, and EPOR were lower than those of the model group, and the effect was better than that of the positive control drug group.

Deer Oil Block the Activation of the NF-κB Pathway Induced by Ethanol

In view of the above-mentioned oxidative stress and inflammation caused by ethanol damage, we clarified the mechanism of deer oil through the NF-κB signaling pathway, which is usually involved in the inflammatory signaling cascade. As shown in **Figure 4**, compared with the normal group, absolute

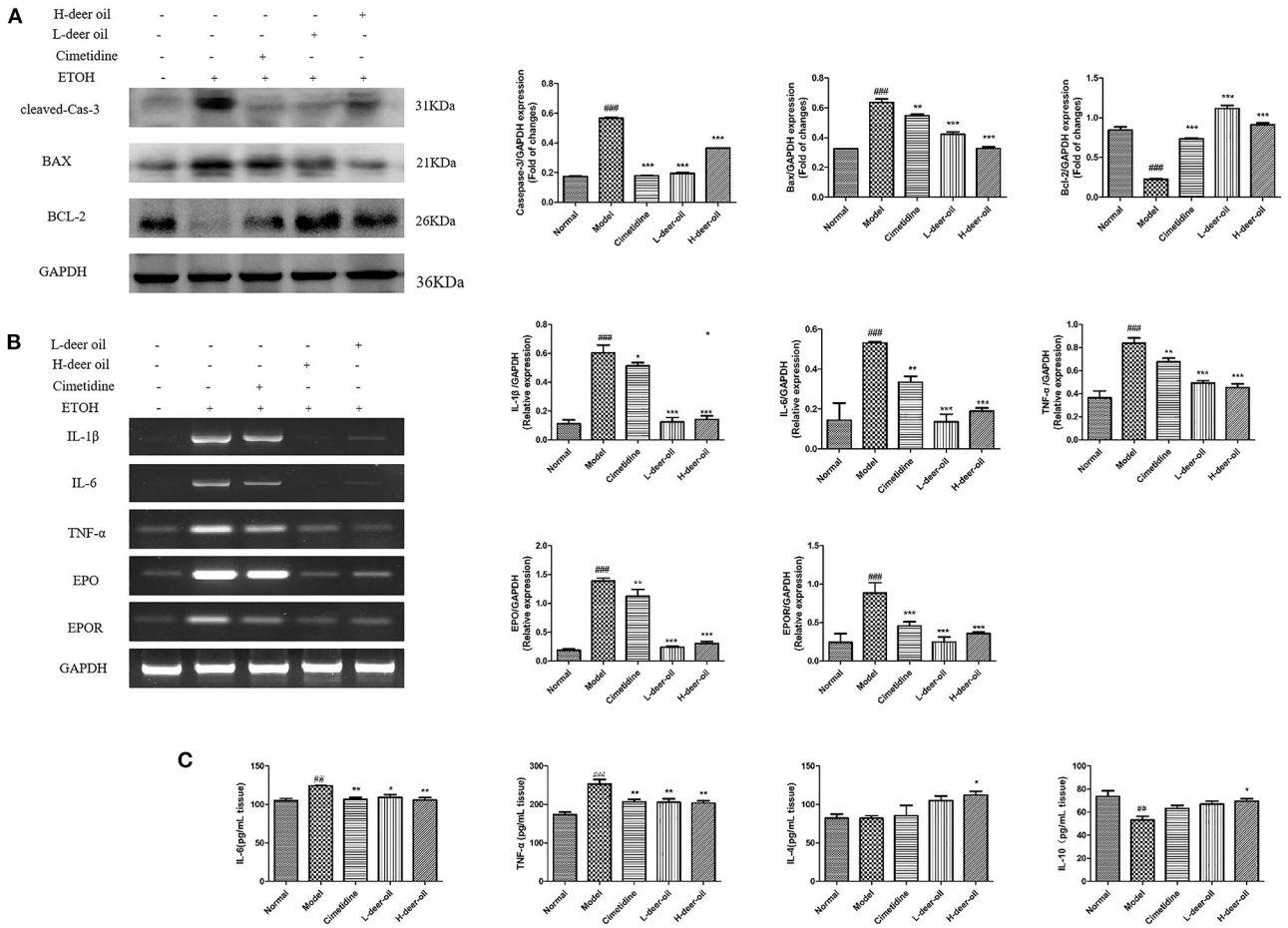

FIGURE 3 | Deer oil weaken the apoptosis and inflammation caused by ethanol in the stomach. **(A)** Western blotting showed the protein expression levels of apoptosis markers. The loading control was GAPDH. **(B)** mRNA expression of inflammatory-related factors and their expression levels. **(C)** Inflammatory factor content in gastric tissue. Data are presented as the means ± SD ($n = 6$). $^{###}p < 0.001$ vs. Normal group, $^{##}p < 0.01$ vs. Normal group, $^{***}p < 0.001$ vs. Model group, $^{**}p < 0.01$ vs. Model group,$^{*}p < 0.05$ vs. Model group.

ethanol stimulation significantly increased the expression of IKK, p-IKBα, and p-NF-κB ($P < 0.01$, $P < 0.001$). Compared with the model group, deer oil significantly reduced the expression of IKK ($P < 0.01$), and the positive control group, deer oil and powdered oil groups all significantly reduced the expression of p-IKBα and p-NF-κB p65 ($P < 0.01$, $P < 0.001$). These results show that deer oil and its powdered oil exert gastric protective effects by blocking the NF-κB signaling pathway, and the effect is better than that of the positive control drug group.

Deer Oil Block the Activation of the MAPK Pathway Induced by Ethanol

Ethanol injury also activated three major subgroups in the MAPK family, namely, p-ERK, p-JNK, and p-p38. As shown in **Figure 5**, compared with the normal group, the expression of p-ERK, p-JNK, and p-p38 in the model group was significantly upregulated ($^{###}P < 0.001$). Compared with the model group, the deer oil had reduced expression of p-ERK, p-JNK, and p-p38 ($^{*}P < 0.05$, $^{**}P < 0.01$, $^{***}P < 0.001$). These results show that deer oil exert gastric protective effects by blocking the MAPK signaling pathway.

DISCUSSION

The extraction rate of deer oil extracted by aqueous enzymatic method is higher than that of conventional boiling method (17), reaching 85.63%, but at the same time the water content is also higher, which is 4.33%. The excess water can be removed by direct drying or vacuum drying. The deer oil extracted by this method has a protein content of 0.12%, a phospholipid content of 0.48 mg/100 g, and a cholesterol content of 44.40 mg/100 g. The content of unsaturated fatty acids in deer oil extracted by aqueous enzymatic method reached 34.87%. This may be because the low-temperature extraction method of aqueous enzymatic method had less effect on the content of unsaturated fatty acids (18). In

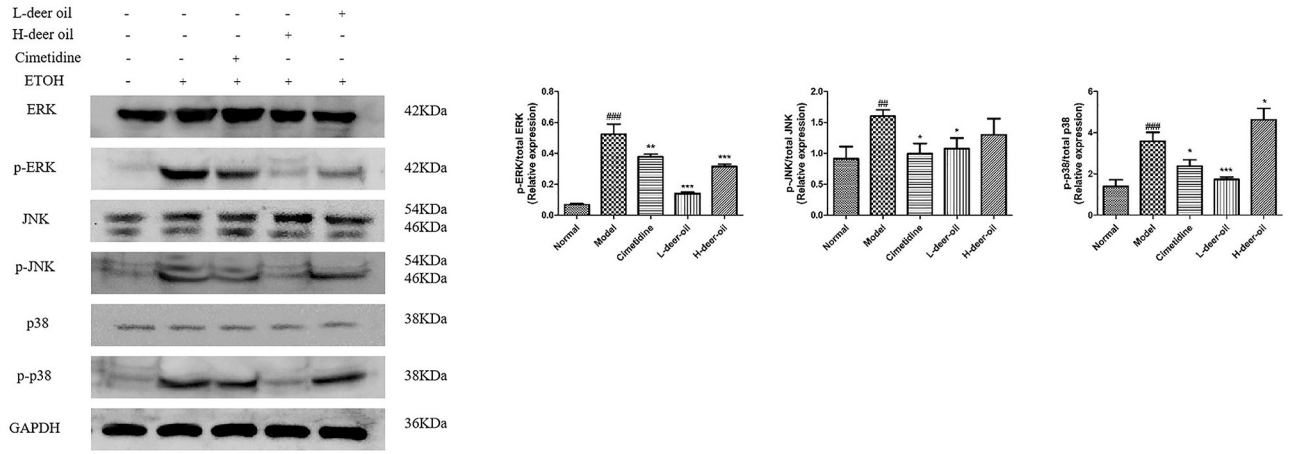

FIGURE 4 | Deer oil blocked ethanol-induced activation of NF-κB pathways. Protein expression levels of the NF-κB signaling pathway were detected by Western blotting. The loading control was GAPDH. Data are presented as the means ± SD ($n = 6$). $^{\#\#\#}p < 0.001$ vs. the normal group, $^{\#\#}p < 0.01$ vs. the normal group, $^{***}p < 0.001$ vs. the model group, $^{**}p < 0.01$ vs. the model group, $^{*}p < 0.05$ vs. the model group.

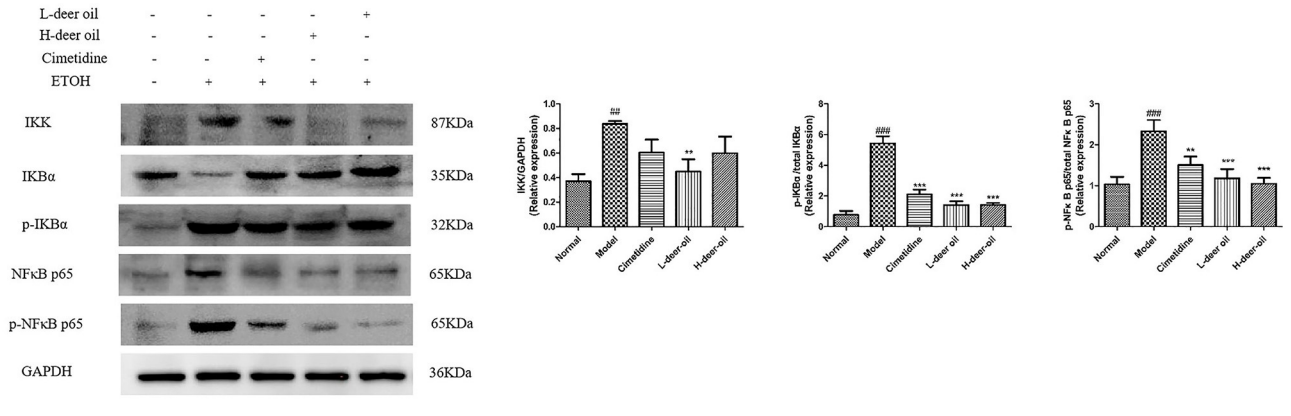

FIGURE 5 | Deer oil blocked ethanol-induced activation of MAPK pathways. Protein expression levels of the MAPK signaling pathway were detected by Western blotting. The loading control was GAPDH. Data are presented as the means ± SD ($n = 6$). $^{\#\#\#}p < 0.001$ vs. the normal group, $^{\#\#}p < 0.01$ vs. the normal group, $^{***}p < 0.001$ vs. the model group, $^{**}p < 0.01$ vs. the model group vs. the model group.

summary, the deer oil extracted by the aqueous enzymatic method is of high quality and lighter in color than the boiled method. It not only has a high extraction rate but also has a small impact on the content of active ingredients. It is a safe and effective green extraction method. The development and utilization of cosmetics and other fields provide a theoretical basis.

Excessive intake of absolute ethanol can cause acute gastric mucosal damage and trigger oxidative stress, apoptosis and inflammatory pathways. The rat gastric tissues swelled and hemorrhaged after being stimulated by absolute ethanol, and the model was successfully established. Compared with the model group, the weight of stomach tissue or body mass in each administration group was significantly reduced, and edema was reduced to a certain extent. Deer oil reduced the acute gastric mucosal injury caused by ethanol, and the effect of the high-dose group was better than that of the low-dose group.

Compared with the normal group, the blood lipid levels of the rats in each administration group increased to a certain extent, but there was no significant difference. This may be due to the small amount of fat given to rats every day, which did not reach the dose that would cause the blood lipid level to rise. Oxidative stress plays a key role in the pathogenesis of gastric mucosal damage. The intake of absolute ethanol will reduce the antioxidant capacity of cells, leading to the occurrence of oxidative stress, which in turn causes the body to produce an

inflammatory response (19). Glutathione peroxidase and SOD are important endogenous antioxidant enzymes and the first line of defense against oxidative damage. Superoxide dismutase activity can reflect the body's ability to scavenge free radicals. Glutathione peroxidase can block the free radicals caused by peroxides from causing damage to the body. Myeloperoxidase is a key indicator to assess the degree of neutrophil infiltration into the gastric mucosa (20). In the present study, a significant decrease of SOD activity and GSH level and increase of MDA level were observed in ethanol-induced gastric mucosal injury. However, deer oil reduced MDA level and increased SOD activity and GSH-Px level, which may has a protective effect on gastric mucosa as seen by the reduction of gastric mucosal injury.

Epidermal growth factor is an important protective factor of the gastrointestinal tract and has a strong protective effect on stomach and duodenal injury. It is an important intermediary factor that regulates ulcer healing. Epidermal growth factor can reduce the poor renewal of gastric mucosal cells and weaken defense ability. Ethanol can also inhibit the responsiveness of EGF to gastric mucosal injury (21). Prostaglandin E2 (PGE2) is an important regulatory mediator of the gastric mucosa that changes when the gastric mucosa is damaged for a variety of reasons. It mainly enhances the protective ability of gastric mucosa by promoting gastric mucus production, inhibiting gastric acid secretion, reducing inflammation, improving gastric mucosal blood circulation, and stimulating the production of gastric mucosal protective growth factors (22). The synthesis and secretion of somatostatin SS (growth hormone release inhibitory hormone) in the stomach is mainly completed by D cells in the stomach and fundus. In the gastric mucosa, it protects and repairs the gastric mucosa by inhibiting the secretion of gastric acid, inhibiting the release of gastrointestinal hormones such as pepsin, motilin, and gastrin, and promoting the healing of gastric injuries. At the same time, SS also participates in the local defense mechanism of gastric mucosa, increases the content of reduced glutathione in cells, improves the ability of gastric mucosa to scavenge oxygen free radicals and lipid peroxides, and reduces gastric mucosal damage (23). These indicators have been used by many researchers to indicate gastric mucosal damage (24). Our results show that deer oil can significantly increase the content of E2, EGF, and SS in the gastric tissue of rats and enhance the defense and repair functions of the gastric mucosa to protect the gastric mucosa.

The pathogenesis of gastric mucosal injury is related to cell apoptosis. The current findings indicate that ethanol triggers gastric apoptosis, which is manifested by the cleavage of caspase-3. The expression of apoptosis-related genes is mainly driven by ROS and proinflammatory signals. In this context, it has been reported that ROS change the protein conformation of pro-apoptotic Bax, causing cytochrome C to escape the mitochondria, thereby activating caspase-3 cleavage (7). Our results show that deer oil can inhibit the cleavage of caspase-3 and the expression of Bax protein, increase the expression of Bcl-2 protein, and reduce cellular apoptosis, thereby playing a role in reducing the gastric damage caused by ethanol.

Acute gastric mucosal injury caused by excessive alcohol leads to the occurrence of inflammation. IL-6, TNF-α, IL-4, and IL-10 are all important inflammation-related factors that are closely related to the occurrence of acute gastric mucosal injury (25). Erythropoietin (EPO) is a hematopoietic factor synthesized and secreted by the kidneys. It is an endogenous cell-protection and inflammation-regulation molecule induced by inflammation. It is one of the endogenous mechanisms of inflammation regulation in the body, and it can inhibit the expression of proinflammatory factors to a certain extent. EPOR is the EPO receptor on the surface of the target cell membrane. Studies have found that EPOR is expressed on the surface of inflammatory cells (26, 27). When the body secretes proinflammatory factors, the expression levels of EPO and EPOR increase to regulate inflammation. The above results provide clear evidence that the model group of rats secreted more proinflammatory factors than the normal group, leading to increased levels of EPO and EPOR. Deer oil pretreatment significantly limited the production of proinflammatory cytokines, increased the secretion of anti-inflammatory cytokines, and effectively inhibited the inflammation of gastric tissue.

Activation of the MAPK cascade and NF-κB transcription pathway occur in many inflammatory and immunomodulatory diseases. Nuclear factor kappa B is a transcription factor that can regulate the expression of a variety of inflammatory mediators, such as TNF-α, IL-6, and IL1β. Pathological disorders of NF-κB signaling are related to the occurrence and development of inflammation, related autoimmune diseases, and cancer (28). Ethanol as an irritant can induce inflammation of gastric mucosal epithelial cells and activate the NF-κB pathway. Studies have shown that the protective effect of Dendrobium nobile polysaccharide on gastric mucosal injury and its mechanism occur through inhibiting the activation of NF-κB and downregulating the ratio of Bax/Bcl2 in gastric mucosa to inhibit cellular apoptosis induced by oxidative stress (29). This is consistent with the results of our study. MAPK, the common pathway of information transmission in cells, participates in the process of extracellular signals from the surface to the inside of the cell. The three main subgroups of MAPK, ERK, JNK, and p38MAPK, require phosphorylation and activation of upstream kinases to perform their biological functions. In the MAPK family, the activation of the main subgroup will regulate the expression of proinflammatory mediators, a phenomenon that has been reported in ethanol-induced gastric ulcers (30). In this study, we found that deer oil pretreatment can prevent the activation of ERK, JNK, p38MAPK, and IKK/IκBα/NF-κB p65 after ethanol stimulation to a certain extent. Therefore, deer oil can inhibit ethanol-induced acute gastric mucosal injury in rats, and its mechanism of action may be through inhibiting the activation of MAPK signaling pathways, thereby inhibiting the nuclear translocation of NF-κB and the expression of downstream inflammatory

cytokines. In turn, the occurrence of gastric mucosal damage is inhibited.

In summary, the deer oil extracted by the aqueous enzymatic method is of good quality, has little effect on the active ingredients, and has a certain protective effect on the acute gastric mucosal injury caused by ethanol.

DATA AVAILABILITY STATEMENT

The original contributions presented in the study are included in the article/**Supplementary Materials,** further inquiries can be directed to the corresponding author/s.

ETHICS STATEMENT

The animal study was reviewed and approved by Institute of Special Animal and Plant, Chinese Academy of Agricultural Sciences.

AUTHOR CONTRIBUTIONS

Y-SX performed the animal experiment and manuscript. D-DR and RM performed the date analysis. P-PB, Y-TZ, and L-jZ collected the samples. L-jZ and CL supervised the research. Y-sS and ZW designed the experiment. All authors listed have made a substantial, direct and intellectual contribution to the work, and approved it for publication.

ACKNOWLEDGMENTS

I would like to thank Z-ML and CL for their nice suggestions on the review.

SUPPLEMENTARY MATERIAL

The Supplementary Material for this article can be found online at: https://www.frontiersin.org/articles/10.3389/fnut.2021.769463/full#supplementary-material

REFERENCES

1. Chen W, Wu D, Jin Y, Li Q, Liu Y, Qiao X, et al. Pre-protective effect of polysaccharides purified from *Hericium erinaceus* against ethanol-induced gastric mucosal injury in rats. *Int J Biol Macromol.* (2020). 159:948–6. doi: 10.1016/j.ijbiomac.2020.05.163
2. Hu J, Luo J, Zhang M, Wu J, Zhang Y, Kong H, et al. Protective effects of radix sophorae flavescentis carbonisata-based carbon dots against ethanol induced acute gastric ulcer in rats: anti-inflammatory and antioxidant activities. *Int J Nanomed.* (2021) 16:2461–75. doi: 10.2147/IJN.S289515
3. Guo M, Yu H, Meng M, Wang C. Research on the structural characteristics of a novel Chinese Iron Yam polysaccharide and its gastroprotection mechanism against ethanol-induced gastric mucosal lesion in a BALB/c mouse model. *Food Funct.* (2020) 9:1–44. doi: 10.1039/C9FO02642H
4. Yu L, Li R, Liu W, Zhou Y, Li Y, Qin Y, et al. Protective effects of wheat peptides against ethanol-induced gastric mucosal lesions in rats: vasodilation and anti-inflammation. *Nutrients.* (2020) 12:2355. doi: 10.3390/nu12082355
5. Wang XY, Yin JY, Zhao MM, Liu SY, Nie SP, Xie MY, et al. Gastroprotective activity of polysaccharide from *Hericium erinaceus* against ethanol-induced gastric mucosal lesion and pylorus ligation-induced gastric ulcer, and its antioxidant activities. *Carbohydr Polym.* (2018) 186:100–9. doi: 10.1016/j.carbpol.2018.01.004
6. Ren SC, Wei Y, Wang RL, Wei SZ, Wen JX, Yang T, et al. Rutaecarpine ameliorates ethanol-induced gastric mucosal injury in mice by modulating genes related to inflammation, oxidative stress and apoptosis. *Front Pharmacol.* (2020) 11:295. doi: 10.3389/fphar.2020.600295
7. Arab HH, Salama SA, Eid AH, Kabel AM, Nancy NS, et al. Targeting MAPKs, NF-κB, and PI3K/AKT pathways by methyl palmitate ameliorates ethanol-induced gastric mucosal injury in rats. *J Cell Physiol.* (2019) 234:1–15. doi: 10.1002/jcp.28807
8. Arab HH, Saad MA, El-Sahar AE, Al-Shorbagy MY. Mechanistic perspective of morin protection against ketoprofen-induced gastric mucosal injury: Targeting HMGB1/RAGE/NF-êB, DJ-1/Nrf2/HO-1 and PI3K/mTOR pathways. *Arch Biochem Biophys.* (2020) 693:108552. doi: 10.1016/j.abb.2020.108552
9. Xia YS, Sun YS, Liu C, Li ZM, Jiang H, Wang Z, et al. Effects of three animal fats on acute gastric mucosal injury in rats. *Food Indus Sci Technol.* (2021) 42:1–10. doi: 10.13386/j.issn1002-0306.2020110238
10. Zhang Y, Chen FZ. New exploration of medicinal value of Northeast sika deer. *Jilin J Tradit Chin Med.* (2012) 32:178–80. doi: 10.13463/j.cnki.jlzyy.2012.02.037
11. Liu HY Li D, Guo SD. Studies on collagen from the skin of channel catfish (*Ictaluru spunctaus*). *Food Chem.* (2007) 101:621–5. doi: 10.1016/j.foodchem.2006.01.059
12. Du J, Li X H, Liu F, Li WQ, Gong ZC Li YJ, et al. Role of the outer inflammatory protein a/cystine–glutamate transporter pathway in gastric mucosal injury induced by *Helicobacter pylori*. *Clin Transl Gastroenterol.* (2020) 178:1–9. doi: 10.14309/ctg.0000000000000178
13. Pereira LC, Nascimento FG, Oliveira SRBD, Lima GC, Freitas ALP, et al. Protective effect against gastric mucosa injury of a sulfated agaran from *Acanthophora spicifera*. *Carbohydr Polym.* (2021) 261:117829. doi: 10.1016/j.carbpol.2021.117829
14. Duran Y, Karaboa H, Polat FR, Polat E, Ylmaz A, Celikkol A, et al. Royal jelly attenuates gastric mucosal injury in a rat ethanol-induced gastric injury model. *Mol Biol Rep.* (2020) 1:1–13. doi: 10.1007/s11033-020-05939-w
15. Li ZM Li SS, Chen LX Qi YL, Sun YS, et al. Protective effects of *Hericium erinaceus* Yangwei granules on acute gastric mucosal injury. *Special Res.* (2018) 40:31–4. doi: 10.16720/j.cnki.tcyj.2018.04.006
16. Ling GT. *Handbook of Health Food Ingredients. 2nd ed.* Beijing: Chemical Industry Press (2007) p. 71–2.
17. Liu H, Zhang TS, Zhang TY, Wang YM, Sun WZ, et al. The process optimization and fatty acid composition analysis of deer oil extraction by ultrasonic-assisted water enzymatic method. *Acta Econ Zool.* (2020) 24:36–41. doi: 10.13326/j.jea.2018.1314
18. Yang FY, Zhao LH, Sun Y, Lv SC, Gao L, et al. Extraction and composition detection of sika deer oil. *Food Res Dev.* (2020) 41:111–6.
19. Verma S, Kumar V L. Attenuation of gastric mucosal damage by artesunate in rat: modulation of oxidative stress and NFκB mediated signaling. *Chem Biol Interact.* (2016) 257:46–53. doi: 10.1016/j.cbi.2016.07.027
20. Li Z M, Shao Z J, Li Shanshan, Hua M, Sun YS, et al. Protective effects of ginseng *Hovenia dulcis* extract on alcoholic liver injury in mice. *Food Indus Sci Technol.* (2019) 40:302–6; 313. doi: 10.13386/j.issn1002-0306.2019.14.050
21. Li ZJ, Kan XB. *Gastric Mucosal Injury and Protection.* Shanghai: Shanghai Science and Technology Press (2004).
22. Robert A, Nezamis JE, Lancaster C, Davis JP, Field SO, Hanchaer AJ, et al. Mild irritants prevent gastric necrosis through "adaptive cytoprotection" mediated by prostaglandins. *Amer J Physiol Heart Circ Physiol.* (1983) 245:113–21. doi: 10.1152/ajpgi.1983.245.1.G113
23. El-Sheikh AA, Morsy MA, Mahmoud MM, Rifaai RA. Protective mechanisms of coenzyme-Q10 may involve up-regulation of testicular P-glycoprotein in

doxorabicin-induced toxicity. *Environ Toxicol Pharmacol.* (2014) 37:772–81. doi: 10.1016/j.etap.2014.02.010
24. Qu B, Pan J, Wang Z, Han X, Qiao R, Hui GE. Relationship of pathological changes of gastric mucosa with prostaglandin E2 and epidermal growth factors in patients with chronic ethanol ingestion. *Chin J Gastroenter Hepatol.* (2011) 20:96–102.
25. Zhang C, Gao F, Gan S, He Y, Zhen ZJ, Liu XW, et al. Chemical characterization and gastroprotective effect of an isolated polysaccharide fraction from *Bletilla striata* against ethanol-induced acute gastric ulcer. *Food Chem Toxicol.* (2019) 131:1–9. doi: 10.1016/j.fct.2019.05.047
26. Luo B W. *Erythropoietin in EAN is an Endogenous Protective Molecule Induced by Inflammation*. Xi'an: Third Military Medical University (2012).
27. Zhang K. *The Effect of EPO/EPOR Autocrine Pathway on the occurrence and Development of Non-Small Cell Lung Cancer and Its Molecular Mechanism*. Xi'an: Northwest University. (2018).
28. El Sheikh A, Morsy MA, Mahmoud MM, Rifaai RA, Abdelrahman AM, et al. Effect of coenzyme-Q10 on doxorubicin-induced nephrotoxicity in rats. *Adv Pharmacol Sci.* (2012) 2012:981461. doi: 10.1155/2012/981461
29. Raish M, Ahmad A, Ansari MA, Alkharfy KM, Aljenoobi FI, Jan BL, et al. *Momordica charantia* polysaccharides ameliorate oxidative stress, inflammation, and apoptosis in ethanol-induced gastritis in mucosa through NFκB signaling pathway inhibition. *Int J Biol Macromol.* (2018) 111:193–9. doi: 10.1016/j.ijbiomac.2018.01.008
30. Zhang Y, Wang H, Mei N, Ma CY, Lou ZX, Lv WP, et al. Protective effects of polysaccharide from *Dendrobium nobile* against ethanol-induced gastric damage in rats. *Int J Biol Macromol.* (2018) 107:230–5. doi: 10.1016/j.ijbiomac.2017.08.175

Conflict of Interest: The authors declare that the research was conducted in the absence of any commercial or financial relationships that could be construed as a potential conflict of interest.

Publisher's Note: All claims expressed in this article are solely those of the authors and do not necessarily represent those of their affiliated organizations, or those of the publisher, the editors and the reviewers. Any product that may be evaluated in this article, or claim that may be made by its manufacturer, is not guaranteed or endorsed by the publisher.

Advantages of publishing in Frontiers

OPEN ACCESS
Articles are free to read for greatest visibility and readership

FAST PUBLICATION
Around 90 days from submission to decision

HIGH QUALITY PEER-REVIEW
Rigorous, collaborative, and constructive peer-review

TRANSPARENT PEER-REVIEW
Editors and reviewers acknowledged by name on published articles

Frontiers
Avenue du Tribunal-Fédéral 34
1005 Lausanne | Switzerland

Visit us: www.frontiersin.org
Contact us: frontiersin.org/about/contact

REPRODUCIBILITY OF RESEARCH
Support open data and methods to enhance research reproducibility

DIGITAL PUBLISHING
Articles designed for optimal readership across devices

FOLLOW US
@frontiersin

IMPACT METRICS
Advanced article metrics track visibility across digital media

EXTENSIVE PROMOTION
Marketing and promotion of impactful research

LOOP RESEARCH NETWORK
Our network increases your article's readership